Pasquale Cavaliere *Editor*

Laser Cladding of Metals

Springer

Laser Cladding of Metals

Pasquale Cavaliere
Editor

Laser Cladding of Metals

Springer

Editor
Pasquale Cavaliere
Department of Innovation Engineering
University of Salento
Lecce, Italy

ISBN 978-3-030-53194-2 ISBN 978-3-030-53195-9 (eBook)
https://doi.org/10.1007/978-3-030-53195-9

This Springer imprint is published by the registered company Springer Nature Switzerland AG
The registered company address is: Gewerbestrasse 11, 6330 Cham, Switzerland

Preface

Laser cladding (LC) for additive manufacturing is a very interesting process for both the production industry and research. Today, LC challenges process engineers and material scientists with many adjustable processes and material parameters, metallurgy, and defects. The development of laser cladding with its unique advantages will continue to advance with additive manufacturing of complex functional and volumetric parts. Additive manufacturing through laser cladding is a nonlinear process depending on many variables. Many models have been developed in order to predict the optimal cladding properties as a function of the fundamental processing parameters governing the deposition. The online continuous process monitoring is fundamental for the final quality of the laser cladded structures. Although laser cladding process is currently well controlled from a manufacturing strategy point of view and allows producing healthy components with a low or nonexistent porosity level, the microstructure of the parts obtained by these techniques is far from being understood and controlled. In metals, the grain size and orientation are essential factors for the control of the properties, especially the mechanical properties. The type of solidification (columnar or equiaxed) and grain size depend on the local solidification conditions, while the grain orientation is strongly conditioned by epitaxy phenomena based on the current orientation of the substrate microstructure. It is therefore very important to be able to model the behavior of the metal during its solidification and to be able to predict what type of solidification will occur. The goal is to correlate the main parameters of this additive manufacturing process with the microstructure generated by them and relate them to the mechanical properties obtained from samples.

The introductory chapters of the book illustrate the potential of Laser Cladding Technology as an optimal additive manufacturing tool. Laser cladding has evolved into a potent three-dimensional additive manufacturing technology by stacking the deposited material layers. Currently, a wide variety of materials can be processed. The ability to functionalize surfaces as well as 3D-printed objects leads to further integration of structural, optomechanical, and thermal properties into these parts. One approach is the combination and encapsulation of optical elements like quartz lenses or laser crystals with custom alloys, thus creating multi-material components.

Additive manufacturing with laser cladding also offers the opportunity to integrate cooling solutions, which reduce mechanical stresses and improve optical properties of the assemblies. These complex structures lead to increasingly complex processes with narrow process and parameter windows within which defects can occur. Several materials can be employed for the production of laser cladding coatings in order to achieve high hardness for wear resistance, thermal and corrosion barriers, and fatigue life improvement.

The book's chapters are devoted to illustrate the model employed for production of the optimal microstructure of laser cladded components. The main aim is to correlate the main parameters of this additive manufacturing process with the microstructure generated by them and relate them to the mechanical properties obtained from samples.

Many examples on laser-cladded superalloys, titanium alloys, and steel are provided. The specific relationship among composition, processing parameters, corrosion, and mechanical properties in laser cladding technology are described.

My special acknowledgments to the passion and cooperation of all the authors and reviewers who made possible the realization of this book and the reduction of the publication time with their hard work and prompt responses. My special thanks to the professionalism of the editorial office manager and assistants.

Lecce, Italy Pasquale Cavaliere

Contents

Nomenclature

3D	Three-Dimensional
AM	Additive Manufacturing
BCC	Body-Centered Cubic
BF	Bright Field
BM	Base Metal
BS	Building Strategy
CAD	Computer Aided Design
CAFE	Computer-Aided Fabrication Environment
CET	Columnar to Equiaxed Transition
CGLs	Continuous Galvanizing Lines
CNC	Computer Numerical Controlled
CS	Cold Spray
CT	Computed Tomography
CTL	Constant Track Length
DEM	Discrete Element Modeling
DF	Dark Field
DMD	Direct Metal Deposition
DMLD	Direct Metal Laser Deposition
DSR	Deep Surface Rolling
DTL	Decreasing Track Length
EDS	Energy Dispersive Spectroscopy
EHLA	Extreme High-Speed Laser Material Deposition
EIS	Electrochemical Impedance Spectra
EMS	Electromagnetic Stirring
ERDF	European Regional Development Fund
FCC	Face-Centered Cubic
FEA	Finite Element Analysis
FEM	Finite Element Modelling
FESEM	Field Emission Scanning Electron Microscopy
fHAp	Fluorapatite
FWR	Fatigue Wear Resistance

GFA	Glass Forming Alloys
GTAC	Gas Tungsten Arc Cladding
HA	Hydroxyapatite
HAZ	Heat Affected Zone
HCP	Hexagonal Close Packed
HEA	High Entropy Alloy
HPDL	High-Power Diode Lasers
IBJs	Insulated Block Joints
IE	Incident Energy
LACS	Laser-Assisted Cold Spray
LAM	Laser Additive Manufacturing
LAMPR	Laser Additive Manufacturing Process Replicator
LC	Laser Cladding
LCD	Laser Cladding
LDMD	Laser Direct Metal Deposition
LENS	Laser Engineered Near Net Shaping
LOF	Lack of Fusion
LPBF	Laser Powder Bed Fusion
LR	Laser Remelting
LSFed	Laser Solid Formed
LSFF	Laser Solid Freeform Fabrication
LST	Laser Surface Treatment
MERC	Materials and Energy Research Center
MMCs	Metal Matrix Composites
MP	Melting Pool
MRI	Magnetic Resonance Imaging
PBF	Powder Bed Fusion
PHT	Post-Heat Treated
PID	Proportional-Integral-Derivative
PLD	Pulsed Laser Deposition
PVA	Polyvinyl Alcohol
RA	Regression Method
RCF	Rolling Contact Fatigue
SBF	Simulated Body Fluids
SCE	Saturated Calomel Electrode
SEBM	Selective Electron-Beam Melting
SFE	Stacking Fault Energy
SGs	Stray Grains
SLD	Supersonic Laser Deposition
SLM	Selective Laser Melting
SMAW	Shielded Metal Arc Welding
SLS	Selective Laser Sintering
SX	Single-Crystal
TBC	Thermal Barrier Coating
TEM	Transmission Electron Microscopy

TGO	Thermally Grown Oxide
TZ	Treated Zone
WG	Water Glass
XRD	X-Ray Diffraction

Chapter 1
Laser Cladding – Additive Manufacturing

Robert Bernhard, Philipp Neef, Henning Wiche, Volker Wesling, Christian Hoff, Jörg Hermsdorf, and Stefan Kaierle

1.1 Introduction to Additive Manufacturing with Laser Cladding

After the discovery of laser technology in 1960, the precision and flexibility of lasers showed great potential for material and surface processing. Due to the high initial costs and the low efficiency of laser beam sources, it took laser cladding until the 1980s to become adopted industry-wide (Corbin et al. 2004). It proved to be a promising alternative to conventional electric arc welding and cladding methods, since the confined heat input results in low dilution and an overall reduction of defects (Morgado and Valente 2018).

At its core, laser cladding is a laser welding process where individual weld beads are aligned and stacked onto a substrate material. In its simplest form, it is used to clad metal surfaces with metals or carbides. Typical applications are the reinforcement of mechanical parts that are used in abrasive or corrosive environments (Lachmayer et al. 2018). The cladding of ductile round stock with a hard and wear-resistant metal improves tribological properties of gears and bearings. Compared to other cladding processes, the laser-based process is very flexible and therefore the higher investment for the laser source is often worthwhile. Additive manufacturing with laser cladding evolved with the need for the repair of worn drawing dies for metal stamping (Levy et al. 2003). In addition, reinforcement of structures with increased complexity used in the automobile industry is possible.

Generally, laser cladding process heads exist in two different configurations, which themselves are distinctive in wire and powder-based filler material. At the

R. Bernhard (✉) · P. Neef · H. Wiche · V. Wesling
Clausthaler Zentrum für Materialtechnik, Clausthal-Zellerfeld, Germany
e-mail: r.bernhard@lzh.de

C. Hoff · J. Hermsdorf · S. Kaierle
Laser Zentrum Hannover e.V., Hannover, Germany

P. Cavaliere (ed.), *Laser Cladding of Metals*,
https://doi.org/10.1007/978-3-030-53195-9_1

same time, both systems can be designed with an off-axis or a coaxial material supply (Lammers et al. 2018).

Laser metal deposition in pure cladding applications is typically set up for maximum deposition rates. Therefore, large amounts of wire or powder filler material are added to the laser processing zone off-axially. For sophisticated additive tasks with higher resolution, a coaxial powder or wire nozzle setup is required.

One of the main advantages of laser cladding for additive manufacturing is the large build volume, where some build-chambers can have the size of multiple cubic meters. The possibility to add onto existing freeform surfaces allows the combination of high-speed conventional machining and specialized additive manufacturing.

Advances in process development enable not only changing complexity, but also the use of special and even hard to weld materials. Laser cladding is not only limited to metals, even ceramics or carbides can be used to disperse into metal surfaces to functionalize 3D-printed parts.

Leveraged through advanced process monitoring and feedback control loops, even larger objects with longer print durations and ultimately safety-relevant aviation parts can be manufactured and repaired.

1.2 Laser Cladding Setup for Additive Manufacturing

A typical laser cladding machine for additive manufacturing consists of a laser source, a processing head, a numeric control, and an enclosure. Material can be added in the form of a wire or a powder feed. The necessary laser power depends on the material and the targeted deposition rate. Typically, 0.5–3 kW near-infrared diode, fiber, or disk lasers are used. The machine presented here has a 680 W diode laser, six independent axes of movement and a build volume of 1000 × 1500 × 1000 mm (W×H×D). It is equipped with a coaxial powder-based processing head. For process control, a pyrometer and a computer-vision system is in place (see Fig. 1.1).

Starting from the laser beam source, the laser light is guided to the process head via an optical fiber. There, the beam propagates through a converging lens that collimates the beam. The beam is reflected at a dichroitic mirror at a 45° angle. The mirror is transmissive for the pyrometer and the camera wavelength. The combined process and sensor beams are focused on a substrate. The work piece is melted locally and through an annular nozzle. Shield gas and metal powder are added coaxially. Moving the process head results in weld beads, which can be oriented in x and y direction. Volumetric buildup is created by stacking layers and remelting previously printed material.

Materials that can be processed by laser cladding are manifold. The main requirement is availability as powder or wire, depending on the used technique. One of the advantages of powder-based materials is that the material composition can easily be modified (see Fig. 1.2) (Neef et al. 2019). Even in situ alloys of incompatible materials like metals and ceramics can be achieved. Printable, atomized metal powder

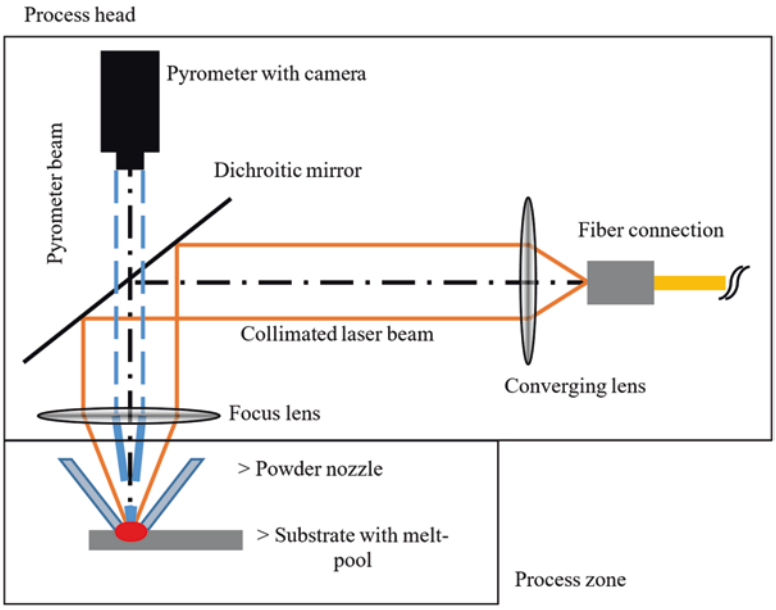

Fig. 1.1 Schematic drawing of a laser cladding process head (Bernhard et al. 2019b)

Fig. 1.2 Iron–nickel powder (Bernhard et al. 2019a)

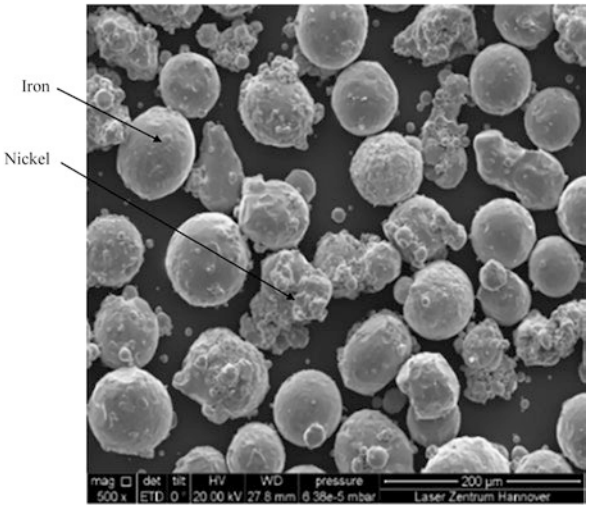

can range from structural steel to special nickel superalloys like CMSX-4 and PWA 1426 (Alfred et al. 2018). Furthermore, due to the fine control of the powder mass-flow, high-resolution parts can be manufactured. In contrast, wire-based laser cladding processes are used for coarser structures. It is a cleaner process since less material is lost by powder overspray. Generally, metal wires are available at lower

Table 1.1 Overview of common materials for laser cladding

Material	Remarks
Structural steel	Mahamood (2018)
Composites	
Nickel-based superalloys	Alfred et al. (2018) and Kaierle et al. (2017)
Cobalt	Brueckner et al. (2017) and Mueller (2019)
Titanium	
Copper	
Molybdenum	Bernhard et al. 2019a, b
Iron–nickel	
316 L steel	Trumpf (2019)
Aluminum	
Bronze	

costs, but with its fixed metallurgic composition, variations of additives can only be done by coating the surface of the wires (Gehling et al. 2019). Powder properties like particle size and distribution in conjunction with their morphology dictate the flowability of the powder due to possible interlocking of individual grains. Compared to powder bed processes, laser cladding is less sensitive to variations of these properties and allows for heterogeneous powder compositions.

An overview of common additive manufacture materials can be seen in Table 1.1.

1.3 Process Parameters of Laser Cladding

Process parameters of laser cladding continue to be the subject of research. Parameter windows are strongly influenced by the material, the substrate, and the geometry of the printed objects. The results of laser cladding are very dependent on the process parameters. One of the most significant parameter sets is the laser power P (W) and the feed rate f (m/s). Their relation is described as linear energy E = P/f (J/m) and it dictates the energy input and therefore the size of the melt pool. Additionally, the amount of powder added to the process zone mainly impacts the resulting deposition rate and temperature of the melt-pool. The feed rate of the processing head has an influence on the process time and the overall volumetric heat input regarding the size of the heat-affected zone and the dilution of the metals. Another main factor is the material used and its inherent properties. These include the melting point, weldability, surface tension of the liquid phase, thermal conductivity, and reflectivity/absorption of laser light.

Furthermore, different parameters can become significant in specific circumstances. In situations where heat dissipation is restricted at, for example, quick geometric changes, the type and flow rate of the shielding gas can become critical. The large number of parameters is a challenge for the process development.

Table 1.2 Iron–nickel parameters for additive manufacturing

Laser power	Laser spot diameter	Laser M^2	Feed rate	Hatch distance
272 W	0.84 mm	115	180 mm/min	0.6 mm
	Top hat			
Layer height	**Standoff distance**	**Powder mass-flow**	**Carrier gas-flow**	**Mean grain size**
0.1 mm	9 mm	2.2 g/min	5000 cm^3/min	60 µm

For a deeper insight into the process and in search of best parameters, the application of design of experiments is indispensable. As an example, the process parameters for additive manufacturing of iron–nickel powder are shown in Table 1.2. These parameters were found by the use of a statistical screening design and a subsequent full factorial design of experiments.

1.4 Power-Based Laser Cladding with its Limitations and Possibilities

Laser cladding has many advantages, including the generation of parts that are not manufacturable by conventional processes, due to their complex shapes, gradual material composition, or undercuts. The powder nature of the filler material and steep thermal gradients can lead to unwanted changes in microscopic and macroscopic appearances. Especially powder processes like laser cladding for additive manufacturing and laser powder bed fusion (LPBF) are prone to defects inside the 3D printed metal (Zhang et al. 2017). The application of novel but hard to weld materials results in increasingly complex processes with narrow process and parameter windows. Inevitably, defects can occur during the print process. Irregularities of a laser cladding process can range from small pores to larger heat-induced cracks as well as bonding defects and cavities, as shown in Fig. 1.3. Bonding defects are typically a result of insufficient energy input that results in elongated pores. Pores are gas-filled, whereas cavities and cracks are a result of shrinkage.

Inclusions inside the printed part can range from segregation to impurities and oxidation. Oxidation is a challenge due to the large build volume that only allows for local inert atmospheres. During the process, oxygen can react with the heated material and form unwanted oxides. This can lead to microscopic defects and irregularities. Another common macroscopic error is a lack of dimensional accuracy. The thermal capacity changes with every layer; especially at corners, the heat is concentrated. An additional limitation for 3D printing is the compromise between complexity and deposition rate. Fine structures with a resolution of 100 µm are possible with powder-based laser cladding. At this resolution, the deposition rate decreases to 0.5–1 g per minute (Kaierle et al. 2012). Larger focus diameters reduce the fidelity significantly but allow deposition rates up to 10 kg/h.

To counteract these defects, efforts are being made to mitigate these effects and make the process more robust. Controlled process environments monitored with

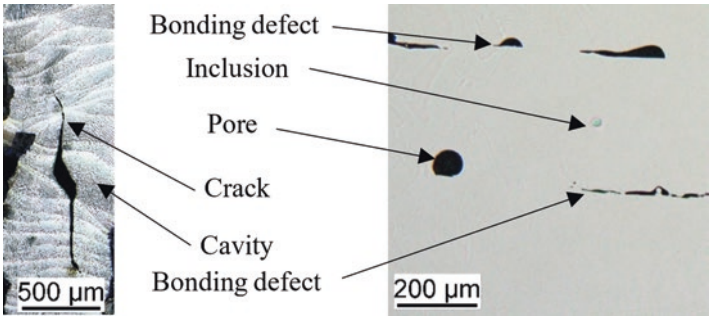

Fig. 1.3 Laser cladding defects visible in a microsection (Bernhard et al. 2019b)

Fig. 1.4 Computer-vision melt-pool identification (a, b), FFT of acoustic emissions (c)

different sensors are key to a reliable and repeatable process. Developments in computing power allow fast image processing of the melt pool. From the captured melt-pool image, the contour is extracted and a convex hull is superimposed (see Fig. 1.4a, b). In-process evaluation of temperature, shape, area, stability, and uniformity with feedback control to the powder mass-flow, feed rate, and laser power greatly improve the printed results. These data in conjunction with acoustic and deposition measurements allow the creation of a visual representation of the data (see Fig. 1.4c).

1.5 Creation of Multi-Material Components

Development is not only limited to the process itself. Newly developed material combinations and even gradient compositions allow the manufacturing of functional parts never seen before. Furthermore, new possibilities include the combination of optical thermal and structural components, where material groups with opposing properties can be combined by specific material adaptation (Neef et al. 2019). Using the additive design freedom, especially multi-material components with laser active materials could benefit from this. In Fig. 1.5, a 3D-printed multi-

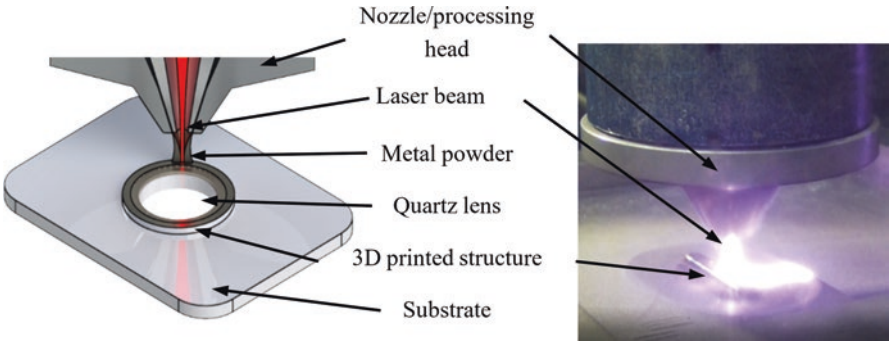

Fig. 1.5 Multi-material processing with additive laser cladding (Bernhard et al. 2019a)

material lens mount is shown. An integration of cooling channels, reducing the part count, bionic, lightweight construction for space applications, and full automation are just some of the future project goals that can be achieved by laser cladding.

1.6 Conclusion and Outlook

Laser cladding for additive manufacturing is a very interesting process for both the production industry and research. In the past 30 years, it has evolved to a robust and very flexible additive process at reasonable costs. Today it challenges process engineers and material scientists with many adjustable process and material parameters, metallurgy, and defects. At the same time, demands for complex, function-integrated, and individualized parts are increasing. Multifunctional and multi-material parts open up the opportunity to cover that demand and are subject to research. Eventually, by sampling process emissions, it will be possible to visualize and qualify the process for safety-related applications. Therefore, the development of laser cladding with its unique advantages will continue to advance with additive manufacturing of complex functional and volumetric parts.

Acknowledgments We thank the Ministry for Science and Culture of Lower Saxony and the European Regional Development Fund (ERDF) for the funding and support.

Duration of implementation: 01.07.2018 – 30.06.2021.

Project number: ZW6-8501 8048 (wGROTESK).

References

Alfred, I., Nicolaus, M., Hermsdorf J., Kaierle, S., Möhwald, K., Maier, H.-J., & Wesling, V. (2018). *Advanced high pressure turbine blade repair technologies*. CIRP conference on photonic technologies (LANE 2018).

Bernhard, R., Neef P., Wiche, H., Wesling, V., Hoff, C., Hermsdorf, J., & Kaierle, S. (2019a). *Process development for additive multi-material components*. 2019 Lasers in manufacturing conference Munich.

Bernhard, R., Neef P., Wiche, H., Wesling, V., Hoff, C., Hermsdorf, J., & Kaierle, S.. (2019b). *Defect detection in additive manufacturing via a toolpath overlayed meltpool-temperature tomography*. 2019 ICALEO conference, Orlando.

Brueckner, F., Riede, M., Mueller, M, Marquardt, F., Knoll, M., Willner, R., Seidel A., Lopéz E., Leyens C., & Beyer E. (2017). *Fabrication of metallic multi-material components using laser metal deposition*. Solid Freeform Fabrication Symposium.

Corbin, S., Khajepour, A., & Toyserkani, E. (2004). *Laser cladding*. Boca Raton: CRC. ISBN 978-1-4200-3917-7.

Gebhardt, A. (2013). *Generative Fertigungsverfahren: Additive Manufacturing und 3D Drucken für Prototyping – Tooling – Produktion*. Munich: Carl Hanser Verlag.

Gehling, T., Treutler, K., & Wesling, V. (2019). Targeted influence on the weld strength of high-strength fine-grain structural steels in the GMA welding process through functionalized weld material surfaces. *Welding in the World, 63*, 783–792. https://doi.org/10.1007/s40194-019-00707-2.

Kaierle, S., Barroi, A., Noelke, C., Hermsdorf, J., Overmeyer, L., & Haferkamp, H. (2012). Review on laser deposition welding: From micro to macro. *Physics-Procedia, 39*.

Kaierle, S., Overmeyer, L., Alfred, I., Rottwinkel, B., Hermsdorf, J., Wesling, V., & Weidlich, N. (2017). Single-crystal turbine blade tip repair by laser cladding and remelting. *CIRP Journal of Manufacturing Science and Technology, 19*, 196–199.

Lachmayer, R., Lippert, R. B., & Kaierle, S. (2018). *Additive Serienfertigung – Erfolgsfaktoren und Handlungsfelder für die Anwendung*. Berlin/Heidelberg: Springer.

Lammers, M., Budde, L., Barroi, A., Hermsdorf, J., & Kaierle, S. (2018). Entwicklung von Laser-Systemkomponenten optimiert für die additive Fertigung mittels SLM. In *Konstruktion für die additive Fertigung*. Berlin/Heidelberg: Springer.

Levy, G. N., Schindel, R., & Kruth, J. (2003). Rapid manufacturing and rapid tooling with layer manufacturing (LM) technologies. *CIRP Annals, 52*.

Mahamood, R. M. (2018). *Laser metal deposition process of metals, alloys, and composite materials*. Cham: Springer. ISBN: 978-3-319-64984-9.

Morgado, T., & Valente, C. (2018). *Development status of LASER Cladding and the new metallic alloys.* https://doi.org/10.20944/preprints201805.0417.v1

Mueller, M. (2019). Metallische Werkstoffe – Pulvertechnologie. *Fraunhofer-Allianz Generative Fertigung*. https://www.generativ.fraunhofer.de/en/research/materials.html. Retrieved 15 October 2019.

Neef, P., Bernhard, R., Wiche, H., Wesling, V., Kranert, F., Budde, J., Wienke, A., Neumann, J., Kracht, D., Lammers, M., Ahlers, H., Grabe, T., Rettschlag, K., & Lachmayer, R. (2019). *Generatives Fertigen optischer, thermaler und struktureller Komponenten für Lasersysteme, NSM 2019/Clausthal-Zellerfeld/Shaker Verlag*. ISBN: 978-3-8440-6471-1.

TRUMPF. (2019). Maschinen AG, Marco Ritz. https://www.technische-rundschau.ch/site/assets/files/44977/09_ritz_kopie.pdf. Retrieved 15 October 2019.

Zhang, B., Li, Y., & Bai, Q. (2017). *Defect formation mechanisms in selective laser melting: A review*. Berlin/Heidelberg: Springe.

Chapter 2
Additive Manufacturing by Laser Cladding: State of the Art

P. Cavaliere, A. Silvello, and A. Perrone

2.1 Introduction

Recently, large research and industrial attention has been devoted to additive manufacturing technologies based on direct energy deposition. High-quality materials coatings with good metallurgical bonds and minimal heat input into the work piece can be achieved by laser cladding through powder or wire feeding.

Many materials can be employed for laser cladding coatings production in order to achieve high hardness for wear resistance, thermal and corrosion barriers, fatigue life improvement. The quality of laser cladded structures is largely influenced by processing parameters (Shim et al. 2016). The authors addresses methods for selecting an appropriate layer thickness setting, which is an important parameter in layer-by-layer deposition manufacturing. A new procedure is proposed for determining the layer thickness setting for use in slicing of a part based on the single-layer height for a given depositing condition. The power, the scanning speed, and the material feeding are the fundamental parameters that can be tuned during processing and they have the largest impact on the final quality of the deposited structure. They all influence the single-layer height while the layer width is mainly governed by the scanning speed, power, and spot size. The laser cladding operational window can be defined in terms of laser power P [W], laser beam scanning speed S [mm/s], and powder feeding rate F [mg/s]. These are the three key parameters as they can be easily controlled and have a strong effect on the final outcome of the clad layer. A complete description of the cladding process is complex as it also depends on additional parameters such as laser beam spot size, laser beam energy distribution,

P. Cavaliere (✉) · A. Perrone
Department of Innovation Engineering, University of Salento, Lecce, Italy
e-mail: pasquale.cavaliere@unisalento.it; angelo.perrone@unisalento.it

A. Silvello
Thermal Spray Centre (CPT), Dto. CMiQF, Universitat de Barcelona, Barcelona, Spain
e-mail: asilvello@cptub.eu

P. Cavaliere (ed.), *Laser Cladding of Metals*,
https://doi.org/10.1007/978-3-030-53195-9_2

carrier and shielding gas used, how exactly the powder is fed, etc. Difficulty with the description of the process is due to many different interactions and various physical phenomena (Nenadl et al. 2014). The key quantities are: the amount of powder provided per unit length of the laser track F/S and the total heat input per unit length of the laser track P/S. It has been shown experimentally that over a wide range of processing parameters, the clad height, H, depends linearly on the F/S parameter with the laser power having a minimal effect. Similarly, the width, w, of the laser track linearly depends on $P/S^{1/2}$ and the clad area, Ac, is controlled by the $P^{1/2}*F/S$ parameter. These empirical dependencies were observed for both, side and coaxial cladding setups with high values of the correlation coefficient ($R > 0.9$) for cladding of Ni- and Co-based coatings on iron-base substrates.

2.2 Materials for Laser Cladding

Different materials behave differently, because of their melting temperatures, surface tension, and specific heat capacities differences. In addition to these inherent physical properties, different materials require different thermal management strategies in order to control, for example, hardening and crack formation. These effects require tailoring of process parameters to each new material processed. Also, since the geometry of the deposit and the fixture used will affect the thermal dissipation and buildup of temperature, process parameters might have to be adjusted during deposition depending on the specific deposit and fixture. High temperature resistant materials are normally selected for laser cladding coatings. For this reason, the whole microstructural and mechanical behavior at high temperature is fundamental for their potential application. Focusing on Co-based alloys, Eutroloy 16,006 was deposited showing clads without pores or cracking retaining high hardness up to 525 °C (de Oliveira et al. 2006). Stellite SF6 was deposited with preheating the substrate at 650 °C in order to avoid cracking and optimize residual stresses. The coating showed hardness up to 880 HV with diffusion of Fe from the substrate leading to improvement in wear and corrosion properties (Jendrzejewski et al. 2008). If thermally cycled at 1050 °C, a strong modification of carbides morphology and precipitation is revealed (d'Oliveira et al. 2002). Tribaloy® T-800 shows similar hardness levels, though its high-temperature corrosion susceptibility limits the application ranges (Navas et al. 2006). Diaz et al. (2012) have proved not only the possibility of performing coatings to repair or improve the properties of the Cr-Mo ASTM A182 F11 steel, but also the fact that these layers can be obtained by means of the laser cladding process. Dendritic microstructures and free crack and porosity coatings were achieved in the case of Stellites® and Tribaloy® T-900, keeping original properties of coating and substrate. Only Tribaloy® T-800 presents crack formation. Preheating of substrate can reduce this tendency of cracking but not completely remove its formation.

The damage of die surface due to cyclic thermo-mechanical loading is detrimental to the service life. In order to enhance the die life, it has been observed that

cladding-based repair is superior to welding or thermal spraying repair techniques. In this study, experimental study of laser cladding of H13 has been carried out. CPM 9 V steel powder has been deposited on H13 tool steel plate for repairing the die surface damage using a CW CO2 laser in conjunction with powder injection system. The effect of laser parameters on clad geometry and clad quality has been investigated (Kattire et al. 2015). The hard vanadium carbide particles increase the clad hardness to an average of four times greater than the substrate hardness. It has been observed that compressive residual stresses are generated in clad, which is desirable for repair applications as it will impede the crack propagation resulting in enhanced die life.

To strengthen Invar alloy, nanostructured carbide-strengthened cobalt-based cladding layers were fabricated on an Invar alloy by laser cladding. The cladding layers contained cubic γ-(Fe, Ni) or Co-based solid solution and hard carbides such as W_2C, Cr_3C_2/V_8C_7, CoCx, and niobium carbide at the grain boundaries. The cladding layers improved the wear and oxidation resistance of the Invar alloy without changing its coefficient of thermal expansion. The results indicated that the friction coefficient of composite coatings decreased by 28.6% compared with that of Invar substrate (Zou et al. 2020). An in situ synthesized high-volume fraction WC-reinforced Ni-based composite coating was fabricated on a mild steel substrate by using a high-power diode laser. Three kinds of single-layer coatings of different amounts of W + C powder and Ni60 powder and a five-layer coating with different amounts of W + C and Ni60 powders in each layer were prepared. This work showed that the multilayer coating possesses the highest hardness among all coatings, and the maximum hardness of the coatings was about 3.7 times more than that of the substrate. The gradient coating technology combined with the feature that WC particles were liable to sink in the bottom of coating were employed as a new idea for preparing the composite coating free of pores and cracks (Shu et al. 2017).

Stellite 6 was deposited by laser cladding of two different chromium-bearing steel substrates (P91 and P22). The results showed less cracking and pore development for Stellite 6 coatings applied to the P22 steel substrate. Further, the Stellite coating on P22 steel was significantly harder than that deposited on the P91 steel. The wear test results showed that the weight loss for the coating on P22 steel was significantly lower than for the P91 steel substrate. The surface topography data showed that the surface roughness for the coating on P22 steel was much lower than for the P91 steel substrate. It is concluded that the residual C content for the deposit on P22 was higher, mainly because the lower concentration of strong carbide formers, compared to P91, reduced the extent of carbon loss in the deposit (Kusmoko et al. 2014).

NiCrAl-based coatings are optimal for high-temperature protection (De Damborenea et al. 1994). Thanks to the formation of ceramic and metallic oxides on the surface of the specimen, which prevent the spread of alloy elements toward the exterior, and the entry of oxygen into the material, the coating exhibits superior high-temperature corrosion resistance. NiCrBSi coatings show very high wear resistance at high temperatures (Guo et al. 2011). Hardness increases with higher concentrations of B, C, Cr, and Si (Conde et al. 2002). Laser cladding NiCrBSi/

WC-Ni composite coating shows better high-temperature wear resistance than NiCrBSi coating, which is due to the formation of hard WC phase in the composite coating. NiCr coatings show a degradation of properties around 600 °C (Yang et al. 2012). Results indicated that the laser clad NiCr/Cr_3C_2 coating consisted of Cr7C3 primary phase and γ-(Fe,Ni)/Cr_7C_3 eutectic colony, while the coating added with WS_2 was mainly composed of Cr_7C_3 and (Cr,W)C carbides, with the lubricating WS_2 and CrS sulfides as the minor phases. The wear tests showed that the friction coefficients of two coatings both decrease with the increasing temperature, while both the wear rates increase. The same behavior is described for NiMoSi coatings (Lu and Wang 2004). Aging of the coating at 800 °C leads to gradual dissolution of the interdendritic eutectic Mo_2Ni_3Si and subsequent formation of a dual-phase structure with equiaxed Mo_2Ni_3Si primary grains distributed in the NiSi single-phase matrix. Because of the strong covalent-dominated atomic bonds and high volume fraction of the ternary metal silicide Mo2Ni3Si, both the original and the aged Mo_2Ni_3Si/NiSi coating has excellent wear resistance under pin-on-disc, high-temperature sliding wear test conditions; although hardness of the aged coating is slightly lower than that of the As-clad coating. NiCrAlY-based coatings show stability up to 1100 °C (Partes et al. 2008). The obtained results suggested that up to 450 h the system was able to form a continuous alumina layer that could protect the substrate from oxygen diffusion. The Fe addition can easily be accomplished in laser cladding process by dilution of the Tribaloy® T-800 coating with the steel substrate. In this work, a comparative study of microstructure, hardness and cracking susceptibility of low and high diluted T-800 and T900 coatings deposited by laser cladding is presented. A lower cracking ratio is obtained for the T-900 coatings at the cost of a lower hardness and wear resistance. No noticeable effect on the cracking susceptibility of the T-800 is found due to dilution with the substrate. However, a change in its microstructure is observed giving superior hardness and wear resistance (Tobar et al. 2008). Intermetallic coatings have good high-temperature wear resistance under sliding wear test conditions (Chen and Wang 2004). The laser clad chromium-alloyed nickel silicide coating has a rapidly solidified microstructure consisting of the Ni2Si primary cellular-dendrites and minor amount of interdendritic Ni2Si/NiSi eutectics. The intermetallic coating has good wear resistance under dry sliding wear test conditions due to the high hardness, refined microstructure, and strong intermetallic atomic bonds (Cai et al. 2003). The LC of single-tracks and 3D (three-dimensional) objects of the Ni3Al intermetallic was successfully prepared. Good metallographic characteristics and interface bonding were obtained. The coating microstructure consisted of γ-Ni3Al. The cladding of the Ni3A1 coating with small dilution into substrate can be obtained only at the appropriate power density of about 2–8 J/mm2 under the laser scan velocity of 100–200 mm/min and the powder feed rate ~ 3.8 g/min. The average micro-hardness of the laser cladded coatings was HV0,1380–1400. The ability of the multilayer LC process to build the Ni3Al intermetallic coatings was successfully shown (Kotoban et al. 2014).

Under high-temperature oxidation tests performed in air furnace at 1100 °C up to 200 h, weight gain of NiCoCrAlY was significantly larger than those of Ni and

CoNi alloy counterparts, and 50 times less than the weight gain of the substrate. This can be understood as a consequence of its larger Al content. Surface morphology was inspected by SEM-EDS, revealing a dense, stable, and continuous Al_2O_3 oxide layer with Ni, Co, Cr, and Y oxide inclusions. The percentage of these oxides is as low as 5% in the NiCoCrAlY coating, reaching about a 50% in the CoNiCrAlY one (Tobar et al. 2014).

By analyzing the deposition of Inconel718 powders, increasing the laser power and decreasing the scanning speed has shown to significantly increase the width of the deposit bead, whilst increasing the powder feeding rate and decreasing the scanning speed has shown to significantly increase the height of the deposit bead. Additionally, a decreased laser standoff distance and increased laser power significantly increased the penetration depth. The top surface straightness was significantly affected by the powder standoff distance where an increased positive distance increased the deviation in the top surface. The microstructure was mainly columnar with long dendrites growing epitaxially in the height direction. However, in the top surface there was a thin section with a dendritically equiaxed structure. This structure was most probably formed due to a lower thermal gradient and the increase of solidification velocity caused by the convection with the shielding gas (Segerstark 2015).

Results indicate the use of laser cladding technique as an alternative to plasma spray or HVOF methods, yielding fully dense coatings with metallurgical bonds to substrate. According to the effect of the three factors on bonding strength, the powder type has the largest dependency, followed by scanning speed. The laser output power has minimal impact. The bonding strength with iron-based powder is much higher than that with the nickel-based powder. The bond strength increases as the laser power increases. No obvious dependence of bonding strength on scanning speed has been found (Xu et al. 2015). Based on the background of the engineering application of automobile mold repair and surface strengthening, the effects of process parameters on the formation and microstructure of laser cladding nickel(Ni)-based alloy coating were studied (Yufan et al. 2020). The optimal parameters were: laser power 2000 W, powder feeding rate 15 g/min, scanning speed 4 mm/s. Under this process, the cladding layer and the substrate can exhibit good metallurgical bonding, and the cladding layer has fine crystal grains and a low dilution ratio. On this basis, different mass fractions of niobium carbide (NbC) powder were added to the nickel-based powder and laser cladding was carried out on the surface of die steel. The results show that with the increasing of niobium carbide addition, the hardness of the cladding layer decreases, and the wear loss of the cladding layer decreases first and then increases. When the niobium carbide addition reaches 6 wt.%, the wear loss of the cladding layer is the least, and the wear resistance is the best.

Surface modification of Ti-6Al-4 V is necessary surface to enhance its tribological properties. Multi-phase and multi component coating development is one of the present research trends in surface engineering arena. In Dhanda et al. (2014) it was attempted to develop a multi-component coating by laser cladding process using a pre-placed powder mixture containing Ni5Al (50 vol%) + hBN (10 vol%) + B4C

(20 vol%) + SiC (20 vol%) on substrate of Ti-6Al-4 V to improve its tribological performance. A nanostructured coating was formed with micro-hardness (780 HV0.05). X-ray diffraction (XRD) identified the presence of compounds like TiC, BN, TiB2, SiC, and intermetallics of Ni-Ti in the coating. The wear behavior of the composite coating was assessed by ball-on-disc type wear and friction monitor at 10 N load at 300 RPM taking a track diameter of 5 mm. Specific wear rate and coefficient of friction (μ) were found to vary from 0.6E-12 to 2.2E-12 m3/N-m and from 0.15 to 0.45, respectively, due to rubbing of coated surface against tungsten carbide ball.

Metal matrix composite (MMC) coatings were fabricated on Ti–6Al–4 V titanium alloy by laser cladding. Co42 self-fluxing powder, B4C, SiC, and Y2O3 were employed as the cladding materials. Results showed that the laser cladding coatings were mainly reinforced by CoTi, CoTi2, NiTi, TiC, TiB2, TiB, Cr7C3, and Ti5Si3. The micro-hardness of the cladding coatings was equivalent to three to four times the Ti–6Al–4 V substrate. Laser cladding coating exhibiting outstanding wear resistance was fabricated with the addition of 20 wt.% B4C, 7 wt.% SiC, and 1 wt.% Y2O3. The wear resistance was enhanced by over ten times compared with the substrate (Weng et al. 2020).

2.3 Clad Geometry

The precise prediction of the clad geometry as a function of the employed processing parameter per each used material is fundamental for additive manufacturing applications such as 3D printing. Many studies report the correlation between the cladding and the processing parameters (Chan et al. 1999). In Narang et al. (2012), the outputs from the welding, such as the weld macrostructure characteristics, were mathematically modeled with respect to the input process variables. Based on the weldment characteristics, including that of the bead contact angle, a mapping technique was developed for the graphical representation of the macrostructure zones' shape profiles. Taking into account the complexity of the laser cladding process governed by the heat transfer among the laser beam, the substrate and powder, and mass transfer between the powder flow and the molten surface, many authors suggest that the best approach should be based on "combined parameters" (Felde et al. 2002). This phenomenological approach uses simple mathematical formulae, derived from a statistical analysis of measured data, to relate the laser cladding parameters with the geometric features of the clad track. Given the required clad height and available laser beam power, the proposed method allows one to calculate values of the scanning speed and powder feed rate, which are used to obtain low dilution, pore-free coatings, fusion bonded to the substrate. Different sets of combined parameters are proposed to predict the track width and height for coaxial and lateral geometry of the powder feeder (De Hosson et al. 2009). In Toyserkani et al. (2003), the proposed model can predict clad geometry as a function of time and process parameters including beam velocity, laser power, powder jet geometry, laser

pulse shaping, and material properties. Suryakumar et al. (2011) modeled the formations of single beads and overlapping multiple beads. While the individual bead's geometry is influenced by the size of the filler wire and the speeds of the wire and torch, the step over increment between the consecutive beads additionally comes into the picture for the multiple bead deposition. So, the geometry prediction is possible over many process windows for both powders and wire-based laser cladding techniques. In Hoadley and Rappaz (1992), a two-dimensional (2D) finite element model is presented for laser cladding by powder injection. The model simulates the quasi-steady temperature field for the longitudinal section of a clad track. It takes into account the melting of the powder in the liquid pool and the liquid/gas free surface shape and position, which must conform to the thermal field in order to obtain a self-consistent solution. The model shows the linear relationship between the laser power, the processing velocity, and the thickness of the deposited layer. Another simplified model was proposed by Picasso et al. (1994). For a given laser power, beam radius, powder jet geometry, and clad height, this model evaluates two other processing parameters, namely, the laser-beam velocity and the powder feed rate. It considers the interactions between the powder particles, the laser beam, and the molten pool. In Naveed Ahsan and Pinkerton (2011) a coupled analytical–numerical solution is presented. Submodels of the powder stream, quasi-stationary conduction in the substrate and powder assimilation into the area of the substrate above the liquidus temperature are combined. An iterative feedback loop is used to ensure mass and energy balances are maintained at the melt pool. The knowledge of temperature, velocity, and composition distribution history is essential for a better understanding of the process and subsequent microstructure evolution and properties. Numerical simulation not only helps to understand the complex physical phenomena and underlying principles involved in this process, but it can also be used in the process prediction and system control. The double-track coaxial laser cladding with H13 tool steel powder injection is simulated using a comprehensive three-dimensional model, based on the mass, momentum, energy conservation, and solute transport equation. Some important physical phenomena, such as heat transfer, phase changes, mass addition and fluid flow, are taken into account in the calculation. The physical properties for a mixture of solid and liquid phase are defined by treating it as a continuum media. The velocity of the laser beam during the transition between two tracks is considered. The evolution of temperature and composition of different monitoring locations is simulated (He et al. 2009). Bax et al. (2018) offers guidelines to evaluate process parameter maps for single tracks, which are a requirement for high-quality claddings and 3D structures. The procedure is executed creating a process map for the parameters laser power, powder feed rate, and scanning speed. The relationship between process parameters and output responses and the interaction among the process parameter are analyzed and discussed in detail for Ti6Al4V. The analysis results indicate that powder feed rate is the dominant factor on the width and height of cladding coating while laser scanning speed has the strongest effect on molten depth of substrate (Sun and Hao 2012). The correlations that exist between key parameters of the process (i.e., laser power, scanning speed, powder feeding rate) and geometrical characteristics for single clads (i.e., height,

width, dilution, and wetting angle) were predicted and analyzed by regression method (RA). The preliminary geometrical considerations allowed to choose the processing parameters that led to high-quality clads with minimum porosity. All considerations finally resulted in the development of a processing map that shows the optimum parameters for laser cladding process (Erfanmanesh et al. 2017). The influence of the laser power, scan speed, and laser beam focal position (focus, positive and negative defocus) on the shape factor, cladding-bead geometry, cladding-bead microstructure (including the presence of pores and cracks), and hardness has been evaluated. The correlation of these process parameters and their influence on the properties and, ultimately, on the feasibility of the cladding process, is demonstrated. The importance of focal position is demonstrated. The different energy distribution of the laser beam cross section in focus plane or in positive and negative defocus plane affects the cladding-bead properties (Riquelme et al. 2016). Ti–6Al–4 V deposits with variable thickness are made to assess the use of laser cladding as a repair technology. Both the effect of the building strategy (BS) and the incident energy (IE) on the metallurgical characteristics of the deposits in relation to their complex thermal history have been studied. It is shown that for the configuration consisting in a decreasing track length (DTL) under high IE, a gradient of cooling rate exists that leads to the presence of different phases within the microstructure. Conversely, homogeneous microstructures are present either for the configuration with a constant track length (CTL) under high IE, and for the strategy obtained from a DTL under low IE (Paydas et al. 2015). Francis (2017) analyzed three different process parameters, power, velocity, and spot size, on melt pool geometry for the electron beam wire feed and laser powder feed processes of Ti6Al4V. Beam spot size has been identified as having a major influence on melt pool geometry. It was also shown that experimental melt pool dimensions can be used to estimate how spot size changes with a focusing parameter in additive manufacturing processes. Increases in spot size have been shown to eliminate the presence of keyholing, and a normalized spot size threshold is proposed to prevent keyholing in five alloys.

Many experimental evidences demonstrate how the cladding properties depend on the substrate material. In Kumar and Roy (2009), a three-dimensional conduction heat transfer model is developed to predict the clad geometry (e.g., height, width, and dilution) and microstructure (scale and morphology) of the solidified layer for a laser cladding process. The effect of controllable input process parameters like absorbed laser power, powder deposition rate, and processing speed on the clad characteristics is critically assessed with the help of dimensionless parameters. A process map is developed that enables operators to pick up the proper process parameters for a feasible laser cladding process with desirable characteristics. Li and Ma (1997) found that the surface roughness (turbulence) of an overlapped cladding layer decreased with the increase of the overlapping ratio in an oscillating manner. At some overlapping ratios the turbulence was at minimum and at some other ratios it was at maximum. Among various single-track sections, overlapping with symmetrical parabolic section single-clad tracks produced the smoothest cladding layer, in which the surface turbulence decreased in an oscillating manner. Lalas

et al. (2007) have taken into account the process speed and feed rate of the powder being supplied for the estimation of clad geometry. The surface tension between the added material and the substrate is used primarily for the calculation of the clad characteristics.

To obtain the powder packing information in the powder bed, dynamic discrete element modeling (DEM) was used (Lee 2015). The results show that negatively skewed particle size distribution, faster scanning speed, low power and low packing density worsen the surface finish quality and promote the formation of balling defects.

In El Cheikh et al. (2012), a mathematical model implemented in the software Mathematica 8© is used to predict the clad cross-section dimensions and obtain an analytical description of the clad geometry. It was experimentally noticed that the cross-section shape is a disk due to the surface tension forces. Analytical relationships are established between the radius and the center of the disk on the one hand and the process parameters on the other hand.

During the layer additive manufacturing, the cross-sectional profile of a single weld bead as well as overlapping parameters is critical for improving the surface quality, dimensional accuracy, and mechanical performance. Xiong et al. (2013) highlights an experimental study carried out to determine the optimal model of the bead cross-section profile fitted with circular arc, parabola, and cosine function, by comparing the actual area of the bead section with the predicted areas of the three models. A necessary condition for the overlapping of adjacent beads is proposed. The results show that different models for the single bead section profile result in different center distances and surface qualities of adjacent beads. The optimal model for the bead section profile has an important bearing on the ratio of wire feed rate to welding speed.

Laser cladding using scanning optics is a relatively little studied matter. Scanning optics makes the adjustment of laser beam interaction zone numerically possible and it is, therefore, a more flexible optical tool than the conventional static optics. A series of cladding tests were conducted using a 5 kW fiber laser and an oscillating linear scanner with dynamic powder feeding to determine the process characteristics and their possibilities and limitations (Pekkarinen et al. 2012). It was noticed that by using scanning optics, it is possible to vary the width and thickness of clad beads on a large scale. With scanning optics, it is possible to affect clad bead geometry so that only a 20% overlapping ratio is used. However, certain cladding parameter combinations expose the clad bead to cladding defects. Also, a fast moving scanned laser beam causes a wave formation to the melt pool that further causes stirring in the melt pool. The dilution was increased with increase in the cladding speed. However, the increase of the dilution was dependent on the scanning amplitude.

Modification of the cladding angle during overlap has been observed experimentally and linked with the formation of an inter-run porosity. There is another group of models of laser cladding process that try to model all physically involved processes, involving some approximation in equations and solve these numerically. Physical phenomena including heat transfer, melting, and solidification phase

changes, mass addition, and fluid flow in the melt pool, were modeled in a self-consistent manner. Interactions between the laser beam and the coaxial powder flow, including the attenuation of beam intensity and temperature rise of powder particles before reaching the melt pool were modeled with a simple heat balance equation. The level-set method was implemented to track the free surface movement of the melt pool, in a continuous laser cladding process. The governing equations were discretized using the finite volume approach. Temperature and fluid velocity were solved for in a coupled manner (Qi et al. 2006). Laser beam cladding of metals by single-step powder delivery is analyzed with a process model that is based on balance equations of energy and mass. Effects like powder heating, clad layer formation, substrate dilution and overlapping of tracks are discussed in dependence of the process parameters. In particular, the powder catchment efficiency and the beam energy redistribution in the material can be optimized by the powder mass flow rate and by the geometrical properties of the beam and of the powder jet (Kaplan and Groboth 2001). A three-dimensional finite element model is presented for precisely simulating laser cladding process with a focus on dilution control (Zhao et al. 2003). Dilution is referred to as an important quality index in the laser cladding process, indicating the contamination level of the properties of clad layer by substrate metals. As regards a good quality of laser clad layer, low dilution as well as metallurgical bond of interface are prerequisite, so the dilution control is essential in the process.

2.4 Textures and Microstructure Evolution

The rapid solidification (in the order of 10^3 K/s) produces many different microstructures in the laser cladded materials. So, the relationships between processing parameters and the final microstructure as well as properties of laser clad coatings are very complex. Conventional chill casting as well as laser surface cladding were used to produce a wide range of solidification Stellite 6 microstructures (Frenk and Kurz 1994). A detailed microstructural study of Stellite 6 coating deposited on a low carbon ferritic steel substrate using preplaced powder method and low-power Nd:YAG pulse laser was performed by Farnia et al. (2013). The shape of solidification front during pulsed laser cladding is similar to the shape of solidification front during continuous cladding with a doubled laser beam scanning speed. Further, OIM reveals the Greninger–Troiano OR between the face centered cubic coating and bcc substrate grains. It is concluded that at the moment of solidification, epitaxial growth of the grains in the coating occurs on the austenitic grains of the substrate and that an austenite–ferrite transformation occurs in the heat-affected zone upon subsequent cooling. High cooling rates during laser cladding of stainless steels may alter the microstructure and phase constitution of the claddings and consequently change their functional properties. Hemmati et al. (2011) showed that an extreme refinement of the solidification structure will influence the phase constitution of the coatings by lowering the Ms (Martensite start) temperature and hence stabi-

lizing the austenite, which results in lower hardness values and increased wear rates in AISI 431 steel. These results confirm that the structural refinement obtained by higher cladding speeds is not helpful for improving the hardness and wear properties of laser-deposited martensitic stainless steel coatings. The single-track formation and the deposition of block sample from 316 L stainless steel powders have been carried out by both SLM and LCD techniques. A comparison on pool shape, cooling rate, columnar grain size and mechanical properties under different processing conditions by LCD and SLM respectively has been studied. It is found that, due to the increase of energy input and the decrease of depth-to-width ratio of melting pool (MP) from SLM to LCD, the primary cellular arm spacing (PCAS) of the sample increases from less than 1.0 μm to more than 15.0 μm, and thus the cooling rate of MP decreases from about 10 K/s in SLM to about 10 K/s in LCD. Furthermore, due to the decrease of cooling rate from SLM to LCD, the columnar grains of the as forming alloy are getting coarser (Ma et al. 2017). The samples of 316 L stainless steel by SLM have much stronger tensile strength but lower elongation than those by LCD, and the main reason is due to the fact that the solidification behavior of the MPs by SLM can form much finer columnar grains than those by LCD.

Alvarez et al. (2018) summarize the influence of the most relevant process parameters in the laser cladding processing of single and compound volumes (solid forms) made from AISI 316 L stainless steel powders and using a coaxial nozzle for their deposition. Process speed, applied laser power, and powder flow are considered to be the main variables affecting the laser cladding in single clads, whereas overlap percentage and overlapping strategy also become relevant when dealing with multiple clads. By setting appropriate values for each process parameter, the main goal of this study is to develop a processing window in which a good metallurgical bond between the delivered powder and the substrate is obtained, trying simultaneously to maintain processing times at their lowest value possible.

The experimental work carried out has consisted in the verification of the viability of three iron-based materials AISI 4340, AISI 430 L, and DIN 16MnCr5 for repair processes using EHLA. For this, an experimental process consisting of four work packages was carried out: (1) analysis of the deposition of a layer of material to select the laser power and feedforward that give low porosity and no bonding defects; (2) selection of the nozzle displacement according to the thickness obtained in the analysis of a layer by the deposition of blocks of five layers; (3) preliminary study of 3 mm to see the behavior of the material in greater thicknesses and choose the best manufacturing strategy; and lastly, (4) buildup of 10 mm samples (Edurne 2018).

The evolution of macro- and microstructures of laser-deposited Al–Si samples was investigated by Dinda et al. (2012). Microstructural observation revealed that the morphology and the length scale of the microstructures are different at different locations of the sample. A periodic transition of microstructural morphology from columnar dendrite to microcellular structure was observed in each layer. Cloots et al. (2016) investigated selective laser melting (SLM) of the nickel-based superalloy IN738LC and the cobalt-based alloy Mar-M509, and identify the influence of process and material parameters on the resulting microstructure. Significant differ-

ences between IN738LC and Mar-M509 were observed with respect to grain size, grain shape, and texture sharpness. Alloy IN738LC exhibits coarse and elongated grains with a sharp texture and thus a pronounced mechanical anisotropy. Alloy Mar-M509 shows smaller grains with only moderate structural and mechanical anisotropy. The different microstructural and mechanical characteristics are attributed to the different recovery and recrystallization behavior of IN738LC and Mar-M509. The high stacking fault energy (SFE) of IN738LC results in pronounced recovery of lattice defects without affecting the basic grain structure, whereas the low SFE in Mar-M509 favors recrystallization with the effect of significant grain refinement and weakening of the solidification texture. During laser deposition of Ni-Cr-B-Si-C alloys with high amounts of Cr and B, various microstructures and phases can be generated from the same chemical composition that results in heterogeneous properties in the clad layer. The combination of EDS and EBSD allowed unequivocal identification of micron-sized precipitates as polycrystalline orthorhombic CrB, single-crystal tetragonal Cr5B3, and single-crystal hexagonal Cr7C3. In addition, TEM characterization showed various equilibrium and metastable Ni-B, Ni-Si, and Ni-Si-B eutectic products in the alloy matrix. The findings of this study can be used to explain the phase formation reactions and to tune the microstructure of Ni-Cr-B-Si-C coatings to obtain the desired properties (Hemmati et al. 2013). In spite of excellent properties, the practical applications of laser claddings are relatively restricted when compared with well-established coating techniques because of their inherent defects identified as cracks, pores, and inclusions. Substantial evidence suggests that the incorporation of an appropriate amount of rare earth in laser claddings can remarkably prevent these defects. Additionally, the presence of rare earth in laser claddings can notably enhance tribo-mechanical properties such as surface hardness, modulus of elasticity, fracture toughness, friction coefficient, and wear rate (Quazi et al. 2016).

AlCoCrFeNi alloys with different amounts of aluminum prepared by arc melting were investigated and compared with the laser beam remelted HEAs with the same composition. Attempts to form HEAs coatings with a direct laser deposition from the mixture of elemental powders were made for AlCoCrFeNi and AlCrFeNiTa composition. A strong influence of solidification rate on the amounts of face-centered cubic and body-centered cubic phase, their chemical composition, and spatial distribution was detected for two-phase AlCoCrFeNi HEAs (Ocelík et al. 2016). Critical issues are related to the rate of (re)solidification, the dilution with the substrate, powder efficiency during cladding, and differences in melting points of clad powders making additive manufacturing processing from a simple mixture of elemental powders a challenging approach.

The melt pool shape evolves in order to minimize surface energy. The final geometry of the melt pool depends on convection, surface tension, and buoyancy as well as processing speed. In particular, the elongation of melt pool depends strongly on the velocity of heat source and thermal conductivity of the solid material around the melt pool. Therefore, it is more elongated for faster heat source and for lower thermal conductivity. Due to directional solidification, which is the result of laser cladding, there is always some preferential texture present in cladded materials.

Significant efforts have been made to investigate the microstructure and mechanical properties of HEA coating by laser cladding (Li et al. 2019). 6FeNiCoSiCrAlTi high-entropy alloy coating with simple BCC solid solution phase has been prepared by laser cladding on a low-carbon steel substrate. The microstructure, hardness, and magnetic properties have been investigated. The experimental results show that the tendency of component segregation in the conventional solidification microstructure of multicomponent alloy is effectively relieved. The microstructure of the coating is mainly composed of equiaxed polygonal grains, discontinuous interdendritic segregation and nanoprecipitates (Zhang et al. 2011a). The polygonal grains and interdendritic segregation have similar BCC structure with lots of low-angle grain boundaries at the interface. After annealing, the columnar grains transform to equiaxed refined grains with the grain boundary misorientation transition from low to high angles. This result supports such an argument that the reheating process in post-stage of solidification plays a key role on the grain refinement during rapid solidification process (Zhang et al. 2011b). The FeCoCrNiBx high-entropy alloy (HEA) coatings with three different boron (B) contents were synthesized on Q245R steel (American grade: SA515 Gr60) by laser cladding deposition technology. Effects of B content on the microstructure and wear properties of FeCoCrNiBx HEA coating were investigated (Liu et al. 2020). The FeCoCrNiBx coatings exhibited a typical dendritic and interdendritic structure, and the microstructure was refined with the increase of B content. Additionally, the coatings were found to be a simple face-centered cubic (FCC) solid solution with borides. In terms of mechanical properties, the hardness and wear resistance ability of the coating can be enhanced with the increase of the B content, and the maximum hardness value of three HEA coatings reached around 1025 HV0.2, which is higher than the hardness of the substrate material. It is suggested that the present fabricated HEA coatings possess potentials in application of wear resistance structures for Q245R steel. Low-cost AlCoCrFe Ni (x = 1.5, 2.5) high-entropy alloy (HEA) coatings were prepared by laser cladding and their microstructural evolutions, mechanical properties, and wear behaviors were investigated. Both Fe–Cr rich disordered BCC(A2) phase and Al–Ni rich ordered BCC(B2) phase were identified in these coatings. At x = 1.5, the coating consisted of B2 matrix and nanoscale A2 precipitates. While, at x = 2.5, A2 matrix with B2 precipitates formed. CALPHAD revealed that addition of Fe changed the solidification sequence of coatings, and was beneficial to the formation of A2 phase, resulting in different A2/B2 morphologies. AlCoCrFe Ni coating exhibited higher strength and better wear resistance, due to the strengthening effect of B2 precipitates was stronger. It was found that the properties of coatings could be improved by regulating the A2/B2 morphology. Moreover, increasing Fe content while maintaining a morphology of A2 matrix with B2 precipitates was a strategy to design high-strength HEA coatings (Zhang et al. 2020).

The preparation of HEA coatings on aluminum has received little attention, and the high efficiency cladding technology with coaxial powder feeding and the wear resistance of the coating have been rarely explored. Coatings with excellent mechanical properties are difficult to prepare on the aluminum alloy surfaces by laser surface engineering because of the low melting point and active chemical

properties of aluminum (Al). Al0.8CrFeCoNiCu0.5Bx coating exhibited a BCC1 + BCC2 + FCC phase when the x < 0.1. When x > 0.2, boride was formed in the Al0.8CrFeCoNiCu0.5Bx coatings, and it became the main phase of the Al0.8CrFeCoNiCu0.5B0.3 and Al0.8CrFeCoNiCuB0.4 coatings; however, no Alrich intermetallic compound with a complex phase structure was formed. When 0 < x < 0.3, the bonding strengths of the Al0.8CrFeCoNiCu0.5Bx coatings were 70.6–176.2 MPa. An increase in the boron content increased the hardness of all the coatings, except the Al0.8CrFeCoNiCu0.5B0.3 coating (Li and Shi 2020).

Due to the different microstructural evolution during cladding production and solidification, the mechanical properties are generally different from the bottom to substrate. In Bhattacharya et al. (2011) AISI 4340 steel was laser deposited on a rolled mild steel substrate by Direct Metal Deposition (DMD) technology. The microstructural investigation of the clad was performed using optical and electron microscopes and X-ray diffraction techniques. The microstructure consisted of ferrite, martensite, and cementite phases. Two types of martensite, lathe-type and plate-type, were observed in the microstructure. Decrease in micro-hardness values from the top layer to the alloy layer proves that the degree of tempering of the martensite phase increases in the same direction. An increase in the scanning speed and a decrease in laser power resulted in a finer microstructure and higher microhardness, and a reduction in the amount of overlap improved the overall microhardness. Cao and Choi (2006) developed a process model of microstructure evolution that indicated it is not the mass transfer but the heat transfer in the melt pool that dominates the solidification process.

The regime of laser cladding could be classified for evolution of coarse, fine, and ultrafine dendrite microstructure from analyses performed with monitoring systems using pyrometers (Kathuria and Tsuboi 1996). Hua et al. (2008) found a relationship between the molten pool temperature and the cladding thickness. The influences of laser processing parameters on the temperature of molten pool was investigated, such as powder feed rate, scanning velocity of laser beam, laser power, spot diameter, shielding gas flow rate, and powder feeding position. The results of Zhang et al. (2012) indicated that thermal history had an important effect on the microstructure, and consequently on the final properties.

TiAlCoCrxFeNi high-entropy alloys (HEAs) coatings were fabricated on the surface of Ti6Al4V by laser cladding. Their microstructural evolution with the increase in x value (x = 0, x = 1.0, x = 2.0) was investigated in detail (Zhang et al. 2020). The results indicated that two kinds of phases (a solid solution with the hexagonal close-packed (HCP) structure and Ti2Ni) were synthesized in the coatings, and the HCP content was gradually increased with the increase in x accompanied with the decrease in Ti2Ni content. An HEA coating only composed of single HCP was successfully prepared when x reached 2.0. The electrochemical and immersion tests all confirmed that the coating with x = 2.0 demonstrated the most excellent corrosion resistance in a0.1 mol·L − 1 HCl solution from different aspects including corrosion tendency and corrosion rate without the applied potential, the formation difficult/stability of the passive film and the dissolution rate in the passive state, and corrosion surface morphology.

2.5 Laser Cladding Monitoring and Control

Although the possibility of applying laser cladding for additive manufacturing of many classes of materials, their final microstructure, mechanical properties, residual stresses, and geometry are difficult to be precisely controlled. Processing parameters can lead to unexpected clads properties especially in layer-by-layer deposition. The process involves many physical and chemical nonequilibrium reactions leading to strong modifications in the clad materials. In order to monitor the process, especially for closed-loop control systems, the identification of simple measurable parameters is needed. So, many researchers focused their studies on the identification of physical parameters that can be directly correlated to the microstructural evolution of the clad materials. The interactive process between high-power laser and metal material, leading to a high temperature and high pressure area, is a complex kinetics process with complicated physicochemical changes. There are many factors contributing to the quality of repair layers, for example, technological parameters and environmental factors (Liu et al. 2017). They provide an overview of the significant signals that have been used to conduct studies on IMAC. The significant signals can be categorized into visual signal, temperature signal, spectrum signal, and acoustical signal in terms of the monitoring objects.

Song and Mazumder (2011) presented a model predictive control system that controls the melt pool temperature. A dual-color pyrometer was used to monitor the melt pool temperature. Laser cladding of H13 tool steel on a substrate with uneven surface showed that the closed-loop process was able to compensate for an underfill with 3 mm depth after 40-layer depositions. An infrared imaging system is developed to monitor surface temperatures during the process as feedback signals. Cooling rates and melt pool temperatures are recorded in real-time to provide adequate information regarding thermal gradients, and thus control the deposition microstructure affected by cooling rates. Results indicate that the closed-loop controller is capable of generating a consistent controlled microstructure during the process in real-time (Farshidianfar et al. 2015). Further study is conducted to evaluate cooling rate effects on grain size, phase transformations and hardness. Cooling rate changes are also studied with respect to the traveling speed, in order to identify a suitable controlling action for a microstructural controller (Farshidianfar et al. 2016). A temperature measurement system has been developed by using a two-color infrared thermometer (Hua et al. 2008). The influences of laser processing parameters on the temperature of molten pool was investigated, such as powder feed rate, scanning velocity of laser beam, laser power, spot diameter, shielding gas flow rate and powder feeding position. The control scheme of the single-layer thickness was discussed and the relationship between the molten pool temperature and the cladding thickness was build. The optimum approach is to use an infrared camera with the temperature calibrated to monitor the laser cladding process. However, this solution is very expensive, and it would cost even more if a high dynamic range were needed (Smurov et al. 2012).

The direct laser metallic powder deposition process was investigated with the aid of a radiant thermometer by building thin walls. The measured infrared (IR) temperature signal showed good correlation with the deposition process and the quality of the deposited samples. Both the deposition process and the measured temperature signal depended strongly on the z-increment. The variation of the melt pool temperature and cooling rate resulted in an inhomogeneous dimension accuracy, microstructure and hardness of the deposited sample (Bi et al. 2006).

The laser aided direct metal/material deposition (DMD) process is a layered manufacturing process able to produce a three-dimensional (3D) part directly from a computer aided design image. A closed-loop feedback control system is considered as a requirement to ensure dimensional accuracy. For conventional control methods, the effectiveness of process control strongly relies on accuracy of the analytical model of the system behavior. In Emamian et al. (2017), real-time cooling rate of Fe-Ti-C Metal Matrix Composites (MMCs) made by Direct Metal Deposition (DMD) are measured to monitor microstructure and carbide morphology. DMD can reduce the lead time for a concept to product by eliminating several intermediate steps. The most attractive feature of the process is that not only can it produce functional parts but it can also be interfaced with the homogenization design method, heterogeneous solid model and computer-aided design software to produce "Designed Material" with desired properties generally not observed in nature (Mazumder et al. 2000). This research proves that carbide morphology developed by DMD of Fe–TiC composite coating on AISI 1020 carbon steel is highly affected by cooling rate and preheat. For this purpose, the DMD process is monitored by a thermal camera to obtain real-time values of the cooling rate resulted from a range of selected scan speeds. Two approaches are studied for the single-track depositions: (a) single speed and (b) dual speeds in which the scan speed changes during the deposition. The dual speed generates different preheat values during deposition and thus deviates the cooling rate. Consequently, the effect of cooling rate and preheat temperature are studied on carbide morphologies. Results show that scan speed plays the main role in the formation and distribution of TiC particles in the deposited layer by affecting the cooling rate and dilution (melt pool composition). Based on this research, it is possible to control the cooling rate in order to achieve specific carbide morphologies in the deposited layer.

Based on high-speed camera recordings, an automated video analysis is developed, which tracks the particles on the melt pool surface, so that there the melt pool, flow velocity field is captured (Wirth 2018). The melt pool flow turns out to be partially turbulent due to the continuous impact of powder particles, which are fed into the melt pool by a powder nozzle. The melt pool flow has only a minor influence on the movement of pores or carbide particles. The interaction time is the main factor, as it determines for a material element the time in the liquid state, which is the available time for a pore to escape from the melt pool or for a carbide particle to accumulate on the melt pool surface or on the melt pool bottom.

Toyserkani and Khajepour (2006) introduce a mechatronics approach for the development of a closed-loop control system utilized in laser powder deposition. The laser powder deposition process, as a manufacturing technique, is combined

with a feedback control system to increase the quality of the final formed parts. The interconnections between the technologies involved in this complex mechatronics system along with the development of a CCD-based optical detector are explained. The optical CCD-based detector monitors the process zone to provide a series of single-pass band images of the near-locus region. A pattern recognition algorithm is incorporated into the feedback device to obtain the clad's height and angle of solid/liquid interface in real-time. This feedback device is blended in a PID-based controller, which is designed using a knowledge-based model, to adjust the laser pulse energy for enhancing the output of the process. The experimental assessments of the developed system are also presented at different process conditions and disturbances when Fe–20%Al was deposited on mild steel. It is shown that the PID-based controller can effectively improve the geometrical characteristics of the clad around the operating point by overcoming the effects of various disturbances. They also developed a feedforward proportional-integral-derivative (PID) controller to effectively control the clad height in laser solid freeform fabrication (LSFF). The architecture of the controller consists of a PID and a feedforward module, which is the inverse of the identified model. The advantage of adding a feedforward path to the PID controller is evaluated experimentally, in which the results show a lower overshoot and faster response times (Fathi et al. 2006). A proportional integral differential such as a fuzzy-logic-based controller was developed for adaptive deposition during the DMD process (Hua and Choi 2005). The controller has the capability of continuously tracking the reference height by varying the laser power adaptively, thus depositing a clad line with varying deposition height and a layer with a curved surface. This feature provides a potential of building 3D parts with nonlinear geometry, such as overhang, while maintaining the accuracy of surface curvature.

The precision, performance, and robustness of model-based controllers depend, to a large extent, on the accuracy of the inverse dynamic model that is incorporated in the design of the controller. Due to complex nature of the laser cladding process and presence of time-varying uncertainties, derivation of an accurate mathematical inverse dynamic model of the process is very difficult, and involves many unknown parameters. The inverse dynamic model of the complex nonlinear laser cladding process, which is difficult to describe mathematically, can be described by a fuzzy-logic-based inverse dynamic model constructed form input–output data. In Zeinali and Khajepour (2010), the development of an adaptive fuzzy inverse dynamic model of the laser cladding process, using a systematic fuzzy modeling approach, is presented. In a closed-loop laser cladding process, the scanning speed of the substrate is required to produce a clad with desired geometry and quality. In this study, a fuzzy inverse dynamic model that describes the scanning speed as a function of the cladding parameters in particular the clad height is developed.

Leung (2017) highlights the development and applications of a LAM process replicator (LAMPR), combined with in operando high-speed synchrotron X-ray imaging and image analysis to study these mechanisms. Using this setup, the sequential powder consolidation phenomena were revealed in LAM of stainless steel (SS316L), an Fe–Ni alloy (Invar36) and bioactive glass (13–93).

2.6 Conclusions

Additive manufacturing through laser cladding is a nonlinear process depending on many variables. Both, processing parameters and design shape play a fundamental role in the definition of the final clad. The nature and properties of the deposited material governs the setting of the optimal processing parameters because of a direct influence on the obtained microstructure both in single-layer and layer-by-layer structures. Many models have been developed in order to predict the optimal glad properties as a function of the fundamental processing parameters governing the deposition. This allows setting the optimal parameters for both powder or wire deposition as a function of the different clad materials also for very complex compositions. Obviously, the on-line continuous process monitoring is fundamental for the final quality of the laser cladded structures, the best available monitoring techniques have been largely reviewed in this chapter.

References

Alvarez, P., Montealegre, M. A., Pulido-Jimenez, J. F., & Arrizubieta, J. I. (2018). Analysis of the process parameter influence in laser cladding of 316L stainless steel. *Journal of Manufacturing and Materials Processing, 2*, 55. https://doi.org/10.3390/jmmp2030055.

Bax, B., Rajput, R., Kellet, R., & Raisacher, M. (2018). Systematic evaluation of process parameter maps for laser cladding and directed energy deposition. *Addit Manuf, 21*, 487–494. https://doi.org/10.1016/j.addma.2018.04.002.

Bhattacharya, S., Dinda, G. P., Dasgupta, A. K., & Mazumder, J. (2011). Microstructural evolution of AISI 4340 steel during direct metal deposition process. *Materials Science and Engineering, A528*(6), 2309–2318. https://doi.org/10.1016/j.msea.2010.11.036.

Bi, G., Gasser, A., Wissenbach, K., Drenker, A., & Poprawe, R. (2006). Investigation on the direct laser metallic powder deposition process via temperature measurement. *Applied Surface Science, 253*(3), 1411–1416. https://doi.org/10.1016/j.apsusc.2006.02.025.

Cai, L. X., Wang, C. M., & Wang, H. M. (2003). Laser cladding for wear-resistant Cr-alloyed Ni2Si–NiSi intermetallic composite coatings. *Materials Letters, 57*(19), 2914–2918. https://doi.org/10.1016/S0167-577X(02)01396-4.

Cao, Y., & Choi, J. (2006). Multiscale modeling of solidification during laser cladding process. *Journal of Laser Applications, 18*(3), 245. https://doi.org/10.2351/1.2227021.

Chan, B., Pacey, J., & Bibby, M. (1999). Modelling gas metal arc weld geometry using artificial neural network technology. *Canadian Metallurgical Quarterly, 38*, 43–51. https://doi.org/10.1179/cmq.1999.38.1.43.

Chen, Y., & Wang, H. M. (2004). High-temperature wear resistance of a laser clad TiC reinforced FeAl in situ composite coating. *Surface and Coating Technology, 179*(2–3), 252–256. https://doi.org/10.1016/S0257-8972(03)00821-1.

Cloots, M., Kunze, K., Uggowitzer, P. J., & Wegener, K. (2016). Microstructural characteristics of the nickel-based alloy IN738LC and the cobalt-based alloy Mar-M509 produced by selective laser melting. *Materials Science and Engineering, A658*, 68–76. https://doi.org/10.1016/j.msea.2016.01.058.

Conde, A., Zubiri, F., & De Damborenea, J. (2002). Cladding of Ni–Cr–B–Si coatings with a high power diode laser. *Materials Science and Engineering, A334*(1–2), 233–238. https://doi.org/10.1016/S0921-5093(01)01808-1.

d'Oliveira, A., Vilar, R., & Feder, C. G. (2002). High temperature behaviour of plasma transferred arc and laser co-based alloy coatings. *Applied Surface Science, 201*, 154–160. https://doi.org/10.1016/S0169-4332(02)00621-9.

De Damborenea, J., Lopez, V., & Vazquez, A. J. (1994). Improving high-temperature oxidation of Incoloy 800H by laser cladding. *Surface and Coating Technology, 70*, 107–113. https://doi.org/10.1016/0257-8972(94)90081-7.

De Hosson, J. T. M., Ocelík, V., de Oliveira, U. O. B., & Vainchtein, D. I. (2009). Fundamental and applied aspects of laser surface engineering. *Indian Journal of Medical Research, 100*, 1343–1360. https://doi.org/10.3139/146.110203.

de Oliveira, U., Ocelik, V., & De Hosson, J. T. M. (2006). Residual stress analysis in co-based laser clad layers by laboratory X-rays and synchrotron diffraction techniques. *Surface and Coating Technology, 201*, 533–542. https://doi.org/10.1016/j.surfcoat.2005.12.011.

Dhanda, M., Haldar, B., & Saha, P. (2014). Development and characterization of hard and wear resistant MMC coating on Ti-6Al-4V substrate by laser cladding. *Procedia Materials Science, 6*, 1226–1232. https://doi.org/10.1016/j.mspro.2014.07.196.

Diaz, E., Amado, J. M., Montero, J., Tobar, M. J., & Yanez, A. (2012). Comparative study of co-based alloys in repairing low Cr-Mo steel components by laser cladding. *Physics Procedia, 39*, 368–375. https://doi.org/10.1016/j.phpro.2012.10.050.

Dinda, G. P., Dasgupta, A. K., & Mazumder, J. (2012). Evolution of microstructure in laser deposited Al–11.28%Si alloy. *Surface and Coating Technology, 206*, 2152–2160. https://doi.org/10.1016/j.surfcoat.2011.09.051.

Edurne, M. M. (2018). *Analyses of the static mechanical properties of iron-based alloys deposited by extreme high-speed laser material deposition for additive manufacturing and repair applications*. PhD thesis, Universidad del Pais Vasco.

El Cheikh, H., Courant, B., Hascoët, J. Y., & Guillén, R. (2012). Prediction and analytical description of the single laser track geometry in direct laser fabrication from process parameters and energy balance reasoning. *Journal of Materials Processing Technology, 212*, 1832–1839. https://doi.org/10.1016/j.jmatprotec.2012.03.016.

Emamian, A., Farshidianfar, M. H., & Khajepour, A. (2017). Thermal monitoring of microstructure and carbide morphology in direct metal deposition of Fe-Ti-C metal matrix composites. *Journal of Alloys and Compounds, 710*, 20–28. https://doi.org/10.1016/j.jallcom.2017.03.207.

Erfanmanesh, M., Abdollah-Pour, H., Mohammadian-Semnani, H., & Shoja-Razavi, R. (2017). An empirical-statistical model for laser cladding of WC-12Co powder on AISI 321 stainless steel. *Optics & Laser Technology, 97*, 180–186. https://doi.org/10.1016/j.optlastec.2017.06.026.

Farnia, A., Malek Ghaini, F., Ocelík, V., & De Hosson, J. T. M. (2013). Microstructural characterization of co-based coating deposited by low power pulse laser cladding. *Journal of Materials Science, 48*, 2714–2723. https://doi.org/10.1007/s10853-012-7069-8.

Farshidianfar, M. H., Khajepour, A., & Gerlich, A. (2015). Real-time control of microstructure in laser additive manufacturing. *International Journal of Advanced Manufacturing Technology, 82*(5), 1173–1186. https://doi.org/10.1007/s00170-015-7423-5.

Farshidianfar, M. H., Khajepour, A., & Gerlich, A. P. (2016). Effect of real-time cooling rate on microstructure in laser additive manufacturing. *Journal of Materials Processing Technology, 231*, 468–478. https://doi.org/10.1016/j.jmatprotec.2016.01.017.

Fathi, A., Khajepour, A., Toyserkani, E., & Durali, M. (2006). Clad height control in laser solid freeform fabrication using a feedforward PID controller. *International Journal of Advanced Manufacturing Technology, 35*(3–4), 280–292. https://doi.org/10.1007/s00170-006-0721-1.

Felde, I., Reti, T., Zoltan, K., Costa, L., Colago, R., Vilar, R., Vero, B. (2002). *A simple technique to estimate the processing window for laser clad coatings*. In 1st ASM international surface engineering conference and the 13th IFHTSE congress. 237–242.

Francis, Z. R. (2017). *The effects of laser and electron beam spot size in additive manufacturing processes*. PhD thesis, Carnegie Mellon University Pittsburgh, PA.

Frenk, A., & Kurz, W. (1994). Microstructural effects on the sliding wear resistance of a cobalt-based alloy. *Wear, 174*(1–2), 81–91. https://doi.org/10.1016/0043-1648(94)90089-2.

Guo, C., Zhou, J., Chen, J., Zhao, J., Yu, Y., & Zhou, H. (2011). High temperature wear resistance of laser cladding NiCrBSi and NiCrBSi/WC-Ni composite coatings. *Wear, 270*, 492–498. https://doi.org/10.1016/j.wear.2011.01.003.

He, X., Yu, G., & Mazumder, J. (2009). Temperature and composition profile during double-track laser cladding of H13 tool steel. *Journal of Physics D: Applied Physics, 43*, 015502. https://doi.org/10.1088/0022-3727/43/1/015502.

Hemmati, I., Ocelík, V., & De Hosson, J. T. M. (2011). The effect of cladding speed on phase constitution and properties of AISI 431 stainless steel laser deposited coatings. *Surface and Coating Technology, 205*, 5235–5239. https://doi.org/10.1016/j.surfcoat.2011.05.035.

Hemmati, I., Rao, J. C., Ocelik, V., & De Hosson, J. T. M. (2013). Electron microscopy characterization of Ni-Cr-B-Si-C laser deposited coatings. *Microscopy and Microanalysis, 19*, 120–131. https://doi.org/10.1017/S1431927612013839.

Hoadley, A. F. A., & Rappaz, M. (1992). A thermal model of laser cladding by powder injection. *Metallurgical and Materials Transactions B, 23*, 631–642. https://doi.org/10.1007/BF02649723.

Hua, Y., & Choi, J. (2005). Adaptive direct metal/material deposition process using a fuzzy logic-based controller. *Journal of Laser Applications, 17*(4), 200. https://doi.org/10.2351/1.2098811.

Hua, T., Jing, C., Xin, L., Fengying, Z., & Weidong, H. (2008). Research on molten pool temperature in the process of laser rapid forming. *Journal of Materials Processing Technology, 198*(1–3), 454–462. https://doi.org/10.1016/j.jmatprotec.2007.06.090.

Jendrzejewski, R., Navas, C., Conde, A., de Damborenea, J. J., & Śliwiński, G. (2008). Properties of laser-cladded stellite coatings prepared on preheated chromium steel. *Materials and Design, 29*, 187–192. https://doi.org/10.1016/j.matdes.2006.10.020.

Kaplan, A. F. H., & Groboth, G. (2001). Process analysis of laser beam cladding. *The Journal of Manufacturing Science and Engineering, 123*, 609–614. https://doi.org/10.1115/1.1344899.

Kathuria, Y. P., & Tsuboi, A. (1996). The effect of beam interaction time on laser cladding process. *Laser Electro-Optics*, 351–352.

Kattire, P., Paul, S., Singh, R., & Yan, W. (2015). Experimental characterization of laser cladding of CPM 9V on H13 tool steel for die repair applications. *Journal of Manufacturing Processes, 20*(3), 492–499. https://doi.org/10.1016/j.jmapro.2015.06.018.

Kotoban, D., Grigoriev, S., & Shishkovsky, I. (2014). Study of 3D laser cladding for Ni85Al15 superalloy. *Physics Procedia, 56*, 262–268. https://doi.org/10.1016/j.phpro.2014.08.170.

Kumar, A., & Roy, S. (2009). Development of a theoretical process map for laser cladding using a three-dimensional conduction heat transfer model. *Numerical Heat Transfer, Part A: Applications, 56*, 478–496. https://doi.org/10.1080/10407780903266489.

Kusmoko, A., Dunne, D., Li, H., & Nolan, D. (2014). Effect of two different energy inputs for laser cladding of Stellite 6 on P91 and P22 steel substrates. *Procedia Materials Science, 6*, 24–36. https://doi.org/10.1016/j.mspro.2014.07.005.

Lalas, C., Tsirbas, K., Salonitis, K., & Chryssolouris, G. (2007). An analytical model of the laser clad geometry. *International Journal of Advanced Manufacturing Technology, 32*, 34–41. https://doi.org/10.1007/s00170-005-0318-0.

Lee, Y. (2015). *Simulation of laser additive manufacturing and its applications*. PhD thesis, The Ohio State University.

Leung, C. L. A. (2017). *X-ray imaging of powder consolidation during laser additive manufacturing*. PhD thesis, The University of Manchester.

Li, Y., & Ma, J. (1997). Study on overlapping in the laser cladding process. *Surface and Coating Technology, 90*, 1–5. https://doi.org/10.1016/S0257-8972(96)03022-8.

Li, Y., & Shi, Y. (2020). Microstructure and wear resistance of the laser-cladded Al0.8CrFeCoNiCu0.5Bx high-entropy alloy coating on aluminium. *Mater Res Expr, 7*, 026517. https://doi.org/10.1088/2053-1591/ab7161.

Li, Q., Zhang, H., Li, D., Chen, Z., Huang, S., Lu, Z., & Yan, H. (2019). WxNbMoTa refractory high-entropy alloys fabricated by laser cladding deposition. *Materials, 12*, 533. https://doi.org/10.3390/ma12030533.

Liu, W. W., Tang, Z. J., Liu, X. Y., Wang, H. J., & Zhang, H. C. (2017). A review on in-situ monitoring and adaptive control technology for laser cladding remanufacturing. *Procedia CIRP, 61*, 235–240. https://doi.org/10.1016/j.procir.2016.11.217.

Liu, D., Zhao, J., Li, Y., Zhu, W., & Lin, L. (2020). Effects of boron content on microstructure and Wear properties of FeCoCrNiBx high-entropy alloy coating by laser cladding. *Applied Sciences, 10*, 49. https://doi.org/10.3390/app10010049.

Lu, X. D., & Wang, H. M. (2004). High-temperature phase stability and tribological properties of laser clad Mo2Ni3Si/NiSi metal silicide coatings. *Acta Materialia, 52*, 5419–5426. https://doi.org/10.1016/j.actamat.2004.08.006.

Ma, M., Wang, Z., & Zeng, X. (2017). A comparison on metallurgical behaviors of 316L stainless steel by selective laser melting and laser cladding deposition. *Materials Science and Engineering, A685*, 265–273. https://doi.org/10.1016/j.msea.2016.12.112.

Mazumder, J., Dutta, D., Kikuchi, N., & Ghosh, A. (2000). Closed loop direct metal deposition: Art to part. *Optics and Lasers in Engineering, 34*(4–6), 397–414. https://doi.org/10.1016/S0143-8166(00)00072-5.

Narang, H. K., Mahapatra, M. M., & Jha, P. K. (2012). Mukherjee I (2012) modelling and predicting the effects of submerged arc weldment process parameters on weldment characteristics and shape profiles. *Proceedings of the Institution of Mechanical Engineers Part B Journal of Engineering Manufacture, 226*, 1230–1240. https://doi.org/10.1177/0954405412441561.

Navas, C., Cadenas, M., Cuetos, J. M., & de Damborenea, J. (2006). Microstructure and sliding wear behaviour of Tribaloy T-800 coatings deposited by laser cladding. *Wear, 260*, 838–846. https://doi.org/10.1016/j.wear.2005.04.020.

Naveed Ahsan, M., & Pinkerton, A. J. (2011). An analytical–numerical model of laser direct metal deposition track and microstructure formation. *Modelling and Simulation in Materials Science and Engineering, 19*(5), 055003. https://doi.org/10.1088/0965-0393/19/5/055003.

Nenadl, O., Ocelik, V., Palavra, A., & De Hosson, J. T. M. (2014). The prediction of coating geometry from main processing parameters in laser cladding. *Physics Procedia, 56*, 220–227. https://doi.org/10.1016/j.phpro.2014.08.166.

Ocelík, V., Janssen, N., Smith, S. N., & De Hosson, J. T. M. (2016). Additive manufacturing of high-entropy alloys by laser processing. *JOM, 68*, 1810–1818. https://doi.org/10.1007/s11837-016-1888-z.

Partes, K., Giolli, C., Borgioli, F., Bardi, U., Seefeld, T., & Vollertsen, F. (2008). High temperature behaviour of NiCrAlY coatings made by laser cladding. *Surface and Coating Technology, 202*, 2208–2213. https://doi.org/10.1016/j.surfcoat.2007.09.010.

Paydas, H., Mertens, A., Carrus, R., Lecompte-Beckers, J., & Tchoufang Tchuindjang, J. (2015). Laser cladding as repair technology for Ti–6Al–4V alloy: Influence of building strategy on microstructure and hardness. *Materials and Design, 85*, 497–510. https://doi.org/10.1016/j.matdes.2015.07.035.

Pekkarinen, I. J., Kujanpää, V., & Salminen, A. (2012). Laser cladding using scanning optics. *Journal of Laser Applications, 24*, 52003. https://doi.org/10.2351/1.4742938.

Picasso, M., Marsden, C. F., Wagniere, J. D., Frenk, A., & Rappaz, M. (1994). A simple but realistic model for laser cladding. *MetTrans, B25*, 281–291. https://doi.org/10.1007/BF02665211.

Qi, H., Mazumder, J., & Ki, H. (2006). Numerical simulation of heat transfer and fluid flow in coaxial laser cladding process for direct metal deposition. *Journal of Applied Physics, 100*, 24903. https://doi.org/10.1063/1.2209807.

Quazi, M. M., Fazal, M. A., Haseeb, A. S. M. A., Yusof, F., Masjuki, H. H., & Arslan, A. (2016). Effect of rare earth elements and their oxides on tribomechanical performance of laser claddings: A review. *Journal of Rare Earths, 34*(6), 549–564. https://doi.org/10.1016/S1002-0721(16)60061-3.

Riquelme, A., Rodrigo, P., Escalera-Rodríguez, M. D., & Rams, J. (2016). Analysis and optimization of process parameters in Al–SiCp laser cladding. *Optics and Lasers in Engineering, 78*, 165–173. https://doi.org/10.1016/j.optlaseng.2015.10.014.

Segerstark, A. (2015). *Influence of laser metal deposition process parameters on microstructural characteristics*. Licentiate Thesis, University West, Trollhättan Sweden.

Shim, D.-S., Baek, G.-Y., Seo, J.-S., Shin, G.-Y., Kim, K.-P., & Lee, K.-Y. (2016). Effect of layer thickness setting on deposition characteristics in direct energy deposition (ded) process. *Optics & Laser Technology, 86*, 69–78. https://doi.org/10.1016/j.optlastec.2016.07.001.

Shu, D., Li, Z., Zhang, K., Yao, C., Li, D., & Dai, Z. (2017). In situ synthesized high volume fraction WC reinforced Ni based coating by laser cladding. *Materials Letters, 195*, 178–181. https://doi.org/10.1016/j.matlet.2017.02.076.

Smurov, I., Doubenskaia, M., & Zaitsev, A. (2012). Complex analysis of laser cladding based on comprehensive optical diagnostics and numerical simulation. *Physics Procedia, 39*, 743–752. ISSN: 1875-3892. https://doi.org/10.1016/j.phpro.2012.10.096.

Song, L., & Mazumder, J. (2011). Feedback control of melt Pool temperature during laser cladding process. *IEEE Transactions on Control Systems Technology, 19*(6), 1349–1356. https://doi.org/10.1109/TCST.2010.2093901.

Sun, Y., & Hao, M. (2012). Statistical analysis and optimization of process parameters in Ti6Al4V laser cladding using Nd: YAG laser. *Optics and Lasers in Engineering, 50*(7), 985–995. https://doi.org/10.1016/j.optlaseng.2012.01.018.

Suryakumar, S., Karunakaran, K. P., Bernard, A., Chandrasekhar, U., Raghavender, N., & Sharma, D. (2011). Weld bead modeling and process optimization in hybrid layered manufacturing. *CAD, 43*, 331–344. https://doi.org/10.1016/j.cad.2011.01.006.

Tobar, M. J., Amado, J. M., Alvarez, C., Garcia, A., Varela, A., & Yanez, A. (2008). Characteristics of Tribaloy T-800 and T-900 coatings on steel substrates by laser cladding. *Surface and Coating Technology, 202*(11), 2297–2301. https://doi.org/10.1016/j.surfcoat.2007.11.025.

Tobar, M. J., Amado, J. M., Yanez, A., Pereira, J. C., & Amigo, V. (2014). Laser cladding of MCrAlY coatings on stainless steel. *Physics Procedia, 56*, 276–283. https://doi.org/10.1016/j.phpro.2014.08.172.

Toyserkani, E., & Khajepour, A. (2006). A mechatronics approach to laser powder deposition process. *Mechatronics, 16*(10), 631–641. https://doi.org/10.1016/j.mechatronics.2006.05.002.

Toyserkani, E., Khajepour, A., & Corbin, S. (2003). Three-dimensional finite element modeling of laser cladding by powder injection: Effects of powder feedrate and travel speed on the process. *Journal of Laser Applications, 15*, 153–160. https://doi.org/10.2351/1.1585087.

Weng, F., Yu, H., Chen, C., & Dai, J. (2020). Microstructures and wear properties of laser cladding Cobased composite coatings on Ti–6Al–4V. *Materials and Design, 80*, 174–181. https://doi.org/10.1016/j.matdes.2015.05.005.

Wirth, F. (2018). *Process understanding, modeling and predictive simulation of laser cladding*. PhD thesis, ETH Zurich.

Xiong, J., Zhang, G., Gao, H., & Wu, L. (2013). Modeling of bead section profile and overlapping beads with experimental validation for robotic GMAW-based rapid manufacturing. *Robotics and Computer-Integrated Manufacturing, 29*, 417–423. https://doi.org/10.1016/j.rcim.2012.09.011.

Xu, M., Li, J., Jiang, J., & Li, B. (2015). Influence of powders and process parameters on bonding shear strength and micro hardness in laser cladding remanufacturing. *Procedia CIRP, 29*, 804–809. https://doi.org/10.1016/j.procir.2015.02.088.

Yang, M.-S., Liu, X.-B., Fan, J.-W., He, X.-M., Shi, S.-H., Fu, G.-Y., Wang, M.-D., & Chen, S.-F. (2012). Microstructure and wear behaviors of laser clad NiCr/Cr3C2–WS2 high temperature self-lubricating wear-resistant composite coating. *Applied Surface Science, 258*, 3757–3762. https://doi.org/10.1016/j.apsusc.2011.12.021.

Yufan, S., Hanguang, F., Xuelong, P., Shuting, S., Jian, L., & Yiongping, L. (2020). Effect of process parameters and niobium carbide addition on microstructure and wear resistance of laser cladding nickel-based alloy coatings. *Materialwissenschaft und Werkstofftechnik, 51*, 54–65. https://doi.org/10.1002/mawe.201800221.

Zeinali, M., & Khajepour, A. (2010). Development of an adaptive fuzzy logic-based inverse dynamic model for laser cladding process. *Engineering Applications of Artificial Intelligence, 23*(8), 1408–1419. https://doi.org/10.1016/j.engappai.2009.11.006.

Zhang, H., Pan, Y., He, Y., & Jiao, H. (2011a). Microstructure and properties of 6FeNiCoSiCrAlTi high-entropy alloy coating prepared by laser cladding. *Applied Surface Science, 257*, 2259–2263. https://doi.org/10.1016/j.apsusc.2010.09.084.

Zhang, H., Pan, Y., & He, Y. (2011b). Grain refinement and boundary misorientation transition by annealing in the laser rapid solidified 6FeNiCoCrAlTiSi multicomponent ferrous alloy coating. *Surface and Coating Technology, 205*(16), 4068–4072. https://doi.org/10.1016/j.surfcoat.2011.02.054.

Zhang, Y., Yu, G., He, X., Ning, W., & Zheng, C. (2012). Numerical and experimental investigation of multilayer SS410 thin wall built by laser direct metal deposition. *Journal of Materials Processing Technology, 212*(1), 106–112. https://doi.org/10.1016/j.jmatprotec.2011.08.011.

Zhang, G. J., Tian, Q. W., Yin, K. X., Niu, S. Q., Wu, M. H., Wang, W. W., Wang, Y. N., & Huang, J. C. (2020). Effect of Fe on microstructure and properties of AlCoCrFe Ni (x=1.5, 2.5) high entropy alloy coatings prepared by laser cladding. *Intermetallics, 119*, 106722. https://doi.org/10.1016/j.intermet.2020.106722.

Zhao, G., Cho, C., & Kim, J.-D. (2003). Application of 3-D finite element method using Lagrangian formulation to dilution control in laser cladding process. *International Journal of Mechanical Sciences, 45*, 777–796. https://doi.org/10.1016/S0020-7403(03)00140-1.

Zou, Y., Ma, B., Cui, H., Lu, F., & Xu, P. (2020). Microstructure, wear, and oxidation resistance of nanostructured carbide strengthened cobalt-based composite coatings on invar alloys by laser cladding. *Surface and Coating Technology, 381*, 125188. https://doi.org/10.1016/j.surfcoat.2019.125188.

Chapter 3
Laser Cladding of Metals by Additive Manufacturing: Moving Toward 3D Printing

Gholamreza Fayaz and Sepideh S. Zakeri

Nomenclature

ALE	arbitrary Lagrangian Eulerian
AM	additive manufacturing
DED	direct energy deposition
DMLS	direct metal laser sintering
EBM	electron beam melting
FDM	finite difference method
FEM	finite element method
LAM	laser-based additive manufacturing
LC	laser consolidation
LD	laser deposition
L-DED	laser-based direct energy deposition
LENS	laser-engineered net shaping
LIBS	laser-induced breakdown spectroscopy
LM	laser melting
LMD	laser metal deposition
L-PBF	laser-based powder bed fusion
MLS	metal laser sintering
PBF	powder bed fusion
SLM	selective laser melting
SLS	selective laser sintering

G. Fayaz (✉)
Physics Department, Tafresh University, Tafresh, Iran
e-mail: reza.fayaz@tafreshu.ac.ir

S. S. Zakeri
Smart Industry Division, FAR Pajouhesh Azma Co. (FARPACO), Tehran, Iran
e-mail: sepideh.zakeri@farpaco.com

P. Cavaliere (ed.), *Laser Cladding of Metals*,
https://doi.org/10.1007/978-3-030-53195-9_3

3.1 Introduction

Would it not be great to be able to fabricate and repair complex-shaped parts with high resolution and fidelity to their digital designs, right on demand, while simultaneously saving time as well as reducing energy usage and material waste? The state-of-the-art technology of additive manufacturing (AM) aims to provide such potentially smart and sustainable solutions by solid translation of a digital design model into its real twin using AM machines.

In contrast to the conventional formative and subtractive manufacturing techniques with concerning issues such as geometry limitations as well as expensive tooling requirements, additive manufacturing follows a layer-by-layer or even pixel-by-pixel fabrication strategy based on a CAD/CAM model to build three-dimensional (3D) complex-shaped components. More importantly, it can be considered as a less environmentally harmful manufacturing method because of the reduced energy usage and material waste. AM technology offers novel capabilities including rapid fabrication/prototyping, multi-materials combinations, tunability of material properties, as well as high resolution. Recent advances in AM technologies have enabled the digital fabrication of different types of materials including ceramics (Zocca et al. 2015), polymers (Melchels et al. 2012), and metals (Frazier 2014; Herzog et al. 2016) for a broad range of applications.

Laser cladding is an intrinsically additive technique that has been extensively studied and used mainly for coating and wear resistance applications (Toyserkani et al. 2004). Following the recent advancement in the laser-based additive manufacturing of metals (LAM) and the emerging tools for design, characterization, and property prediction of the additively manufactured components, laser cladding by additive manufacturing is distinguishably equipped with improved integrated feedback control that enables smart optimization of the process. This capability is, undoubtedly, a step forward toward increased readiness for the digital revolution.

The main objective of this chapter is to briefly introduce laser-based additive manufacturing of metals and then summarize the currently emerging computational, experimental, and processing innovations that are expanding the scope for implementation of LAM for future generations of advanced laser cladding systems. Moreover, current open challenges as well as the outlook on the market-value of metal AM are also discussed.

3.2 Additive Manufacturing of Metals: Processes and Materials

Over the past two decades, metal additive manufacturing has emerged into a promising technology to print 3D metallic components, thanks to the advances in industrial lasers, metal powder technology, and computational hardware/software. These developments have rapidly enabled diverse applications of metal AM, ranging from

aerospace (Fasel et al. 2020; Froes and Boyer 2019; Pollock 2016), energy, oil and gas (Burns and Wangenheim 2019), automotive (Leal et al. 2017), machining (Traxel and Bandyopadhyay, 2019), welding and cladding (Bax et al. 2018), medical (Murr 2020) to construction (Buchanan and Gardner 2019).

Despite the promising aspects of metal AM, however, the complex thermal cycles in the nature of the AM processes are still challenging for additive manufacturing of defect-free and operational components. During the past decades, the field of metal additive manufacturing has experienced significant developments aiming to unravel the scientific and technical complexities associated with various metal AM processes.

3.2.1 Description of AM Processes

The fabrication of a metallic layer during an AM process is performed by rapid melt and solidification of a deposited metal using a heat source. Depending on the material feedstock, energy source, and build volume, different techniques can be defined for metal additive manufacturing. Lasers are one of the main energy sources used in AM processes (Hyub Lee et al. 2017) together with other sources such as electron beam, plasma arc, gas metal arc (Donghong Ding et al. 2015; Jin et al. 2020). According to the American Society for Testing and Materials (ASTM) standard F2792, the main techniques for metal AM are classified into powder bed fusion (PBF) and direct energy deposition (DED).

The powder bed fusion (PBF), also known as selective laser sintering (SLS), direct metal laser sintering (DMLS), laser melting (LM), selective laser melting (SLM), LaserCusing, and electron beam melting (EBM), is currently one of the promising techniques for AM of metallic components. As illustrated schematically in Fig. 3.1, in a PBF technique, a predefined fine layer of metal powder from a powder reservoir is spread over a solid substrate plate by a leveling powder delivery system, which can be blade, brush, or roller. The beam of a heat source, either laser (Khairallah et al. 2016) or electrons (Sames et al. 2014), then selectively melts thin layers of the metal powder onto the substrate plate according to a sliced CAD data and simultaneously fuses them to the substrate plate as the scanning beam moves away. The powder bed is then lowered equal to the thickness of a layer and the process is repeated until the entire component geometry is generated. The unexposed powder can then easily be recycled as it remains loose.

The direct energy deposition (DED), also known as direct metal deposition (DMD), laser engineered net shaping (LENS), laser additive manufacturing (LAM), laser metal deposition (LMD), is one of the main AM techniques for metal AM. DED technique is based on simultaneous intersection of a concentrated energy source and the feedstock material at a common focal point, generally in the presence of an inert shield gas. Powder (Kakinuma et al. 2016), wire (Heralić et al. 2012), or combination of both (Syed et al. 2006) can be used as the feedstock material and the heat

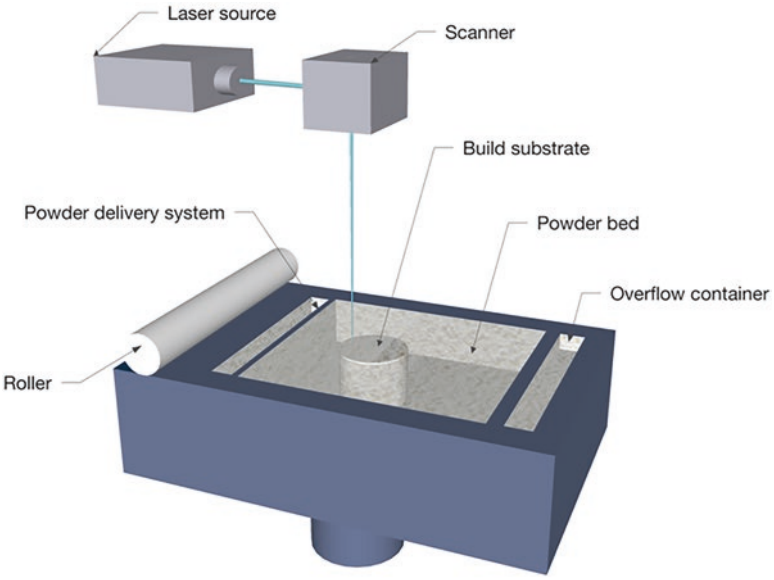

Fig. 3.1 Schematic illustration of a laser-based additive manufacturing technique known as powder bed fusion (L-PBF): Predefined fine layer of metal powder is first spread over a solid substrate plate by a roller. Laser beam then selectively melts thin layers of the metal powder onto the substrate plate according to a sliced CAD data and simultaneously fuses them to the substrate plate as it moves away. The powder bed is then lowered equal to the thickness of a layer and the process is repeated until the entire component geometry is generated

source can be either laser (Keist and Palmer 2016), electron beam (Brandl et al. 2012), plasma arc (Williams et al. 2016), or gas metal arc (Xiong et al. 2017).

In laser-based direct energy deposition (L-DED) process, a moving laser beam melts the surface of the substrate and instantly creates a melt pool. Powder is simultaneously injected into the melt pool through a coaxial or multi-jet nozzle. A clad is then fabricated on the surface by rapid solidification of the melt pool. A schematic illustration of the laser-based DED process is shown in Fig. 3.2.

Both PBF and DED techniques have their own advantages and disadvantages. Therefore, proper choice of the AM process depends on different criteria including availability of knowledge about the relationships between processing, microstructure, properties, and performance as well as desired geometrical dimensions, surface roughness, etc. of the AM materials. Selected process parameters for the L-PBF and L-DED techniques are compared in Table 3.1.

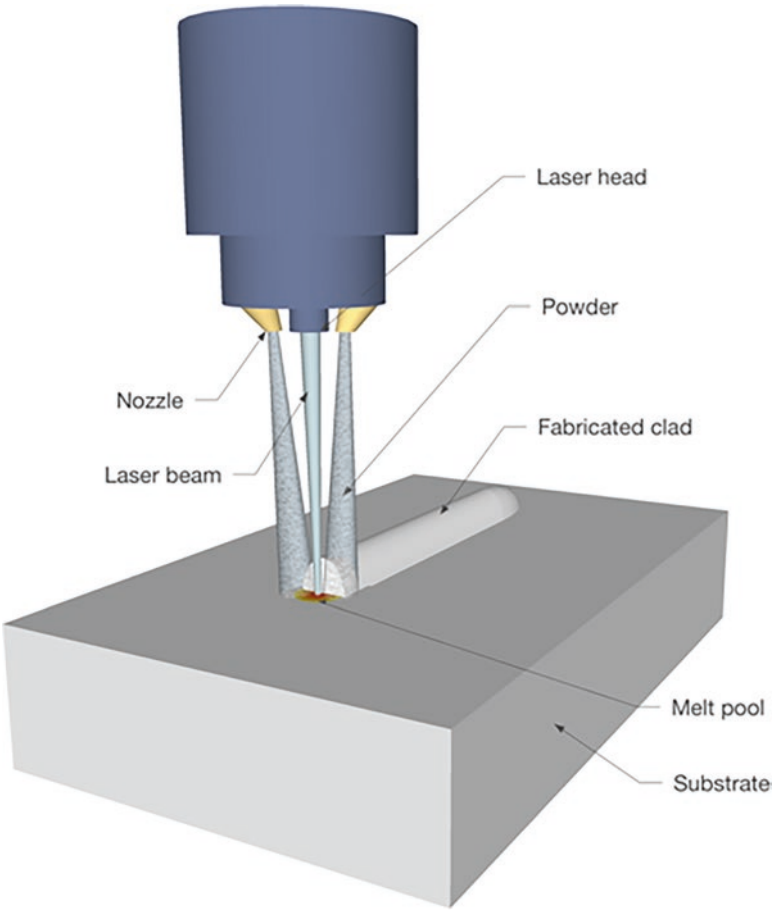

Fig. 3.2 Schematic illustration of a laser-based additive manufacturing known as direct energy deposition (L-DED): A moving laser beam strikes the substrate creating a melt pool into which the feedstock powder is injected through a nozzle. A clad is then fabricated by rapid solidification of the melt pool

Table 3.1 Comparison of the selected process parameters for laser-based additive manufacturing of metals: L-PBF vs. L-DED. (DebRoy et al. 2018)

Process	L-PBF	L-DED
Laser power (W)	50–1000	100–3000
Scan speed (mm/s)	10–1000	5–20
Max. Build size (mm × mm × mm)	500 × 280 × 320	2000 × 1500 × 750
Max. Feed rate (g/s)	NA	0.1–1.0
Dimensional accuracy (mm)	0.04–0.2	0.5–1.0
Surface roughness (μm)	7–20	4–10

3.2.2 Common Alloys Currently Used for Additive Manufacturing of Metals

So far, only a few numbers of alloys have been reported to be reliably additively manufactured (Lewandowski and Seifi 2016) and nearly more than 5500 alloys are not available for AM processes. The directional heat extraction, rapid solidification, and repeated melting, as the intrinsic thermal features of the AM processes (Hu Zhang et al. 2016) create complex microstructures and properties, consequently limiting the number of applicable alloys and slowing down metal additive manufacturing to reach its full potential. A list of printable alloys currently used in AM applications are represented in Table 3.2.

Furthermore, recent studies suggest that effective use of nanomaterials in the feedstock can improve printability and quality of the final fabricated part (Fayaz and Kazemzadeh 2018; Martin et al. 2017).

3.2.3 Common Potential Defects Forming during AM of Metals

Several classes of defects, which can be spherical, irregular, or elongated in shape, can potentially form during AM processes. Such inherent AM anomalies can occur thousands of time in a single component, playing an important role in quality and operationality of the additively manufactured parts. In Table. 3.3, common process-induced defects and the reason for their potential formations during AM processes are summarized. Images associated with these defects are also presented in Fig. 3.3. For a review on defect generation during AM processes, see for example, Bauereiß et al. (2014).

Table 3.2 Common alloys used in additive manufacturing of metals and their applications (Milewski 2017)

Alloy	Application (s)
Titanium-based	Aerospace, medical, automotive, marine, corrosion resistance, high temperature, machinability and weldability
Aluminum-based	Aerospace, automotive, machinability and weldability, consumer products
Nickel-based superalloys	Aerospace, marine, corrosion resistance, high temperature, machinability and weldability
Stainless steel	Aerospace, medical, energy, oil & gas, automotive, marine, corrosion resistance, high temperature, machinability and weldability, tools and molds, consumer products
Cobalt chrome	Aerospace, medical, corrosion resistance
Maraging steel	Tools and molds
Precious metals	Medical, consumer products

Table 3.3 Common potentially process-induced defects associated with AM (Duyao Zhang et al. 2018)

Defect	Reason(s) for formation
Gas porosities	(1) entrapped gas inside the powder particles during the powder atomization process; (2) powder-carrying/shielding gas entrapped in the melt pool in the blown powder process with a high powder flow rate; (3) moisture on the powder particle surface and dissolved hydrogen within the powder
Keyholes	Vaporization of constituents with high vapor pressure within the alloy in a fusion-based metal AM process, when the energy density is too high
Lack of fusion or incomplete melting	Insufficient energy to melt all the powder particles and the surface of the previous layer
Rough build surfaces	Metallic balls formed due to (1) high thermal gradients in the first track when the power is cold, (2) the capillary instability of the melt pool when the total surface of the melt pool is larger than that of a sphere with the same volume and the viscosity is too low; (3) hydrodynamic instability driven by the Marangoni effect; (4) spattering and denudation, which causes non-melted powder particles around the melt pool entrained/expulsed by vapor-induced surrounding gas flow/recoil pressure as the result of evaporation of the melt; (5) ejection of liquid drops due to splashing of the melt at high melt-pool surface temperatures or high velocities of melt flow; and (6) change in melt flow direction due to changes in surface tension with higher dissolved oxygen contents in iron
Cracks and distortion	Residual stresses built up due to high temperature gradients, large amounts of thermal expansion, and shrinkage or nonuniform plastic deformation during heating and cooling cycles

Clearly, a comprehensive understanding of the laser–metal interaction during the processing could have major outcomes for the quality of the components produced by AM. However, other additional types of defects can also be induced by equipment, model (or design for additive choice), and quality of the feedstock (Grasso and Colosimo 2017). Therefore, in order to reduce or eliminate all these types of defect-inducing mechanisms, more efforts with focus on the characterization and understanding of the AM materials as well as optimization and testing methodologies are highly required.

3.3 Predictive Tools for Optimization of Metal AM Processes

While the concept behind AM of metal is simply joining single layers of materials together to shape a part, the scientific and engineering issues during preprocessing, processing, and post-processing (e.g., heat treatment, HIP) are still complex (Nazmul Ahsan and Khoda 2016), resulting in unique processing characteristics that can have significant impacts on the structural integrity and microstructure of the fabricated components and their overall performance and functionality. On the other hand, an overarching goal in the AM technology is to fabricate components that can

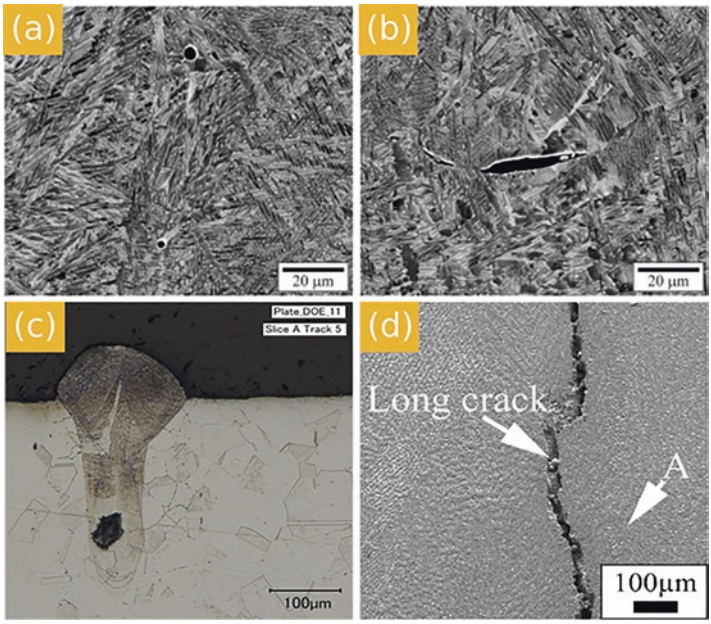

Fig. 3.3 Examples of process-induced defects in AM. (**a**) Two circular gas pores, (**b**) a more irregular lack of fusion pore, (**c**) keyhole, (**d**) long crack. | Images (**a**) and (**b**) are adapted from Tammas-Williams et al. (2015); (**c**) is adapted from King et al. (2014); (**d**) is adapted from Zhao et al. (2009)

reliably be used even in high safety-critical applications. This contradiction has motivated and initiated many of the current research attempts toward optimization of the AM processes by integration of the predictive tools in order to accelerate advances in the technology.

The predictive models for metal AM processes can be built by physics-based modeling as well as experimental measurements. Undoubtedly, maintaining a strong feedback loop between the two approaches is essential to effectively build reliable and well-tested predictive models. These approaches are briefly discussed in the following.

3.3.1 Physics-Based Modeling

During the AM process, complex thermal cycles including absorption or reflection of the heat source, convection, conduction, evaporation, and heat radiation occur simultaneously. Due to the layer-by-layer nature of the AM processes, however, conventional experimental techniques measuring temperature at the surface cannot provide the critical information about the thermal events occurring in the underlying layers. Thus, to further monitor and optimize AM processes, accurate modeling

techniques can be used to provide perspective on the temperature and velocity fields and their relationships with the characteristic features of the AM processes including the properties of laser (power, density distribution, scanning speed) as well as powder (feed rate, chemical composition, particle size, velocity of the powder particles).

An accurate 3D calculation of the transient temperature requires coupled modeling of the heat transfer and fluid flow. A rather comprehensive model (Manvatkar et al. 2014) can be described by solving the governing equations for conservation of mass, momentum, and energy, respectively, as

$$\frac{\partial\left(\rho u_i\right)}{\partial x_i}=0, \tag{3.1}$$

$$\frac{\partial\left(\rho u_i\right)}{\partial t}+\frac{\partial\left(\rho u_j u_i\right)}{\partial x_i}=\frac{\partial}{\partial x_i}\left(\mu\frac{\partial u_j}{\partial x_i}\right)+S_j, \tag{3.2}$$

$$\rho\frac{\partial h}{\partial t}+\frac{\partial\left(\rho u_i h\right)}{\partial x_i}=\frac{\partial}{\partial x_i}\left(\frac{k}{C_p}\frac{\partial h}{\partial x_i}\right)-\rho\frac{\partial\Delta H}{\partial t}-\rho\frac{\partial\left(u_i\Delta H\right)}{\partial x_i}. \tag{3.3}$$

Here ρ is the density, t is the time, x_i is the distance along the i direction, and u_i and u_j are the velocity vectors along the i and j directions, respectively. μ is the dynamic viscosity, h is the heat, C_p is the specific heat, k is the thermal conductivity, S_j is a source term for the momentum equation, and ΔH is the latent heat content. In DED processes, the power density distribution of the heat source (I) with a modified Gaussian distribution (including the interactions between the heat source and the feedstock materials) can be described as

$$I=\frac{fP}{\pi r_b^2 t_l}\left[\eta_p+\left(1-\eta_p\right)\eta_l\right]\exp\left(-f\frac{r^2}{r_b^2}\right), \tag{3.4}$$

where f is the distribution factor, P is the total power of the heat source, r_b is the radius of the beam heat source, r is the radial distance of any point from the axis of the heat source, η_l refers to the absorption coefficient of the deposit, η_p is the fraction of energy absorbed by the powder during flight (zero in PBF processes), and t_l is the layer thickness.

By solving the coupled Eqs. 3.1, 3.2, and 3.3 with appropriate initial and boundary conditions (Manvatkar et al. 2014), the transient temperature in the entire built part and the velocity fields in the melt-pool region can be obtained. Moreover, information about cooling rates and parameters associated with the solidification, as additional intriguing features of the process can be retrieved.

Different analytical and numerical approaches have been used to model various features of the AM processes. The approaches include analytical (Huang et al. 2016, 2019; Picasso et al. 1994), heat conduction models using finite element method

(FEM) (Zeng et al. 2015), heat transfer and fluid flow models using finite difference method (FDM) (Manvatkar et al. 2015; Raghavan et al. 2013; Yuan and Gu 2015), level-set method (He and Mazumder 2007; Morville et al. 2012; Qi et al. 2006; Wen and Shin 2010), Lattice Boltzmann and arbitrary Lagrangian Eulerian (ALE) methods (Khairallah and Anderson 2014; Klassen et al. 2014; Moser et al. 2016) and volume of fluid method (Lee et al. 2014).

These approaches have been used to model key features such as powder stream and laser interaction, melt-pool dynamics, as well as microstructure. As examples, snapshots of the computed temperature and velocity fields during laser cladding by direct metal deposition obtained by perform of FEM simulations are shown in Fig. 3.4. Additionally, cross section of the multi-physics simulations of the turn point dynamics during a PBF process using ALE is presented in Fig. 3.5, for better understanding of the mechanism for pore formation and depression at a turn point. For a review on the modeling of PBF see for example, Schoinochoritis et al. (2015) and on the modeling of DED, see for example, Guan and Zhao (2020).

A selection of the reported modeling approaches classified by different performance characteristics associated with DED processes is presented in Table 3.4.

3.3.2 In Situ Monitoring and Control

Quality of the fabricated parts in AM techniques can be highly affected by small variations in the process parameters and conditions. So far, limited improvements have been achieved in the quality of the additively manufactured components using data-driven controls obtained by experiments. Clearly, this makes in situ monitoring and control of the AM processes far more desirable and essential for quality assurance in critical industrial applications.

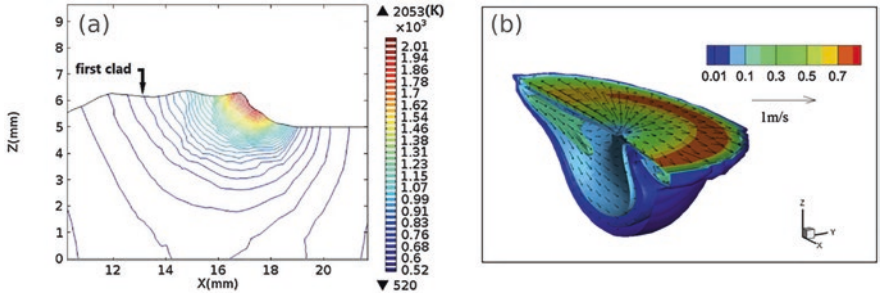

Fig. 3.4 Snapshots of the output results for the temperature and velocity fields during laser cladding by direct metal deposition, obtained by FEM simulations. (**a**) Cross section showing isothermal contours of the temperature during laser cladding of nickel alloy 625 powder mixed with nano-CeO_2 on AISI 4140 (Fayaz and Kazemzadeh, 2018). (**b**) Distribution of the velocity fields during multilayer laser additive manufacturing of Ni-based alloy on cast iron (Gan et al. 2017)

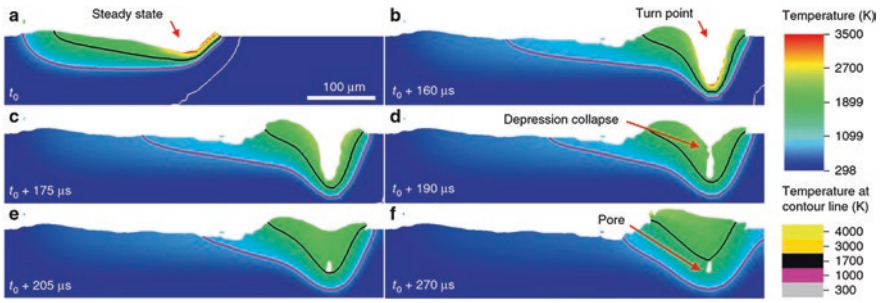

Fig. 3.5 Cross section of 3D multi-physics simulations of a pore formation and depression at turn point during an L-PBF process. (**a–f**) show evolution of a single frame of the simulation at different time steps. The color map describes the thermal gradients in the material and the black contour line represents the melt-pool boundary. The image is adapted from Martin et al. (2019)

There have been a number of reports on the use of in situ and real-time techniques as attempts to understand the underlying interactions during AM processes, mostly focusing on measurements of the temperature as well as geometry of the melt pool. For a review on this topic, see for example, Everton et al. (2016).

Depending on the processing conditions, temperature (Tapia and Elwany 2014) can be controlled by use of pyrometers (Fathi et al. 2008; Rodriguez et al. 2015) such as digital cameras and photodiodes, and also by thermocouples (Heigel et al. 2015). In contrast to the thermocouples that are usually preplaced in the substrate and are in contact only with the first layer, flexibility in positioning of the pyrometers enables noncontact measurements at the surface of the desired regions during the process. Now both pyrometers and thermocouples are commonly used.

Due to local accumulation of the heat in some regions as well as the nonhomogeneous heating and cooling cycles, dynamics of the melt pool may not remain uniform and can highly vary during the processing, which could further degrade final component quality. Direct observation of the geometry of the melt pool can be performed by use of high-speed cameras that can probe subsurface phenomena by capturing many successive images of the process in a short amount of time.

In a recent report, in situ transmission X-ray imaging was applied to probe laser–metal interactions and elucidate the mechanisms leading to the keyhole pore formation and depression at a turn point during L-PBF processing of Ti–6Al–4 V (Martin et al. 2019). In another recent work by Wirth et al., dynamics of the melt pool in laser cladding by direct metal deposition was analyzed based on evaluation of the images captured by an automated high-speed camera (see left panel in Fig. 3.6). In their experiment, the structural steel S235JRC + C was used as the substrate material and a mixture of 1% by weight of titanium carbide particles and 99% MetcoClad® 625 as the deposited powder (Wirth et al. 2018).

In addition to the imaging techniques, spectroscopy-based techniques can also be applied for the monitoring and control of the AM processes. Lednev et al. (see the right panel in Fig. 3.6) reported on the first use of laser-induced breakdown spectroscopy (LIBS) to perform in situ quantitative multielemental analysis during laser

Table 3.4 Selected studies on the different approaches to model DED process

Performance characteristics	Modeling approach			
	analytical	numerical	both	Reference (s)
Surface roughness related	×			Gharbi et al. (2013)
		×		Morville et al. (2012)
Topology and dimensional accuracy related	×			Ahsan et al. (2011), Lin (1999), Pinkerton and Li (2004)
		×		Adalsteinsson and Sethian (1995), Li et al. (2012), Morville et al. (2012), Mughal et al. (2006), Mukherjee et al. (2017), Zhang et al. (2006)
			×	Ahsan and Pinkerton, (2011), Peyre et al. (2008)
Mechanical properties and microstructure related	×			Ahsan et al. (2011), Lin (1999)
		×		Costa et al. (2005), Ghosh and Choi (2005), Kumar et al. (2010), Yang and Wang (2009)
			×	Ahsan and Pinkerton (2011), Crespo (2011)
Droplet kinematics and flow phenomena related	×			Dhiman and Chandra (2005), Shakeri and Chandra (2002)
		×		Bussmann et al. (2000), Fachinotti et al. (2012) Kumar et al. (2010), Li et al. (2012), Lim et al. (2009) Pasandideh-Fard et al. (1998, 2002), Tian et al. (2008), Zhou et al. (2013)
Heat transfer + other characteristics related	×			Pinkerton (2007)
		×		Ding et al. (2014), Fachinotti et al. (2012), Foroozmehr and Kovacevic (2010), Ghosh and Choi (2005), Kumar et al. (2010), Li et al. (2012), Michaleris (2014), Mughal et al. (2006), Mukherjee et al. (2017), Pasandideh-Fard et al. (1998), Roberts et al. (2009)
			×	Ahsan and Pinkerton, (2011), Peyre et al. (2008)
Heat transfer (exclusively)		×		Bai et al. (2013), Kelly and Kampe (2004), Qi et al. (2006)

cladding by additive manufacturing to characterize the melt-pool dynamics (Lednev et al. 2019).

Additionally, laser displacement sensor, as another monitoring technique, has been used for in situ distortion measurements during AM processes (Heigel et al.

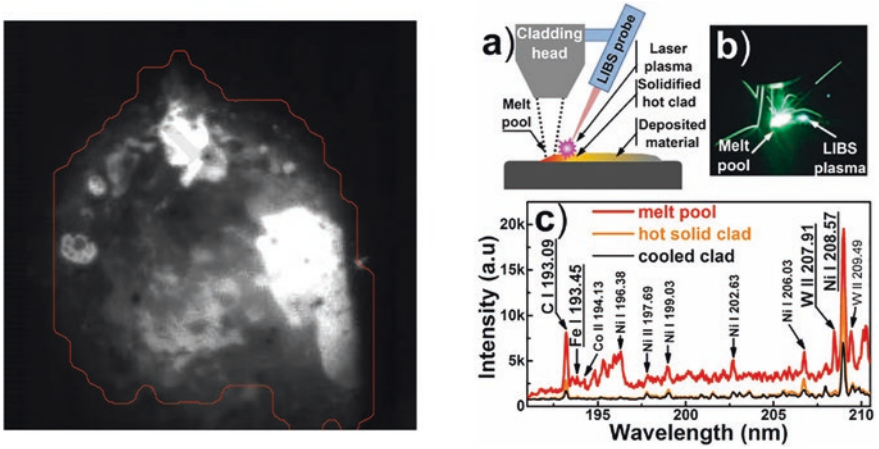

Fig. 3.6 (left panel): High-speed camera image together with the border of the detected metal powder particle obtained during laser cladding by direct metal deposition where the structural steel S235JRC + C and a mixture of 1% by weight of titanium carbide particles and 99% MetcoClad® 625 were used as the substrate and powder, respectively (Wirth et al. 2018). (Right panel): in situ elemental analysis of laser cladding by DED using laser-induced breakdown spectroscopy (LIBS); (**a**) scheme of sampling zones, (**b**) photograph taken during hot solid clad sampling by LIBS, (**c**) plasma spectra for different sampling spots (Lednev et al. 2019)

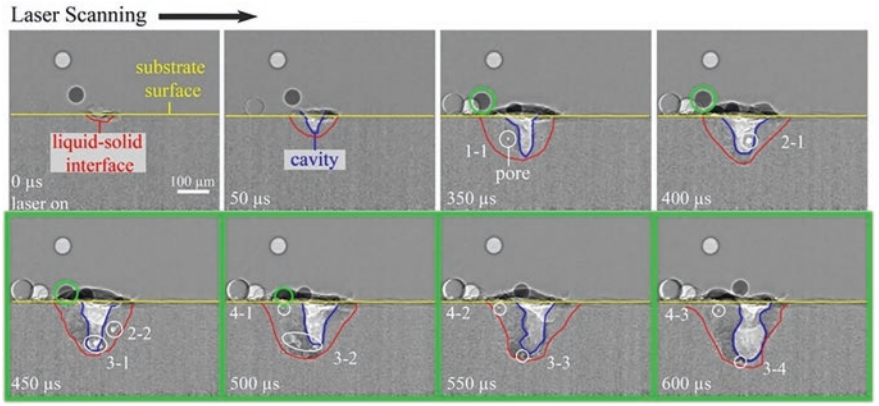

Fig. 3.7 Image frames captured by a high-speed camera for in situ monitoring of the cavity, melt pool, and porosity evolution as mass was added during a laser cladding by AM process (laser power of 250 W and a scan speed of 100 mm/s) using a piezo-driven powder delivery system (Wolff et al. 2019)

2015). Moreover, improved powder delivery systems such as a piezo-driven system have also been used together with high-speed camera for better understanding of the melt pool and evolution of porosity (see Fig. 3.7), allowing in situ monitoring of the cladding process by AM (Wolff et al. 2019).

Finally, to ensure the consistency and quality of the additively manufactured components, big data generated during sensing approaches and nondestructive evaluations is needed to be collected and analyzed, requiring highly efficient and powerful computations. By revealing real-time and accurate information on the laser additive manufacturing processes, the technology is now smarter, more robust and more suitable for industrial applications (Mazumder 2015).

3.4 Further Aspects of AM for Metals: Industrial Market and Current Challenges

3.4.1 Industrial Market: History and Outlook

The field of metal AM has experienced significant growth over the past decades with considerable attention received both from academia and industry (particularly, the aerospace, medical devices, automotive, and defense sectors). The investments and pulls by various giant industry leaders to improve and capitalize the value-added properties of the fabricated components have undoubtedly accelerated the evolution and implementation of metal AM technology. Selected major technological events (achievements and investments) that are mostly relevant to the commercialization of metal additive manufacturing are displayed in a timeline in Fig. 3.8.

With the fast development of AM techniques, intensive efforts have also been made to incorporate the technology into real commercial systems. In Table 3.5, the commercial systems that are already available in the market for additive manufacturing of metals are listed and categorized based on the ASTM classification.

The increasing number of machines sold and the number of produced components can be considered as indicators of the growing use of AM technology for production applications. According to the most recent Wohlers report (Wohlers Report 2019), the sale of AM products and services could likely exceed US$23.9 billion worldwide by 2022, and reach US$35.6 billion by 2024 (see Fig. 3.9). Moreover,

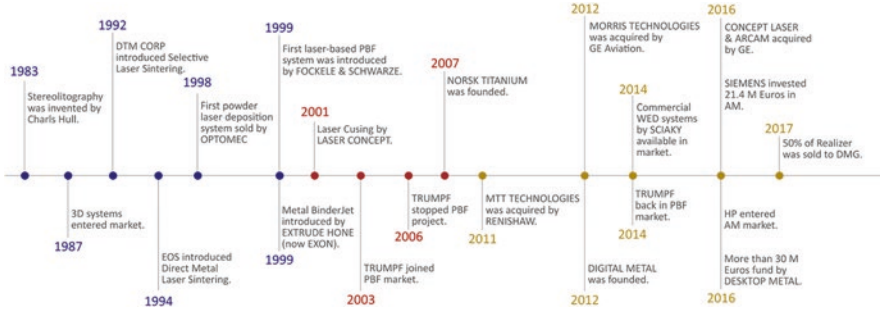

Fig. 3.8 Timeline depicting the major technological events (achievements and investments) toward commercialization of metal additive manufacturing

Table 3.5 Commercial systems already available for additive manufacturing of metals

Manufacturer	ASTM classification	Commercial name	Heat source
Concept Laser	PBF	SLM	Fiber laser
Sisma	PBF	LMF	Fiber laser
SLM Solutions	PBF	SLM	Fiber laser
Matsuura	PBF	SLM	
Realizer	PBF	SLM	Fiber laser
Renishaw	PBF	LM	Optical fiber
Farsoon	PBF	MLS	Yb-fiber laser
EOS	PBF	DMLS	Yb-fiber laser
Arcam AB	PBF	EBM	Electron beam
Phenix (3D Systems)	PBF	SLS	Fiber laser
Optomec	DED	LENS	IPG fiber laser
Sciaky	DED (wire-fed)	EBDM	Electron beam
Trumpf	PBF/ DED (powder-fed)	LD	
DM3D Technology	DED	DMD	Diode/disc/fiber laser
Accufusion	DED	LC	Nd:YAG laser
Irepa Laser	DED	LD	
ExOne	Binder Jet		
Fabrisonic	Sheet Lamination		Ultrasonic vibration sonotrode

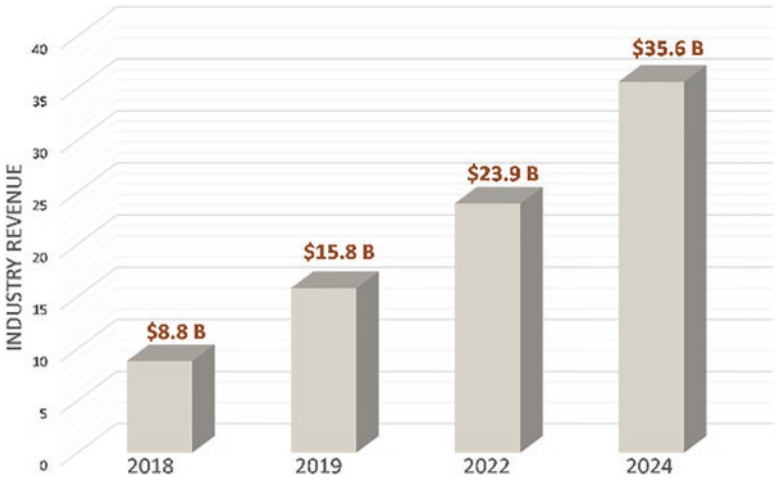

Fig. 3.9 Estimated market value for additive manufacturing

revenue from metals is estimated to grow 41.9%, continuing a five-year streak of more than 40% growth each year.

Many interesting promising impacts are provisioned for industrial implementation of AM, such as feasibility to print on demand with reduced lead-time, capacity to create parts with high-level of shape-complexity, reduction in weight and part count, ease of design modification, improved prototyping abilities, potential cost-effectiveness, potential environmental efficiency, etc. Thus, industrial leaders are motivated to actively invest toward improving readiness and sustainment of AM technologies. As industrial examples of AM technology, images of an additively manufactured fuel nozzle (already being used in a LEAP engine for aerospace application) by GE and a hybrid manufactured closed impeller by Sulzer are shown in Fig. 3.10.

Despite recent progresses, however, there are still many problems in the field of metal AM, resulting in the reduction of the process accuracy and the rate of qualified components. Thus, to fully realize the potential of the AM technology, particularly in fracture-critical applications (e.g., aerospace, biomedical, and automotive parts), extensive research and development efforts are needed to address and resolve the current challenges in the field, keeping the scientists and engineers busy in the foreseeable future.

Fig. 3.10 (Top panel): Image of an already flying additively manufactured fuel nozzle (Courtesy of GE Additive). | (Bottom panel): Hybrid manufacturing of a closed impeller by combination of DED and subtractive milling. (Courtesy of Sulzer)

3.4.2 Current Challenges

Despite the substantial progresses that have been made in the understanding and development of metal additive manufacturing, there are still major scientific, technological and economic challenges to overcome in this field (DebRoy et al. 2019) and researchers are now encouraged to fill the current knowledge gaps associated with these challenges.

Scientific challenges rise from a more fundamental level due to the complicated thermal processes that occur during each AM technique causing formation of defects and some microstructure features that can affect properties and functionality of the additively manufactured parts. Scientific challenges such as the complex relationships between processing, microstructure, properties and performance of the printed components (Mukherjee and DebRoy 2019), control of the microstructure (Liu et al. 2018; Wu and Fan 2020), formation of defects (Bisht et al. 2018; Martin et al. 2019), solidification structure (Mukherjee and DebRoy 2019), and the grain structure and topology (Hitzler et al. 2018) can be addressed as the main pertinent challenges that need to be resolved.

Moreover, progress toward the full implementation of AM in industry has been slowed down due to the current existing technological challenges. Issues such as qualifications and certification, geometric limitations and complexities, scale-up of the building strategies, process design and printing sequence, post-processing as well as safety and health are the main targets that need to be resolved from the technology perspective.

Additionally, economic challenges such as cost competitiveness, low market share, lack of standards, compatibility of the feedstock material, intellectual property and cyber-security, as well as the severe lack of practical and targeted guidance for AM processing are currently assumed as the major barriers to the improvement of the AM technology from economic aspects. Ironically, while the association between the full implementation of AM and economic benefits for the industry is very promising, these barriers can affect the current acceleration of the technology. The above-discussed critical challenges to the rapid and widespread deployment of metal additive manufacturing are presented in Fig. 3.11. A question can now arise as how these three categories of challenges are interconnected and to what extent they have impacts, particularly on the development and implementation of metal additive manufacturing. To address this in detail, further research and exploration need to be performed. For more insights on these challenges and the potential solutions, see Bonnín Roca et al. (2016) and DebRoy et al. (2019).

To sum, the scientific, technological, and economic challenges constitute areas in which researcher, engineers, and decision makers need to cooperate effectively in order to further expand implementation of AM and build up a smarter and more sustainable framework for manufacturing.

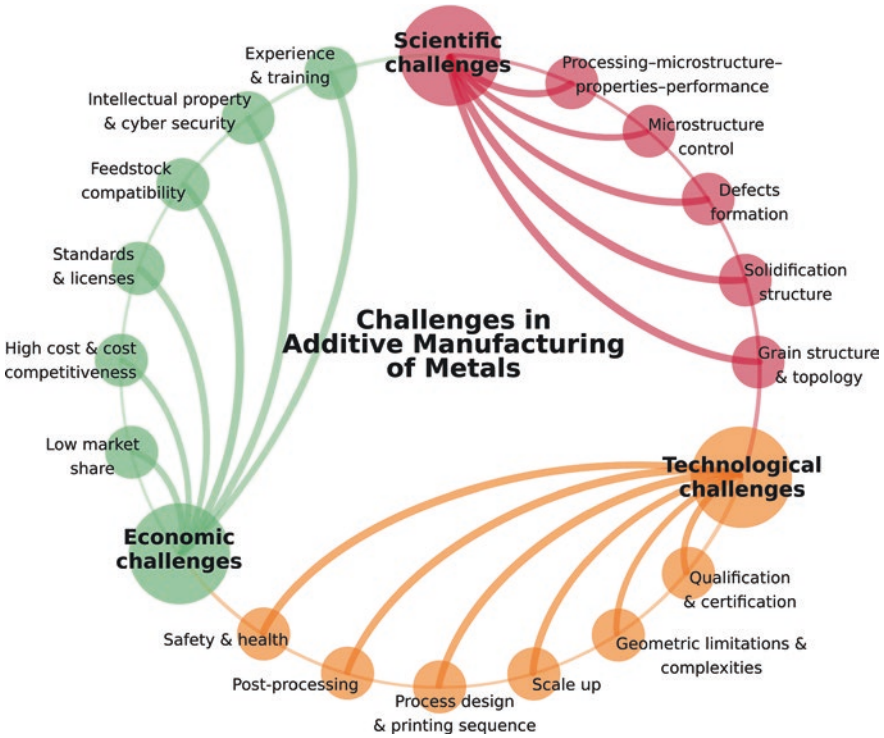

Fig. 3.11 Current scientific, technological, and economic challenges in the field of additive manufacturing of metals. The challenges are not listed in any particular order or assumed priority

3.5 Conclusion

AM is one of the most promising technologies in the field of manufacturing that allows processing of a wide spectrum of materials with improved or at least similar mechanical properties as those of their cast counterparts. AM technology is directing toward cost-optimization, value-addition, and sustainability, thus, receiving considerable interest from both industry and academia. So far, different AM processing techniques have already been in use for 3D fabrication of metallic components, none of them is without limitations, either in terms of material compatibility, accessible feature sizes and the integrability of diverse functional components. This makes development of robust in situ monitoring techniques and implementation of closed loop process controls to prequalify parts before post-processing and/or assembly, a necessity for further development of the technology (Mazumder 2015).

Laser cladding or laser-based direct energy deposition, as an additive manufacturing technique with excellent net-shape manufacturing capacity and more enhanced integrated closed loop control, is now considered as a state-of-the-art

solution for many applications, that is, hybrid manufacturing/remanufacturing and fabrication of functionally graded materials, etc.

The deeper understanding of the metal AM processes together with the implementation of smart optimization techniques will surely bring more added-value to the manufacturing industry and facilitate its penetration into the market. However, as technology evolves, so do challenges. Therefore, acquiring adequate knowledge and experience through collective efforts from scientists, engineers, and decision makers is needed to resolve the scientific, technological, and economic issues associated with metal additive manufacturing.

Acknowledgments The authors wish to gratefully acknowledge the help from Setareh Zakeri to improve the graphics of some figures.

References

Adalsteinsson, D., & Sethian, J. A. (1995). A level set approach to a unified model for etching, deposition, and lithography I: Algorithms and two-dimensional simulations. *Journal of Computational Physics, 120*(1), 128–144. https://doi.org/10.1006/jcph.1995.1153.

Ahsan, N., & Khoda, B. (2016). AM optimization framework for part and process attributes through geometric analysis. *Additive Manufacturing, 11*, 85–96. https://doi.org/10.1016/j.addma.2016.05.013.

Ahsan, M. N., & Pinkerton, A. J. (2011). An analytical–numerical model of laser direct metal deposition track and microstructure formation. *Modelling and Simulation in Materials Science and Engineering, 19*(5), 055003. https://doi.org/10.1088/0965-0393/19/5/055003.

Ahsan, M. N., Paul, C. P., Kukreja, L. M., & Pinkerton, A. J. (2011). Porous structures fabrication by continuous and pulsed laser metal deposition for biomedical applications; modelling and experimental investigation. *Journal of Materials Processing Technology, 211*(4), 602–609. https://doi.org/10.1016/j.jmatprotec.2010.11.014.

Bai, X., Zhang, H., & Wang, G. (2013). Improving prediction accuracy of thermal analysis for weld-based additive manufacturing by calibrating input parameters using IR imaging. *International Journal of Advanced Manufacturing Technology, 69*(5), 1087–1095. https://doi.org/10.1007/s00170-013-5102-y.

Bauereiß, A., Scharowsky, T., & Körner, C. (2014). Defect generation and propagation mechanism during additive manufacturing by selective beam melting. *Journal of Materials Processing Technology, 214*(11), 2522–2528. https://doi.org/10.1016/j.jmatprotec.2014.05.002.

Bax, B., Rajput, R., Kellet, R., & Reisacher, M. (2018). Systematic evaluation of process parameter maps for laser cladding and directed energy deposition. *Additive Manufacturing, 21*, 487–494. https://doi.org/10.1016/j.addma.2018.04.002.

Bisht, M., Ray, N., Verbist, F., & Coeck, S. (2018). Correlation of selective laser melting-melt pool events with the tensile properties of Ti-6Al-4V ELI processed by laser powder bed fusion. *Additive Manufacturing, 22*, 302–306. https://doi.org/10.1016/j.addma.2018.05.004.

Bonnín Roca, J., Vaishnav, P., Fuchs, E. R. H., & Morgan, M. G. (2016). Policy needed for additive manufacturing. *Nature Materials, 15*(8), 815–818. https://doi.org/10.1038/nmat4658.

Brandl, E., Schoberth, A., & Leyens, C. (2012). Morphology, microstructure, and hardness of titanium (Ti-6Al-4V) blocks deposited by wire-feed additive layer manufacturing (ALM). *Materials Science and Engineering A, 532*, 295–307. https://doi.org/10.1016/j.msea.2011.10.095.

Buchanan, C., & Gardner, L. (2019). Metal 3D printing in construction: A review of methods, research, applications, opportunities and challenges. *Engineering Structures, 180*, 332–348. https://doi.org/10.1016/j.engstruct.2018.11.045.

Burns, M., & Wangenheim, C. (2019, March 15). *Metal 3D printing applications in the oil & gas industry*. Paper presented at the SPE Middle East Oil and Gas Show and Conference, Manama, Bahrain

Bussmann, M., Chandra, S., & Mostaghimi, J. (2000). Modeling the splash of a droplet impacting a solid surface. *Physics of Fluids, 12*(12), 3121–3132. https://doi.org/10.1063/1.1321258.

Costa, L., Vilar, R., Reti, T., & Deus, A. M. (2005). Rapid tooling by laser powder deposition: Process simulation using finite element analysis. *Acta Materialia, 53*(14), 3987–3999. https://doi.org/10.1016/j.actamat.2005.05.003.

Crespo, A. N. (2011). Modelling of heat transfer and phase transformations in the rapid manufacturing of titanium components. In A. Ahsan (Ed.), *Convection and conduction heat transfer*. Rijeka: IntechOpen. https://doi.org/10.5772/19836.

DebRoy, T., Wei, H. L., Zuback, J. S., Mukherjee, T., Elmer, J. W., Milewski, J. O., et al. (2018). Additive manufacturing of metallic components – Process, structure and properties. *Progress in Materials Science, 92*, 112–224. https://doi.org/10.1016/j.pmatsci.2017.10.001.

DebRoy, T., Mukherjee, T., Milewski, J. O., Elmer, J. W., Ribic, B., Blecher, J. J., et al. (2019). Scientific, technological and economic issues in metal printing and their solutions. *Nature Materials, 18*(10), 1026–1032. https://doi.org/10.1038/s41563-019-0408-2.

Dhiman, R., & Chandra, S. (2005). Freezing-induced splashing during impact of molten metal droplets with high Weber numbers. *International Journal of Heat and Mass Transfer, 48*(25), 5625–5638. https://doi.org/10.1016/j.ijheatmasstransfer.2005.05.044.

Ding, J., Colegrove, P., Mehnen, J., Williams, S., Wang, F., & Almeida, P. S. (2014). A computationally efficient finite element model of wire and arc additive manufacture. *International Journal of Advanced Manufacturing Technology, 70*(1), 227–236. https://doi.org/10.1007/s00170-013-5261-x.

Ding, D., Pan, Z., Cuiuri, D., & Li, H. (2015). Wire-feed additive manufacturing of metal components: Technologies, developments and future interests. *International Journal of Advanced Manufacturing Technology, 81*(1), 465–481. https://doi.org/10.1007/s00170-015-7077-3.

Everton, S. K., Hirsch, M., Stravroulakis, P., Leach, R. K., & Clare, A. T. (2016). Review of in-situ process monitoring and in-situ metrology for metal additive manufacturing. *Materials and Design, 95*, 431–445. https://doi.org/10.1016/j.matdes.2016.01.099.

Fachinotti, V. D., Cardona, A., Baufeld, B., & Van der Biest, O. (2012). Finite-element modelling of heat transfer in shaped metal deposition and experimental validation. *Acta Materialia, 60*(19), 6621–6630. https://doi.org/10.1016/j.actamat.2012.08.031.

Fasel, U., Keidel, D., Baumann, L., Cavolina, G., Eichenhofer, M., & Ermanni, P. (2020). Composite additive manufacturing of morphing aerospace structures. *Manufacturing Letters, 23*, 85–88. https://doi.org/10.1016/j.mfglet.2019.12.004.

Fathi, A., Khajepour, A., Durali, M., & Toyserkani, E. (2008). Geometry control of the deposited layer in a nonplanar laser cladding process using a variable structure controller. *Journal of Manufacturing Science and Engineering, 130*(3). https://doi.org/10.1115/1.2823085.

Fayaz, G., & Kazemzadeh, S. (2018). Towards additive manufacturing of compressor impellers: 3D modeling of multilayer laser solid freeform fabrication of nickel alloy 625 powder mixed with nano-CeO2 on AISI 4140. *Additive Manufacturing, 20*, 182–188. https://doi.org/10.1016/j.addma.2018.02.001.

Foroozmehr, E., & Kovacevic, R. (2010). Effect of path planning on the laser powder deposition process: Thermal and structural evaluation. *International Journal of Advanced Manufacturing Technology, 51*(5), 659–669. https://doi.org/10.1007/s00170-010-2659-6.

Frazier, W. E. (2014). Metal additive manufacturing: A review. *Journal of Materials Engineering and Performance, 23*(6), 1917–1928. https://doi.org/10.1007/s11665-014-0958-z.

Froes, F. H., & Boyer, R. (2019). *Additive manufacturing for the aerospace industry*. Amsterdam: Elsevier Science.

Gan, Z., Liu, H., Li, S., He, X., & Yu, G. (2017). Modeling of thermal behavior and mass transport in multi-layer laser additive manufacturing of Ni-based alloy on cast iron. *International Journal of Heat and Mass Transfer, 111*, 709–722. https://doi.org/10.1016/j.ijheatmasstransfer.2017.04.055.

Gharbi, M., Peyre, P., Gorny, C., Carin, M., Morville, S., Le Masson, P., et al. (2013). Influence of various process conditions on surface finishes induced by the direct metal deposition laser technique on a Ti–6Al–4V alloy. *Journal of Materials Processing Technology, 213*(5), 791–800. https://doi.org/10.1016/j.jmatprotec.2012.11.015.

Ghosh, S., & Choi, J. (2005). Three-dimensional transient finite element analysis for residual stresses in the laser aided direct metal/material deposition process. *Journal of Laser Applications, 17*(3), 144–158. https://doi.org/10.2351/1.1961688.

Grasso, M., & Colosimo, B. M. (2017). Process defects andin situmonitoring methods in metal powder bed fusion: A review. *Measurement Science and Technology, 28*(4), 044005. https://doi.org/10.1088/1361-6501/aa5c4f.

Guan, X., & Zhao, Y. F. (2020). Modeling of the laser powder–based directed energy deposition process for additive manufacturing: A review. *International Journal of Advanced Manufacturing Technology*. https://doi.org/10.1007/s00170-020-05027-0.

He, X., & Mazumder, J. (2007). Transport phenomena during direct metal deposition. *Journal of Applied Physics, 101*(5), 053113. https://doi.org/10.1063/1.2710780.

Heigel, J. C., Michaleris, P., & Reutzel, E. W. (2015). Thermo-mechanical model development and validation of directed energy deposition additive manufacturing of Ti–6Al–4V. *Additive Manufacturing, 5*, 9–19. https://doi.org/10.1016/j.addma.2014.10.003.

Heralić, A., Christiansson, A.-K., & Lennartson, B. (2012). Height control of laser metal-wire deposition based on iterative learning control and 3D scanning. *Optics and Lasers in Engineering, 50*(9), 1230–1241. https://doi.org/10.1016/j.optlaseng.2012.03.016.

Herzog, D., Seyda, V., Wycisk, E., & Emmelmann, C. (2016). Additive manufacturing of metals. *Acta Materialia, 117*, 371–392. https://doi.org/10.1016/j.actamat.2016.07.019.

Hitzler, L., Merkel, M., Hall, W., & Öchsner, A. (2018). A review of metal fabricated with laser- and powder-bed based additive manufacturing techniques: Process, nomenclature, materials, achievable properties, and its utilization in the medical sector. *Advanced Engineering Materials, 20*(5), 1700658. https://doi.org/10.1002/adem.201700658.

Huang, Y., Khamesee, M. B., & Toyserkani, E. (2016). A comprehensive analytical model for laser powder-fed additive manufacturing. *Additive Manufacturing, 12*, 90–99. https://doi.org/10.1016/j.addma.2016.07.001.

Huang, Y., Khamesee, M. B., & Toyserkani, E. (2019). A new physics-based model for laser directed energy deposition (powder-fed additive manufacturing): From single-track to multi-track and multi-layer. *Optics and Laser Technology, 109*, 584–599. https://doi.org/10.1016/j.optlastec.2018.08.015.

Jin, W., Zhang, C., Jin, S., Tian, Y., Wellmann, D., & Liu, W. (2020). Wire arc additive manufacturing of stainless steels: A review. *Applied Sciences, 10*(5). https://doi.org/10.3390/app10051563.

Kakinuma, Y., Mori, M., Oda, Y., Mori, T., Kashihara, M., Hansel, A., et al. (2016). Influence of metal powder characteristics on product quality with directed energy deposition of Inconel 625. *CIRP Annals, 65*(1), 209–212. https://doi.org/10.1016/j.cirp.2016.04.058.

Keist, J. S., & Palmer, T. A. (2016). Role of geometry on properties of additively manufactured Ti-6Al-4V structures fabricated using laser based directed energy deposition. *Materials and Design, 106*, 482–494. https://doi.org/10.1016/j.matdes.2016.05.045.

Kelly, S. M., & Kampe, S. L. (2004). Microstructural evolution in laser-deposited multilayer Ti-6Al-4V builds: Part II. Thermal modeling. *Metallurgical and Materials Transactions A, 35*(6), 1869–1879. https://doi.org/10.1007/s11661-004-0095-7.

Khairallah, S. A., & Anderson, A. (2014). Mesoscopic simulation model of selective laser melting of stainless steel powder. *Journal of Materials Processing Technology, 214*(11), 2627–2636. https://doi.org/10.1016/j.jmatprotec.2014.06.001.

Khairallah, S. A., Anderson, A. T., Rubenchik, A., & King, W. E. (2016). Laser powder-bed fusion additive manufacturing: Physics of complex melt flow and formation mechanisms of pores, spatter, and denudation zones. *Acta Materialia, 108*, 36–45. https://doi.org/10.1016/j.actamat.2016.02.014.

King, W. E., Barth, H. D., Castillo, V. M., Gallegos, G. F., Gibbs, J. W., Hahn, D. E., et al. (2014). Observation of keyhole-mode laser melting in laser powder-bed fusion additive manufacturing. *Journal of Materials Processing Technology, 214*(12), 2915–2925. https://doi.org/10.1016/j.jmatprotec.2014.06.005.

Klassen, A., Scharowsky, T., & Körner, C. (2014). Evaporation model for beam based additive manufacturing using free surface lattice Boltzmann methods. *Journal of Physics D: Applied Physics, 47*(27), 275303. https://doi.org/10.1088/0022-3727/47/27/275303.

Kumar, A., Ghosh, S., & Dhindaw, B. K. (2010). Simulation of cooling of liquid Al–33wt.% Cu droplet impinging on a metallic substrate and its experimental validation. *Acta Materialia, 58*(1), 122–133. https://doi.org/10.1016/j.actamat.2009.08.063.

Leal, R., Barreiros, F. M., Alves, L., Romeiro, F., Vasco, J. C., Santos, M., et al. (2017). Additive manufacturing tooling for the automotive industry. *International Journal of Advanced Manufacturing Technology, 92*(5), 1671–1676. https://doi.org/10.1007/s00170-017-0239-8.

Lednev, V. N., Sdvizhenskii, P. A., Asyutin, R. D., Tretyakov, R. S., Grishin, M. Y., Stavertiy, A. Y., et al. (2019). In situ multi-elemental analysis by laser induced breakdown spectroscopy in additive manufacturing. *Additive Manufacturing, 25*, 64–70. https://doi.org/10.1016/j.addma.2018.10.043.

Lee, Y., Nordin, M., Babu, S. S., & Farson, D. F. (2014). Effect of fluid convection on dendrite arm spacing in laser deposition. *Metallurgical and Materials Transactions B: Process Metallurgy and Materials Processing Science, 45*(4), 1520–1529. https://doi.org/10.1007/s11663-014-0054-7.

Lee, H., Lim, C. H. J., Low, M. J., Tham, N., Murukeshan, V. M., & Kim, Y.-J. (2017). Lasers in additive manufacturing: A review. *International Journal of Precision Engineering and Manufacturing-Green Technology, 4*(3), 307–322. https://doi.org/10.1007/s40684-017-0037-7.

Lewandowski, J. J., & Seifi, M. (2016). Metal additive manufacturing: A review of mechanical properties. *Annual Review of Materials Research, 46*(1), 151–186. https://doi.org/10.1146/annurev-matsci-070115-032024.

Li, H., Wang, P., Qi, L., Zuo, H., Zhong, S., & Hou, X. (2012). 3D numerical simulation of successive deposition of uniform molten Al droplets on a moving substrate and experimental validation. *Computational Materials Science, 65*, 291–301. https://doi.org/10.1016/j.commatsci.2012.07.034.

Lim, T., Han, S., Chung, J., Chung, J. T., Ko, S., & Grigoropoulos, C. P. (2009). Experimental study on spreading and evaporation of inkjet printed pico-liter droplet on a heated substrate. *International Journal of Heat and Mass Transfer, 52*(1), 431–441. https://doi.org/10.1016/j.ijheatmasstransfer.2008.05.028.

Lin, J. (1999). A simple model of powder catchment in coaxial laser cladding. *Optics and Laser Technology, 31*(3), 233–238. https://doi.org/10.1016/S0030-3992(99)00046-8.

Liu, L., Ding, Q., Zhong, Y., Zou, J., Wu, J., Chiu, Y.-L., et al. (2018). Dislocation network in additive manufactured steel breaks strength–ductility trade-off. *Materials Today, 21*(4), 354–361. https://doi.org/10.1016/j.mattod.2017.11.004.

Manvatkar, V., De, A., & DebRoy, T. (2014). Heat transfer and material flow during laser assisted multi-layer additive manufacturing. *Journal of Applied Physics, 116*(12), 124905. https://doi.org/10.1063/1.4896751.

Manvatkar, V., De, A., & DebRoy, T. (2015). Spatial variation of melt pool geometry, peak temperature and solidification parameters during laser assisted additive manufacturing process. *Materials Science and Technology, 31*(8), 924–930. https://doi.org/10.1179/1743284714Y.0000000701.

Martin, J. H., Yahata, B. D., Hundley, J. M., Mayer, J. A., Schaedler, T. A., & Pollock, T. M. (2017). 3D printing of high-strength aluminium alloys. *Nature, 549*(7672), 365–369. https://doi.org/10.1038/nature23894.

Martin, A. A., Calta, N. P., Khairallah, S. A., Wang, J., Depond, P. J., Fong, A. Y., et al. (2019). Dynamics of pore formation during laser powder bed fusion additive manufacturing. *Nature Communications, 10*(1), 1987. https://doi.org/10.1038/s41467-019-10009-2.

Mazumder, J. (2015). Design for metallic additive manufacturing machine with Capability for "Certify as You Build". *Procedia CIRP, 36*, 187–192. https://doi.org/10.1016/j.procir.2015.01.009.

Melchels, F. P. W., Domingos, M. A. N., Klein, T. J., Malda, J., Bartolo, P. J., & Hutmacher, D. W. (2012). Additive manufacturing of tissues and organs. *Progress in Polymer Science, 37*(8), 1079–1104. https://doi.org/10.1016/j.progpolymsci.2011.11.007.

Michaleris, P. (2014). Modeling metal deposition in heat transfer analyses of additive manufacturing processes. *Finite Elements in Analysis and Design, 86*, 51–60. https://doi.org/10.1016/j.finel.2014.04.003.

Milewski, J. O. (2017). *Additive manufacturing of metals: From fundamental technology to rocket nozzles, medical implants, and custom jewelry*. Cham: Springer International Publishing.

Morville, S., Carin, M., Peyre, P., Gharbi, M., Carron, D., Le Masson, P., et al. (2012). 2D longitudinal modeling of heat transfer and fluid flow during multilayered direct laser metal deposition process. *Journal of Laser Applications, 24*(3), 032008. https://doi.org/10.2351/1.4726445.

Moser, D., Pannala, S., & Murthy, J. (2016). Computation of effective thermal conductivity of powders for selective laser sintering simulations. *Journal of Heat Transfer, 138*(8). https://doi.org/10.1115/1.4033351.

Mughal, M. P., Fawad, H., & Mufti, R. (2006). Finite element prediction of thermal stresses and deformations in layered manufacturing of metallic parts. *Acta Mechanica, 183*(1), 61–79. https://doi.org/10.1007/s00707-006-0329-4.

Mukherjee, T., & DebRoy, T. (2019). A digital twin for rapid qualification of 3D printed metallic components. *Applied Materials Today, 14*, 59–65. https://doi.org/10.1016/j.apmt.2018.11.003.

Mukherjee, T., Zhang, W., & DebRoy, T. (2017). An improved prediction of residual stresses and distortion in additive manufacturing. *Computational Materials Science, 126*, 360–372. https://doi.org/10.1016/j.commatsci.2016.10.003.

Murr, L. E. (2020). Metallurgy principles applied to powder bed fusion 3D printing/additive manufacturing of personalized and optimized metal and alloy biomedical implants: An overview. *Journal of Materials Research and Technology, 9*(1), 1087–1103. https://doi.org/10.1016/j.jmrt.2019.12.015.

Pasandideh-Fard, M., Bhola, R., Chandra, S., & Mostaghimi, J. (1998). Deposition of tin droplets on a steel plate: Simulations and experiments. *International Journal of Heat and Mass Transfer, 41*(19), 2929–2945. https://doi.org/10.1016/S0017-9310(98)00023-4.

Pasandideh-Fard, M., Chandra, S., & Mostaghimi, J. (2002). A three-dimensional model of droplet impact and solidification. *International Journal of Heat and Mass Transfer, 45*(11), 2229–2242. https://doi.org/10.1016/S0017-9310(01)00336-2.

Peyre, P., Aubry, P., Fabbro, R., Neveu, R., & Longuet, A. (2008). Analytical and numerical modelling of the direct metal deposition laser process. *Journal of Physics D: Applied Physics, 41*(2), 025403. https://doi.org/10.1088/0022-3727/41/2/025403.

Picasso, M., Marsden, C. F., Wagniere, J. D., Frenk, A., & Rappaz, M. (1994). A simple but realistic model for laser cladding. *Metallurgical and Materials Transactions B: Process Metallurgy and Materials Processing Science, 25*(2), 281–291. https://doi.org/10.1007/BF02665211.

Pinkerton, A. J. (2007). An analytical model of beam attenuation and powder heating during coaxial laser direct metal deposition. *Journal of Physics D: Applied Physics, 40*(23), 7323–7334. https://doi.org/10.1088/0022-3727/40/23/012.

Pinkerton, A. J., & Li, L. (2004). Modelling the geometry of a moving laser melt pool and deposition track via energy and mass balances. *Journal of Physics D: Applied Physics, 37*(14), 1885–1895. https://doi.org/10.1088/0022-3727/37/14/003.

Pollock, T. M. (2016). Alloy design for aircraft engines. *Nature Materials, 15*(8), 809–815. https://doi.org/10.1038/nmat4709.

Qi, H., Mazumder, J., & Ki, H. (2006). Numerical simulation of heat transfer and fluid flow in coaxial laser cladding process for direct metal deposition. *Journal of Applied Physics, 100*(2), 024903. https://doi.org/10.1063/1.2209807.

Raghavan, A., Wei, H. L., Palmer, T. A., & DebRoy, T. (2013). Heat transfer and fluid flow in additive manufacturing. *Journal of Laser Applications, 25*(5), 052006. https://doi.org/10.2351/1.4817788.

Roberts, I. A., Wang, C. J., Esterlein, R., Stanford, M., & Mynors, D. J. (2009). A three-dimensional finite element analysis of the temperature field during laser melting of metal powders in additive layer manufacturing. *International Journal of Machine Tools and Manufacture, 49*(12), 916–923. https://doi.org/10.1016/j.ijmachtools.2009.07.004.

Rodriguez, E., Mireles, J., Terrazas, C. A., Espalin, D., Perez, M. A., & Wicker, R. B. (2015). Approximation of absolute surface temperature measurements of powder bed fusion additive manufacturing technology using in situ infrared thermography. *Additive Manufacturing, 5*, 31–39. https://doi.org/10.1016/j.addma.2014.12.001.

Sames, W. J., Unocic, K. A., Dehoff, R. R., Lolla, T., & Babu, S. S. (2014). Thermal effects on microstructural heterogeneity of Inconel 718 materials fabricated by electron beam melting. *Journal of Materials Research, 29*(17), 1920–1930. https://doi.org/10.1557/jmr.2014.140.

Schoinochoritis, B., Chantzis, D., & Salonitis, K. (2015). Simulation of metallic powder bed additive manufacturing processes with the finite element method: A critical review. *Proceedings of the Institution of Mechanical Engineers, Part B: Journal of Engineering Manufacture, 231*(1), 96–117. https://doi.org/10.1177/0954405414567522.

Shakeri, S., & Chandra, S. (2002). Splashing of molten tin droplets on a rough steel surface. *International Journal of Heat and Mass Transfer, 45*(23), 4561–4575. https://doi.org/10.1016/S0017-9310(02)00170-9.

Syed, W. U. H., Pinkerton, A. J., & Li, L. (2006). Combining wire and coaxial powder feeding in laser direct metal deposition for rapid prototyping. *Applied Surface Science, 252*(13), 4803–4808. https://doi.org/10.1016/j.apsusc.2005.08.118.

Tammas-Williams, S., Zhao, H., Léonard, F., Derguti, F., Todd, I., & Prangnell, P. B. (2015). XCT analysis of the influence of melt strategies on defect population in Ti–6Al–4V components manufactured by Selective Electron Beam Melting. *Materials Characterization, 102*, 47–61. https://doi.org/10.1016/j.matchar.2015.02.008.

Tapia, G., & Elwany, A. (2014). A review on process monitoring and control in metal-based additive manufacturing. *Journal of Manufacturing Science and Engineering, 136*(6). https://doi.org/10.1115/1.4028540.

Tian, D.-W., Wang, C.-Q., & Tian, Y.-H. (2008). Effect of solidification on solder bump formation in solder jet process: Simulation and experiment. *Transactions of Nonferrous Metals Society of China, 18*(5), 1201–1208. https://doi.org/10.1016/S1003-6326(08)60205-8.

Toyserkani, E., Khajepour, A., & Corbin, S. F. (2004). *Laser cladding*. Boca Raton: CRC Press.

Traxel, K. D., & Bandyopadhyay, A. (2019). First demonstration of additive manufacturing of cutting tools using directed energy deposition system: Stellite™-Based cutting tools. *Additive Manufacturing, 25*, 460–468. https://doi.org/10.1016/j.addma.2018.11.019.

Wen, S., & Shin, Y. C. (2010). Modeling of transport phenomena during the coaxial laser direct deposition process. *Journal of Applied Physics, 108*(4), 044908. https://doi.org/10.1063/1.3474655.

Williams, S. W., Martina, F., Addison, A. C., Ding, J., Pardal, G., & Colegrove, P. (2016). Wire + Arc additive manufacturing. *Materials Science and Technology, 32*(7), 641–647. https://doi.org/10.1179/1743284715Y.0000000073.

Wirth, F., Arpagaus, S., & Wegener, K. (2018). Analysis of melt pool dynamics in laser cladding and direct metal deposition by automated high-speed camera image evaluation. *Additive Manufacturing, 21*, 369–382. https://doi.org/10.1016/j.addma.2018.03.025.

Wohlers Report. (2019). Wohlers Associates, USA.

Wolff, S. J., Wu, H., Parab, N., Zhao, C., Ehmann, K. F., Sun, T., et al. (2019). In-situ high-speed X-ray imaging of piezo-driven directed energy deposition additive manufacturing. *Scientific Reports, 9*(1), 962. https://doi.org/10.1038/s41598-018-36678-5.

Wu, H., & Fan, G. (2020). An overview of tailoring strain delocalization for strength-ductility synergy. *Progress in Materials Science, 113*, 100675. https://doi.org/10.1016/j.pmatsci.2020.100675.

Xiong, J., Lei, Y., Chen, H., & Zhang, G. (2017). Fabrication of inclined thin-walled parts in multi-layer single-pass GMAW-based additive manufacturing with flat position deposition. *Journal of Materials Processing Technology, 240*, 397–403. https://doi.org/10.1016/j.jmatprotec.2016.10.019.

Yang, J., & Wang, F. (2009). 3D finite element temperature field modelling for direct laser fabrication. *International Journal of Advanced Manufacturing Technology, 43*(11), 1060–1068. https://doi.org/10.1007/s00170-008-1785-x.

Yuan, P., & Gu, D. (2015). Molten pool behaviour and its physical mechanism during selective laser melting of TiC/AlSi10Mg nanocomposites: Simulation and experiments. *Journal of Physics D: Applied Physics, 48*(3), 035303. https://doi.org/10.1088/0022-3727/48/3/035303.

Zeng, K., Pal, D., Gong, H. J., Patil, N., & Stucker, B. (2015). Comparison of 3DSIM thermal modelling of selective laser melting using new dynamic meshing method to ANSYS. *Materials Science and Technology, 31*(8), 945–956. https://doi.org/10.1179/1743284714Y.0000000703.

Zhang, H.-O., Kong, F.-R., Wang, G.-L., & Zeng, L.-F. (2006). Numerical simulation of multiphase transient field during plasma deposition manufacturing. *Journal of Applied Physics, 100*(12), 123522. https://doi.org/10.1063/1.2399341.

Zhang, H., Zhu, H., Qi, T., Hu, Z., & Zeng, X. (2016). Selective laser melting of high strength Al–Cu–Mg alloys: Processing, microstructure and mechanical properties. *Materials Science and Engineering A, 656*, 47–54. https://doi.org/10.1016/j.msea.2015.12.101.

Zhang, D., Sun, S., Qiu, D., Gibson, M. A., Dargusch, M. S., Brandt, M., et al. (2018). Metal alloys for fusion-based additive manufacturing. *Advanced Engineering Materials, 20*(5), 1700952. https://doi.org/10.1002/adem.201700952.

Zhao, X., Lin, X., Chen, J., Xue, L., & Huang, W. (2009). The effect of hot isostatic pressing on crack healing, microstructure, mechanical properties of Rene88DT superalloy prepared by laser solid forming. *Materials Science and Engineering A, 504*(1), 129–134. https://doi.org/10.1016/j.msea.2008.12.024.

Zhou, W., Loney, D., Degertekin, F. L., Rosen, D. W., & Fedorov, A. G. (2013). What controls dynamics of droplet shape evolution upon impingement on a solid surface? *AIChE Journal, 59*(8), 3071–3082. https://doi.org/10.1002/aic.14050.

Zocca, A., Colombo, P., Gomes, C. M., & Günster, J. (2015). Additive manufacturing of ceramics: Issues, potentialities, and opportunities. *Journal of the American Ceramic Society, 98*(7), 1983–2001. https://doi.org/10.1111/jace.13700.

Chapter 4
CET Model to Predict the Microstructure of Laser Cladding Materials

M. Renderos, A. Torregaray, M. E. Gutierrez-Orrantia, E. Lacoste, and F. Girot Mata

4.1 Introduction

Despite the clear progress made by laser cladding, it has limitations that mean that this technology has not yet been systematically implemented in many industrial sectors. The current limits are due to (i) the peripheral or complementary processes (prior material handling, post-processing, quality control) that in many cases condition its viability, and (ii) the ignorance of how to design products or successfully reorient industrial activities through the integration of these technologies (Bourell et al. 2009). These limitations are certainly not insuperable, and pose challenges for research, technological development, and innovation, which are being analyzed by teams of researchers and companies around the world.

The case for many metallic materials shows that the available variety of alloys is smaller than for the subtractive and/or shaping methods. In addition, the purchase cost is also higher. These problems of availability and cost of the raw material are inherent to the current low volumes of consumption, since there is a vicious circle of low demand, which does not justify the necessary investment in the production of new materials and the unit cost that discourages the increase of consumption (PNAS 2012). The current problems concern:

M. Renderos (✉) · A. Torregaray · M. E. Gutierrez-Orrantia
Faculty of Engineering, University of the Basque Country, Bilbao, Spain
e-mail: marioalfredo.renderos@ehu.eus; amaia.torregaray@ehu.eus; esther.gutierrez@ehu.eus

E. Lacoste
I2M, University of Bordeaux, Talence, France
e-mail: eric.lacoste@u-bordeaux.fr

F. Girot Mata
Faculty of Engineering, University of the Basque Country, Bilbao, Spain

IKERBASQUE, Basque Foundation for Science, Bilbao, Spain
e-mail: frank.girot@ehu.eus

P. Cavaliere (ed.), *Laser Cladding of Metals*,
https://doi.org/10.1007/978-3-030-53195-9_4

- The surface quality of the parts and the productivity: these aspects are associated, since the productivity influences the finish quality of the surface.
- The quality of the product and the repetitiveness of the process: laser cladding has problems of processing capacity and repetitiveness, that is, they cannot guarantee the dimensional precision with which one part and the next will be manufactured. In the same way, the stability of the physical properties of the product (hardness, elasticity, resistance to traction and fatigue, metallurgy, etc.) is a critical aspect for the qualification of parts and processes in certain sectors (automotive, aeronautics, medical, etc.) (Gibson et al. 2010). It is currently the main problem to relate the microstructure of the component obtained with the parameters of the process and after with the mechanical and physical properties of the product.
- The limited size of the components: the maximum volume of the part that can be done today is limited, although there is an AM process that improves this aspect (WAAM).
- The cost of the equipment: this is a problem similar to the cost of the raw material, and due to the current limited market, the cost of the equipment is a brake on the development of the technology.

Although laser cladding process is currently well controlled from a manufacturing strategy point of view and allows producing healthy components with a low or nonexistent porosity level, the microstructure of the parts obtained by these techniques is far from being understood and controlled. In metals, the grain size and orientation are essential factors for the control of the properties, especially the mechanical properties. The type of solidification (columnar or equiaxed) and the grain size depend on the local solidification conditions (thermal gradient G_L and solidification growth rate V), while the grain orientation is strongly conditioned by epitaxy phenomena based on the current orientation of the substrate microstructure. Therefore, it is common to find stray grains of several sizes (normally from microns to mm) oriented in completely random directions. This leads to traction and/or thermal fatigue properties that may be low compared to the characteristics of the base material, because when the constituents needed for grain boundary strengthening are eliminated the high-temperature creep resistance and thermal fatigue behavior as in nickel-based superalloys is improved (Liu and Qi 2014).

It is therefore very important to be able to model the behavior of the metal during its solidification and to be able to predict what type of solidification will occur and what size of grain will be obtained.

This contribution presents an analytical model of crystallization, growth, and morphology for Inconel 718 during the manufacture or repair of components by laser cladding.

The objective is to correlate the main parameters of this additive manufacturing process with the microstructure generated by them and relate them to the mechanical properties obtained from samples. Emphasis is placed on maintaining the simplicity of the model with the aim of enabling the influence of each of the parameters and their effects to be clarified factor-by-factor.

4.2 State of the Art

Laser cladding has a lot of similarity with the welding processes because in both a small melted area is generated (in this case created via high-power laser), where particles of powder or filler wire are incorporated.

Although there are some publications on solidification conditions in the case of laser cladding (Fayazfar et al. 2018; Ma et al. 2017; Toyserkani et al. 2005; Zhong and Liu 2010), the available literature can be extended using, in this case, the analog process of welding (Anderson 2010; Park et al. 2003; Pinkerton and Li 2004; Vitek et al. 2012).

These processes can have a detrimental effect on the properties of the material, especially in the molten zone, where both the composition (with the filler material) and the microstructure change. In particular, the formation of a completely columnar grain structure in the molten zone results in a very low resistance of that zone at room temperature (Villaret et al. 2013a). It is possible, however, under certain conditions, to modify the morphology of the grains in the molten zone from a columnar to equiaxed structure (Flemings 1974; Greer et al. 2003).

This type of microstructure significantly improves the ductility of the melted zones (Petersen 1973) and lowers the transition temperature (Lakshminarayanan et al. 2009), especially if the grain obtained is small (Bayraktar et al. 2006). This transition from columnar grains to equiaxed grains, called CET (Columnar to Equiaxed Transition), depends on the temperature field and its evolution in the solidification area. Two parameters have a particular importance in the solidification morphology: the thermal gradient G_L in the liquid isotherm solidification front and the growth speed V of this front. It is generally accepted that a decrease in the G_L/V ratio promotes CET (Kurz and Fisher 1998), normally associated with an increase in the constitutional supercooling (Anderson 2010).

The dominant theory to explain CET involves the nucleation and growth of new equiaxed grains in the subcooled liquid near the solidification front that blocks the growth of the columnar grain, by mechanical interaction (Kurz et al. 2001), or by solutal interaction (Martorano et al. 2003). The cooling conditions that promote a high subcooling in the liquid near the solidification front, that is a low G_L/V ratio, favors the nucleation of new equiaxed grains and, consequently, the CET. In laser cladding or welding, an increase in the displacement speed can decrease the G_L/V ratio, thus facilitating the appearance of equiaxed grains and improving the ductility of the melted zone (Bayraktar et al. 2006).

However, the number of nuclei that give equiaxed grains, formed in the subcooled liquid, is controlled mainly by the composition of the molten zone, and especially by the content in some elements that favor the formation of nucleation sites.

Titanium, for example, has a very active role in the morphology of solidification grains for many alloys (Ostrowski and Langer 1979). In the case of ferritic stainless steels, it has been shown that titanium forms intermetallic compounds in the liquid alloy that provide heterogeneous nucleation sites for equiaxed grains (Villaret et al. 2013b) (Fig. 4.1). The exact nature of these compounds is not always identified, and

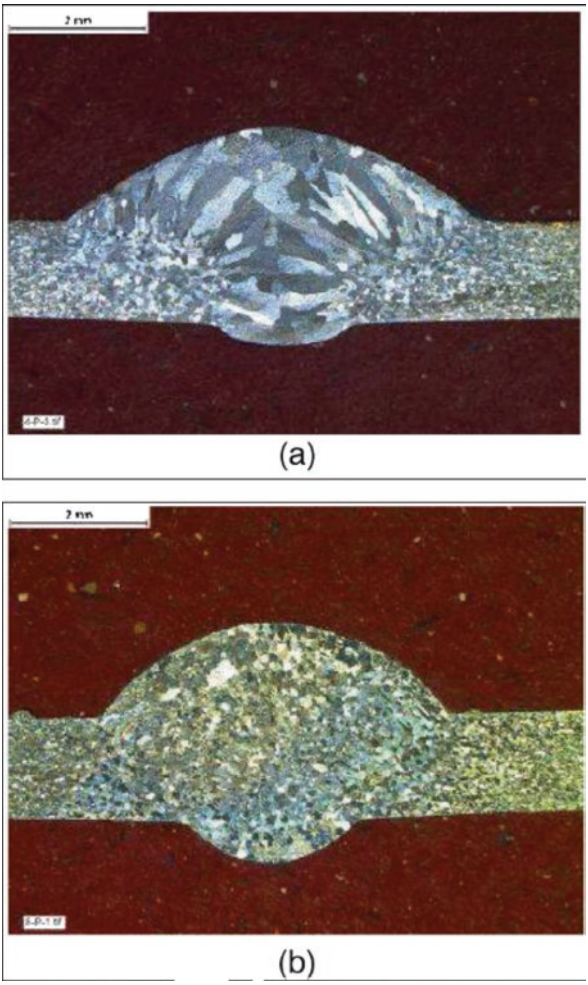

Fig. 4.1 Morphology of the melted zone microstructure for a ferritic stainless steel with 0.07% Ti (**a**), and 0.15%Ti (**b**) (Villaret et al. 2013b)

seems to vary according to the composition and cooling conditions (Villafuerte and Kerr 1990; Villafuerte et al. 1995).

As the grain structure formed in the fusion zone is of paramount importance in the mechanical properties of that area, some models have been developed to try to predict the microstructure formed after welding or laser cladding process.

Models based on cellular automation, generally coupled to the finite element method (CAFE), have been used to predict with fairly good precision the grain structure formed during solidification of ingots (Carozzani et al. 2012; Rappaz et al. 1996), or for the solidification of welds (Chiocca et al. 2015), but it needs a quite long computing time.

By contrast, classical models based on Hunt's theory (Hunt 1984) are simpler methods to predict whether CET occurs or not during solidification (Kurz et al.

2001), but require the preliminary determination of the number of heterogeneous nucleation sites N_0, which is not predictable by the model, and which may change, depending on the cooling rate (Gäumann et al. 1997).

In the Hunt's model of unidirectional steady-state solidification (Hunt 1984), a decrease in nucleation subcooling ΔT_N or an increase in the number of heterogeneous nucleation sites N_0 facilitates blockage of columnar grains and, consequently, the appearance of CET. Likewise, the incorporation of inoculants into the alloys allows the CET to occur earlier compared with alloys without inoculants, confirming the predictions of the Hunt's model (Martorano et al. 2003; Sturz et al. 2005).

The final equation of the Hunt model indicates that the CET occurs when the following condition is achieved (Eq. 4.1):

$$G_L < 0.617 N_0^{1/3} \Delta T_t \left(1 - \left(\frac{\Delta T_N}{\Delta T_t} \right)^3 \right) \tag{4.1}$$

It is assumed that a certain number of equiaxed grains per unit volume N_0 nucleates instantaneously ahead of the columnar front when the liquid reaches a subcooling of $\Delta T_N = T_L(C^o) - T_N$, where $T_L(C^o)$ is the temperature of liquidus corresponding to the initial composition of the alloy (C^o) and T_N is the nucleation temperature. The subcooling temperature of the columnar tips is $\Delta T_t = T_L(C^o) - T_t$, where T_t is the temperature in the columnar tips, which is calculated from an empirical relation as a function of the speed of the isotherm.

Gäumann et al. (2001) and Kurz et al. (2001) have improved the Hunt's model using a dendrite growth model that explains the effects of rapid solidification to predict CET in processes with large temperature gradients and growth solidification rates.

As shown in Fig. 4.2 (Gäumann et al. 1999), the speed of the isotherms V depends on the location and is linked to the velocity of the heat source v. Along the center

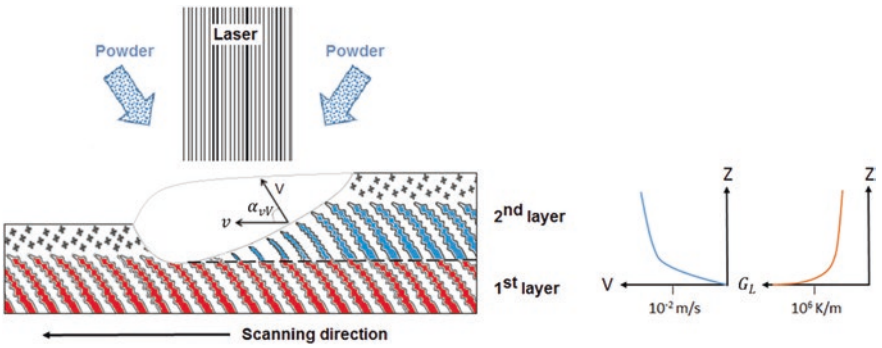

Fig. 4.2 Diagram of the longitudinal section along the central line of the clad during the laser cladding process and evolution of the solidification velocity V and the temperature gradient G_L along the solid/liquid interface (Gäumann et al. 1999)

line, V increases rapidly from zero at the bottom of the clad to a value close to v at the surface. The temperature gradient G_L is higher in the lower part of the clad and decreases as it approaches the surface. Unlike castings, where solidification is generally controlled by nucleation and growth processes, laser coatings that are very similar to welding exhibit primarily an epitaxial growth of the adjacent molten substrate. Therefore, the initial metal solidification assumes a crystallographic orientation identical to that of the contiguous solid in the melting line.

For the first layer, the columnar grains begin to grow epitaxially from the substrate and their growth is blocked by the formation of equiaxed grains in the upper part of the layer. The columnar grains in the second layer also grow epitaxially from the columnar grains of the upper part of the first layer since the equiaxed grains have been remelted. There is a competitive growth of grains with different orientations and those closely aligned with the flow direction of maximum heat in the solid/liquid interface obtain a preferential growth. However, equiaxed grains are also formed in the upper part of the second layer. Similar processes of grain growth take place during the deposition of subsequent layers (Renderos et al. 2017).

The Gäumann's model is a generalization of the Hunt's model for multicomponent alloys, adapted to laser cladding process. This model starts from the temperature gradient conditions in the liquid inside the boundary of the molten bath G_L, the growth velocity V, the number of nucleation sites N_0, the volumetric fraction of equiaxed grains ϕ, and a pair of constants of the material a and n. It has a validity range for processes of the order of $V \approx 0.01$ m.s^{-1} and $G_L \approx 10^6$ K.m^{-1}. The model defines that the CET (columnar to equiaxed) occurs when (Eq. 4.2):

$$\frac{{G_L}^n}{V} < a\left[\sqrt[3]{\frac{-4\pi N_0}{3\ln(1-\phi)}}\,\frac{1}{n+1}\right]^n \tag{4.2}$$

Kobryn et al. (Kobryn and Semiatin 2003) have developed columnar/equiaxed transition maps for the Ti-6Al-4V alloy for various castings and laser glazes processes that allow determining the morphology of the microstructure as a function of the solidification velocity V and the thermal gradient G_L (Fig. 4.3).

These maps are actually three-dimensional (3D) surfaces with the volume fraction of the equiaxed phase (ϕ) on the third axis. The representation proposed by Kobryn et al. is a projection in the V/G_L plane of a 3D evolution of the fraction ϕ.

This contribution focuses on the development of a model applied to the cladding laser process, which takes into account the specificity of this additive manufacturing process, and which allows predicting the type of structure that will be obtained during the solidification of the clad material.

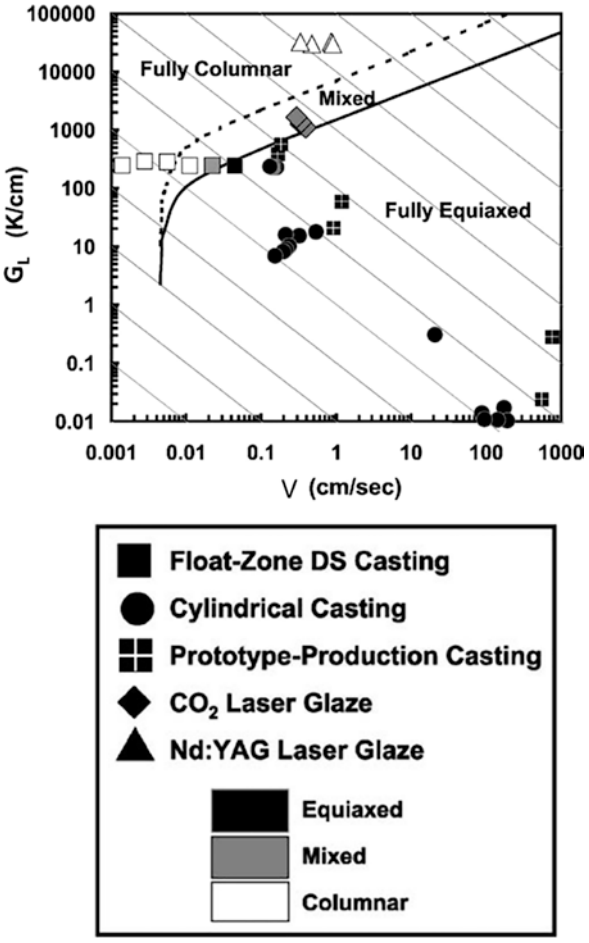

Fig. 4.3 The Ti–6Al–4V solidification map showing both the measured/predicted values of G_L and V, and the observed macrostructures for various castings and laser glazes (Kobryn and Semiatin 2003)

4.3 Modeling of Laser Cladding Process

The laser cladding process is based on the injection of material (usually metallic powder or wire) into a previously melted pool over the substrate material. The surface of the part where the material is being deposited is melted via a high-power laser and the filler external material is deposited and melted together with the base material (Toyserkani et al. 2005).

The solidification conditions are obtained from the model based on an analytical heat source (3D) of general type in quasi-stable state, moving over a semi-infinite substrate, which allows applying specific boundary conditions to the heat source (as the effect of powder attenuation) and the effect of the same on the substrate. A code has been programmed that allows obtaining from the solidification conditions the steady-state variations of the temperature gradient (G_L) and the solidification growth velocity (V).

The model is divided into the following steps or submodels:

1. Attenuation of the laser beam by powder
2. Energy balance on the surface of the substrate
3. Application of energy balance to obtain temperature field by means of a heat source
4. Obtaining the local solidification conditions
5. Solidification model CET based on the standard cumulative distribution function of Gumbel (*cdf*) or Extreme Value Type I Distribution
6. Observation of the effect in the variation of process parameters in the microstructure of added material
7. Experimental validation
8. Proposal of a method for obtaining constants of material for a CET model

It is assumed:

Assumption 1 Particles are considered perfectly spherical, and their distribution in size is taken on basis of a weighted average of the diameter distribution.

Assumption 2 It has been assumed steady state, with constant properties of drag gas for the powder (isothermal).

Assumption 3 Only those particles that come in contact with the melt pool created by laser beam adhere to the substrate.

Assumption 4 The size of the melt pool is approximately the same as of the area of incidence of laser beam over the substrate (in the focal plane of work).

Assumption 5 The working fluid for deposition and drag of material in the laser cladding process is considered to be a two-phase compound. A continuous phase that serves as a carrier medium (it is usually a noble gas), and a disperse phase that consists of solid particles (powder). Physical parameters both phases (velocity, temperature, density, etc.), will be described by average values.

Assumption 6 The velocity of drag gas flow determines the behavior of the dragged powder (both speeds are coupled, but are not necessarily the same).

Assumption 7 A Gaussian distribution of powder concentration in the working plane of consolidation is assumed.

Assumption 8 The density of the particles is high in relation to the amount of volume that they occupy, that is, they do not shadow each other (they do not interact during the travel nozzle-melt pool).

To develop the experimental part of this model, a nickel-base superalloy (Inconel 718) is used and emphasis is placed on maintaining the simplicity of the model in order to weigh the influence of each process parameter.

All the symbols and abbreviations used in the model are given in Appendix 1.

4.3.1 Attenuation of Laser Beam on Subtract by Effect of the Powder Shadow

The attenuation model for a coaxial nozzle developed by Pinkerton (Pinkerton 2007) has been used as basis with certain modifications (Fig. 4.4).

The velocity conditions of powder and gas are assumed as steady state at the output of nozzle and the powder velocity remains constant until the substrate is reached. However, the powder velocity is not considered the same as the gas velocity. There is a so-called sliding velocity between the two speed values.

The gas velocity is defined as (Eq. 4.3):

$$v_g = \frac{Q_g}{4\pi r_n r_o} \tag{4.3}$$

It is very difficult to estimate the final velocity of the particles by the effect of the speed of the drag gas stream. In general, the geometry of a coaxial nozzle involves a tortuous path for the powder particles in order to guide them as precisely as possible to the working area (the concentration area below the nozzle, which is usually the focal point of the laser beam). In addition, the carrier gas shares the same working space in the area of the nozzle tip with the protective gas (at different velocity). In this model, it is assumed that most of the particles velocity component is due to the carrier gas inside the nozzle, and not the protective stream gas. This

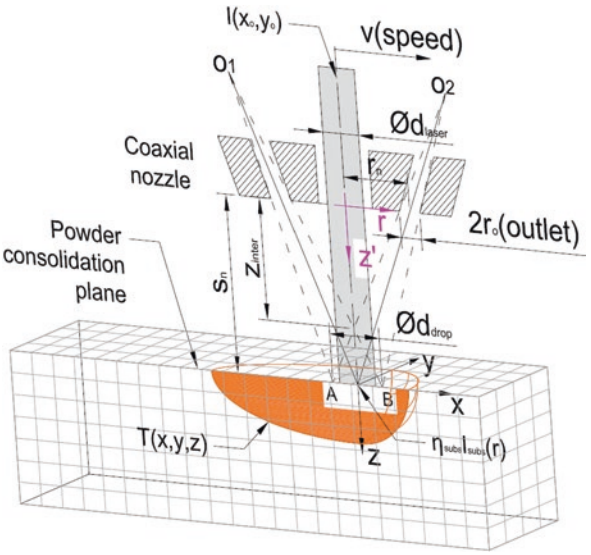

Fig. 4.4 Schematic powder stream diagram of a coaxial laser cladding deposition nozzle, and its interaction with laser beam and substrate (Pinkerton 2007)

simplification is valid when the ratio between the velocity of the protective gas and carrier gas is close to 0.8 with low speeds, which are the most suitable for laser cladding process (Arrizubieta et al. 2014).

The use of a ratio factor between particle velocity and carrier gas velocity is to model that the net losses in powder velocity due to its multiple collisions within the nozzle must be somehow compensated for by the entraining effect of the carrier gas velocity. As a reference value Agarwal (2005) has established that the ratio between particle velocity and drag velocity is about 0,8.

Experimentally, empirical equations have been developed for powder flows dragged by gas under different conditions. One of the most popular is the Hinkle ratio (Hinkle 1953) for horizontal tubes, in which the sliding velocity of solid particles with respect to the gas velocity stream by which it is drawn can be defined as (Eq. 4.4):

$$\frac{v_p}{v_g} = 1 - 0.044 d_p{}^{0.3} \rho_p{}^{0.5} \tag{4.4}$$

This correlation allows obtaining approximate values of sliding velocities according to the results of (Agarwal 2005), as function of factors relatively simple to quantify: the mean diameter of the particles and their density. For that reason, the Hinkle ratio has been chosen for this model. Therefore, the velocity of the particle in steady state will be (Eq. 4.5):

$$v_p = \frac{Q_g \left(250 - 11 d_p{}^{0.3} \rho_p{}^{0.5}\right)}{1000 \pi r_n r_o} \tag{4.5}$$

This equation will be valid while the biphasic flow regime is laminar ($\mathrm{Re}_p < 1000$); therefore, it is necessary to check this condition using (Tabernero et al. 2010) Eq. 4.6:

$$\mathrm{Re}_p = \frac{\rho_p d_p \left| v_g - v_p \right|}{\mu_{\mathrm{gas}}} \tag{4.6}$$

In the case of $\mathrm{Re}_p \geq 1000$ the velocity of the powder particles will be taken as directly coupled to the velocity of the carrier gas $v_p = v_g$ (Pinkerton 2007). From Pinkerton (2007) it is assumed that the main direction of velocity that attenuates the laser beam is the vertical component (in z' direction), where it is calculated as (Eq. 4.7):

$$v_{pz'} = \frac{v_p s_n}{\sqrt{s_n^2 + r_n^2}} \tag{4.7}$$

The relative Reynolds number should be calculated for each point (with its respective local velocities) in the space between the nozzle and the substrate where the

powder + gas interaction exists. However, taking into account only the velocities in the z' direction (Eq. 4.7) and according to Assumption 5, the values of v_g, v_p, and v_{pz} will be taken as representative of the entire biphasic stream.

In Fig. 4.4, the points A–B define the diameter where the value of the powder mass flow concentration (Assumption 7) has fallen to a value e^{-2} of the maximum concentration value and this fall allows delimiting the part of the powder stream that effectively intervenes in the attenuation of the laser beam.

In practical mode, the value of distances A–B and s_n can be obtained from the study of images of the nozzle (in this case coaxial), as long as it is fulfilled that the dispersion of the powder jet from its tip is approximately linear (as it is shown by the lines drawn in Fig. 4.5.

From Fig. 4.4, the z coordinate according to the $[r,z']$ coordinate frame of reference where the powder attenuation starts can be deduced and this is given by Eq. 4.8:

$$z'_{\text{inter}} = \frac{s_n\left(d_i - \phi d_{\text{laser}}\right)}{\phi d_{\text{drop}} + d_i} \tag{4.8}$$

where $d_i = 2(r_n - r_o)$

From Pinkerton (2007) it is known that the powder flow, assumed with a Gaussian density as a function of r coordinate (symmetrical to the z' axis), is variable up to a consolidation plane. This plane, parallel to the r axis, is located in the $z' = S_n$ coordinate, as seen in Fig. 4.4. The following relation gives the powder mass flow concentration (Eq. 4.9):

$$P\left(z',r\right) = \frac{C_0}{\pi r_s^2}\left[\exp\left(-\frac{2a_1^2}{r_s^2}\right) + \exp\left(-\frac{2a_2^2}{r_s^2}\right)\right] \tag{4.9}$$

$$\text{where } a_1 = \left|\left(\frac{s_n - z'}{s_n}\right)r_n - r\right|, \quad a_2 = \left|\left(\frac{s_n - z'}{s_n}\right)r_n + r\right| \text{ and } r_s = r_o + \frac{z'\left(\phi d_{\text{drop}} - 2r_o\right)}{2s_n}.$$

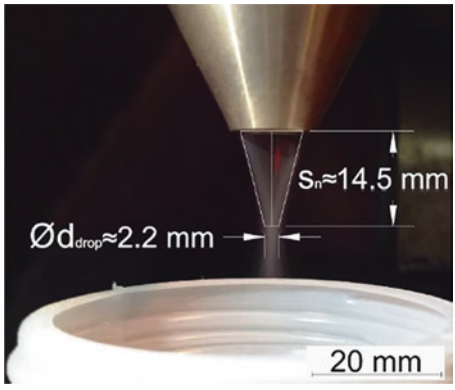

Fig. 4.5 Example of photography with image processing from which it is possible to obtain an estimate value of the distances A–B and S_n

It is necessary to establish the value of C_0, since the peak concentration value (expressed by $P(z',r)$) is variable as the powder mass concentration is consolidated until reaching the working plane (Arrizubieta et al. 2014; Tabernero et al. 2010). This can be calculated by considering a mass balance for different planes before reaching the work plane in $z' = S_n$.

For a plane at distance z' = constant, the total mass flow (m') must be the same (m' = constant $\forall\ z'_{\text{plane}}$), therefore the density in powder flux is only a function of r (Fig. 4.4). Thus, $P = P(r)_{z\ \text{constant}}$ and from the Cylinder Method (Leithold 1996) the total mass flow of powder will be (Eq. 4.10):

$$m' = 2\pi \int_0^{\ell_{\text{catch}}} r * P(r)\,dr = 2\pi \int_0^{\ell_{\text{catch}}} r \left\{ \frac{C_0}{\pi r_s^2} \left[\exp\left(-\frac{2a_1^2}{r_s^2} \right) + \exp\left(-\frac{2a_2^2}{r_s^2} \right) \right] \right\} dr \quad (4.10)$$

where $\ell_{\text{catch}} = r_n + 2r_o$

The upper limit of integral (ℓ_{catch}) has been defined in such a way that it encompasses the entire space of powder outlet from the nozzle, then integrating Eq. 4.10 and clearing C_0 (Eq. 4.11):

$$C_0 = \frac{-2m' \exp(b_1) \cdot b_2}{\left\{ \exp\left(\frac{16 \cdot \phi d_{\text{drop}} r_n^{\,2} s_n}{b_3^{\,2} b_2} \right) \cdot \left[\sum_{j=0}^{1} \exp\left(\frac{32 r_n \boldsymbol{s}_n \cdot c_j}{b_2^{(j+1)} b_3} \right) - 2 \exp\left(\frac{8 s_n \ell_{\text{catch}} \left(2 r_n z' b_3 + s_n \left(\sum_{k=0}^{1} c_k \left(2r_n - (2k-1)\ell_{\text{catch}} \right) \right) \right)}{b_3 b_2^{\,2}} \right) \right] b_2 + 2\sqrt{2}\sqrt{\pi} r_n \exp(b_1) \cdot (z' - s_n) \left[\sum_{i=-1}^{1} (3|i| - 2) * erf\left(\frac{2\sqrt{2} \cdot c_i)}{b_2} \right) \right] \right\}} \quad (4.11)$$

where

$c_i = r_n z' - r_s s_n + i s_n \ell_{\text{catch}}$

$c_j = (1 - j)\ell_{\text{catch}} + j \cdot \phi d_{\text{drop}}$

$c_k = \phi d_{\text{drop}}(1 - k) + 2kr_o$

$$b_1 = \frac{8 s_n \left(2 r_n \ell_{\text{catch}} z' \left(\phi d_{\text{drop}} - 2r_o \right)^2 + s_n \left(\phi d_{\text{drop}}{}^2 \left(r_n^{\,2} + 2 r_n \ell_{\text{catch}} + \ell_{\text{catch}}{}^2 \right) - 4 \cdot \phi d_{\text{drop}} r_o \ell_{\text{catch}}{}^2 - 4 r_o{}^2 \ell_{\text{catch}} \left(2r_n - \ell_{\text{catch}} \right) \right) \right)}{\left(\phi d_{\text{drop}} - 2r_o \right)^2 \cdot \left(z' \left(\phi d_{\text{drop}} - 2r_o \right) + 2 r_o s_n \right)^2}$$

$b_2 = z' \left(\phi d_{\text{drop}} - 2r_o \right) + 2 r_o s_n$

$b_3 = (\phi d_{\text{drop}} - 2r_o)$

The effect of the variable C_0 in powder flux as it consolidates on the working plane is presented in Fig. 4.6 for a powder mass flow and a nozzle of dimensions both of arbitrary values.

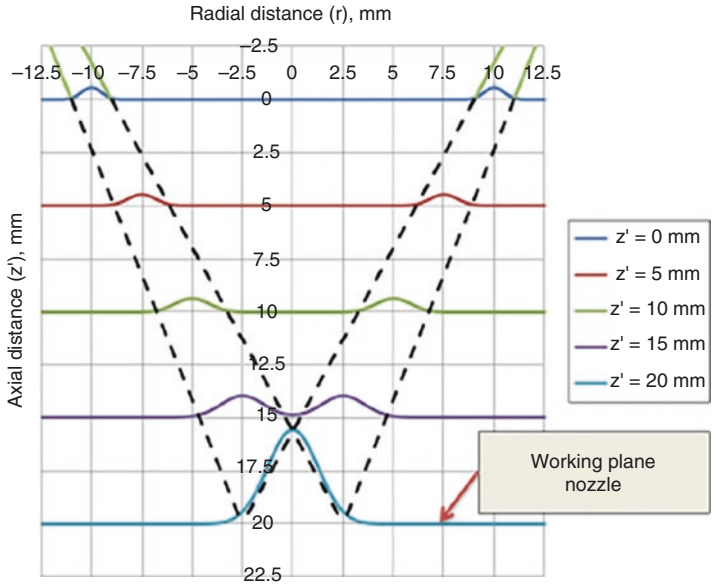

Fig. 4.6 Effect of C_0 value over the powder flux concentration for a nozzle with arbitrary powder mass flow and fixed dimensions: $\phi d_{\text{drop}} = 5$, $r_0 = 1$, $S_n = 20$ and $r_n = 10$. All dimensions in mm

4.3.2 *Energy and Mass Balance on the Substrate Surface by Interaction of Powder and Laser Beam*

From Pinkerton (2007) the intensity of the laser beam taking into account the total attenuation due to the "shadow accumulated" as result of the powder flow for different z' planes (from coordinate z'_{inter} to S_n) for any distribution with cylindrical symmetry (respect to the z' axis), is given by (Eq. 4.12):

$$I_{\text{att}}\left(z',r\right) = \varepsilon_m * f_{\substack{\text{shape}\\ \text{energy}}}\left(0,r\right) * \left(1 - \frac{3}{2v_{pz'}d_p\rho_p}\int_{z'_{\text{inter}}}^{s_n} P dz'\right) \tag{4.12}$$

where ε_m models the maximum value of energy density for a given distribution as a function of P_{laser} and ϕd_{laser}. In Eq. 4.12, $f_{\text{shape energy}}$ determines the radial distribution of the laser beam energy in the $z' = 0$ plane (before interaction with powder) for any value of r coordinate. Table 4.1 presents the formulas of $f_{\text{shape energy}}$ and ε_m for the Cylindrical, Gaussian, and TEM01 energy distributions (Eqs. 4.13, 4.14 and 4.15).

Table 4.1 Energy density distributions for different types of laser beams with circular symmetry

Cylindrical:	
$f_{\substack{\text{shape} \\ \text{cylindrical}}}(0,r) = \frac{1}{2} - \frac{\text{sgn}\left(2\lvert r\rvert - \phi d_{\text{laser}}\right)}{2}$	(4.13)
With $\varepsilon_{m\_\text{cylindrical}} = \frac{4P_{\text{laser}}}{\pi \cdot \phi d_{\text{laser}}{}^2}$, boundary condition $P_{\text{laser}}(r \mid r > \phi d_{\text{laser}}/2) = 0$	
Gaussian:	
$f_{\substack{\text{shape} \\ \text{gaussian}}}(0,r) = \exp\left(\frac{-8r^2}{\phi d_{\text{laser}}{}^2}\right)$	(4.14)
With $\varepsilon_{m\_\text{gaussian}} = \frac{8P_{\text{laser}}}{\pi \cdot \phi d_{\text{laser}}{}^2}$, and $P_{\text{laser}}(r \mid r = \phi d_{\text{laser}}/2) = \varepsilon_{m\_\text{gaussian}} e^{-2}$	
TEM01:	
$f_{\substack{\text{shape} \\ \text{TEM01}}}(0,r) = \frac{r^6 \exp\left(\frac{-32r^2}{\phi d_{\text{laser}}{}^2}\right)}{\phi d_{\text{laser}}{}^6}$	(4.15)
With $\varepsilon_{m\_\text{TEM01}} = \frac{524288e^8 P_{\text{laser}}}{\pi \cdot \phi d_{\text{laser}}{}^2 \left(3e^8 - 379\right)}$, and	
$P_{\text{laser}}(r \mid r = \phi d_{\text{laser}}/2) = \varepsilon_{m\_\text{TEM01}}(512/27)e^{-5}$	

4.3.3 Energy Quantification for Powder Temperature by Use of Negative Enthalpy

In addition to the net effect of the shadow of particles as a whole in the attenuation of energy available from the laser beam to form the melt pool in the substrate area, the powder itself absorbs part of energy. This "powder energy" (expressed as high temperature of itself) is not all useful, since a part of the stream of particles falls out of the useful area of work (determined by ϕd_{laser}, where it is assumed that all the material that hits the zone adheres). The quantification of this energy is expressed as a set of temperatures of the particles that reach the substrate (T_{powder}). Depending on the local value for temperature of powder particles when it reaches the substrate, it is possible that there is a contribution or a decrease of the local energy for the melt pool formation.

This enthalpy can be positive or negative, or both for different locations, depending on process parameters and position of hitting of powder particles within melt pool. The power value of laser beam that increases the powder temperature by interaction with it will be taken as the one that would be reached without effects of attenuation by shadow of other powder particles above. This effect occurs while the powder reaches the consolidation in the working plane coordinates ($z' = S_n$). Therefore, the power useful in the heating of powder particles will be the intensity (I_{laser}) corresponding to the ($z' = 0$, r) coordinate, that is, $f_{\text{shape energy}}(S_n,r) = f_{\text{shape energy}}(0,r)$. For a small spherical particle, the energy balance is expressed as (Pinkerton et al. 2007) Eq. 4.16:

$$\eta_{\text{powder}} * \varepsilon_m * f_{\substack{\text{shape} \\ \text{energy}}}(0,r) * \left(\frac{\pi d_p^{\,2}}{4}\right)\Delta t = \frac{\pi d_p^{\,3}\rho_p c_p \Delta T}{6} \tag{4.16}$$

For simplification, the powder temperature will be taken as the average of the temperatures in the limit conditions of its trajectories (Pinkerton, 2007), that is to say the temperature of the particles that reach the middle zone of laser beam diameter $T_{\text{powder}}(S_n,0)$ and that of the end in the zone of interaction $T_{\text{powder}}(S_n, \pm \phi d_{\text{laser}}/2)$.

Thus, clearing the value of ΔT and calculating the value of Δt as the time of interaction $\Delta t = \Delta \ell_{\text{interaction laser beam}}/v_{pz}$, from Eq. 4.16 is obtained (Eq. 4.17):

$$T_{\text{powder}}(s_n,0) = \frac{3\eta_{\text{powder}}\varepsilon_m f_{\substack{\text{shape} \\ \text{energy}}}(s_n,0)}{2d_p v_{pz'}\rho_p c_p} * \ell_{\substack{\text{powder\_center} \\ \text{laser\_beam}}} + T_{\text{o\_powder}} \tag{4.17}$$

where $\ell_{\substack{\text{powder\_center} \\ \text{laser\_beam}}}$ is the interaction length for the radius $r = 0$ in the coordinate $z' = S_n$ from focus O_1 or O_2 (according to each case), which from Fig. 4.4, is given by Eq. 4.18:

$$\ell_{\substack{\text{powder\_center}\\ \text{laser\_beam}}} = \frac{\phi d_{\text{laser}} \sqrt{\left(r_n^2 + s_n^2\right)}}{2r_n} \tag{4.18}$$

In the case of $T_{\text{powder}}(s_n, \pm\phi d_{\text{laser}}/2)$, the temperature is given by Eq. 4.19:

$$T_{\text{powder}}\left(s_n, \phi d_{\text{laser}}/2\right) = \frac{3\eta_{\text{powder}} \varepsilon_m \underset{\text{energy}}{f_{\text{shape}}}\left(s_n, \phi d_{\text{laser}}/2\right)}{2 d_p v_{pz'} \rho_p c_p} * \ell_{\substack{\text{powder\_edge}\\ \text{laser\_beam}}} + T_{\text{o\_powder}} \tag{4.19}$$

where $\ell_{\substack{\text{powder\_edge}\\ \text{laser\_beam}}}$ is the interaction length from focus O_1 or O_2 (according to each case), to the coordinate $r = \pm \phi d_{laser}/2$ (+ for stream from vertex O_1 and – for stream from focus O_2) in the $z' = s_n$ plane. From Fig. 4.4, $\ell_{\substack{\text{powder\_edge}\\ \text{laser\_beam}}}$ is given by Eq. 4.20:

$$\ell_{\substack{\text{powder\_edge}\\ \text{laser\_beam}}} = \frac{1}{2}\left(\frac{\phi d_{\text{laser}} \sqrt{\left(\phi d_{\text{drop}}{}^2 + 4 \cdot \phi d_{\text{drop}}\left(r_n - r_o\right) + 4\left(r_n^2 - 2 r_n r_o + r_o^2 + s_n^2\right)\right)}}{\phi d_{\text{drop}} + 2\left(r_n - r_o\right)} \right) \tag{4.20}$$

where the ½ factor before the parenthesis in Eq. 4.20 represents an average that must be interpreted in that way: when observing Fig. 4.4, a particle of powder starting from $O_1 \rightarrow A$ will suffer a zero heating (in no time it touches the laser beam), compared with a particle with $O_1 \rightarrow B$ trajectory that passes completely through laser beam. By symmetry, the same can be said of the particles leaving the powder focus O_2 and therefore only the positive coordinate $r = \phi d_{\text{laser}}/2$ for the calculation of temperature is taken and the factor ½ is added.

The mass flows for the same coordinates of powder temperature ($r = 0$ and $r = \phi d_{\text{laser}}/2$ in $z' = S_n$ plane) can be calculated from Eq. 4.9 and is given by (Eqs. 4.21 and 4.22):

$$P\left(s_n, 0\right) = \frac{8m'}{\pi \cdot \phi d_{\text{drop}}{}^2} \tag{4.21}$$

$$P\left(s_n, \phi d_{\text{laser}}/2\right) = \frac{8m'}{\pi \cdot \phi d_{\text{drop}}{}^2} \exp\left(-2 \frac{\phi d_{\text{laser}}{}^2}{\phi d_{\text{drop}}{}^2} \right) \tag{4.22}$$

From Pinkerton et al. (2007), the total energy flow that is carried by the powder will be (Eq. 4.23):

$$I_{\text{powder}}\left(s_n, |r|, r \le d_{\text{laser}}/2\right) = c_p * P\left(s_n, r\right) * \left(T_{\underset{\text{powder}}{\text{melt}}} - T\left(s_n, 0\right) \right) \exp\left(\frac{r^2}{2\lambda_{\text{powder}}{}^2} \right) \tag{4.23}$$

where

$$\lambda_{\text{powder}} = \frac{\sqrt{2}\cdot\phi d_{\text{laser}}}{4\ln\left(\frac{P\left(s_n,\phi d_{\text{laser}}/2\right)*\left[T\left(s_n,\phi d_{\text{laser}}/2\right)-T_{\text{melt}}\right]}{P\left(s_n,0\right)*\left[T\left(s_n,0\right)-T_{\text{melt}}\right]}\right)}$$

It is assumed that no powder falling out of $A_{\text{spot laser}} = \pi.\phi d_{\text{laser}}^2/4$ area adheres to the substrate; therefore, all energy acquired by this powder steam when heated by the laser beam is lost. Thus (Eq. 4.24),

$$I_{\text{powder}}\left(s_n,\mathrm{I}\, r,\left|r\right\rangle\phi d_{\text{laser}}/2 \wedge r < -\phi d_{\text{laser}}/2\right) = 0 \tag{4.24}$$

This energy flow (I_{powder}) can be interpreted as a function of the melting temperatures of powder particles (T_{melt}) and the temperatures of boundary zones in the interaction zone of the melt pool with the substrate $T(S_n,0)$ and $T(S_n,d_{\text{laser}}/2)$. This means actually how much energy is expressed in the form of a negative enthalpy (subtraction of energy from the substrate by impacting of the powder "half melt" against it). The subtraction of that energy will be necessary to achieve the complete liquefaction of the powder particles.

Finally, the energy balance on the surface of the substrate in the working plane $z' = S_n$, expressed as intensity I_{subs} is equal to (Eq. 4.25):

$$I_{\text{subs}} = I\left(s_n,r\right) = I_{\text{att}}\left(s_n,r\right) - I_{\text{powder}}\left(s_n,\left|r,\right|r \le \phi d_{\text{laser}}/2\right) \tag{4.25}$$

The first term on the right side of Eq. 4.25 is a purely geometric factor, and it is independent of the temperature conditions of powder particles (except in the case that the particles melt, which would cause them to lose their spherical shape). However, due to the effect of surface tension, the particles will tend to maintain their spherical shape even though they are melted.

On the other hand, the second term of Eq. 4.25 depends very much on the relative difference between temperatures $T(S_n,r) - T_{\text{melt}}$. This is important since the greater the difference between these two values, the lesser the energy intensity that will reach the substrate. Therefore, it is necessary to establish as precisely as possible the powder temperature to correctly quantify the amount of energy available.

4.3.4 Modeling of Phase Change for Inconel 718 and Temperature-Dependent Thermal Properties

Assuming temperature-independent properties in a process that involves temperatures can lead to a large error when modeling values of characteristics of the medium (e.g., the thermal field itself). The properties of materials are in general temperature-dependent.

A phase change is an important problem, as it leads to a discontinuity in the values of thermal properties. One way of solving this is to make use of modified properties via a corrector that takes into account the latent fusion heat (ΔL_f), as in the case of specific heat in the solidification range (Peyre et al. 2008). The same can be done for the enthalpies associated with this phase change for the different temperature ranges (Kamara et al. 2011). Thus, from Bandyopadhyay (2002), Kamara et al. (2011), and Mishra and Yadava (2013), and Eqs. 4.26–4.28, for each range of temperature in the material it is possible to elaborate the table of properties for Inconel 718 over a wide temperature range (Table 4.2). The reference temperature for the properties is T_0 = 298 K.

$$\text{For the range}: T \le T_S \qquad \mathrm{H}(T) = \rho \int_{T_0}^{T} c_p dT \tag{4.26}$$

$$\text{For the range}: T_S < T \le T_L \qquad \mathrm{H}(T) = \rho \int_{T_0}^{T_S} c_p dT + \rho L_f \left(\frac{T - T_S}{T_L - T_S} \right) \tag{4.27}$$

$$\text{For the range}: T > T_L \qquad \mathrm{H}(T) = \rho \int_{T_0}^{T_S} c_p dT + \rho L_f + \rho \int_{T_L}^{T} c_p dT \tag{4.28}$$

Table 4.2 Properties of Inconel 718 as a function of temperature

Temperature (K)	Density (kg/m^3)	Enthalpy (J/m^3)	Specific heat (J/(kg.K))	Thermal conductivity (W/(m.K))	Thermal diffusivity (m^2/s)*10^{-6}
298	8240	0	439	10.3	2.85
373	8221	2.73E+08	454	11.5	3.08
473	8193	6.51E+08	473	13.2	3.41
573	8162	1.05E+09	493	15	3.73
673	8130	1.46E+09	512	16.9	4.06
773	8095	1.88E+09	532	18.8	4.37
873	8058	2.33E+09	551	20.9	4.71
973	8019	2.79E+09	582	22.8	4.89
1073	7978	3.26E+09	604	23.8	4.94
1173	7934	3.75E+09	626	25.8	5.19
1273	7889	4.25E+09	648	28	5.48
1373	7841	4.77E+09	670	30.2	5.75
1473	7792	5.30E+09	692	32.4	6.01
1533 (S)	7761	5.63E+09	710	33.7	6.12
1617 (L)	7579	7.34E+09	769	26.8	4.60
1723	7483	8.00E+09	736	28.2	5.12
1800	7414	8.36E+09	712	29.4	5.57
1973	7258	9.83E+09	659	31.7	6.63
2100	7143	9.90E+09	619	33.5	7.57

S solidus temperature, *L* liquidus temperature

The thermophysical properties of the liquid phase are different from those of the solid alloy (e.g., thermal conductivity and thermal diffusivity). The values of the thermophysical properties in the "mushy zone" will depend on the amount of liquid and solid fraction. The solid fraction differs with the cooling rate, then the thermophysical ratios and temperature ratios also differ with the cooling rate (Mills, 2002). As a simplification to this model and in order to avoid discontinuities of the thermal properties values within the "mushy zone," a linear behavior is assumed, and is given by Eq. 4.29:

For the range: $T_S < T \leq T_L$

$$Th_{\text{prop}}\left(T_{\underset{\text{zone}}{\text{mushy}}}\right) = \frac{Th_{\text{prop}}\left(T = T_L\right) * \left(T_{\underset{\text{zone}}{\text{mushy}}} - T_S\right) + Th_{\text{prop}}\left(T = T_S\right) * \left(T_L - T_{\underset{\text{zone}}{\text{mushy}}}\right)}{\Delta T_{\text{Liq\_Sol}}} \quad (4.29)$$

4.3.5 *Determination of Powder Temperature as Function of Laser Beam Power and Thermal Properties of Material*

The method consists in establishing an iterative loop between the material properties (starting from a given temperature), and the temperature obtained with the properties from that initial temperature until a balance of energy is stablished.

If the temperature of the material does not coincide within a certain range with the calculated temperature based on the thermal properties, an average of the values of both temperatures (material and thermal properties) is calculated and the loop is reinitiated with the new "average temperature."

The convergence of the iteration cycle (based on the difference between the powder temperature and that calculated in the previous cycle on the basis of thermal properties), is less than a certain threshold, the final value of temperature get from loop will be the used as the "good value" of both temperature material and thermal properties for that material. The scheme of loop is shown in Fig. 4.7. It should be taken into account that a basic idea of the model is that each powder particle has essentially the same instantaneous temperature in its entire volume (Biot number << 1). For laser cladding process, this Biot number of powder particles is in the order of $d_p/6$ so a "lumped" model for the temperature of particles is justified (Ibarra-Medina and Pinkerton 2010; Zohdi 2015).

Temperature changes by laser–powder interaction are important because although the powder interaction time in the laser beam is very short (Meriaudeau et al. 1997), the high powers involved (in the order of $10^7 \sim 10^8$ W/m^2) can result in a phase change (Solidus–Liquidus), or a change of the energy carried by the powder depending on its sensible temperature (enthalpy). For this specific model, it is established that the $\Delta T_{\text{setpoint}} = |T_{\text{powder}} - T_i| \leq 1$ K.

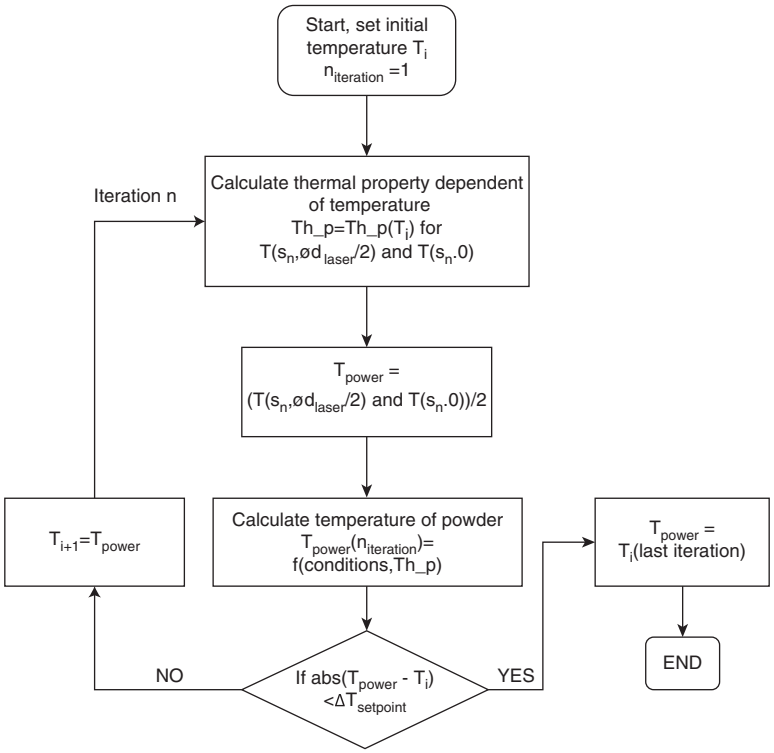

Fig. 4.7 Iteration scheme to find the actual temperature of powder reaching the substrate taking into account the temperature-dependent properties of material

4.3.6 Effect of Change in Values of the Main Variables for Powder Attenuation over the Available Laser Beam Power for Substrate

The effect of parameters interaction will be tested for a constant nozzle geometry ($[r_n, r_0, S_n]$ = constant), and for some material and process variables staying constants ($[Q_g, \mu_{gas}, \rho_p, \phi d_{drop}, \eta_{powder}]$ = constant).

Instead we will vary $d_{p(mean)}$ = [60, 120] μm, m' = [10, 15, 20] gr/min, and P_{laser} = [200, 600] W (ϕd_{laser} = 1 mm, with cylindrical power distribution). The results are presented in Figs. 4.8, 4.9, 4.10 and 4.11.

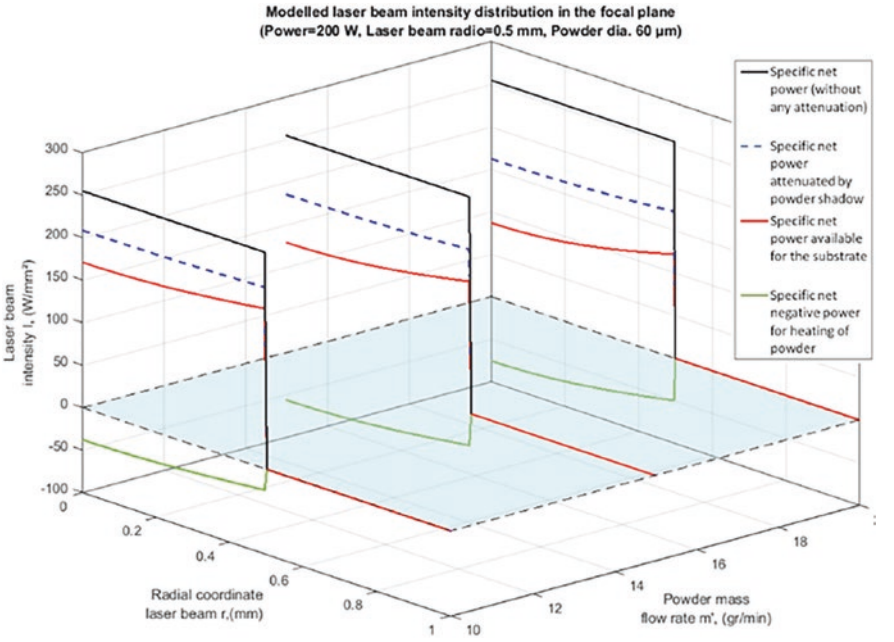

Fig. 4.8 Effect on the net power available for melt pool formation on the substrate by interaction of laser beam with powder for a given nozzle geometry and with variation of the powder flux (P_{laser} = 200 W, $d_{p\text{mean}}$ = 60 µm)

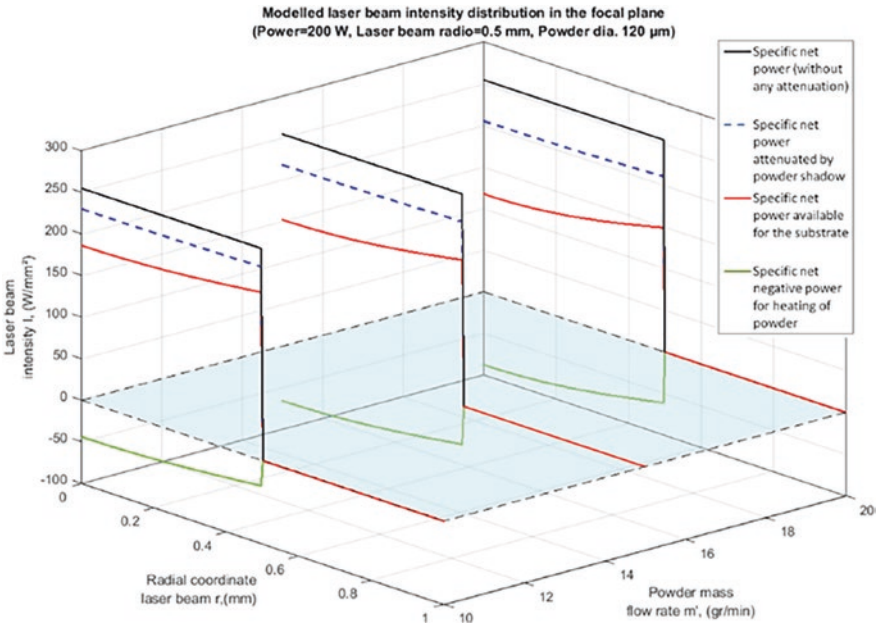

Fig. 4.9 Effect on the net power available for melt pool formation on the substrate by interaction of laser beam with powder for a given nozzle geometry and with variation of the powder flux (P_{laser} = 200 W, $d_{p\text{mean}}$ = 120 µm)

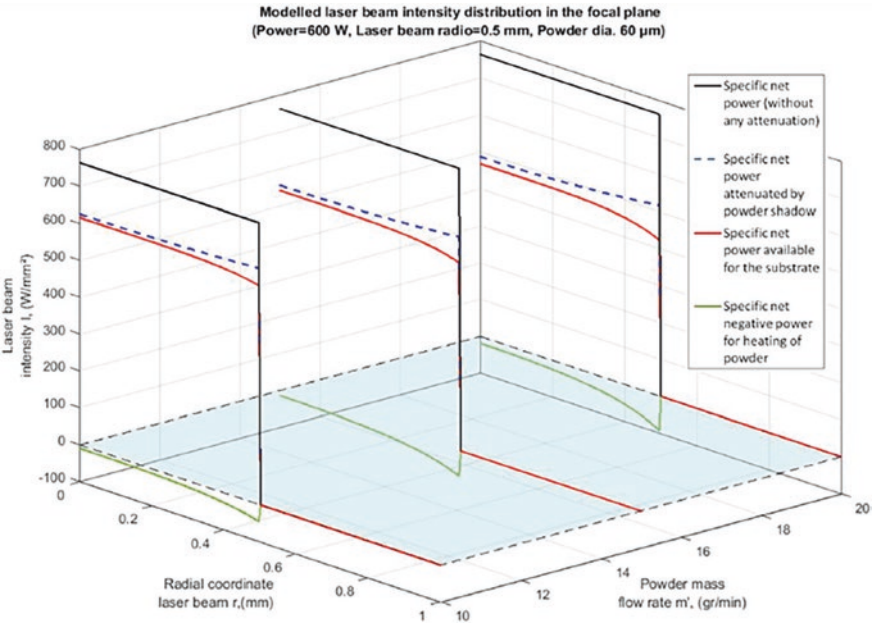

Fig. 4.10 Effect on the net power available for melt pool formation on the substrate by interaction of laser beam with powder for a given nozzle geometry and with variation of the powder flux (P_{laser} = 600 W, $d_{p\text{mean}}$ = 60 µm)

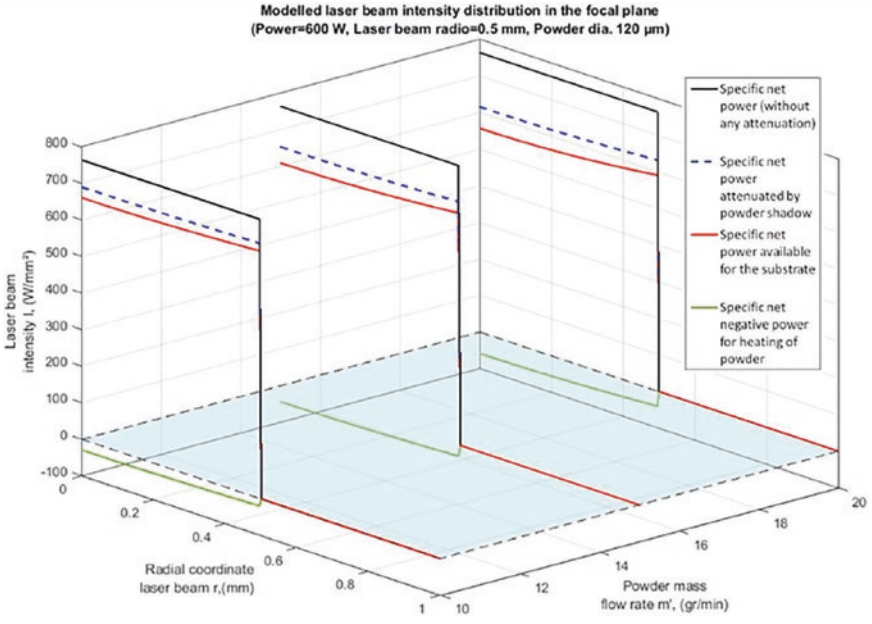

Fig. 4.11 Effect on the net power available for melt pool formation on the substrate by interaction of laser beam with powder for a given nozzle geometry and with variation of the powder flux (P_{laser} = 600 W, $d_{p\text{mean}}$ = 120 µm)

4.3.7 Application of Energy Balance by Means of a General Type Heat Source on the Substrate to Obtain the Temperature Field

Analytical heat sources are very useful in describing the temperature field in areas both inside and outside the melt pool. Some examples of analytical heat sources of various types can be found in these references (Darmadi et al. 2011; Peyre et al. 2008; Pinkerton and Li 2004; Van Elsen et al. 2007). In the case of this model, the solution obtained by Levin (2008) will be used as base because it has the following advantages.

Its formulation is general, that is to say the surface energy density can have any shape necessary on the substrate and not limited to "classic" energy distributions like the Gaussian, Top Hat, Point Source, Cylindrical, etc. This is important due to the fact that, for example, in the case of Point Source energy distribution, singularities are generated within the melt pool (such as infinite temperatures), giving rise to unrealistic thermal fields (Darmadi et al. 2011). In our case, the attenuation of powder results in a nonstandard laser beam energy distribution that the Levin's Analytical Solution is capable of handling.

The heat source formulation when the differential equation is solved (in steady state), takes into account the particular contour conditions generated due to a heat source moving in a mobile frame of reference. The use of a moving frame of reference for solving the heat equation is because analytical solutions are either too complicated to implement by time dependence or because is inconsistent with the character of source intensity, which supposed to be constant in time and symmetric along axis of moving direction. Using proposed exponential transformation of moving coordinates (Levin's analytical solution), one can express the fundamental solution of the problem as the generalization of the Poisson's equation solution (Levin 2008). This result in the fact that the cooling rates reached after the solidification of the melt pool can be modeled by this formulation, but not by simpler ones. The advantage of this is that, for example, the formation of martensitic structures at relatively high scanning speeds of laser beam in the substrate can be explained with a relatively simple model.

For a heat source type heat flux with intensity $I=I(x_0, y_0)$ [W/m^2] in local coordinates of frame of reference (x_0, y_0), constant in time, moving at velocity v over the surface of a semi-infinite solid ($z \geq 0$), with z pointing toward the interior of a homogeneous and isotropic solid in Cartesian coordinates in solidarity with the frame of reference of the heat source according to Fig. 4.4, the following mathematical formulation can be applied (Eq. 4.30):

$$\frac{\partial^2 T}{\partial x^2}+\frac{\partial^2 T}{\partial y^2}+\frac{\partial^2 T}{\partial z^2}+\frac{v}{\alpha}\frac{\partial T}{\partial x}=-\frac{I\left(x_0,y_0\right)}{k}\delta\left(z\right) \tag{4.30}$$

Under the boundary condition $T|_{(x^2+y^2+z^2)\to\infty} = 0$. The solution for Eq. 4.30 is expressed by Eq. 4.31:

$$T(x,y,z) = 2\int_{-\infty}^{\infty}\int_{-\infty}^{\infty} G_R\begin{pmatrix} x,y,z, \\ x_0,y_0,0 \end{pmatrix}\frac{I(x_0,y_0)}{k}dx_0dy_0 \tag{4.31}$$

where $R = \sqrt{(y-y_0)^2+z^2}$ is a radial coordinate, and is the principal part of the Green's function, associated with Laplacian operator and boundary conditions for analytical solution of Eq. 4.30.

$$G_R\begin{pmatrix} x,y,z \\ x_0,y_0,0 \end{pmatrix} = \frac{v\exp\left(-\frac{v(x-x_0)}{\alpha}\right)}{4\pi\alpha}\left[\left(\left(1-\exp\left(-\frac{v(x-x_0)}{\alpha}\right)\right)^2+\left(\frac{Rv}{\alpha}\exp\left(-\frac{v(x-x_0)}{\alpha}\right)\right)^2\right)^{-\frac{1}{2}}\right.$$
$$\left.-\left(\left(1+\exp\left(-\frac{v(x-x_0)}{\alpha}\right)\right)^2+\left(\frac{Rv}{\alpha}\exp\left(-\frac{v(x-x_0)}{\alpha}\right)\right)^2\right)^{-\frac{1}{2}}\right]$$

The (x_0, y_0) coordinates that define the energy density in the surface plane of the substrate that according to Fig. 4.4 lie in the same coordinate of powder consolidation plane and working distance of the nozzle ($z' = S_n$), therefore the heat flux $I(x_0, y_0) = I_{subs}$.

First a transformation of coordinates is necessary to apply the Eq. 4.31 from I_{subs} (Eq. 4.25) to $I(x_0, y_0)$. The I_{subs} is defined solely as a function of r in the working plane $z' = S_n$, therefore $I_{subs} = I(S_n, r)$ becomes only $I_{subs} = I_{subs}(r)$. In addition, and since the heat source moves exclusively on the surface of the solid, ($z = 0$) and the z' axis of the nozzle is in the same direction as that of the substrate (z), the transformation of coordinates for Eq. 4.31 is given by the radial coordinate $r = f(x_0, y_0)$, (Eq. 4.32):

$$r = \sqrt{x_0^2 + y_0^2} \tag{4.32}$$

Finally, taking into account the absorptivity of the substrate η_{subs} and the coordinate transformation, the temperature field in the melt pool is given by Eq. 4.33:

$$T(x,y,z) = 2\int_{-\infty}^{\infty}\int_{-\infty}^{\infty} G_R\begin{pmatrix} x,y,z, \\ x_0,y_0,0 \end{pmatrix}\frac{\eta_{subs}I_{subs}(r)}{k}dx_0dy_0 \tag{4.33}$$

It is important to remember that the thermal properties over time (not space) remain constant.

4.3.8 Determination of Melt Pool Temperatures as a Function of Attenuated Laser Beam and Thermal Properties of Material

In the same way that temperature-dependent thermal properties values $Th_{\text{prop}}(T)$ have been used to calculate powder temperatures, and in turn it has been used to calculate the temperature of particles (assumed as uniform) through an iterative loop, it is possible to establish an analogous procedure to determine the thermal field from the incident energy of the laser beam in the substrate (η_{subs}. $I_{\text{subs}}(r)$).

Unlike the procedure for calculating the temperature of the powder (which assumes a uniform temperature in the volume of itself), the substrate size is much larger (assumed to be semi-infinite), and therefore it is not possible to assign to the same in its entire dimension (and especially to the melt pool that is formed), values of temperature-dependent thermal properties uniform. The reason for this last is that each point within the (x, y, z) coordinate system in the domain of the substrate may, in general, have a different value of temperature.

Another important difference is the phase change. In the case of powder heating, the melting of the particle is an undesirable effect (it is simpler for powder particle to lose its spherical shape and complicate a lot the modeling of the heating of them). In the case of substrate, the melt pool formation is essential to carry out the cladding process. The temperature gradient (G_L) and solidification growth velocity (V) values are very dependent on local properties, and it is necessary to take this effect into account in some way for better precision of the model.

In order to solve the problem of assigning values to the thermal temperature-dependent properties in the substrate, an approximate solution has been chosen. The analytical heat source of Levin (Eq. 4.33) allows calculating of temperatures in discrete points considering the thermal properties of material as constant and the thermal field only a function of the relative position of the heat source energy distribution (x_0, $y_0 \mid z' = S_n$) with respect to a substrate coordinate system (x, y, z).

When a thermal property is defined as constant within a volume, it is the same as saying that a temperature has been "chosen" for all the thermal properties of the work volume (substrate). The natural question is: what is the temperature that best represents the phenomenon of the thermal field via the values of temperature-dependent properties?

A method is proposed to solve the previous question and overcome this limitation inherent to an analytical resolution method. It consists of establishing an "approximate temperature function" within the melt pool and taking the temperature-dependent properties as a function of that set of "representative temperatures" especially in its nearby area (in the zone of influence of the laser beam).

The method is summarized in the following steps.

First is necessary to define a working domain in two dimensions of discrete points (center in the heat source origin $x_0 = 0$, $y_0 = 0$); with low step density in its plane of symmetry (xz plane) (Fig. 4.4). It is necessary to divide the substrate domain into small sections characterized by their length (called steps), in order to

implement the mathematical solution (step length in x and z axes). A convenient dimension to use as a base is the radio of the laser beam. This is because the higher temperature gradients will be found near the melt pool, which is defined by the variable ϕd_{laser} (Assumption 4). In high power density energy sources ($10^7 \sim 10^9$ W/m^2), the most abrupt change in the thermal field is in the vicinity of the heat source reference system (in this case an attenuated modified laser beam) (Araya and Gutierrez 2006; Pinkerton 2007; Van Elsen et al. 2007). Therefore, all the step sizes for discretization of domain (and the domain size itself) will be a function of the $r_{laser} = \phi d_{laser}/2$ value. Another phenomenon to take into account is that normally analytical heat sources are symmetrical (Darmadi et al. 2011; Fassani and Trevisan 2003; Picasso et al. 1994; Trujillo Guillen 2005), and this allows simplifying the calculation of the number of nodes to calculate the temperature field.

Second, the proposed domain dimensions are (based on the observation that the greatest change in the temperature gradient occurs around the area of incidence of the laser beam): domain length along the x axis (in the xz plane) of $-3r_{laser} \leq x \leq 3r_{laser}$, with step $\Delta x = r_{laser}/4$. For the z axis the length of the domain is defined *as* $0 \leq z \leq 2r_{laser}$, with $\Delta z = r_{laser}/5$. The dimension in the z domain is justified by the fact that for analytical solutions the high-power heat sources are assumed to be of a superficial nature (Araya and Gutierrez 2006; Trujillo Guillen 2005), and that the effects toward the interior of the substrate are rapidly attenuated with depth.

Third, within the domain created in substrate in the second step (xz plane), the iteration scheme of Fig. 4.12 is applied with a similar principle to that used for the thermal temperature-dependent properties of powder. The difference is that it is not possible in "respect to the properties" to assume the temperature within the melt pool as uniform (as lumped system for powder). Instead of an "unvarying temperature" (referred to a constant value for thermal properties), a representative "set" of them inside the melt pool will be established, and with it, a set of representative thermal temperature-dependent properties via functions $Th_{prop}(T)$ for each point on the domain in the proximity of the origin of coordinates of heat source (i.e., approximately the same area of the melt pool).

Fourth, once the corresponding $Th_{prop}(T)$ properties are calculated, they will be used in the calculation of thermal field via the analytical solution of Eq. 4.33. The approximate thermal properties are calculated by layers for different z values along x local coordinates for each z-coordinate; thus, the thermal properties will become of the $Th_{prop}(T_{aprox}(z))$ form.

In the case of temperature profiles that are calculated using the algorithm showed in Fig. 4.12 and applied to specific case for $r_{laser} = 0.5$ mm (plane xz of Fig. 4.4), it is important to note that a possible problem can occur at the domain ends ($-3r_{laser} \leq x \leq 3r_{laser}$) (Fig. 4.14).

Near domain ends the temperature profiles have almost crossed one over another (overlap), which is at the level of thermal field physically impossible. If that case occurs, it means that there is something wrong in the convergence criterion (via algorithm) for the mathematical solution for the temperature field. The proximity of the lines for temperature profiles for different substrate depths is much less in the central region for each one of the z planes (near x axis origin). This is because in that

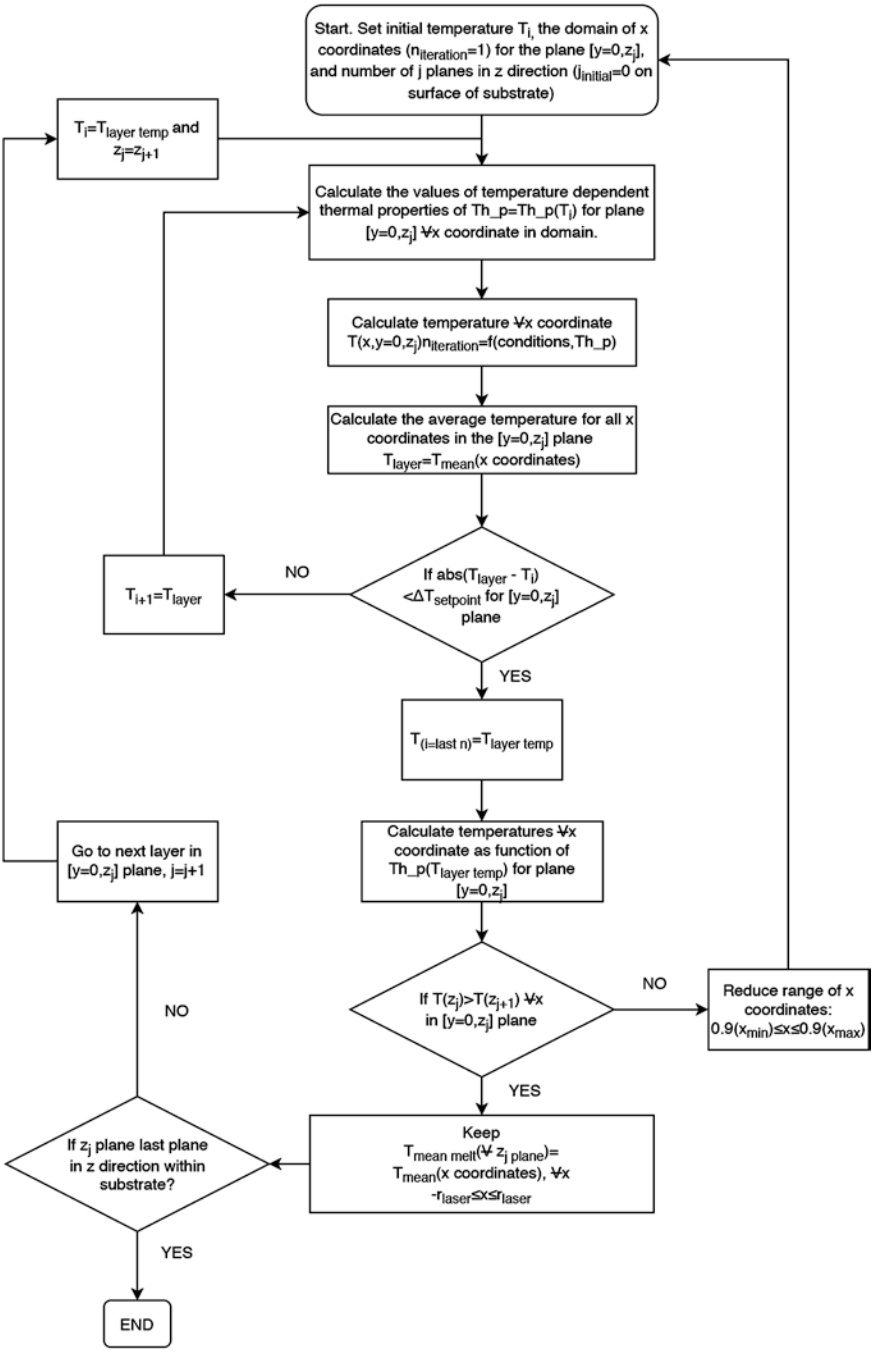

Fig. 4.12 Interaction scheme to determine thermal properties as function of approximate temperatures for the melt pool volume and nearby zones

zone a higher temperature gradient for different z planes is found. Because it has not been possible to find data for thermal properties of alloy Inconel 718 for very high temperatures, it has been decided to use the average temperature over a certain domain of the x-coordinate to avoid extrapolating thermal η properties in a range beyond that defined in Table 4.2. This range has been defined as $-r_{laser} \leq x \leq r_{laser}$, and can be modified according to the scheme of Fig. 4.12 to achieve the convergence of the solution by algorithm.

The schemes of Figs. 4.7 and 4.12 are applied to a specific case (Table 4.3).

Applying Eqs. 4.3–4.29 for powder heating, Table 4.2, and the algorithm of Fig. 4.7, the quantification of energies for the interaction of the laser beam with powder (Eq. 4.25) is given in Fig. 4.13.

The approximate temperature profiles in the melt pool for different distances (planes) from the surface of the substrate ($z = 0$) for the xz plane of Fig. 4.4 are calculated from the specific power available for substrate. This power is obtained from the interaction of laser beam-powder showed on Fig. 4.13 and Eq. 4.33. The resulting temperature profiles are shown in Fig. 4.14.

From Fig. 4.14, in the $z = 0$ coordinate for the approximate value $x = 0$, $T \approx 2300$ K. On the other hand, from Table 4.2, the temperature-dependent thermal properties ($Th_{prop}(T)$) are not defined for those specific conditions. The maximum values available for thermal properties are defined up to the temperature of $T = 2100$ K. The algorithm of Fig. 4.12 foresees this problem, and what it does to solve it is to average the temperature values that are too high for specific x values over an x range, which is initially taken as $-r_{laser} \leq x \leq r_{laser}$ (point values of temperature are replaced by the average of the values around that specific x coordinate).

In the case of Fig. 4.14, the average temperatures for $z_{surf} = 0 \leq z \leq z_{max} = 1$ (mm) allow defining an approximate temperature function within the melt pool in the diameter range of the laser beam source ($d \leq \phi d_{laser}$), as function of the z coordinate in substrate. The range of this function ($d \leq \phi d_{laser}$) can be different depending on the range that has been defined to calculate the average temperatures within the melt pool that is to say $\phi d_{laser} = [-r_{laser}, r_{laser}]$ in length. This function $T(x) = f(T_{mean})$ is obtained from the average temperature values instead of the point values according to the x coordinate for each z plane in consideration.

This approach is useful because it allows the temperature-dependent thermal properties to be calculated quickly in the solidification volume inside the melt pool at relatively low computational cost. By applying the numerical method described

Table 4.3 Example parameters for application of thermal field model for a specific laser cladding process

$Q_{g(normalized)} = 4.33\ 10^{-5}$ m^3/s	$\phi d_{drop} = 2.2$ mm
$\mu_{gas} = 2.125\ 10^{-5}$ kg/(m.s) [argon]	$\phi d_{laser} = 1$ mm
$r_n = 5.275$ mm	$m' = 1.463\ 10^{-4}$ kg/s
$2r_0 = 0.45$ mm	P_{laser} (cylindrical) = 571 W
$S_n = 14.5$ mm	$\eta_{powder} = \eta_{subs} = 0.4$
$\rho_p = \rho_{subs} = 8240$ kg/m^3	$v = 8.7$ mm/s
$d_{p(mean)} = 80$ μm	

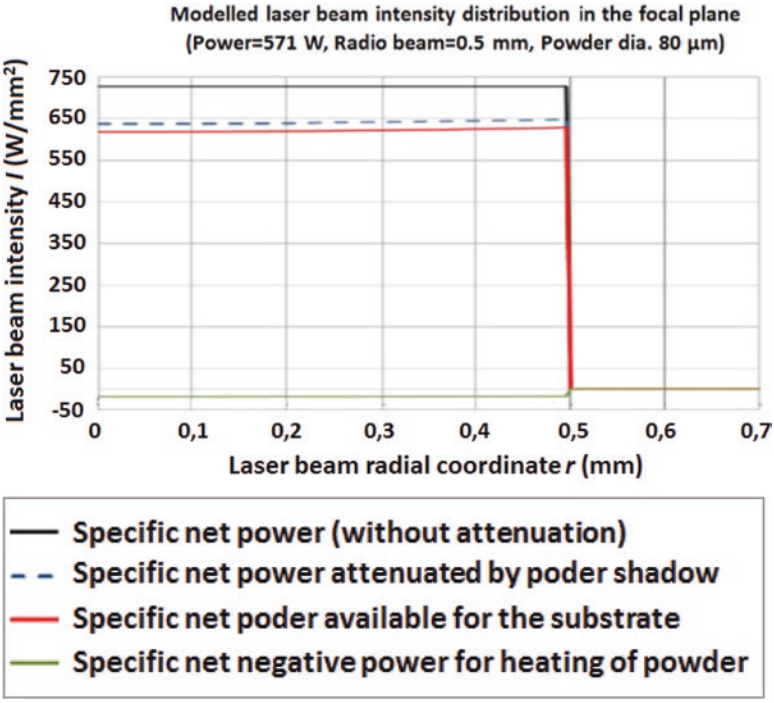

Fig. 4.13 Total specific energy available for substrate as function of parameters in Table 4.3 at the focal plane of laser beam (red line). The figure takes into account the quantification of the effects on power by the interaction between laser beam and powder (Eq. 4.25)

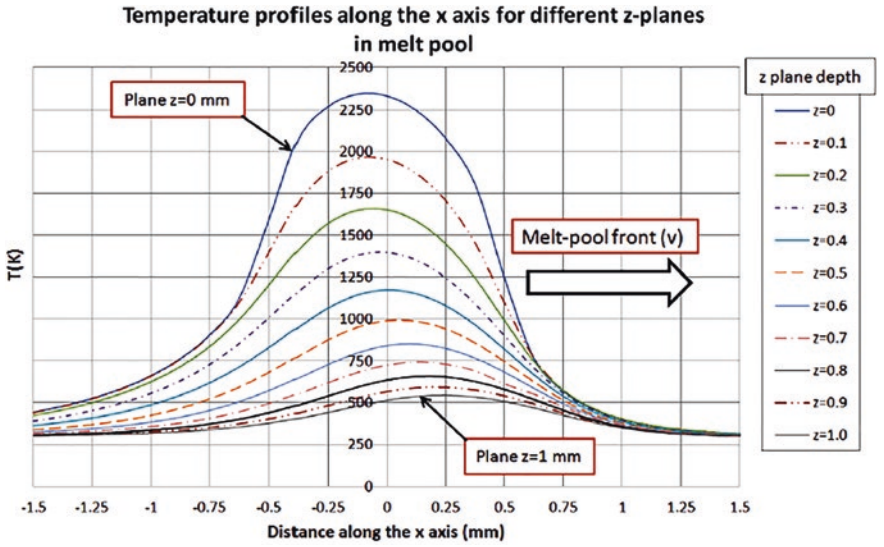

Fig. 4.14 Approximate temperatures profiles for different z planes of reference (surface $z = 0$) to determine the approximate thermal properties of the melt pool in the vicinity of the origin of x axis (origin of the heat source) (Fig. 4.4)

in Fig. 4.12, it is possible to overcome one of the major limitations of an analytical solution, which is that the thermal properties remain constant as a function of a single temperature, along with the difficulty of determining the "good" temperature that models the phenomenon without making an excessive error.

When applying the verification condition for convergence according to the solution algorithm of Fig. 4.12, where for each value of temperature within the substrate (at a specific value of x), the temperature profiles do not "cross" each other as in Fig. 4.14 for different z planes, the average calculated values of temperature can be used to assign values to the thermal properties (again according to the z coordinate).

The idea is to extend the concept of a temperature-dependent thermal property to a position-dependent thermal property when the temperature in different positions is known. Using thermal properties that are variable in the melt pool space is more accurate than simply choosing a fixed temperature as "good value" for the whole volume of molten zone.

For example, by combining the T_{mean} data from Fig. 4.14 over $-r_{laser} \leq x \leq r_{laser}$ for different z planes with Table 4.2 (in the case of thermal conductivity k), a $k(T_{mean}(z))$ composite function can be obtained (Fig. 4.15).

When thermal properties have been approximately estimated as a function of the z coordinate in the substrate, the next step is to define a division of the domain in it (mesh) for the calculation of the thermal gradients (in other words, the step for each coordinate-dependent temperature calculation within the x, y, z coordinates in the substrate), to apply Eq. 4.33.

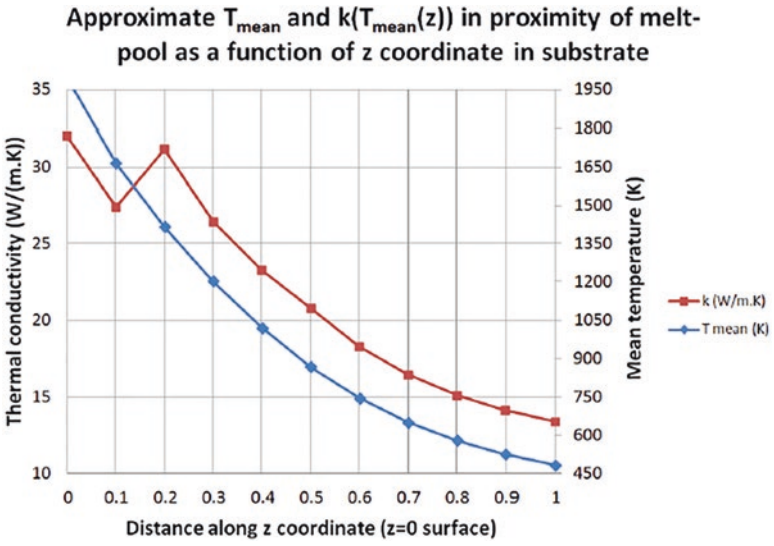

Fig. 4.15 Approximate temperature in the melt pool zone as a function of the z coordinate to define its inner thermal properties in the range of the laser beam ($-r_{laser} \leq x \leq r_{laser}$). It also shows the application of $T_{mean}(z)$ to a specific temperature-dependent thermal property (thermal conductivity) to define the $k(T_{mean}(z))$ function

It is not appropriate to apply a time-dependent convergence criterion such as the one used for the numerical method of finite differences to solve the thermal field (in discrete x, y, z coordinates), since Eq. 4.30 does not depend on it. Therefore, a discretization by coordinates in the domain will be chosen finely enough to have a "good resolution" within the volume of the melt pool (Peyre et al. 2008).

For simplicity, the pitch of the domain discretization that has been defined to obtain the temperatures within the melt pool will be a function of the radius of the laser beam. Thus, the size of mesh pitch for the x, y, z coordinates will be Eq. 4.34:

$$\Delta x = \Delta y = \Delta z = \frac{r_{\text{laser}}}{25} \tag{4.34}$$

It is not necessary to establish the same range size for the calculation of the thermal gradients and for the approximate temperature-dependent thermal properties ($-3.r_{\text{laser}} \leq x \leq 3.\ r_{\text{laser}}$). From the Assumption 3 of this model, the size of the melt pool is given approximately by ϕd_{laser}, and therefore (and to ensure a sufficient domain size for gradient calculation), the maximum and minimum range coordinates for x and y will be defined as Eq. 4.35:

$$x_{\min} = y_{\min} = -1.5r_{\text{laser}} \wedge x_{\max} = y_{\max} = 1.5r_{\text{laser}} \tag{4.35}$$

From the data and parameters of Tables 4.2 and 4.3, applying the algorithms of Figs. 4.7 and 4.12 and Eq. 4.33 with the range and domain pitch density of Eqs. 4.34 and 4.35, the corresponding surface isotherms for the temperatures T_{Liquidus} and T_{Solidus} (this has been calculated with of a programming code made in Matlab (R)) for $T\ \forall\ (x, y, z)$ discrete domain points are presented in Fig. 4.16.

4.3.9 *Calculation of Temperature Gradient (G_L) for Liquid Isotherm and the Grow Rate (V) in the Melt Pool*

For the calculation of temperature gradients within the data set, the Method of Central Difference is used. For the edges in the same data set, the Single-Sided Differences Method is used (LeVeque 2007). A unique temperature gradient value (G_L and G_S) must be established for each coordinate within the thermal field based on the reference frame of Fig. 4.4.

The solidification in the melt pool (taking into account its symmetry) is given in the rear part of the same (with respect to the direction of movement of the laser beam), specifically from the plane that is located in the lower z coordinate of the solidus temperature T_{Solidus} over the surface in the isotherm that is the boundary of the melt pool (Fig. 4.17).

The criterion for establishing a unique value of G_L and G_S is that every point in the surfaces of the isotherms must be crossed by the same vector-line starting from

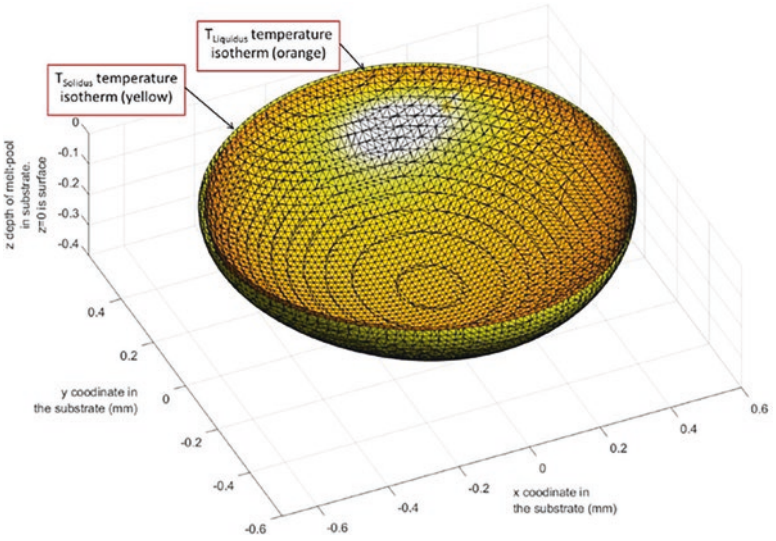

Fig. 4.16 Isothermal surfaces for the calculation of temperature gradients at the T_{Liquidus} and T_{Solidus} boundary. In this figure, the origin of the coordinate system ($x_0 = 0$, $y_0 = 0$, $z_0 = 0$) coincides with that of the semi-infinite substrate of Fig. 4.4. The positive x coordinates coincide with the direction of advance (v) of the laser beam

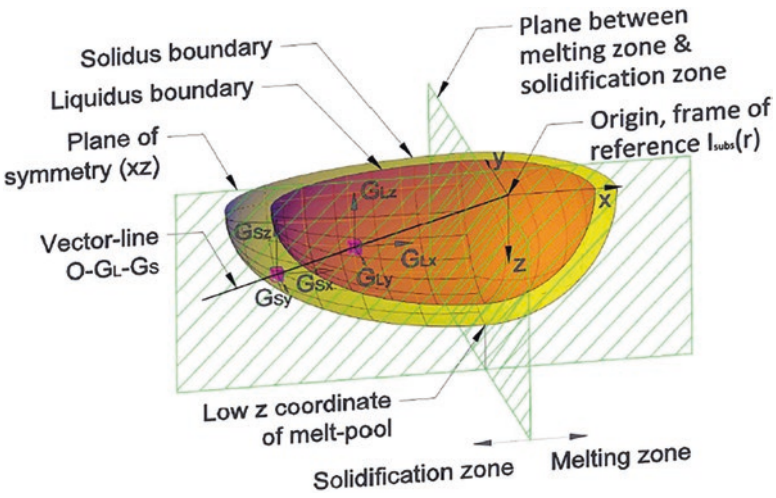

Fig. 4.17 Scheme for the calculation of temperature gradients G_L and G_S in melt pool. Note that the lowest z coordinate within the melt pool over the surface of isotherm does not coincide with the origin of the frame of reference for the vectors-lines to define the coordinates for the simultaneous calculation of G_L and G_S

the origin of the frame of reference of the laser beam. As the mesh in the melt pool domain is regular (and defined for an [x, y, z] orthogonal system), and the volume of the melt pool in mushy state is relatively small (Fig. 4.16), the projection line *Origin*-G_L to a specific coordinate (x_{GL}, y_{GL}, z_{GL}) automatically defines the G_S coordinate by its extrapolation (x_{GS}, y_{GS}, z_{GS}). The use of this approach allows practically the same coordinate density as that of the isotherm of Liquidus temperature.

Once the gradients have been calculated for each domain coordinate in the corresponding conditions for both Liquidus (G_{Lx}, G_{Ly}, G_{Lz}) and Solidus (G_{Sx}, G_{Sy}, G_{Sz}) boundaries, the modules of the same will be calculated (Eqs. 4.36 and 4.37):

$$\left|G_L\right| = \sqrt{G_{Lx}{}^2 + G_{Ly}{}^2 + G_{Lz}{}^2} \tag{4.36}$$

$$\left|G_S\right| = \sqrt{G_{Sx}{}^2 + G_{Sy}{}^2 + G_{Sz}{}^2} \tag{4.37}$$

When the temperature gradients have been calculated, it is necessary to use solidification theory to determine an extra parameter needed to define the grain morphology originated by the local conditions of solidification (e.g., with the use of a Solidification Map for a certain alloy). This extra parameter is V the growth velocity of the solidification front of during the change of phase Liquid to Solid.

The temperature gradients across the solid–liquid interface are assumed in steady state and are a function of an energy balance that remains in equilibrium (that is to say, there is no change in the interface velocity with time) (Flemings 1974) since Eq. 4.33 is itself a representation of a steady state. It is possible to make such energy balance between the Liquidus and Solidus boundaries based on the observation of Fig. 4.16, where the distance between Liquidus and Solidus boundaries in the melt pool isotherms is very small. This is because the temperature gradient in the laser cladding process is very high (Levin 2008) and that in turn leads to a rapid solidification.

Assuming that the distance between Liquidus and Solidus boundaries is small, the energy balance for the growth front of grains can be assumed as that of a plane front. Applying the method for plane growing of grains (Flemings 1974), whose formulation is presented in Eq. 4.38, it is possible to estimate the value of V from G_L and G_S, and the temperature-dependent thermal properties of Table 4.2, thus:

$$k_S G_S - k_L G_L = \rho_S L_f V \tag{4.38}$$

where the properties k_S, ρ_S refer to the values of thermal properties at T_{Solidus} temperature, and k_L to the values at T_{Liquidus} temperature. Clearing V and reordering Eq. 4.38, the growth velocity V can be estimated as (Eq. 4.39):

$$V = \frac{G_S k_S - G_L k_L}{L_f \rho_S} \tag{4.39}$$

Equation 4.39 indicates that the growth velocity is not directly dependent on the temperature gradient, but on the difference $G_S.k_S - G_L.k_L$. Since k_S, ρ_S, k_L and L_f are properties of the material (fixed values), the gradient in the Liquidus phase (G_L) will be directly proportional to the heat flow at the Liquidus–Solidus interface. It should be noted that Eq. 4.39 is of a general formulation and does not take into account sub-cooling phenomena or composition gradients.

Furthermore, Eq. 4.39 does not indicate anything about the final morphology after grain solidification. To overcome the latter (and establish a way to estimate the grain morphology based on the laser cladding process parameters), it is necessary to use the model described later in this document. To justify the use of a CET model, it is necessary first to understand the particular metallurgical characteristics of the laser cladding process.

4.3.10 Metallurgy of Laser Cladding Process

Metallurgy refers to the science and technology of metals. The subject area can be considered as a combination of chemistry, physics, and mechanics with special reference to metals.

There are two types of metallurgy: Physical Metallurgy, which is related to physical properties, where these are a function of the phases present in the alloy (or the transformation of them), and Chemical Metallurgy, which is related to the reduction/oxidation of metals (corrosion) (Seetharaman 2005). This chapter will be mainly focused on the concepts associated with Physical Metallurgy.

The concept of metallurgy in coatings processes that use lasers as source of energy to the process itself (the case of laser cladding) is associated with the guarantee of the quality of the bond between the clad and the substrate materials.

The union is by fusion (and not a union by diffusion) of a small portion of the surface (melt pool), together with the added material (Vuoristo et al. 2005). This union by fusion is much localized, since the source of energy used to create this small foundry (the laser source), is generally of a small size and a very high energy density. The existence of a high energy density (in the order of MW/m^2), is one of the main factors to determine the magnitude of the heat flow (through the value of G_L), which together with the shape and characteristics of the melt pool are key to determining the microstructure that will form when the molten material solidifies.

Along with the reduced size of the melt pool of the process itself (in the scale of millimeters), other important differences with the traditional casting processes are:

– The high cooling rate (because the change of phase liquid/solid takes place on a substrate that is in general many times larger than the melt pool generated on it and acts as a thermal sink).
– The highly directional conduction of the heat flow (this is general for all LAM processes, resulting in columnar grain epitaxial growth from the substrate when

the feeding material is similar to the base). However, under certain circumstances, equiaxed grain growth will also be possible (Ma et al. 2017).

Regarding raw materials, it is most common to use filler material consisting of the same type of alloy as the substrate, although it is nevertheless possible to mix different kinds of metal powder if the application requires it. The use of different types of metal powders makes it possible for both physical and chemical metallurgical reactions to occur when the melt is formed (Zhong and Liu 2010), since materials with very different physical properties (melting points, thermal conductivities, coefficients of thermal expansion, etc.) can be used. A very interesting study of different combinations for both substrate and powder materials is presented in Toyserkani et al. (2005), which mentions the importance of convection as phenomenon inside the melt pool (which allows the homogenization of its constituent components), and that can be characterized by the "tension number" (*S*), (Eq. 4.40), which is much related to the laser cladding process and thermal properties of the material:

$$S = \frac{\left|d\gamma_{\text{sup}} / dT\right| \phi d_{\text{laser}} \eta P}{A_{\substack{\text{spot} \\ \text{laser}}} \mu_{\text{melt}} vk} \tag{4.40}$$

This equation allows characterizing the convection within the melt pool itself, as a function of several parameters of the same process and of the thermal properties of the material itself. It is established that for values lower than 45,000, the convection is negligible (Almeida et al. 2001). However, this strong convection within the liquid phase of the material acts for a very short time, since the solidification is in turn very fast. The balance between the processes of melting, mixing, and solidification is very complex, and depends on, among other things, the size of the laser spot, the speed of laser beam with respect to the substrate, the amount of powder flow, the absorptivity of the laser beam by the materials during the laser cladding process itself, and the kind of protection gas and its flow (Zhong and Liu 2010).

However, even if a good metallurgical union is reached (apparently), its behavior may not be satisfactory because the high temperatures and energies involved give rise to some of the components within the melt pool itself reacting and forming insoluble phases with very high melting point, such as for example in Al-Nb systems, which can form intermetallic Al_3Nb (Almeida et al. 2001). Some of these phases are very hard and fragile, and therefore their appearance must be avoided as they can generate cracks or fragile starting points of rupture within the cladded material itself or within the metallurgical union.

Due to large temperature gradients, solid solubility limits for solutes are much higher than expected from equilibrium phase diagrams, plus considerable increases in phase transformation temperatures (Kar and Mazumder 1989; Zhong and Liu 2010). This leads to the formation of metastable alloys with extended solid solubility (Agrawal et al. 1993). An excellent study for laser cladding applied to eutectic and isomorphic binary alloys can be found in Toyserkani et al. (2005). There are

special cases that make it difficult to obtain a homogeneous alloy during the formation of the clad. This is the case with multi-component alloys, where there are the difficulty by the formation of intermediate compounds between the powder and the substrate during the formation of the melt pool (due to the high temperatures involved), giving rise to problems of crack formation or low quality of substrate/clad union usually due to the formation of brittle or intermetallic phases (Cárcel et al. 2014).

For single phase alloys, such as 316L stainless steel, many of the physical properties will depend on the grain size. Some classic relationships used in traditional type casting are applicable to the laser cladding process for these cases (Ma et al. 2017). For example, the one that expresses the grain size as a function of the cooling rate ($\dot{T}$), Eq. 4.41:

$$d_{gr} = a_{gr} + \frac{b_{gr}}{\sqrt{\dot{T}}} \tag{4.41}$$

Another special feature of laser cladding metallurgy is the creation of very fine grain microstructure within the clad material (with very small primary and secondary dendritic distances), in addition to the associated increase in dislocations density, and the distortion of the lattice structure (Zhong and Liu 2010), this last a consequence of rapid solidification.

The refinement of the microstructure is explained by the phenomenon of constitutional supercooling. In Toyserkani et al. (2005) the phenomenon is explained qualitatively for a eutectic alloy (Fig. 4.18), where in steady-state conditions it is assumed that the interface in the solidification zone remains at constant temperature, the solidification front is flat and moves at constant speed, the solid diffusion effects are neglected due to the high solidification rates, the convection in the melt pool (mixture) is limited to a mass transport by diffusion of the solute in the liquid phase, and the partition coefficient (k_e) can be determined from the equilibrium phase diagram of the alloy.

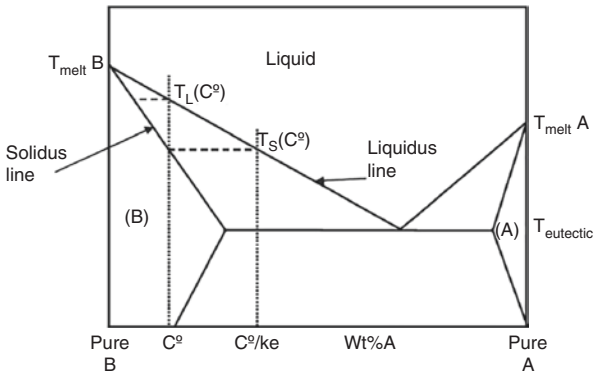

Fig. 4.18 A schematic of a hypothetical phase diagram indicating steady-state solidification conditions (Toyserkani et al. 2005)

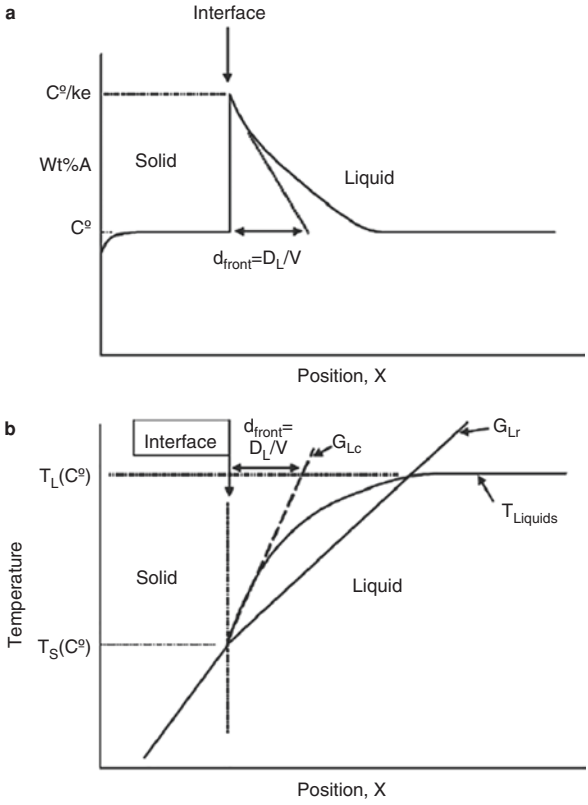

Fig. 4.19 (**a**) Compositional gradient, (**b**) temperature gradient at the solid/liquid interface during steady-state solidification (Toyserkani et al. 2005)

The result is a concentration profile through the solid/liquid interface similar to Fig. 4.19, where the Liquidus Temperature is determined by the composition of the liquid itself that experiences a part of the solidification front (when there is a high proportion of solute). This zone experiences a "real" temperature (given by the gradient G_{Lr}), which is below the solidification temperature determined by the gross composition of the alloy. This phenomenon is called constitutional supercooling.

The critical temperature gradient (G_{Lc}) for the establishment of stable solidification conditions is defined in Eq. 4.42. Above this value, no constitutional supercooling will occur, and the solidification front will remain flat.

$$G_{Lc} > \frac{\Delta T\left(C^o\right)}{D_L / V} \tag{4.42}$$

The alloys used in engineering practice have in general a significant solidification range; therefore, they are prone to solidify with a dendritic structure and it is very difficult to fulfill a small $\Delta T(C^o)$ that can originate a flat solidification interface. Therefore, as the solid grows, the solidification front needs to reject more solute at the front of the solid/liquid interface.

For a binary alloy solidifying at high speed, the solute trapping phenomenon is generated, where the partition coefficient becomes dependent on the solidification velocity (k_V) (Wang et al. 1997) (Eq. 4.43):

$$k_V = \frac{k_e + a_o V / D_L}{1 + a_o V / D_L} \tag{4.43}$$

The morphology of microstructures due to growth in unstable state is very sensitive to disturbances, and the whole phenomenon is not well understood, although it is believed to be related to the waves on the solidification front that produce instability. On a practical level, empirical relations are used in the form of power, Eq. 4.44, in which λ_{gr} represents a characteristic of spacing in the microstructure after solidification (Srivatsan and Sudarshan 1993).

$$\lambda_{gr} = B\left(\partial T / \partial t\right)^{-n_\lambda} \tag{4.44}$$

Finally, the refinement of the microstructure finally comes from the fact that the most efficient way to generate the concentration gradient by rejection of the solute (related to k_V as a first approximation) is by reducing the dendritic radius tip or through the creation of a cellular-type solidification structure (thus generating more surface for rejection), and therefore originating a refinement over the entire microstructure volume of the clad material. Because the solidification rate varies within the height of melt pool, it is expected that the microstructure of the clad should also be refined across the same (Toyserkani et al. 2005).

Recently, Liang et al. (2016a, b, 2017) have established models for Nickel SX-based alloys to estimate: microsegregation for rapid solidification multicomponent alloys, processing microstructure maps, and primary dendritic arm spacing, respectively.

The general conclusion of the above text is that the modeling of the crystallization process (including CET), in laser cladding process is very complicated, mainly due to phenomena of high cooling rates that can greatly deviate the conditions of solidification from equilibrium.

The conditions of instability have their origin in the particularities of the process itself. However, it is not advisable to avoid the use of this technology due to the great advantages that it offers; especially to its metallurgy particularities (it is possible to precisely control the resulting microstructure).

To overcome this limitation, there is experimental information about solidification conditions and structure generated through experimental solidification maps for complex alloys that are available as a function of V and G_L. It should be remembered that solidification maps for alloys illustrate the effect of temperature gradient and solidification rate on the morphology and scale of solidification structures (Blecher et al. 2014).

4.4 Crystallization Model

4.4.1 Relationship Between a Solidification Map and Gäumann's Crystallization Model

There are basically two ways of predicting CET for a given multicomponent alloy during a solidification process. One is by means of a mathematical model such as Gäumann's, (Gäumann et al. 1999) and another by the use of solidification maps of experimental type.

By means of mathematical models as for example the deterministic one in Eq. 4.46, (knowing the values of N_0, a and n for a given alloy), ϕ will express the fraction of equiaxial grain ($\phi \rightarrow 1$) or columnar grain ($\phi \rightarrow 0$) that will originate under certain conditions in a solidification process, knowing the local values of V and G_L. The CET models can be classified as stochastic or deterministic (Martorano et al. 2003) – we use in this chapter a deterministic one.

Another way to predict the behavior of the resulting microstructure after solidification is by means of solidification maps (Fig. 4.3). These maps are of experimental type (Hunt 1984; Nastac et al. 2001), and in them it is possible to plot for the local conditions of solidification V and G_L as coordinates and get not only the morphology of the microstructure, but (depending on the information available in the experimental map) other characteristics such as SDAS and porosity. In this chapter, only information related to the CET from these maps will be taken into account.

In summary, a solidification model is an approximation, by means of a mathematical adjustment (based on physical constants), of the behavior observed in an experimental solidification map.

The model of Gäumann (Gäumann et al. 2001) is defined as (Eq. 4.45):

$$\frac{G_L{}^n}{V} = a\left[\sqrt[3]{\frac{-4\pi N_o}{3\ln(1-\phi)}}\,\frac{1}{n+1}\right]^n \tag{4.45}$$

Clearing ϕ, assuming [V, a, n, N_0] = constant, and replacing in Eq. 4.45 results in:

$$\phi = 1-\exp\left[-\frac{4\pi N_0\left(G_L{}^n/(Va)\right)^{-3/n}}{3(n+1)^3}\right] = 1-\exp\left(-a_1 G_L{}^{-3}\right) \tag{4.46}$$

where $a_1 = f(V) = \dfrac{4\pi N_0 (Va)^{3/n}}{3(n+1)^3}$.

As G_L normally is expressed for a logarithmic scale coordinate system, for a space in linear coordinates the appropriate change of variables is defined as $\log_{10}(G_L) = G_L'$. Then clearing G_L, and replacing in (Eq. 4.46):

$$\phi = 1 - \exp\left(-a_1 G_L^{-3}\right) = 1 - \exp\left[-a_1\left(\exp\left(-a_2 G_L^{'}\right)\right)\right] \tag{4.47}$$

where $a_2 = 3\ln(10)$.

The graphical representation of Eq. 4.46 expressed as a three-dimensional surface of the form φ=f (G,V) for the specific case of the model of CMSX-4 alloy based on the constants of (Anderson 2010), ($N_0 = 2 \times 10^{15}\,\mathrm{m}^{-3}$, $a = 1.25 \times 10^6\,\mathrm{K^n m^{-1}\,s^{-1}}$ and $n = 3.4$) results in the following graph (Fig. 4.20).

The experimental solidification map for the same alloy is presented in Fig. 4.21, where two graphs of contour lines (the lines are the same as the one in the lower left graph of Fig. 4.20), for the mathematical model of Gäumann for $\phi = 0$ and $\phi = 1$, have been superimposed (red lines). The graph shows that the mathematical model correctly describes the CET behavior of the alloy for conditions with solidification velocities greater than approximately 10^{-2} m/s. In the case of V less than 10^{-2} m/s, the model quickly loses accuracy (the real boundary between the equiaxial and columnar grain morphology is delimited by the thick-curved black line).

The alloy constants for Fig. 4.20 obtained from (Anderson 2010) are not calculated uniquely. The procedure for obtaining the constants used in the representation of Fig. 4.20 requires the use of numerical methods to adjust the shape of the mathematical curve, although this method makes no physical sense. For example, a second set of constants for the Gäumann model for CMSX-4 alloy is given in Table 4.4.

There is nothing to guarantee that the numerical method will converge, nor that the values of the constants obtained are optimal ones.

There are excellent mathematical models such as Gäumann et al. (2001) and Martorano and Biscuola (2009), but they have the same limitations in their range of application and do not clearly describe the behavior in the columnar/equiaxial transition. To "describe" the behavior in the mixed zone means to establish with certain accuracy the percentage of equiaxed or columnar grain formation within the zone. Later on it will be demonstrated that, for example, for a value V = constant, a value of G_L found at the mean distance between the isocurves $\phi = 0$ and $\phi = 1$ will not have an equiaxial grain formation percentage of 50%. Later it will be shown that the crystallization model within the mixed zone is asymmetric, and that their behavior is adjusted to a special type of statistical distribution.

On the other hand, solidification maps such as those in Gäumann et al. (2001), Kobryn and Semiatin (2003), Martorano et al. (2003), and Nastac et al. (2001) are not sufficiently exploited, because it is not easy to adapt them to a useful form for use for example in a computer program as it is possible in mathematical models. A very useful idea would be to take the data from a given solidification map and convert it into a formula based on some key data or easily transform the information contained in a solidification map into the constants necessary for a model such as that of Gäumann (with unique values and with some physical sense that allows verifying the numerical fitting by means of key data). Another difficulty with experimental solidification maps is to model the behavior in areas of mixed columnar/equiaxed when the CET transition occurs only using graphics, as in Fig. 4.3. The

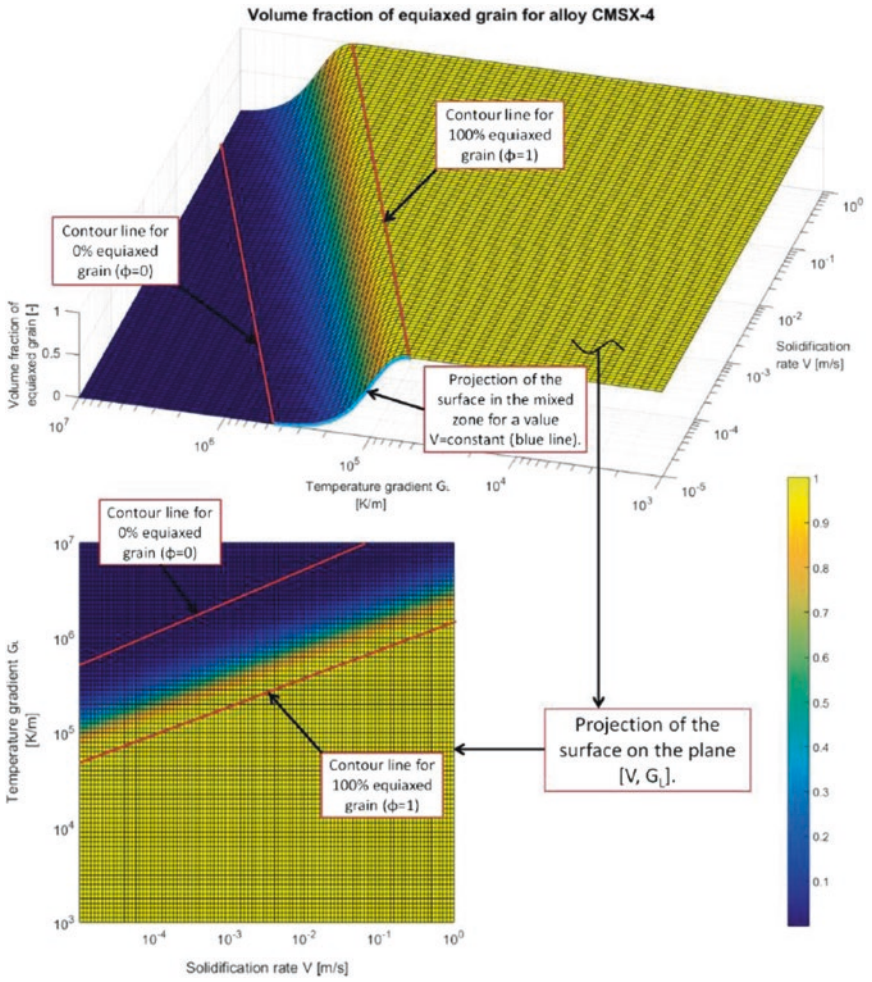

Fig. 4.20 Representation of equation of the volumetric fraction of equiaxed grains of Gäumann's model (Gäumann et al. 2001) for CMSX-4 alloy

solidification maps have in general well-defined CET boundaries, but they do not give information about the behavior in the mixed zone. For this document the model of (Gäumann et al. 2001) will be used as basis.

4.4.2 Objectives of the Crystallization Model

1. Describe the mathematical structure on which Gäumann's CET model is based, and use it to create an extended deterministic mathematical model for steady-state in unidirectional solidification.

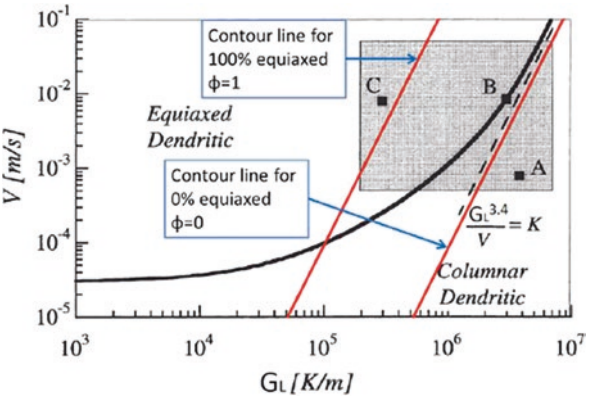

Fig. 4.21 Microstructure selection map for superalloy CMSX-4 under the experimental conditions described in the text (Gäumann et al. 2001), showing the expected solidification morphology as a function of temperature gradient, G, and solidification velocity, V

Table 4.4 The original and optimized parameters for the calculation of SG volume fraction (Anderson et al. 2010)

	Original	Optimized
N_0 (m^{-3})	2×10^{15}	1.18×10^{15}
a ($K^n.m^{-1}.s^{-1}$)	1.25×10^6	2.03×10^6
N	3.4	5.3

2. Based on the above objective, accurately and intuitively establish the behavior of the mixed zone in the columnar/equiaxed transition $\phi = f(V, G_L)$.
3. Extend the application range of Gäumann's model for low solidification speeds V.
4. Establish a methodology to determine both the constants for the model to be proposed in this document and for Gäumann's model, based on experimental solidification maps. The aim is a method of searching for constants that result in a unique set of them that make physical sense. At the same time, this will avoid the use of numerical methods that can result in multiple sets of values for the constants (without physical sense).
5. Establish a practical method for calculating the value of the constant N_0 based on EBSD test images, and based on that the constant a, for example, to use it in Gäumann's model.

4.4.3 Model of Crystallization Based on Gäumann's Model as a Probability Distribution

It will be shown that Gäumann's model has the same mathematic basic structure as a probability distribution of Extreme Value Type I, and from this fact the necessary constants will be deduced to extend the range of use of the original model through a deterministic mathematical model for steady-state in unidirectional solidification.

If in Eq. 4.47, $\xi = G_L'$ and $a_1 = a_2 = 1$ (only for clarification), the resulting expression is equivalent in canonical shape to the formulation of the minimum standard cumulative distribution function (cdf) of Gumbel or Extreme Value Type I Distribution (NIST/SEMATECH 2012), which is defined in Eq. 4.48:

$$\mathrm{cdf}_{\mathrm{Gumbel}} = 1 - \exp\left[-\exp\left(\xi\right)\right] \tag{4.48}$$

From the comparison of Eq. 4.48 with Eq. 4.47, it is observed that both share the same basic structure, that is to say, the same canonical shape, from which it can be deduced that the behavior of Gäumann's model can be represented by a specific cumulative distribution function *or cdf* (Gumbel).

Both the probability density function (*pdf*) and cdf of Gumbel's function are biased in terms of the probabilities calculated from them (for different values of ξ) (NIST/SEMATECH 2012). Therefore, they do not follow the pattern of the Normal Distribution (symmetry for both *pdf* and *cdf*). Thus by analogy, Gäumann's model will present this phenomenon of asymmetry when used to calculate the volume fraction of equiaxed grains (ϕ) as function of G_L and V especially in the mixed zone of CET (Figs. 4.20 and 4.22).

4.4.4 *Deduction of the Crystallization Model Based on the* cdf *of Gumbel*

Since it has been demonstrated by means of Eqs. 4.47 and 4.48, that the Gäumann equation is of the Gumbel's cdf type, the next step is to adapt a general form of the equation to a surface similar to that shown in Fig. 4.20. The general equation of the *cdf* of the Gumbel Distribution is represented by the Eq. 4.49:

$$\phi_{\mathrm{Gum}} = 1 - \exp\left(-\exp\left(\frac{\xi - \mu}{\beta}\right)\right) \tag{4.49}$$

where μ is the location parameter and β is the scale parameter.

The objective is to obtain, on the basis of relatively easy to get key data from graphs similar to those in Fig. 4.3, the constants μ and β as a function of G_L and V.

4.4.4.1 Equivalence of ξ for the Crystallization Model Based on *cdf* of Gumbel

The variable ξ has a precise meaning within the crystallization model based on Gumbel. It is the statistical equivalent of the "location parameter" (i.e. the position of the cfd curve over a coordinate axis). The effect of varying such a parameter can be understood visually by observing the behavior of the variable ϕ (in a 2d graph),

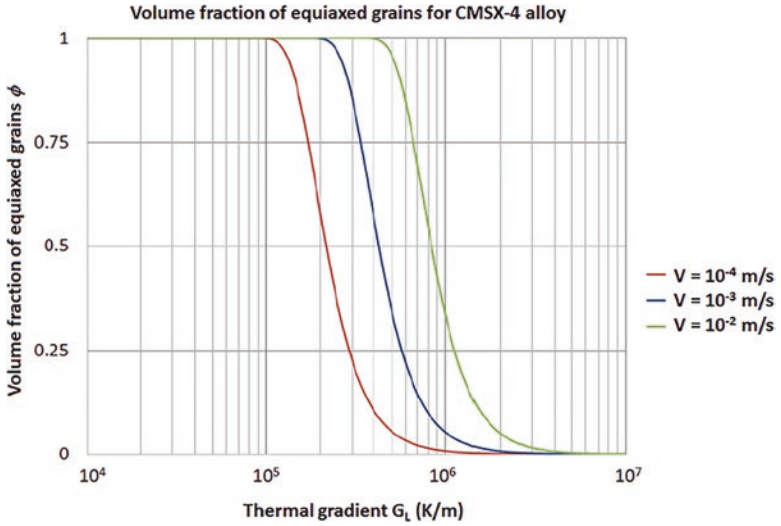

Fig. 4.22 Volume fraction of equiaxed grains formation for alloy CMSX-4 for different V from 1×10^{-4} to 1×10^{-2} (m/s) as function of G_L(K/m)

when the coefficients [N_0, a] are taken as constants. In this example the values of (Gäumann et al. 2001), will be used as a typical value. With the above it is possible to plot the Eq. 4.46 as a function $\phi = f(G_L)$. For the alloy CMSX-4 (Fig. 4.20), and by taking of specific values for V from $V = 10^4$ to $V = 10^{-2}$, it is possible to obtain a figure that represents the projection of the "surface" (2D graph), of probability for the formation of equiaxed grains as function of G_L for different V (Fig. 4.22). The values of V are taken in that range because they appear in the middle of the experimental graph of the CMSX4 alloy, and therefore are representative of the entire range of work of such alloy (Fig. 4.21).

From the analysis of Fig. 4.22, it can be seen easily that in logarithmic scale coordinates, the plotting of $\phi = f(G_L)$ for a given V is equivalent to the value of $\phi = f(\xi)$ for the Eq. 4.49 and by applying the appropriate change of base (from logarithmic scale to linear scale), Eq. 4.50:

$$\xi = \log_{10}\left(G_L\right) \tag{4.50}$$

4.4.4.2 Deduction of μ and β for the Crystallization Model Based on *cdf* of Gumbel

Particularities of Solidification Maps

The next step is to deduce relationships that allow, from visual analysis and through simple calculations over graphs similar to the one in Fig. 4.3, obtaining of the values of μ and β for Eq. 4.49.

The effect of the scale parameter is to stretch out the graph (NIST/SEMATECH 2012), as the probability distribution of the Eq. 4.49. From the analysis in Fig. 4.22, it is observed that the shape (stretch) of the function $\phi = f(G_L)$ remains constant in "shape" for different values of V, and therefore β (the scale parameter) must remain constant.

Other observations (from the graph in Fig. 4.3) that allow us to obtain the above parameters (μ and β) are:

- The graphs of solidification maps for alloys such as the one in Fig. 4.3 normally present boundary lines that limit the areas for the regions of 100% equiaxed grain ($\phi = 1$) and fully columnar morphology ($\phi = 0$).
- The relative distance between the boundary line where the grain volume is 100% equiaxed and 100% columnar remains constant for a typical solidification map like that of Fig. 4.3 (for the zone where the slope of both lines is linear and constant).
- The Eq. 4.46 is able to represent that behavior (relative distance between $\phi = 0$ and $\phi = 1$ is constant). This is demonstrated from Fig. 4.22, where a change with the same delta value of V (on the logarithmic scale), produces probability curves that are at the same relative distance from one another.

Therefore, if the scale parameter β is kept constant for different values of V (or what is the same, for different location parameters μ), it should be possible to establish a relationship between the relative distances only as a function of $\log_{10}(G_L)$.

Proposed Method for the Deduction of β Based on the Solidification Map Parameter G_L

As mentioned earlier, the effect of the scale parameter (β) is to stretch out the graph. The idea is to establish in such a way that it is able to represent the projection of the surface graph for a given alloy (for a model of crystallization), for a value of constant, as shown in Fig. 4.20 in the detail marked as "Projection of the surface in the mixed zone for a value V = constant (blue line)."

The following method is proposed to derive the variable β based on the Solidification Map Parameter G_L (starting from Eq. 4.46), when the volumetric grain fraction takes the value of $\phi = 0$, $\phi = ½$, $\phi = 1$ for certain a, V and, N_0, that remain constant. The scale parameter (β) can be deduced as a function of these values of ϕ, taking them as values of probability that fit in the Gumbel function located on the axis $\log_{10}(G_L)$ in an arbitrary position, that is to say $\mu = f(V)$.

On the one hand, Eq. 4.45 is not defined for $\phi = 0$ and $\phi = 1$, since the evaluation at either values of ϕ is indeterminate or ∞. To solve the problem of indetermination for (Eq. 4.45), when ϕ=0 and ϕ=1, it has been decided to use as methodology numerical limits near those values with the desired precision. For convenience of numerical management, we have chosen values related to the exponential number to replace the values of ϕ near zero and one by Eqs. 4.51 and 4.52:

$$\phi \approx 0 = \frac{1}{e^{\kappa}} \tag{4.51}$$

$$\phi \approx 1 = 1 - \frac{1}{e^{\kappa}} \tag{4.52}$$

where κ is an integer. Replacing the values of Eqs. 4.51 and 4.52 in Eq. 4.45, clearing out $G_{L(\phi \approx 0)}$ and $G_{L(\phi = 1)}$, and applying logarithm to base 10 result in Eqs. 4.53 and 4.54:

$$\log_{10}\left(G_{L(\phi \approx 0)}\right) = \frac{3\ln\left(\left(Va\left(\frac{(n+1)^3\left(\kappa - \ln\left(e^{\kappa}-1\right)\right)}{N_0}\right)^{-n/3}\right)^{1/n}\right) + \ln\left(\frac{4\pi}{3}\right)}{3\ln(10)} \tag{4.53}$$

$$\log_{10}\left(G_{L(\phi \approx 1)}\right) = \frac{3\ln\left(\left(Va\left(\frac{\kappa(n+1)^3}{N_0}\right)^{-n/3}\right)^{1/n}\right) + \ln\left(\frac{4\pi}{3}\right)}{3\ln(10)} \tag{4.54}$$

For the case of ϕ = ½, and repeating the same procedure as in Eqs. 4.53 and 4.54, results in Eq. 4.55:

$$\log_{10}\left(G_{L(\phi = 1/2)}\right) = \frac{3\ln\left(\left(Va\left(\frac{(n+1)^3}{N_0}\right)^{-n/3}\right)^{1/n}\right) - \ln\left(\frac{3\ln(2)}{4\pi}\right)}{3\ln(10)} \tag{4.55}$$

Then calculating the ratio between the relative distances over the horizontal axis of the logarithms ($\log_{10}(G_L)$) for the different values of ϕ (from ϕ = ½ to $\phi \approx 1$ and from $\phi \approx 0$ to $\phi \approx 1$) (Eq. 4.56):

$$\text{Ratio}_{\log_{10}(G_L)} = \frac{\log_{10}\left(G_{L(\phi=1/2)}\right) - \log_{10}\left(G_{L(\phi \approx 1)}\right)}{\log_{10}\left(G_{L(\phi \approx 0)}\right) - \log_{10}\left(G_{L(\phi \approx 1)}\right)} = \frac{\ln\left(\frac{\ln(2)}{\kappa}\right)}{\ln\left(\frac{\kappa - \ln\left(e^{\kappa}-1\right)}{\kappa}\right)} \tag{4.56}$$

The value of $\text{Ratio}_{\log_{10}(G_L)}$ depends solely on κ (for convenience defined as an integer $\kappa > 1$). Table 4.5 shows the result of evaluating the function for different κ along

Table 4.5 Evaluation of the function $\text{Ratio}_{\log_{10}(G_L)} = f(\kappa)$ for different values of κ, along with the relative error rate for the term $\kappa + 1$

$\text{Ratio}_{\log 10(GL)} = f(\kappa)$	Relative error (%) $(f(\kappa + 1) - f(\kappa))/f(\kappa)$	Relative difference in % of error	Convergence condition
0.404	11.0%	1.64%	No
0.360	9.4%	1.13%	No
0.326	8.2%	0.86%	No
0.299	7.4%	0.69%	No
0.277	6.7%	0.57%	No
0.259	6.1%	0.48%	No
0.243	5.6%	0.40%	<1% in the last four terms

with the relative error difference for the term $\kappa + 1$. We have defined the criterion that the value of κ shall be taken from the last term whose difference between its last four consecutive evaluations is not greater than 1%.

From Table 4.5, $\kappa = 8$ and substituting in Eq. 4.56, results in Eq. 4.57:

$$\text{Ratio}_{\log_{10}(G_L)} = \frac{\log_{10}\left(G_{L(\phi=1/2)}\right) - \log_{10}\left(G_{L(\phi\approx1)}\right)}{\log_{10}\left(G_{L(\phi\approx0)}\right) - \log_{10}\left(G_{L(\phi\approx1)}\right)} = \frac{\ln\left(\frac{\ln(2)}{8}\right)}{\ln\left(\frac{8-\ln\left(e^8-1\right)}{8}\right)} \quad (4.57)$$

Finally, the value of β can be obtained from the following reasoning:

- Equation 4.46 can be interpreted as a probability of volumetric equiaxed grain formation, with a value always between 0 and 1, that is to say, a probability function. It has been demonstrated that its representation is consistent with that of a Gumbel's *cdf*.
- It is known that there is a relationship for the equiaxed grain volume fraction between the values of $\phi \approx 0$, $\phi \approx ½$ and $\phi \approx 1$ as $f(\log_{10}G_L)$ (Eq. 4.57), this relation is shown in Fig. 4.23.

From the previous paragraphs, it is therefore possible to know the value of β, from Eq. 4.49, clearing the value of μ, and then resolving β for the two known conditions (the distance ratio of Eq. 4.57).

Clearing μ from Eq. 4.49, rename μ as μ_V (because $\mu = f(V)$), and applying the above proposed method results in (Eq. 4.58):

$$\mu_V = \beta \ln\left(-\ln\left(1-\phi_{\text{Gum}}\right)\right)+\xi \tag{4.58}$$

The conditions to be replaced in Eq. 4.58 will be those corresponding to Eqs. 4.59 and 4.60.

– Condition 1:

$$\left(\xi_1 = \log_{10}\left(G_{L(\phi\approx 1)}\right), \phi_{\text{Gum}} \approx 1 = 1-1/e^8\right) \tag{4.59}$$

– Condition 2:

$$\left(\begin{array}{l}\xi_2 = \log_{10}\left(G_{L(\phi\approx 1)}\right)+\left|\log_{10}\left(G_{L(\phi\approx 1)}\right)-\log_{10}\left(G_{L(\phi\approx 0)}\right)\right| \\ *\text{Ratio}_{\log_{10}(G_L)}, \phi_{\text{Gum}} = 1/2\end{array}\right) \tag{4.60}$$

Operating and clearing β for the above conditions (Eq. 4.61):

$$\beta = -\frac{\left|\log_{10}\left(G_{L(\phi\approx 1)}\right)-\log_{10}\left(G_{L(\phi\approx 0)}\right)\right|}{\ln\left(1-\dfrac{\ln\left(e^8-1\right)}{8}\right)} \tag{4.61}$$

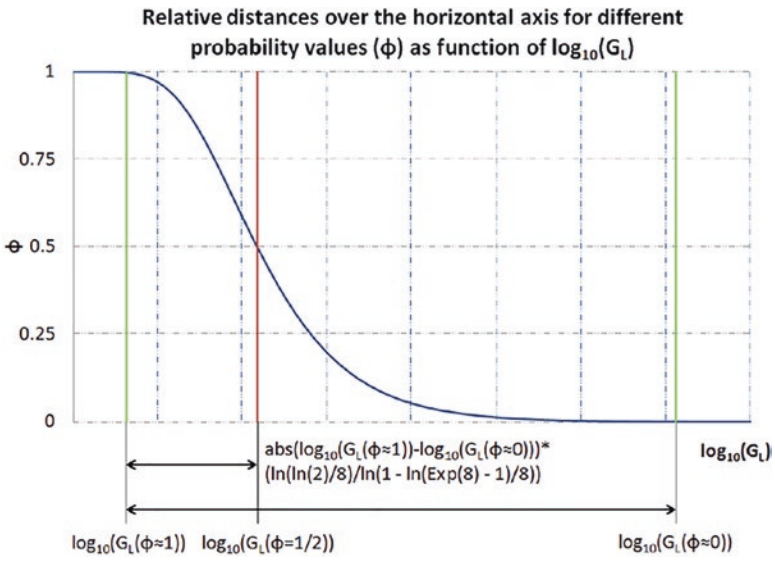

Fig. 4.23 Relative distance over the horizontal axis for the coordinate $\log_{10}(G_{L(\phi\approx 1)})$ for a volumetric equiaxed grain fraction ϕ = ½ as a function of $|\log_{10}(G_{L(\phi\approx 0)}) - \log_{10}(G_{L(\phi\approx 1)})|$

where $V_{(\phi \approx 1)} = V_{(\phi \approx 0)} = V_\phi \; \forall \; G_{L(\phi \approx 1)} \wedge G_{L(\phi \approx 0)}$; see Fig. 4.24 for details about the coordinates associated with Eq. 4.61.

Different tests have been done using Eq. 4.61 to estimate the value of β in the zone where the lines of constant slope for the volumetric fractions (ϕ close to 0 and 1), for graphs similar to the one shown in Fig. 4.3.

A phenomenon has been observed. Between the visual estimation of what mathematically is $\phi \approx 0$ and $\phi \approx 1$, and the real mathematical calculation, there is an underestimation of the value of β close to a factor of 1.7, whose origin is the definition of the limits of ϕ that have been applied to Eq. 4.45.

The volumetric equiaxed grain fraction is derived from an "approximation" of $\phi = 0$ or $\phi = 1$ by itself (Eqs. 4.51 and 4.52). This "almost" ϕ value of 0 or 1 makes the value chosen in the ξ variable defined according to Eq. 4.50 very sensitive, as well as the β value that derives from Eq. 4.61, which means that a correction factor needs to be established for β, from now on defined as β_G (because $\beta = f(G_L)$); therefore, Eq. 4.61 is transformed with the respective correction into Eq. 4.62:

$$\beta = \beta_G = -\frac{1.7\left|\log_{10}\left(G_{L(\phi\approx 1)}\right) - \log_{10}\left(G_{L(\phi\approx 0)}\right)\right|}{\ln\left(1 - \dfrac{\ln\left(e^8 - 1\right)}{8}\right)} \tag{4.62}$$

Having obtained the parameter β_G, the next one (the location parameter μ_V) shall be estimated.

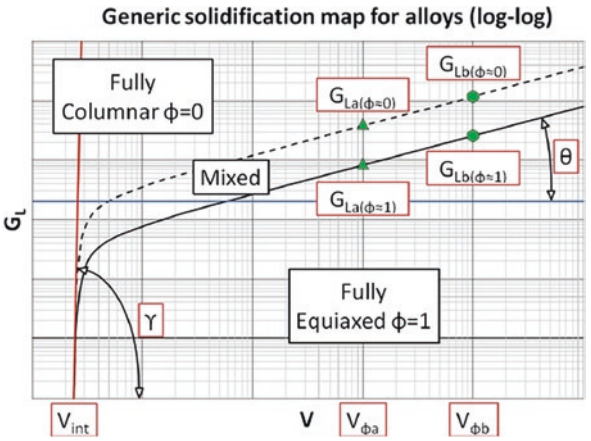

Fig. 4.24 Coordinates associated to the calculation of coefficients for the model of volumetric fraction of equiaxed grain for a generic solidification map $\phi = f(G_L, V)$

Proposed Method for the Deduction of μ Based on the Solidification Map Parameter V

The effect of location parameter (μ) is that it shifts the graph left or right over an axis (NIST/SEMATECH 2012). For this model, μ will be the parameter responsible for shift the projected curve defined by β_G over the axis of coordinates V.

In the graph of Fig. 4.20, if the projection indicated by the detail "Projection of the surface in the mixed zone for a value V = constant (blue line)" is "anchored" to one of the contour lines (either for $\phi = 0$ or $\phi = 1$), then it is possible to define the parameter μ (that will move the projection creating the surface of the model of crystallization) as a function of V, since any of the contour lines to "anchor" will be a function of V and in turn $\mu = f(\ell_{\log})$.

Therefore, the first step will be to deduce the line of projection in logarithmic scale that represents one of the contour curves, that is to say $\ell_{\log} = f(V)$, in this document for the case where $\phi = 1$.

From the analysis of Fig. 4.3, it is observed that in the area where the slope of the lines for $\phi \approx 0$ and $\phi \approx 1$ are constant in the logarithmic graph, it is possible that their representation can be made by a straight-line function in logarithmic coordinates (Eq. 4.63):

$$F(\xi) = \xi^m 10^{b_1} \tag{4.63}$$

where $F(\xi) = G_L$ and $\xi = V$. Replacing and applying logarithm to base 10:

$$\log_{10}(G_L) = m \log_{10}(V) + b_1 \tag{4.64}$$

For the graph of Fig. 4.20, where the value of contour line is $\phi = 1$ (straight line), and applying the concept of point-slope equation in logarithmic coordinates ($\ell_{\log}$), it is possible to determine for Eq. 4.64 the constants m and b_1 (Eq. 4.65):

$$\ell_{\log} = \log_{10}(G_L) = \frac{\ln\left(G_{L(\phi\approx 1)}\right) + m\left(\ln(V) - \ln\left(V_{(\phi\approx 1)}\right)\right)}{\ln(10)} \tag{4.65}$$

where

$$m = \tan\theta = \frac{1}{n} = \frac{\ln\left(\dfrac{G_{La(\phi\approx 1)}}{G_{Lb(\phi\approx 1)}}\right)}{\ln\left(\dfrac{V_{\phi a}}{V_{\phi b}}\right)} \tag{4.66}$$

The associated coordinates related to the Fig. 4.3 for Eqs. 4.65 and 4.66 are displayed in Fig. 4.24.

Physical Meaning of the Material Constant n with Respect to an Experimental Solidification Map

In this model, the slope of an equation of a straight line in logarithmic coordinates being $m = 1/n$ (where n is a constant of material) for the Eq. 4.45 is very useful, because it allows the usage of bibliography data from Gäumann et al. (2001), Kobryn and Semiatin (2003), Martorano et al. (2003), Nastac et al. (2001), or in other words its deduction from graphs like that of Fig. 4.3 or by Eq. 4.66. The validity of the above argument is demonstrated from Eq. 4.45, clearing G_L (Eq. 4.67):

$$G_L = \frac{6^{2/3}\pi^{1/3}\left[Va\left(\frac{\left(-N_0/\ln(1-\phi)\right)^{1/3}}{n+1}\right)^n\right]^{(1/n)}}{3} \tag{4.67}$$

If N_0 = constant (it is assumed that the number of heterogeneous nucleation sites is constant for a given solidification process like laser cladding), and applying logarithm to base 10 (to use the same base as in the graph of Fig. 4.3), results in Eq. 4.68:

$$\log_{10}(G_L) = \log_{10}\left(\frac{6^{2/3}\pi^{1/3}}{3}\right) + \frac{1}{n}\left[\log_{10}(V) + \log_{10}\left(a\left(\frac{\left(-N_0/\ln(1-\phi)\right)^{1/3}}{n+1}\right)^n\right)\right] \tag{4.68}$$

Equation 4.68 presents the generic shape of a straight line in logarithmic space such as Eq. 4.64. Therefore, its slope can be found by defining the auxiliary variables $\Psi^* = \log_{10}(G_L)$ and $\xi^* = \log_{10}(V)$, and deriving respect to Ψ^* knowing that $d\Psi^*/d\xi^* = \tan\theta$, thus (Eq. 4.69):

$$\frac{d}{d\xi_*}\left(\log_{10}\left(\frac{6^{2/3}\pi^{1/3}}{3}\right) + \frac{1}{n}\left[\xi_* + \log_{10}\left(a\left(\frac{\left(-N_0/\ln(1-\phi)\right)^{1/3}}{n+1}\right)^n\right)\right]\right) = \frac{1}{n} \tag{4.69}$$

And this results in Eq. 4.70:

$$m = \tan\theta = \frac{1}{n} \tag{4.70}$$

In Eq. 4.70 it is shown that the material constant n for the Gäumann model is equivalent to the inverse of the slope of the boundary line that defines the zones for CET

in an experimental solidification map for a given alloy (in the zones where the lines have linear behavior), expressed in logarithmic coordinates.

4.4.4.3 Modification of Parameters to Model the Volumetric Fraction ϕ for Low Solidification Speeds V

Preliminarily, the value of the model coefficient $\mu = \mu_V$ in Eq. 4.49 for a logarithmic base coordinate system can be defined as the sum of Eq. 4.65 (the line that defines the fully equiaxed grain volume boundary of Fig. 4.3 where the slope is linear and constant), plus the ratio deduced in Eq. 4.57 multiplied by the distance $|\log_{10}(G_{L(\phi \approx 0)}) - \log_{10}(G_{L(\phi \approx 1)})|$, that is to say, Eq. 4.71a and 4.71b:

$$\mu_V = \frac{\ln\left(G_{L(\phi\approx 1)}\right) + m\left(\ln(V) - \ln\left(V_{(\phi\approx 1)}\right)\right)}{\ln(10)} + \frac{\left|\log_{10}\left(G_{L(\phi\approx 0)}\right) - \log_{10}\left(G_{L(\phi\approx 1)}\right)\right| \ln\left(\frac{\ln(2)}{8}\right)}{\ln\left(\frac{8 - \ln\left(e^8 - 1\right)}{8}\right)} \tag{4.71a}$$

$$\mu_V = \ell_{\log} + \frac{\left|\log_{10}\left(G_{L(\phi\approx 0)}\right) - \log_{10}\left(G_{L(\phi\approx 1)}\right)\right| \ln\left(\frac{\ln(2)}{8}\right)}{\ln\left(\frac{8 - \ln\left(e^8 - 1\right)}{8}\right)} \tag{4.71b}$$

Representing ϕ_{Gum} (Eq. 4.49) in conjunction with Eqs. 4.62 and 4.71, the result will be similar to the generic shape of the surface of Gäumann's model (Eq. 4.46) or graphics similar to the one of Fig. 4.20. For a complete representation of the volumetric fraction of equiaxed grains at low solidification rates V, it is necessary to modify Eq. 4.49, specifically the set $(\xi - \mu)/\beta$ by means of an appropriate "scale factor"

The adjustment of the representation via an equation of scale will be made in two stages. The first step is to define a scale function over the logarithmic straight line of Eq. 4.65. It is necessary to establish a scale function in the same range as the variable V (via multiplication factor), over Eq. 4.65. The effect on equation 4.65 will be to minimize the function and establishing the "cut" boundary V_{int} as shown in Fig. 4.24, The boundary V_{int} is a border value defined between the morphology zone of the 100% equiaxed grain and the 100% columnar grain.

The general idea of this "scaling factor function" is shown in Fig. 4.25, where the same scale will always have a range between 0 and 1.

The scale function must have the next desirable characteristics:

– The maximum value within the range of the "scale function" must be 1, and it must be maintained at that value asymptotically regardless of the value of the domain, in this case when $V \rightarrow \infty$.
– The fall in the value "created" by the scale function ($f(V \rightarrow V_{int}) = 0$) within the range of V must be very abrupt, and must reflect in the V_{int} coordinate value an asymptotic, monotonic, and strictly decreasing behavior.
– It is preferable that the associated function to the scale factor will be in some way related to exponential functions, since ϕ_{Gum} is defined in those terms.

For convenience, the scale function Ψ^{**} (scale factor for the vertical axis) in the same domain of axis V (through the auxiliary variable ξ^{**}) has been chosen as follows:

$$\Psi ** = \frac{\left(n_1 - \coth\left(\xi ** + \chi\right) + 1\right)}{n_1} \tag{4.72}$$

where χ is a location parameter of the function itself, and n_1 is a parameter that relates the slope of the function Ψ^{**} over the coordinate axis V to the value V_{int}.

This function (Eq. 4.72), will be defined in the domain $0 < (\xi^{**} + \chi) < +\infty$, where it is asymptotic in $\Psi^{**} = 1$. It is possible to deduce the constant n_1 from an analysis of the left-hand graph of Fig. 4.25. At the coordinate $\xi^{**} = \log_{10}(V)$ if it is assumed that the temperature gradient is equal to zero ($G = \Psi^{**} = 0$), it is possible first to determine the value of ξ^{**}, and then that of n_1 (Eq. 4.73):

$$G_L = 0 = \frac{\left(n_1 - \coth\left(\xi ** + \chi\right) + 1\right)}{n_1} \tag{4.73}$$

And clearing ξ^{**}:

$$\xi ** = \frac{\ln\left(\frac{n_1 + 2}{n_1}\right)}{2} + \chi \tag{4.74}$$

Derivation of Eq. 4.73, and equaling it to the tangent of the angle tanγ, at the coordinate (V_{int}, $G_L = 0$) as shown in Fig. 4.24, results in Eqs. 4.75 and 4.76:

$$n_1 = \tan\gamma - 2, V < 90^{\circ} \tag{4.75}$$

$$\chi = \frac{\ln\left(\frac{\sin\gamma}{\sin\gamma - 2\cos\gamma}\right)}{2} - \log_{10}\left(V_{int}\right) \tag{4.76}$$

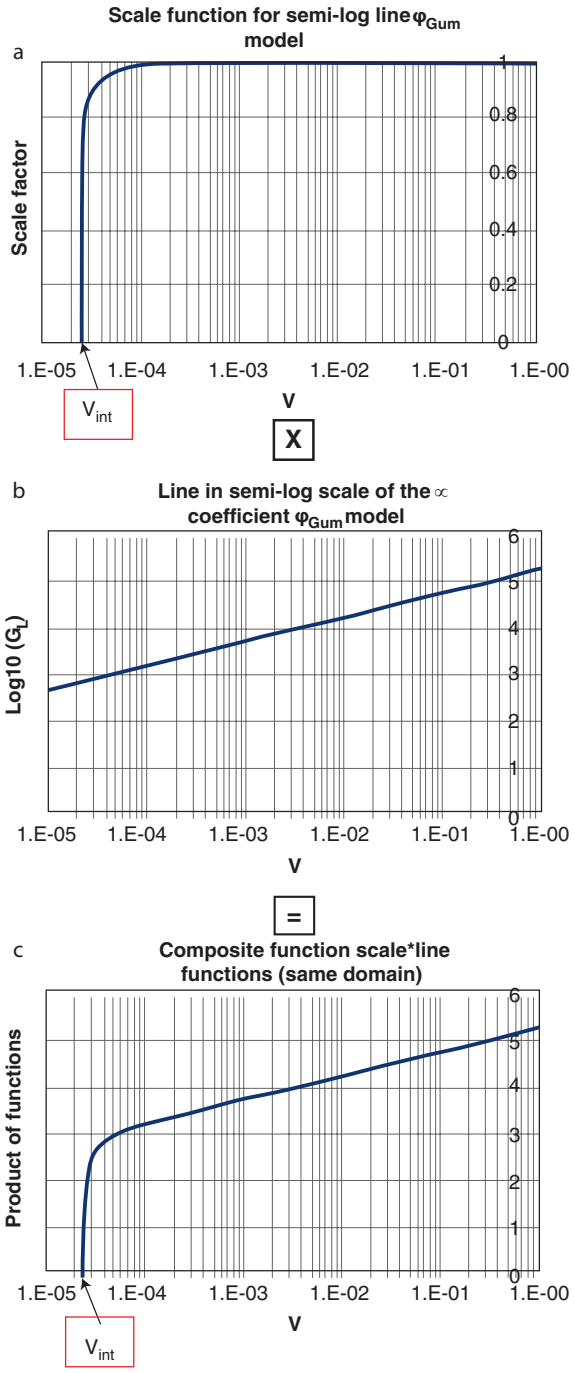

Fig. 4.25 Scheme of the effect of the "scaling factor function" over the μ_V location parameter function in semi-log coordinates for the same V domain. Left: scale function, middle: straight line representing the behavior of the preliminary model for the logarithmic straight lines with constant slope. Right: product of both functions on the same domain

To restrict the fact that the Eq. 4.72 is also defined for values of $(\xi^{**} - \chi) < 0$, a unitary step function (Heaviside step function) will be used to restrict its range, so Eq. 4.72 will be transformed into Eq. 4.77:

$$\Psi** = \left[\frac{\left(n_1 - \coth\left(\log_{10}\left(V\right) + \chi\right) + 1\right)}{n_1}\right] H\left(V - V_{\text{int}}\right) \tag{4.77}$$

where V_{int} is the boundary value on the axis V between the CET areas in a solidification map, and $H(V - V_{\text{int}})$ is the unitary step function (Heaviside), for the domain $V \geq V_{\text{int}}$.

From Fig. 4.22, it has previously been shown that the value of the variable scale factor β of Eq. 4.49 should remain constant; that is to say, "the width" of the S-shape graph of the probability function (ϕ) does not vary as the value of V variable changes.

The latter is valid for a model like the one shown in Fig. 4.20, where the "relative distance" between the isocurves for $\phi \approx 1$ and $\phi \approx 0$ remains constant. However, for alloys solidification maps typically found in the literature such as that of Fig. 4.3, and remembering that $\beta = \beta_G$ (Eq. 4.62), there must be a variation (i.e., a change in width for the S-shaped curve of the probability function) in the vicinity of V_{int}, as shown in Fig. 4.26.

The variation in width of β_G is very small except in the coordinates very close to V_{int}. It is therefore necessary to include in Eq. 4.49 a factor that directly affects β_G, and therefore model its change as seen in Fig. 4.26 (Eq. 4.78):

$$\phi = 1 - \exp\left[-\exp\left(-f_{\text{esc}}\left(\frac{\xi - \mu}{\beta}\right)\right)\right] \tag{4.78}$$

where f_{esc} is a scaling factor for $\beta = \beta_G$.

An equation is proposed based on Eq. 4.77 such that $f_{\text{esc}} \to \infty \; \forall \; V \to V_{\text{int}}$, or the same $\beta = \beta_G \to 0$. On the one hand, it must be taken into account the condition that for a relatively little change on the value of the coordinate when the V value grows moving away from V_{int}, the value $f_{\text{esc}} \to 1$, that is to say, $\beta = \beta_G \to$ constant.

The slope of the γ angle of Fig. 4.24 is also taken into account as a parameter to measure of the "abrupt fall" of β_G value when $V \to V_{\text{int}}$. Therefore, of the above, the scaling factor proposed is:

$$f_{\text{esc}} = \beta_G \left(e^7 \left(1 - \Psi**^{\frac{1}{\tan\gamma}}\right)\right) + 1 \tag{4.79}$$

Equation 4.79 completes the determination of all parameters necessary for use in Eq. 4.49 as a model to establish the volumetric fraction of equiaxed grains in the form of a mathematical equation of form $\phi = f(G_L, V)$.

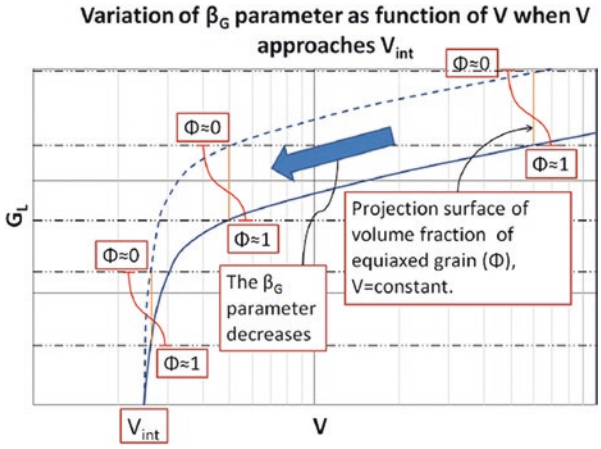

Fig. 4.26 Variation of the location parameter (β_G) with the consequent narrowing in the projection (*S*-shaped graph orange line) over the width of the equiaxed grain fraction function close to the V_{int} coordinates

4.4.5 Summary of the Crystallization Model and Associated Parameters

Rearranging the Eqs. 4.49, 4.62, 4.65, 4.66, 4.77, 4.78, and 4.79, and renaming the variables $\Psi^{**} = f_{multi}p$, $\mu = \mu_V$ and $\beta = \beta_G$, Table 4.6 is presented as the summary of the model.

4.4.6 Example of Application of the Model for the Experimental Solidification Map of Inconel 718

The model will be applied to Fig. 4.27, specifically for the case of the solidification map of the INCONEL 718 alloy (Nastac et al. 2001). Inconel 718 alloy has been chosen for the reason that it will be used in the experimental validation of this model.

First, the image will be preprocessed to place the coordinates of G_L and V (Fig. 4.27) in the same scale of (1:1) for the horizontal and vertical axes. Once this is done, the key values to be introduced in Eqs. 80 through 86, according to the references of Fig. 4.24, will be obtained.

The results are summarized in Table 4.7.

For simplicity, we have applied the model through a contour graph for the volume of equiaxed grain formation $\phi = 0.01$, $\phi = 0.5$ and $\phi = 0.99$ (Fig. 4.28), adjacent

Table 4.6 Summary of constitutive equations of the equiaxed grain volume fraction model (ϕ) based on solidification maps for alloys. The associated coordinates to the model are referred to Fig. 4.24

$\phi\left(G_L,V\right)=\left[1-\exp\left(-G_L^{-\left(\frac{f_{\text{esc}}}{\beta_G\ln(10)}\right)}\cdot\exp\left(\frac{f_{\text{esc}}\mu_V}{\beta_G}\right)\right)\right]\cdot H\left(V-V_{\text{int}}\right)$	(4.80)
$\beta_G=-\dfrac{1.7\left\lvert\log_{10}\left(G_{L(\phi\approx0)}\right)-\log_{10}\left(G_{L(\phi\approx1)}\right)\right\rvert}{\ln\left(1-\dfrac{\ln\left(e^8-1\right)}{8}\right)}$	(4.81)
$\mu_V=\left[\ell_{\log}+\dfrac{\left\lvert\log_{10}\left(G_{L(\phi\approx0)}\right)-\log_{10}\left(G_{L(\phi\approx1)}\right)\right\rvert\ln\left(\dfrac{\ln(2)}{8}\right)}{\ln\left(\dfrac{8-\ln\left(e^8-1\right)}{8}\right)}\right]\cdot f_{\text{multip}}$	(4.82)
$f_{\text{esc}}=\beta_G\left(e^7\left(1-f_{\text{multip}}^{\frac{1}{\tan\gamma}}\right)\right)+1$	(4.83)
$\ell_{\log}=\dfrac{\ln\left(G_{L(\phi\approx1)}\right)+m\left(\ln(V)-\ln\left(V_{(\phi\approx1)}\right)\right)}{\ln(10)}$	(4.84)
$f_{\text{multip}}=\left(\dfrac{\sin\gamma\left(V^{\frac{2}{\ln(10)}}-V_{\text{int}}^{\frac{2}{\ln(10)}}\right)\left(2\cos\gamma-\sin\gamma\right)}{V^{\frac{2}{\ln(10)}}\sin\gamma\left(2\cos\gamma-\sin\gamma\right)+V_{\text{int}}^{\frac{2}{\ln(10)}}\left(3\cos^2\gamma-4\sin\gamma\cos\gamma+1\right)}\right)H\left(V-V_{\text{int}}\right)$	(4.85)
$m=\tan\theta=\dfrac{1}{n}=\dfrac{\ln\left(\dfrac{G_{La(\phi\approx1)}}{G_{Lb(\phi\approx1)}}\right)}{\ln\left(\dfrac{V_{\phi a}}{V_{\phi b}}\right)}$	(4.86)

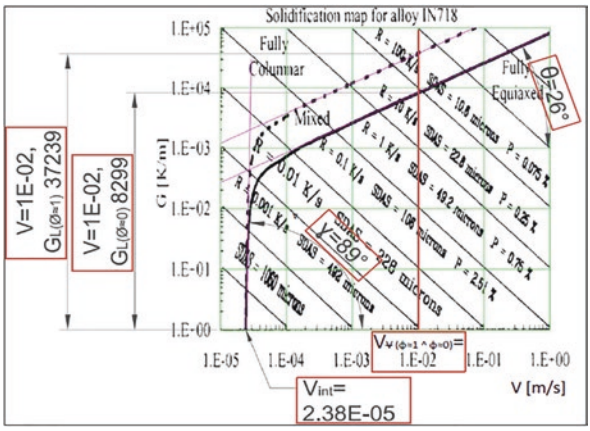

Fig. 4.27 Solidification map of INCONEL718 with the horizontal and vertical axes scaling at same size to obtain the value of coefficients for the equiaxed grain volume fraction model (ϕ)

Table 4.7 Coefficients calculated for the application of the Table 4.6 model from the solidification map for the INCONEL 718 alloy (Fig. 4.27)

$V_{int} = 2.38 * 10^{-5}$ (m. s^{-1})	$\theta = 26.3^{\circ} \rightarrow \tan\theta = m = 0.495$
$V_{\forall(\phi \approx 0 \wedge \phi \approx 1)} = 1 * 10^{-2}$ (m. s^{-1})	$\gamma = 89^{\circ}$
$G_{L(\phi \approx 0)} \approx 10^{3.919} = 8299$ (K. m^{-1})	$G_{L(\phi \approx 1)} \approx 10^{4.571} = 37,239$ (K. m^{-1})

with the original solidification map for the INCONEL 718 alloy for the purpose of comparison.

The correlation in Fig. 4.28 is very good. A very important detail is that the fraction of the equiaxed grain formation volume is not symmetrical in the "mixed morphology" grain zone. This is observed in the relative distance between the fractions $\phi = 0.01$ and $\phi = 0.5$, and from $\phi = 0.5$ to $\phi = 0.99$, which is not equidistant (Fig. 4.28a). On the other hand, the model of Table 4.6 reflects very well the asymptotic behavior at low solidification rates and low temperature gradients.

4.5 Application of the Model for a Metal Powder Reconditioning Method

4.5.1 Experimental Setup

A series of probes has been manufactured based on the optimized parameters of Renderos et al. (2017). The original objective of that research was to develop a method of reconditioning the INCONEL 718 to take advantage (reuse) of the metallic powder not adhered to the substrate. The methodology consisted in the

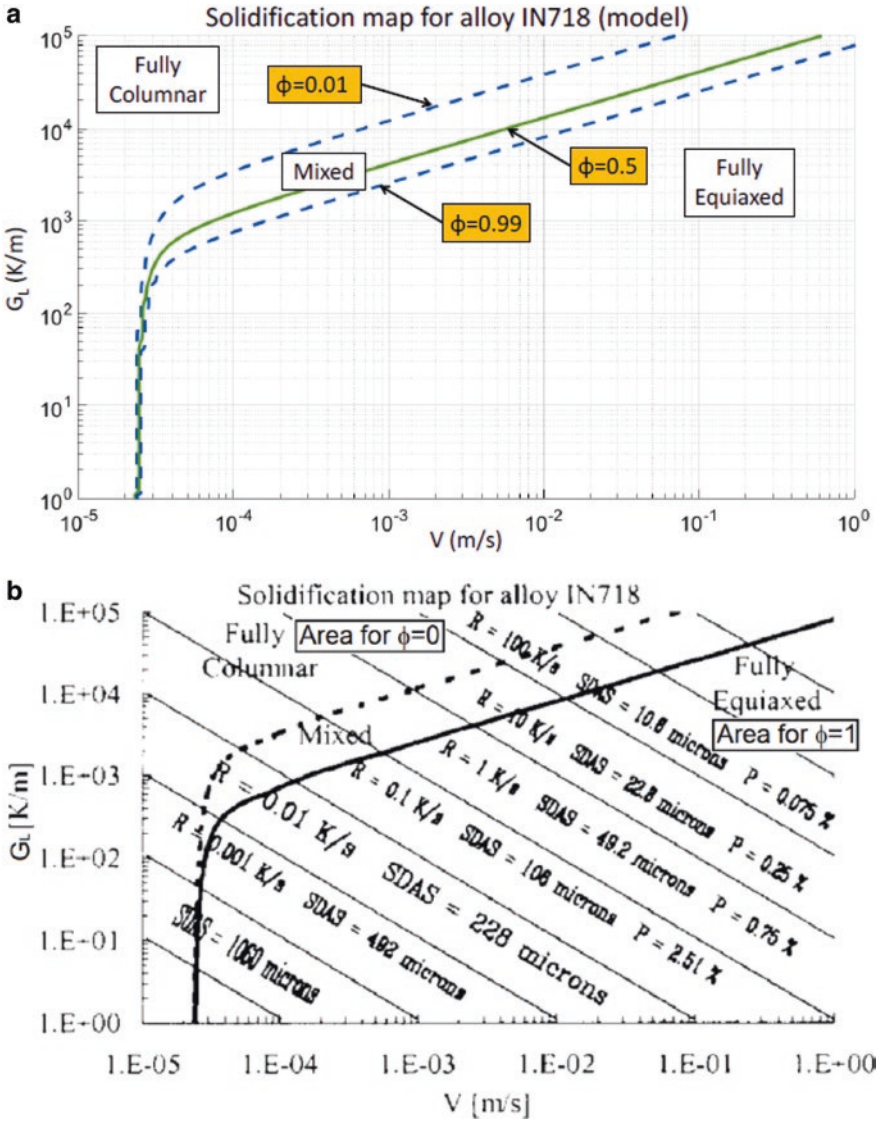

Fig. 4.28 (**a**) Comparison between the solidification map generated from the proposed model by means of the isocurves $\phi = 0.01$, $\phi = 0.5$, and $\phi = 0.99$ (blue and green lines), versus (**b**) the experimental solidification map for the Inconel 718 alloy (Nastac et al. 2001)

manufacture of specimens from new powder, of which an evaluation of mechanical and metallurgical properties would be made.

These specimens generate during their manufacture a waste of unadhered powder, which once collected and reconditioned, would be used as raw material to manufacture a new series of samples, which in turn must generate more unadhered powder and so on (up to a total of 4 times) without adding "fresh" (new) metallic powder.

Due to the heating of the powder as it passes through the laser beam, a certain amount of it oxidizes, superficially changing the original absorptivity of laser beam with respect to the new powder, that is, the amount of energy absorbed by the powder itself is greater as it is more opaque (Sainte-Catherine et al. 1991); in addition, a change in the distribution of the mean size of the powder was originated. The continuous repetition of that cycle (collection of unadhered powder and production of samples with the same) according to the number of reuses of powder was increasing, is the origin in the modification of the process parameters. The consecutive reuse of the powder modifies the properties of the surface itself, which makes it necessary to modify the working conditions in the system through the process parameters.

Along with the evolution on the physical properties (surface properties and average powder size), an effect of heat accumulation on the substrate was observed during the sample manufacturing. The first layers deposited were processed on a "cold" substrate (assumed at room temperature, $T_{0(\text{first layers})} \approx 298$ K); on the other hand, the layers manufactured in the final stages of the samples with reconditioned powder were raised on a "hot" substrate (approximately of $T_{0(\text{last layers})} \approx 573$ K).

The summary that will serve as the basis to establish the local coordinate conditions for their application in both the model for laser cladding process and the proposed model for equiaxed grain volumetric fraction (ϕ) applied to the INCONEL 718 alloy (and obtain the variation in the local conditions of G_L and V) is presented in Table 4.8.

The rest of the parameters (which remain constant), for the application of both the analytical model during the manufacturing of the probes in Renderos et al. (2017) by means of laser cladding process, and that for the proposed model for volumetric fraction of equiaxed grain (ϕ) are presented in Table 4.9.

4.5.2 Results

The evaluation and verification of the laser cladding model (Eqs. 4.3–4.29 and Eqs. 4.31–4.39), and of the volumetric fraction of equiaxed grain Table 4.6, are presented in Fig. 4.29. This graph describes the summary of test results in which a series of specimens manufactured under the conditions of Tables 4.8 and 4.9 have been submitted for an EBSD examination.

Table 4.8 Evolution in raw material properties and process variables for sample manufacturing in research about reconditioning of metallic powder for laser cladding process on INCONEL 718 (Renderos et al. 2017)

Condition 1:	**Condition 2:**
State of powder: New	State of powder: New
Equivalent powder mean diameter: 68.1 μm	Equivalent powder mean diameter: 68.1 μm
Surface condition powder: shiny (not oxidized), $\eta_{powder} = 0.3$	Surface condition powder: shiny (not oxidized), $\eta_{powder} = 0.3$
$T_{0(\text{first layers})} \approx 298$ K (not preheating)	$T_{0(\text{last layers})} \approx 523$ K (preheating)
Surface condition substrate: shiny (not oxidized), $\eta_{subs} = 0.3$	Surface condition substrate: opaque (oxidized), $\eta_{subs} = 0.59$
Condition 3:	**Condition 4:**
State of powder: Used (4 times)	State of powder: Used (4 times)
Equivalent mean diameter: 81.1 μm	Equivalent mean diameter: 81.1 μm
Surface condition powder: Opaque (oxidized), $\eta_{powder} = 0.4$	Surface condition powder: Opaque (oxidized), $\eta_{powder} = 0.4$
$T_{0(\text{first layers})} \approx 298$ K(not preheating)	$T_{0(\text{last layers})} \approx 573$ K (preheating)
Surface condition substrate: Shiny (not oxidized), $\eta_{subs} = 0.3$	Surface condition substrate: Opaque (oxidized), $\eta_{subs} = 0.61$

Table 4.9 Constant parameters for verification of laser cladding model and application of the proposed volumetric fraction of equiaxed grain model

$Q_{g(\text{normalized})} = 2.6$ (l.min^{-1})	$\phi d_{\text{drop}} = 2.2 * 10^{-3}$ (m)
$\mu_{\text{gas}} = 2.125 * 10^{-5}$ (kg. m^{-1}s^{-1}) [Argon]	$\phi d_{\text{laser}} = 1 * 10^{-3}$ (m)
$r_n = 5.275 * 10^{-3}$ (m)	$m' = 1.463 * 10^{-4}$ (kg. s^{-1}) = 8.78 (gr.min^{-1})
$2r_o = 0.45 * 10^{-3}$ (m)	P_{laser}(cylindrical energy distribution) = 571 W
$s_n = 14.5 * 10^{-3}$ (m)	$v = 8.7 * 10^{-3}$ (m. s^{-1}) = 522 (mm.min^{-1})
$\rho_p = \rho_{subs} = 8240$ (kg. m^{-3})	

The EBSD test technique has allowed characterizing of the distribution in size and geometry of the grains generated during solidification based on the average local conditions of V and G_L. It is desired to verify the following aspects.

First, if the equiaxed fraction model is capable of correctly describing the morphology of the grain generated during solidification.

Second, if the laser cladding model as function of the input process parameters itself has been capable of generating sufficiently precise local values of V and G_L.

Finally, the EBSD images together with the related points associated with the local conditions of solidification were superimposed on the proposed crystallization model graph (it is a probability surface in two variables V and G_L), for the different process conditions of Tables 4.8 and 4.9, as shown in Fig. 4.29.

EBSD images have been taken at the bottom and top of the specimen samples for both new powder and reconditioned powder (Renderos et al. 2017). The results shown in Fig. 4.29 indicate grain morphology strongly dependent on local

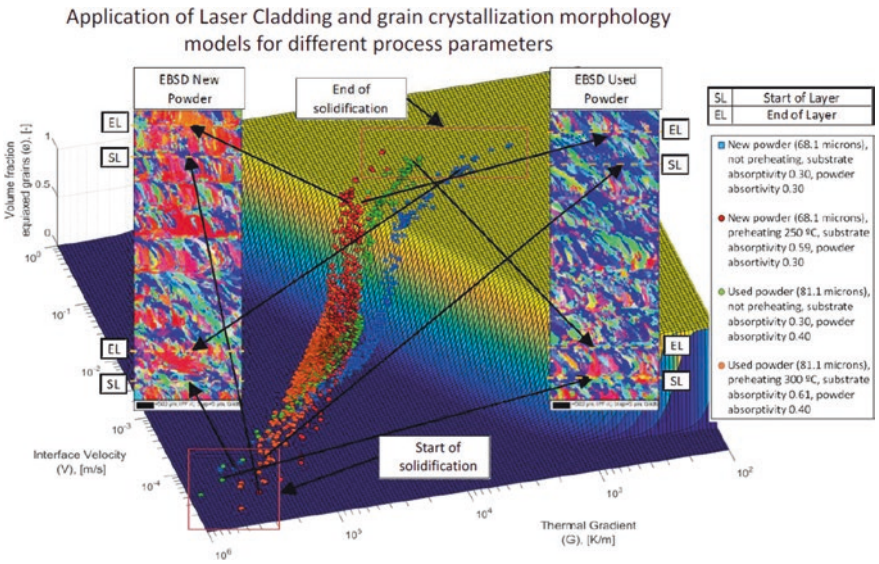

Fig. 4.29 Representation of the solidification model of the equiaxed grain fraction for the alloy INCONEL 718 for the laser cladding processes based on the parameters of Tables 4.8 and 4.9

solidification conditions with the tendency of equiaxed grain formation in the upper part in the blocks of alloy manufactured by means of laser cladding process.

4.5.3 Discussion of the Results

Figure 4.29 indicates the beginning and end of the melt pool hardening process (beginning and end of solidification), for each set of laser cladding process (Conditions 1–4, Tables 4.8 and 4.9). In the graph (EBSD map), this is indicated by dotted lines in orange with the abbreviation SL (start of layer) and EL (end of layer). With black arrows, the coordinates of the different stages for the manufacturing of the blocks from which the test probes were made, are indicated on the EBSD figure of the crystallization model. It is also indicated with red line boxes on the graph itself, the beginning and the end of each of the cat layers (the labels "Start of solidification" and "End of solidification").

Each layer in the substrate always starts with solidification in columnar morphology (indicated by the arrow pointing to the bottom of each cladding layer in the EBSD graph), which is dependent on the maximum gradient of temperature (the cladded material in direct contact with the substrate conducts the temperature better). It is also observable that the solidification concludes with morphology of mixed grain or completely equiaxed (again depending on the local conditions of cladding and temperature gradient). It should also be noted that with each layer of material

that is deposited, part of the equiaxed fraction on the previous layer is remelting by the next one; this effect is most evident in the upper layers.

A very particular phenomenon has been observed in Fig. 4.29 while examining the interface between layers: when one layer adheres consecutively to the other, the amount (depth) of remelting depends on the difference between the temperature of the melt pool and the initial temperature of the previous layer (T_0). The above is deduced from the process conditions shown in Tables 4.8 and 4.9. For different process conditions, the initial average temperature (T_0) at the top of the blocks for the manufacturing of the samples always was higher.

In a solidification map for alloys such as that of Fig. 4.28, low temperature gradients tend to generate equiaxed grain morphology (this is an effect of the substrate being hot, since the temperature difference between two points within the sample will be smaller). However, in a hot substrate the amount of melt pool will penetrate a greater distance into the substrate since the laser beam does not have to use a lot of energy to "heat" the base (substrate) where the material is deposited.

The evidence with EBSD indicates that at least for the experimental conditions used in the verification of this model, the second effect (the melting of a part of the surface in the previous substrate with the tendency to create grain with columnar morphology), has been more important than the tendency of the temperature gradients to form grain with equiaxed morphology structure (governed by the local conditions V and G_L of solidification and described by the experimental solidification map of the alloy).

All the previous comments have been well reflected in Fig. 4.29, both by the laser cladding model (which serves as the basis for obtaining the average local conditions of V and G_L), and by the grain crystallization morphology model (to know the fraction of equiaxed grain for each local condition $\phi = f(G_L, V)$). Therefore, both models are considered valid.

In Appendix 2, a method is proposed for deduction of number of nucleation sites per unit of volume (N_0) for laser cladding process.

4.6 Conclusions

An analytical model for the laser cladding process has been proposed. The model takes into account the main parameters, and "develops" the effect of each of them independently so that it is possible to separate the consequences of each parameter separately.

The model takes into account the attenuation of the energy supplied by the laser beam on the surface due to the shadow effect of the powder (delivered by a coaxial nozzle), taking into account the effect of drag velocity because of the protective gas.

An iterative methodology has been proposed to define the temperature-dependent properties for the energy balance in the metallic powder interacting with the laser beam, and thus obtain a more accurate energy balance for the substrate (via negative enthalpy).

In the application of the laser cladding model for the calculation of the thermal field in the substrate, a general solution in a steady stable state was used. In the calculation of the thermal field a methodology has been proposed to be able to make the solution "dependent" on the thermal properties of the material, which helped to calculate accurately the temperature values within the melt pool, taking into account the change of phase, and therefore to calculate the values of temperature to determine the thermal gradient.

The calculation of the thermal gradient together with the growth velocity in the solidification front was used as input variables to determine the CET behavior of an alloy. To model the CET behavior of an alloy, the use of a solidification model based on experimental Solidification Maps combined with the behavior of a Gumbel's probability distribution is proposed.

The use of a deterministic model for columnar/equiaxed grain formation is justified by the difficulty of modeling the behavior of a multicomponent alloy. The relationship between the CET-model and the experimental-type solidification maps that served as basis has been established.

The proposed model: extends the range of application of the base model to values of low solidification speeds, intuitively explains the CET behavior in the mixed zone (the behavior is modeled based on a well-known probability distribution), and determines in a unique way with a physical sense the constants of material for other models, taking advantage of the information contained in experimental solidification maps.

A method is included to obtain an estimate for the number of nucleation sites per unit volume, and it is concluded that this value is highly dependent on the solidification process involved. For laser cladding process, its value is very high compared to traditional casting processes, due mainly to temperature gradients.

The model was tested by means of an experimental essay where different types of raw material (new metallic powder and reconditioned metallic powder to be recycled again) are used to build specimens that were analyzed by means of EBSD images. The results of the powder solidification CET morphology are compared with both the proposed model for laser cladding and proposed model for CET crystallization, with good correlation between the predictions and the experimental results.

Acknowledgments The authors would like to acknowledge the support from the Join Cross Border Laboratory ÆNIGME (Aquitaine Euskadi Network In Green Manufacturing and Ecodesign) between the University of the Basque Country, the University of Bordeaux, and Arts et Métiers Institute of Technology. The authors also gratefully acknowledge the helpful comments and suggestions of the reviewers, which have improved the presentation.

Appendices

Appendix 1: Nomenclature and Abbreviations

cdf:	Cumulative distribution function
Pdf:	Probability density function
AM:	Additive manufacturing
CAFE:	Cellular automata finite element
CET:	Columnar to Equiaxed transition
EBSD:	Electron backscatter diffraction
EL:	End of layer
LAM:	Laser additive manufacturing
LMD:	Laser metal deposition
SDAS:	Secondary dendrite arm spacing
SG:	Stray grain (synonymous of equiaxed grain)
SL:	Start of layer
SLM:	Selective laser melting
SX:	Single-crystal
TEM:	Transvers electromagnetic mode
WAAM:	Wire arc additive manufacturing

$A_{\text{spot}}^{\text{laser}}$:	Spot area of laser beam in work plane at $z' = s_n$ (m^2)
a:	Alloy related constant for Gäumann's crystallization model ($K^n.m^{-1}\ s^{-1}$)
a_1, a_2:	Distance, auxiliary variable (m)
a_{gr}, b_{gr}:	Alloy-related constant for grain size in traditional casting alloy formula (*)
$A_{\text{grain}}^{\text{mean}}$:	Mean area of the projection of set of grains valid for analysis (m^2)
a_o:	Characteristic value of the thickness of the interface for nonequilibrium solidification (m)
B, n_λ:	Alloy-related constants for empiric model for microstructure size in rapid solidification
b_1:	Intercept for the equation of the straight line in logarithmic coordinates (−)
C_0:	Powder mass flow rate ($Kg.s^{-1}$)
C^o:	Solute concentration to the initial composition of the alloy (%)
c_p:	Specific heat capacity at constant pressure ($J.Kg^{-1}\ K^{-1}$)
d_{gr}:	Grain size (m)
d_i:	Diameter, auxiliary variable (m)
D_L:	Thermal diffusivity in liquid phase ($m^2.s^{-1}$)
d_p:	Mean diameter of the powder particles (m)
f_{esc}:	Scaling factor function for the β_G parameter of Gumbel distribution (−)

$f_{\text{shape energy}}$:	Radial energy distribution of the laser beam in the $z' = 0$ plane (−)
G_L:	Temperature gradient in liquid isotherm (K.m^{-1})
G_R:	Green's function (m^{-1})
G_S:	Temperature gradient in solid isotherm (K.m^{-1})
$H(X)$:	Unitary step function (Heaviside) for the domain X (−)
I:	Intensity of laser beam (W.m^{-2})
k:	Thermal conductivity (W.m^{-1} K^{-1})
k_e:	Equilibrium partition coefficient (*)
k_V:	Nonequilibrium partition coefficient (*)
ℓ:	Distance, auxiliary variable (m)
L_f:	Latent heat of fusion (J.Kg^{-1})
$\ell_{\text{square grain}}$:	Equivalent side length for the area projection by EBSD test (m)
m:	Slope for the equation of the straight line in logarithmic coordinates (−)
m':	Powder feed rate (Kg.s^{-1})
n:	Alloy-related constant for Gäumann's crystallization model (−)
N_0:	Number of heterogeneous nucleation sites (m^{-3})
P:	Powder mass flux (Kg.m^{-2} s^{-1})
P_{laser}:	Laser beam power (W)
Q_g:	Gas volumetric flow rate (m^3.s^{-1})
r:	Radial coordinate in the frame of reference of nozzle (m)
R:	Radial auxiliary variable (m)
Re_p:	Relative Reynolds number for particles (−)
r_{laser}:	Laser beam radius (m)
r_n:	Centre radius of nozzle outlet (m)
r_o:	Half of the gap distance of nozzle outlet (m)
r_s:	Distance, auxiliary variable (m)
s_n:	Coordinate on the z' axis of the powder consolidation plane (m)
T:	Temperature (K)
t:	Time (s)
Th_{prop}:	Thermophysical properties in the mushy zone melt pool (K)
$\dot{T}$:	Cooling rate (K.s^{-1})
V:	Solidification grow rate (m.s^{-1})
v:	Scanning speed of laser beam (m.s^{-1})
v_g:	Initial carrier gas velocity (m.s^{-1})
V_{int}:	Boundary value on the axis V between the areas of 100% equiaxed grain and 100% columnar grain in a solidification map.
v_p:	Mean speed of the particles (m.s^{-1})
$v_{pz'}$:	Component of v_p in the z' direction in the frame of reference of nozzle (m.s^{-1})

$V_{\text{cell}}^{\text{unit}}$:	Volume of the equivalent cubic cell grain from grain projection (m^3)
x, y, z:	Coordinate in frame of reference system on semi-infinite substrate (m)
x_0, y_0:	Local coordinates that define the energy density in the surface of substrate (m)
z':	Axial coordinate in the frame of reference of nozzle (m)
z'_{inter}:	Coordinate on the z' axis of start of interaction of centerlines of powder streams with laser beam (m)
α:	Thermal diffusivity ($m^2.s^{-1}$)
α_1, α_2:	Auxiliary variable for deduction of cdf Gumbel's distribution (*)
α_{vV}	Angle between the normal direction of the growth solidification interface and the travel direction of scanning the speed of laser beam (−)
β, β_G:	Scale parameter for Gumbel distribution (generalized extreme value distribution type-I) (*)
χ:	Location parameter for the scaling factor function (*)
δ:	Dirac's δ-function (m^{-1})
ε_m:	Peak value of energy density for a given distribution of laser beam ($W.m^{-2}$)
η:	Laser absorptivity of material (−)
ϕ:	Volumetric fraction of equiaxed grains (−)
ϕd_{drop}:	Diameter where the value of the powder mass flow concentration has fallen to a value e^{-2} of the maximum concentration (m)
ϕd_{laser}:	Laser beam diameter (m)
γ:	Angle between the horizontal coordinate axis V and the tangent line to the coordinate V_{int} in a solidification map (−)
γ_{sup}:	Surface tension ($N.m^{-1}$)
H(T):	Enthalpy from the reference temperature T_0 ($J.m^{-3}$)
κ:	Numerical counter (integer), auxiliary variable (−)
λ:	Radius, auxiliary variable (m)
λ_{gr}:	Representation of a characteristic of spacing (dimension) in the microstructure (m)
$\ell_{\log}$:	Equation of straight line in logarithmic coordinates for the variable $\log_{10}(G_L)$ (*)
μ_{gas}:	Dynamic viscosity of carrier gas ($kg.s^{-1}\ m^{-1}$)
μ_{melt}:	Viscosity of the melt pool (Pa.s)
μ, μ_V:	Location parameter for Gumbel distribution (generalized extreme value distribution type-I) (*)
ρ_p:	Density of a particle within carrier gas ($kg.m^{-3}$)
θ:	Angle for the equation of the straight line in logarithmic coordinates (−)
ξ:	Variable for the calculation of Gumbel's cdf (−)
$\xi*$, $\Psi*$:	Auxiliary variable for deduction of constant of material n (*)
$\xi**\Psi**$, f_{multip}	Auxiliary variable for deduction of the scaling factor function for the μ_V location parameter (*)

Appendix 2: Method for Deduction of Number of Nucleation Sites per Unit of Volume (N_0) for Laser Cladding Process

Importance of the Constant N_0 and Its Relation to the Material Constant *a* for Crystallization Models

As mentioned before, one of the limitations in the use of a crystallization model is the availability of experimental data. In this section we will explain the deduction of the number of homogeneous nucleation sites (N_0) for the Gäumann model (Gäumann et al. 2001), and its subsequent application for the deduction of the constant of material "*a*" (Eq. 4.45). Once this value is deduced, it is possible to extrapolate the calculation for the model deduced in this chapter since the value for this material constant is the same for both.

On the other hand, Gäumann et al. (1997) show that the influence of the number of nucleation sites on CET is important in the higher velocity growth region (V), because once nucleation occurs, the volume of fraction of equiaxed grains is mainly linked to the number of nucleation sites. Thus, if the number of nucleation sites is reduced, then the columnar microstructure is stabilized. The above together with the undercooling are parameters that are specific to the equiaxed grains and for the control of the formation of nuclei.

Therefore, a good estimate of the material constant N_0 is important for the prediction and control of the microstructure during a solidification process.

Proposed Method for the Deduction of N_0 Based on EBSD Images

Clearing *a* from Eq. 4.46 results in (Eq. 4.87):

$$a = \frac{G_L^n \left(\frac{4\pi}{3}\right)^{-n/3} \left(\frac{\left(-\frac{N_0}{\ln(1-\phi)}\right)^{\frac{1}{3}}}{n+1} \right)^{-n}}{V} \tag{4.87}$$

Since it is possible to evaluate the volumetric fraction of equiaxed grain (ϕ) by means of an image analysis of the EBSD test as proposed (Gäumann et al. 2001), the method to deduce N_0 will follow an analogous procedure.

It basically consists in counting the number of grains per unit of volume by means of the analysis of the projection of the number of grains per unit of area from images, obtained through an EBSD test, from two different directions of the same volume to be analyzed. The methodology is the same used by Brahme et al. (2006),

where the images with the projection of the grains from the EBSD test from two different directions were taken perpendicularly at 90° to each other.

In this case, instead of proposing the strict use of images taken at 90°, it will be taken as a criterion if the image is able to show the change of texture in the microstructure.

Or in other words, if it is possible to characterize the microstructure of the grains taking into account the variable morphology of the same for different directions. This is important because the laser cladding process is highly directional (Hu et al. 2012).

In Fig. 4.30, where the projection of the grains by EBSD images corresponding to two different classes of powder (new and reconditioned) is shown, the morphology of solidification is in the advance direction; that is to say, the cut view section is parallel to the direction of movement of the laser beam.

The morphology of grain for an image taken in a perpendicular direction (transversal to the direction of the laser beam movement) however presents a different grain characteristic. Or in other words, it is possible to distinguish, for example, a section view of an image of the longitudinal direction (L) from a transverse one (T), as shown in Fig. 4.30.

The grain size distribution for an EBSD image can be done with specialized and even free software, such as MTEXT (Nolze and Hielscher 2016). By example, for the longitudinal section view of used powder (discounting the grains at the periphery of the image for being incomplete), the grains "valid" for the calculation of their density per unit area are shown in Fig. 4.31.

From the selection of "valid" grains, it is possible to obtain the total area of the grains and the number of then, as well as varied statistics to characterize their size distribution. Table 4.10 presents the results for the cross-sectional and longitudinal areas for new and reconditioned powder (Figs. 4.30 and 4.31).

From the statistics of Table 4.10, it is observed that there is a great data dispersion, which does not allow using of the assumption that the grains can be approximated by ellipsoids homogeneous as in Brahme (2006) (where it is postulated that their size is approximately uniform). As our assumption, we will admit that the projected sections of the "valid" grains (those not found on the periphery of the EBSD image) are squares. The reason for this assumption will be explained later.

The next step is to calculate an equivalent side length for each "square" type grain according to its corresponding area projection (in this case for L and T views), as shown in Eq. 4.88:

$$\ell_{\substack{\text{square}\\\text{grain}}} = \sqrt{A_{\substack{\text{mean}\\\text{grain}}}} = \sqrt{A_{\substack{\text{grains}\\\text{projection}}} / n_{\text{grains}}} \tag{4.88}$$

The volume of the equivalent cubic cell grain will be assumed as the product of the equivalent length of the grain projection in the longitudinal (L) and transverse (T) directions by the average of both previous lengths for the third direction.

The use of the average of the grain lengths (in the L and T directions), to estimate the value in the third dimension, is the reason why cubic-shaped cells have been

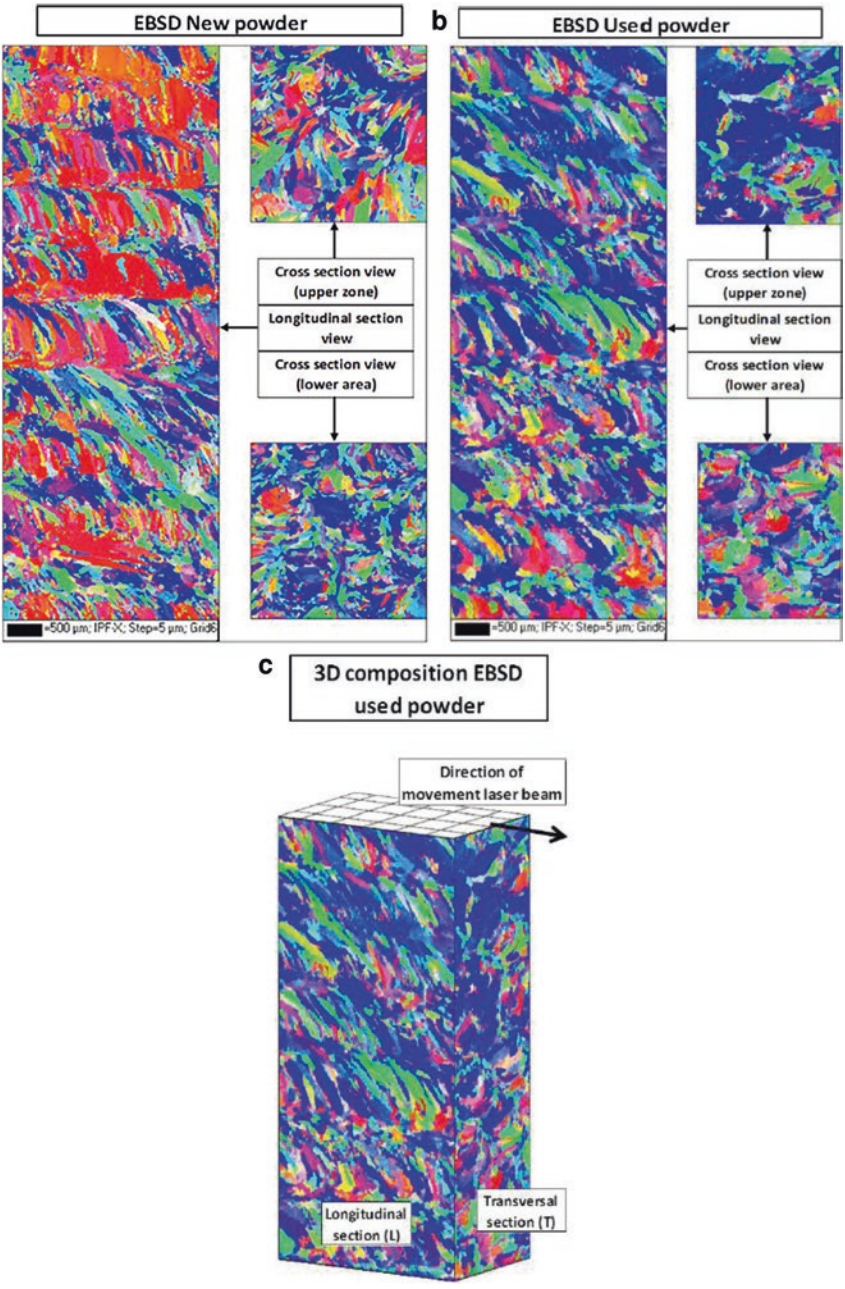

Fig. 4.30 Morphological distribution of microstructure of grain from images based on EBSD tests (**a**) for new and (**b**) reconditioned powder in the longitudinal (L) and transversal (T) directions, respect to (**c**) the laser beam path (used powder)

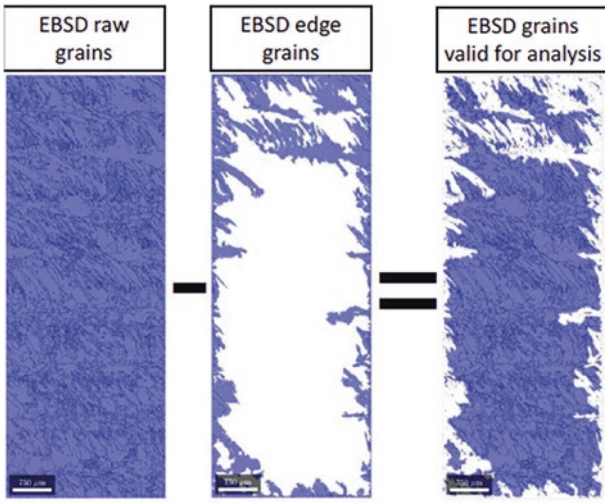

Fig. 4.31 Grains filtering in an EBSD image to calculate the number of heterogeneous grain growth sites (N_0) based in view sections, in this case for reconditioned powder (longitudinal section)

Table 4.10 Grain size statistics for transversal (T) and longitudinal (L) sections views for new and used powder based in process parameters described in Tables 4.8 and 4.9

	Transversal (T)		Longitudinal (L)	
	New powder	Used powder	New powder	Used powder
Mean (μm^2)	1358.2	1409.5	1094.8	1341.4
Median (μm^2)	75	75	75	75
Mode (μm^2)	25	25	25	25
Standard deviation (μm^2)	7421.6	10,138.9	12,960.5	10,378.1
Minimum (μm^2)	25	25	25	25
Maximum (μm^2)	257,800	450,800	1,562,300	675,375
Total grain area (μm^2)	8,931,400	9,027,925	30,633,950	18,359,125
Kurtosis	457.3	1036.0	7974.2	1592.5
Number of grains	6576	6405	27,981	13,687

chosen (it is a simple geometric shape that allows to estimate the missing dimension to calculate the volume of each cell). The above is calculated through Eq. 4.89:

$$V_{\text{cell}}^{\text{unit}} = \frac{\ell_{\text{grain (L)}}^{\text{square}} * \ell_{\text{grain (T)}}^{\text{square}} * \left(\ell_{\text{grain (L)}}^{\text{square}} + \ell_{\text{grain (T)}}^{\text{square}} \right)}{2} \tag{4.89}$$

Table 4.11 Calculation of the equivalent cubic cell grain volume and number of heterogeneous nucleation sites for a laser cladding process with two different types of clad material (new and used metallic powder)

	New powder		Used powder	
	Trans. (T)	Long. (L)	Trans. (T)	Lon. (L)
Length of grain side in equivalent cubic shape $\ell_{square\ grain}$ (μm)	36.9	33.1	37.5	36.6
Length mean value (μm)	35.0		37.1	
Volume unit cell (m^3)	4.26E-14		5.10E-14	
Number of heterogeneous nucleation sites N_0 (m^{-3})	2.35E+13		1.96E+13	

Results and Discussion

The results from Eqs. 4.88 and 4.89 and from the data of Table 4.10 are presented in Table 4.11, together with the number of heterogeneous nucleation sites for each kind of powder. The number of heterogeneous nucleation sites is defined as the inverse of the volume of the equivalent cubic cell grain in appropriate units.

From Table 4.11, it should be noted that the value of N_0 is very uniform even for different laser cladding process parameters, but it is very sensitive and dependent on the solidification process, where for example in the case of Pautrat (2013), the density of germination sites for the same alloy but for a different solidification process is in the order of 8×10^7 [m^{-3}].

Between the factors that have the greatest effect on the number of nucleation sites, the temperature gradient is one of the most important (in general, for a smaller temperature gradient larger grain size) (Nastac et al. 2001). In the case of the laser cladding process, since the gradients are very high, the effect will be a small grain size (or a high N_0 value).

Finally, from Table 4.11 the value of N_0 suitable for the laser cladding process will be chosen to replace it in Eq. 4.87, and deduce the *a* alloy-related constant needed to complete the data availability for any model. In this chapter, two cases have been presented as an example (with new and used powder), and the N_0 adequate should mean the one that best represents the process to be controlled.

References

Agarwal, A. T. (2005). Theory and design of dilute phase pneumatic conveying systems. *Powder Handling and Processing, 17*, 18–22.

Agrawal, G., Kar, A., & Mazumder, J. (1993). Theoretical studies on extended solid solubility and nonequilibrium phase diagram for Nb-Al alloy formed during laser cladding. *Scripta Metallurgica et Materialia, 28*, 1453–1458. https://doi.org/10.1016/0956-716X(93)90498-H.

Almeida, A., Petrov, P., Nogueira, I., & Vilar, R. (2001). Structure and properties of Al-Nb alloys produced by laser surface alloying. *Materials Science and Engineering A, 303*, 273–280. https://doi.org/10.1016/S0921-5093(00)01838-4.

Anderson, T. D., DuPont, J. N., & DebRoy, T. (2010). Origin of stray grain formation in single-crystal superalloy weld pools from heat transfer and fluid flow modeling. *Acta Materialia, 58*, 1441–1454. https://doi.org/10.1016/j.actamat.2009.10.051.

Araya, G., & Gutierrez, G. (2006). Analytical solution for a transient, three-dimensional temperature distribution due to a moving laser beam. *International Journal of Heat and Mass Transfer, 49*, 4124–4131. https://doi.org/10.1016/j.ijheatmasstransfer.2006.03.026.

Arrizubieta, J. I., Tabernero, I., Ruiz, J. E., Lamikiz, A., Martinez, S., & Ukar, E. (2014). Continuous coaxial nozzle design for LMD based on numerical simulation. *Physics Procedia, 56*, 429–438. https://doi.org/10.1016/j.phpro.2014.08.146.

Bandyopadhyay, S., Sundar, J. K. S., Sundararajan, G., & Joshi, S. V. (2002). Geometrical features and metallurgical characteristics of Nd:YAG laser drilled holes in thick IN718 and Ti-6{A}1-4V sheets. *Journal of Materials Processing Technology, 127*, 83–95.

Bayraktar, E., Moiron, J., & Kaplan, D. (2006). Effect of welding conditions on the formability characteristics of thin sheet steels: Mechanical and metallurgical effects. *Journal of Materials Processing Technology, Achievements in Mechanical & Materials Engineering, 175*, 20–26. https://doi.org/10.1016/j.jmatprotec.2005.04.007.

Blecher, J. J., Palmer, T. A., & Debroy, T. (2014). Solidification map of a nickel-base alloy. In *Metallurgical and materials transactions A: Physical metallurgy and materials science* (pp. 2142–2151). Boston: Springer. https://doi.org/10.1007/s11661-013-2149-1.

Bourell, D. L., Leu, M. C., & Rosen, D. W. (2009). *Roadmap for additive manufacturing identifying the future of freeform processing*. https://wohlersassociates.com/roadmap2009A.pdf

Brahme, A., Alvi, M. H., Saylor, D., Fridy, J., & Rollett, A. D. (2006). 3D reconstruction of microstructure in a commercial purity aluminum. *Scripta Materialia, 55*, 75–80. https://doi.org/10.1016/J.SCRIPTAMAT.2006.02.017.

Cárcel, B., Serrano, A., Zambrano, J., Amigó, V., & Cárcel, A. C. (2014). Laser cladding of TiAl intermetallic alloy on Ti6Al4V -process optimization and properties. *Physics Procedia, 56*, 284–293. https://doi.org/10.1016/J.PHPRO.2014.08.173.

Carozzani, T., Digonnet, H., Bellet, M., & Gandin, C.-A. (2012). 3D CAFE simulation of a macrosegregation benchmark experiment. In *IOP conference series: Materials science and engineering* (p. 012087). Bristol: IOP Publishing. https://doi.org/10.1088/1757-899X/33/1/012087.

Chiocca, A., Soulie, F., Bordreuil, C., & Deschaux-Beaume, F. F. (2015). *Microstructure generation during CuNi bead on plate: Comparison of experimental results and CA prediction*.

Darmadi, D., Norrish, J., & Tieu, A. (2011). Analytic and finite element solutions for temperature profiles in welding using varied heat source models. *Proceedings of World Academy of Science, Engineering and Technology, 81*, 154–162. https://ro.uow.edu.au/engpapers/4621.

Fassani, R. N. S., & Trevisan, O. V. (2003). Analytical modeling of multipass welding process with distributed heat source. *Journal of the Brazilian Society of Mechanical Sciences and Engineering, 25*, 302–305. https://doi.org/10.1590/S1678-58782003000300013.

Fayazfar, H., Salarian, M., Rogalsky, A., Sarker, D., Russo, P., Paserin, V., & Toyserkani, E. (2018). A critical review of powder-based additive manufacturing of ferrous alloys: Process parameters, microstructure and mechanical properties. *Materials and Design, 144*, 98–128. https://doi.org/10.1016/j.matdes.2018.02.018.

Flemings, M. C. (1974). Solidification processing. In *Materials science and technology*. Weinheim: Wiley-VCH Verlag GmbH & KGaA. https://doi.org/10.1002/9783527603978.mst0173.

Gäumann, M., Trivedi, R., & Kurz, W. (1997). Nucleation ahead of the advancing interface in directional solidification. *Materials Science and Engineering A, 226–228*, 763–769. https://doi.org/10.1016/S0921-5093(97)80081-0.

Gäumann, M., Henry, S., Cléton, F., Wagnière, J.-D., & Kurz, W. (1999). Epitaxial laser metal forming: Analysis of microstructure formation. *Materials Science and Engineering A, 271*, 232–241. https://doi.org/10.1016/S0921-5093(99)00202-6.

Gäumann, M., Bezençon, C., Canalis, P., & Kurz, W. (2001). Single-crystal laser deposition of superalloys: Processing–microstructure maps. *Acta Materialia, 49*, 1051–1062. https://doi.org/10.1016/S1359-6454(00)00367-0.

Gibson, I., Rosen, D. W., & Stucker, B. (2010). *Additive manufacturing technologies: Rapid prototyping to direct digital manufacturing*. Boston: Springer. https://doi.org/10.1007/978-1-4419-1120-9.

Greer, A. L., Cooper, P. S., Meredith, M. W., Schneider, W., Schumacher, P., Spittle, J. A., & Tronche, A. (2003). Grain refinement of aluminium alloys by inoculation. *Advanced Engineering Materials, 5*, 81–91. https://doi.org/10.1002/adem.200390013.

Hinkle, B. L. (1953). *Acceleration of particles and pressure drops encountered in horizontal pneumatic conveying*. Georgia: Georgia Institute of Technology.

Hu, B., Hu, F. Y., & Huang, X. R. (2012). Directionally solidified laser cladding. *Advances in Materials Research, 557–559*, 1708–1711. https://doi.org/10.4028/www.scientific.net/AMR.557-559.1708.

Hunt, J. D. (1984). Steady state columnar and equiaxed growth of dendrites and eutectic. *Materials Science and Engineering, 65*, 75–83. https://doi.org/10.1016/0025-5416(84)90201-5.

Ibarra-Medina, J., & Pinkerton, A. J. (2010). A CFD model of the laser, coaxial powder stream and substrate interaction in laser cladding. *Physics Procedia, 5*, 337–346. https://doi.org/10.1016/j.phpro.2010.08.060.

Kamara, A. M., Wang, W., Marimuthu, S., & Li, L. (2011). Modelling of the melt pool geometry in the laser deposition of nickel alloys using the anisotropic enhanced thermal conductivity approach. *Proceedings of the Institution of Mechanical Engineers, Part B: Journal of Engineering Manufacture, 225*, 87–99. https://doi.org/10.1177/09544054JEM2129.

Kar, A., & Mazumder, J. (1989). Extended solid solution and nonequilibrium phase diagram for Ni-Al alloy formed during laser cladding. *Metallurgical Transactions A, 20*, 363–371. https://doi.org/10.1007/BF02653915.

Kobryn, P. A., & Semiatin, S. L. (2003). Microstructure and texture evolution during solidification processing of Ti-6A1-4V. *Journal of Materials Processing Technology, 135*, 330–339. https://doi.org/10.1016/S0924-0136(02)00865-8.

Kurz, W., & Fisher, D. J. (1998). *Fundamentals of solidification* (4th ed.). Uetikon-Zuerich: CRC Press.

Kurz, W., Bezençon, C., & Gäumann, M. (2001). Columnar to equiaxed transition in solidification processing. *Science and Technology of Advanced Materials, 2*, 185–191. https://doi.org/10.1016/S1468-6996(01)00047-X.

Lakshminarayanan, A., Shanmugam, K., & Balasubramanian, V. (2009). Effect of autogenous arc welding processes on tensile and impact properties of ferritic stainless steel joints. *Journal of Iron and Steel Research, International, 16*, 62–16. https://doi.org/10.1016/S1006-706X(09)60012-1.

Leithold, L. (1996). *The calculus 7*. HarperCollins College Pub. ISBN:13: 9780673469137.

LeVeque, R. J. (2007). *Finite difference methods for ordinary and partial differential equations: Steady-state and time-dependent problems*. Society for Industrial and Applied Mathematics.

Levin, P. (2008). A general solution of 3-D quasi-steady-state problem of a moving heat source on a semi-infinite solid. *Mechanics Research Communications, 35*, 151–157. https://doi.org/10.1016/j.mechrescom.2007.09.003.

Liang, Y.-J., Cheng, X., & Wang, H.-M. (2016a). A new microsegregation model for rapid solidification multicomponent alloys and its application to single-crystal nickel-base superalloys of laser rapid directional solidification. *Acta Materialia, 118*, 17–27. https://doi.org/10.1016/j.actamat.2016.07.008.

Liang, Y.-J., Li, A., Cheng, X., Pang, X.-T., & Wang, H.-M. (2016b). Prediction of primary dendritic arm spacing during laser rapid directional solidification of single-crystal nickel-base superalloys. *Journal of Alloys and Compounds, 688*, 133–142. https://doi.org/10.1016/j.jallcom.2016.06.289.

Liang, Y.-J., Cheng, X., Li, J., & Wang, H.-M. (2017). Microstructural control during laser additive manufacturing of single-crystal nickel-base superalloys: New processing–microstructure maps involving powder feeding. *Materials and Design, 130*, 197–207. https://doi.org/10.1016/j.matdes.2017.05.066.

Liu, Z., & Qi, H. (2014). Mathematical modeling of crystal growth and microstructure formation in multi-layer and multi-track laser powder deposition of single-crystal superalloy. *Physics Procedia, 56*, 411–420. https://doi.org/10.1016/J.PHPRO.2014.08.144.

Ma, M., Wang, Z., & Zeng, X. (2017). A comparison on metallurgical behaviors of 316L stainless steel by selective laser melting and laser cladding deposition. *Materials Science and Engineering A, 685*, 265–273. https://doi.org/10.1016/j.msea.2016.12.112.

Martorano, M. A., & Biscuola, V. B. (2009). Predicting the columnar-to-equiaxed transition for a distribution of nucleation undercoolings. *Acta Materialia, 57*, 607–615. https://doi.org/10.1016/J.ACTAMAT.2008.10.001.

Martorano, M. A., Beckermann, C., & Gandin, C. A. (2003). A solutal interaction mechanism for the columnar-to-equiaxed transition in alloy solidification. *Metallurgical and Materials Transactions A, 34 A*, 1657–1674. https://doi.org/10.1007/s11661-003-0311-x.

Meriaudeau, F., Truchetet, F., Grevey, D., & Vannes, A. B. (1997). Laser Cladding process and image processing. *Journal of Lasers in Engineering, 6*, 161–187. https://doi.org/10.1101/gr.133546.111.

Mills, K. C. (2002). *Recommended values of thermophysical properties for selected commercial alloys*. Cambridge: Woodhead.

Mishra, S., & Yadava, V. (2013). Modeling and optimization of laser beam percussion drilling of nickel-based superalloy sheet using Nd: YAG laser. *Optics and Lasers in Engineering, 51*, 681–695. https://doi.org/10.1016/j.optlaseng.2013.01.006.

Nastac, L., Valencia, J. J., Tims, M. L., & Dax, F. R. (2001). Advances in the solidification of IN718 and RS5 alloys. In *Superalloys 718, 625, 706 and various derivatives* (pp. 103–112). Warrendale: TMS. https://doi.org/10.7449/2001/Superalloys_2001_103_112.

NIST/SEMATECH. (2012). *E-handbook of statistical methods* [WWW Document]. Probab. Distrib. https://www.itl.nist.gov/div898/handbook/eda/section3/eda366g.htm. Accessed 10.24.18.

Nolze, G., & Hielscher, R. (2016). Nolze and Hielscher orientations-perfectly colored research papers. *Journal of Applied Crystallography, 49*, 1786–1802. https://doi.org/10.1107/S1600576716012942.

Ostrowski, A., & Langer, E. W. (1979). Precipitation of titanium carbonitrides in as-cast 17% chromium stainless steels. *Scandinavian Journal of Metallurgy, 8*(4), 153–160.

Park, J.-W., Babu, S. S., Vitek, J. M., Kenik, E. A., & David, S. A. (2003). Stray grain formation in single crystal Ni-base superalloy welds. *Journal of Applied Physics, 94*, 4203–4209. https://doi.org/10.1063/1.1602950.

Pautrat, A. (2013). *Étude expérimentale quantitative de la solidification de l'inconel 718 en fonderie*. Français: Ecole Nationale Supérieure des Mines de Paris. https://tel.archives-ouvertes.fr/pastel-00998532/.

Petersen, W. A. (1973). Fine grained weld structures. In: *53rd AWS annual meeting*. Welding Research Supplement, Detroit, pp. 74–79.

Peyre, P., Aubry, P., Fabbro, R., Neveu, R., & Longuet, A. (2008). Analytical and numerical modelling of the direct metal deposition laser process. *Journal of Physics D: Applied Physics, 41*. https://doi.org/10.1088/0022-3727/41/2/025403.

Picasso, M., Marsden, C. F., Wagniere, J. D., Frenk, A., & Rappaz, M. (1994). A simple but realistic model for laser cladding. *Metallurgical and Materials Transactions B: Process Metallurgy and Materials Processing Science, 25*, 281–291. https://doi.org/10.1007/BF02665211.

Pinkerton, A. J. (2007). An analytical model of beam attenuation and powder heating during coaxial laser direct metal deposition. *Journal of Physics D: Applied Physics, 40*, 7323–7334. https://doi.org/10.1088/0022-3727/40/23/012.

Pinkerton, A. J., & Li, L. (2004). An analytical model of energy distribution in laser direct metal deposition. In *Proceedings of the Institution of Mechanical Engineers, Part B: Journal of Engineering Manufacture* (pp. 363–374). London: Sage. https://doi.org/10.1243/095440504323055498.

Pinkerton, A. J., Moat, R., Shah, K., Li, L., Preuss, M., & Withers, P. J. (2007). A verified model of laser direct metal deposition using an analytical enthalpy balance method. *Proceedings of the 26th International Congress on Applications of Lasers and Electro-optics, 2007*, 1806. https://doi.org/10.2351/1.5061038.

PNAS, National Academy of Engineering. (2012). *Frontiers of engineering: Reports on leading-edge engineering from the 2011 symposium*. Washington, DC: The National Academies Press. https://doi.org/10.17226/13274.

Rappaz, M., Gandin, C. A., Desbiolles, J. L., & Thévoz, P. (1996). Prediction of grain structures in various solidification processes. *Metallurgical and Materials Transactions A: Physical Metallurgy and Materials Science, 27*, 695–705. https://doi.org/10.1007/BF02648956.

Renderos, M., Torregaray, A., Gutierrez-Orrantia, M. E., Lamikiz, A., Saintier, N., & Girot, F. (2017). Microstructure characterization of recycled IN718 powder and resulting laser clad material. *Materials Characterization, 134*, 103–113. https://doi.org/10.1016/J.MATCHAR.2017.09.029.

Sainte-Catherine, C., Jeandin, M., Kechemair, D., Ricaud, J.-P., & Sabatier, L. (1991). Study of dynamic absorptivity at 10.6 μm (CO2) and 1.06 μm (ND-YAG) wavelengths as a function of temperature. *Journal de Physique IV, 01*, C7-151–C7-157. https://doi.org/10.1051/jp4:1991741.

Seetharaman, S. (2005). *Fundamentals of metallurgy*. Cambridge: Woodhead Pub. and Maney Pub. on behalf of the Institute of Materials, Minerals and Mining.

Srivatsan, T. S., & Sudarshan, T. S. (1993). *Rapid solidification technology: An engineering guide*. Lancaster: Technomic Pub.

Sturz, L., Drevermann, A., Pickmann, C., & Zimmermann, G. (2005). Influence of grain refinement on the columnar-to-equiaxed transition in binary Al alloys. *Materials Science and Engineering A, 413–414*, 379–383. https://doi.org/10.1016/j.msea.2005.08.199.

Tabernero, I., Lamikiz, A., Ukar, E., López De Lacalle, L. N., Angulo, C., & Urbikain, G. (2010). Numerical simulation and experimental validation of powder flux distribution in coaxial laser cladding. *Journal of Materials Processing Technology, 210*, 2125–2134. https://doi.org/10.1016/j.jmatprotec.2010.07.036.

Toyserkani, E., Corbin, S., & Khajepour, A. (2005). *Laser cladding*. Boca Raton: CRC Press.

Trujillo Guillen, M. (2005). *Función de Green para la ecuación hiperbólica de transmisión del calor*. Riunet. Universitat Politècnica de València, Valencia (Spain). https://doi.org/10.4995/Thesis/10251/1905.

Van Elsen, M., Baelmans, M., Mercelis, P., & Kruth, J.-P. (2007). Solutions for modelling moving heat sources in a semi-infinite medium and applications to laser material processing. *International Journal of Heat and Mass Transfer, 50*, 4872–4882. https://doi.org/10.1016/J.IJHEATMASSTRANSFER.2007.02.044.

Villafuerte, J., & Kerr, H. (1990). Grain structures in gas tungsten-arc welds of austenitic stainless steels with ferrite primary phase. *Metallurgical Transactions A*. https://doi.org/10.1007/BF02656582.

Villafuerte, J. C., Kerr, H. W., & David, S. A. (1995). Mechanisms of equiaxed grain formation in ferritic stainless steel gas tungsten arc welds. *Materials Science and Engineering A, 194*, 187–191. https://doi.org/10.1016/0921-5093(94)09656-2.

Villaret, V., Deschaux-Beaume, F., Bordreuil, C., Fras, G., Chovet, C., Petit, B., & Faivre, L. (2013a). Characterization of Gas Metal Arc Welding welds obtained with new high Cr-Mo ferritic stainless steel filler wires. *Materials and Design, 51*, 474–483. https://doi.org/10.1016/j.matdes.2013.04.054.

Villaret, V., Deschaux-Beaume, F., Bordreuil, C., Rouquette, S., & Chovet, C. (2013b). Influence of filler wire composition on weld microstructures of a 444 ferritic stainless steel grade. *Journal of Materials Processing Technology, 213*, 1538–1547. https://doi.org/10.1016/j.jmatprotec.2013.03.026.

Vitek, J. M., Babu, S. S., Park, J.-W., & David, S. A. (2012). *Analysis of stray grain formation in single-crystal nickel-based superalloy welds* (pp. 459–465). https://doi.org/10.7449/2004/superalloys_2004_459_465.

Vuoristo, P., Tuominen, J., & Nurminen, J. (2005). Laser coating and thermal spraying – Process basics and coating properties. In`*Thermal spray 2005: Thermal spray connects: Explore its surfacing potential!* (pp. 1270–1277). DVS-ASM.

Wang, G. X., Prasad, V., & Matthys, E. F. (1997). Solute distribution during rapid solidification into an undercooled melt. *Journal of Crystal Growth, 174*, 35–40. https://doi.org/10.1016/S0022-0248(96)01058-5.

Zhong, M., & Liu, W. (2010). Laser surface cladding: The state of the art and challenges. *Proceedings of the Institution of Mechanical Engineers, Part C: Journal of Mechanical Engineering Science, 224*, 1041–1060. https://doi.org/10.1243/09544062JMES1782.

Zohdi, T. I. (2015). On the thermal response of a surface deposited laser-irradiated powder particle. *CIRP Journal of Manufacturing Science and Technology, 10*, 77–83. https://doi.org/10.1016/j.cirpj.2015.05.001.

Chapter 5
Laser Additive Manufacturing of Single-Crystal Superalloy Component: From Solidification Mechanism to Grain Structure Control

Chaoyue Chen, Jiang Wang, Hanlin Liao, Zhongming Ren, and Shuo Yin

5.1 Introduction

Nickel-based superalloys are materials of choice for manufacturing the hot-section components in the gas turbine due to their superior mechanical properties at high temperatures (Han et al. 2019; Luo et al. 2019). Notably, the nickel-based superalloys in the form of single crystal (SX) are manufactured through directional solidification techniques to obtain one single grain in the whole component. Compared with polycrystalline alloys, the superior creep and thermal fatigue resistance can be obtained for the SX superalloy through the absence of grain boundaries (Anderson et al. 2010; Vitek 2005). As a result, the SX superalloys have been widely applied as the desired material selections for the high-temperature turbine section of aero and industrial gas turbine engines (Kong et al. 2019; Inaekyan et al. 2019; Wang and Chou 2017). However, the SX superalloy parts will experience unavoidable damage under the extremely severe service environment with high temperature, high pressure, and severe corrosion. Due to the high manufacturing cost of such SX components, the effective repair techniques for the damaged SX superalloy are highly desired to extend the service life of the hot-section components, such as blades, blisks, and vane seal segments. For this moment, the popular welding techniques

C. Chen · J. Wang · Z. Ren
State Key Laboratory of Advanced Special Steels, School of Materials Science and Engineering, Shanghai University, Shanghai, China
e-mail: cchen1@shu.edu.cn; jiangwang@i.shu.edu.cn; zmren@shu.edu.cn

H. Liao
ICB UMR 6303, CNRS, Univ. Bourgogne Franche-Comté, UTBM, Belfort, France
e-mail: hanlin.liao@utbm.fr

S. Yin (✉)
Department of Mechanical and Manufacturing Engineering, Trinity College Dublin, The University of Dublin, Dublin 2, Ireland
e-mail: yins@tcd.ie

P. Cavaliere (ed.), *Laser Cladding of Metals*,
https://doi.org/10.1007/978-3-030-53195-9_5

like TIG with high energy input and high-thermal-affected area cannot avoid the formation of stray grain as well as cracks within the repaired SX component (Gäumann et al. 1999; Basak and Das 2016; Chauvet et al. 2018a).

Among the various methods, laser additive manufacturing (LAM) has become an effective technique to realize the repair of damage SX components (Vilar and Almeida 2015; Gäumann et al. 2001). The high-energy laser beam is used to melt the feedstock metals to form the molten pool, whereas the feedstock materials can be the powder bed, powder feeding, and the wires (Herzog et al. 2016; Körner 2016; DebRoy et al. 2018). Due to the small spot size and high energy density, the LAM technique can achieve the damage repair with limited heat-affected zone and low distortion caused by thermal stress (Li et al. 2019). Coordinated with the industrial robot, the high-resolution LAM technique is able to realize the repair and restoration of the damaged components with complex geometry. However, due to the complex melting and solidification process, the columnar growth in the LAM process cannot be precisely controlled to obtain the SX structure. During this process, if specific solidification conditions are satisfied, the epitaxial growth of columnar cells/dendrites along the original orientation in the substrate occurs, and no equiaxed stray grains (SGs) will form. Otherwise, columnar-to-equiaxed transition (CET) takes place, and equiaxed SGs are produced, indicating the failure of the repairing process. Thus, the processing parameters should be carefully chosen to obtain the desired epitaxial growth of single-crystalline alloys based on the SX substrate so as to realize the repair of the SX turbine blade and make a right consistency of the mechanical properties between the repaired and substrate regions.

Existing work mainly focused on the solidification mechanism, processing parameter optimization, and cracking development. So far, a systematic summarization and review of these topics are still lacking. Therefore, in this chapter, the existing work on the LAM of SX superalloys was summarized and reviewed for the purpose of systematically introducing the recent progress.

5.2 Laser Additive Manufacturing Techniques

Different from the traditional subtraction manufacturing, the metallic additive manufacturing (AM) is a novel technology that joins materials to generate three-dimensional parts directly from CAD models based on the discrete-stacking principle (Han et al. 2019; Luo et al. 2019; Anderson et al. 2010; Vitek 2005; Kong et al. 2019; Inaekyan et al. 2019). Metallic AM techniques have various eye-catching advantages in comparison with other manufacturing technologies, such as the freedom of design and manufacturing, a short manufacturing cycle, and less material waste (Wang and Chou 2017; Gäumann et al. 1999). In addition, metallic AM technology has spread into various fields, such as the mold industry (Basak and Das 2016), the aerospace (Chauvet et al. 2018a), automotive fields (Vilar and Almeida 2015), etc.

Recently, the powder bed fusion (PBF) method has become the most distinguished metallic AM technique, including selective laser melting (SLM) (Yan et al. 2018, 2019) and selective electron-beam melting (SEBM) (Herzog et al. 2016). It is worth noting that SLM technology is more easily applied in the fabrication of metallic molds that have conformal cooling channels and functional parts with complicated geometries. Such unique advantages can be attributed to its flexibility in geometric design, high spatial resolution, and smaller amounts of material waste (Körner 2016; DebRoy et al. 2018).

This method can either flexibly add alloying elements (laser surface alloying) to the molten pool during the rapid melting or directly melt the alloy powder (laser cladding) that is simultaneously conveyed on the surface of the part to solidify quickly (Herzog et al. 2016; Gu et al. 2013; King et al. 2015). It is able to obtain the coating material with the characteristics of fine and uniform rapid solidification and nonequilibrium structure, which is different from the composition of the substrate material. It can also directly integrate material design, material preparation, and rapid near-net forming to produce complex structural parts. Laser additive manufacturing can adjust the solidification structure by adjusting the process parameters, not only the small equiaxed crystal structure but also the long columnar crystal structure epitaxially grown from the substrate (Basak and Das 2016). Thus, the integration from material composition and structural design to part manufacturing and forming is genuinely realized. Therefore, additive manufacturing is hailed as a representative technology that is expected to become the "third industrial revolution" and is a leading technology for the development of mass-production models to personalized manufacturing models.

At present, the most representative of laser additive manufacturing technology is selective laser melting (SLM), with powder bed as the technical feature, and laser direct metal deposition (LDMD), with synchronous powder feed as the technical feature. As shown in Fig. 5.1a, SLM technology is based on selective laser sintering (SLS) technology (Herzog et al. 2016; Dadbakhsh et al. 2014). Due to the development and application of high-power lasers, SLM technology can completely melt powder particles. In addition, the powder size of the SLM technology is smaller, and the laser beam with a smaller spot size is used, so the surface accuracy of the formed part is higher. However, due to the limitation of the printing chamber, SLM can only process precision parts with small size and complicated structure and cannot manufacture some large integral metal components. As shown in Fig. 5.1b,c, the LDMD technology is based on laser cladding technology (Yan et al. 2014; Ren et al. 2017). It is not limited by the fabrication chamber and can manufacture some large-sized metal components. Besides, it can control the process parameters to achieve the directional growth of the metal structure to prepare columnar crystal structure and single-crystal structure to achieve the effect of rapid repair of damaged parts. In addition, functionally graded composite materials and metal-based composite materials can be prepared by mixing different materials.

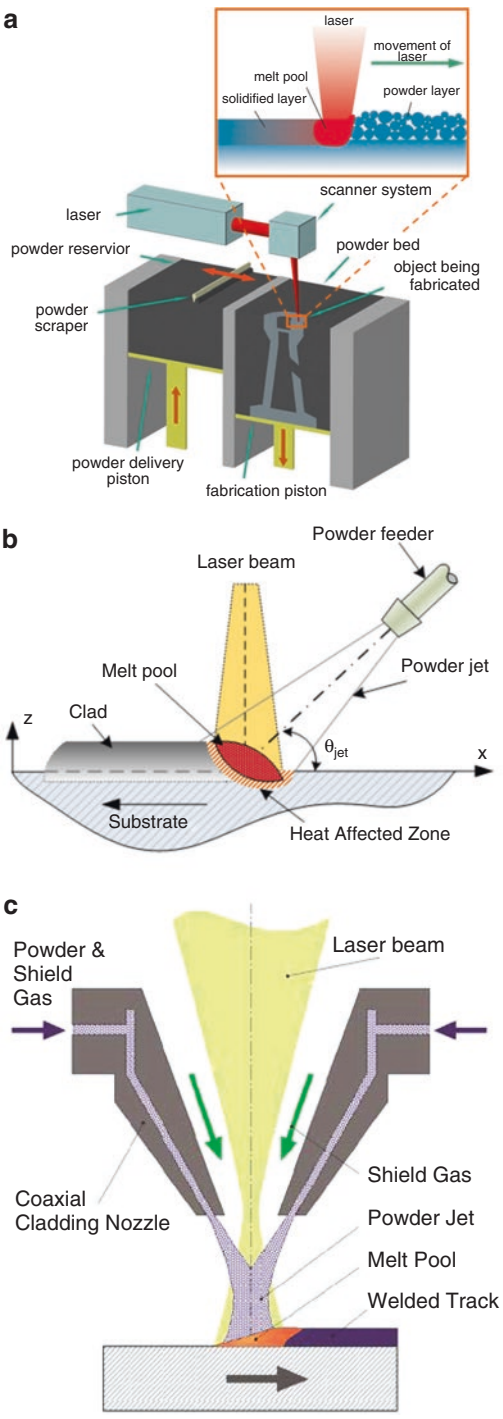

Fig. 5.1 Schematic diagram of laser additive manufacturing process: (**a**) SLM; (**b**) side powder feed LDMD; (**c**) coaxial powder feed LDMD

5.3 Solidification Mechanism of SX via AM

In order to obtain the single-crystal solidification during the laser additive manufacturing process, the key is to find the relation between the processing parameters and the solidification structure. Characterized by the high cooling rate and thermal gradient, the laser additive manufacturing presents distinct solidification features from the traditional solidification processes. For both the LAM of polycrystalline and the epitaxial growth of single-crystalline alloys, enormous efforts have been attributed to reveal the solidification structure diagram according to the temperature gradient and growth rate as well as the processing parameters.

For example, in AM Ti6Al4V samples by laser or electron beam, the columnar prior β grain is found to dominate the solidified microstructure, leading to the strong microstructural textures and anisotropy of the mechanical properties (Ren et al. 2017; Liu and Shin 2019). Similarly, the columnar grain morphology composed of γ phases is dominating the AM Ni-based superalloys along the building direction, leading to a typical attributed <001> texture (DebRoy et al. 2018; Hosseini and Popovich 2019). Such epitaxially growing columnar crystal from the substrate material or previously deposited layer is mainly due to the extremely high thermal gradient along the building direction during laser additive manufacturing. However, under certain thermal conditions, the epitaxially growing columnar structure can be interrupted and replaced by the formation of equiaxed grains. Such columnar-to-equiaxed transition (CET) occurs when nucleation of sufficiently numerous equiaxed dendrites takes place in the constitutionally undercooled liquid adjacent to the columnar dendritic front. The stability of the solidification front is controlled by the extent of the constitutional undercooling ahead of the advancing interface. Such stability is influenced by the presence of alloying or impurity elements, local grain growth rate, R, and the thermal gradient in the molten pool, G. As shown in Fig. 5.2, the higher ratio between G and R, namely, the G/R, results in a planar solidification front. At lower G/RL ratios, the morphology changes to cellular, cellular-dendritic, or dendritic, depending on the constitutional undercooling at the advancing solidification front (see Fig. 5.2). Thus, for the given material system with specific element composition, the grain morphology, as well as the CET, is mainly determined by the ratio between thermal gradient of G and solidification velocity of R. A fully columnar structure can be obtained at a sufficiently G/R value, while the equiaxed grains are emerging as the value G/R is higher than a critical value.

Figure 5.3 shows a typical cross-sectional microstructure of the laser-deposited CMSX-4 sample on a single-crystal substrate (Acharya et al. 2014). It can be seen that the epitaxial growth dendrite along the [001] direction. However, it is also evident that the CET was formed at the top of the deposited layer, where the stray grain formation appears as misoriented and equiaxed grains in the deposited microstructure. The control of CET and suppression of stray grain formation become the major challenges for the manufacturing of SX superalloy via the LAM technique. As shown in Fig. 5.4, the variation of solidification speed V and thermal gradient G is illustrated within the molten pool along the building direction of the z-axis

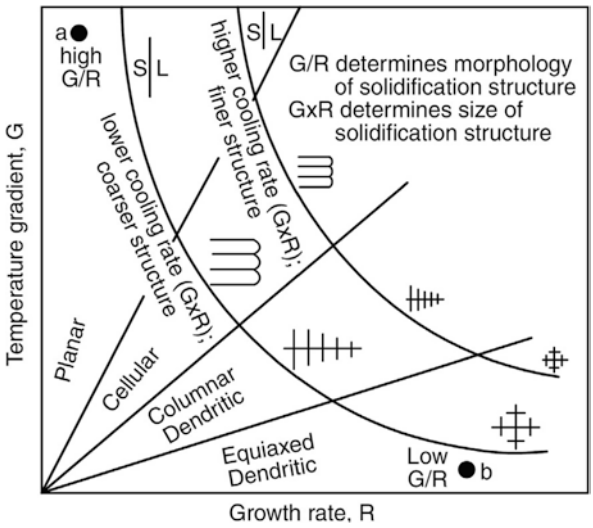

Fig. 5.2 Effect of temperature gradient *G* and growth rate *R* on the morphology and size of solidification microstructure (Kou 2003)

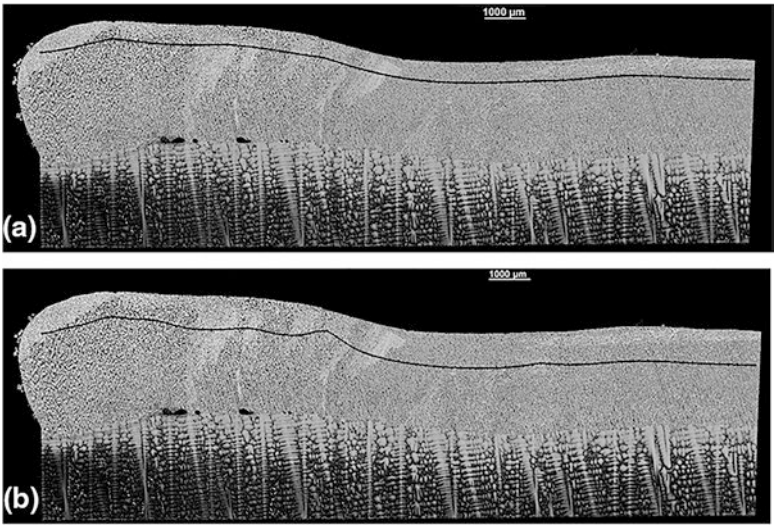

Fig. 5.3 Representative CMSX-4 sample (**a**) with the CET initiation indicated by the black line and (**b**) showing termination of [001] growth to [100] growth or OMT (Acharya et al. 2014)

(Gäumann et al. 1999). It can be seen that the solidification speed of *V* rapidly increases from zero at the bottom to the maximum value at the surface of the molten pool. On the contrary, the temperature gradient *G* is highest at the bottom of the molten pool, which gradually decreases as the surface is approached. As a result, the epitaxial growth of columnar dendrites is most likely to form from the molten pool, whereas the stray grains can be formed with the ratio of *G*/*V* that gradually decreases with the deposition process. The key is to control the vulnerable to columnar-to-equiaxed transition (CET) process of Ni-based SX superalloy by revealing the

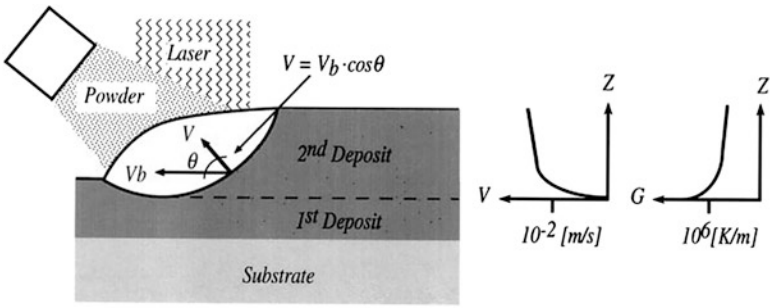

Fig. 5.4 Schematic longitudinal section along the clad centerline presenting the laser metal-forming process and the evolution of the solidification velocity *V* and temperature gradient *G* along with the solid/liquid interface (Gäumann et al. 1999)

relation between thermal history (thermal gradient and solidification speed) and epitaxial solidification model in the rapid solidification process of LAM.

In order to better control the epitaxial growth of the single crystal from an SX substrate, enormous efforts have been made to predict the CET with a quantitative equation to describe the relation between *G* and *R* (Gäumann et al. 2001; Liang et al. 2016, 2017a, b). It is then able to obtain the solidification structure from columnar to equiaxed grains in the LAM materials by controlling the processing parameters like laser powder and scanning speed. To quantitatively investigate this crucial phenomenon prevalent in solidification, Hunt (1984) developed the first analytical CET model for the casting process based on the growing competition between columnar dendrites and new equiaxed grains at the solidification front. At the sufficient constitutional supercooling, the mechanism of stray grain formation in the casting process is the nucleation and growth of equiaxed grains ahead of the solidification interface, which is determined by the ratio between thermal gradient and solidification velocity. Hunt proposed that the fully equiaxed growth occurs if the volume fraction of equiaxed grains Φ is higher than 49%, whereas the structure is becoming entirely columnar if Φ is lower than 0.66%. In order to quantitatively describe the CET model of the laser melting process, Gäumann et al. (1999, 2001) subsequently adapted the Hunt's model to the rapid solidification conditions by using the Kurz-Giovanola-Trivedi (KGT) model (Kurz et al. 1986). Gäumann found that the constitutional undercooling at the solidification front is the dominant factor for the CET at a lower thermal gradient and lower solidification velocity, which means that the formation of equiaxed grains is more easily to be triggered at a lower nucleation undercooling degree. However, the quantity of nucleation sites plays a more vital role in the case of rapid solidification cases with higher thermal gradients. Thus, to easily relate CET to the solidification conditions, a simplified CET criterion for complex multicomponent alloys was further derived (Gäumann et al. 2001):

$$\frac{G^n}{v} = K_{\mathrm{CET}} = \alpha \left[\sqrt[3]{\frac{-4\pi N_0}{3\ln(1-\phi)}} \times \frac{1}{n+1} \right]^n \tag{5.1}$$

where G is the thermal gradient, v is the solidification velocity, N_0 is nuclei density, Φ is the fraction of equiaxed grains, and a and n are the material-dependent constants. While the G^n/v is higher than the critical value of K_{CET}, the CET will be triggered during the laser additive manufacturing process. As shown in Fig. 5.5, the microstructure selection map for superalloy CMSX-4 under the experimental conditions is illustrated to predict the solidification morphology as a function of temperature gradient, G, and solidification velocity, V. For example, a microstructure selection map of superalloy CMSX-4 for a nuclei density $2 \times 10^{15}/m^3$ was built to predict the formation of columnar and equiaxed structure (Gäumann et al. 2001). It should be noted that CET is critical to the quality of the single-crystal deposit because it limits the height of columnar dendrite growth. The rectangular insert shows the range of conditions which is typical for the LMF process.

Besides, it should be noticed that the different LAM techniques present distinct microstructure selection patterns due to their thermal history. As can be seen in Fig. 5.6, the selective laser melting (SLM) presents a notably higher G/V ratio than

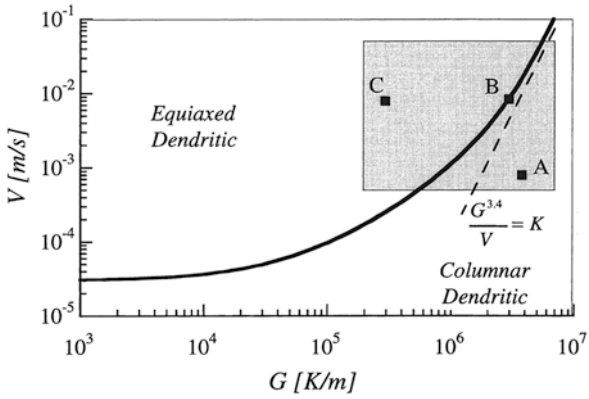

Fig. 5.5 Microstructure selection map for superalloy CMSX-4 (Gäumann et al. 1999)

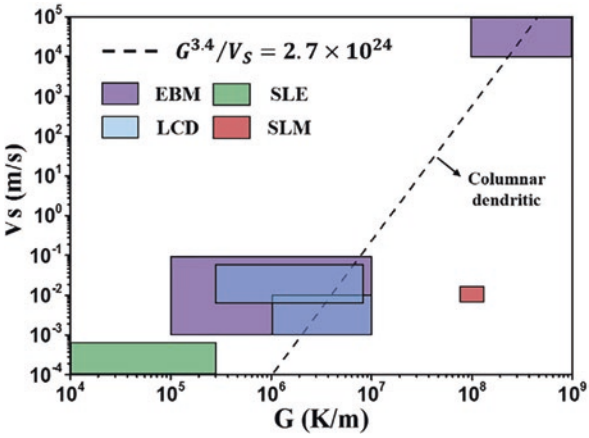

Fig. 5.6 Comparison of G and Vs among several kinds of LAM technologies (Yang et al. 2019)

the methods like laser cladding deposition due to its higher energy density with a smaller laser spot size (around 100 μm). Thus, the SLM can be another potential technique to realize the fabrication of the SX superalloy component. However, the control of the columnar misorientation angle becomes the key challenge under the complex laser scanning strategy.

5.4 Influence of Laser Processing Parameters

M. Gäumann et al. (1999, 2001) reported the first attempt to fabricate the single-crystal deposits using the epitaxial laser metal forming. Figure 5.7 shows the cross-sectional morphology of a CMSX-4 deposit on the single-crystal substrate, where the left column is the OM (optical microscopy) images and the right one is the EBSD patterns. From both the OM and EBSD images, it is evident that the deposit shows a columnar dendritic structure at the bottom of the deposit. Meanwhile, the equiaxed grains can be observed at the top of the layer indicating the CET occurrence, which is induced due to the insufficient thermal gradient as the LAM process (Fig. 5.8).

Various researchers have made vast efforts on the epitaxial growth of the SX superalloy under different processing parameters. Santos et al. (2011) used the laser metal deposition to fabricate the SX CMSX-4 deposit on the Rene N4 substrate. By optimizing the processing parameter and deposition orientation, the SX deposit layer was obtained on the substrate, whereas the height of the SX region can occupy 30–40% of each deposited layer. As shown in Fig. 5.9, the deposit layer growth epitaxially from the substrate along the [001] direction, which is the same as the maximum thermal gradient. It is obvious that the CET occurred at the top layer of deposit (see Fig. 5.9), where the equiaxed grain was formed along the [100] direction. However, during the continuous deposition process, the equiaxed grain region can be remelted, and the epitaxial growth can be continued from the columnar region to form the subsequent SX deposit layer. Thus, the crystallographic orientation of the SX structure can be preserved across the successive layers. As shown in Fig. 5.9, the CMSX-4 sample composed of ten layers of epitaxial growth can be obtained with the misorientation different from the less than 2°. Meanwhile, it is also evident that the interior columnar structure was surrounded by the equiaxed grains at the exterior of the sample.

In order to predict the epitaxial growth of the dendritic grains based on the SX substrate, Liu and Qi (2014, 2015a) established a three-dimensional finite element model to simulate the temperature field of the direct laser deposition. The effects of laser power, scanning speed, and powder feeding rate were accounted for in the finite element simulation and the experimental investigations. It is found that the processing parameters can directly determine the shape of the molten pool and, in turn, affected the epitaxial growth features of the deposited layer. As can be seen in Fig. 5.10a–c, at the laser power of 300 W, the height ratio between the epitaxial columnar dendritic region and that of the total deposit along the [001] orientation

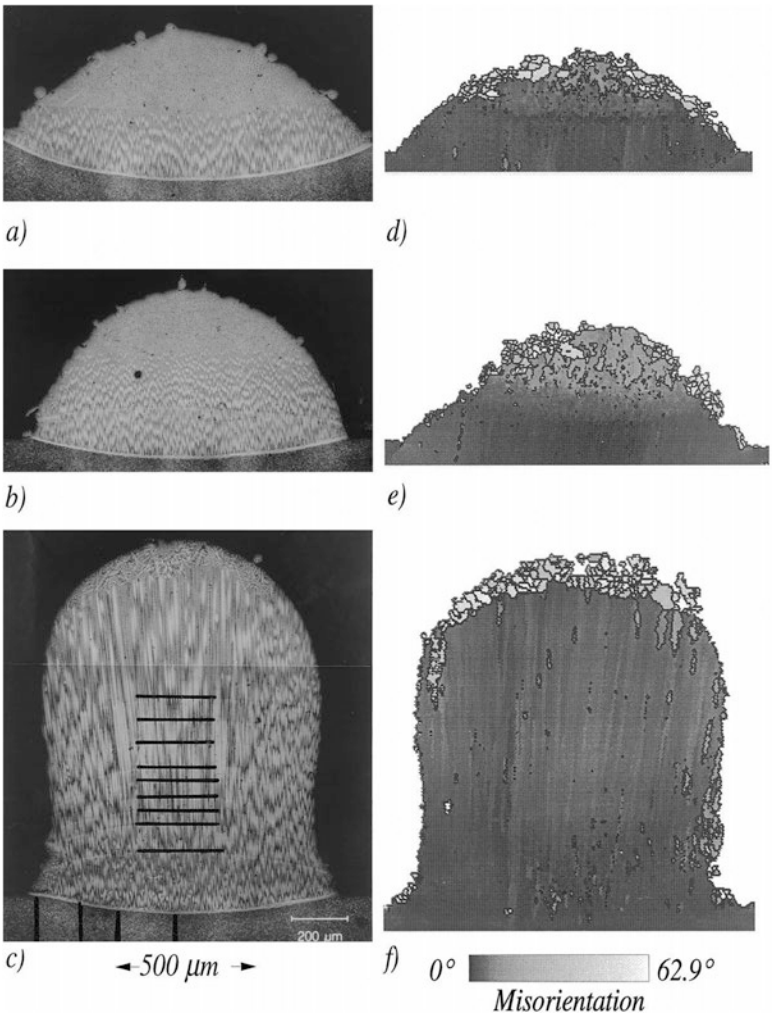

Fig. 5.7 (**a**–**c**) Optical micrographs of a transverse section of a laser formed plate-like deposit after one, two, and ten layers, respectively. (**d**–**f**) Corresponding electron backscattered diffraction (EBSD) grain structure maps

can increase from 42.0% to 48.3% as the laser scanning speed is increased from 5 mm/s to 10 mm/s. As shown in Fig. 5.10d, the height ratio of epitaxial columnar dendritic has a similar trend with the change of laser speed, whereas the height ratio can reach as high as 52% at a laser power of 200 W and speed of 10 mm/s. To further investigate the effect of laser power, the height ratio of columnar dendrite decreases from 44.8% to 43.0% as laser power increases from 200 W to 300 W (see Fig. 5.10b, d, which is also illustrated in Fig. 5.10f). It is also obvious that the simulation results agree reasonably well with the experimental results of the epitaxial

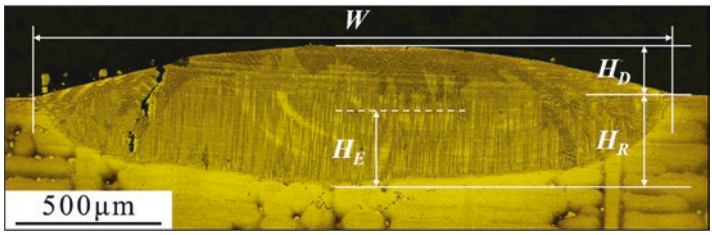

Fig. 5.8 Transverse-section microstructure of a laser cladding, i.e., a single-layer laser deposit, schematically showing several geometric dimensions crucial to SXLAM process (Liang et al. 2017a)

height ratio. According to the heat transfer simulation, the competitive growth of the grains along different crystallographic orientations can be obtained by comparing each critical CET value of $G^{3.4}/V$. Thus, the value of $G^{3.4}/V$ increases less rapidly along with the building direction at the higher laser scanning speed, which indicates the promoted epitaxial growth of columnar dendrite and the larger region of epitaxial growth. At the same time, the higher laser power can significantly decrease the thermal gradient at a higher energy input, which causes the lower value of $G^{3.4}/V$ and lower epitaxial grain height. As a result, the CET occurrence during the epitaxial growth can be directly determined by optimizing the processing parameter, and the finite element modeling of the heat transfer process provides more insights into the mechanism behind the parametric optimization.

Similar relationships between the processing parameters and the solidification conditions were also reported by Liang through the LMD of the René N5 deposit (Liang et al. 2017a). As shown in Fig. 5.11, a higher thermal gradient (G) is obtained at a lower heat input, which means the lower laser power is favorable to promote the epitaxial growth of the dendrite columnar. The solidification velocity (V) increases with early increasing laser speed (V_b) and then becomes almost unchanged with further increasing V_b. Moreover, a higher laser power (P) can further increase the solidification velocity. Wang et al. (2018) also studied the laser scanning speed on the remelted microstructure of the SX Ni-based superalloy. It is found that the equiaxed grains of [010] region are about twice as big as the area of $[0\bar{1}0]$ along the laser scanning direction on (001). Meanwhile, the primary dendritic spacing decreases with the increase of laser scanning speed, indicating a significant influence on the cooling rate during the laser remelting process.

In addition to the laser direct deposition technique, selective laser melting was also used to attempt the epitaxial growth of the SX SR999 superalloy. As another typical metal additive manufacturing technology, SLM based on the powder bed fusion possesses a higher thermal gradient, solidification velocity, and also the value of G^n/V, which makes it more likely to avoid CET during epitaxial growth of SX. From work by Yang et al. (2019), the columnar SX structure with a height of 2 mm can be obtained by using the SLM technique. Meanwhile, it should be noted that the extremely fine dendrite structure is present in the SLM SX layer with the

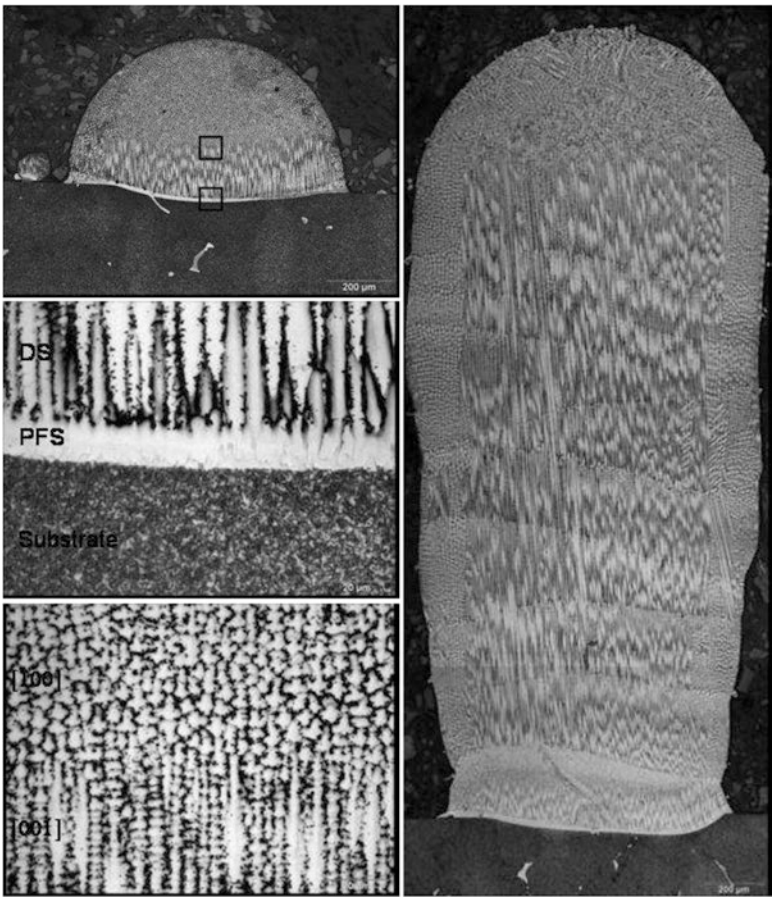

Fig. 5.9 (**a**) Cross section of a single clad; (**b**) SEM interface between the substrate and the clad; (**c**) optical micrograph of the [001]/[100] transition region (P = 500 W, v = 4 mm/s, f = 1 g/min and d = 1 mm, clad height = 495 μm); (**d**) cross section of a 10-layer deposit. The deposition direction is parallel to [100] (P = 500 W, v = 4 mm/s, f = 1 g/min and d = 1 mm, clad height = 2.5 mm) (Santos et al. 2011)

primary dendrite spacing around 1 μm and 2 μm, which is almost two orders of magnitude lower than that of the cast one (~320 μm) (see Fig. 5.12).

5.5 Influence of Substrate Conditions on Microstructure

Apart from the laser processing parameters, the condition of the SX substrate plays a crucial role in the epitaxial laser forming process. For example, the initial substrate temperature can directly influence the thermal gradient as well as the

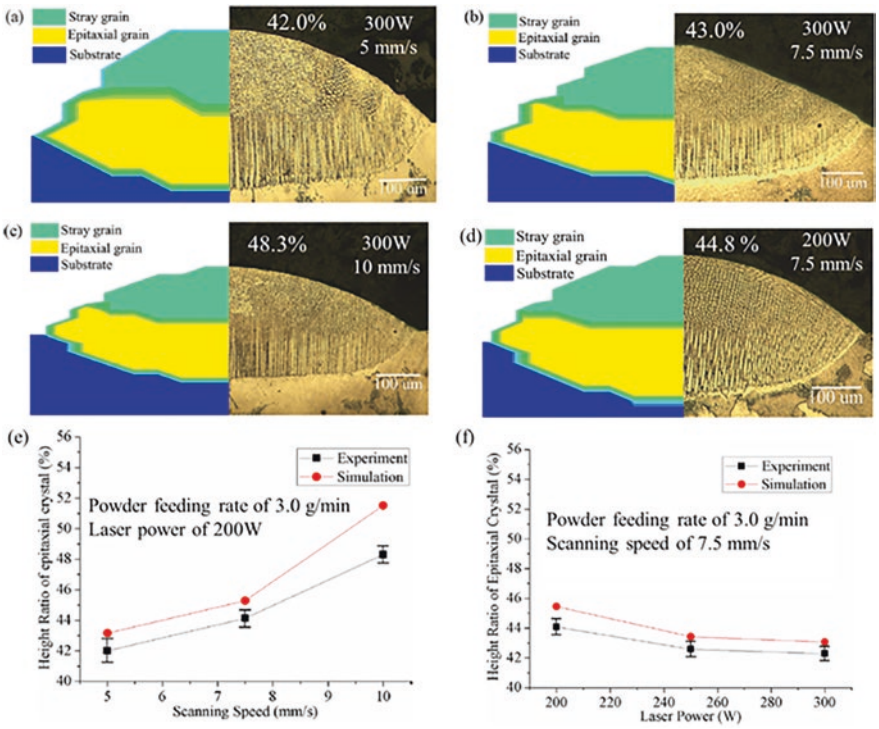

Fig. 5.10 The comparison of microstructure between the simulation and experimental deposited beads with powder feeding rate of 3.0 g/min, different laser power, and scanning speed: (**a**) 300 W, 5 mm/s; (**b**) 300 W, 7.5 mm/s; (**c**) 300 W, 10 mm/s; and (**d**) 200 W, 7.5 mm/s (Liu and Qi 2015a)

solidification velocity at the liquid/solid front and determine the grain structure during rapid solidification. Thus, the adjustment of the substrate temperature makes it possible to control the epitaxial growth of the columnar dendrite during LAM. Apart from grain structure, the misorientation of the columnar grain is another crucial factor evaluating the quality of the epitaxial deposit layer. The influence of the crystallographic orientation of the primary SX stem should be included in the study of the laser epitaxial forming process. As a result, focusing on the substrate conditions, various researches have been conducted to reveal the influence mechanism of substrate temperature and crystallographic orientation during the laser epitaxial growth process (Liu and Qi 2015b; Wang et al. 2015; Wang and Wang 2016; Liu and Wang 2018).

Liu and Wang (2018) studied the effect of initial substrate temperature on epitaxial crystal growth and microstructure formation in laser powder deposition of Ni-based SX superalloy. As shown in Fig. 5.13, it can be found that the molten pool morphology changes little as the substrate temperature increases from −30 °C to +210 °C. However, the enhanced stray grain formation and restrained epitaxial growth of columnar dendrites can be observed with the increase of substrate

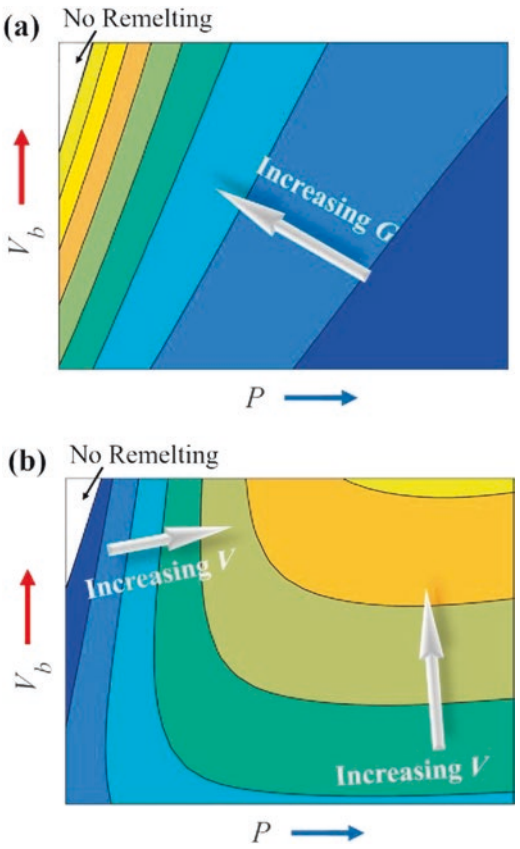

Fig. 5.11 Schematics of the variation trends of (**a**) temperature gradient G and (**b**) solidification velocity V with laser power P and scanning velocity V_b (Liang et al. 2017a)

temperature. It indicates that the lower substrate temperature can benefit the epitaxial growth of columnar dendrites and suppress the stray grain formation. At the same time, the significantly refine columnar dendrites can be found in the epitaxial deposit at a lower substrate present temperature. Such phenomena can be considered due to the enhanced $|G_{001}|^{3.4}/|V_{001}|$ ratio and weakened disturbance by molten pool fluctuation, which can in turn affect the primary dendrite arm distance. As a result, the control of the substrate provides more possibility to enhance the epitaxial growth of columnar dendrites. However, it should be noted that the high thermal gradient and cooling rate may cause more prominent cracking during the solidification of Ni-based superalloy (Qiu et al. 2019; Zhou et al. 2018). Thus, the control of thermal conditions during the laser epitaxial growth of the SX superalloy is crucial to improve the metallurgical quality.

Besides the substrate temperature, various researchers have reported the effect of crystallographic orientation on the epitaxial growth of columnar dendrites. Wang et al. (Wang et al. 2015; Wang and Wang 2016) studied the competitive growth of the dendrites with different preferential orientations during the laser remelting process of SX substrates with different crystallographic orientations. As shown in

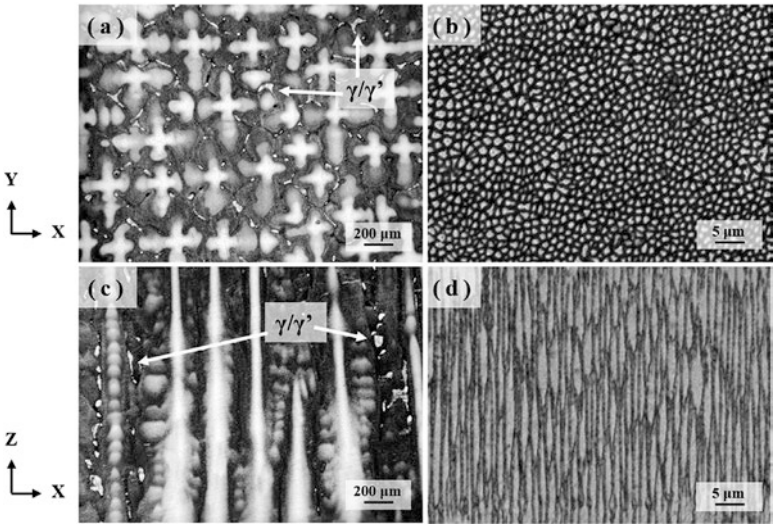

Fig. 5.12 Microstructure of the substrate and SLM sample: (**a** and **c**) horizontal and vertical microstructure of the substrate; (**b** and **d**) horizontal and vertical microstructure of SLM sample

Fig. 5.14, the crystallographic orientation of the SX stems was controlled through the rotation of the SX substrate around the axes of X and Z.

As the crystallographic orientation of the SX substrate was rotated around the x-axis by 15°, the dendritic grains formed along [0 $\bar{1}$ 0] were found to move upward at the left side of the molten pool. By further rotating the crystallographic orientation by 45° around x-axis, the [0 $\bar{1}$ 0] dendritic grains disappeared from the molten pool. The [010] dendrites have a similar tendency as the crystallographic is rotated around z-axis. The solidification structure of the molten pool was replaced by the epitaxial [001] grains at the bottom and [0 $\bar{1}$ 0] and [100] dendrites at the top. However, the area fraction of the epitaxial growth region of the SX dendrite has been hardly changed through the rotation around x- and z-axes.

It is interesting to find that the [100] dendrite gradually moves upward in the molten pool with the crystallographic orientation that is clockwise rotated around y-axis, and the region of the epitaxial [001] grains increases accordingly. As the crystallographic orientation is rotated around y-axis by 45°, the [001] dendrite is dominating the central area as a result of epitaxial growth, whereas the [100] dendrite has been eliminated. On the contrary, the boundary of [100]/[001] gradually moves downward as the crystallographic orientation was rotated around y-axis counterclockwise.

Similarly, Liu and Qi (2015b) also reported the variation of the solidification structure through the crystallographic orientation change of the SX substrate. It is found that the height ratio of the epitaxial crystal exhibits a notable increase from 9% to 94% as the inclination angle of the substrate crystallographic orientation changes from −30° to +30°. Based on the theoretical analysis (Wang et al. 2015,

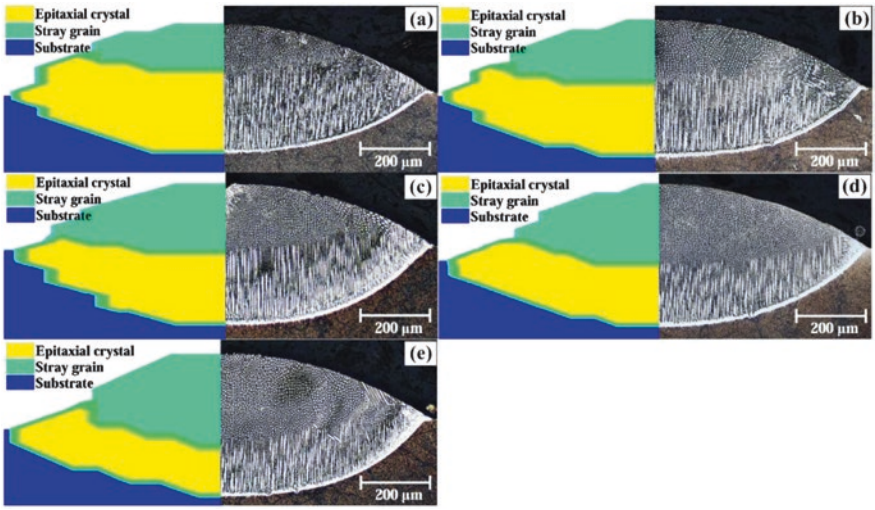

Fig. 5.13 Comparison of geometrical size and microstructure formation in the transverse section of simulation and experimental deposited bead with the Tsub = (**a**) −30 °C; (**b**) +30 °C; (**c**) +90 °C; (**d**) +150 °C; (**e**) +210 °C

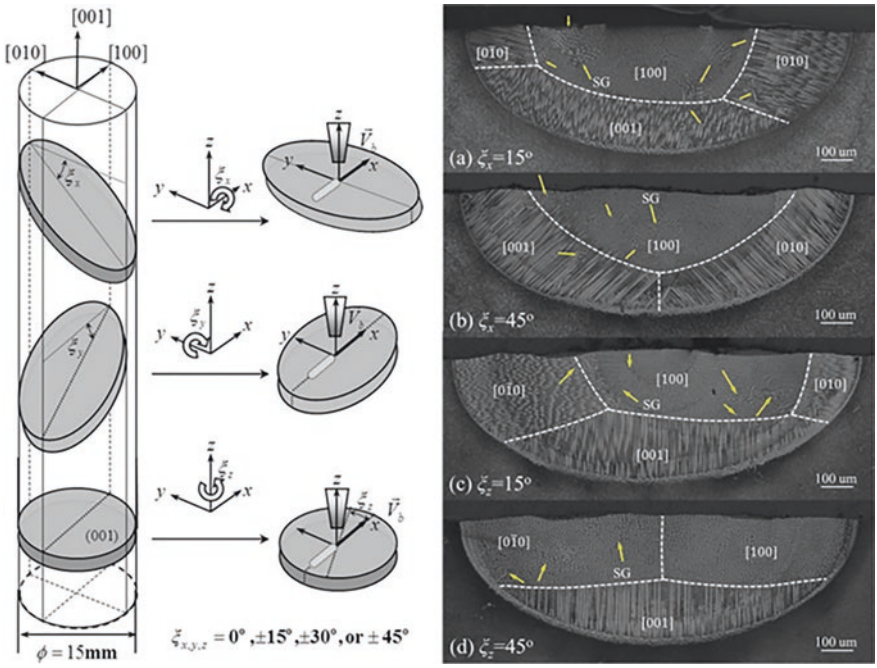

Fig. 5.14 Transverse-section micrographs for different orientations via x- and z-axis rotations

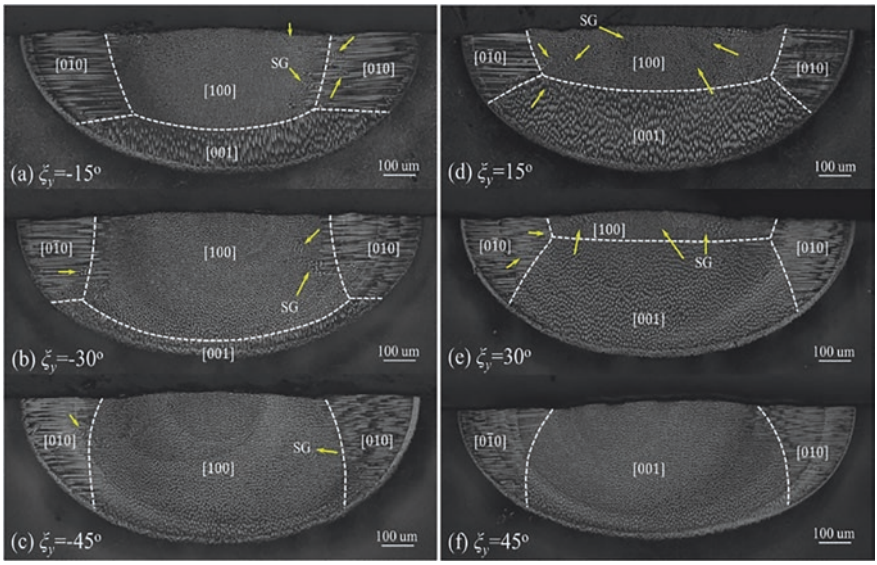

Fig. 5.15 Transverse-section micrographs for different orientations via *y*-axis rotation (Hunt 1984)

2016; Wang and Wang 2016), it can be found that the laser scanning direction toward the crystallographic orientation of the SX substrate after clockwise rotation around y-axis can produce the highest thermal gradient and promote the epitaxial growth of [001] columnar dendrite. Such phenomena indicate that epitaxial growth can be significantly influenced and promoted by controlling the crystallographic orientation of the SX substrate (Figs. 5.14 and 5.15).

5.6 Crack Formation Mechanism

With the increased demand for high-temperature mechanical properties, the Ni-based superalloy is designed and produced with increasing alloying elements to achieve the better γ' strengthening and solid solution strengthening. However, the varying melting temperature of the alloying elements to obtain such high γ' volume fractions is usually non-weldable. It also increases the difficulty of the laser-based additive manufacturing process. Especially, the majority of heavily alloyed Ni-based superalloy often suffers from cracking during the LAM process, which has become one of the main restrictions from its further application. Apart from the control of dendrite growth, the controlling of crack development has become another major issue for the LAM fabrication of single-crystal superalloy. Currently, various efforts have been made to investigate the cracking development and understand the cracking mechanisms during LAM of Ni-based superalloys.

Currently, the liquation cracking and solidification cracking are widely accepted as two primary mechanisms for crack development of Ni-based superalloys (Qiu et al. 2019; Zhou et al. 2018). Solidification cracking that is also known as the hot cracking usually occurs under the high contraction stress at the terminal stage of solidification above the solidus as a result of its low ductility. Meanwhile, the liquation cracking happens typically in the heat-affected zone of the already deposited layers, where the cyclic thermal history can cause the remelting of eutectic phases. Both types of cracking require the presence of liquid films.

In the direct laser-deposited Inconel 718 alloy, the liquation cracking is found along with low-melting-point Laves phase at grain boundaries (Chen et al. 2016; Nie et al. 2014). Similarly, the low-temperature ($\gamma + \gamma'$) eutectics along GBs are found to be responsible for the liquation cracking of laser-deposited Inconel 738 alloy (Zhong et al. 2005). In a low-carbon version of Inconel 738 (i.e., Inconel 738LC), solidification cracking was observed instead and was attributed to the formation of low-melting-point liquid films enriched in Zr and B along GBs after SLM (Cloots et al. 2016). For laser-deposited Inconel 625, solidification cracking due to low-melting-point (γ + Laves) eutectics along GBs was reported (Hu et al. 2017). It was also suggested that high-angle GBs are particularly prone to the development of solidification cracking (Chauvet et al. 2018b; Wang et al. 2004). It was argued that the high-angle GBs with higher grain boundary energy values are more likely to create a significant critical coalescence undercooling, which may lead to consequent cracking under stress.

Zhou et al. (2018) investigated the crack formation of Ni-based single-crystal superalloy using laser powder deposition of single walls and block samples. Experimental results show that the thin-wall samples exhibited crack-free single-crystal structures with the orientation of [001] as a result of epitaxial growth from the SX substrate. On the contrary, some cracks can be found in the as-deposited block samples due to the continuous layer-by-layer heating process. The EBSD shows that the large misorientation angle at the grain boundary in the cracking regions played significant roles in the crack initiation and its further propagation. Furthermore, the solidification cracking can be formed due to the columnar interdendritic shrinkage cavities. Meanwhile, the carbides with a high melting point that is formed in the interdendritic region at the early stage of the solidification can hinder the liquid flow to fill the shrinkage. Due to the pinning of carb at the liquid-filled channel, the liquid film was easy to be torn apart during the filling process. At the same time, the interdendritic low-melting-point structure may melt in heat-affected zone to form the liquid films, and the liquid films act as the initiation of the liquation cracking. Similarly, the susceptibility of the liquation cracking will also increase with the misorientation angle increasing (Fig. 5.16).

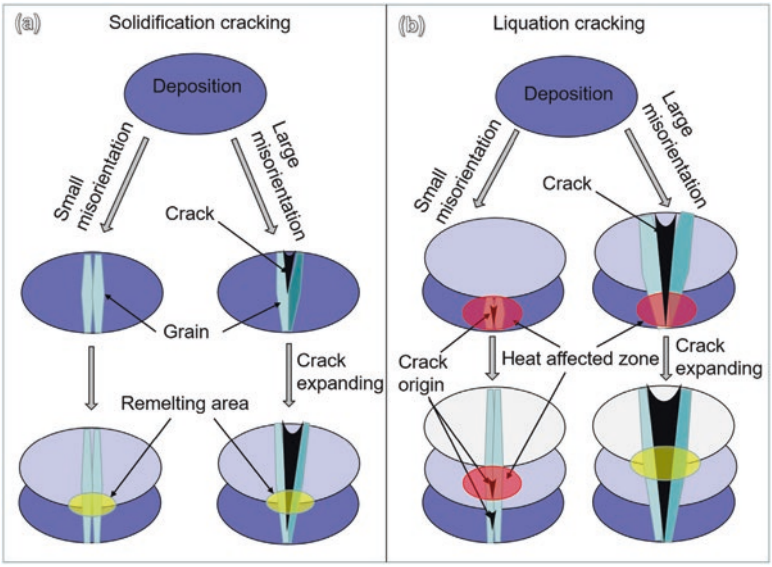

Fig. 5.16 Diagram of the cracking expanding modes. (**a**) Solidification cracking mechanism; crack formed in the region with large misorientation but not in the region with small misorientation, and it expanded during the laser remelting process. (**b**) Liquation cracking mechanism; crack origin appeared in the heat-affected zone and further cracked in the region with large misorientation, while it did not expand in the region with small misorientation (Zhou et al. 2018)

5.7 Conclusion and Perspectives

LAM technique has attracted increasing attention due to its high freedom of fabrication and design, reduction of material waste, and increase of sample complexity. Due to the small spot size and high energy density, the LAM technique can achieve the damage repair with limited heat-affected zone and low distortion caused by thermal stress. Another outstanding feature of the LAM is the ability to control the microstructure evolution by adjusting the heat transfer through the laser-related parameters. Based on the extremely high thermal gradient, the typical columnar dendrite can provide the possibility of epitaxial growth of single crystal from the SX substrate. In order to provide the potential guidance, vast efforts have been made to understand the underlying theory of epitaxial growth in LAM process and the relationship between the microstructure change and laser processing parameters. For example, the microstructure prediction has been investigated based on the model of thermal gradient and solidification, which are further understood as the laser power and scanning speed. The influence of powder feeding rate on the change of molten pool shape and the heterogeneous nuclei number are also included. Besides, the effects of the substrate conditions like columnar orientation and initial temperature have been also widely studied to ameliorate the epitaxial growth of single crystal.

However, the manufacturing of SX still remains as a major challenge for the LAM technique due to the following unsolved problems. Firstly, the precise control of the temperature field is still a major challenge during the layer-by-layer manufacturing in LAM process. The cyclic laser movement on the previously deposited layer may lead to the heat accumulation and decrease of thermal gradient and increase of solidification speed. Thus, the formation of stray grain at the top of the deposited layer is increasingly difficult to avoid with the successive buildup process, even though the partial remelting can provide the possibility of epitaxial growth. It further increases the difficulty in the manufacturing of single-crystal superalloy component with complex geometry. The control of dendrite orientation at the curved surface with specific geometry should also be accounted by manipulating the laser-related parameters. Thus, it should further enhance the understanding of rapid solidification theory in LAM process. Secondly, the development of cracking is another fact hindering the fabrication of high-quality SX superalloy by LAM technique. Besides, the segregation of alloying elements with various melting points should be accounted during the rapid solidification process of LAM. Such segregation may affect the precipitation of carbides and intermetallic compounds within the matrix material. Furthermore, the heat treatment study of the LAM SX superalloys should be made to achieve the homogenization and precipitation hardening. At last, the mechanical properties in room-temperature and high-temperature period should be investigated to reveal the distinct features of LAM SX superalloys.

References

Acharya, R., Bansal, R., Gambone, J. J., & Das, S. (2014). A microstructure evolution model for the processing of single-crystal alloy CMSX-4 through scanning laser epitaxy for turbine engine hot-section component repair (Part II). *Metallurgical and Materials Transactions B, 45*(6), 2279–2290.

Anderson, T. D., DuPont, J. N., & DebRoy, T. (2010). Origin of stray grain formation in single-crystal superalloy weld pools from heat transfer and fluid flow modeling. *Acta Materialia, 58*(4), 1441–1454.

Basak, A., & Das, S. (2016). Epitaxy and microstructure evolution in metal additive manufacturing. *Annual Review of Materials Research, 46*(1), 125–149.

Chauvet, E., Tassin, C., Blandin, J.-J., Dendievel, R., & Martin, G. (2018a). Producing Ni-base superalloys single crystal by selective electron beam melting. *Scripta Materialia, 152*, 15–19.

Chauvet, E., Kontis, P., Jägle, E. A., Gault, B., Raabe, D., Tassin, C., Blandin, J.-J., Dendievel, R., Vayre, B., Abed, S., & Martin, G. (2018b). Hot cracking mechanism affecting a non-weldable Ni-based superalloy produced by selective electron beam melting. *Acta Materialia, 142*, 82–94.

Chen, Y., Lu, F., Zhang, K., Nie, P., Elmi Hosseini, S. R., Feng, K., & Li, Z. (2016). Dendritic microstructure and hot cracking of laser additive manufactured Inconel 718 under improved base cooling. *Journal of Alloys and Compounds, 670*, 312–321.

Cloots, M., Uggowitzer, P. J., & Wegener, K. (2016). Investigations on the microstructure and crack formation of IN738LC samples processed by selective laser melting using Gaussian and doughnut profiles. *Materials and Design, 89*, 770–784.

Dadbakhsh, S., Hao, L., & Kruth, J. P. (2014). Selective laser melting towards manufacture of three dimensional in situ Al matrix composites: A review. In *High value manufacturing: Advanced research in virtual and rapid prototyping* (pp. 303–308).

DebRoy, T., Wei, H. L., Zuback, J. S., Mukherjee, T., Elmer, J. W., Milewski, J. O., Beese, A. M., Wilson-Heid, A., De, A., & Zhang, W. (2018). Additive manufacturing of metallic components – Process, structure and properties. *Progress in Materials Science, 92*(Supplement C), 112–224.

Gäumann, M., Henry, S., Cléton, F., Wagnière, J. D., & Kurz, W. (1999). Epitaxial laser metal forming: Analysis of microstructure formation. *Materials Science and Engineering A, 271*(1), 232–241.

Gäumann, M., Bezençon, C., Canalis, P., & Kurz, W. (2001). Single-crystal laser deposition of superalloys: Processing–microstructure maps. *Acta Materialia, 49*(6), 1051–1062.

Gu, D. D., Meiners, W., Wissenbach, K., & Poprawe, R. (2013). Laser additive manufacturing of metallic components: Materials, processes and mechanisms. *International Materials Review, 57*(3), 133–164.

Han, Q., Gu, Y., Setchi, R., Lacan, F., Johnston, R., Evans, S. L., & Yang, S. (2019). Additive manufacturing of high-strength crack-free Ni-based Hastelloy X superalloy. *Additive Manufacturing, 30*, 100919.

Herzog, D., Seyda, V., Wycisk, E., & Emmelmann, C. (2016). Additive manufacturing of metals. *Acta Materialia, 117*, 371–392.

Hosseini, E., & Popovich, V. A. (2019). A review of mechanical properties of additively manufactured Inconel 718. *Additive Manufacturing, 30*, 100877.

Hu, Y. L., Lin, X., Yu, X. B., Xu, J. J., Lei, M., & Huang, W. D. (2017). Effect of Ti addition on cracking and microhardness of Inconel 625 during the laser solid forming processing. *Journal of Alloys and Compounds, 711*, 267–277.

Hunt, J. D. (1984). Steady state columnar and equiaxed growth of dendrites and eutectic. *Materials Science and Engineering, 65*(1), 75–83.

Inaekyan, K., Kreitcberg, A., Turenne, S., & Brailovski, V. (2019). Microstructure and mechanical properties of laser powder bed-fused IN625 alloy. *Materials Science and Engineering A, 768*, 138481.

King, W., Anderson, A., Ferencz, R., Hodge, N., Kamath, C., Khairallah, S., & Rubenchik, A. (2015). Laser powder bed fusion additive manufacturing of metals; physics, computational, and materials challenges. *Applied Physics Reviews, 2*(4), 041304.

Kong, D., Ni, X., Dong, C., Zhang, L., Yao, J., Man, C., Wang, L., Xiao, K., & Li, X. (2019). Anisotropic response in mechanical and corrosion properties of hastelloy X fabricated by selective laser melting. *Construction and Building Materials, 221*, 720–729.

Körner, C. (2016). Additive manufacturing of metallic components by selective electron beam melting – A review. *International Materials Review, 61*(5), 361–377.

Kou, S. (2003). *Welding metallurgy* (pp. 431–446). Hoboken: Wiley.

Kurz, W., Giovanola, B., & Trivedi, R. (1986). Theory of microstructural development during rapid solidification. *Acta Metallurgica, 34*(5), 823–830.

Li, N., Huang, S., Zhang, G., Qin, R., Liu, W., Xiong, H., Shi, G., & Blackburn, J. (2019). Progress in additive manufacturing on new materials: A review. *Journal of Materials Science and Technology, 35*(2), 242–269.

Liang, Y.-J., Li, A., Cheng, X., Pang, X.-T., & Wang, H.-M. (2016). Prediction of primary dendritic arm spacing during laser rapid directional solidification of single-crystal nickel-base superalloys. *Journal of Alloys and Compounds, 688*, 133–142.

Liang, Y.-J., Li, J., Li, A., Cheng, X., Wang, S., & Wang, H.-M. (2017a). Experimental optimization of laser additive manufacturing process of single-crystal nickel-base superalloys by a statistical experiment design method. *Journal of Alloys and Compounds, 697*, 174–181.

Liang, Y.-J., Cheng, X., Li, J., & Wang, H.-M. (2017b). Microstructural control during laser additive manufacturing of single-crystal nickel-base superalloys: New processing–microstructure maps involving powder feeding. *Materials and Design, 130*, 197–207.

Liu, Z., & Qi, H. (2014). Mathematical modeling of crystal growth and microstructure formation in multi-layer and multi-track laser powder deposition of single-crystal superalloy. *Physics Procedia, 56*, 411–420.

Liu, Z., & Qi, H. (2015a). Effects of processing parameters on crystal growth and microstructure formation in laser powder deposition of single-crystal superalloy. *Journal of Materials Processing Technology, 216*, 19–27.

Liu, Z., & Qi, H. (2015b). Effects of substrate crystallographic orientations on crystal growth and microstructure formation in laser powder deposition of nickel-based superalloy. *Acta Materialia, 87*, 248–258.

Liu, S., & Shin, Y. C. (2019). Additive manufacturing of Ti6Al4V alloy: A review. *Materials and Design, 164*, 107552.

Liu, Z., & Wang, Z. (2018). Effect of substrate preset temperature on crystal growth and microstructure formation in laser powder deposition of single-crystal superalloy. *Journal of Materials Science and Technology, 34*(11), 2116–2124.

Luo, S., Huang, W., Yang, H., Yang, J., Wang, Z., & Zeng, X. (2019). Microstructural evolution and corrosion behaviors of Inconel 718 alloy produced by selective laser melting following different heat treatments. *Additive Manufacturing, 30*, 100875.

Nie, P., Ojo, O. A., & Li, Z. (2014). Numerical modeling of microstructure evolution during laser additive manufacturing of a nickel-based superalloy. *Acta Materialia, 77*, 85–95.

Qiu, C., Chen, H., Liu, Q., Yue, S., & Wang, H. (2019). On the solidification behaviour and cracking origin of a nickel-based superalloy during selective laser melting. *Materials Characterization, 148*, 330–344.

Ren, Y. M., Lin, X., Fu, X., Tan, H., Chen, J., & Huang, W. D. (2017). Microstructure and deformation behavior of Ti-6Al-4V alloy by high-power laser solid forming. *Acta Materialia, 132*, 82–95.

Santos, E. C., Kida, K., Carroll, P., & Vilar, R. (2011). Optimization of laser deposited Ni-based single crystal superalloys microstructure. *Advanced Materials Research, 154-155*, 1405–1414.

Vilar, R., & Almeida, A. (2015). Repair and manufacturing of single crystal Ni-based superalloys components by laser powder deposition – A review. *Journal of Laser Applications, 27*(S1), S17004.

Vitek, J. M. (2005). The effect of welding conditions on stray grain formation in single crystal welds – Theoretical analysis. *Acta Materialia, 53*(1), 53–67.

Wang, X., & Chou, K. (2017). Effects of thermal cycles on the microstructure evolution of Inconel 718 during selective laser melting process. *Additive Manufacturing, 18*, 1–14.

Wang, L., & Wang, N. (2016). Effect of substrate orientation on the formation of equiaxed stray grains in laser surface remelted single crystal superalloys: Experimental investigation. *Acta Materialia, 104*, 250–258.

Wang, N., Mokadem, S., Rappaz, M., & Kurz, W. (2004). Solidification cracking of superalloy single- and bi-crystals. *Acta Materialia, 52*(11), 3173–3182.

Wang, L., Wang, N., Yao, W. J., & Zheng, Y. P. (2015). Effect of substrate orientation on the columnar-to-equiaxed transition in laser surface remelted single crystal superalloys. *Acta Materialia, 88*, 283–292.

Wang, G. W., Liang, J. J., Zhou, Y. Z., Jin, T., Sun, X. F., & Hu, Z. Q. (2016). Effects of substrate crystallographic orientations on microstructure in laser surface-melted single-crystal superalloy: Theoretical analysis. *Acta Metallurgica Sinica-English Letters, 29*(8), 763–773.

Wang, G., Liang, J., Yang, Y., Shi, Y., Zhou, Y., Jin, T., & Sun, X. (2018). Effects of scanning speed on microstructure in laser surface-melted single crystal superalloy and theoretical analysis. *Journal of Materials Science and Technology, 34*(8), 1315–1324.

Yan, M., Dargusch, M. S., Ebel, T., & Qian, M. (2014). A transmission electron microscopy and three-dimensional atom probe study of the oxygen-induced fine microstructural features in as-sintered Ti–6Al–4V and their impacts on ductility. *Acta Materialia, 68*, 196–206.

Yan, X., Yin, S., Chen, C., Huang, C., Bolot, R., Lupoi, R., Kuang, M., Ma, W., Coddet, C., Liao, H., & Liu, M. (2018). Effect of heat treatment on the phase transformation and mechanical

properties of Ti6Al4V fabricated by selective laser melting. *Journal of Alloys and Compounds, 764*, 1056–1071.

Yan, X., Yin, S., Chen, C., Jenkins, R., Lupoi, R., Bolot, R., Ma, W., Kuang, M., Liao, H., Lu, J., & Liu, M. (2019). Fatigue strength improvement of selective laser melted Ti6Al4V using ultrasonic surface mechanical attrition. *Materials Research Letters, 7*(8), 327–333.

Yang, J., Li, F., Pan, A., Yang, H., Zhao, C., Huang, W., Wang, Z., Zeng, X., & Zhang, X. (2019). Microstructure and grain growth direction of SRR99 single-crystal superalloy by selective laser melting. *Journal of Alloys and Compounds, 808*, 151740.

Zhong, M., Sun, H., Liu, W., Zhu, X., & He, J. (2005). Boundary liquation and interface cracking characterization in laser deposition of Inconel 738 on directionally solidified Ni-based superalloy. *Scripta Materialia, 53*(2), 159–164.

Zhou, Z., Huang, L., Shang, Y., Li, Y., Jiang, L., & Lei, Q. (2018). Causes analysis on cracks in nickel-based single crystal superalloy fabricated by laser powder deposition additive manufacturing. *Materials and Design, 160*, 1238–1249.

Chapter 6
Laser Cladding: Fatigue Properties

P. Cavaliere and A. Silvello

6.1 Introduction

Laser cladding can be employed for restoration and repair of crucial components (Lu et al. 2018; DebRoy et al. 2018). One of the main properties to be monitored in laser cladded components is the fatigue resistance. First of all, fatigue behavior is affected by the difference in yield strength between the coating and the substrate (Vundru et al. 2018). Obviously, residual stresses are a crucial aspect (Mukherjee et al. 2018). Tensile residual stresses are detrimental for fatigue life; however, heat treatment can be employed to induce compressive residual stresses with positive improvement of the fatigue and crack behavior (Fang et al. 2019). Many materials can be employed as substrates, e.g., carbon–manganese or stainless steel as well as titanium nickel, copper, and aluminum. In order to improve the surface properties of these substrates, mainly cobalt-, nickel-, and iron-based alloys are employed for cladding. CO_2 lasers are used for large-area surface treatments with the obtaining of several millimeter thicknesses; otherwise, Nd:YAG lasers are employed for precision coating production with thickness less than 1 mm (Mazumder 2017). Two main techniques are normally proposed: a two-step deposition with pre-placed powder for cladding and a one-step deposition where the cladding material is fed into the melted pool. The two-step method is very simple as additive manufacturing of layer-by-layer structures (Fig. 6.1).

In order to successfully produce sound coatings, the pre-placed material must possess a strong bond to the substrate, and the particles must adhere to each other. This high cohesion strength is required in order to avoid the particle removal during

P. Cavaliere (✉)
Department of Innovation Engineering, University of Salento, Lecce, Italy
e-mail: pasquale.cavaliere@unisalento.it

A. Silvello
Thermal Spray Centre (CPT), Dto. CMiQF, Universitat de Barcelona, Barcelona, Spain
e-mail: asilvello@cptub.eu

P. Cavaliere (ed.), *Laser Cladding of Metals*,
https://doi.org/10.1007/978-3-030-53195-9_6

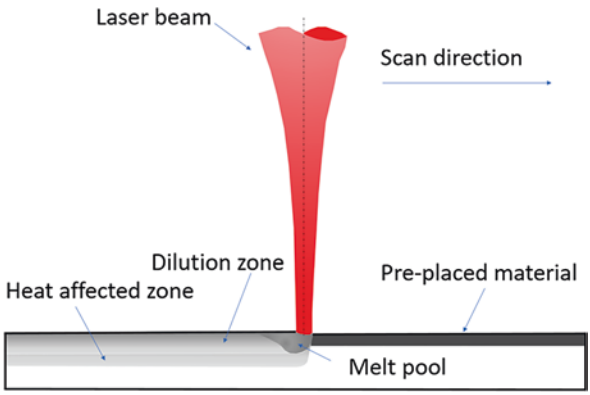

Fig. 6.1 Two-step laser cladding

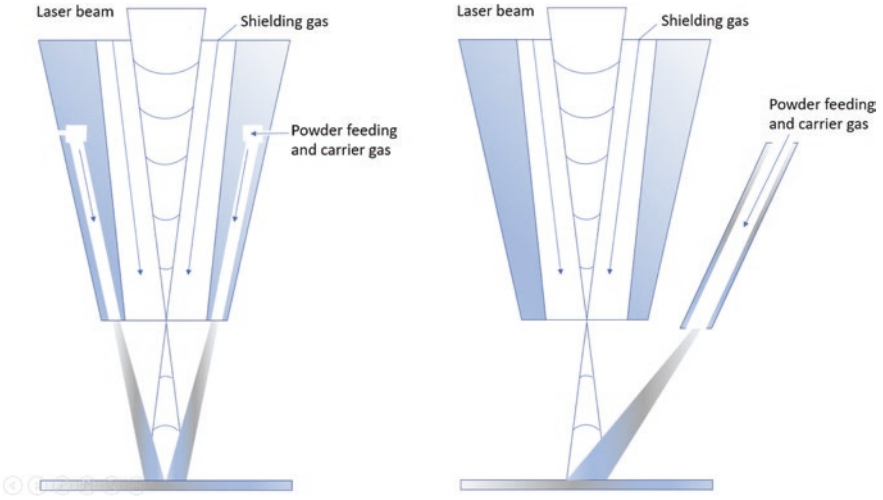

Fig. 6.2 Coaxial (left) and lateral (right) laser cladding

the melting as a consequence of the shielding gas pressure. This is the reason why the powders are glued with special chemical binder even if this solution can lead to high porosity due to the binder evaporation during melting (Valente et al. 2020). The coating formation procedure includes the melt pool formation as a consequence of the heat input of the laser power, the expansion of the melt pool due the conduction of the heat, and the heat penetration into the substrate with the consequent bond creation.

In the one-step process, mainly three types of feeding materials are employed: powders, wires, or pastes; the feeding material is deposited on the substrate contemporary to the laser beam heat input. By moving the substrate during the process, different configurations of the cladded surface are produced (Li et al. 2019). Different ways are employed in order to deliver the coating material on the surface, mainly coaxially or laterally to the laser beam (Fig. 6.2).

Powders, after mixing with a binder, are placed on the substrate before cladding; this can be applied only on flat surfaces, and the bind removal could lead to excessive porosity (Zhang et al. 2019). The powder–paste binder can be employed by depositing the coating material at the same time of laser irradiation. Here, the feeding control is crucial (Liu et al. 2017; Man et al. 2008). For complex geometries, coating material supply into the form of wire is preferred. This configuration can lead to excessive porosity, cracks, and low adhesion because only a reduced portion of the laser power is absorbed (Garmendia et al. 2019). Through helium or argon gases, the powder is fed into the melt pool. With this method, lower porosity coatings with improved corrosion and mechanical properties are produced. Given these advantages, powder feeding has become very widely used for laser cladding (Bourahima et al. 2019).

In the second case, wire is fed instead of powders (Fig. 6.3).

Wire system is less expensive with respect to the powder feeding one; in addition, porosity due to the binder evaporation is avoided (Zhang et al. 2020).

In laser cladding by paste feeding, the paste is positioned on the surface during heating. Here again, the binder interaction with the heat input and the related inconveniences govern the coating quality (Bidron et al. 2020).

The main advantages of laser cladding are low dilution, high wear properties of the coatings, low thermal distortion and residual stresses, high precision, repairing, and reduced production times.

On the other hand, the laser cladding process can be characterized by defect formation such as incomplete or irregular fusion, hot cracking, pores or inclusions, and interface irregularities in the layer-by-layer deposition. In addition, uncontrolled residual stresses can influence the mechanical properties especially the fatigue ones due to plastic and elastic property gradients. All these influence crack initiation and growth during cyclic loading (Chew et al. 2017).

Now, very few papers are published on the correlation between process defects and fatigue behavior of laser cladded coatings. In this chapter, a critical review of the state of the art will be presented.

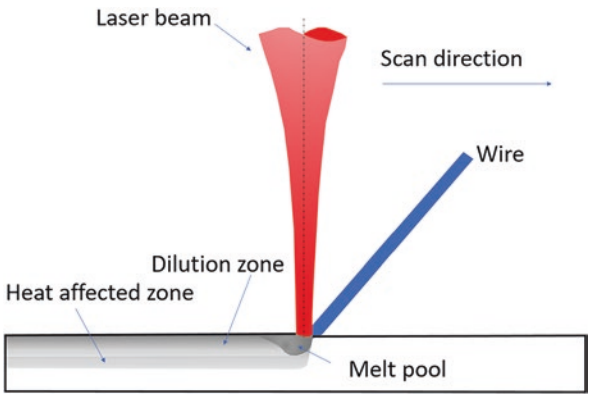

Fig. 6.3 Wire feeding laser cladding

6.2 Microstructure of Laser Cladded Materials

The focused heat input belonging to the laser melting leads to the typical shape of the clad which appear as an ellipse with the main axis in the direction perpendicular to the main laser beam (Fig. 6.4).

After laser fusion, the final structure is characterized by the fused coating, the heat-affected zone (HAZ), and the unaffected substrate (Fig. 6.5).

Normally, the clad microstructure is not uniform due to different thermal histories (Fig. 6.6). This will influence the residual stresses and consequently the fatigue properties, especially the crack propagation rate toward different strength materials.

Another important aspect is the dilution. Dilution is achieved in laser cladding processes which relies on diffusion bonding (Barekat et al. 2016). The main features of laser cladding process are the low penetration band of the clad on the substrate as well as the low dilution with the substrate. Therefore, the study of the dilution of the clad has attracted a large number of researchers' attention. The existence of the dilution leads to the formation of a metallurgical bonding between the clad and the substrate. In order to form a strong bond for laser clads, the molten pool must penetrate into the substrate. Additionally, the dilution phenomenon in the clad materials leads to improvement of the clad's quality. The dilution is generated via the fusion bonding which forms between the solid and liquid by fusion. The fusion bond is usually strong and has a high resistance to mechanical and thermal shocks. The melting of the substrate as well as the dilution is necessary to attain the strong bonding if the brittle phase at the interface does not form (Pinkerton 2010). Therefore, the melting of the substrate as well as the dilution is necessary; however, for high dilution values, it has a detrimental effect on the clad quality and geometry. This aspect is largely described in the chapter entitled "Laser Cladding of NiCr-Cr_2C_3 Coatings on γ-TiAl Substrate."

So the chemical composition changes influence the mechanical properties across the coating, especially the fatigue ones.

Many scientific evidences underline how the hardness profile shows high values on the surface and that this value decreases by approaching the interface. So, it can

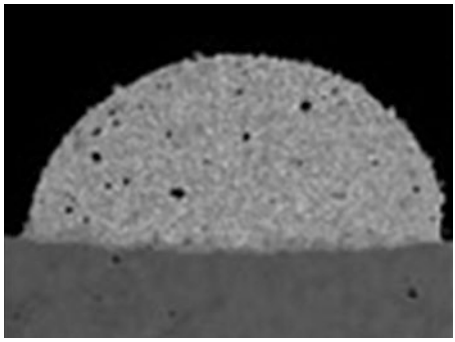

Fig. 6.4 Typical shape of a laser clad

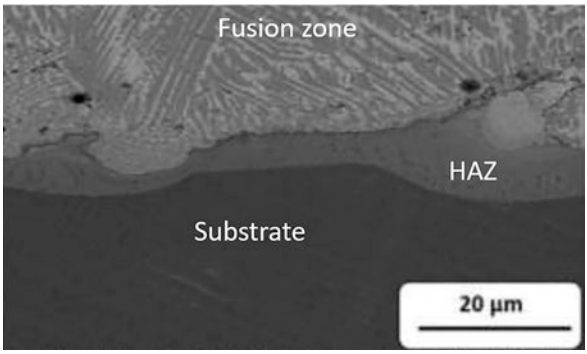

Fig. 6.5 Different zones of the laser cladded structure

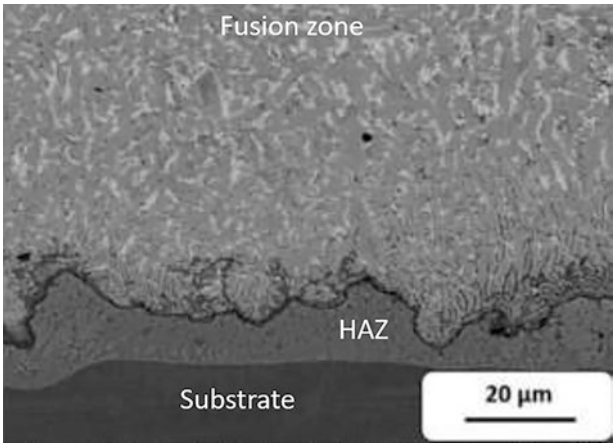

Fig. 6.6 Different microstructures of the laser cladded coating

be imagined that the clads have high resistance to crack initiation but the cracks grow very quickly by approaching the substrate.

Cracking in the laser cladding is typical in these kinds of applications. This is due to the thermal shocks during solidification, to the formation of hard brittle particle segregation, and to the presence of inclusions or impurities. Thermal stresses are normally regulated by the substrate preheating that reduces the temperature gradients. The addition of carbides or ceramic particles reduces the tendency to cracking (Zhou et al. 2008).

Inter-track porosity or gas porosity is another typical inconvenience. Porosity is strongly related to the choice of the correct processing parameters. Porosity acts as crack initiation sites leading to a strong decrease in fatigue resistance (Fig. 6.7).

During laser cladding, the size of the melt pool expands as a result of continuous heat input from the laser beam. Due to the expansion of the melt pool size, the temperature in the outer region of the melt pool is reduced since it is no longer heated by the laser beam, which in turn reduces the ability to dissolve the injected powder (Sun et al. 2006), and causes inter-track porosity formation. One way to reduce the

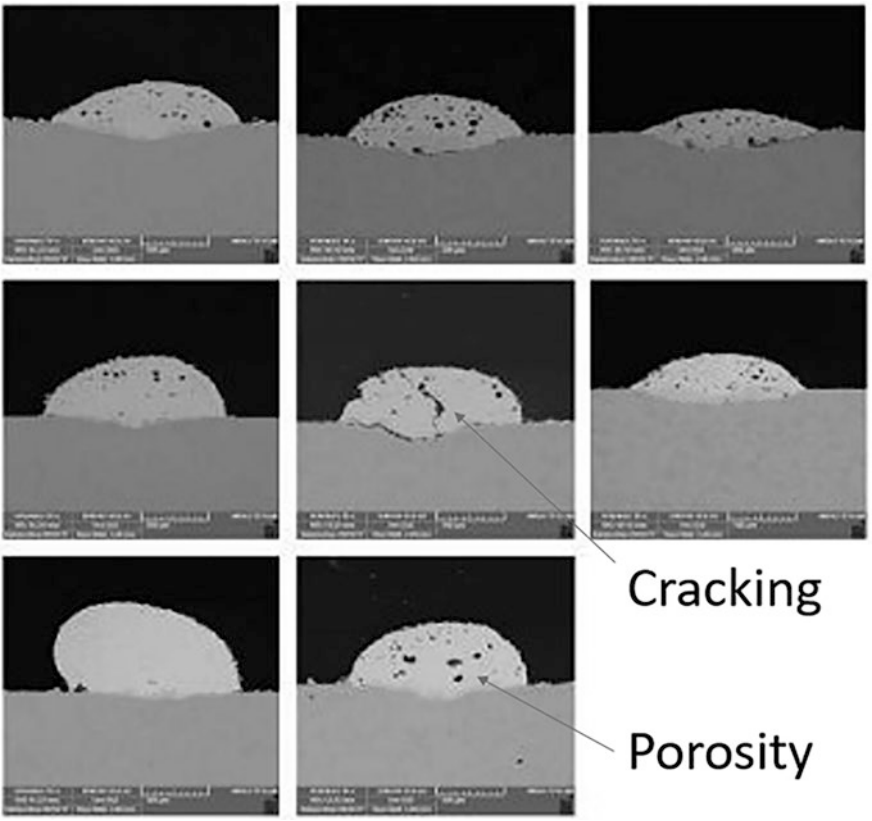

Fig. 6.7 Cracking in the clad due to void formation

presence of inter-track porosity is by using higher laser power and finer cladding powder size.

6.3 Effect of Preheating

Many experimental evidences indicate that the substrate preheating is very effective in improving the fatigue life of the laser cladded specimens. We tested AISI 316 L stainless steel where cladding was performed with a 6 kW CO_2 laser. The coating materials were MoB/CoCr and MoB/CoTi deposited on four layers of overlay in order to obtain a thickness of 3.5 mm. The specimens were then machined in order to obtain a thickness of 3 mm by eliminating the effect of surface defects. Rotating bending fatigue tests were performed on standardized cylindrical specimens. The Kaplan–Meier survival analysis allowed for the estimation of the fatigue failure of the cladded specimens. The appearance of fracture at the same stress level for

different preheating was analyzed. The alternating stress was 400 MPa, with a mean stress of 0 and stress range of 800 MPa. Two different temperatures were imposed as preheating of the substrate before laser cladding: 150 and 300 °C. Figure 6.8 shows the results of this analysis for the tested specimens.

The main result to be underlined is that preheating is very beneficial in improving the fatigue behavior of the laser cladded structures. The substrate preheating is

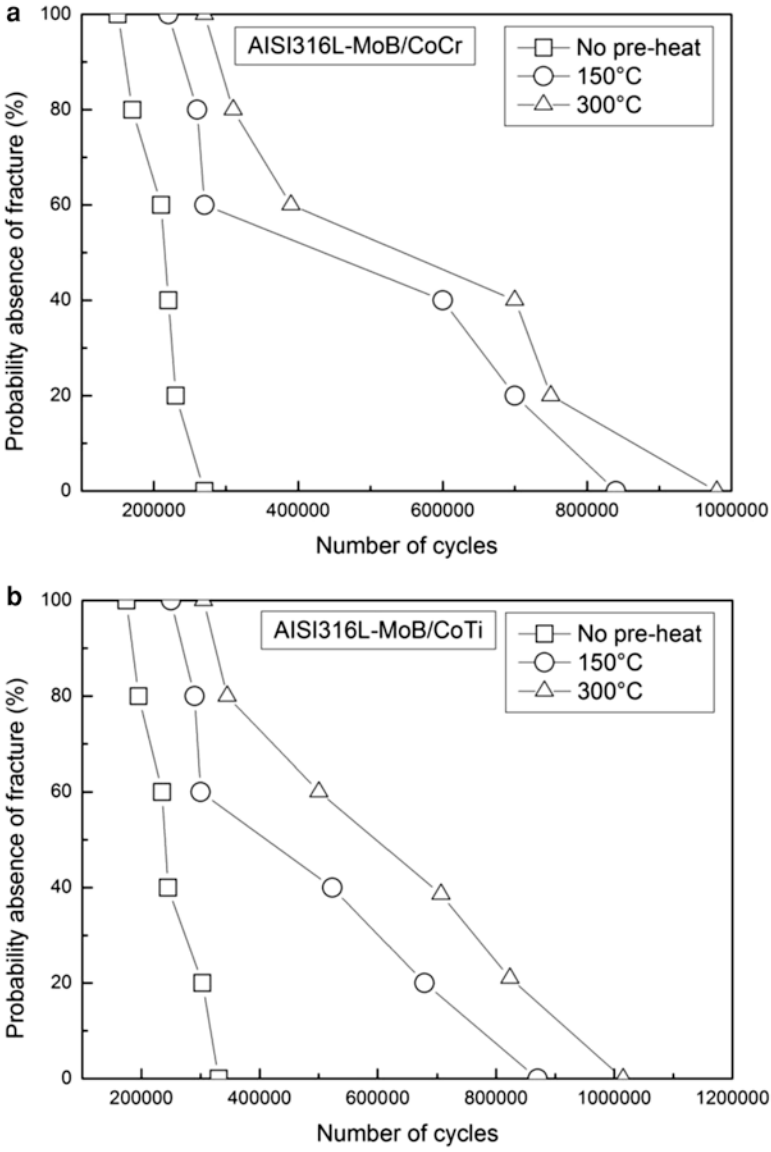

Fig. 6.8 The Kaplan–Meier analysis of the studied laser cladding coatings

very beneficial especially at the highest loading cycles. Normally, no preheating of the substrate leads to nonuniform microstructure in the clads with a strong decrease of fatigue properties especially in crack propagation rates.

6.4 Effect of Residual Stresses

In our studies, residual stresses in the laser cladded specimens were measured after machining in order to correlate the real stresses to the fatigue life. The processing parameters as well as the substrate preheating influence the residual stress behavior. Obviously, superficial compressive residual stresses are expected to be beneficial in improving fatigue life. The residual stress profiles of the laser cladded coatings are shown in Fig. 6.9.

As summarized by the residual stress profile, the substrate preheating is beneficial in inducing surface residual stresses in both axial and circumferential directions, hence demonstrating the improvement in the previously shown fatigue properties.

Hutasoit et al. (2015) investigated the fatigue life of Stellite 6 and Deloro 40G on AISI 4130 steel substrate under rotary bending fatigue test. They explained that the presence of tensile residual stresses in the clad region reduced the fatigue life compared to substrate of the same size. The presence of higher compressive residual stress in substrate region and lower tensile residual stresses in coating region in specimen laser clad with Stellite 6 generated longer fatigue life compared to the specimen laser clad with Deloro 40G, at similar coating thickness levels. With the same final structure size, increasing the coating thickness reduced the fatigue life of laser clad specimens as the result of tendency toward the presence of higher tensile residual stress in axial stress direction in coating region. Koehler et al. (2012) clad Stellite 21 alloy powder on cylindrical substrates of X5CrNi18–10 and 42CrMo4 and obtained the fatigue S–N curve of the specimens under cyclic four-point bending loading. Cladding was performed at the center parallel section and maintains a clad thickness of approximately 1.28 mm after grinding. It was reported that both types of clad specimens exhibited lower fatigue strength with the 42CrMo4 clad specimens having more markedly reduced fatigue performance due to tensile residual stresses. They also demonstrated in their numerical model that inclusion of cladding residual stresses in the computation yielded fatigue limit predictions that were closer to experimental results. In Köhler et al. (2014), the influence of processing and post-processing strategies on resulting residual stresses is determined by neutron diffraction. A low-alloy as well as high-alloy steel has been considered within this study, both cladded with the Co-based superalloy Stellite 21. Processing speed and posttreatment by laser annealing and by deep rolling strategies have been tested. Residual stresses in low-alloy steel show high sensitivity on applied treatment strategies. In this study, only deep rolling induced compressive residual stress close to the part surface. In high-alloy steel, compressive stress in this area resulted directly

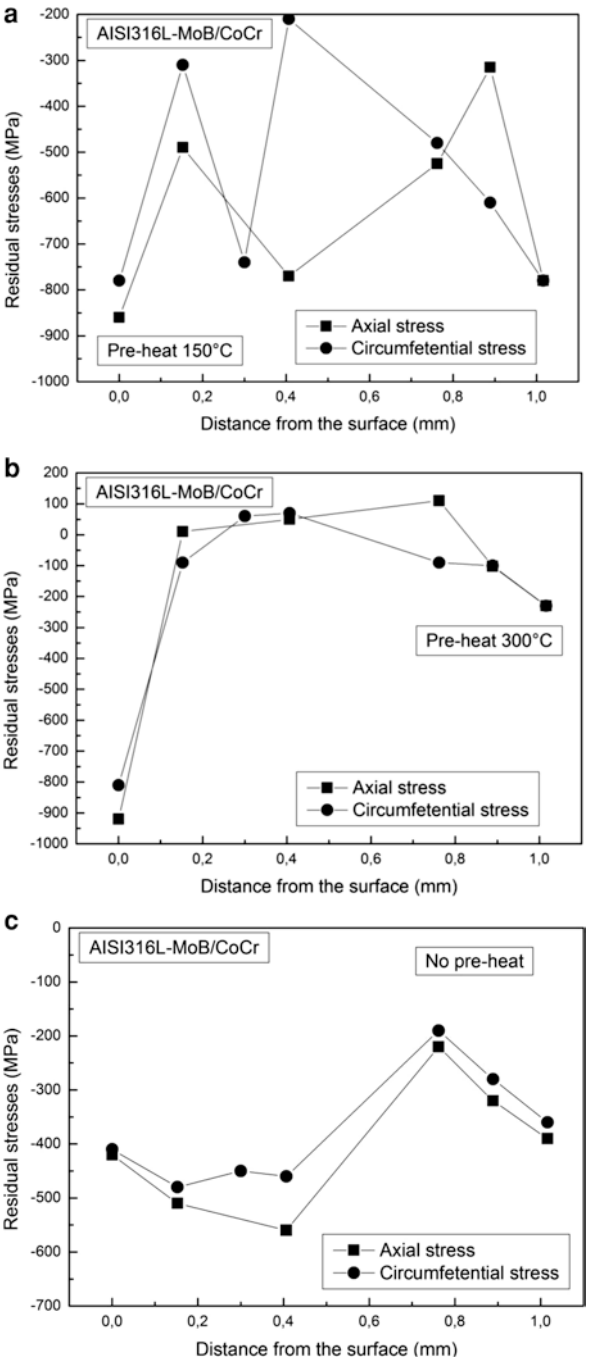

Fig. 6.9 Residual stresses measured for the AISI 316 L coated with MoB/CoCr

after laser cladding, where its magnitude depends on processing speed. A compressive residual stress state which is suspected to be beneficial for fatigue strength could be achieved at the two representative steels. Process parameters applied for laser cladding as well as thermal and mechanical posttreatment proved to influence resulting residual stresses in steels. For both investigated steels, it can be found that residual stresses of the three principal axes show qualitatively similar distributions. Constant peak temperatures along the process trajectory are appropriate to realize a highly homogeneous residual stress situation along a part. In the present study, this could be realized by temperature control based on ratio-pyrometric temperature measurements. The emissivity compensated monitoring of induced temperature fields by the IMS CHIPS Q-Pyrocam provided enhanced process information in terms of temperature gradients. Within a wide span of applied laser powers and feed velocities, these could be evaluated despite of scattered and reflected heat radiation on surrounding objects. Depending on steel grade and processing and post-processing strategy, highly diverse stress situations result from the respective combinations. In as-cladded steel X5CrNi18-10 (AISI 304), compressive residual stress toward the specimen surface can be evaluated, where its amplitude is depending on the applied processing speed. Within the cladding, the balance of stresses to zero indicates a mean stress of about 0 MPa. In as-cladded steel 42CrMo4 (AISI 4140), tensile residual stresses toward the specimen surface result independently of applied processing speed. In thermally post-processed condition by laser annealing, a residual stress situation comparable to the as-cladded state after applying moderate speed can be evaluated. Within the study only in mechanically post-processed condition by deep rolling, a significant impact on the residual stress situation in low-alloy steel can be determined. This method leads to an increase of tensile residual stress within the specimen core and, estimated by the balance of stress, compressive stress within the cladding, having a maximum in axial direction of more than −200 MPa.

Tensile and fatigue properties of laser cladded medium carbon steel with two clad layers of Co–Cr alloy were studied by Niederhauser and Karlsson (2003), and it was noted that the residual stress created during cladding had a significant effect on the stress versus number of cycles to failure test results particularly for fatigue tests with small strain amplitudes. Fatigue studies on laser clad specimens of Stellite 21 on AISI 316 L stainless steel with pre-cladding machined cavity by Ganesh et al. (2010) show superior fatigue strength under rotating bending loading, as fatigue crack nucleation in all specimens took place in the substrate. The presence of the clad layer can suppress fatigue crack initiation from the surface and improve fatigue performance. Tuominen et al. (2015) investigated the fatigue performance of 42CrMo4 steel bar clad with Inconel 625 and S355 structural steel clad with Stellite 21 under four-point bending and torsion fatigue test. The clad specimen generally exhibited reduced fatigue strength except for Inconel 625 clad specimen at higher applied stress. The lower fatigue lives were attributed to high tensile residual stress measured by hole drilling and the presence of defects such as inclusions and porosity. Post-weld heat treatment was also found to have insignificant impact on fatigue performance for both clad–substrate material pairs.

The disadvantage of ultrahigh-strength steels is their susceptibility to fatigue resulting in brittle fracture. The primary interest of the aerospace industry is to improve the structural integrity by repair and maintenance of parts. Ultrahigh-strength steels in fatigue critical aerospace military components are very difficult to repair using conventional arc-based technology and are usually replaced when the damage, such as by fatigue and wear, exceeds dimensional limits. In Lourenço et al. (2016), it was shown how by repairing AerMet 100 high-strength steel with the same material through laser cladding, high compressive residual stresses are measured on the clad surface. The fatigue tests were performed under variable amplitude loading with a maximum stress of 1000 MPa. Both the as-clad and postheat-treated (PHT) samples were compared to a baseline sample with an artificial notch to simulate damaged condition. Results show that laser cladding significantly improves fatigue life, as compared to the baseline sample with a notch. However, the fatigue life of the as-clad sample is lower as compared to a baseline sample without a notch. The fracture modes in the as-clad specimen consisted mainly of tearing topology surface and some regions of decohesive rupture through the columnar austenite grains. The PHT condition however was not effective in improving the fatigue life. The fracture modes showed mainly decohesive rupture and, as a consequence, reduced the fatigue life.

Ultrahigh-strength steels such as AISI 4340 and AerMet 100 are materials used widely in modern aircraft structure, particularly in critical applications such as under carriages. However, they are highly sensitive to damage caused by corrosion, fatigue, and stress corrosion cracking and, in some of these applications, to impact damage from foreign objects. High-strength steels achieve their strength at the expense of toughness, and as a result any damage which promotes crack development and propagation increases the risk of unpredicted catastrophic failure. Discovering even the smallest cracks (in the submillimeter scale) will usually require some attention, since the components are usually managed on a safe-life (no detectable cracks) basis. Grind-out is a technique traditionally used to remove the damage. However, aircraft components are geometrically optimized, leaving very little material to safely grind-out. This method is viable only if the grind-out does not exceed the dimensional limits. Sun et al. (2014) in recent work evaluated the mechanical properties of laser cladding repair of AISI 4340 and AerMet 100 powder on AISI 4340 substrate in an attempt to restore and improve its fatigue properties especially addressing the airworthiness certification issue important to the aerospace industry. In their study, a certain level of degradation in the mechanical properties of AISI 4340 as-clad was found. However, by changing the material of the clad layer to AerMet 100, the fatigue properties were improved.

The test results showed that the crack propagation lives from a common initial depth of 0.25 mm for the as-clad samples were significantly longer than the baseline samples by a factor of three to four. The longer life is attributed to the beneficial compressive residual stresses resulting from the repair process. The model predictions are found to correlate well with the results of quantitative fractography measurements from samples tested under variable amplitude cyclic loads (Walker et al. 2017).

Residual stresses arising in a body post-manufacture are beneficial or detrimental to the fatigue life of a component depending on their nature. Methods such as shot-peening and autofrettage are known to induce compressive residual stresses, providing fatigue life improvement. However, welding processes and dissimilar joints, as with most machining processes, are typically known to induce tensile residual stresses, therefore shortening fatigue life. The weld cladding can be described as a dissimilar joint in essence. Where possible, it would be desirable to select specific material combinations and deposition processes to induce compressive residual stresses, particularly at the surface of the component, where operational stresses are often highest. Residual stresses are elastic and self-equilibrating in nature, arising from various mechanisms. In weld cladding, thermally generated residual stresses arise due to the nonuniform heating and cooling operations, resulting in constraint on thermal expansion and contraction in the component. Possible modification of the residual stress distribution arising in the nickel alloy clad component is discussed (Shnier et al. 2014). The use of a stainless steel clad material demonstrates that compressive residual stresses can be obtained in the clad layer and into the substrate. The potential of laser cladding is also highlighted, allowing thinner clad layers and HAZs. Metallurgical studies show good fusion of the clad material and substrate, with no defects or inclusions in the weld material due to the weld cladding process. Laser cladding produces certain regions of micro-segregation, requiring process refinement to eliminate these undesirable features. Alloy segregation arises in the HAZs, producing high-hardness regions in alloy-rich areas. Increased homogeneity in the weld clad HAZ is achieved through PWHT.

Given the aspect related to fatigue life governed by microstructural inhomogeneities, laser cladded structures require new models to be developed in order to focus their fatigue behavior. Fatigue test on laser clad AISI 4340 steel specimens shows that multiple surface cracks initiate from the clad-toe region due to clad bead overlap features deposited in a raster scan pattern. The multiple surface cracks propagating from the clad-toe region spend a significant part of their fatigue lives as small surface cracks especially at applied stress range near the fatigue limit. Fatigue crack growth modeling of such small periodic surface cracks is required to predict the total fatigue life of laser clad steel specimens. The initial crack size for fracture mechanics analysis can be determined using the equivalent initial crack size approach to account for fatigue life spent during the early crack growth phase for estimating the total fatigue life. A fatigue crack growth modeling algorithm capturing the observed fatigue behavior of periodic multiple coplanar semielliptical cracks initiated from these features was developed based on crack closure concepts for small cracks to predict the fatigue S–N curve of laser clad AISI 4340 steel specimens. New solutions for stress intensity factor and clad-toe magnification factor (Mk factor) are presented for surface cracks propagating from the laser clad-toe region. The fatigue life prediction model is able to start from multiple clad-toe surface cracks propagating from the clad-toe region which coalesce into a dominant surface crack or edge crack before final failure. The fatigue life prediction result was compared to the experiment S–N curve test data and gave good agreement (Chew and Pang 2016).

Chen et al. (2017) used pre-cracked EA4T steel samples repaired with laser cladding technique in order to evaluate the fatigue bending behavior after repairing. They demonstrated that laser cladding repairing is very useful in retarding crack initiation and growth improving the overall fatigue behavior. This was also due to the fact that the hardness of the cladded layer was higher with respect to the substrate, thanks to the optimization of processing parameters during cladding.

Although laser cladding is used to improve the functional surface properties or to refurbish worn-out parts, it has some essential drawbacks. In the as-clad components, the overlapping clad traces generate a wavy surface with sharp notches. Low side-bead angles and surface ripples from overlapping clads create a rough surface that generates stress peaks during fatigue loading conditions which can initiate cracking (Alam et al. 2010). Laser cladding produces high-density homogeneous coatings; however, defects such as lack of fusion (LOF), hot cracks, pores, or inclusions both at the layer substrate interface and inside the clad layer and particularly at the interfaces of overlapping layers can be generated. Basically, these pore and void defects can be divided into three categories: inter-track, interlayer, and intralayer defects. Inter-track porosity is caused by the horizontally aligned or offset tracks of incompatible aspect ratios.

It forms near the base of deposited tracks. Interlayer LOF porosity is caused by incomplete bonding between vertically aligned deposits. The orientation of LOF relative to the loading direction plays an important role on fatigue life. Intralayer porosity is often a spherical area of porosity within a layer. It is most commonly attributed to small amounts of trapped gas or oxide between the powder particles, but a study of laser welding indicated that it can also be caused by the presence of moisture in industrial-grade shroud gases. Co-based powder (Stellite 21) and Ni-based powder (Inconel 625) were deposited on structural steel (S355) bars and on hardened and tempered steel (42CrMo4) bars by laser cladding by Alam et al. (2013). Fatigue cracking of laser clad bars is initiated from the maximum stress location that depends on the macro-load conditions plus stress rising from the defect with the most critical combination of type, location, and orientation. From its surface maximum, the macro-stress field strongly decays in the vertical direction for bending or torsional loads, while an axial load tends toward uniform stress throughout. Semispherical pores at the clad–substrate interface or spheres in the clad layer are the least critical; pores become increasingly critical if just below the surface or just intercepting it, strongly raising the stress the shorter this distance is; toward side edges, this surface impact contributes once more, which can cause the most critical combination. The notches from wavy as-laser clad surfaces raise the stress fields—particularly for smaller notch radii and angles; a wavy clad–substrate interface is a very weak stress raiser. The clad orientation relative to the tensile stress is important. Planar inner defects like LOF or hot cracks can under load be considered as propagating cracks; they accelerate vertically in both directions but faster toward the surface. Again, the orientation angles are most critical normal to the tensile load, i.e., as vertical planes.

Sandhu and Shahi (2016) investigated the fatigue performance of AISI 304 L austenitic stainless steel with a single layer of Inconel 625 weld cladding using

shielded metal arc welding (SMAW) process. They observed better fatigue performances for specimens with higher amount of clad IN625 content and the base substrate AISI 304L stainless steel exhibiting lowest fatigue strength.

Kaplan et al. (2013) investigated the fatigue and crack initiation and growth behavior in laser cladded components under various geometrical and stress conditions. Cylindrical and square section bars are compared for axial, bending, and torsional load conditions, which induces the macro-stress field with corresponding stress peaks. Defects from laser cladding such as pores, cracks, or the surface roughness superimpose additional stress raising action on this stress field. The geometrical position and orientation of the defects has strong impact on the induced maximum stress level. For surface pores, it is demonstrated by the fractography that their occurrence within a critical azimuthal range can initiate fatigue cracking. The different conditions of sample geometry, load situations, materials, and defects are compared and discussed. In particular, advanced illustration methods are applied for improved and generalized documentation and explanation of the trends, both qualitatively and quantitatively. The maximum stress in a laser clad component, which is likely to initiate fatigue cracking, is generated from a superposition of the macro-stress field (from load and component geometry), stress raisers by defects (from laser cladding), and residual stress (generated during laser cladding). For defects, their location and orientation in the macro-field is often more important for their generation of stress raisers than the defect size. Experimental evidence was found where a surface pore has initiated fatigue cracking. When a crack propagates in the vicinity of a defect, it will be locally deflected and accelerated, in general lowering fatigue life; however, the defect is not wide-ranging.

The influence of the severe shot-peening process on the fatigue life of the laser cladded Inconel 718 specimens which can be employed during refurbishment of components enduring high mechanical cyclic loads such as gas turbine components was described by Ghorashi et al. (2019). The effectiveness of severe shot-peening treatment on restoring the fatigue performance of the laser cladded (LC) Inconel 718 specimens has been experimentally investigated by conducting a series of uniaxial fatigue tests. Prior to this investigation, the detrimental effect of laser cladding process on the fatigue strength of specimens was verified experimentally. This detrimental effect was also predicted by performing a finite element analysis (FEA) based on a cyclic plasticity model with nonlinear kinematic hardening in order to assess the distribution of residual stresses caused by the laser cladding process. This assessment of FEA for the residual stresses was experimentally verified by conducting incremental center hole drilling. It is worth noting that the performed microstructure analysis has indicated that in the clad-toe zone, the microstructures suffer some weakness due to the presence of more carbides compared with other areas and also diffusion of carbides into substrate. Aggregation of carbides as a brittle phase in this zone could make it prone to crack initiation in the cyclic loadings. The investigation reveals a major advantage of shot-peening treatment for LC specimens in restoring their deteriorated fatigue strength caused by laser cladding. Particularly, at higher values for the maximum stress in fatigue tests, this deterioration was observed at significant amounts of about 40% in the conducted experiments, and this signifi-

cant deterioration was almost restored by the conducted shot-peening post-process. The usefulness of severe shot-peening treatment in restoring the fatigue strength of LC specimens can be justified by the well-known facts of the occurrence of compressive residual stresses and the presence of grains with finer sizes near the surface after the treatment. The results also indicate that the clad-toe zone is the weakest area concerning fatigue issues in all LC specimens with or without shot-peening post-process. Thus, paying attention to this zone by pursuing activities like geometrical modification of the zone with chamfering or filleting would be promising.

The coarse columnar grains and special interface in laser solid formed (LSFed) Inconel 718 superalloy workpieces seriously affect their mechanical properties. To improve the microstructure and mechanical properties of LSFed Inconel 718 superalloy, electromagnetic stirring (EMS) was introduced to alter the solidification process of the molten pool during LSF (Liu et al. 2018). The results show that EMS could not completely eliminate the epitaxially growing columnar grains; however, the strong convection of liquid metals can effectively influence the solid–liquid interface growing mode. The segregation of alloying elements on the front of solid–liquid interface is inhibited, and the degree of constitutional supercooling decreases correspondingly. Comparing the microstructures of samples formed under different process parameters, the size and amount of the c + Laves eutectic phases formed in interdendritic area decrease along with the increasing magnetic field intensity, resulting in more uniformly distributed alloying elements. The residual stress distribution is proved to be more uniform, which is beneficial to the grain refinement after recrystallization. Mechanical property testing results show an improvement of 100 MPa in tensile strength, and 22% in elongation was obtained after EMS was used. The high cycle fatigue properties at room temperature were also improved from 4.09×10^4 cycles to 8.21×10^4 cycles for the as-deposited samples and from 5.45×10^4 cycles to 12.73×10^4 cycles for the heat-treated samples, respectively.

The deep surface rolling (DSR) technology can substantially increase the fatigue life of metallic materials due to the introduction of deep compressive residual stresses in the material surface. These beneficial compressive residual stresses can be achieved up to a depth of 1 mm. The DSR technology also produces a good surface finish unlike bead peening technology.

In Liu et al. (2014), the main objectives were (1) to study the feasibility of DSR for fatigue life improvement of high-strength aluminum alloy (7075-T651) repaired with laser cladding technology and (2) to investigate the effect of thermal stressing on the fatigue life improvement of DSR. Previously published results have shown that postheat treatment of laser clad high-strength Al alloy coupons improved their fatigue life. The experimental results in this paper show that the fatigue life was substantially increased using the DSR technique on laser clad 7075-T6 aluminum alloy compared to laser cladding alone and laser cladding, followed by postheat treatment. Roughness-induced crack closure found in the deep surface-rolled specimens could also be a contributor to improving fatigue performance. Further research is required to understand material microstructure and texture modification induced by the deep surface rolling (Zhuang et al. 2014).

6.5 Fretting

The laser cladding is a method using metals with better mechanical and tribological performances that can be welded on top of the original substrate material. This method cannot only produce a cladding coating with better wear and damage resistance but also repair the worn wheel or rail surface. Lewis et al. (2015) investigated the fatigue characteristics of different laser cladding materials which are used to repair damaged rail. Guo et al. (2015) explored the microstructure and wear characteristic of laser cladding Co-based alloy coating on single wheel or rail material, and the wear rate of the wheel/rail system was reduced by the deposition of the laser cladding layer on either the rail or the wheel. How to obtain better wear and fatigue damage resistance of the laser cladding coating is becoming an important studying issue.

The results indicate that the wheel/rail rollers with laser cladding form a uniform and compacted coating without any cracks or stomata (Wang et al. 2014). The laser cladding coating markedly improves wear resistance of wheel/rail rollers. The wear mechanism of wheel/rail rollers undergoing laser cladding is plowing and abrasive wear. However, the wheel/rail rollers without laser cladding exhibit visible adhesion wear and serious spalling damage. Furthermore, there are obvious fatigue cracks in both the surface and subsurface. Excellent wear resistance of laser cladding coating can effectively alleviate surface damage and prolong wear life of heavy-haul wheel/rail.

Wang et al. (2016a) explored the role of lanthanum oxide on the wear and contact fatigue damage resistance of laser cladding Fe-based alloy coating on the wheel and rail materials under oil lubrication condition using a rolling–sliding wear machine. The lanthanum oxide is beneficial for refining the microstructure of the laser cladding Fe-based alloy coating due to the activity of La element. The lanthanum oxide has no obvious influence on the surface hardness of the cladding coating. However, it improves the wear resistance and decreases the wear rate of the laser cladding coating. The cladding Fe-based alloy coating on the wheel and rail materials decreases the rolling contact fatigue damage of the rollers under the oil lubrication condition due to favorable deformation resistance. The addition of lanthanum oxide further enhances the fatigue resistance of wheel and rail rollers. There is an optimum amount of La_2O_3 content (in this case:1.2% La_2O_3) in the laser cladding Fe-based alloy coating for obtaining outstanding wear and fatigue damage resistance under the oil lubrication condition.

Wheel–rail lubrication has a vital influence on decreasing the wear of wheel and rail materials. The results show that a given friction coefficient value can be correlated to a given morphology that characterizes the localization of the mixture in the contact, whereas the relative quantity of oil and particles in the mixture probably determines its specific rheology. It should be noted that the wear and rolling contact fatigue resistance of laser cladding coating is significant for prolonging the service life. Therefore, the wear resistance and fatigue damage characteristics of wheel and rail materials with or without laser cladding coating were investigated under oil

lubrication by means of various examinations. Furthermore, the formation of crack damage to the wheel and rail rollers was discussed. The laser cladding Co-based alloy coating improves the wear resistance of wheel and rail rollers under oil lubrication. Serious spalling is dominant for untreated wheel and rail rollers, and the wheel and rail rollers undergoing laser cladding with Co-based alloy show abrasive wear and slight plowing. The laser cladding Co-based alloy coating exhibits excellent fatigue damage resistance, and there are no obvious fatigue cracks on the surface and subsurface of wheel and rail rollers with laser cladding under oil lubrication. The laser cladding Co-based alloy coating is beneficial to repair the worn wheel tread or rail in the field to improve the wear and fatigue resistance of wheel and rail materials (Wang et al. 2016b).

The treatment of rails and other track components by laser cladding to improve rail durability shows good potential as a method for reducing wear and increasing the RCF life of rails. Tests which simulated an IBJ have shown that laser cladding of the rail head around the area of the end post can reduce the tendency for the rail to lip across the joint. Lewis et al. (2017) report on a series of tests which were carried out on full-scale sections of rail that had been treated by laser cladding aiming to create a layer (1–2 mm) of high-performance material on the rail head. Experiments were designed to measure wear, lipping of insulated block joints (IBJs), and bending fatigue of clad samples. The wear rate of the clad samples was between 78% and 89% lower than that of the standard R260 reference sample. Cladding of either side of an insulated block joint greatly improves its lipping resistance and allows it to withstand approximately three times the energy input into the contact compared to a standard unclad IBJ.

The macrostructure of the laser cladded titanium alloys often exhibits periodical layer bands due to reheating treatment and coarse columnar prior β grains approximately parallel to building direction due to high-temperature gradients. And the microstructure of the laser cladded titanium alloys exhibits a basket-weave microstructure with fine lamellar or lath-like microstructures as a result of high cooling rate. Titanium alloys made by laser cladding often possess high strength due to refined microstructure and high residual stress. Laser cladding is proved to be a viable method to obtain high mechanical properties due to obtained refined microstructure. Ti6Al4V alloy was fabricated on pure titanium substrate using laser cladding (Song et al. 2016). The effect of scanning speed on microstructure, hardness, and wear performance of the Ti6Al4V cladding was investigated. The layer-band-like zone, which consists of coarse basket-weave microstructure with short-lamellar α phase and β phase, decreases with the increase of scanning speed. Layer-band-free cladding is obtained at a high scanning speed. With the increase of the scanning speed, the microstructure of the cladding evolves from lamellar or lath-like α/α′ phase to refined acicular α/α′ phase. The ultrafine microstructure with submicron scaled acicular α/α′ phases (60–400 nm in width) and β phase is obtained under the scanning speed of 600 mm min^{-1}. The clad exhibits a high hardness of 7.6 GPa, a high elastic modulus of 136.4 GPa, a reduced friction coefficient of 0.46, and a low wear loss of 0.5 mg in dry sliding wear tests. The main worn mechanisms are fatigue and abrasive wear. A rational high scanning speed is beneficial to the enhancement

of wear performance of the Ti6Al4V cladding, due to the obtained ultrafine microstructure, high residual stress, high hardness, and fatigue strength.

The nickel-based coatings are widely used in various industries both for reconstructing worn-out parts and for improving the surface quality of new products (rollers, gear wheels, etc.) subject to high contact loads. Correspondingly, the ability of the coatings to resist such loads needs to be estimated. For many applications of Ni-based coatings, an important characteristic is their ability to withstand repetitive contact loads. Contact fatigue is the process of damage accumulation and development of material surface layer failure induced by variable contact stresses causing the formation of pits (pitting) or cracks (cracking) and reducing durability. The given scheme of contact-fatigue tests may be effective for evaluation of contact endurance of materials after various surface-related and strengthening treatments. This is because under contact fatigue as per pulsating contact load, the initiation of cracks begins from the surface. The behavior of NiCrBSi coatings obtained by laser cladding from powders with various chromium, carbon, and boron contents has been investigated under contact loading through microindentation with a Vickers indenter and via nonimpact cyclic loading as per "sphere-to-surface" contact scheme. The microindentation data shows that the ability of the investigated coatings to withstand higher contact loads before plastic deformation increases with the growth of carbon and substitution elements in the coating composition and, correspondingly, the amount and hardness of strengthening phases. The restrictions of the processes of plastic deformation and cracking for the more heavily alloyed and harder coating under contact fatigue loading are substantially due to its increased ability to deform predominantly in the elastic region under the used cyclic loading conditions. This is indicated by the obtained microindentation data, and, therefore, the microindentation method (one-time indentation) can be used to assess the ability of the laser clad NiCrBSi coatings to withstand repeated contact loads (Savrai et al. 2016).

Chen et al. (2015) presented a study on the improvement of laser surface treatment on rolling contact fatigue resistance of gray cast iron. Sample surface covered with carbon powder was coupled with localized treatment by high-energy laser beam—a process defined as "laser cladding (LC)." With this method, the optimum precoating thickness was experimentally studied. Compared to the region treated by laser remelting, the crystal in LC region was finer, more compact, and uniform. Mechanical property testing showed not only high microhardness of LC region but also improved tensile and compressive resistance of treated material. Fatigue wear tests and thorough analysis of fatigue detects suggested that LC treatment significantly improved fatigue wear resistance (FWR). Improved FWR was likely facilitated by delayed initiation and propagation of cracks, as well as the reduction of contact stress on substrate. Additionally, formations of fatigue defects on sample surface were thoroughly discussed.

Degradation of contact surfaces is inherent in wheel–rail contact. Such degradation includes wear and rolling contact fatigue (RCF) damage. Degradation rates are higher in some components such as turnouts, which are subjected to more severe wheel–rail contact conditions. Failure to effectively manage the degradation

increases the risk of failure, sometimes with tragic consequences. Repair or rebuilding of worn and damaged surfaces is one means by which component lives can be extended. In the recent advancement of manufacturing techniques, laser cladding has become a promising repair technique because of its ability to produce a sound metallurgical bond with a wide range of deposition materials onto the substrate. The advantages of laser cladding techniques include strong fusion bond, low heat input, superior process control, high deposition rates, and the ability to produce minimal distortion and minimum micro-cracking. Evaluation of the mechanical performance and metallurgical characteristics of premium hypereutectoid rails after cladding is vital in the development of future rail repairing strategies in heavy-haul railways. To develop a laser cladding technique for repairing rail surface damages due to rolling contact, wear and rolling contact fatigue characteristics of a set of laser cladded rails were investigated using a roller-on-disc test machine. Three deposition materials, 410 L, SS420, and Stellite 6, were chosen to clad a premium hypereutectoid steel rail under two different heat treatment processes. In the first heat treatment, only preheating at 3500C was conducted, and in the second heat treatment, preheating at 3500C, postheating at 3500C (1 h), then slow cooling to room temperature was conducted. Preheating the substrate was insufficient to prevent martensite formation resulting from the rapid cooling rate, whereas postheat treatment was beneficial for refining the lamellar spacing and eliminating martensite formation in the clad layer and heat-affected zone. Following the roller-on-disc tests, wear loss was calculated from wear track profiles using a laser optical profilometer. The level of surface degradation, surface cracking, and spalling was investigated using an optical microscope. Experimental results revealed that SS420 cladding had the highest wear-resistant behavior but severe surface cracks and spalling were found in the worn area. Stellite 6 cladding showed similar wear resistance as the parent substrate rail and the best fatigue resistance behavior among the three cladded rail samples. Based on this research, Stellite 6 is the most promising deposition material for repairing rails by laser cladding (Roy et al. 2018).

In Zhu et al. (2019), cladding materials are deposited at a small section of wheel surfaces in order to repair wheels with local defects. 316 L, 410, and 420 stainless steels were used as cladding materials on wheel discs, while rail discs are unclad. Twin-disc tests were performed to study wear and rolling contact fatigue (RCF) behaviors of clad wheels. Results indicate that adhesion coefficients do not have notable difference between clad and unclad discs. All three clad wheel discs have slightly lower wear rates compared to the unclad wheel discs. The wear rates decrease with increased hardness of the clad materials. Plastic deformation and ratcheting is found on the surface of unclad samples/zones. Only small surface cracks can be found. Deep cracks are found at the boundary between clad and unclad zones leading to a large chunk of material loss. The cracks may be initiated from where maximum shear stress presents below the surface and further propagate along the boundary due to the difference in deformation between clad and unclad materials.

Laser cladding is developed as a new preparation technique, because it is capable of producing a wide range of composite coatings with many unique required

properties, such as good metallurgical bonding between coating and substrate and dense microstructure. TiB_2 particle and TiB short-fiber-reinforced titanium matrix composite coatings were prepared utilizing in situ synthesized technique by laser cladding on the surface of Ti6Al4V alloy (Lin et al. 2016). Through the experiment, it was found that the surface of the single-track coatings appeared in the depression, but it can be improved by laser track overlapping. With the increase of laser power density, the amount of TiB short fiber was increased, and the distribution of TiB_2 and TiB became more uniform from the top to bottom. The microhardness of TiB_2/TiB coating showed a gradient decreasing trend, and the average microhardness of the coatings was twofold higher than that of the substrate. Due to the strengthening effect of TiB_2 particle and TiB short fiber, the wear volume loss of the center of the coating was approximately 30% less than that of the Ti6Al4V substrate, and the wear mechanism of the coating was mild fatigue particle detachment.

Fe-Cr_3C_2 hard coatings with varying Cr_3C_2 content were produced on 35CrMo steel substrates by laser cladding (Han et al. 2013). The experimental results showed that the coatings were uniform, continuous, and free of cracks. High adhesions between all produced coatings and their corresponding substrates were obtained due to the metallurgical interfaces between them. The microstructures of the coatings were mainly composed of austenitic dendrites and M_7C_3. The microhardness gradually increased from the bottom to the top of the coating and increased with elevation of Cr_3C_2 content. The Fe-Cr_3C_2 coatings improved the sliding wear resistance of the 35CrMo steel substrates obviously, and the dominant wear mechanism was spalling fatigue, with plowed grooves on the worn surfaces.

Savrai (2018) described the contact endurance of laser clad chromium–nickel coatings of the NiCrBSi system with different contents of chromium, boron, and carbon (PG-SR2, containing 0.48% C, 14.8% Cr, 2.1% B wt %, and PG-10 N-01, containing 0.92% C, 18.2% Cr, 3.3% B wt %) and with additions of carbides of titanium TiC (15 and 25 wt %) and chromium Cr3C2 (15 wt %) upon contact fatigue loading according to the scheme of the pulsing nonimpact "sphere-to-surface" contact. It has been established that the contact endurance of chromium–nickel coatings with different chemical compositions and different dispersities of structure is determined by their ability to resist plastic deformation under the conditions of repeated elastic–plastic deformation upon the mechanical nonimpact contact action. This study has shown that composite coatings can be created, which contain large (50–150 μm) particles of the strengthening phases, whose contact endurance will not be substantially inferior to the contact endurance of coatings with fine (1–10 μm) strengthening phases. An estimation of the ability of the surface of the coatings to resist the mechanical contact action was made with the use of the data on microindentation. It has been shown that the method of microindentation (single loading) can be used for determining the ability of chromium–nickel coatings to withstand repeated contact loadings.

6.6 Conclusions

Laser cladding is used for restoration and repair of critical components. One of the main properties to be monitored in laser cladded components is the fatigue resistance. First of all, fatigue behavior is affected by the different mechanical properties between the coating and the substrate. Residual stresses are fundamental in governing the fatigue behavior. Tensile residual stresses are detrimental for fatigue life; however, post-cladding treatments can be employed to induce compressive residual stresses with positive improvement of the fatigue and crack behavior. The laser cladding process can be characterized by defects formation such as incomplete or irregular fusion, hot cracking, pores or inclusions, and interface irregularities in the layer-by-layer deposition. In addition, uncontrolled residual stresses can influence the mechanical properties especially the fatigue ones due to plastic and elastic property gradients. All these influence crack initiation and growth during cyclic loading. Substrate preheating is very beneficial in improving the fatigue behavior of the laser cladded structures. The substrate preheating is very beneficial especially at the highest loading cycles. Normally, no preheating of the substrate leads to nonuniform microstructure in the clads with a strong decrease of fatigue properties especially in crack propagation rates. As summarized by the residual stress results, the substrate preheating is beneficial in inducing surface residual stresses in both axial and circumferential directions, hence demonstrating the improvement in the fatigue properties.

References

Alam, M. M., Barsoum, Z., Jonsen, P., Kaplan, A. F. H., & Häggblad, H. Å. (2010). The influence of surface geometry and topography on the fatigue cracking behaviour of laser hybrid welded eccentric fillet joints. *Applied Surface Science, 256*, 1936–1945. https://doi.org/10.1016/j.apsusc.2009.10.041.

Alam, M. M., Kaplan, A. F. H., Tuominen, J., Vuoristo, P., Miettinen, J., Poutala, J., Näkki, J., Junkala, J., Peltola, T., & Barsoum, Z. (2013). Analysis of the stress raising action of flaws in laser clad deposits. *Materials and Design, 46*, 328–337. https://doi.org/10.1016/j.matdes.2012.10.010.

Barekat, M., Razavi, R. S., & Ghasemi, A. (2016). Nd: YAG laser cladding of Co–Cr–Mo alloy on γ-TiAl substrate. *Optics & Laser Technology, 80*, 145–152. https://doi.org/10.1016/j.optlastec.2016.01.003.

Bidron, G., Doghri, A., Malot, T., Fournier-dit-Chabert, F., Thomas, M., & Peyre, P. (2020). Reduction of the hot cracking sensitivity of CM-247LC superalloy processed by laser cladding using induction preheating. *Journal of Materials Processing Technology, 277*, 116461. https://doi.org/10.1016/j.jmatprotec.2019.116461.

Bourahima, F., Helbert, A. L., Rege, M., Ji, V., Solas, D., & Baudin, T. (2019). Laser cladding of Ni based powder on a Cu-Ni-Al glassmold: Influence of the process parameters on bonding quality and coating geometry. *Journal of Alloys and Compounds, 771*, 1018–1028. https://doi.org/10.1016/j.jallcom.2018.09.004.

Chen, Z., Zhou, T., Zhao, R., Zhang, H., Yang, W., Zhou, H., Zhang, P., & Ren, L. (2015). Influence of carbon pre-coating prior to laser deposition on rolling contact fatigue of gray cast iron. *Journal of Materials Research, 30*(20), 3104–3115. https://doi.org/10.1557/jmr.2015.288.

Chen, W., Chen, H., Li, C. C., Wang, X., & Cai, Q. (2017). Microstructure and fatigue crack growth of EA4T steel in laser cladding remanufacturing. *Engineering Failure Analysis, 79*, 120–129. https://doi.org/10.1016/j.engfailanal.2017.03.005.

Chew, Y., & Pang, J. H. L. (2016). Fatigue life prediction model for laser clad AISI 4340 specimens with multiple surface cracks. *International Journal of Fatigue, 87*, 235–244. https://doi.org/10.1016/j.ijfatigue.2016.01.025.

Chew, Y., Pang, J. H. L., Bi, G., & Song, B. (2017). Effects of laser cladding on fatigue performance of AISI 4340 steel in the as-clad and machine treated conditions. *Journal of Materials Processing Technology, 243*, 246–257. https://doi.org/10.1016/j.jmatprotec.2016.12.020.

DebRoy, T., Wei, H. L., Zuback, J. S., Mukherjee, T., Elmer, J. W., Milewski, J. O., Beese, A. M., Wilson-Heid, A., De, A., & Zhang, W. (2018). Additive manufacturing of metallic components – Process, structure and properties. *Progress in Materials Science, 92*, 112–224. https://doi.org/10.1016/j.pmatsci.2017.10.001.

Fang, J. X., Dong, S. Y., Li, S. B., Wang, Y. J., Xu, B. S., Li, J., Liu, B., & Jiang, Y. L. (2019). Direct laser deposition as repair technology for a low transformation temperature alloy: Microstructure, residual stress, and properties. *Materials Science and Engineering, A748*, 119–127. https://doi.org/10.1016/j.msea.2019.01.072.

Ganesh, P., Moitra, A., Tiwari, P., Sathyanarayanan, S., Kumar, H., Rai, S. K., Kaul, R., Paul, C. P., Prasad, R. C., & Kukreja, L. M. (2010). Fracture behavior of laser-clad joint of Stellite 21 on AISI 316L stainless steel. *Materials Science and Engineering A, 527*(16–17), 3748–3756. https://doi.org/10.1016/j.msea.2010.03.017.

Garmendia, I., Pujana, J., Lamikiz, A., Flores, J., & Madarieta, M. (2019). Development of an intra-layer adaptive toolpath generation control procedure in the laser metal wire deposition process. *Materials, 12*(3), 352. https://doi.org/10.3390/ma12030352.

Ghorashi, M. S., Farrahi, G. H., & Movahhedy, M. R. (2019). Effect of severe shot peening on the fatigue life of the laser-cladded Inconel 718 specimens. *International Journal of Advanced Manufacturing Technology, 104*, 2619–2631. https://doi.org/10.1007/s00170-019-04082-6.

Guo, H. M., Wang, Q., Wang, W. J., Guo, J., Liu, Q. Y., & Zhu, M. H. (2015). Investigation on wear performance of laser cladding co-based alloy on single wheel or rail material. *Wear, 328–329*, 329–337. https://doi.org/10.1016/j.wear.2015.03.002.

Han, B., Li, M., & Wang, Y. (2013). Microstructure and Wear resistance of laser clad Fe-Cr3C2 composite coating on 35CrMo steel. *Journal of Materials Engineering and Performance, 22*, 3749–3754. https://doi.org/10.1007/s11665-013-0708-7.

Hutasoit, N., Luzin, V., Blicblau, A., Yan, W., Brandt, M., & Cottam, R. (2015). Fatigue life of laser clad hardfacing alloys on AISI 4130 steel under rotary bending fatigue test. *International Journal of Fatigue, 72*, 42–52. https://doi.org/10.1016/j.ijfatigue.2014.11.001.

Kaplan, A. F. H., Alam, M. M., Tuominen, J., Vuoristo, P., Miettinen, J., Poutala, J., & Barsoum, Z. (2013). Stress raising in laser clad components depending on geometry and defects. In A. Kaplan & H. Engström (Eds.), *The 14th Nordic laser materials processing conference, NOLAMP 14, August 26th – 28th 2013, Gothenburg, Sweden* (Nordic laser materials processing conference) (pp. 281–292). Luleå: Luleå University of Technology, Department of Engineering Sciences and Mathematics.

Koehler, H., Schumacher, J., Schuischel, K., Partes, K., Bomas, H., Jablonski, F., Vollertsen, F., & Kienzler, R. (2012). An approach to calculate fatigue properties of laser cladded components. *Production Engineering, 6*(2), 137–148. https://doi.org/10.1007/s11740-012-0369-7.

Köhler, H., Rajput, R., Khazan, P., & Rebelo Kornmeier, J. (2014). On the influence of laser cladding and post-processing strategies on residual stresses in steel specimens. *Physics Procedia, 56*, 250–261. https://doi.org/10.1016/j.phpro.2014.08.169.

Lewis, S. R., Lewis, R., & Fletcher, D. I. (2015). Assessment of laser cladding as an option for repairing/enhancing rails. *Wear, 330–331*, 581–591. https://doi.org/10.1016/j.wear.2015.02.027.

Lewis, S. R., Lewis, R., Goodwin, P. S., Fretwell-Smith, S., Fletcher, D. I., Murray, K., & Jaiswal, J. (2017). Full-scale testing of laser clad railway track; Case study – Testing for wear, bend fatigue and insulated block joint lipping integrity. *Wear, 376–377*, 1930–1937. https://doi.org/10.1016/j.wear.2017.02.023.

Li, N., Huang, S., Zhang, G., Qin, R., Liu, W., Xiong, H., Shi, G., & Blackburn, J. (2019). Progress in additive manufacturing on new materials: A review. *Journal of Materials Science and Technology, 35*(2), 242–269. https://doi.org/10.1016/j.jmst.2018.09.002.

Lin, Y., Yao, J., Lei, Y., Fu, H., & Wang, L. (2016). Microstructure and properties of TiB2–TiB reinforced titanium matrix composite coating by laser cladding. *Optics and Lasers in Engineering, 86*, 216–227. https://doi.org/10.1016/j.optlaseng.2016.06.013.

Liu, Q., Zhuang, W., & Sharp, P. K. (2014). Fatigue life improvement of laser clad 7075 Aluminium alloy by deep surface rolling technique. *Advances in Materials Research, 891-892*, 115–120. https://doi.org/10.4028/www.scientific.net/AMR.891-892.115.

Liu, J., Hu, H., Chen, C., Weng, F., & Dai, J. (2017). Research and development status of laser cladding on magnesium alloys: A review. *Optics and Lasers in Engineering, 93*, 195.210. https://doi.org/10.1016/j.optlaseng.2017.02.007.

Liu, F., Cheng, H., Yu, X., Yang, G., Huang, C., Lin, X., & Chen, J. (2018). Control of microstructure and mechanical properties of laser solid formed Inconel 718 superalloy by electromagnetic stirring. *Optics and Lasers in Engineering, 99*, 342–350. https://doi.org/10.1016/j.optlastec.2017.09.022.

Lourenço, J. M., Sun, S. D., Sharp, K., Luzin, V., Klein, A. N., Wang, C. H., & Brandt, M. (2016). Fatigue and fracture behavior of laser clad repair of AerMet 100 ultra-high strength steel. *International Journal of Fatigue, 85*, 18–30. https://doi.org/10.1016/j.ijfatigue.2015.11.021.

Lu, S., Wei, X., Zhao, J., & Ling, X. (2018). Wear resistance of nickel-based alloy coating formed by multilayer laser cladding. *Materials Research Express, 5*(12), 126508. https://doi.org/10.1088/2053-1591/aae01b.

Man, H. C., Leong, K. H., & Ho, K. L. (2008). Process monitoring of powder pre-paste laser surface alloying. *Optics and Lasers in Engineering, 46*(10), 739–745. https://doi.org/10.1016/j.optlaseng.2008.05.006.

Mazumder, J. (2017). Laser-aided direct metal deposition of metals and alloys. In *Laser additive manufacturing* (pp. 21–53). Elsevier. https://doi.org/10.1016/B978-0-08-100433-3.00001-4.

Mukherjee, T., Zhang, W., & DebRoy, T. (2018). An improved prediction of residual stresses and distortion in additive manufacturing. *Computational Materials Science, 126*, 360–372. https://doi.org/10.1016/j.commatsci.2016.10.003.

Niederhauser, S., & Karlsson, B. (2003). Mechanical properties of laser cladded steel. *Materials Science and Technology, 19*(11), 1611–1616. https://doi.org/10.1179/026708303225008103.

Pinkerton, A. (2010). Laser direct metal deposition: Theory and applications in manufacturing and maintenance. In *Advances in laser materials processing* (pp. 461–491). Elsevier. https://doi.org/10.1533/9781845699819.6.461.

Roy, T., Lai, Q., Abrahams, R., Mutton, P., Paradowska, A., Soodi, M., & Yan, W. (2018). Effect of deposition material and heat treatment on wear and rolling contact fatigue of laser cladded rails. *Wear, 412–413*, 69–81. https://doi.org/10.1016/j.wear.2018.07.001.

Sandhu, S. S., & Shahi, A. S. (2016). Metallurgical, wear and fatigue performance of Inconel 625 weld claddings. *Journal of Materials Processing Technology, 233*, 1–8. https://doi.org/10.1016/j.jmatprotec.2016.02.010.

Savrai, R. A. (2018). Resistance of laser-clad chromium–nickel coatings to failure under contact fatigue loading. *The Physics of Metals and Metallography, 119*(10), 1070–1078. https://doi.org/10.1134/S0031918X18100113.

Savrai, R. A., Makarov, A. V., Soboleva, N. N., Malygina Yu, I., & Osintseva, A. L. (2016). The behavior of gas powder laser clad NiCrBSi coatings under contact loading. *Journal of Materials Engineering and Performance, 25*, 1068–1075. https://doi.org/10.1007/s11665-016-1925-7.

Shnier, G., Wood, J., & Galloway, A. (2014). Investigating the effects of process variables on the residual stresses of weld and laser cladding. *Advances in Materials Research, 996*, 481–487. https://doi.org/10.4028/www.scientific.net/AMR.996.481.

Song, L., Xiao, H., Ye, J., & Li, S. (2016). Direct laser cladding of layer-band-free ultrafine Ti6Al4V alloy. *Surface and Coating Technology, 307*, 761–771. https://doi.org/10.1016/j.surfcoat.2016.10.007.

Sun, S., Brandt, M., Harris, J., & Durandet, Y. (2006). The influence of stellite 6 particle size on the inter-track porosity in multi-track cladding. *Surface and Coating Technology, 201*, 998–1005. https://doi.org/10.1016/j.surfcoat.2006.01.008.

Sun, S. D., Liu, Q., Brandt, M., Luzin, V., Cottam, R., & Janardhana, M. (2014). Effect of laser clad repair on the fatigue behaviour of ultra-high strength AISI 4340 steel. *Materials Science and Engineering, A606*, 46–57. https://doi.org/10.1016/j.msea.2014.03.077.

Tuominen, J., Näkki, J., Poutala, J., Miettinen, J., Peltola, T., Vuoristo, P., Rasehorn, I., Alam, M. M., & Kaplan, A. F. H. (2015). Fatigue behavior of laser clad round steel bars. *Journal of Laser Applications, 27*(1), 012006. https://doi.org/10.2351/1.4903351.

Valente, C., Morgado, T., & Sharma, N. (2020). LASER Cladding—A Post processing technique for coating, repair and re-manufacturing. In K. Gupta (Ed.), *Materials forming, machining and post processing. Materials forming, machining and tribology*. Cham: Springer. https://doi.org/10.1007/978-3-030-18854-2_10.

Vundru, C., Paul, S., Singh, R., & Yan, W. (2018). Numerical analysis of multi-layered laser cladding for die repair applications to determine residual stresses and hardness. *Procedia Manufacturing, 26*, 952–961. https://doi.org/10.1016/j.promfg.2018.07.122.

Walker, K. F., Lourenço, J. M., Sun, S., Brandt, S. M., & Wang, C. H. (2017). Quantitative fractography and modelling of fatigue crack propagation in high strength AerMet100 steel repaired with a laser cladding process. *International Journal of Fatigue, 94*, 288–301. https://doi.org/10.1016/j.ijfatigue.2016.06.031.

Wang, W. J., Hu, J., Guo, J., Liu, Q. Y., & Zhu, M. H. (2014). Effect of laser cladding on wear and damage behaviors of heavy-haul wheel/rail materials. *Wear, 311*, 130–136. https://doi.org/10.1016/j.wear.2014.01.011.

Wang WJ, Fu ZK, Cao X, Guo J, .Liu QY, Zhu MH (2016a) The role of lanthanum oxide on wear and contact fatigue damage resistance of laser cladding Fe-based alloy coating under oil lubrication condition. Tribology International 94:470–478. doi:https://doi.org/10.1016/j.triboint.2015.10.017.

Wang WJ, Fu ZK, Cao X, Guo J, .Liu QY, Zhu MH (2016b) Investigation on wear resistance and fatigue damage of laser cladding coating on wheel and rail materials under the oil lubrication condition. Tribology Transactions 59:810–817. doi:https://doi.org/10.1080/10402004.2015.1107926.

Zhang, Y., Xu, P., Liu, C., Ren, J., & Gong, H. (2019). The influence of carbides on the microstructure, grain growth, and oxidation resistance of nanostructured carbides-strengthened cobalt-based multi-track laser-cladding layers. *Applied Surface Science, 469*, 495–504. https://doi.org/10.1016/j.apsusc.2018.11.084.

Zhang, Z., Kong, F., & Kovacevic, R. (2020). Laser hot-wire cladding of Co-Cr-W metal cored wire. *Optics and Lasers in Engineering, 128*, 105998. https://doi.org/10.1016/j.optlaseng.2019.105998.

Zhou, S., Zeng, X., Hu, Q., & Huang, Y. (2008). Analysis of crack behavior for Ni-based WC composite coatings by laser cladding and crack-free realization. *Applied Surface Science, 255*, 1646–1653. https://doi.org/10.1016/j.apsusc.2008.04.003.

Zhu, Y., Yang, Y., Mu, X., Wang, W., Yao, Z., & Yang, H. (2019). Study on wear and RCF performance of repaired damage railway wheels: Assessing laser cladding to repair local defects on wheels. *Wear, 430-431*, 126–136. https://doi.org/10.1016/j.wear.2019.04.028.

Zhuang, W., Liu, Q., Djugum, R., Sharp, P. K., & Paradowska, A. (2014). Deep surface rolling for fatigue life enhancement of laser clad aircraft aluminium alloy. *Applied Surface Science, 320*, 558–562. https://doi.org/10.1016/j.apsusc.2014.09.139.

Chapter 7
Corrosion Protection of Metal Alloys by Laser Cladding

Patrizia Bocchetta, Katy Voisey, Liana Anicai, Teodor Visan, and Filippo Selleri

7.1 Introduction

As pointed out in previous chapters, laser cladding is one of the most important coating processes where a metallic powder is melted on a surface via a high-power laser and a layer connected metallurgically with the basic material is produced (Draper and Ewing 1984).

Thanks to the high level of precision, LC can be fruitfully exploited for a wide range of cost-effective engineering applications, including fabrication or repair of coatings with great hardness and erosion and corrosion resistance (Yao et al. 2012; Sexton et al. 2002; Kim and Peng 2000; Dubourg and Archambeault 2008). It is worth nothing that of the 837 papers found in a December 2019 Web of Science search on laser clad and corrosion over half were related to wear and/or erosion.

P. Bocchetta (✉)
Dipartimento di Ingegneria dell'Innovazione, Università del Salento, Lecce, Italy
e-mail: patrizia.bocchetta@unisalento.it

K. Voisey
Faculty of Engineering, The University of Nottingham, Nottingham, England
e-mail: Katy.Voisey@nottingham.ac.uk

L. Anicai
Center of Surface Science and Nanotechnology, University Politehnica of Bucharest, Bucharest, Romania
e-mail: liana.anicai@cssnt-upb.ro

T. Visan
Department of Inorganic Chemistry, Physical Chemistry and Electrochemistry, University Politehnica of Bucharest, Bucharest, Romania
e-mail: t_visan@catedra.chfiz.pub.ro

F. Selleri
Eco Salento S.n.c, Lequile (LE), Italy
e-mail: info@ecoanalisisalento.it

P. Cavaliere (ed.), *Laser Cladding of Metals*,
https://doi.org/10.1007/978-3-030-53195-9_7

Corrosion phenomena are a strong limitation to the physical integrity and functionality of almost every solid material exposed to the environment and for the great economical losses connected to the detrimental process (for example, in the USA, corrosion costs are reported to be $276 bn/year, more than an order of magnitude compared to hurricanes (Ackerman et al. 2008). Corrosion represents a worldwide crucial problem that strongly affects natural and industrial environments, and for this reason the design of relevant corrosion protection techniques for specific materials and structures is indispensable. The application of a highly corrosion-resistant layer on a metal or alloy in order to separate it from the aqueous attacking solution is often used. The technique of deposition of a protective coating on a metal is typically selected depending on the economical value of the metallic structure to be protected from corrosion (Table 7.1). Painting is the best choice for low-cost and large parts (pipes and bridges), while zinc electroplating is commonly used for higher value parts (panels or chassis). On the contrary, LC is the preferred coating method for very expensive components requiring high corrosion resistance performance (strong wear and thermal conditions, aerospace engineering, power stations, etc.) (Mahmood et al. 2011a, b).

The feedstock material conventionally used in LC coating techniques is made of metal spheres with sizes ranging from units to hundreds of micron. Mainly due to the cost of these spherical, gas-atomized powders, the use of the LC coating technique is normally considered an expensive coating technique. However, recent works have shown that powders produced by recycling titanium and other metal machining swarf have been successfully laser-clad for corrosion protection. The use of this kind of raw material increases the sustainability and dramatically reduces the material costs as well as increases the range of applications of the method (Nazari et al. 2018; Mahmood et al. 2011a, b, 2012).

Figure 7.1 schematically illustrates the laser cladding technique. The particles are driven on the surface of the material to be coated through a protective gas feeding system and suddenly melted together with a thin layer of the surface substrate by a laser. A melt pool is generated and the corrosion resistant coating is formed by its solidification (Valkov et al. 2018). The entire surface of the material is covered thanks to the simultaneous movement of the particles and the laser across the surface. The coating thickness usually ranges from a few hundred micrometers to several millimeters (Valkov et al. 2018; Toyserkani et al. 2005).

The LC technique facilitates the generation of optimal functionalities of the material vs. corrosion, abrasion, and wear resistance by resulting in strong metallurgical bonding between the substrate and the laser clad material, minimal dilution

Table 7.1 Coating methods in corrosion protection

Structure	Coating method
Cheap components (pipes,…)	Painting
Expensive components (car chassis/panels,….)	Zinc electroplating
Very expensive components (aerospace engineering, power station)	Laser cladding

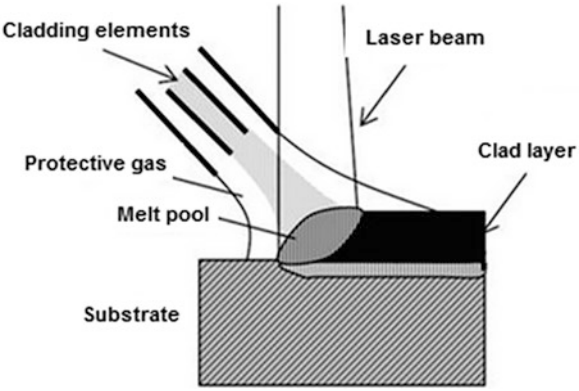

Fig. 7.1 A schematic view of the laser cladding technique. (Adapted from Valkov et al. 2018)

of the metal, low porosity coatings without cracking, and minimal heat affected zones. Moreover, LC processes offer significantly faster deposition times with respect to other coating techniques.

There is an intense scientific, technical, and technological activity related to the laser cladding equipment and processes (Pekkarinen et al. 2012; Lison et al. 2019; Syed et al. 2005; Heralič et al. 2008; Nowotny et al. 2015; Pekkarinen et al. 2014) so readers may refer to these cited works and to the other chapters of the book for detailed information.

This chapter will focus on information regarding the laser cladding of corrosion-protective layers on various metallic substrates, including steels and Ni-based alloys as well as Mg-based alloys.

At the beginning, some general information regarding the electrochemical fundamental aspects of the corrosion process will be discussed. Afterward, an overview of the recent advances made in the field of laser clad coatings in order to improve the corrosion performance of the metallic substrates will be presented.

7.2 General Aspects of Electrochemical Corrosion

Electrochemical corrosion is defined as the physico-chemical phenomena leading to the destruction of metallic materials caused by interaction with the environment. Corrosion is a natural process sustained by the chemical affinity of a metal or metal alloy to some compounds like oxygen and hydrogen ions and can be considered the reverse of an extractive metallurgical process (Fig. 7.2). Metals are extracted from mineral oxides through metallurgical processes by providing energy and are used in several applications where they convert to the initial oxidized state via thermodynamically favored chemical reactions, thus completing their life cycle (Fontana and Green 1967).

Corrosion can occur in dry and humid environments through two fundamentally different mechanisms. Dry corrosion is governed by chemical thermodynamics,

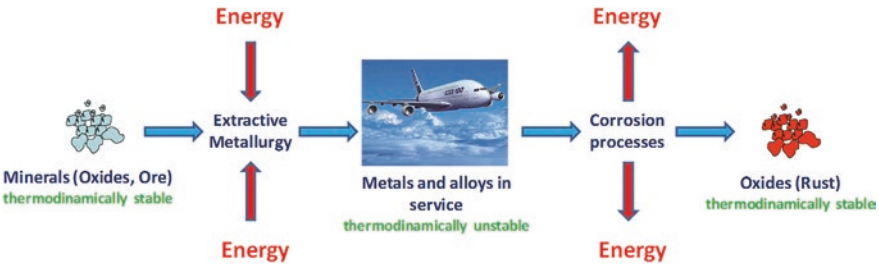

Fig. 7.2 Metallurgy and metallurgy in the reverse cycle

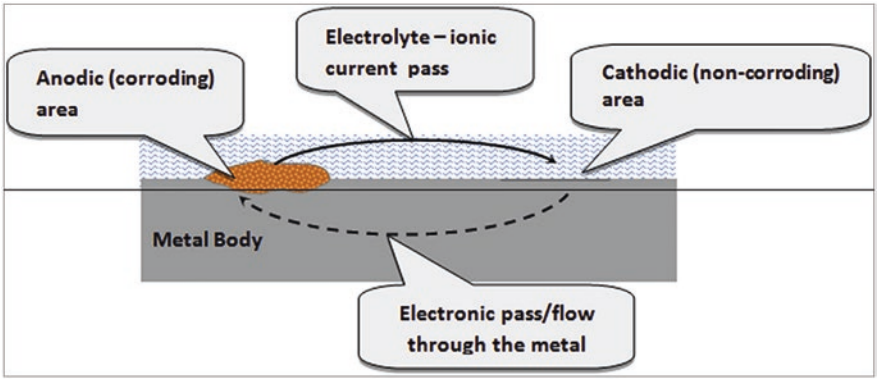

Fig. 7.3 Corrosion cell on the metal surface. Reprinted from (Riskin and Khentov 2019), Copyright (2019), with permission from Elsevier

while humid corrosion (the more significant) is an electrochemical process, thus following the thermodynamic and kinetic laws of electrochemistry. In humid corrosion, the electrochemical process consists of the anodic reaction of metal oxidation, the reduction reaction of chemical species coming from the environment (generally O_2 or H^+), the ionic transport through the aqueous media over the metal, and the electron transport through the metal itself. The two half-reactions occur in separate areas of the metal surface (sometimes macroscopically visible), as schematized in Fig. 7.3.

7.2.1 Thermodynamics and Kinetic Aspects

Thermodynamics determines if a metal is susceptible to electrochemical corrosion in a given chemical environment. The corrosive process of a general metal M in contact with an aqueous solution can be divided into two half-processes: (1) the anodic process (oxidation) where metal atoms are transferred into the solution through oxidation leaving electrons on the metal surface and (2) the cathodic process (reduction) where a reduction reaction sustained by relevant chemical species

in the solution, usually O_2 and/or H^+, consumes the electrons produced by the anodic reaction. In the simplest case, they can be indicated as follows:

$$\begin{aligned}
&\text{Anodic half-reaction: } M \rightarrow M^{m+} + me^- \\
&\text{Cathodic half-reaction: } O_2 + 4e^- + 2H_2O \rightarrow 4OH^- \\
&\qquad\qquad \text{and/or} \qquad 2H^+ + 2e^- \rightarrow H_2 \\
&\text{Global corrosion reaction: } M + O_2 + 2H_2O \rightarrow M^{m+} + 4OH^- \\
&\qquad\qquad \text{and/or} \qquad M + mH^+ \rightarrow M^{m+} + m/2\ H_2
\end{aligned} \tag{7.1}$$

The two half-reactions are independent, but they occur at the same rate (which means equal numbers of exchanged electrons per unit time), otherwise an excess or a depletion of charge in the metal would be generated, which is incompatible with the electro-neutrality law.

The global corrosion reaction is thermodynamically spontaneous only if the equilibrium electrode potential of the metal oxidation $E^{eq}_{Me^{m+}/Me}$ is more negative than that of the cathodic reaction. For this reason, metals with high positive standard equilibrium potentials (Au and Pt) have high thermodynamic stability also in highly aggressive environments (Riskin and Khentov 2019).

Understanding if a particular metal or alloy is resistant in a predefined environment is fundamental for the design of the materials to be used in a particular structure. An immediate view of the metal thermodynamic behavior in aqueous environment is given by the Pourbaix diagrams (Pourbaix 1974). They are constructed on the basis of thermodynamic chemical and electrochemical equilibrium reactions involved in the corrosion process. Pourbaix diagrams can be obtained by expressing these thermodynamic data as functions of potential and pH. The result is reported in Fig. 7.4 for the aerated iron–water system at 25 °C as example.

All the equilibrium data are calculated considering the activity of metal ions equal to 10^{-6} N. Three different stability fields can be immediately identified: immunity, corrosion, and passivity of iron. In the immunity area the metallic form of iron is thermodynamically stable, while the metal oxides and hydroxides are stable at high pH and potentials where the passivity zone is defined. Passivity means that the corrosion products form protective layers on the metal surface that are able to limit corrosion. At high potentials and low pH the corrosion process, i.e., the dissolution of the metal takes place.

However, the Pourbaix diagrams cannot predict the information on the kinetics of corrosion, and how fast the metal will corrode in a given environment is a fundamental factor because it decides the service lifetime of metal structures. On the basis of the Pourbaix diagrams, some metals dissolve in aqueous environment, but their corrosion rate is so slow that the materials exist for a very long time. On the contrary, low-carbon steel has such a high corrosion rate in HCl that it is destroyed in a very short period.

When a corrosion process is active, the global corrosion reaction is no longer in the electrochemical equilibrium conditions at which the global reaction rate is null,

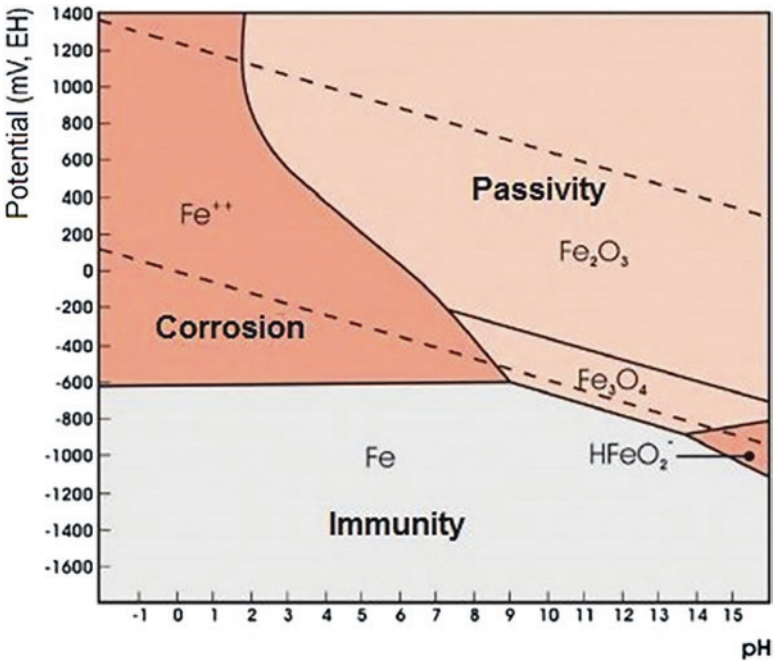

Fig. 7.4 Pourbaix diagram of iron–water system, without chloride, at 25 °C. (Reproduced from Rivetti et al. 2018 under the terms of the Creative Commons Attribution 3.0 License)

but occurs in a thermodynamically favored direction (to the right in Eq. 7.1). The potential of the metal electrode corroding in aqueous solution is called "corrosion potential," and its value is higher than the equilibrium potential $E^{eq}_{Me^{m+}/Me}$ in the presence of a suitable reduction reaction. This occurs,, for the same reason, for every electrochemical anodic polarization process: the equilibrium potential of the metal is shifted to a more positive value by a quantity called anodic overpotential (η_a) $E_{Me} = E^{eq}_{Me^{m+}/Me} + \eta_a$. In these conditions, the anodic oxidation of the metal is favored with respect to the metal ion reduction, generating a mass flow of metal ions into the solution (i.e., metal consumption) sustained by the presence of a coupled thermodynamically suitable cathodic process.

The kinetics of corrosion processes are properly described by Evans diagrams (Evans 1937), as schematically shown in Fig. 7.5a. In the same graph anodic and cathodic potential vs. current density curves of the two corrosion half-reactions are reported. Of course, the graphs are strictly dependent on the experimental conditions, such as the nature and concentration of the chemical species in the solution, crystallography, composition and finishing of the metal surface, temperature, pressure, and agitation of the solution.

When the ohmic overpotential is negligible, the corrosion potential (E_{corr}) and the current density (i_{corr}) of the corroding system are defined by the point where the two curves meet. In other words, at the corrosion point the oxidation (consumption) rate

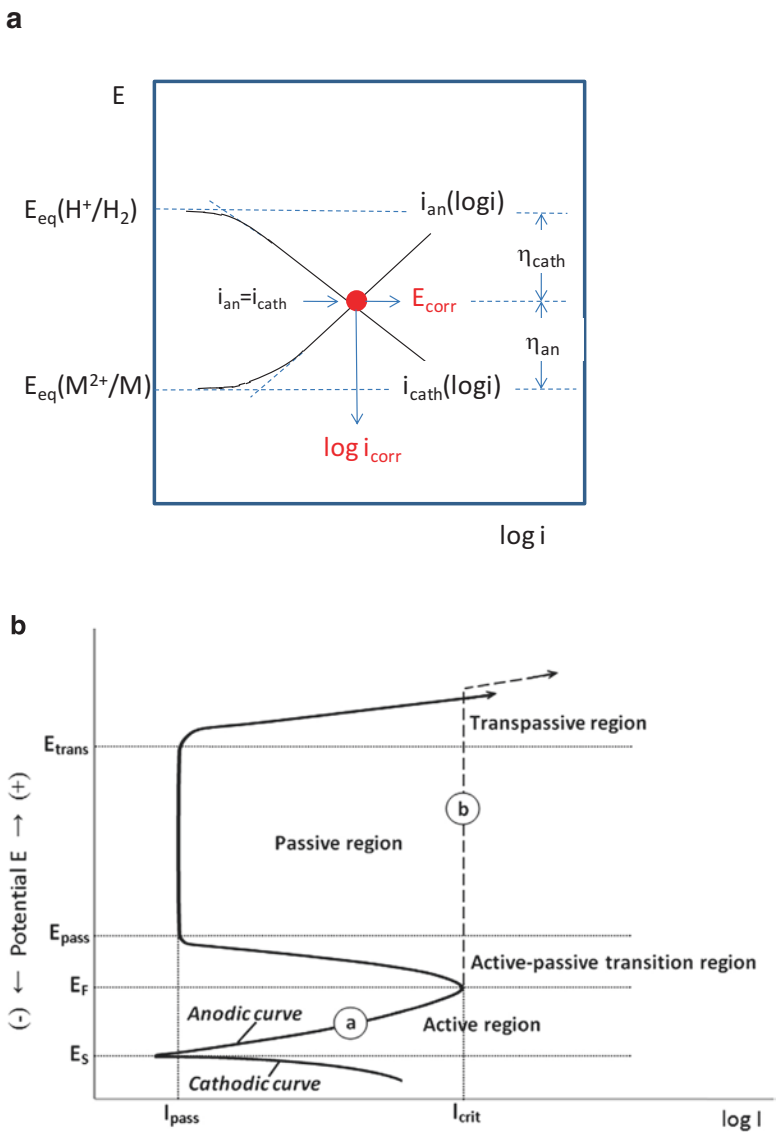

Fig. 7.5 Potential–current diagram of (**a**) anodic and cathodic reactions for a corroding metal in acid solution;(**b**) Anodic polarization of a generic metal with active–passive behavior. Reprinted from (Riskin and Khentov 2019), Copyright (2019), with permission from Elsevier

of the metal is equal to the reduction rate of the oxidant (usually oxygen or H^+) and the E_{corr} and i_{corr} values can be analytically or experimentally extracted from the graph. The anodic oxide films formed by metal passivation can be stabilized by certain chemical species, such as chromates (CrO_4^{2-}), with passivating action.

It is worth noting that the anodic and cathodic reactions also produce important modifications at the metal–solution interface changing the chemical composition of the nearby aqueous environment. The variations of pH and the metal ion concentration in the solution are often responsible for secondary chemical reactions leading to an increase of pH or to the precipitation of metal compounds, such as oxides, hydroxides, and salts. The physico-chemical properties of the corrosion subproducts (rust is a classic example), such as their electric conductivity and morphology, can substantially affect the initial corrosion rates, in a very few cases forming protective layers.

7.2.2 General and Localized Corrosion

Corrosion processes may affect the entire metal surface (general corrosion) or only some areas (localized corrosion). When corrosion is extended to the whole surface, the anodic and cathodic areas are small, approximately uniformly distributed, and move across the surface so that the damage in terms of depth is constant and its rate maintains the order of mm/year.

An average corrosion rate is not meaningful for localized corrosion because in some areas the penetration of the corrosive attack may be significant and in other zones the metal remains in pristine conditions. Localized corrosion may be very dangerous because the attack cannot be detected and monitored and thus may cause the failure of a device or an infrastructure.

One of the most common examples of localized corrosion is pitting. It begins with the formation of small cavities (pits) in the metal often covered by corrosion products. It often occurs simultaneously with uniform corrosion and can develop very rapidly. The main reason feeding the pitting corrosion is the presence of chlorides in the solution in contact with the metal.

7.2.3 Metals with Active–Passive Behavior

In relevant conditions, metals and alloys may oxidize giving rise to the formation of a metal oxide film on their surface (passivation). Under these conditions, the metal is not reactive and thus the corrosion rate is negligible. This phenomenon is really important for engineering because many materials which are thermodynamically susceptible to corrosion are, in contrast, highly resistant in aggressive solutions. This resistance is explained by the presence of a protective layer formed on their surface during corrosion. Metals displaying active-passive behavior on the course of their anodic polarization curve are Fe, Cr, Ni, Ti, Al (anodized aluminum is a classic example) and their alloys. In Fig. 7.5b, a typical S-shaped anodic polarization curve of active-passive metal is shown.

The metal corrodes by injecting metal ions into the solution (active state) from the equilibrium potential up to the flade potential (E_f). In this region the metal oxide is formed; however, it is not yet compact enough to protect the metal. At a certain potential, called passivation potential (E_P), the current density of the metal anodization curve radically decreases to negligible values. At this point the metal enters the passive region and the corrosion rate becomes minimal and independent of the metal potential. The passive oxide is uniform on the entire metal surface.

During the corrosion process (active state) the metal can protect itself by passivation. In fact, a protective metal oxide can electrochemically form on the metal surface if the coupled cathodic process (O_2 or H^+ reduction) generates a corrosion potential higher than the equilibrium potential of the anodic reaction of oxide formation. Once the surface passivity has been established, as the anodic potential is increased further, different phenomena may occur. These can make the metal move into the transpassivation region highlighted by a sharp increase of the current density (Fig. 7.5b). The possible causes can be: (1) the presence of aggressive ions that dissolve the passive film (Cl^- for inox, Fe, Al) in some points generating pitting corrosion; (2) the potential reaches the oxidation potential of the metal toward more soluble metal anions, for example, chromium ($Cr^{3+} \rightarrow CrO_4^{2-}$) or manganese ($MnO_4^{2-} \rightarrow Mn^{3+}$); and (3) the potential reaches the potential of oxygen evolution (in this case the anodic film needs to be a good electronic conductor).

7.3 Corrosion Protection by Laser Cladding

Corrosion can essentially be prevented unlike many other natural phenomena such as volcanic eruptions. The corrosion rate can be reduced to negligible levels by decreasing the kinetics of the electrochemical reactions or changing the physico-chemical conditions of the environment in order to control the thermodynamics of the process. Three fundamental methods of corrosion protection are used depending on the cost of the technique, the physico-chemical properties of the environment, the presence of wear and abrasion, and the required appearance and value of the metallic component: (1) protective coatings, (2) electrochemical protection, and (3) corrosion inhibitors. Coating protection is usually selected for marine and industrial environments (Sorensen et al. 2009).

Among the numerous techniques of corrosion protection, we focus on the coating method, which is based on the interposition of a corrosion resistant material between the metal and the aggressive environment. The coating may consist of (1) a metal chemically different from the substrate, (2) a metal oxide formed by oxidation of the metal/alloy substrate, or (3) an organic compound.

The mechanisms of corrosion protection in the presence of a coating are generally more sophisticated than a simple inert barricade between the metal and the aggressive atmosphere. The coating material is usually chosen so that it passivates in the relevant environment. This leads to an extensive use of stainless steels (Wen et al. 2019) and materials such as Inconel 625 (Olakanmi et al. 2019) as laser clad

coatings. Laser clad coatings are rarely designed to provide protection via a sacrificial anode mechanism. This is due to the large thickness of the clad layer.

7.3.1 Mechanism of Corrosion Protection

The simplest description of laser cladding is that a layer of corrosion resistant material is added to the substrate surface. The substrate is then protected from corrosion as it is now physically separated from the corrosive environment by a barrier. In addition to being a physical barrier, the clad material itself must be corrosion resistant in the relevant environment. The majority of laser clad coatings achieves this via passivation, hence the widespread use of materials such as stainless steels and Inconel 625. It is important to note that a laser clad layer of alloy X can be very different from bulk alloy X. There may be both compositional and microstructural differences between a laser clad material and the "equivalent" bulk material, which can of course lead to differences in corrosion behavior.

A laser clad layer has different demands than the equivalent bulk material. It has to both be able to be laser clad and to be corrosion resistant. It can be necessary to amend the alloy composition in order to ensure crack-free clad layers can be produced (Baldridge et al. 2013).

Generating metallurgical bonding with the substrate requires some inevitable mixing and dilution of the clad layer. This dilution will change the composition of the clad layer. High dilution levels are generally undesirable, and there are many examples where excessive dilution results in the clad layer not delivering the required corrosion resistance (Liu et al. 2017). Dilution is of particular relevance to corrosion work. There are various different methods of determining dilution, some are based on the geometry of the clad cross-section (Li et al. 2019), others directly measure the composition, e.g., via EDS. The extent of dilution can also vary from site-to-site within the clad layer, leading to spatial variation in composition. Care, therefore, needs to be taken in understanding dilution data (Song et al. 2016). EDS line or, better, area scans are recommended.

Uneven distribution of alloying elements in SS316 has been reported to have a detrimental effect on passivation behavior (Wen et al. 2019). This can result both from spatial variation in dilution and segregation during solidification (Liu et al. 2017). Spatial variation in microstructure and/or composition is undesirable as this can lead to generation of galvanic cells and localized corrosion. An issue in laser cladding is that there is an almost always inherent spatial difference in the thermal cycles the material undergoes due to the need to build up clad layers from multiple overlapping tracks. The extent of overlap is a balance between the efficiency and speed of the process and the uniformity of the resulting laser clad surface.

There is a body of work in the general laser processing literature on the thermal fields generated by different laser paths (Catchpole-Smith et al. 2017). This is as applicable to laser cladding as it is for any other laser material processing methods (Gong et al. 2017). The importance of the thermal cycle to the final clad coating is

highlighted by work that uses the melt pool temperature as a process control parameter (Bi et al. 2006). Compositional differences can also arise from loss of alloying elements via differential evaporation during laser cladding (Wang and Liu 2019). A system has been developed to use emission spectroscopy analysis of the evaporated plume as a method for real-time monitoring of clad composition (Wang and Liu 2019). Laser cladding generates rapidly solidified microstructures. Such refined grain structures are known to influence corrosion behavior (Singh et al. 2005).

7.3.2 Cladding Systems

In Table 7.2 a number of specific laser cladding systems are reported. They typically use a fiber laser, with a wavelength of approximately 1 μm, set up so that an out of focus beam spot with a diameter of several mm is incident on the substrate surface. Individual tracks are approximately the same width as the spot diameter.

Translation speeds tend to be of the order of a few mm/s. In order to generate full surface coverage some overlap of adjacent tracks is required, a 30% overlap is typical. The thickness of the coating generated varies between a few hundred micrometers to several millimeters.

Table 7.2 Laser parameters for selected laser cladding systems

References	Material	Laser	Laser parameters	Feedstock type	Coating thickness	Dilution
Liu et al. (2019)	Al HEA	Fiber	2400 W, 4.6 mm beam diameter, 5ss/s 40% overlap	Powder		53%
Zhang et al. (2015)	Fe–Ti–V–Cr–C–CeO_2	Fiber	1.0kw, 2 mm beam diameter, 5 mm/s, 30% overlap	Preplaced mixed powders plus binder	Approx. 1 mm	
Hu et al. (2019)	Mo, Ni60, Cr and B mixed powders	Fiber	800 W, 3 mm/s 30% overlap, spot diameter 5 mm	45 um powder	Approx. 500um	
Jiao et al. (2018)	T15M powder, in which five alloying elements are uniformly mixed in the iron-based powder including W, Mo, Cr, V and co.	CO_2	0.6 kW, 3 mm spot diameter,		1.67 mm	
Wen et al. (2019)	CaCO3, CaF2, TiO2, Si, Mn, 316 L stainless steel powders and epoxy resin	Fiber	2.9 kW 4 mm/s, 3.5 mm spot diameter	Preplaced powders		

An important difference between laser cladding and the closely related additive manufacturing technique of laser-powder bed fusion is that laser cladding generally only forms a single layer deposit. In cases where multiple layers are used it must be noted that layer-to-layer variation in dilution and properties can be expected (D' Oliveira et al. 2002).

7.3.3 Selection of Laser Cladding Parameters

Laser parameter selection is a balance between multiple factors: uniformity of the clad coating, dilution minimization, process time, and efficiency optimization (Olakanmi et al. 2019). Inappropriate selection of laser cladding parameters can lead to problems such as coating cracking (Baldridge et al. 2013), inclusion of porosity, incomplete melting, and incomplete metallurgical bonding as well as excessive dilution (Liu et al. 2017).

Substrate preheating can be used to decrease crack initiation (Baldridge et al. 2013; Liu et al. 2019). Cracking can also be controlled by the use of an interlayer (Stanciu et al. 2016). Protection of the molten pool from oxidation can be achieved using a shielding gas, often argon (Liu et al. 2019). Parameter selection is often done not only by a set of experimental trials including metallurgical examination of cross-sections of clad tracks but also numerical modeling. Magnesium alloys are known to be difficult to laser clad due to their high rates of evaporation during the process, requiring selection of lower powers to decrease material loss (Zhu et al. 2015). These alloys also need particularly thorough control of the local atmosphere to ensure oxidation does not occur during cladding (Liu et al. 2017).

7.3.4 Feedstock Material

As is evident from Table 7.3, the majority of reported laser cladding work is done using powder feedstock. This is not the only form of feedstock that can be used. There is interest in laser cladding with wire feedstock. This has the advantage of increased deposition efficiency, compared to powder-based processes (Abioye et al. 2015). There are also advantages related to enhanced ease of handling of the feedstock material, as well as elimination of the risks associated with fine metallic powders. Laser cladding can also be carried out on preplaced coatings (Voisey et al. 2006; Zhang et al. 2015; Jiao et al. 2018). This has been done using thermally sprayed coatings (Voisey et al. 2006); however, the added expense makes this unlikely to be viable to scale up to industrial processes. Direct preplacement of a powder mix (Jiao et al. 2018) or the use of a slurry or a mixture of the powder and a suitable binder (Zhang et al. 2015) is a more straightforward and cheaper way to preplace a material onto the substrate surface prior to laser irradiation, which will produce a metallurgical bond.

Table 7.3 Web of Science results (December 2019) using search terms laser clad[a] AND.....(term listed at the top of the column)

Year	Powder	Wire	Preplaced	Slurry	Corrosion	Total (laser clad[a])
2019	191	17	11	4	120	728
2018	209	22	6	4	119	787
2017	158	27	5	1	67	778
2016	137	21	5	1	56	690
2015	116	16	4	3	52	623
2010	92	8	5	0	32	485
2005	72	6	2	1	20	378
2000	44	12	3	0	10	237
1995	16	1	1	0	9	136
1990	1	0	0	0	0	20

This approach can be particularly useful when only small quantities of the coating material can be prepared or when dissimilar particle sizes and/or masses may cause concerns about uniform deposition of a mixed particle feedstock.

7.3.5 Nanostructured Laser Clad Coatings

During the laser cladding process, feedstock material melts and re-solidifies, hence any nanoscale features in the final coating can only be generated by the solidification and cooling processes (Zhang et al. 2015) or by the inclusion of additives which survive the melting process. Nanoscale microstructures generated during the solidification process include in-situ generated cermets. In the case of nanoscale additions, such as TiC, these are included to enhance the hardness and wear resistance.

7.3.6 Metallic Glasses/High Entropy Alloys

The enhanced hardness and good corrosion resistance of high-entropy alloys (HEA), also referred to as glass forming alloys (GFA), make them attractive coating materials. The rapid quenching rates generated in laser cladding make laser cladding of HEA an area of interest (Manna et al. 2006). Laser cladding of various Fe-based HEAs is detailed in Sect. 7.3.2. Laser clad CoCrBFeNiSi HEAs (Shu et al. 2019) have greater corrosion resistance with greater amorphous content. AlCoCrCuFeNi HEA has been laser clad on Mg in order to improve corrosion resistance (Yue et al. 2014).

7.3.7 Sustainability Considerations

Laser cladding is a solvent- and chemical-free coating process, as opposed to the competitor technology of electrodeposited coatings. There is generally good deposition efficiency, hence little waste of feedstock material. It is clear that the use of a laser as well as the usual gas-atomized feedstock, powder does make laser cladding an inherently energy-intensive process. However, as with all corrosion management work, the lifetime extensions that can be achieved justify the cost and energy input of the process. This is particularly relevant for any retrofitting work which eliminates the need for manufacture of new structures or components.

7.4 Laser Clad Corrosion Resistant Coatings

7.4.1 LC Coatings on Steel-Based Substrates

Carbon and low or high-alloyed steels represent materials having diverse applications in all industrial fields. They are widely available, strong, weldable, and versatile. However, their use is sometimes limited by their low oxidation and corrosion resistance. In order to improve these properties, besides the tuning of the materials' microstructures, laser surface alloying or laser cladding are recommended, as modern surface modification techniques (Vilar 2012; Polsky et al. 2016).

Even if laser surface alloying is advantageous as a method for the production of high corrosion resistance surface alloys, it presents some difficulties related to the achievement of the targeted chemical composition, and a proper reproducibility or uniformity of the composition. The processing parameters are chosen so that the clad material is metallurgically bound to the substrate, but dilution is kept as low as possible.

An extensive literature may be found regarding the laser cladding and related processes applied on carbon and low-alloy steels as well as on different high alloyed ones, so that the following sections will present only several examples.

Laser cladding represents a cost-effective method to produce surface layers having compositions similar to almost any grade of stainless steel on carbon and low alloy steels in order to create a composite material with a good compromise between corrosion resistance and mechanical strength.

Surface layers with specific compositions may be produced by laser surface alloying, adding alloying elements such as Cr, Ni, and Mo to a laser-generated melt pool. However, in order to achieve high corrosion resistance, galvanic effects must be avoided, so the surface must present a uniform chemical composition and be free of defects. This requires that the laser beam/material interaction time to be sufficiently long for the alloying element particles to dissolve completely and the melt to homogenize. Under these circumstances, laser cladding is advantageous because uniform surface composition is easily provided by the use of prealloyed powders.

Nevertheless, the contamination of the surface layer by carbon must be avoided as this can result in the occurrence of localized corrosion and sensitization due to chromium carbide precipitation (Vilar 2012).

7.4.1.1 Laser Cladding on Mild Steel

Carbon steel substrates have been corrosion protected by laser clad coatings on austenitic stainless steels. Stainless steel powders of two grades (AISI 304 and AISI 316) with grain sizes in the range of 50 and 100 μm and a 1.5 kW continuous wave CO_2 laser (Fouquet et al. 1994) have been used as feedstock material. The coatings presented good performance in terms of thickness uniformity, adherence, compactness, and chemical homogeneous distribution. The corrosion behavior of the 304 clad layers has been assessed in 0.1 M Na_2SO_4 (at two pH values of 7 and 3) and 30 g/L NaCl solutions by processing the polarization curves recorded at 1 $mV.s^{-1}$ scan rate after stabilization of the corrosion potential, E_{corr}. Very low current densities were measured, of about 1 $\mu A.cm^{-2}$ or less, even after 48 h of immersion in the aggressive electrolyte, indicating an excellent uniform corrosion resistance.

Li et al. (1996a, b) reported the laser surface cladding of UNS S31254 super austenitic stainless steel on a mild steel base material. Usually the super stainless steels have been developed to improve the poor pitting corrosion resistance noticed in marine applications and other chloride and perchloride containing environments, benefitting from the presence of Mo, N, and Cr (Parvathavarthini et al. 1992; McCafferty and Moore 1986). The authors used radiation from a continuous-wave CO_2 laser operating at 2.2 kW and the UNS S31254 alloy powder was delivered into the molten pool by using argon gas. Additional argon was used as the shielding gas to avoid excessive oxidation during laser processing. Surface layers free from cracks and pores have been obtained, consisting of fine austenitic cellular dendrites. The chemical composition was found to be quite uniform at the macroscale level; however, not so homogeneous at the microscale level. The corrosion performance of the laser surface clad UNS S31254 has been investigated using potentiodynamic anodic polarization in 4 M NaCl, 0.1 M and 1 M $FeCl_3$ solutions and by long-term immersion tests in 1 M $FeCl_3$ at pH 0.4. The performed studies showed that the UNS S31254 surface alloy produced by laser surface cladding exhibited excellent passive performance in chloride solutions. After immersion for 2 months in 1 M $FeCl_3$ at pH 0.4 pitting corrosion has been localized in the surface areas at low Cr and Mo contents.

Majumdar et al. (Majumdar et al. 2005) reported on the laser clad deposition of multiple layers of 316 L stainless steel on mild steel by using gas atomized powders and a diode laser. It was found that the microstructure of the clad layer is predominantly cellular with an average diameter of 10 μm and is dependent on the laser parameters. The microhardness of the laser clad coatings reaches higher values (from 170 to 278 VHN) than conventionally grown 316 L protective layers and depends on laser power density and scan speed that govern grain refinement and laser melting and rapid solidification. The corrosion resistance of the coating with

the highest microhardness (in a 3.56% NaCl solution) has been analyzed by recording potential–current potentiodynamic curves. Pitting corrosion begins to occur at 550 mV vs. saturated calomel electrode (SCE), a value higher compared to conventionally processed 316 L stainless steel.

As is already known, the use of Mo either as an alloying element or as a component of a coating has a beneficial effect on the corrosion performance, especially in aggressive environments. Wang et al. (2017a) investigated the influence of the Mo content on the microstructure, hardness, wear, and corrosion resistance of the stainless steel coatings produced by laser cladding on 45 steel. The assessment of the corrosion performance of the laser cladding layers has been based on electrochemical investigations by recording the potentiodynamic polarization curves in 3.5% NaCl solution at a scan rate of 0.5 $mV.s^{-1}$, at 25 °C.

The results demonstrated that great metallurgical bonding between the SS coating and the alloy substrate was attained. The wear resistance of the 6.0 wt. % Mo coating was found to be about 3.7 times higher than that of the Mo-free coating. According to the recorded polarization curves, as shown in Fig. 7.6, the presence of the laser clad coating significantly improved the corrosion performance as compared to the uncoated alloy.

A displacement of the corrosion potential toward more positive values was seen, suggesting a protective behavior. However, for Mo contents in the coating higher than 2 wt.%, the corrosion resistance decreased. The SEM and EDS investigations

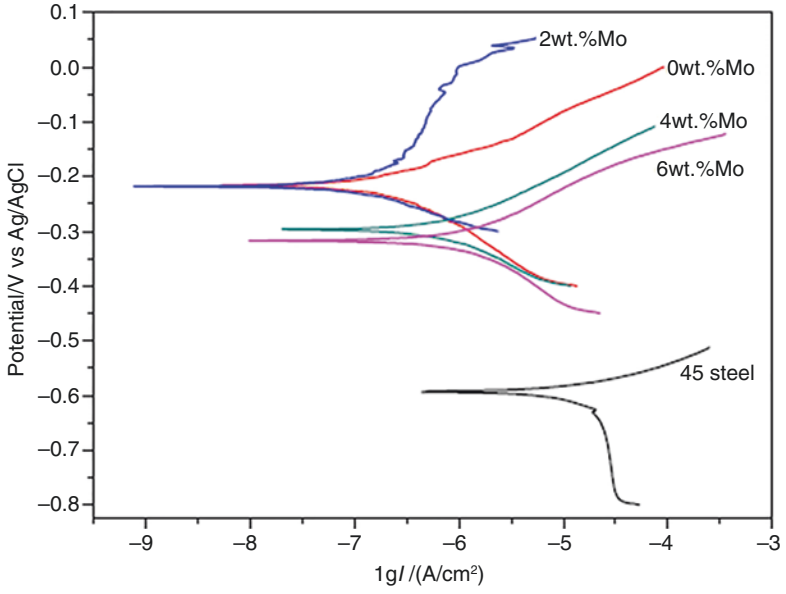

Fig. 7.6 Comparative potentiodynamic polarization curves of 45 steel substrate and different stainless steel laser cladding layers with various Mo contents in 3.5% NaCl. (Reported from Wang et al. 2017a, b)

showed a higher concentration of the Mo element at the grain boundaries. This uneven distribution may be responsible for reducing the corrosion resistance.

In order to improve the corrosion behavior of the metal and alloy materials in the whole service period, the so-called solution treatment was also considered, especially for the materials with high-Cr content (Yang et al. 2011; Cai et al. 2003). Therefore, He et al. (2020) explored the influence of the solution-treated 316 L layer fabricated by laser cladding onto the 45# medium carbon steel (0.45% C) substrate on the interaction of corrosion and wear behavior. The solution treatment consisted of subjecting the laser clad 316 L to 1050 °C environment for 1 h in a heat treatment furnace in dry air. The corrosion performance has been evaluated using the copper-accelerated acetic acid salt spray (CASS) test, according to ISO 9227-2006. Based on the SEM, XRD, and microhardness associated analysis, it was shown that the solution treatment increased the microhardness of the layer by more than 40%, which was beneficial for the overall corrosion and wear performance improvement.

In the last decade, the use of Fe-based amorphous coatings attracted in-creased interest due to their remarkable mechanical, physical, and chemical properties, including excellent corrosion resistance and wear resistance, which makes them suitable for industrial applications (Wang et al. 2017a, b; Huang et al. 2018a, b; Farmer et al. 2009; Katakam et al. 2014; Zhou and Kong 2019). The corrosion resistance of these layers depends on the porosity and amorphous character of the clad coating material. It has been recently observed (Wang et al. 2017a, b; Katakam et al. 2014) that even the porosity would decrease or disappear in laser clad coatings; the corrosion protection of the metal/alloy is mainly dictated by the crystalline grade of the coating.

Fe-based amorphous coatings with increased compactness can be laser clad by using crystalline Fe-based alloy plates as feedstock materials with the composition of $Fe_{44.72}Co_{8.57}Cr_{14.95}Mo_{26.9}C_{3.2}B_{1.28}Y_{3.01}$ (wt%), instead of the amorphous powders (Wang et al. 2017a, b). The effect of pulse frequency and laser power on the morphological and corrosion resistance properties has been evaluated. The thicknesses of the clad layers are measured in the order of hundreds of microns maintaining a perfect metallurgical bonding at the metal/coating interface. However, upon increasing the laser power, the thickness increases and some cracks appear.

Potentiodynamic polarization curves at 1 mV s^{-1} scan rate in 3.5% NaCl solution at 25 °C reveals that the clad coatings have excellent corrosion performance (Fig. 7.7).

The laser clad coatings exhibit a stable passive region up to about 1.0 V without transpassive behavior, indicating the absence of localized corrosion. If the laser power is increased, the current density of the laser clad coating slowly grows though remaining under the values relating to 316 L stainless steel (lower than 1 μA cm^{-2}). The obtained results suggest that great corrosion resistance of LC coatings can be achieved by using fine grain and passivation elements (Cr, Mo, B, Y, and Co) within the clad coatings. The same conclusions are confirmed by Huang et al. (2018a, b) for $Fe_{37.5}Cr_{27.5}C_{12}B_{13}Mo_{10}$ amorphous laser clad coatings on 45 steel.

Cr–Ni-based stainless steel coatings formed by laser cladding on AISI 1045 carbon steel have been investigated by Zhang et al. (Zhang et al. 2016). The obtained

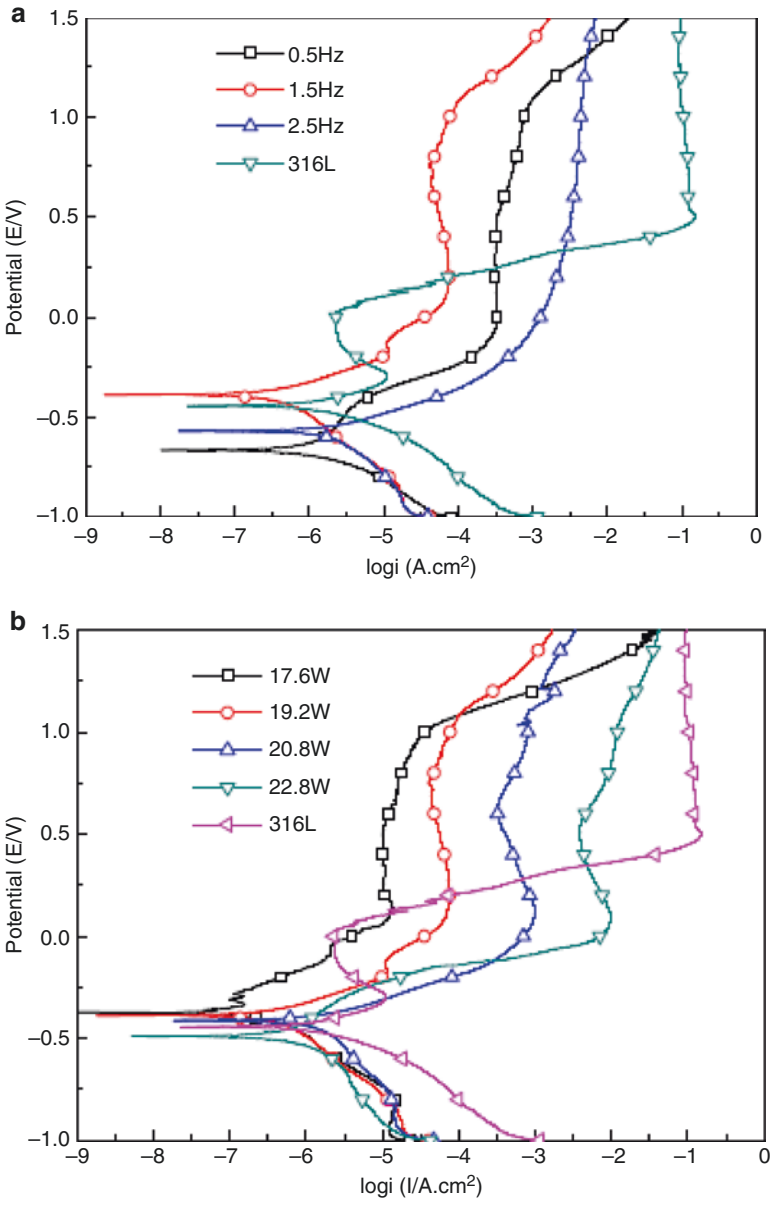

Fig. 7.7 Comparative potentiodynamic polarization curves of the $Fe_{44.72}Co_{8.57}Cr_{14.95}Mo_{26.9}C_{3.2}B_{1.2}{}_{8}Y_{3.01}$ laser clad coatings on Q235 carbon steel with different parameters and stainless steel 316 L (as reference) in 3.5% NaCl solution: (**a**) pulse frequency and (**b**) power. (Reported from Wang et al. 2017a, b)

results showed a better corrosion resistance of the cladding layer as compared to both AISI 1045 and 304 L steels, demonstrated by a nobler corrosion potential and a lower corrosion current. It is reported that these LC materials are not susceptible to passivation in the analyzed potential range.

Other important materials which deserve to be cited as laser clad coatings are nickel silicide alloys because of their high yield strength, abnormal strength–temperature relationship, and outstanding corrosion resistance. In the work of Wang et al. (2003) Ni_2Si/NiSi coatings on a 0.2% C carbon steel were deposited by laser cladding using Ni–40 at.% Si elemental powder blends. The laser clad Ni_2Si/NiSi coating shows excellent corrosion and wear resistance.

7.4.1.2 Laser Cladding on Stainless Steel

Stainless steel is extensively used to produce components to be used in aggressive environments, especially marine ones that are characterized by particular features, including high salinity, high temperature, relative humidity, and UV light. Under these severe exploitation conditions, significant pitting corrosion has been evidenced. On the other hand, producing complex workpieces of stainless steel is not simple. In this frame, laser manufacturing technology has provided great advances, in particular in automotive and aerospace industries, due to the capability to directly prepare workpieces with definite characteristics (Lei et al. 2019; Xu et al. 2019; Niu et al. 2015; Hussaini et al. 2015; Kurgan and Varol 2010; Yan et al. 2014; Thompson et al. 2015).

Currently, significant effort has been made to study laser cladding of corrosion protective layers on 316 L stainless steel. Stellite-F alloy has been laser clad on 316 L stainless and the corrosion resistance improvement was proved by Zhong et al. (Zhong et al. 2019). The addition of CeO_2 to a cobalt-based powder clad on 316 L stainless steel has been demonstrated to increase the mechanical properties of the base material (Niu et al. 2015).

Lei et al. (Lei et al. 2019) prepared 316 stainless steel (316SS) layers onto 304 stainless steel (304SS) using a ring-shaped laser beam for cladding. The cladding metal was 316SS powder prepared by the atomization method, composed of C 0–0.08, Si 0–1.0, Mn 0–2.0, Ni 10.0–14.0, Cr 16.0–18.0, Mo 2.0–3.0, and Fe Bal. (wt%). This procedure diminishes the dilution rate of the cladding material and allows a good metallurgical bonding between the substrate and the laser clad coating by decreasing sintering and increasing the compactness of the microstructure. The smoothness of the laser clad coating is also guaranteed by a powder feeding system internal to the laser beam, which allows higher utilization ratio of feedstock powders and improved cladding efficiency (Shi et al. 2017). Corrosion behavior has been evaluated involving the traditional 3.5% NaCl solution at room temperature, by recording the potentiodynamic polarization curves at 5 mV s^{-1} after the stabilization of the open circuit potential and the electrochemical impedance spectra (EIS). The obtained results showed a better corrosion performance of the clad layers as

compared to the bare substrate. Moreover, it has been noticed that the overlap ratio slightly influences the corrosion resistance, which is maximized for a value of 30%.

Xu et al. explored the influence of rare-earth oxide additions to the 316 L stainless steel laser clad coating on the 316 L stainless steel substrate (Xu et al. 2019). The presence of rare-earth oxides positively affects the hardness of the laser clad layer by grain refinement, while leaving its chemical composition almost unchanged. Improvements in the corrosion potential and the passive current density of the laser clad 316 L stainless steel have been recorded, as shown in Fig. 7.8.

The addition of rare-earth oxide to the laser clad material improves the corrosion resistance, but it does not completely eliminate the pitting events.

7.4.2 LC Coating on Mg-Based Alloys

Currently, laser cladding on magnesium alloys is a novel research area closely related to their involvement in building different components for various industrial applications.

Magnesium alloys are attractive, lightweight structural materials due to their properties, including low density (from 1.74 to 1.85 g.cm^{-3}), high specific strength, rigidity and thermal conductivity, good electromagnetic resistance, and outstanding machinability. In addition, they are characterized by good thermal and electrical conductivities, with proper vibration and shock adsorption properties. Under these circumstances, magnesium alloys are largely used in various applications from automotive, communication, to electronics and aerospace industries (Gupta and Wong 2015; Kulekci 2008).

However, magnesium alloys present high chemical reactivity, low hardness, and poor corrosion resistance and wear characteristics due to the lack of formation of a self-healing passive surface film (Paital et al. 2012; Gray and Luan 2002; Subramanian et al. 1991), which limits their widespread use in some applications,

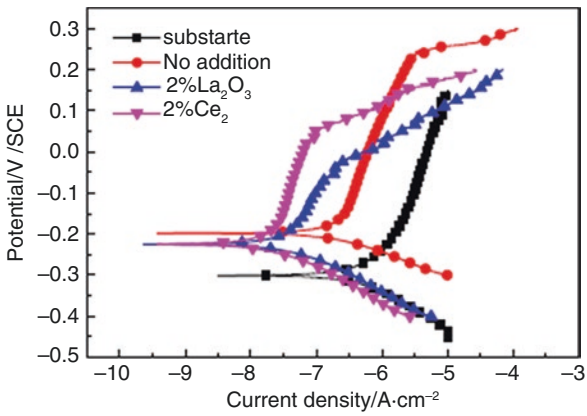

Fig. 7.8 Comparative polarization curves of 316 L stainless steel before and after rare-earth oxide-modified laser cladding in 3.5 wt % NaCl solution. (Reported from Xu et al.(2019)

especially in automotive and aircraft industries (Fini and Amadeh 2013; Rashad et al. 2016).

Among the different surface treatments adopted to improve the mechanical properties and corrosion performance of magnesium alloys, laser surface treatments such as laser surface alloying, laser re-melting, and laser cladding have attracted great attention in recent years (Dutta and Manna 2013; Paital et al. 2012; Subramanian et al. 1991; Liu et al. 2017).

As pointed out in Sect. 7.3.3, numerous processing parameters (laser power, scanning rate, beam size, and focal position) affect the cladding geometry, dilution rate, coating thickness, and aspect ratio as well as the microstructure and the mechanical properties of the final coating (Gao et al. 2009; Wang and Yue 2001; Riquelme et al. 2016).

In addition, the cladding materials are also important in controlling the microstructure and characteristics of the clad coatings. Pure aluminum powder has been used (Ignat et al. 2004), but heterogeneous cladding materials have been preferred in the last few years for better corrosion and wear resistance of magnesium alloys (Liu et al. 2017). Among them, Al-based alloys (Gao et al. 2006; Wang and Yue 2001), Fe-based alloys (Yue et al. 2001), ceramic materials (Gao et al. 2007), and more recently amorphous alloys (Yue et al. 2007) and high entropy alloys (denoted HEAs) were the subject of several studies (Yue et al. 2014).

In order to increase the strength of magnesium, aluminum is typically added to form a solid solution. The different phases formed in laser cladding can be predicted from the thermodynamical equilibrium of Al–Mg elements (Wang et al. 1993; Liu et al. 2017). Wang et al. (1993) reported improved corrosion resistance in 3.5% NaCl of the laser-clad $Mg_{27}Al_{73}$ with respect to laser-clad Mg-2 wt % Zr, Mg-5 wt % Zr, cast AZ91B, and cast magnesium. Laser clad $Mg_{80}Al_{20}$ on ZM5 magnesium alloy substrate using a CO_2 laser provides a better corrosion performance in sea water solution thanks to the fine dispersion of intermetallic phases and extended Al solid solutions obtained by laser rapid solidification (Chen et al. 2007).

It is known that Al-Si alloys have melting points quite close to those of Mg alloys, so many studies have been devoted to the fabrication of Al–Si coatings by laser cladding, exhibiting finer microstructure, better mechanical properties, and enhanced corrosion resistance (Liu et al. 2017; Rolink et al. 2014; Gao et al. 2006).

The deposition of laser clad Al–Si using commercial Al/Si powder onto different Mg alloy substrates by optimizing the Nd:YAG laser power and deposition speed for each alloy type decreases the coating porosity and increases its hardness, wear, and corrosion resistance (Carcel et al. 2011).

In recent years, high entropy alloys (denoted as HEAs) have been intensively studied because of their excellent wear and corrosion resistance and low electrical and thermal conductivities (Liu et al. 2017; Huang et al. 2018a, b). HEAs are constituted by five or more elements in an equal molar ratio and have simple BCC and/or FCC solid solution phases. By using a HEA material in laser clad coating, the mixing entropy with the substrate becomes very high. Therefore, the molten pool size notably decreases. To date, HEAs have been used for laser cladding both on

steel and magnesium alloys (Li et al. 2013; Qiu and Liu 2013; Meng et al. 2015; Huang et al. 2018a, b).

Huang et al. reported the fabrication of $Al_{0.5}CoCrCuFeNi$ high-entropy alloy coating on a AZ91D magnesium alloy substrate by laser cladding using mixed elemental powders (Huang et al. 2018a, b). Dry sliding wear tests and potentiodynamic polarization curves showed that the LC coating provided better corrosion and wear resistance than the AZ91D matrix.

As shown in Fig. 7.9, the HEA coating fabricated by laser cladding presented a corrosion potential approx. 500 mV more positive compared to the uncoated substrate and a lower corrosion current indicating a better corrosion resistance. This result can be ascribed to the presence of Cr, Al, and Ni in the coating that forms dense oxides, which hinder the diffusion of corrosion aggressive Cl^-ions.

7.4.3 Optimization of Laser Clad Coating by Modeling

Parameter selection is often done by a set of experimental trials including metallurgical examination of cross-sections of clad tracks. Prior work on similar systems can of course be used as a starting point for parameter selection, and it should be noted that this chapter reports a summary of the wide body of the published literature on laser clad corrosion resistant layers. Systematic variation of individual parameters can also be done to generate process maps such as that generated by Ocelik et al. (2007) for Co-based coatings on cast iron. The full factorial approach used by Riveiro et al. (2014) found that melt depth, and hence dilution, is decreased by increasing mass flow rate and translation speed. They include process cost in their analysis and highlight that the main cost is associated with feedstock material, hence optimizing powder deposition efficiency is key to minimizing process cost (Riveiro et al. 2014). El Cheikh et al. (2012) have developed a set of analytical

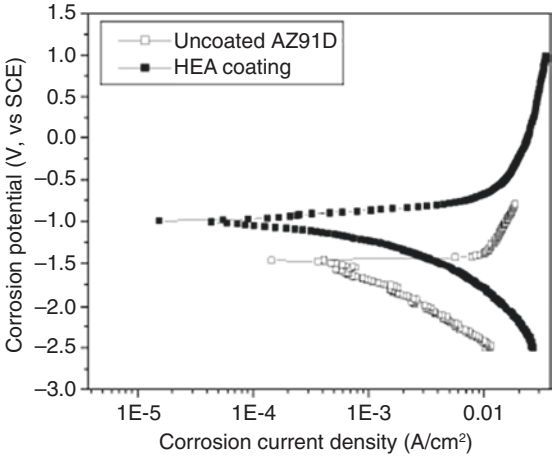

Fig. 7.9 Potentiodynamic polarization curves of AZ91D substrate and of the HEA coating in 3.5 wt % NaCl at a scan rate of 1 mV.s-1. (Reported from Huang et al. 2018a, b)

relationships between laser cladding parameters and clad track geometry for SS316 clad on mild steel: track height is found to be proportional to $(P/Qm)^{(1/4)}(Qm/V)$ and track width to $P^{(3/4)}V^{-(1/4)}$, where P is power, V is velocity, and Qm is mass feed rate. An approach to determining appropriate parameters for 5-axis laser cladding has been described by Calleja et al. (2014).

There is a body of laser cladding work that uses designs of experimental methods including ANOVA and Taguchi analysis (Mondal et al. 2013; Liu and Kovacevic 2014; Zhang and Kovacevic 2016). The range of output responses which can be optimized include track height and width, process efficiency, dilution, extent of heat-affected zone, and bond quality (Bourahima et al. 2019). It must be noted that different applications may need different output responses optimized. For corrosion work, dilution and lack of cracking may be of particular interest. In like-for-like cladding of Ti alloy TC4 the ANOVA analysis carried out by Sun et al. (Sun and Hao 2012) showed track dimensions dominated by powder feed rate, whereas melt depth, and hence dilution, is most strongly affected by translation speed. Increasing speed and decreasing powder feed rate was seen to improve bonding in the cladding of Ni powder on a Cu-Ni-Al alloy (Bourahima et al. 2019), whereas track dimensions decreased with increasing translation speed, an observation easily explained by heat input per unit length and reported elsewhere (Riveiro et al. 2014).

There are also a number of theoretical and modeling approaches which can support the parameter selection process. The combination of existing CFD (computational fluid dynamics) and thermal models was done by Tabernero et al. (2012), which allows them to predict track height and width to be within 20%. Hofman et al. (2011) have applied FEM (finite element modeling) for dilution control in laser cladding. They saw good correlation between experimental and modeled results and noted that melt pool width is a good indicator of dilution level. Roy and Kumar (2009) have used a 3D finite volume heat transfer model and dimensionless parameters to develop a process map for laser cladding. As highlighted by Mackwood and Crafer's review (2005), the extensive existing work on thermal modeling of laser welding has a lot of applicability to the related process of laser cladding.

The recent review on numerical modeling of laser cladding by Tamanna et al. (2019) separates the laser cladding process into three key parts: powder flow dynamics, the melt pool, and clad properties. They report that discretized models can be used to optimize parameters in each stage but note that an all-encompassing model has yet to be achieved. The work concludes by highlighting the need to use experimental results alongside numerical simulations to optimize laser cladding. Given the complexity of the laser cladding process, such a combined approach is a sensible method to optimize laser cladding parameters.

7.5 Conclusions

The provided laser cladding parameters are suitably optimized. LC is a flexible technique with an almost unlimited range of applications. The reduction of capital cost of lasers and the use of novel feedstock materials have turned laser cladding

into a cost-effective technique for corrosion protection to generate resistant coatings in a wide number of substrate–environment systems.

References

Abioye, T. E., McCartney, D. G., & Clare, A. T. (2015). Laser cladding of Inconel 625 wire for corrosion protection. *Journal of Materials Processing Technology, 217*, 232–240.

Ackerman, F., & Stanton, E. A. et al. (2008). The cost of climate change – What we'll pay if global warming continues unchecked. In F Ackerman, E A. Stanton et al. (Eds.), *NRDC (Natural Resources Defense Council)*, New York, USA.

Baldridge, T., et al. (2013). Laser cladding of Inconel 690 on Inconel 600 superalloy for corrosion protection in nuclear applications. *Optics and Lasers in Engineering, 51*, 180–184.

Bourahima, F., et al. (2019). Laser cladding of Ni based powder on a Cu-Ni-Al glassmold: Influence of the process parameters on bonding quality and coating geometry. *Journal of Alloys and Compounds, 771*, 1018–1028.

Bi, G. J., et al. (2006). Identification and qualification of temperature signal for monitoring and control in laser cladding. *Optics and Lasers in Engineering, 44,* 1348–1359.

Cai, D., Yao, M., Nie, P., & Liu, W. (2003). Influence of solution treatment temperature on mechanical properties of a Fe–Ni–Cr alloy. *Materials Letters, 57*, 3805–3809.

Calleja, A., et al. (2014). Improvement of strategies and parameters for multi-axis laser cladding operations. *Optics and Lasers in Engineering, 56*, 113–120.

Carcel, B., Sampedro, J., Ruescas, A., & Toneu, X. (2011). Corrosion and wear resistance improvement of magnesium alloys by laser cladding with Al–Si. *Physics Procedia, 12*, 353–363.

Cheikh, H. E., Courant, B., Branchu, S., Hasco, J. Y., & Guille, R. (2012). Analysis and prediction of single laser tracks geometrical characteristics in coaxial laser cladding process. *Optics and Lasers in Engineering, 50*, 413–422.

Chen, C. J., Wang, M. C., Wang, D. S., Jin, R., & Liu, Y. M. (2007). Laser cladding of Mg20Al80 powder on ZM5 magnesium alloy. *Corros Eng SciTechn, 42*, 130–136.

Catchpole-Smith, S., et al. (2017). Fractal scan strategies for selective laser melting of 'unweldable' nickel superalloys. *Additive Manufacturing, 15,* 113–122.

Draper, C. W., & Ewing, C. A. (1984). Laser surface alloying: A bibliography. *Journal of Materials Science, 19*, 3815–3825. 1984.

Dubourg, L., & Archambeault, J. (2008). Technological and scientific landscape of laser cladding process in 2007. *Surface and Coatings Technology, 202*(24), 5863–5869.

Dutta Majumdar, J., & Manna, I. (2013). Laser treatment to improve the corrosion resistance of magnesium (Mg) alloys. In G. L. Song (Ed.), *Corrosion prevention of magnesium alloys* (1st ed.). Oxford: Woodhead Publ.

D'Oliveira, A., et al. (2002). Microstructural features of consecutive layers of Stellite 6 deposited by laser cladding. *Surface & Coatings Technology, 153,* 203–209.

Evans, U. R. (1937). *Metallic corrosion and protection*. London Book chapter: Edward Arnold.

Farmer, J. C., Choi, J. S., & Saw, C. (2009). Iron-based amorphous metals: High-performance corrosion-resistance material development. *Metallurgical and Materials Transactions A: Physical Metallurgy and Materials Science, 40*, 1289–1305.

Fini, M. H., & Amadeh, A. (2013). Improvement of wear and corrosion resistance of AZ91 magnesium alloy by applying Ni–SiC nanocomposite coating via pulse electrodeposition. *Transactions of the Nonferrous Metals Society of China, 23*, 2914–2922.

Fontana, M. G., & Green, N. D. (1967). *Corrosion engineering*. New York: MmcGrow-Hill.

Fouquet, F., Sallamand, P., Millet, J., Frenk, A., & Wagniere, J. (1994). Austenitic stainless steels layers deposited by laser cladding on a mild steel: Realization and characterization. *Journal de Physique, Colloque, C4*(4), 89–92.

Gao, Y., Wang, C., Lin, Q., Liu, H., & Yao, M. (2006). Broad-beam laser cladding of Al–Si alloy coating on AZ91HP magnesium alloy. *Surface and Coating Technology, 201*, 2701–2706.

Gao, Y., Wang, C., Yao, M., & Liu, H. (2007). The resistance to wear and corrosion of laser–cladding Al2O3 ceramic coating on Mg alloy. *Applied Surface Science, 253*, 5306–5311.

Gao, Y., Xiong, D., Wang, C., & Chen, Y. (2009). Influences of laser powers on microstructure and properties of the coatings on the AZ91HP magnesium alloy. *Acta Metallurgica Sinica (English Letters), 22*, 167–173.

Gray, J. E., & Luan, B. (2002). Protective coatings on magnesium and its alloys – A critical review. *Journal of Alloys and Compounds, 336*, 88–113.

Gupta, M., & Wong, W. L. E. (2015). Magnesium–based nanocomposites: Lightweight materials of the future. *Materials Characterization, 105*, 30–46.

Gong, X. Y., et al. (2017). Effect of scanning path on temperature field in laser cladding. 4th International Conference on Advanced Composite Materials and Manufacturing Engineering, Bristol, Iop Publishing Ltd. 207.

He, B., Zhang, L., Zhu, Q., Wang, J., Yun, X., Luo, J., & Chen, Z. (2020). Effect of solution treated 316L layer fabricated by laser cladding on wear and corrosive wear resistance. *Optics and Laser Technology, 121*, 105788.

Heralič, A., Christiansson, A. K., Hurtig, K., Ottosson, M., & Lennartson, B. (2008, July 6–11). Control design for automation of robotized laser metal-wire deposition. *Proceedings of the 17th World Congress*. The International Federation of Automatic Control, Seoul, Korea. https://doi.org/10.3182/20080706-5-KR-1001.2361.

Hofman, J. T., et al. (2011). FEM modeling and experimental verification for dilution control in laser cladding. *Journal of Materials Processing Technology, 211*, 187–196.

Hu, Z. W., Li, W. G., & Zhao, Y. T. (2019). Microstructure and properties of M3B2-type boride-based cermet coatings prepared by laser cladding synthesis. *Coatings, 9*, 476.

Huang, G., Qu, L., Lu, Y., Wang, Y., Li, H., Qin, Z., & Lu, X. (2018a). Corrosion resistance improvement of 45 steel by Fe-based amorphous coating. *Vacuum, 153*, 39–42.

Huang, K., Chen, L., Lin, X., Huang, H., Tang, S., & Du, F. (2018b). Wear and corrosion resistance of Al0.5CoCrCuFeNi high-entropy alloy coating deposited on AZ91D magnesium alloy by laser cladding. *Entropy, 20*, 915.

Hussaini, S. M., Krishna, G., Gupta, A. K., & Singh, S. K. (2015). Development of experimental and theoretical forming limit diagrams for warm forming of austenitic stainless steel 316. *Journal of Manufacturing Processes, 18*, 151–158.

Ignat, S., Sallamand, P., Grevey, D., & Lambertin, M. (2004). Magnesium alloys laser (Nd: yag) cladding and alloying with side injection of aluminium powder. *Applied Surface Science, 225*, 124–134.

Jiao, X. Y., Wang, J., Wang, C. M., Gong, Z. Q., Pang, X. X., & Xiong, S. M. (2018). Effect of laser scanning speed on microstructure and wear properties of T15M cladding coating fabricated by laser cladding technology. *Optics and Lasers in Engineering, 110*, 163–171.

Katakam, S., Kumar, V., & Dahotre, N. B. (2014). Laser assisted Fe-based bulk amorphous coating: Thermal effects and corrosion. *Journal of Alloys and Compounds, 604*, 266–272.

Kim, J. D., & Peng, Y. (2000). Melt pool shape and dilution of laser cladding with wire feeding. *Journal of Materials Processing Technology, 104*(3), 284–293.

Kulekci, M. K. (2008). Magnesium and its alloys applications in automotive industry. *International Journal of Advanced Manufacturing Technology, 39*, 851–865.

Kumar, A., & Roy, S. (2009). Development of a theoretical process map for laser cladding using two-dimensional conduction heat transfer model. *Numerical Heat Transfer Part a-Applications, 56*, 478–496.

Kurgan, N., & Varol, R. (2010). Mechanical properties of P/M 316L stainless steel materials. *Powder Technology, 201*, 242–247.

Lei, J., Xie, J., Zhou, S., Song, H., Song, X., & Zhou, X. (2019). Comparative study on microstructure and corrosion performance of 316 stainless steel prepared by laser melting deposition with ring-shaped beam and Gaussian beam. *Optics and Laser Technology, 111*, 271–283.

Li, R., Ferreira, M. G. S., Anjos, M. A., & Vilar, R. (1996a). Localized corrosion of laser surface cladded UNS S31254 superaustenitic stainless steel on mild steel. *Surface and Coating Technology, 88*, 90–95.

Li, R., Ferreira, M. G. S., Anjos, M. A., & Vilar, R. (1996b). Localized corrosion performance of laser surface cladded UNS S44700 superferritic stainless steel on mild steel. *Surface and Coating Technology, 88*, 96–102.

Li, Q. H., Yue, T. M., Guo, Z. N., & Lin, X. (2013). Microstructure and corrosion properties of AlCoCrFeNi high entropy alloy coatings deposited on AISI 1045 steel by the electrospark process. *Metallurgical and Materials Transactions A: Physical Metallurgy and Materials Science, 44*, 1767–1778.

Lison, M., Devesse, W., de Baere, D., Hinderdael, M., & Guillaume, P. (2019). Hyperspectral and thermal temperature estimation during laser cladding. *Journal of Laser Applications, 31*(2), 022313. https://doi.org/10.2351/1.5096129.

Liu, J., Yu, H., Chen, C., Weng, F., & Dai, J. (2017). Research and development status of laser cladding on magnesium alloys: A review. *Optics and Lasers in Engineering, 93*, 195–210.

Liu, J., Liu, H., Chen, P. J., & Hao, J. B. (2019). Microstructural characterization and corrosion behaviour of AlCoCrFeNiTix high-entropy alloy coatings fabricated by laser cladding. *Surface and Coating Technology, 361*, 63–74.

Li, X. F., et al. (2019). Microstructure and properties of the laser cladding ODS layers on CLAM steel. *Surface & Coatings Technology, 357,* 172–179.

Liu, S. and R. Kovacevic (2014). Statistical analysis and optimization of processing parameters in high-power direct diode laser cladding. *International Journal of Advanced Manufacturing Technology, 74,* 867–878.

Mackwood, A. P., & Crafer, R. C. (2005). Thermal modelling of laser welding and related processes: A literature review. *Optics and Laser Technology, 37*, 99–115.

Mahmood, K., Syed, W. U. H., Andrew, J., & Pinkerton, A. J. (2011a). Innovative reconsolidation of carbon steel machining swarf by laser metal deposition. *Optics and Lasers in Engineering, 49*, 240–247.

Mahmood, K., Stevens, N., Syed, W. U. H., & Pinkerton, A. J. (2011b). Material-efficient cladding for corrosion resistance. *30th International Congress on Applications of Lasers and Electro-Optics*, ICALEO 2011 Congress Proceedings, Laser Institute of America.

Mahmood, K., Nicholas Stevens, N., Andrew, J., & Pinkerton, A. J. (2012). Laser surface modification using Inconel 617 machining swarf as coating material. *Journal of Materials Processing Technology, 212*, 1271–1280.

Majumdar, J. D., Pinkerton, J. A., Liu, Z., Manna, I., & Li, L. (2005). Mechanical and electrochemical properties of multiple-layer diode laser cladding of 316L stainless steel. *Applied Surface Science, 247*, 373–377.

Manna, I., Majumdar, J. D., Chandra, B. R., Nayak, S., & Dahotre, N. B. (2006). Laser surface cladding of Fe-B-C, Fe-B-Si and Fe-BC-Si-Al-C on plain carbon steel. *Surface and Coating Technology, 201*, 434–440.

McCafferty, E., & Moore, P. G. (1986). Corrosion behavior of laser surface melted and laser surface alloyed steels. *Journal of the Electrochemical Society, 133*, 1090–1096.

Meng, G., Yue, T. M., Lin, X., Yang, H., Xie, H., & Ding, X. (2015). Laser surface forming of AlCoCrCuFeNi particle reinforced AZ91D matrix composites. *Optics and Laser Technology, 70*, 119–127.

Mondal, S., et al. (2013). Application of Taguchi-based gray relational analysis for evaluating the optimal laser cladding parameters for AISI1040 steel plane surface. *International Journal of Advanced Manufacturing Technology, 66*, 91–96.

Nazari, K. A., Rashid, R. A. R., Palanisamy, S., Xia, K., & Dargusch, M. S. (2018). A novel Ti-Fe composite coating deposited using laser cladding of low cost recycled nano-crystalline titanium powder. *Materials Letters, 229*(2018), 301–304.

Niu, L. Y., Cao, Y. L., Tong, X., Lin, J. X., Li, G. Y., & Wang, W. Q. (2015). Effect of CeO2 on microstructure and corrosion resistance of laser cladding Co-based composite coating on 316L stainless steel. *Appl Laser, 35*, 304–308.

Nowotny, S., Brueckner, F., Thieme, S., Leyens, C., & Beyer, E. (2015). High-performance laser cladding with combined energy sources. *Journal of Laser Applications, 27*, S17001.

Ocelik, V., et al. (2007). Thick Co-based coating on cast iron by side laser cladding: Analysis of processing conditions and coating properties. *Surface & Coatings Technology, 201*, 5875–5883.

Olakanmi, E. O., et al. (2019). Multi-variable optimisation of the quality characteristics of fiber-laser cladded Inconel-625 composite coatings. *Surface & Coatings Technology, 357,* 289–303.

Paital, S. R., Bhattacharya, A., Moncayo, M., Ho, Y. H., Mahdak, K., Nag, S., Banerjee, R., & Dahotre, N. B. (2012). Improved corrosion and wear resistance of Mg alloys via laser surface modification of Al on AZ31B. *Surface and Coating Technology, 206*, 2308–2315.

Parvathavarthini, N., Dayal, R. K., Sivakumar, R., KamachiMudali, U., & Bharati, A. (1992). Pitting corrosion resistance of laser surface alloyed 304 stainless steel. *Materials Science and Technology, 8*, 1070–1074.

Pekkarinen, I. J., Kujanp, V., & Salminen, A. (2012). Laser cladding using scanning optics. *Journal of Laser Applications*. https://doi.org/10.2351/1.4742938.

Pekkarinen, J., Salminen, A., & Kujanp, V. (2014). Laser cladding with scanning optics: Effect of scanning frequency and laser beam power density on cladding process. *Journal of Laser Applications, 26*(3), 032002. https://doi.org/10.2351/1.4868895.

Polsky, V. I., Yakushin, V. L., Dzhumaev, P. S., Petrovsky, V. N., & Safonov, D. V. (2016). Increasing corrosion resistance of carbon steels by surface laser cladding. *IOP Conference Series: Materials Science and Engineering, 130*, 012011. https://doi.org/10.1088/1757-899X/130/1/012011.

Pourbaix, M. (1974). *Atlas of electrochemical equilibria in aqueous solutions*. National Association of Corrosion Engineers. 2nd 2d English ed. Houston, Tex.

Qiu, X., & Liu, C. (2013). Microstructure and properties of Al2CrFeCoCuTiNix high–entropy alloys prepared by laser cladding. *Journal of Alloys and Compounds, 553*, 216–220.

Rashad, M., Pan, F., Lin, D., & Asif, M. (2016). High temperature mechanical behavior of AZ61 magnesium alloy reinforced with graphene nanoplatelets. *Materials and Design, 89*, 1242–1250.

Riquelme, A., Rodrigo, P., Escalera–Rodríguez, M. D., & Rams, J. (2016). Analysis and optimization of process parameters in Al–SiCp laser cladding. *Optics and Lasers in Engineering, 78*, 165–173.

Riskin, J., & Khentov, A. (2019). Corrosion basics in electrocorrosion and protection of metals. In J. Riskin & A. Khentov (Eds.), *Corrosion basics* (2nd ed.). Amsterdam: Elsevier.

Riveiro, A., et al. (2014). Laser cladding of aluminium on AISI 304 stainless steel with high-power diode lasers. *Surface & Coatings Technology, 253*, 214–220.

Rolink, G., Weisheit, A., Biermann, T., Bobzin, K., Öte, M., Linke, T. F., Schulz, C., & Kelbassa, I. (2014). Investigations of laser clad, thermal sprayed and laser remelted AlSi20–coatings on magnesium alloy AZ31B under constant and cycling thermal load. *Surface and Coating Technology, 259*, 751–758.

Rivetti M L S, da Silva Andrade Neto J, de Amorim Júnior N S, Véras Ribeiro D (2018). Corrosion Inhibitors for Reinforced Concrete. In: Aliofkhazraei M (ed), Corrosion Inhibitors, Principles and Recent Applications, IntechOpen

Sexton, L., Lavin, S., Byrne, G., & Kennedy, A. (2002). Laser cladding of aerospace materials. *Journal of Materials Processing Technology, 122*, 63–68.

Shi, T., Lu, B., Shi, S., Meng, W., & Fu, G. (2017). Laser metal deposition with spatial variable orientation based on hollow-laser beam with internal powder feeding technology. *Optics and Laser Technology, 88*, 234–241.

Singh, R., Martin, M., & Dahotre, N. B. (2005). Influence of laser surface modification on corrosion behavior of stainless steel 316L and Ti-6Al-4V in simulated biofluid. *Surface Engineering, 21*, 297–306.

Song, B., Hussain, T., & Voisey, K. T. (2016). Laser cladding of Ni50Cr: A parametric and dilution study. In M. Schmidt, F. Vollertsen, & C. B. Arnold (Eds.), *Proceedings of laser assisted net shape engineering 9 international conference on photonic technologies*, pp. 706–715.

Sorensen, P. A., Kiil, S., Dam-Johansen, K., & Weinell, C. E. (2009). Anticorrosive coatings: A review. *Journal of Coating Technology and Research, 6*(2), 135–176.

Subramanian, R., Sircar, S., & Mazumder, J. (1991). Laser cladding of zirconium on magnesium for improved corrosion properties. *Journal of Materials Science, 26*, 951–956.

Sun, Y. W., & Hao, M. Z. (2012). Statistical analysis and optimization of process parameters in Ti6Al4V laser cladding using Nd:YAG laser. *Optics and Lasers in Engineering, 50*, 985–995.

Syed, W. U. H., Pinkerton, A. J., & Li, L. (2005). A comparative study of wire feeding and powder feeding in direct diode laser deposition for rapid prototyping. *Applied Surface Science, 247*, 268–276.

Shu, F. Y., et al. (2019). Effects of laser power on microstructure and properties of laser cladded CoCrBFeNiSi high-entropy alloy amorphous coatings. *Surface & Coatings Technology, 358,* 667–675.

Stanciu, E. M., et al. (2016). Dual Coating Laser Cladding of NiCrBSi and Inconel 718. *Materials and Manufacturing Processes, 31,* 1556–1564.

Tabernero, I., et al. (2012). Geometric modelling of added layers by coaxial laser cladding. *Physics Procedia, 39*, 913–920.

Tamanna, N., et al. (2019). Progress in numerical simulation of the laser cladding process. *Optics and Lasers in Engineering, 122*, 151–163.

Thompson, S. M., Bian, L., Shasaei, N., & Yadollahi, A. (2015). An overview of direct laser deposition for additive manufacturing; Part I: Transport phenomena, modeling and diagnostics. *Additive Manufacturing, 8*, 36–62.

Toyserkani, E., Khajepour, A., & Corbin, S. (2005). *Laser cladding*. Boca Raton: CRC Press.

Valkov, S., Ormanova, M., & Petrov, P. (2018). Surface manufacturing of materials by high energy fluxes. In M. A. Chowdhury (Ed.), *Advanced surface engineering research*. London: IntechOpen. https://doi.org/10.5772/intechopen.79874.

Villar, R. (2012). Laser surface modification of steels and cast irons for corrosion resistance. In C. T. Kwok (Ed.), *Laser surface modification of alloys for corrosion and Erosion resistance* (1st ed.). Oxford: Woodhead Publishing.

Voisey, K. T., Liu, Z., & Stott, F. H. (2006). Inhibition of metal dusting using thermal spray coatings and laser treatment. *Surface and Coating Technology, 201*, 637–648.

Wang, S. Y., & Liu, C. S. (2019). Real-time monitoring of chemical composition in nickel-based laser cladding layer by emission spectroscopy analysis. *Materials, 12*, 2637.

Wang, A. H., & Yue, T. M. (2001). YAG laser cladding of an Al–Si alloy onto an Mg/SiC composite for the improvement of corrosion resistance. *Composites Science and Technology, 61*, 1549–1554.

Wang, A. A., Sircar, S., & Mazumder, J. (1993). Laser cladding of Mg–Al alloys. *Journal of Materials Science, 28*, 5113–5122.

Wang, H. M., Wang, C. M., & Cai, L. X. (2003). Wear and corrosion resistance of laser clad Ni2Si/NiSi composite coatings. *Surface and Coating Technology, 168*(2–3), 202–208.

Wang, K., Chang, B., Chen, J., Fu, H., Lin, Y., & Lei, Y. (2017a). Effect of molybdenum on the microstructures and properties of stainless steel coatings by laser cladding. *Applied Sciences, 7*, 1065.

Wang, S. L., Zhang, Z. Y., Gong, Y. B., & Nie, G. M. (2017b). Microstructures and corrosion resistance of Fe-based amorphous/nanocrystalline coating fabricated by laser cladding. *Journal of Alloys and Compounds, 728*, 1116–1123.

Wen, X., et al. (2019). Underwater wet laser cladding on 316L stainless steel: A protective material assisted method. *Optics and Laser Technology,111,* 814–824

Xu, Z., Wang, Z., Chen, J., Qiao, Y., Zhang, J., & Huang, Y. (2019). Effect of rare earth oxides on microstructure and corrosion behavior of laser-cladding coating on 316L stainless steel. *Coatings, 9*, 636.

Yan, C., Hao, L., Hussein, A., Young, P., & Raymont, D. (2014). Advanced lightweight 316L stainless steel cellular lattice structures fabricated via selective laser melting. *Materials and Design, 55*, 533–541.

Yang, Y. H., Yan, B., Wang, J., & Yin, J. L. (2011). The influence of solution treatment temperatureon microstructure and corrosion behavior of high temperature ageing in 25% Cr duplex stainless steel. *Journal of Alloys and Compounds, 509*, 8870–8879.

Yao J. H., Zhang, Q. L., & Kong, F. Z. (2012). Laser remanufacturing to improve the erosion and corrosion resistance of metal components. In C. T. Kwok (Ed.), *Engineering laser surface modification of alloys for corrosion and erosion resistance*, Woodhead Publishing Series in Metals and Surface, pp. 320–354.

Yue, T. M., Hu, Q. W., Mei, Z., & Man, H. C. (2001). Laser cladding of stainless steel on magnesium ZK60/SiC composite. *Materials Letters, 47*, 165–170.

Yue, T. M., Su, Y. P., & Yang, H. O. (2007). Laser cladding of Zr65Al7.5Ni10Cu17.5 amorphous alloy on magnesium. *Materials Letters, 61*, 209–212.

Yue, T. M., Xie, H., Lin, X., Yang, H. O., & Meng, G. H. (2014). Solidification behaviour in laser cladding of AlCoCrCuFeNi high–entropy alloy on magnesium substrates. *Journal of Alloys and Compounds, 587*, 588–593.

Zhang, Z., & Kovacevic, R. (2016). Multiresponse optimization of laser cladding steel plus VC using Grey relational analysis in the Taguchi method. *JOM, 68*, 1762–1773.

Zhang, H., Zou, Y., Zou, Z. D., & Wu, D. T. (2015). Microstructure and properties of Fe-based composite coating by laser cladding Fe-Ti-V-Cr-C-CeO2 powder. *Optics and Laser Technology, 65*, 119–125.

Zhong, X. K., Wang, X. F., & Han, F. S. (2019). Electrochemical corrosion behavior of laser cladding stellite-F alloy layer on 316L stainless steel surface. *Heat Treatment of Metals, 44*, 176–179. (in Chinese).

Zhou, J., & Kong, D. (2019). Effects of Ni addition on corrosion behaviors of laser cladded FeSiBNi coating in 3.5% NaCl solution. *Journal of Alloys and Compounds, 795*, 416–425.

Zhu, R. D., Li, Z. Y., Li, X. X., & Sun, Q. (2015). Microstructure and properties of the low-power-laser clad coatings on magnesium alloy with different amount of rare earth addition. *Applied Surface Science, 353*, 405–413.

Zhang, Z. and R. Kovacevic (2016). Multiresponse Optimization of Laser Cladding Steel plus VC Using Grey Relational Analysis in the Taguchi Method. JOM, 68, 1762-1773.

Chapter 8
Laser Cladding of Titanium Alloy

Shakti Kumar and Amitava Mandal

8.1 Introduction to Titanium Alloy

Titanium consists of either in the form of pure titanium or titanium alloys having high tensile strength and toughness at elevated temperatures. Titanium alloys mainly consist of titanium, aluminum, vanadium, and molybdenum along with other metallic elements to build strong lightweight alloy. The elements like aluminum and vanadium (4–6 by weight %) increase the solid solubility with high condensation temperature. Though its density is approximately 60% lower than steel, it exhibits good mechanical strength with better heat transfer capacity and higher melting point than the steel depending on compositions of aluminide content on the titanium alloy. It also possesses high strength-to-weight ratio and corrosion resistance nonmagnetic properties. The properties of titanium are shown in Table 8.1.

Titanium alloys exist in different structural categories with unique mechanical properties. The different grades of titanium alloys based on the commercial as well as noncommercial applications are presented in Tables 8.2 and 8.3 (Donachie 2000).

8.2 Backgrounds and Need for Laser Cladding of Titanium

In the last 4–5 decades, titanium and its alloys create an industrial revolution in the field of aerospace, marine, power plant, and chemical industries. However, there are various restrictions in the direct use of titanium and its alloys due to poor tribological properties, lower hardness, and inability to withstand at high temperatures and harsh working environments. Also with direct contact with the metal, it got oxidized

S. Kumar (✉) · A. Mandal
Department of Mechanical Engineering, Indian Institute of Technology(ISM) Dhanbad, Dhanbad, Jharkhand, India
e-mail: amitava@iitism.ac.in

P. Cavaliere (ed.), *Laser Cladding of Metals*,
https://doi.org/10.1007/978-3-030-53195-9_8

Table 8.1 Properties and classification of titanium alloy

Properties		Description
Atomic number		22
Atomic weight		47.90
Atomic volume		10.6w/d
Covalent radius		1.32 Å
Crystal structure	Alpha	Close pack hexagonal
	Beta	Body center cubic
Color		Dark gray
Density		4.1 gm/cm3
Melting point		1668^0c
Boiling point		3260^0c
Specific heat		11.4 w/mk
Thermal conductivity		440 kj/kg
Specific gravity		4.5
Hardness		460 HV
Shapes		Bar, sheet, tube, plate, etc.

Table 8.2 Structural categories of titanium and its properties

Titanium structure	Tensile strength	Properties	
Alpha (α)	290–740	Non-heat treatable and strong willing to its welding capability	Low to medium strength, good toughness, excellent mechanical properties at cryogenic temperature, highest corrosion resistance, high temperature creep strength, and oxidation resistance
Alpha and beta (α&β)	620–1250	Heat treatable and welding capability lower than alpha	Medium to high strength, lower high temperature creep strength, Ti6Al4V
Beta(β)		Fully heat treatable, rarely generally, weldable, high strength, BCC allotropic	Creep resistance up to intermediate temperature, excellent formability, Ti3Al8V6Cr4Mo4Zr

at high temperature which reduced the life of the titanium alloy. In the medical field application, titanium alloys fail due to the corrosion effect as it comes in contact with the body fluid and forms aluminum ion which creates a harmful effect on the body (Dai et al. 1997; Fu and Batchelor 1998; Guo et al. 2010; Azevedo 2003; Suarez-Fernandez et al. 1999; Weng et al. 2014). In order to overcome these problems, various surface modification techniques have been adopted such as heat treatment, alloying, laser cladding, surface coating, etc. Laser-based cladding is one of the most widely used heat energy-dependent nonconventional-type surface modification techniques on the metallic surface (Tian et al. 2005). It has a quick processing

Table 8.3 Different grades of titanium and its mechanical properties

Designation	Tensile strength	Yield strength	Commerciality
Unalloyed grade			Commercially pure (1,2,3,4)
ASTM grade 1	240	170	
ASTM grade 2	340	280	
ASTM grade 3	450	380	Ti/Pd alloy (7,11)
ASTM grade 4	550	480	
ASTM grade 7	340	280	
ASTM grade 11	240	170	
α and near-α alloy			Commercially pure
Ti-0.3Mo-0.8Ni	480	380	
Ti-5Al-2.5Sn	790	760	
Ti-5Al-2.5Sn-ELI	690	620	
Ti-8Al-1Mo-1 V	900	830	
Ti-6Al-2Sn-4Zr-2Mo	900	830	
Ti-6Al-2Nb-1Ta-0.8Mo	790	690	
Ti-2.25Al-11Sn-5Zr-1Mo	1000	900	
Ti-2.25Al-11Sn-5Zr-1Mo	1030	910	
α-β alloy			(a) Commercial but its strength can be increased by surface modification process (b) Commercial but its strength cannot be increased, particularly used in deep and sour well technology (c) Semicommercial not significantly used
Ti-6Al-4 V(a)	900	830	
Ti-6Al-4 V-ELI(a)	830	760	
Ti-6Al-6 V-2Sn(a)	1030	970	
Ti-7Al-4Mo(a)	1170	760	
Ti-7Al-4Mo(a)	1125	970	
Ti-6Al-2Sn-4Zr-6Mo(b)	1030	1100	
Ti-3Al-2.5 V(d)	620	520	
Ti-4Al-4Mo-2Sn-0.5Si	1000	960	
Ti-5Al-2Sn-2Zr-4Mo-4Cr(b)(c)	1125	970	
Ti-6Al-2Sn-2Zr-2Mo-2Cr(c)	1030	520	
β- alloys			Commercial, metastable contain high beta stable (molybdenum, silicon, and vanadium)
Ti-10 V-2Fe-3A	1170	1100	
Ti-13 V-11Cr-3Al	1170	1100	
Ti-8Mo-8 V-2Fe-3A	1170	1100	
Ti-3Al-8 V-6Cr-4Mo-4Zr	900	830	
Ti-11.5Mo-6Zr-4.5Sn	960	620	
Ti-15 V-3Cr-3Al-3Sn	1000	965	

time as well as high accuracy, better surface finishing, smooth grain refinement, and high bonding strength between the substrate and the powder material. Also mixing of different compositions of powders enhances the metallurgical and mechanical properties together (Mittal 2004).

8.2.1 Principle Behind Laser Cladding Process

The principle behind laser cladding is the interaction between the laser beam and the substrate material. In this process, a laser beam is used to melt the surface of the substrate along with reinforcement material and deposited; this can be performed with the help of either wire, powder, or strips, as shown in Fig. 8.1. Laser processing is commonly performed with the CO_2, Nd:YAG, and nowadays the fiber laser (Abkowitz et al. 1990). The laser beam is focused on the substrate surface where either powder material is already deployed, or it is to be sprayed through a system coaxially to the laser beam. While laser beam interacts with the powder material, it may be possible that some amount of energy disappeared to the environment, but a large part of the energy is incident to the working place where powder got sufficient energy to melt and diffuse into the substrate and make a layer of higher quality as compared to that of the substrate material, which improves the life span of the substrate. But during this process, in order to avoid oxidation and defects such as the inclusion of gases and micro-cracks, shielding has been provided with the help of argon gas. In the laser melting and deposition process due to high scanning rate and appropriate energy density leads to minimum dilution, porosity and maintian better uniformity in the top surface of clad. The clad material experienced a rapid natural quenching when cooling down after deposition, which results in the fine-grain microstructure (Gnanamuthu 1980). However, laser power and stand of distance are

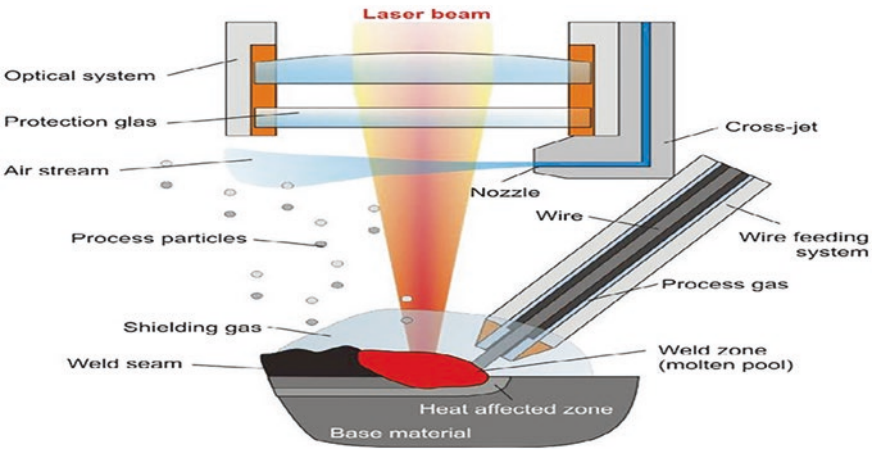

Fig. 8.1 Principle of the laser cladding process (Klocke et al. 2010)

significant parameters in the laser cladding process which enable the clad to prevent overheating/burn or the formation of crack and defect at the intersection zones.

8.3 Classification of Laser Cladding

Laser cladding can be classified on the basis of the deposition technique of metallic powder on the surface of the substrate, as powder bed fusion and direct energy deposition technique. In the case of direct energy deposition technique, powder spray and wire feeding technique are the most common (Everton et al. 2016).

8.3.1 Selective Laser Melting Process

The schematic diagram of laser cladding through melting and deposition is shown in Fig. 8.2. The laser surface modification through the melting and deposition process is the prominent successful method of laser cladding technique, as shown in Fig. 8.2. In this process, cladding powder either in the form of single, binary, or composite is mixed together with the help of binary agents, i.e., a mixture of polyvinyl alcohol (PVA) and distilled water in a specific ratio to make a paste. After creating micro-features on the surface of the substrate using low-grade sandpaper and cleaning with acetone or alcohol, the prepared powder paste is preplaced on the substrate with uniform thickness. Thereafter, the sample consisting of preplaced powder is kept in the oven at certain elevated temperature above the room temperature to remove the moisture content and dry properly in order to avoid oxidation and crack formation. The sample is kept in the inert environment by continuous supplying argon gases during cladding, and the high-intensity laser beam is passed over the samples in a programmed specific path to form laser clad. The deposited preplaced pasted layer gets fused under the influence of laser beam and creates a molten pool which consists of both powder and parent material, which creates a strong

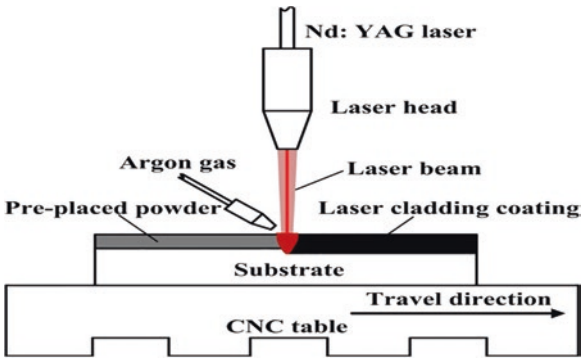

Fig. 8.2 Schematic of the laser preplaced cladding process (Tan et al. 2015)

metallurgical bond, however under the effect of cooling solidified and deposited on the substrate, which improves the mechanical properties of the base metal. This method is easy for the analysis of the controlled process parameter, which shows some advantages such as low porosity, minimum crack, and better surface quality (Kumar et al. 2018). However, others than preplaced method for the cladding process, the deposition of powder directly placed over the substrate without making paste and deposition of laser beam that travels over the substrate, but the major drawback are lots of powder material scattered and spread into the environment which may lead to health hazards or loss of powder material. So to overcome this, preplaced method is used.

8.3.2 Direct Metal Deposition Process

Figure 8.3 shows the schematic diagram of the coaxial nozzle, which consists of different parts for the passes of the laser beam, powder plus carrier gas, and shielding gas. Figure 8.4 shows the actual operation performed by the sprey nozzle which shows the laser beam to help in the deposition of powder over the substrate material and formed track of deposited material. It is a process where the powder is used as a direct deposition material that passes through a coaxial nozzle with a laser beam delivery system. The applied powders completely melt by the high-intensity laser beam. The nozzle also provides local inert atmosphere and allows oxidation-free

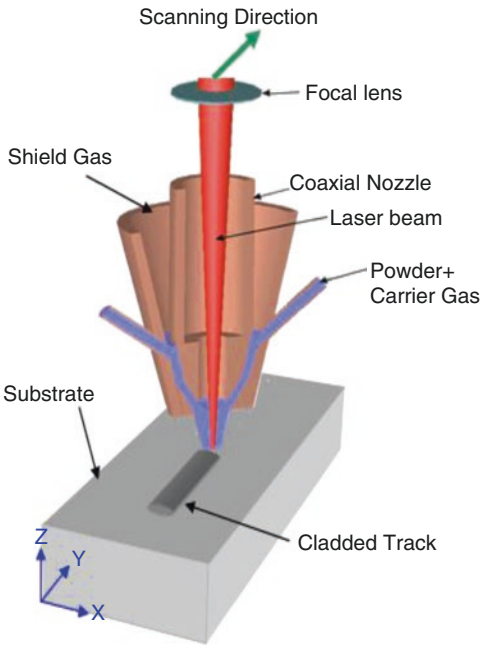

Fig. 8.3 Schematic diagram of the nozzle (Kheloufi and Amara 2008)

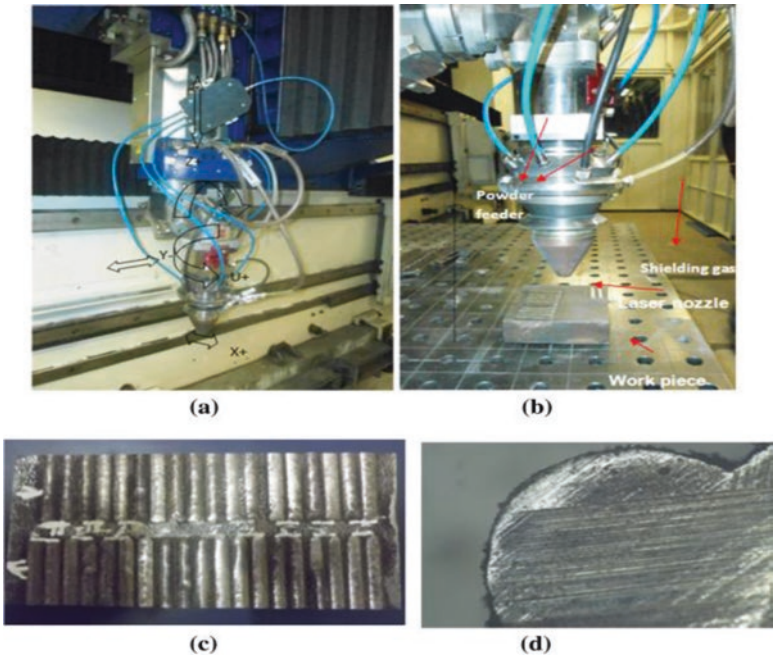

Fig. 8.4 Laser cladding operation forming track and cross section of clad (Kattire et al. 2015)

deposition. Coaxial nozzle optimizes the processing heat occure during the laser operation and quick set on the laser head that provides high protection to both clad and substrate, which allows a wide range of deposition of material without using shielding environment with high mass efficiency and low powder waste, mostly used in the industrial applications to generate 3D surface, repairing process, wear protection applications, etc.

8.3.3 Wire Feeding Technique

Laser cladding can also be done through the wire feeding technique, as shown in Fig. 8.5, which is the advanced version of the welding process which contains a high-power laser, deposition system, robot arm, and inert gas environment. The deposition tool mainly consists of an optical system from where the laser beam generated contains collimator, focusing lens, wire feeder, laser scanner, and process camera. The wire feeder is a self-regulator push–pull mechanism that is mounted on the nozzle to control the feed rate. The wire is melted by the laser beam and partially heated from the molten pool, and after the solidification process is over, the bead is generated. As shown in Fig. 8.5, the bead is deposited side by side with respect to the pattern forming a layer with the desired contour; the process is repeated for a

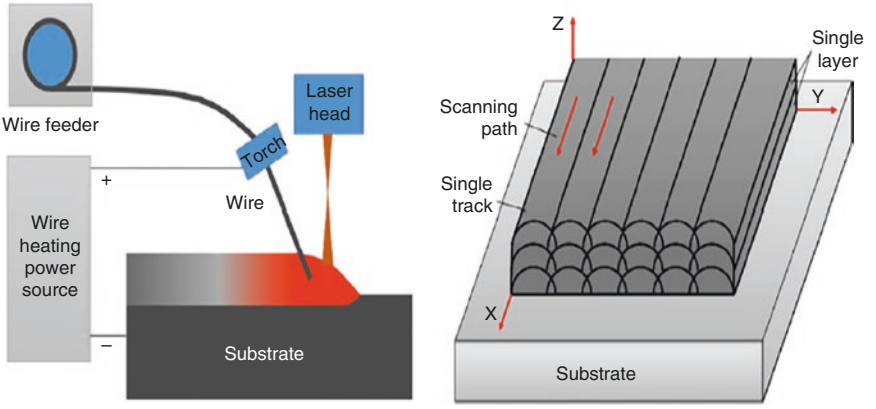

Fig. 8.5 Schematic diagram of wire feeding technique and deposition (Wei et al. 2018)

sufficient number of layers till the desired height with a flat surface is obtained. Preheating of wire is also carried out and then injected into the molten pool using argon gas as a shield to avoid oxidation.

However, in present day in order to overcome the process of wire feeding and preplaced technique, thermal spray technique has been developed, but the constraint is to develop proper shielding to overcome the oxidation that occurs; the thermal spray process is rarely used to replace the preplaced method of cladding due to the occurrence of high residual stress and difficulties in the characterization of the clad after machining process (Chi et al. 2018; Staia et al. 2000).

8.4 Effect of Process Parameter on Laser Cladding

8.4.1 Effect of Laser Power and Scanning Speed on the Clad

The process parameters in surface modification by the laser cladding technique are laser scanning speed, laser power, and spot diameter to get the desired mechanical properties of the clad. The amount of substrate material melted during the cladding process is one of the main factors that decide the quality of cladding which provides a good metallurgical bond between the substrate and powder material. Melting of substrate material should be properly controlled to minimize the dilution of the substrate material with reinforcement which may lead to degradation of the mechanical properties of clad formed (Li and Ma 1997). In the laser cladding process, the base material should just reach the melting temperature in order to make the bond with the clad, but practically it is not possible. So for the effective control of the substrate, melting process parameter is studied (Goodarzi et al. 2015). Among all the process parameters, laser power and scanning speed plays a vital role in laser cladding as shown in Fig. 8.6.

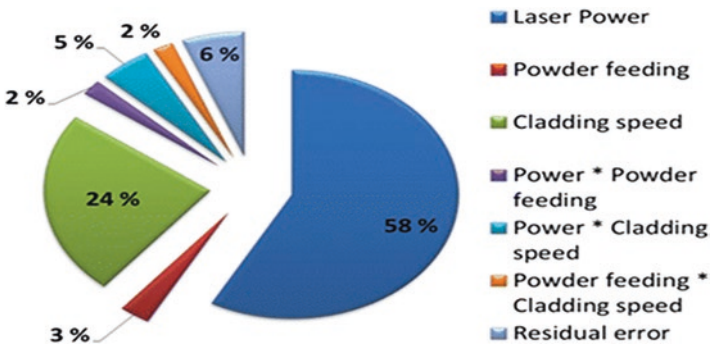

Fig. 8.6 Significance of process parameter in the cladding process (Goodarzi et al. 2017)

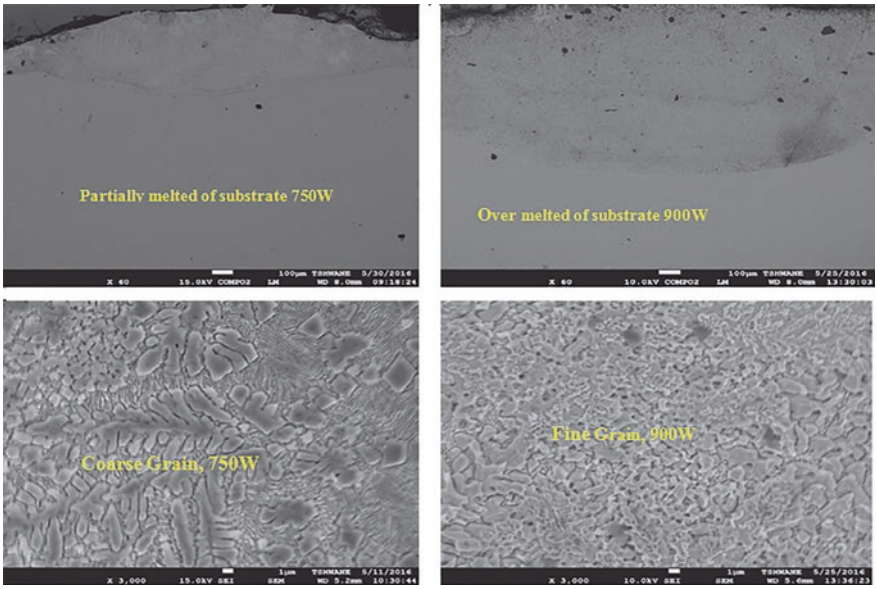

Fig. 8.7 Substrate melting and microstructure change with variation of laser power

The laser power plays an important role in the clad formation and depth of penetration beneath the substrate. At high laser power, depth of penetration is high, as the larger heat input melts more depth of the substrate and gives larger molten zone as well as grain structure changes from coarser to finer as the laser power increases, as shown in Fig. 8.7. If the laser power is not used in a controlled manner, the substrate will melt more which results in the high diffusion of substrate material to the powder material which reduces the clad quality (Adesina and Popoola 2017).

Apart from laser power, scanning speed is another important core-cladding parameter that affects the clad formation. At lower scanning speed, the laser spent more time over the cladding zone and hence resulted in over-melting or burning the

clad. On the other hand, if the scanning speed increases to a limit, the laser beam passes so quickly over the substrate that powder material will not fuse properly and poor bonding strength between the substrate and deposited materials is obtained. Since microstructure plays a vital role in the improvement of mechanical properties like hardness, wear resistance, and strength of the clad formed, the solidification process during the laser cladding depends on the scanning speed which ultimately leads to the formation of microstructure. At optimal scanning speed, the microstructure gets finer as compared to lower scanning speed; it might be due to a higher scanning speed. The cooling rate is high as a result of the formation of fine-grain structure and less prone to the formation of defects like pores and crack, which also leads to high wear resistance and significantly increased microhardness (Hemmati et al. 2011).

The cross section of the clad surface is shown in Fig. 8.8, which shows that a number of blocky particles are observed at different scanning speeds, and cellular dendrites are uniformly distributed over the clad zone; it is observed that with the increase in scanning speed, the size of reinforcement decreases gradually, and at higher scanning speed, the particles are fine and uniformly distributed over the clad. The microstructure of the coating significantly changed with the scanning speed or cooling rate, which improves the wear resistance properties of the clad.

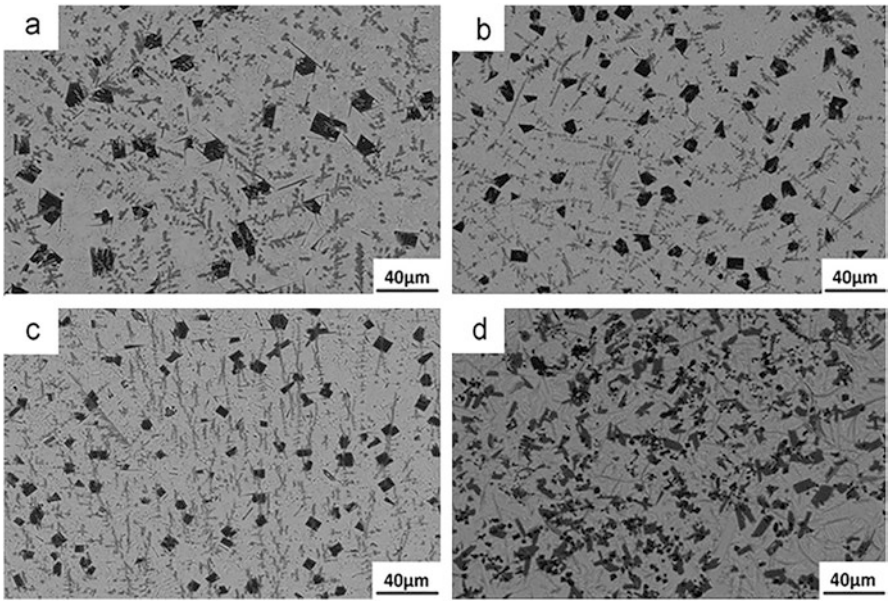

Fig. 8.8 SEM microscope image of the coatings at scanning speeds of (**a**) 5 mm/s, (**b**) 10 mm/s, (**c**) 15 mm/s, and (**d**) 20 mm/s (Chen et al. 2015)

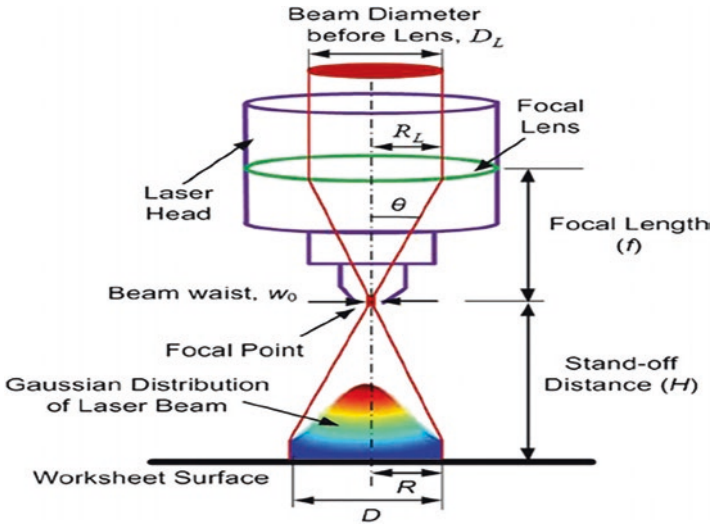

Fig. 8.9 Schematic diagram of laser beam profile (Kant et al. 2015)

8.4.2 Effect of Stand of Distance and Spot Diameter

Figure 8.9 shows the schematic diagram of the laser beam profile. It shows the different parameters associated with the beam profile, i.e., focal lens, laser head, focal length, standoff distance, Gaussian beam distribution, and a spot diameter of the laser beam. Standoff distance is the height above the workpiece surface to the beam waist (W_0), and spot diameter (D) is the base of the Gaussian profile as shown. Stand of distance and spot diameter play an important role in the formation of the clad surface to maintain a good correlation between the layer thickness and width of the clad track. The layer thickness (coating thickness) increases with increase in spot diameter and then decreases further because of a smaller diameter of beam leads to more energy concentrated and dilution rate enhanced and substrate become over-melt contrary as the diameter increases the powder material deposited more over the surface, and width of the clad track initially increases and then decreases with further increase in the spot diameter due to scattering. With the constant spot diameter, the standoff distance of the nozzle determines the mass concentration of powder over the substrate and geometrical dimension of the clad formation (Tan et al. 2018). Similarly, in the case of preplaced technique as the spot diameter increases to the desired limit, the energy got distributed and powder material did not fuse properly and scattered rather than melted.

8.5 Cladding Material System of Titanium Alloy

Materials used in cladding play a vital role in its durability, quality, and mechanical properties to withstand the working environment. On this basis, reinforcement is selected; it may be pure, binary, and composite depending on the application. A brief discussion of the deposition material system is presented below.

8.5.1 Pure Metal and Binary Alloy Coating with Titanium Alloy

This section is basically focused on the enhancement of the surface properties of titanium and its alloys by the addition of the pure titanium powder or the addition of one or two more metallic powders which improve the desired quality of the substrate. Initially, the cladding operation was performed with the addition of pure titanium powder over the surface, which is very much utilized for the repair in industrial application by the same material deposited over the titanium alloy without changing the mechanical properties (Nabhani et al. 2018). However, these are not a very significant enhancement of the hardness of the clad layer due to the same properties of the base material (Kistler et al. 2019). Apart from pure metal powder, the mixture of powders with different properties has been added to increase the mechanical properties of cladding, which helps in the formation of compounds like TiO2, Ni, TiN, Co, AlN, TiC, SiC, Ti-Ni, etc. These compounds lead to the enhancement of the multiple mechanical properties of the clad such as hardness, wear resistance, and corrosion resistance of the clad simultaneously. The formation of compounds like TiO_2, TiAl, TiNi, TiNi5ZrO2, and $TiNi10ZrO_2$ on the clad surface with dendrite and flower-like microstructure is shown in Fig. 8.10. This microstructure improves the hardness as well as wear resistance of the clad. The addition of aluminum in the clad results in the adhesion wear, but the presence of compound like ZrO2 and TiN leads to resist plastic deformation, which improves wear resistance (Sharman et al. 2018; Obadele et al. 2015a).

As titanium alloy fails to resist corrosion when it is subjected to several chemical attacks, cladding of Ti6Al4V powder on the Ti6Al4V substrate has been performed

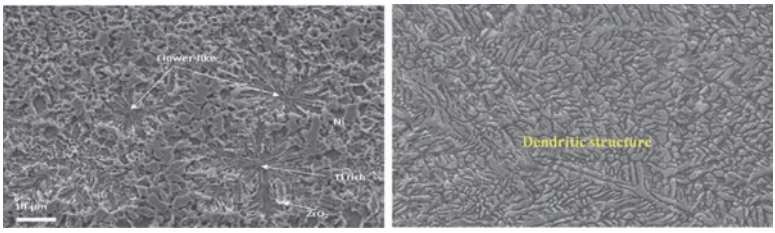

Fig. 8.10 Flower-like microstructure and dendrite structure

and tested with different chemicals like NaCl, H_2SO_4, and HCl. It is observed that corrosion resistance of the cladding samples increases remarkably in the case of NaCl and H_2SO_4 but decreases in the case of HCL (Atapour et al. 2010). Since microstructure plays an important role in the corrosion resistance of the clad material formed, because finer the grain structure of the clad formed enhanced the corrosion resistance, and vice versa in case of coarser grain. Laser cladding on the Ti6Al4v substrate with a pure commercial titanium powder clad was performed, which shows the improvement in the corrosion resistance of the clad (Obadele et al. 2015b). Phase transformation during the melting process in laser clading while selective melting of soft matrix and hard phase compound, which enable the substrate material to increases its hardness and strength simultaneously due to the formation of hard metallic compound which inhibit the grain refinement and grain growth form dendrite structure, improve the wear resistance of Ti6Al4V (Li et al. 2018). The microstructural in-homogeneity is the common problem found in the post-cladding process; so to overcome this, the homogeneity of the microstructure in the laser cladding of titanium alloy has been checked, which forms a martensitic structure that shows lower elastic module which increases with beneath of the clad in the form of lamellae structure, as shown in Fig. 8.11b (Cho et al. 2019). Nickel-based alloy cladding was performed which improves the hardness and the strength of the clad (Zhao et al. 2017). Since titanium and its alloys possess high tendency to get oxidized at high temperature which limits its use at high-temperature working environment, Liu et al. performed an experiment to study about the microstructure, phase constituents, solidification procedure, and oxidation morphology of the clad are investigated, and it has been found that β Ti phase, Ni3Ti phase, and Ni phase of the solidification process depend on the heat dissipation pattern, as shown in Fig. 8.11a. Heat is basically dissipated from the substrate; hence, solidification occurs at a high rate at the bottom of the molten zone, i.e., from the substrate to the top surface of the clad, solidification rate decreases (Liu et al. 2016).

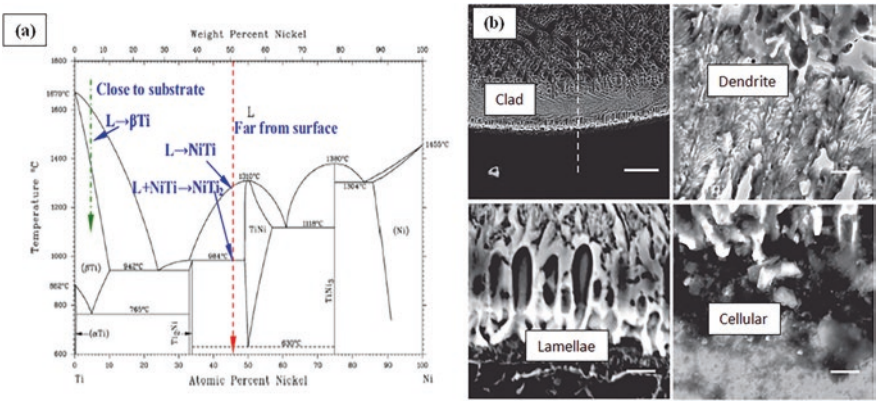

Fig. 8.11 (**a**) Phase transformation based on the binary phase diagram of Ti-Ni [Liu et al. 2016 (47)]; (**b**) cellular, lamellae, and dendrite structure (Liu et al. 2016)

In the case of pure, binary coating and unitary cladding, only the unique properties of the substrate are improved instead of enhancement in different mechanical properties simultaneously. Therefore, applications of composite coating are getting attention nowadays.

8.5.2 *Composite Cladding*

In laser composite cladding or the laser cladding of composite material where, two or more powder materials are mixed together to enhance and deposited over the substrate. In this regard, the composite coating of the mixture of Ti, TiC, and WS_2 was successfully done, and the formation of (Ti_2SC + TiS) compound enhances the tribological properties of titanium alloy (Zhai et al. 2017). Besides improvement in hardness of the clad, Wang et al. also improved the tribological behavior of the titanium alloy through the formation of (Ti, Zr) dendrites and (Ti, Zr) + TiFe + Zr_2Fe eutectic compound over the clad surface. It is seen that the addition of Zr improves the grain structure of clad (Wang and Dong 2015). The composite coating raises the wear resistance and hardness of the clad by the incorporation of hard metallic powder, such as TiC, WC, AlN, TiN, SiC, TiB_2, TiC, SiC, $NiTi_2$, and B_4C over the titanium alloy work surface [Zhao et al. 2017]. Since metals are subjected to high temperature region or in the extreme working environment where liquid lubrication did not work, so the material have been developed to become self lubricated. In order to enhance these phenomena of seld lubrication cladding are most advanced technique have been used now today, the mechanism behind, Self-lubricant wear resistance coatingare formed by the formation of chemical compound in the clad such as c-NiCrAlTi/TiC + TiWC2/CrS + Ti2CS Fe3Al, Ti3Al, and TiC (Li

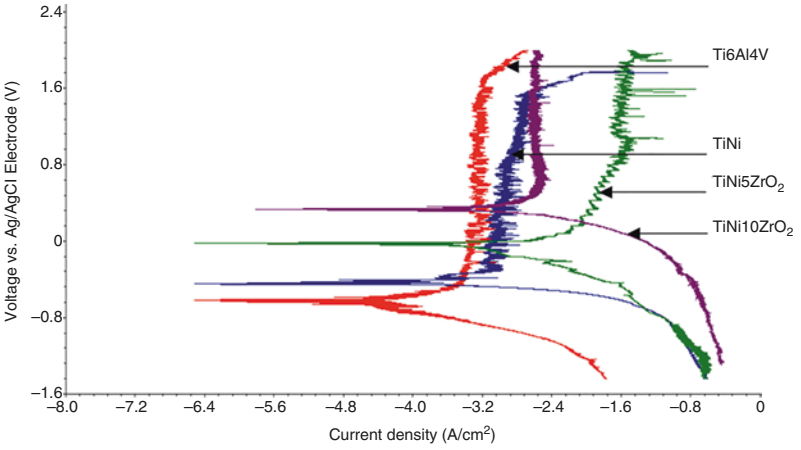

Fig. 8.12 Potentio-dynamic polarization curves for Ti6Al4V substrate, laser clad *TiNi* TiNi5ZrO_2, and TiNi10ZrO_2 composite coatings (Obadele et al. 2015c)

et al. 2013). The tribe corrosion and wear resistance coating have been formed when coated with nickel and zirconium and chromium-based powder clad over the titanium alloy to form the composite of TiNiZrO2, Ti2SC/CrS, and NiCr/Cr3C2 antiwear self-lubricating composite coating over Ti6Al4V alloy (Obadele et al. 2015c). Figure 8.12 shows the photodynamic polarization curve for the analysis of the corrosion resistance of different compounds of zirconium and nickel, which exhibit that corrosion resistance of the coating is higher as compared to the titanium substrate and lowest in case of $TiNi_3ZrO_2$. The composite structure of in situ TiN-TiB was synthesized using laser cladding. TiN nucleated and grew to the dendrite caused by rapid solidification, and the needle platelet with TiB is related to the crystal structure of TiB (B27) structure. TiB tends to grow on the surface of TiN, as shown in Fig. 8.13.

The composite cladding of Co + TiN on ti6al4v alloy has been fabricated for the study of the microhardness and wear resistance analysis. It explains the phase formation, solidification process, and energy distribution during the cladding process as shown in the figure. Figure 8.14a shows the initially added TiN in the cladding material, C (Co) and diluted Ti. At the time of the cladding process, TiN acquires energy and dissolves into Ti and N atom (Fig. 8.14b). In this case, small Ti particles melt properly and large Ti particles melt partially. Uniformly distributed dissolved atom is shown in Fig. c, and then TiN and TiC are formed, as shown in Fig. 8.14d. The undissolved TiN acted as the basement for the TiC growth in the molten pool, as shown in Fig. 8.14e. Further, TiN and TiC react to form phase TiC0.3 N0.7, as shown in Fig. 8.14f. Similarly, the corresponding Fig. 8.15 shows the elemental distribution at the clad surface for the confirmation of the phase formation TiC0.3 N0.7 (Weng et al. 2016).

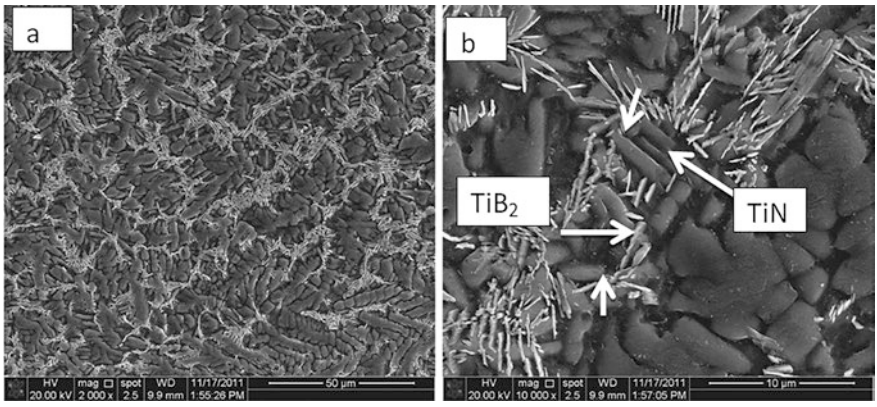

Fig. 8.13 Subsection image of laser clad etched in HF-HNO_3 solution with high solubility: (**a**) the clad microstructure at a low magnification and (**b**) the clad microstructure at a higher magnification

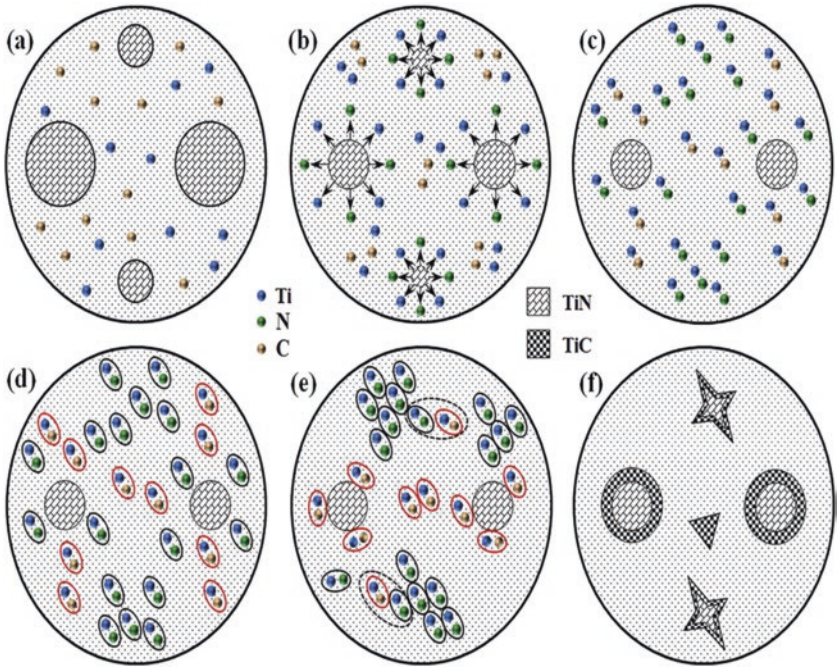

Fig. 8.14 The diagram illustration for the formation mechanism of *TiN* TiC and TiC0.3 N0.7 in the molten pool: (**a**) Ti, C atoms in the molten pool and the initially added TiN; (**b**) dissolution of TiN; (**c**) partially melted large TiN particles and the well-distributed Ti, N, and C atoms; (**d**) reaction between the atoms, forming TiN and TiC; (**e**) the growth of *TiN* TiC and the formation of TiC0.3 N0.7; (**f**) solidified matrix and the formed TiN- and TiC-reinforced phases (TiC0.3 N0.7 is not annotated here) (Weng et al. 2016)

8.5.3 Biocompatible Laser Cladding

This bare Ti6Al4V alloy will subject to corrosion; this phenomenon is called tribo-corrosion. To overcome this tribo-corrosion, Ti6Al4V is added with bioceramics like Ti and Al oxides (Al_2O_3). These bioceramics restrict diffusion of the metallic substrate. The lack of bioactivity leads to the effect of bone integration between implants and the surrounding tissue. Usually, metallic implants do not possess antibacterial capacity. To address these issues, an Ag-HA nanocomposite layer is prepared on Ti6Al4V using laser cladding by combining nanosilver and nano-hydroxyapatite powders. These nanocomposite additions show good bonding with Ti6Al4V and have good bioactivity along with antibacterial capability. Positively charged ions of Ag attach to negatively charged bacteria, which causes cell lysis and death, but higher Ag content may affect surrounding cells (Liu and Man 2017). Cao-SiO_2 cladding on Ti6Al4V and these coatings are obtained by using CeO_2 and Y_2O_3 as coating materials. The addition of CeO_2 and Y_2O_3 refined the microstructure of the ceramic layer. Compounds like $CaTiO_3$, CaO, α-Ca_2

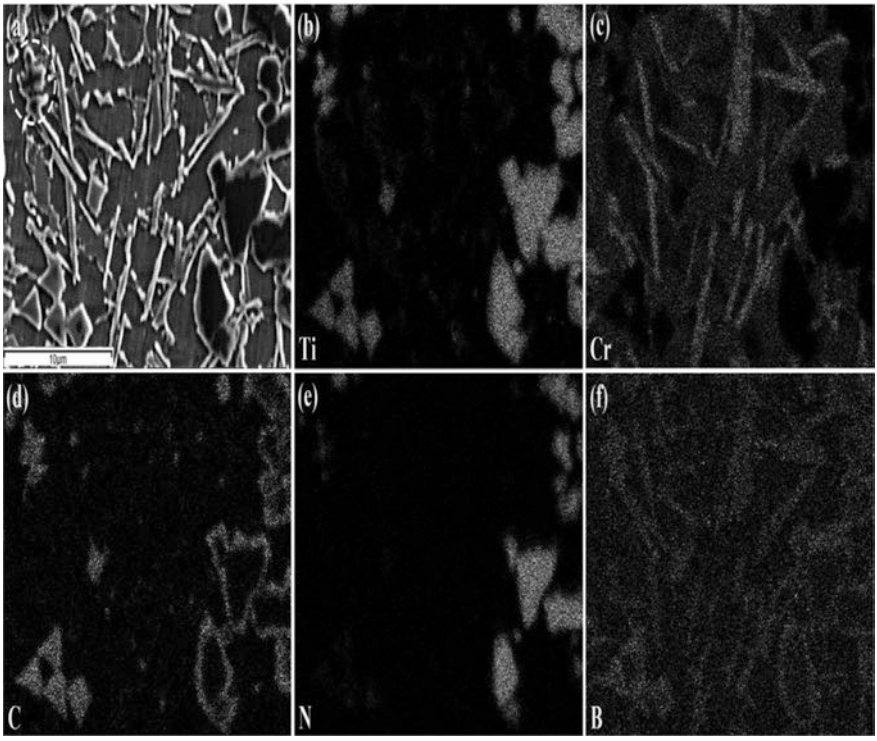

Fig. 8.15 SEM image and the corresponding elemental distributions of the typical microstructure in specimen corresponding to the formation mechanism of TiN, TiC and TiC0.3N0.7 (Weng et al. 2016)

(SiO_4), SiO_2, TiO2, and CaO are formed. The formation of glass ceramics like calcium phosphates leads to bone integration of implants enhanced and these improve the surface bioactivity and also with the addition of CeO_2 and Y_2O_3 degradation of metal is decreased (Li et al. 2015). In the cladding process, the common problem occurred: the detachment of coating from the substrate due to applied stress. Detachments lead to adverse effects on the body due to coating materials. Hence, to improve biocompatibility, a novel texture design is introduced. A line-shaped texture is created on Ti6Al4V with the help of Nd:YAG laser and subsequent laser sintering of hydroxyapatite powder on the substrate. The coating is nontoxic and showed improved living cell density on the coating surface and improved wear resistance and biocompatibility by the formation of the compound of Co-Cr-Mo on the alloy surface (Krishna et al. 2008). TiB-TiN reinforcements are synthesized during laser deposition of premixed BN with Ti6Al4V powder. These implants can be used as orthopedic implants due to their wear resistance, biocompatibility, and high stiffness which improved due to TiB-TiNm (Das et al. 2014). Bioceramic laser cladding of HA $CaTiO_3$, TiO_2, CaO, α-tricalcium phosphate, and β-tricalcium phosphate was produced on Ti6Al4V substrates by the addition of $CaHPO_4.2H_2O$ and $CaCO_3$

powders (Zheng et al. 2008) to improve bioactivity, tribological property, and antibacterial ability of Ti6Al4V. Ca-Si-based coatings are doped with copper particles. Ti6Al4V cladded with CaO, SiO_2, and Cu powder reinforcement to fabricate new phases consisting of Ca_2SiO_4, $CaTiO_3$, and Cu_2O, and these coatings form a sound metallurgical bond with the substrate. Since wetting plays a very important role when a biomaterial is implanted on the body or into the biological system, a clad with different amounts of Ca, SiO, and CaTiO was fabricated with varying scanning speed. By investigating the different coating, it is found that the relative amount of Ca and SiO phase increases with the decrease in the scanning speed. This is because of the increase in the contact angle of the body fluid solution which increases the wettability.

FTIR analysis as shown in Fig. 8.16 of the clad sample confirms the presence of the apatite-like phase on the surface of the clad which improves the in vitro biocompatibility on the textured sample as compared to ti6al4v substrate and improves the load-bearing capacity for the implant applications.

The in vitro biocompatibility of the sample was tested by the culture of the mouse MC3T3-E1 process. It studied the line spacing and appropriate phase on the biocompatibility of the coated sample; cell morphology after 1-day culture of MC3T3-E1 shows osteoblast-like cells are found in the structure. To overcome the traditional coating process, the direct metal deposition technique is effective in achieving good metallurgical bond with minimum dilution; HAP (Hydroxyapatite) was mixed together with Ti6Al4V powder to form a clad on the Ti6Al4V plate to

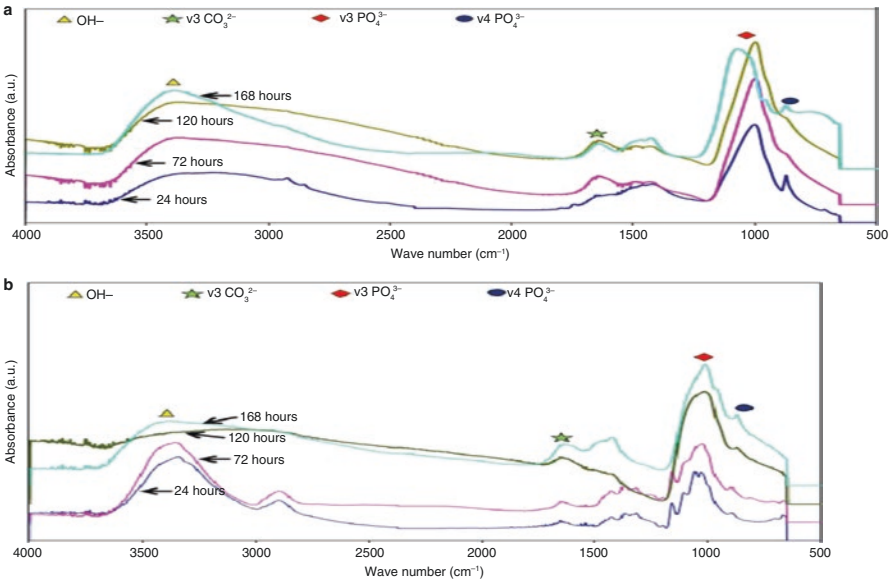

Fig. 8.16 FTIR spectra of laser processed samples: (**a**) 137 J cm-2, 100 lm line spacing, and (**b**) 137 J cm-2, 200 lm line spacing, and following immersion in SBF for different time periods (Paital et al. 2011)

improve the bio-implant capability. The microstructure, chemical composition, and bioactivities of the coated sample were studied; it was found that laser power has much influence on the evolving microstructure, the mechanical properties, and the existence of HAP on the surface of the coating. The higher metallurgical bond will reveal the long service life of the materials; the soak test was performed to study about the unmelted crystal of HAP. The CaP ratio conducted on the soaked coating was found to be 2.00 which shows the presence of tetracalcium phosphate.

In the process parameter which decides the morphology and density of the coated layer which demonstrate the appearance of the surface, since bioceramic cladding has good mechanical properties, in comparison with the bulk material, bioceramic coating has high-strength clad formed. Now, in addition of TCP in the reinforcement material improves the biocompatibility of the sample. HAP crystal was preserved in the coating as shown in the figure, and some HAP particle was not completely melted on the top surface, and some HAPs were in flake form which partially covered the oxidized layer, as shown in Fig. 8.17a. Figure 8.17b shows the best enlarged view of the HAP crystal which freely moves the phosphate ion during cladding. TTCP is one of the calcium phosphate materials which can be used for bone and teeth replacement (Paital et al. 2011).

8.5.4 Laser Cladding of Titanium with Rare Earth Element

In the process of laser cladding technique, different alloy and metal matrix composites can easily be formed which improves the mechanical properties of the clad; laser cladding has been applied on the titanium alloy to alter the properties of the titanium alloy. However, in almost all the cladding process, some voids, cracks, and

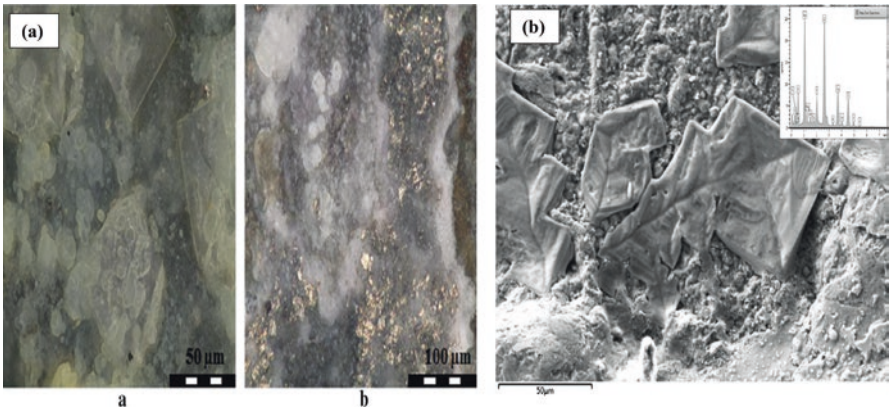

Fig. 8.17 (**a**) Micrograph of the HAP clad after soaking in Hanks' solution: (a) 750W laser power and (**b**) 1 kW laser power. (b) SEM-EDS of a 750Wclad after soaking in Hanks' solution (Paital et al. 2011)

other defects are found on the clad surface or in the interface zone which affect the properties of the clad and ultimately reduce the life span of the matrix formed. The rare earth materials such as cerium oxide, lanthanum oxide, niobium pentoxides, and ytterbium oxide are some of the elements that are widely used in laser cladding process to reduce the cracks and pore formation as well as to alter the microstructure of the clad which ultimately improves mechanical properties of the clad. Ni-based self-melting alloy powder with a small amount (2%) of La_2O_3 has been added to the titanium (TC4) alloy; the morphology, microstructure, and microhardness and friction properties have been studied and compared with and without rare earth elements. The additions of la2o3 La_2O_3 effectively improve the rate of laser irradiation. Larger numbers of Ti-rich phases are formed, and fine and uniform microstructure is observed on the clad surface, but the hardness and friction coefficient are found to be reduced due to excessive element diffusion from the TC matrix into the diffusion zone (Xinghua et al. 2017). The effect of La_2O_3 has been studied on the composite coating of NiCr-Cr_3C_2 powder on the TiAl alloy, which forms Cr_7C_3-TiC composite on the clad surface. With the comparison of la2o3 La_2O_3 and without additions of the rare earth element (La_2O_3), no crystallographic phase is formed on the clad except a high cooling rate which solidifies microstructure consisting of the primary hard Cr_7C_3 and TiC carbides and Cr_7C_3 eutectics distributed in the tough nickel solid solution matrix. Good finishing coatings can be achieved under a proper amount of the addition of La_2O_3 and suitable laser processing parameters. The additions of rare earth oxide La_2O_3 can refine and purify the microstructure of coatings, relatively decrease the volume fraction of primary blocky Cr_7C_3 to Cr_7C_3 eutectics, reduce the dilution of clad material from base alloy, and increase the microhardness of the coatings. When the addition of La_2O_3 is approximately 4 wt. %, the laser clad composite coating possesses the highest hardness and toughness. The composite coating with the addition of 4 wt. % La_2O_3 can result in the best enhancement of wear resistance of about 30%. However, the too little or excessive additional amount of La_2O_3 has no better influence on wear resistance of the composite coating. The refinement of the microstructure is beneficial to improve the hardness, strength, and toughness of the coatings. The purification and compactness of the coatings are in favor of the wear resistance. All the effects of La_2O_3 on microstructure and wear behaviors are mainly due to the inherent chemical and physical characteristics (Liu and Yu 2007). The addition of Y_2O_3 and its effect on the laser clad of Ti6Al4V substrate form a composite compound that contains TiC and TiB particles which are uniformly dispersed in the coarse cellular dendrite and interdendritic eutectic structure. However, the addition of Y_2O_3 refines the phase and improves the microstructural uniformity and increases the volume of TiC on the clad surface which improves the hardness as well as fracture toughness. From the analysis of dry sliding test, it has been observed that cladding with the addition of Y_2O_3 has excellent resistance to the micro-cutting and cracking. Analyses of the cross sections from the wear tracks revealed that the surface of the coating without Y_2O_3 was covered with many fine cracks which caused the de-bonding of the fragments from the surface of the coating. The wear mechanism of the coating with

Y_2O_3 was defined as oxidative wear. Measurement results of the worn mass loss and friction coefficient values further verified the positive effect of Y_2O_3 on the improvement of wear resistance (Liu et al. 2013). TiN reinforcement of composite coating was fabricated by laser cladding of Co42 self-fluxing alloy, TiN, and Y_2O_3 mixed powder composite on the ti6al4v alloy. The effect of rare earth compound Y_2O_3 has been investigated before and after the cladding process. γ-Co/Ni, TiN, Cosi, CoTi2, NiTi, TiC, Cr7C3, TiB, and TiC0.3 N0.7 phases are formed over the coatings improves metallurgical bonding free of pores and cracks with the substrate as well as mechanical strength of the clad. With the addition of 1.0 weight percentage of Y_2O_3 shows microstructure of the coating was refined significantly and hence the microhardness and dry sliding wear resistance of the clad enhanced due to were enhanced further. But also observed that the effects of Y_2O_3 were attributed to the residual Y_2O_3 and decomposed Y atoms and increase overall mechanical strength and quality of the clad surface.

Figure 8.18 shows the mechanism of Y_2O_3 in the grain refinement of TiN formation in the clad surface. The partial decomposition of Y and O atom and the addition of TiN dissolve into the molten pool (Fig. 8.18a). In the molten pool, the O atom reacts with B and Si in the self-fluxing alloy which forms a low-density oxidation product which is floating on the surface of the molten pool; thereafter, TiC was synthesized for the reformation of TiN (Fig. 8.18b). After that, TiC grew to form a core–shell structure (Fig. 8.18c). The TiN is restricted to these core–shell structures, and y atom is distributed in the interface zone (Weng et al. 2015a). The composite coating of YPSZ/CeO_2 on the clad surface and Fe3Al/Co42B + YPSZ/CeO_2 powder were synthesized successfully on the Ti6Al4V plate through laser cladding surface modification process which increases the wear resistance of the clad with the addition of TiC; the longevity of the molten pool decreased, leading to the decrease of

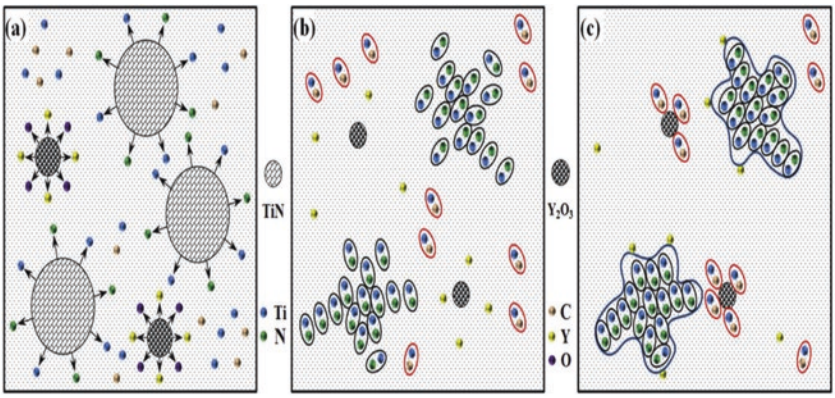

Fig. 8.18 The diagram illustration for the action mechanism of Y2O3: (**a**) dissolution of Y2O3 and TiN, (**b**) reformation of TiN and in situ formation of TiC, (**c**) growth of *TiN* TiC and the distribution of Y atoms

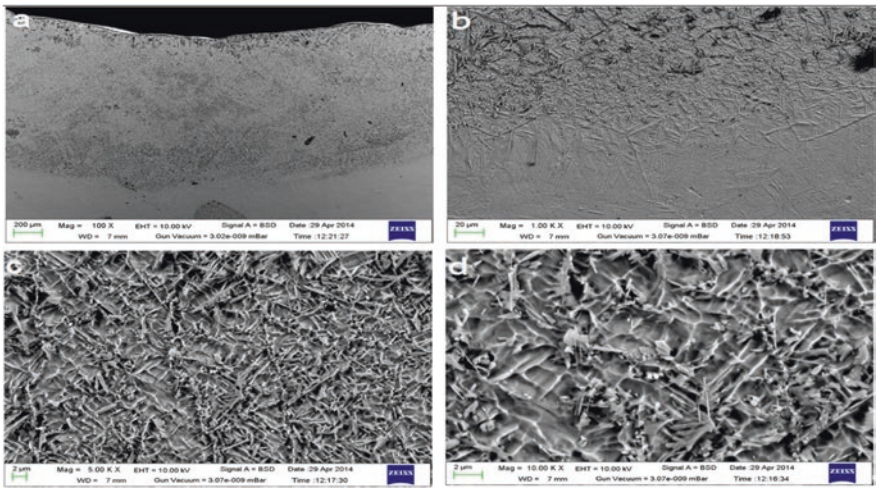

Fig. 8.19 FESEM microstructure in BSE mode of sample with the addition of Y2O3 (P-4200 W, V-10 mm/s) showing (**a**) full thickness of alloyed layer at magnification 100X, (**b**) substrate–alloyed layer interface at magnification 1000X, (**c**) middle portion of alloyed layer at lower magnification (5000X), and (**d**) middle portion of alloyed layer at higher magnification (10,000X)

growth time of the precipitates and the content of CuSi, TiNi, Ali, Ti3Al, and TiB phases (Li et al. 2012; Quazi et al. 2016). Rare earth oxide (Y_2O_3) is added to the mixture of Ti + SiC+h-BN to form different phases of TiN, TiB, Si3N4, Ti5Si3, BN, and Ti2N over the clad surface which improve the hardness up to two to three times as compared to substrate.

The interface zone and the microstructure of the clad are shown; it is visualized that with the addition of rare earth oxide Y_2O_3 at constant machining process parameter, microstructure is very fine compared to without the addition of rare earth, as shown in Fig. 8.19. This leads to improved mechanical properties as well as almost defect-free coated surface have been generated (Weng et al. 2015b).

8.6 Application and Development Tendency

8.6.1 Aerospace Application

Titanium is used in engine applications such as rotors, compressor blades, hydraulic system components, and nacelles. Titanium 6AL-4 V alloy accounts for almost 50% of all alloys used in aircraft applications. In fact, about two-thirds of all titanium metal produced is used in aircraft engines and frames.

8.6.2 Industrial Application

Due to their high tensile strength-to-density ratio, high corrosion resistance, and ability to withstand moderately high temperatures without creeping, titanium alloys are used in aircraft, armor plating, naval ships, spacecraft, and missiles.

8.6.3 Consumer and Architectural Applications

Titanium metal is used in automotive applications, particularly in automobile or motorcycle racing, where weight reduction is critical while maintaining high strength and rigidity. Titanium is used in many sporting goods: tennis rackets, golf clubs, lacrosse stick shafts, cricket, hockey, lacrosse and football helmet grills, and bicycle frames and components. Titanium alloys are also used in spectacle frames. The two most common titanium alloys used in the cycling industry are 6AL-4 V (grade 5) and 3AI-2.5 V (grade 9). These two different alloys are both high-strength titanium and fairly common in the industry.

8.6.4 Medical Applications

Because it is biocompatible (nontoxic and is not rejected by the body), titanium is used in different medical applications including surgical implements and implants, such as hip balls and sockets (joint replacement) that can stay in place for up to 20 years. Titanium has the inherent property to osseointegrate, enabling use in dental implants that can remain in place for over 30 years. This property is also useful for orthopedic implant applications. Titanium is also used for the surgical instruments in image-guided surgery, as well as wheelchairs, crutches, and any other products where high strength and low weight are desirable. The unique qualities of titanium also prove to be MRI (magnetic resonance imaging) and CT (computed tomography) compatible.

8.7 Current Research Trends and Scope of Future Work

Recent studies regarding the formation of a composite coating on the titanium alloy have principally localized on enhancing the hardness and abrasion wear resistance. From the literature review, it has been found that the composite of WC + NiCrBSi coating by laser surface engineering improves surface properties such as hardness and wear resistance of numerous engineering materials. However, the published work related to this cladding composite with high content of the WC ceramic on

titanium alloys is scarce. This high percentage of WC has not yet been studied reflecting the limitation of crack formation because of the tough titanium substrate. Furthermore, it is preferable to increase the wear resistance levels of Ti-6Al-4 V in order to extend its service life in applications such as aircraft turbine, engine components, aircraft structural components, etc. Ni-based alloys exhibit better high-temperature and wear and corrosion resistance properties. Because they are easier to bond to the substrate, they were selected with the hard ceramic WC. The challenge is to create a hard coating of crack-free, nonporous structure with a high level of hardness and abrasion wear resistance than that already achieved by other studies. At present, composite coating development is one of the best research areas in surface engineering applications. Nowadays, most of the research work areas are focused on improving the tribological properties of titanium by the use of different types of coating to get the desired mechanical and tribological properties. In the present scenario, the titanium alloy application has widely increased in the field of biomedical application. One of the major advantages of titanium alloy is having a high tissue affinity and good biocompatibility, but due to poor tribological and wear properties, lots of research are carried out to improve their properties and widen their biomedical application. In the laser cladding process, some voids, cracks, and other defects are found on the clad surface or in the interface zone which affects the properties of cladding which ultimately reduces the coating life of the matrix. To overcome this problem, the use of rare earth metal is currently investigated. Recently, with the development of metal matrix composites (MMCs), high-performance depositing composite coatings on low-grade substrate materials have become an interesting area of research. Particularly, various carbide-reinforced MMC coatings have been developed to modify wear and corrosion resistance. Metal matrix composites (MMCs) fortified with hard earthenware particles have gotten significant interest in light of the fact that they can offer enhanced quality, stiffness, and wear resistance contrasted with their counterparts. Nonetheless, poor strength of metal network composite forces a genuine limitation on the creation of the mass materials for auxiliary application. Then again, wear is a surface-subordinate debasement that may be enhanced by a suitable alteration of the small-scale structure and/or arrangement of the close surface locale. Henceforth, rather than the mass fortification, if a composite layer is produced on the close surface locale, it would upgrade the wear resistance property fundamentally without influencing the durability.

References

Abkowitz, S., Heussi, H. L., Ludwig, H. P., Rowell, D. M., & Kraus, S. A. (1990). U.S. Patent No. 4,968,348. Washington, DC: U.S. Patent and Trademark Office.

Adesina, O. S., & Popoola, A. P. I. (2017). A study on the influence of laser power on microstructural evolution and tribological functionality of metallic coatings deposited on Ti-6Al-4V alloy. *Tribology-Materials, Surfaces & Interfaces, 11*(3), 145–155. https://doi.org/10.1080/17515831.2017.1367150.

Atapour, M., Pilchak, A., Frankel, G. S., Williams, J. C., Fathi, M. H., & Shamanian, M. (2010). Corrosion behavior of Ti-6Al-4V with different thermomechanical treatments and microstructures. *Corrosion, 66*(6), 065004–065004. https://doi.org/10.5006/1.3452400.

Azevedo, C. R. F. (2003). Failure analysis of a commercially pure titanium plate for Osteosynthesis. *Engineering Failure Analysis, 10*, 153–164. https://doi.org/10.1016/S1350-6307(02)00067-5.

Chen, J. L., Li, J., Song, R., Bai, L. L., Shao, J. Z., & Qu, C. C. (2015). Effect of the scanning speed on microstructural evolution and wear behaviors of laser cladding NiCrBSi composite coatings. *Optics & Laser Technology, 72*, 86–99. https://doi.org/10.1016/j.optlastec.2015.03.015.

Chi, Y., Gu, G., Yu, H., & Chen, C. (2018). Laser surface alloying on aluminum and its alloys: A review. *Optics and Lasers in Engineering, 100*, 23–37. https://doi.org/10.1016/j.optlaseng.2017.07.006.

Cho, J. Y., Xu, W., Brandt, M., & Qian, M. (2019). Selective laser melting-fabricated Ti-6Al-4V alloy: Microstructural inhomogeneity, consequent variations in elastic modulus and implications. *Optics & Laser Technology, 111*, 664–670. https://doi.org/10.1016/j.optlastec.2018.08.052.

Dai, Z. D., Pan, S. C., Wang, M., Yang, S. R., Zhang, X. S., & Xue, Q. J. (1997). Improving the fretting Wear resistance of titanium alloy by laser beam quenching. *Wear, 213*, 135–139. https://doi.org/10.1016/S0043-1648(97)00160-9.

Das, M., Bhattacharya, K., Dittrick, S. A., Mandal, C., Balla, V. K., Kumar, T. S., et al. (2014). In situ synthesized TiB–TiN reinforced Ti6Al4V alloy composite coatings: Microstructure, tribological and in-vitro biocompatibility. *Journal of the Mechanical Behavior of Biomedical Materials, 29*, 259–271. https://doi.org/10.1016/j.jmbbm.2013.09.006.

Donachie, M. J. (2000). *Titanium: A technical guide*. Ohio: ASM international.

Everton, S. K., Hirsch, M., Stravroulakis, P., Leach, R. K., & Clare, A. T. (2016). Review of in-situ process monitoring and in-situ metrology for metal additive manufacturing. *Materials & Design, 95*, 431–445. https://doi.org/10.1016/j.matdes.2016.01.099.

Fu, Y. Q., & Batchelor, A. W. (1998). Laser Nitriding of pure titanium with Ni, Cr for improved wear performance. *Wear, 214*, 83–90. https://doi.org/10.1016/S0043-1648(97)00204-4.

Gnanamuthu, D. S. (1980). Laser surface treatment. *Optical Engineering, 19*(5), 195783. https://doi.org/10.1117/12.7972604.

Goodarzi, D. M., Pekkarinen, J., & Salminen, A. (2015). Effect of process parameters in laser cladding on substrate melted areas and the substrate melted shape. *Journal of Laser Applications, 27*(S2), S29201. https://doi.org/10.2351/1.4906376.

Goodarzi, D. M., Pekkarinen, J., & Salminen, A. (2017). Analysis of laser cladding process parameter influence on the clad bead geometry. *Welding in the World, 61*(5), 883–891. https://doi.org/10.1007/s40194-017-0495-0.

Guo, C., Zhou, J. S., Chen, J. M., Zhao, J. R., Yu, Y. J., & Zhou, H. D. (2010). Improvement of the oxidation and Wear resistance of pure Ti by laser cladding at elevated temperature. *Surface and Coating Technology, 205*, 2142–2151. https://doi.org/10.1007/s11249-011-9756-z.

Hemmati, I., Ocelík, V., & De Hosson, J. T. M. (2011). The effect of cladding speed on phase constitution and properties of AISI 431 stainless steel laser deposited coatings. *Surface and Coatings Technology, 205*(21–22), 5235–5239. https://doi.org/10.1016/j.surfcoat.2011.05.035.

Kant, R., Joshi, S. N., & Dixit, U. S. (2015). An integrated FEM-ANN model for laser bending process with inverse estimation of absorptivity. *Mechanics of Advanced Materials and Modern Processes, 1*(1), 6. https://doi.org/10.1186/s40759-015-0006-1.

Kattire, P., Paul, S., Singh, R., & Yan, W. (2015). Experimental characterization of laser cladding of CPM 9V on H13 tool steel for die repair applications. *Journal of Manufacturing Processes, 20*, 492–499. https://doi.org/10.1016/j.jmapro.2015.06.018.

Kheloufi, K., & Amara, E. H. (2008, September). A multiphase approach in numerical modeling of laser cladding process with coaxial powder injection. In *AIP conference proceedings* (vol. 1047, No. 1, pp. 172–175). AIP. https://doi.org/10.1063/1.2999928

Kistler, N. A., Corbin, D. J., Nassar, A. R., Reutzel, E. W., & Beese, A. M. (2019). Effect of processing conditions on the microstructure, porosity, and mechanical properties of Ti-6Al-4V repair fabricated by directed energy deposition. *Journal of Materials Processing Technology, 264*, 172–181. https://doi.org/10.1016/j.jmatprotec.2018.08.041.

Klocke, F., Brecher, C., Heinen, D., Rosen, C. J., & Breitbach, T. (2010). Flexible scanner-based laser surface treatment. *Physics Procedia, 5*, 467–475. https://doi.org/10.1016/j.phpro.2010.08.169.

Krishna, B. V., Xue, W., Bose, S., & Bandyopadhyay, A. (2008). Functionally graded Co–Cr–Mo coating on Ti–6Al–4V alloy structures. *Acta Biomaterialia, 4*(3), 697–706. https://doi.org/10.1016/j.actbio.2007.10.005.

Kumar, S., Mandal, A., Das, A. K., & Dixit, A. R. (2018). Parametric study and characterization of AlN-Ni-Ti6Al4V composite cladding on titanium alloy. *Surface and Coatings Technology, 349*, 37–49. https://doi.org/10.1016/j.surfcoat.2018.05.053.

Li, Y., & Ma, J. (1997). Study on overlapping in the laser cladding process. *Surface and Coatings Technology, 90*(1–2), 1–5. https://doi.org/10.1016/S0257-8972(96)03022-8.

Li, J., Chen, C., Wang, D., & Li, W. (2012). Microstructures and wear properties of YPSZ/CeO2 reinforced composites deposited by laser cladding. *Composites Part B: Engineering, 43*(3), 896–901. https://doi.org/10.1016/j.compositesb.2011.10.003.

Li, Y. J., Wu, N., Wei, S. Z., & Zheng, D. S. (2013). Improving the tribological properties of a titanium alloy by means of a Fe 3 Al/Ti 3 Al+ TiC laser-clad ceramic layer. *Lasers in Engineering* (Old City Publishing), p. 26.

Li, H. C., Wang, D. G., Chen, C. Z., & Weng, F. (2015). Effect of CeO2 and Y2O3 on microstructure, bioactivity and degradability of laser cladding CaO–SiO2 coating on titanium alloy. *Colloids and Surfaces B: Biointerfaces, 127*, 15–21. https://doi.org/10.1016/j.colsurfb.2015.01.016.

Li, W., Xu, P., Wang, Y., Zou, Y., Gong, H., & Lu, F. (2018). Laser synthesis and microstructure of micro-and nano-structured WC reinforced Co-based cladding layers on titanium alloy. *Journal of Alloys and Compounds, 749*, 10–22. https://doi.org/10.1016/j.jallcom.2018.03.235.

Liu, X., & Man, H. C. (2017). Laser fabrication of Ag-HA nanocomposites on Ti6Al4V implant for enhancing bioactivity and antibacterial capability. *Materials Science and Engineering: C, 70*, 1–8. https://doi.org/10.1016/j.msec.2016.08.059.

Liu, X. B., & Yu, R. L. (2007). Effects of La2O3 on microstructure and wear properties of laser clad γ/Cr7C3/TiC composite coatings on TiAl intermatallic alloy. *Materials Chemistry and Physics, 101*(2–3), 448–454. https://doi.org/10.1016/j.matchemphys.2006.08.013.

Liu, P., Li, H. X., & Zhang, Y. B. (2013). Effect of rare earth element (RE) oxides on diffusive behaviour and wear resistance of a laser clad TiC/TiB 2 reinforced coating on a Ti-3Al-2V alloy. *Lasers in Engineering* (Old City Publishing), p. 26.

Liu, F., Mao, Y., Lin, X., Zhou, B., & Qian, T. (2016). Microstructure and high temperature oxidation resistance of Ti-Ni gradient coating on TA2 titanium alloy fabricated by laser cladding. *Optics & Laser Technology, 83*, 140–147. https://doi.org/10.1016/j.optlastec.2016.04.005.

Mittal, K. L. (Ed.). (2004). *Polymer surface modification: Relevance to adhesion* (Vol. 3). Boca Raton: CRC Press.

Nabhani, M., Razavi, R. S., & Barekat, M. (2018). An empirical-statistical model for laser cladding of Ti-6Al-4V powder on Ti-6Al-4V substrate. *Optics & Laser Technology, 100*, 265–271. https://doi.org/10.1016/j.optlastec.2017.10.015.

Obadele, B. A., Andrews, A., Mathew, M. T., Olubambi, P. A., & Pityana, S. (2015a). Improving the tribocorrosion resistance of Ti6Al4V surface by laser surface cladding with TiNiZrO2 composite coating. *Applied Surface Science, 345*, 99–108. https://doi.org/10.1016/j.apsusc.2015.03.152.

Obadele, B. A., Olubambi, P. A., Andrews, A., Pityana, S., & Mathew, M. T. (2015b). Electrochemical behaviour of laser-clad Ti6Al4V with CP Ti in 0.1 M oxalic acid solution. *Journal of Alloys and Compounds, 646*, 753–759. https://doi.org/10.1016/j.jallcom.2015.06.079.

Obadele, B. A., Andrews, A., Mathew, M. T., Olubambi, P. A., & Pityana, S. (2015c). Improving the tribocorrosion resistance of Ti6Al4V surface by laser surface cladding with TiNiZrO2 composite coating. *Applied Surface Science, 345*, 99–108. https://doi.org/10.1016/j.apsusc.2015.03.152.

Paital, S. R., Bunce, N., Nandwana, P., Honrao, C., Nag, S., He, W., & Dahotre, N. B. (2011). Laser surface modification for synthesis of textured bioactive and biocompatible Ca–P coatings on

Ti–6Al–4V. *Journal of Materials Science: Materials in Medicine, 22*(6), 1393–1406. https://doi.org/10.1007/s10856-011-4321-8.

Quazi, M. M., Fazal, M. A., Haseeb, A. S. M. A., Yusof, F., Masjuki, H. H., & Arslan, A. (2016). Effect of rare earth elements and their oxides on tribo-mechanical performance of laser claddings: A review. *Journal of Rare Earths, 34*(6), 549–564. https://doi.org/10.1016/S1002-0721(16)60061-3.

Sharman, A. R. C., Hughes, J. I., & Ridgway, K. (2018). Characterisation of titanium aluminide components manufactured by laser metal deposition. *Intermetallics, 93*, 89–92. https://doi.org/10.1016/j.intermet.2017.11.013.

Staia, M. H., Cruz, M., & Dahotre, N. B. (2000). Microstructural and Tribological characterization of an A-356 aluminum alloy superficially modified by laser alloying. *Thin Solid Films, 377*, 665–674. https://doi.org/10.1016/S0040-6090(00)01448-6.

Suarez-Fernandez, M. B., Soldado, A. B., Sanz-Medel, A., Vega, J. A., Novelli, A., & Fernandez-Sanchez, M. T. (1999). Aluminum-induced degeneration of astrocytes occurs via apoptosis and results in neuronal death. *Brain Research, 835*, 125–136. https://doi.org/10.1016/S0006-8993(99)01536-X.

Tan, H., Luo, Z., Li, Y., Yan, F., Duan, R., & Huang, Y. (2015). Effect of strengthening particles on the dry sliding wear behavior of Al2O3–M7C3/Fe metal matrix composite coatings produced by laser cladding. *Wear, 324*, 36–44. https://doi.org/10.1016/j.wear.2014.11.023.

Tan, H., Shang, W., Zhang, F., Clare, A. T., Lin, X., Chen, J., & Huang, W. (2018). Process mechanisms based on powder flow spatial distribution in direct metal deposition. *Journal of Materials Processing Technology, 254*, 361–372. https://doi.org/10.1016/j.jmatprotec.2017.11.026.

Tian, Y. S., Chen, C. Z., Li, S. T., & Huo, Q. H. (2005). Research progress on laser surface modification of titanium alloys. *Applied Surface Science, 242*(1–2), 177–184. https://doi.org/10.1016/j.apsusc.2004.08.011.

Wang, C., & Dong, C. (2015). Design and laser cladding of Ti–Fe–Zr alloy coatings. *Materials Today Communications, 3*, 43–51. https://doi.org/10.1016/j.mtcomm.2015.02.005.

Wei, S., Wang, G., Shin, Y. C., & Rong, Y. (2018). Comprehensive modelings of transport phenomena in laser hot-wire deposition process. *International Journal of Heat and Mass Transfer, 125*, 1356–1368. https://doi.org/10.1016/j.ijheatmasstransfer.2018.04.164.

Weng, F., Chen, C., & Yu, H. (2014). Research status of laser cladding on titanium and its alloys: A review. *Materials & Design, 58*, 412–425. https://doi.org/10.1016/j.matdes.2014.01.077.

Weng, F., Yu, H., Chen, C., Liu, J., & Zhao, L. (2015a). Microstructures and properties of TiN reinforced co-based composite coatings modified with Y2O3 by laser cladding on Ti–6Al–4V alloy. *Journal of Alloys and Compounds, 650*, 178–184. https://doi.org/10.1016/j.jallcom.2015.07.295.

Weng, F., Yu, H., Chen, C., Liu, J., & Zhao, L. (2015b). Microstructures and properties of TiN reinforced Co-based composite coatings modified with Y2O3 by laser cladding on Ti–6Al–4V alloy. *Journal of Alloys and Compounds, 650*, 178–184. https://doi.org/10.1016/j.jallcom.2015.07.295.

Weng, F., Yu, H., Chen, C., Liu, J., Zhao, L., & Dai, J. (2016). Microstructure and property of composite coatings on titanium alloy deposited by laser cladding with Co42+ TiN mixed powders. *Journal of Alloys and Compounds, 686*, 74–81. https://doi.org/10.1016/j.jallcom.2016.05.319.

Xinghua, H., Xiaojing, X., Xiaolan, G., Jun, T., Yiying, Z., Qinghui, L., & Guilan, W. (2017). F101 Ni-based coating containing La2O3 by laser cladding on TC4 titanium alloy. *Rare Metal Materials and Engineering, 46*(4), 1074–1079.

Zhai, Y. J., Liu, X. B., Qiao, S. J., Wang, M. D., Lu, X. L., Wang, Y. G., et al. (2017). Characteristics of laser clad α-Ti/TiC+ (Ti, W) C1− x/Ti2SC+ TiS composite coatings on TA2 titanium alloy. *Optics & Laser Technology, 89*, 97–107. https://doi.org/10.1016/j.optlastec.2016.09.044.

Zhao, W., Zha, G. C., Kong, F. X., Wu, M. L., Feng, X., & Gao, S. Y. (2017). Strengthening effect of incremental shear deformation on Ti alloy clad plate with a Ni-based alloy laser-clad

layer. *Journal of Materials Engineering and Performance, 26*(5), 2411–2416. https://doi.org/10.1007/s11665-017-2615-9.

Zheng, M., Fan, D., Li, X. K., Li, W. F., Liu, Q. B., & Zhang, J. B. (2008). Microstructure and osteoblast response of gradient bioceramic coating on titanium alloy fabricated by laser cladding. *Applied Surface Science, 255*(2), 426–428. https://doi.org/10.1016/j.apsusc.2008.06.078.

Chapter 9
Improving Wear and Corrosion Performance of AISI 316L Stainless Steel Substrate in Liquid Zinc by MoB/CoCr and MoB/CoTi Gas Tungsten Arc Clad Composite Coatings

Hosein Ziaei, Zeinab Marfavi, Behzad Sadeghi, and Pasquale Cavaliere

9.1 Introduction

The most common problem in galvanizing industries is failures of pot hardware facilities; the following three issues are the main contributors for these failures: (1) wear of supporting bearings in the stabilizer rolls and sink rolls, (2) corrosion of hardware facilities in molten zinc bath, and (3) the nucleation and presence of intermetallic compounds formed on the surface of rolls (Liu et al. 2005). Submerged pot hardware is not only exposed to friction by strip, rollers, and severe wear due to rotation of zinc liquid, but it is also contaminated by molten zinc experiencing friction and corrosion. These facilities lose their surface quality, and the liquid zinc gets polluted and results in reduction in quality of galvanized sheets. Due to these reasons, sink rolls have to be frequently replaced (Ren et al. 2007). Galvanizers must periodically stop continuous galvanizing lines (CGLs) to replace hardware components, resulting in significant economic losses with unplanned stoppages. Prolonging lifetime of hot-dip galvanizing equipment is a pivotal issue in these industries which would result in a decrease in frequency of line shutdowns and save lots of energy and costs for steel manufacturing factories (Yamaguchi and Hisamatsu 1979).

Methods such as thermal spraying and plasma spraying have been largely investigated, and they were able to increase the lifetime of sink rolls, but they have some

H. Ziaei · B. Sadeghi
State Key Laboratory of Metal Matrix Composites, School of Materials Science and Engineering, Shanghai Jiao Tong University, Shanghai, People's Republic of China
e-mail: b.sadeghi@sjtu.edu.cn

Z. Marfavi
Department of Material Engineering, Isfahan University of Technology, Isfahan, Iran

P. Cavaliere (✉)
Department of Innovation Engineering, University of Salento, Lecce, Italy
e-mail: Pasquale.cavaliere@unisalento.it

P. Cavaliere (ed.), *Laser Cladding of Metals*,
https://doi.org/10.1007/978-3-030-53195-9_9

weaknesses such as limitation in thickness of the coating, presence of porosities, and crack formation which would finally lead to downtime of sink rolls. Inevitably sprayed MMC coatings are accompanied by microgalvanic and interfacial corrosion mechanisms as well as porosity. Consequently, the method to improve the surface wear and corrosion resistance of steels by gas tungsten arc cladding (GTAC) grabs lots of attention. The gas tungsten arc cladding is a low-cost and widely accepted surface alloying industrial process and can be easily applied on industrial scale. Furthermore, fast processing speed, relative cleanliness, high heating/cooling rate, and high solidification velocity are some of the advantages (Majumdar et al. 2009; Gholipour et al. 2011). Gas tungsten arc cladding provides much higher thickness of coatings, in the range of a few mm which is thicker than coating prepared by other methods such as HVOF which is in micrometer scale. Mostly, coatings which are deposited by this method provide a wide range of materials such as metals or intermetallic compound with hardening additive which helps the substrate to have better performance during its application. This method is also able to deposit coatings on complex shapes with different dimensions. The main role of welding is fusion and mixing of the coating with sublayer and establishing strong bond between substrate and coating.

Materials can be classified into two groups, namely, soluble and insoluble materials in molten zinc. Soluble materials get wet in molten zinc, and the main reason for their failure is melting corrosion, while insoluble materials do not make solid solution in their phase diagram with zinc (Ma et al. 2011). To be more specific, they are not wettable with molten zinc (Yan et al. 2012). The main reason for failure of insoluble materials is reported to be pit corrosion or cracks (Zhang et al. 2013).

Insoluble materials such as Mo-W and Fe-B intermetallic compounds can suppress the penetration of zinc, but the problem is that they have poor shock resistance, or they are as much as expensive that they are not practically usable for industrial usage. Many researches had been devoted to investigate performance of different types of steels in zinc bath and revealed that all stainless steels were aggressively attacked by liquid zinc. However, austenitic stainless steel outperformed martensitic stainless steel, which, in turn, performed better than low-carbon steel (Zhang and Battiston 2002).

AISI 316 stainless steel is widely used in stabilizer and sink roll as base metal in zinc baths because of its high corrosion resistance, processability, and low cost. Co-based superalloys such as Stellite 6 and Tribaloys were common materials in submerged facilities such as sleeve and bush materials in continuous hot-dip galvanizing where wear performance is fundamental. While Stellite 6 strengthening is due to its carbides, Tribaloys get their superior wear resistance relying on a large percentage of a hard intermetallic Laves phase dispersed in a cobalt solid solution (Halstead and Rawlings 1985). Besides, the efficiency of WC/Co coatings prepared by HVOF spraying had been investigated and proved they show better performance in molten zinc, due to the presence of W_3C and Co_6W_6C in their composition (Tomita et al. 1993).

MoB/CoCr is a cermet material which had been deposited by thermal spraying for usage in galvanizing bath outperforming WC/Co coatings; however, problems

such as high thermal expansion coefficient, high brittleness, and defects such as cracks in coatings would accelerate the zinc penetration. High temperatures of the molten zinc bath and severe wearing condition shorten service life of these facilities and increase the need of designing and proposing appropriate materials or coating for better performance under this circumstance. Hence, the aim of this study is to compare the potential of MoB/CoCr and MoB/CoTi deposited on 316L stainless steel substrate through GTAC for being used in zinc bath plating line. As well as investigating corrosion resistance of coatings in molten zinc, their wear behavior at 480 °C and room temperature was also examined.

9.2 Experimental Procedure

Powders with purity over 99% from German Merck company were used. Sizes of powders are listed in Table 9.1.

The composition of two clads, namely, Cr-Clad and Ti-Clad, and also the composition of substrate are reported in Table 9.2. Stainless steel 316 L stripes were used as substrate with 20 mm thickness in 50 × 100 mm size.

For preparing coatings, 150 g of each coating mixture was mixed in a high-energy mixing machine PM-100 Ritch model. The container was made of high chromium steel, and ten balls made of grade 52,100 steel with 20 mm diameter were used in the mixing machine to obtain uniform mixture. The milling process was applied with 200 rpm speed and ball to powders 5:1 weight ratio for 2 h. Before applying coatings on the stainless steel substrate, surface of substrates was cleaned completely by means of acetone. The coating mixture powders were deposited on the surface through gum tragacanth, and thickness of dough was 3 mm. Samples were heated in the oven up to 100 °C in order to dry the dough and help the vaporization of its water for further cladding process.

For applying coatings on the substrate, the gas tungsten arc welding was employed with nonconsumable electrode with 3.2 mm diameter which contained 2% thorium. Preventing the oxidation of the samples and decreasing the porosity, the argon gas with 99.99% was flowed over the sample during cladding. Cladding parameters are reported in Table 9.3.

Table 9.1 Dimensions of the employed powders

Powder	Average size (μm)
Mo	<30
Cr	<63
Co	<10
Ti	<63
B	<10

Table 9.2 Chemical composition of substrate and coatings (wt.%)

	C	Mn	Si	P	S	Ni	N	Mo	Co	B	Cr	Ti
Substrate	0.03	2	0.75	0.045	0.03	13	0.1	3			18	
Cr-clad								50	22	8	20	
Ti-clad								50	22	8		20

Table 9.3 GTAC parameters

Parameters	Cr-clad	Ti-clad
Argon flow (l/min)	8	8
Voltage	22	22
Electrode diameter (mm)	3.2	3.2
Electrode polarity	DC	DC
Current (A)	160	185
Speed (cm/min)	1.2×10^{-3}	7.2×10^{-4}

Phase characterization was investigated through X-ray diffraction analysis with a Philips MPD-XPERT model with Cu Kα beam λ = 1.542 A˚. The microstructural characterization of the coatings was performed by means of optical microscopy and scanning electron microscopy with a Philips XL30 model equipped by energy dispersive X-ray for chemical analyzing. Specimens were prepared by grinding with grit papers from 80 to 2400 and then polished with abrasive cloth plus 0.5 μm alumina powder. The electroetching was performed with 6v voltage and 10% oxalate solution used for coatings, and for the base metal, the solution was a mixture of 12% hydrochloric acid, 9% nitric acid, and 79% distilled water.

Wear resistance tests were performed through pin on disk tests at ambient temperature and at 480 °C which is the temperature of galvanization bath that coatings are supposed to work. Disks were made from steel grade 52,100 with 50 mm diameter after getting uniform smooth surface through magnetic polishing; samples experienced heat treatment in order to obtain the 900 Vickers hardness. Disks were annealed at 920 °C for 1 h and quenched in oil.

Pin samples were cut out from the cladded samples and the base metal. All the tests were applied for three groups of samples Cr-Clad, Ti-Clad, and base metal. Regarding the ASTM G99 standard, three different forces 35, 50, and 65 N were applied at 100 rpm speed and humidity was 30%. During test, the pin specimen was kept stationary while the circular disk was rotating. All the parameters were kept stable for tests at both ambient temperature and 480 °C. Hardness of coatings was defined according to ASTM-E384 standard with 30 N force and 10 s. For each sample, measurement was repeated five times, and the average quantity is reported. For investigating the corrosion resistance of coatings and diffusion of zinc into them, five cylindrical samples with 30 mm diameter were cut out from coatings and base metal (totally 15 samples). Samples were immersed in three different ceramic containers filled with 99% zinc liquid and kept in induction furnace after various test durations 120, 240, 360, 720, and 840 h. One sample was retrieved after mentioned times from each container for further investigation by scanning electron microscopy and EDS examination.

9.3 Results and Discussion

Morphology and size of the employed powders have direct influence on the quality of coatings; the SEM micrograph and EDS analyses of the powders are shown in Fig. 9.1 and Table 9.4, respectively. From EDS results, it can be seen that powders are uniformly mixed; however, the boron powders due to their small size are not recognizable with SEM, but boride phases which are detected by XRD are a proof for the presence of boron in the coatings.

Considering XRD pattern and EDS results in Fig. 9.2, it was found that double boride phases such as $CoMo_2B_2$, CoMoB, and Mo_2B and single boride phases are formed in Mo-rich solid solution. Besides, phases such as FeCrC carbides are formed in Cr-Clad in Co-rich regions. XRD pattern for Ti-Clad shows the existence of oxides such as TiO and TiO_2 which probably were formed during cladding process due to interaction between Ti and oxygen. Intermetallic compounds such Co_3Ti and NiTi were formed in Ti-Clad too.

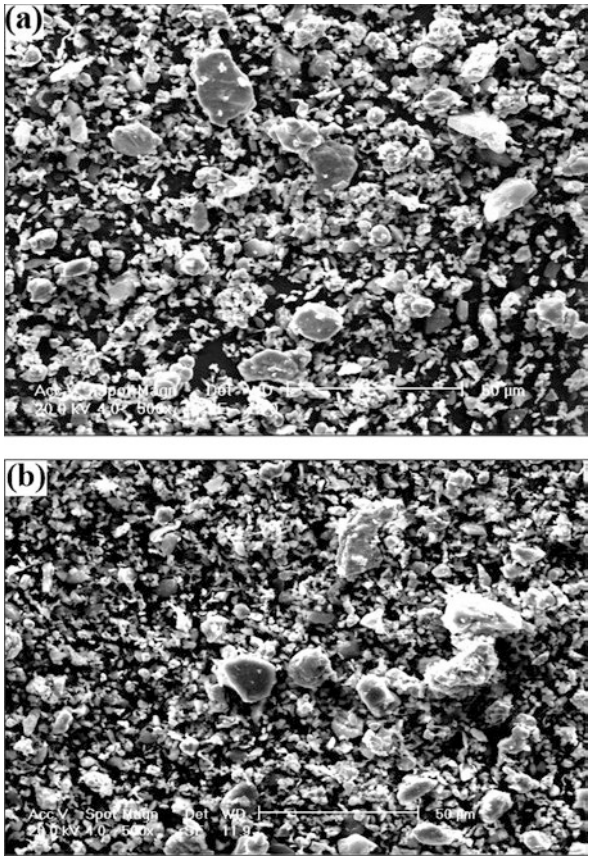

Fig. 9.1 SEM micrograph of (**a**) Cr-Clad powders (**b**) Ti-Clad powders

Table 9.4 Powder composition after mixing (wt. %)

	Mo	Co	Cr	Ti	B
Cr-clad	50	24.4	22.3		
Ti-clad	30.9	30.2		19.8	

Surface and transverse sections of base metal and coatings were investigated by means of scanning electron microscope and optical microscope as shown in Figs. 9.3 and 9.4.

In Cr-Clad transverse section, as the distance from the interface increases, a region of equiaxed grains was observed. By moving closer to the surface of the coating, dendrite structure is pervasive as well as top surface which is covered by dendrite microstructure. In addition, it was observed that at substrate/Cr-Clad interface, the grains choose epitaxial growth and planar growth toward the coating. This type of growth is likely happening in similar metal cladding. In this type, grain boundaries start to form from the boundaries of base metal and then grow perpendicular to the weld interface into the weld pool. The main reason for epitaxial growth is similarities in crystal structure and chemical composition. Considering EDS results reported in Table 9.5, it is clear that dendrites are mostly enriched with Mo and B which according to XRD results are double boride phases and interdendritic region is a solid solution rich in Fe and Co.

In Ti-Clad micrographs (Fig. 9.3), gray area (A) is a solid solution rich in Mo and Fe. Higher concentration of Fe is due to higher current in GTAC process which resulted in diffusion of Fe from sublayer to the coating. Brighter regions (B) according to XRD and EDS results contain titanium oxides such as TiO2 and TiO.

In gas tungsten arc welding process, the geometry and displacement of welding nozzle leads to nonuniform temperatures in melting bath and Marangoni movements (Xu et al. 2014). These features result in different thermal gradients, and consequently there would be a variety of cooling rates. The different microstructure from top surface of the coating to substrate is due to these different heating and cooling rates. Regarding the solidification theory, the morphology of solidified structure is controlled by the stabilizing factor between solid and liquid interfaces (G/R) where G means temperature gradient and R shows the solidification rate. Equation 9.1 compares the (G/R) ratio for interface substrate/coating interface (center line) and on top of the coating (fusion line), as described in Eq. (9.1).

$$\left(\frac{G}{R}\right)_{\text{center line}} \ll \left(\frac{G}{R}\right)_{\text{fusion line}} \tag{9.1}$$

Consequently, the solidification structure changes from the dendrite structure to cellular from the surface to the interface throughout the melt zone (Kou 2003).

Line scanning was applied to investigate the uniformity of alloying elements in coatings, as shown in Fig. 9.5.

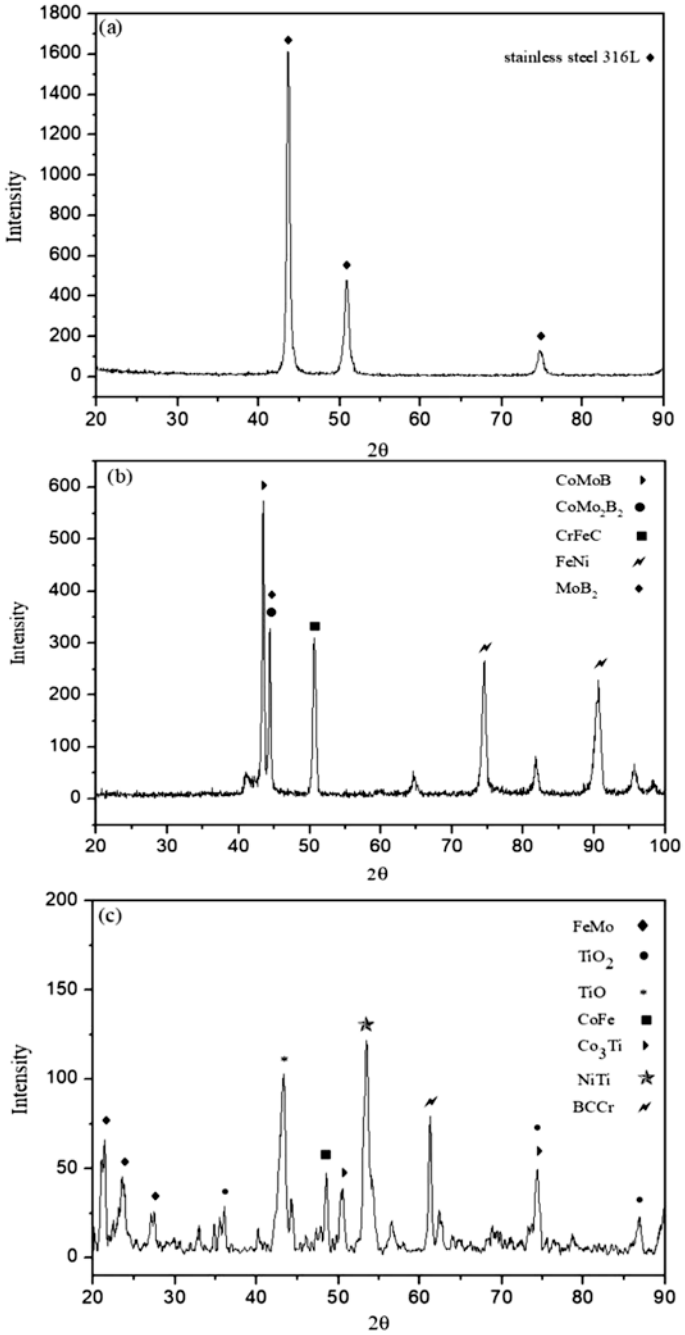

Fig. 9.2 XRD pattern obtained from (**a**) base metal, (**b**) Cr-Clad, and (**c**) Ti-Clad

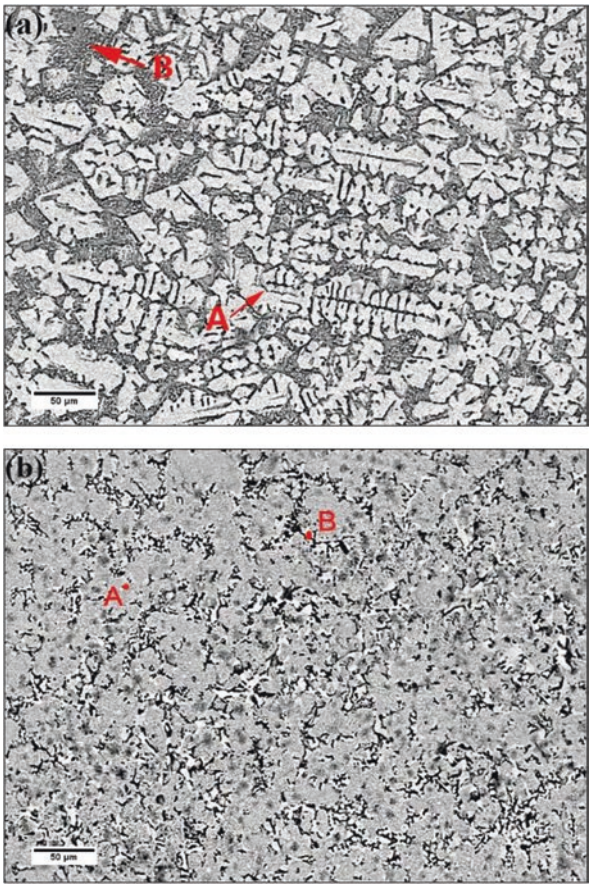

Fig. 9.3 SEM micrographs of (**a**) Cr-Clad (**b**) Ti-Clad

The distribution of substrate elements, especially Fe, in the coatings was observed, and uniform distribution of alloying elements in the coating was proved. Dilution of sublayer elements such as Fe and Ni results in higher toughness and better corrosion resistance but a decrease in hardness (Lin and Chen 2006; Asphahani et al. 1987). According to the hardness measurements of Table 9.6, the lower hardness of Ti-Clad also can be attributed to higher dilution of Fe from substrate to Ti-Clad. The main reason for hardness increment in coatings is solution strength and the presence of phases such as intermetallic compounds, borides, and carbides reported in XRD result (Fig. 9.2). Another important factor is high cooling rate during cladding which led to finer structure especially for Cr-Clad which has the highest hardness.

Microhardness profile of coatings (Fig. 9.6) revealed that due to finer size of grains near surface of the coatings, the microhardness for both coatings decreases by increment in distance from surface to the coating/substrate interface.

Higher cooling rate on the surface of weld bath during cladding process mostly results in finer structure and consequently higher hardness at top surface. Besides,

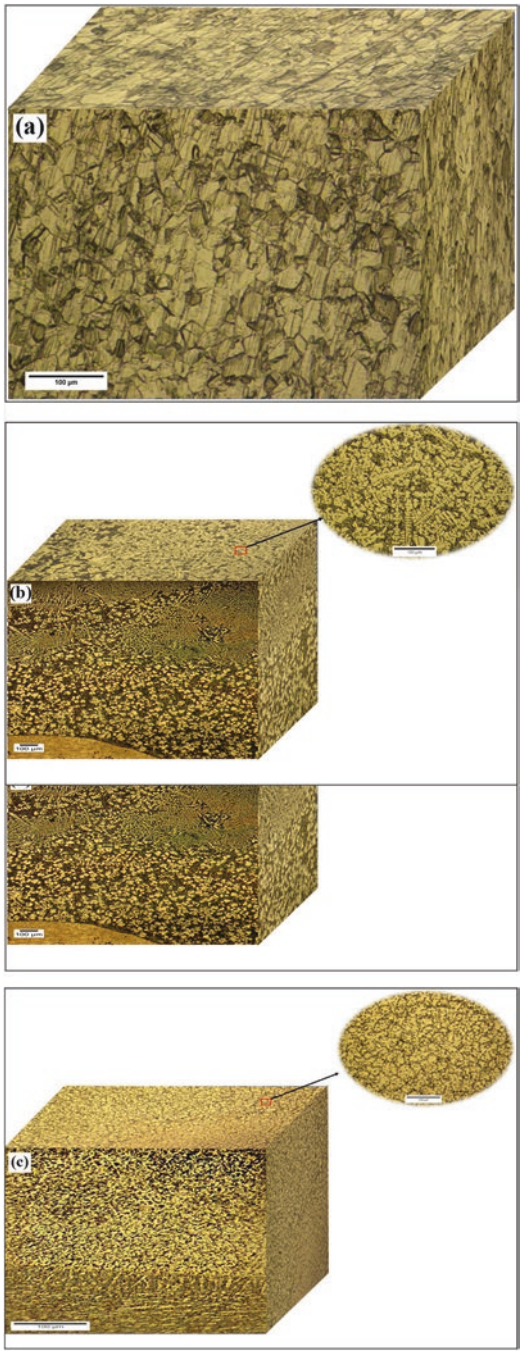

Fig. 9.4 3D optical microscope micrographs of (**a**) base metal, (**b**) Cr-Clad, and (**c**) Ti-Clad

Table 9.5 Composition of coatings

	Element concentration (wt.%)						Results
Area	Mo	Cr	Fe	Co	Ni	Ti	
Cr-Clad-A	45.4	17.6	21.9	12.5	3.5	–	Rich in Mo
Cr-Clad-B	6.6	17.3	31.5	35.8	7.8	–	Rich in Fe and Co
Ti-Clad-A	23.0	12.9	45.5	8.9	6.9	1.5	Rich in Mo and Fe
Ti-Clad-B	11.1	13.9	32.3	12.3	5.3	26.5	Rich in Ti

diffusion of substrate elements (mostly Fe) to the coating resulted in lower microhardness adjacent to the coating/substrate interface. Similarly, higher concentration of Fe in Ti-Clad can be considered as a factor for Ti-Clad lower hardness.

In order to investigate the wear resistance of the coatings, pin on disk wear tests were performed. From weight loss measured after the test and as it is reported in Fig. 9.7 in all three different load conditions (35, 50, 65 N), the Cr-Clad showed the best wear resistance due to its finer structure and higher hardness. The formed solid solution in Cr-Clad and the presence of borides and carbides led to higher hardness and improving wear resistance of the samples.

Solidified microstructure with dendrites shows better resistance toward material removal process because of its more integrated and compact structure (Liu et al. 2007). Surprisingly, increasing the force for Cr-Clad and uncoated sample did not increase the weight loss, and Cr-Clad performed better even at higher forces. The main reason is easier synthesis of separated particles to top of the pins at higher forces. This phenomenon compensated some part of the weight loss for Cr-Clad and base metal. For Ti-Clad, the presence of oxide layers such as TiO and TiO2 prevents further welding of separated particles to Ti-Clad pin during wear test, and that is the reason why its weight loss increases with increasing applied force. The average friction coefficient measured for all the samples is reported in Table 9.7. The lowest friction coefficient is for Ti-Clad and the highest quantity belongs to Cr-Clad, which shows that having lower friction coefficient does not mean having lower weight loss and better wear resistance. However, both composite coatings showed lower average friction coefficient in comparison to uncoated sample. It is also reported that the friction coefficient value reflects the adhesive extent in fractional surfaces under conditions of dry sliding friction.

Regarding the temperature of the zinc bath, wear resistance of samples was investigated at 480 °C with the same parameters as room temperature tests. It was proved that Cr-Clad maintained its best wear resistance property at 480 °C too. But the weight loss behavior was different from room temperature (Fig. 9.8).

In contrast to decrement in weight loss by increasing the force at room temperature, at 480 °C, high temperature facilitates formation of oxide layers which prevent welding of separated particles to the pin. To be more specific, at 480 °C, increasing the force leads to more loss in material for all the samples. EDS results from the worn-out surface of pins showed that Ti-Clad had higher amount of oxygen in comparison to Cr-Clad in both room temperature and 480 °C, and all the samples at 480 °C contained more concentration of oxygen compared with their counterparts

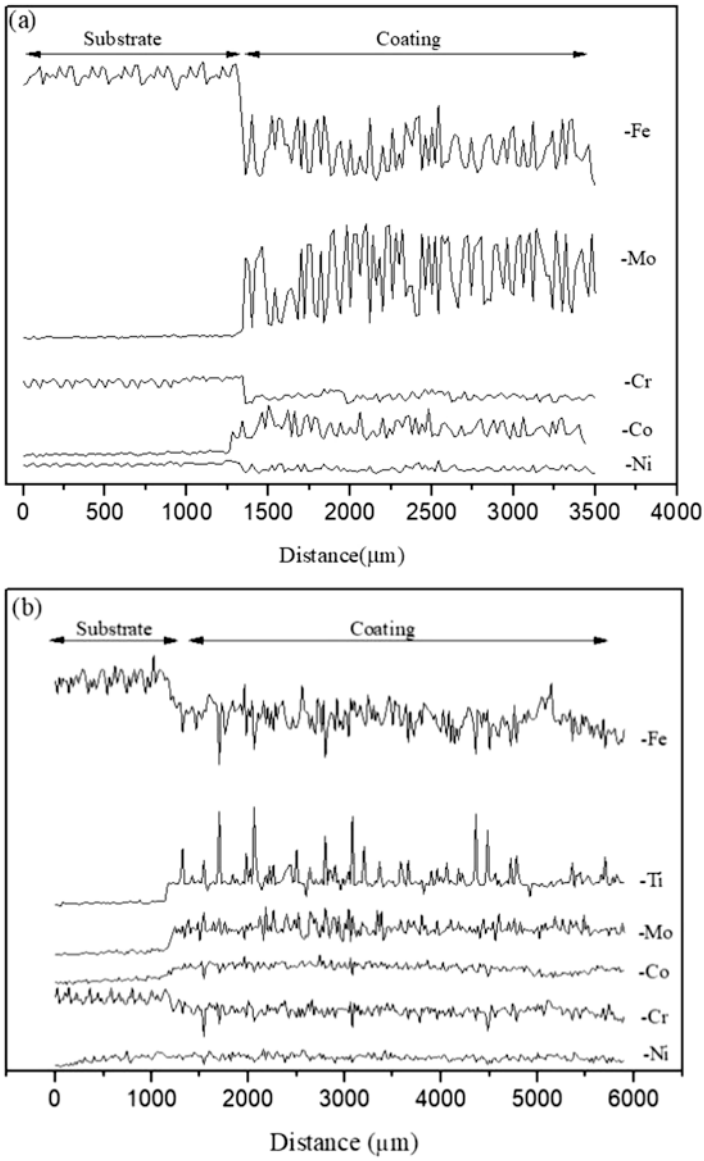

Fig. 9.5 Linear composition from sublayer to coatings: (a) Cr-Clad and (b) Ti-Clad

Table 9.6 Composition of coatings

	Hardness (HV)
Base metal	149.6 ± 1.69
Cr-Clad	692.2 ± 20
Ti-Clad	576.4 ± 20

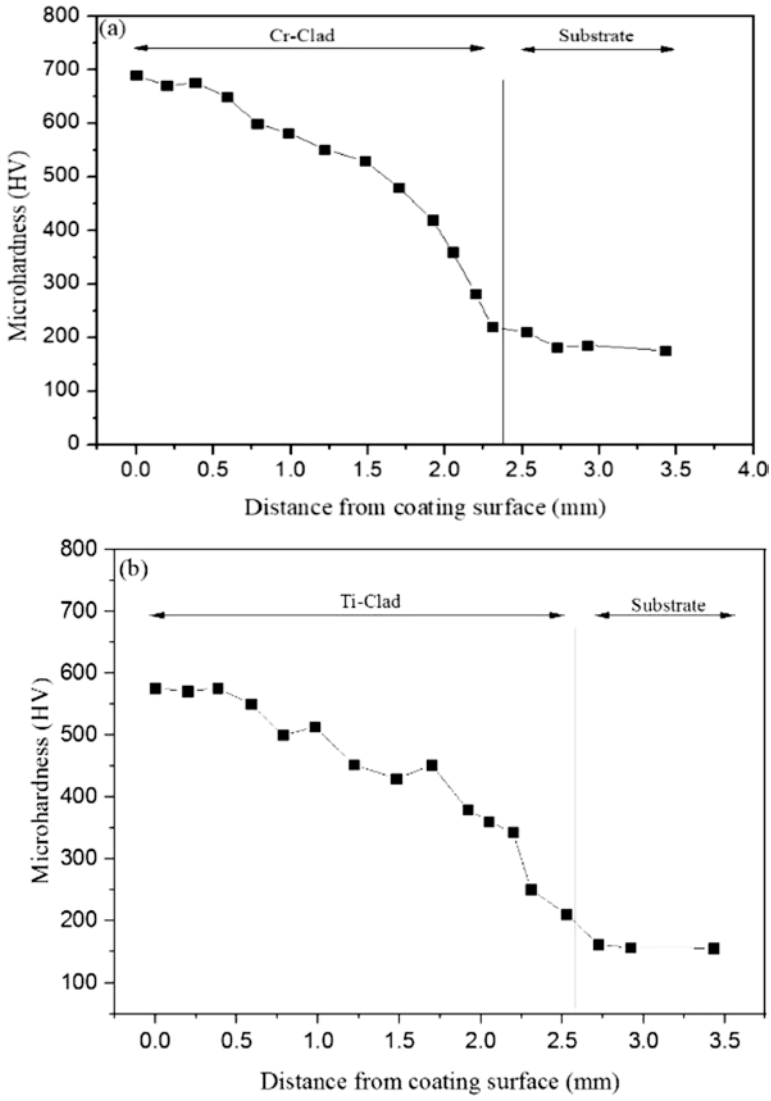

Fig. 9.6 Linear composition from sublayer to coatings: (**a**) Cr-Clad and (**b**) Ti-Clad

at room temperature. Friction coefficient of the samples is reported in Table 9.8. Increment of friction coefficient does not mean an increment in wear. Always increasing the force results in increasing the friction coefficient, but maybe there was no obvious relation with weight loss. In other words, we can say that friction is the main reason for energy loss but not material loss.

Formation of oxide layers such as Cr_2O_3 for Cr-Clad and base metal and TiO and TiO_2 for Ti-Clad on top of the pins prevents the pins from huge weight loss. Also,

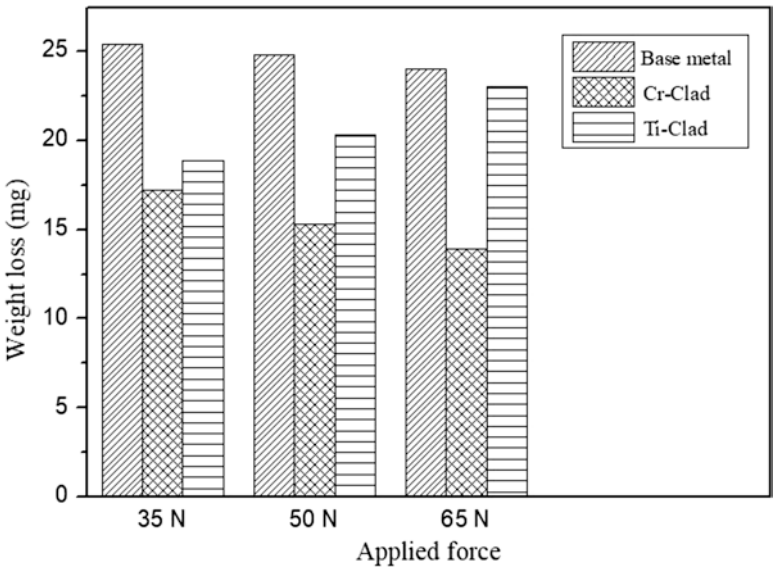

Fig. 9.7 Weight loss of samples at three different vertical loads at room temperature for 1000 m traveled distance

Table 9.7 Average friction coefficient at room temperature

Load	Base metal	Cr-Clad	Ti-Clad
35 N	0.11	0.10	0.09
50 N	0.15	0.13	0.12
65 N	0.17	0.15	0.14

some of the separated particles remain between the pin and disk and experience oxidation at high pressure and temperature. These particles sintered to each other and to the pin and compensate part of the weight loss too; however, particles with lower amount of oxidation have more chance to weld to the pin. It is reported that at temperatures higher than 150 °C, these layers are denser. In other words, at room temperature, also these oxides are formed and sintered to the pin, but they cannot play the role of covering shield for the pin because of their lower amount and lower densification.

Tips of the pins after wear test with 35 N load were investigated by scanning electron microscopy (Fig. 9.9).

9.4 Conclusions

Results showed that the area subjected to wear at room temperature is wider than its counterparts at 480 °C for all the samples, and this result is completely compatible with previous weight loss results. For uncoated sample at room temperature, the

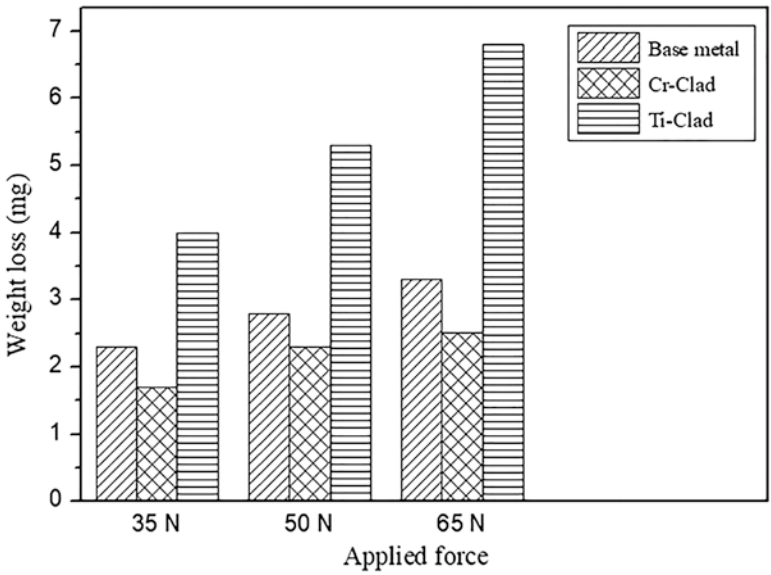

Fig. 9.8 Weight loss of samples at three different loads at 480 °C for 1000 m traveled distance

Table 9.8 Average friction coefficient at room temperature

Force	Base metal	Cr-Clad	Ti-Clad
35 N	0.12	0.11	0.10
50 N	0.13	0.11	0.10
65 N	0.15	0.16	0.12

dominant wear mechanism was abrasive wear, and the scratches can be seen obviously in Fig. 9.9a, while increasing temperature to 480 °C changed the wear mechanism to adhesive mechanism (Fig. 9.9b). Cr-Clad and Ti-Clad coatings both experienced abrasive mechanism at room temperature and 480 °C; however, at high temperature, adhesive wear was also observed, but still the main mechanism is abrasive wear. During the wearing process, dislocation density on the surface is not so high, and the work hardening acts at very low rate. As the traveled distance increases, dislocations accumulate on the narrower space on the surface and result in making some holes on the surface, and when these holes join to each other, they create a crack which is parallel to the surface, and by increasing the length of the crack when it goes higher than the critical length, it breaks and gets separated from the pin. There is a sign of grooves on the surface of coatings, and mostly it is covered by a transferred layer, while noticeable plastic deformation can be seen on worn surface of uncoated sample at 480 °C. The solution strength is the main reason for improving wear resistance of the samples. The presence of carbides and borides which mostly occupy the interstitial position in the FCC matrix structure will prevent dislocations from slipping leading to higher microhardness as well as wear resistance of the composite coatings.

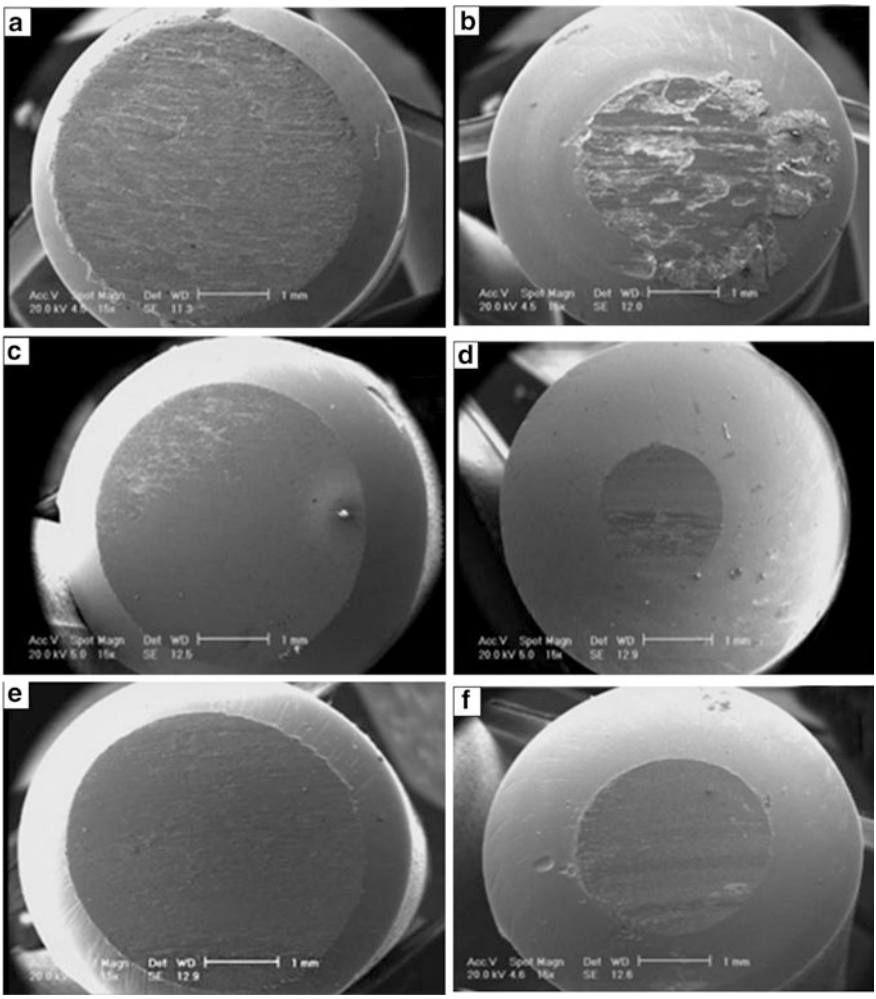

Fig. 9.9 SEM micrographs of worn-out surface of samples in 35 N applied force a, c, e room temperature b, d, f 480 °C, (**a**–**b**) base metal, (**c**–**d**) Cr-Clad, and (**e**–**f**) Ti-Clad

Investigation of the products of wear test at 35 N load at 480 °C with scanning electron microscopy (Fig. 9.10) revealed that the major wear mechanism was abrasive cutting wear for both coatings due to flake products.

The shape of the products depends on the applied tension and geometry of the holes. When products are in the form of microchips, they are the emblem of abrasive wear, while the products with sharp edges are the proof for adhesive wear mechanism. A huge amount of debris in both coating powders can prove that detached particles play the role of abrasives during wear test (Kim et al. 2003).

Comparing oxide concentration in both coatings, it was observed that Ti-Clad has higher oxide percentage which is due to the presence of Ti and its higher suscep-

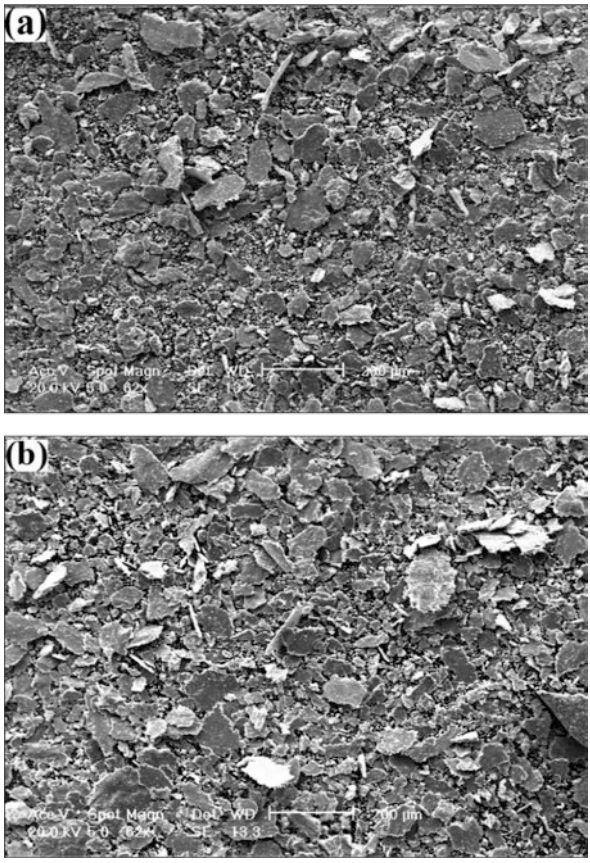

Fig. 9.10 SEM micrographs of powder products of wear test at 35 N at 480 °C for (**a**) Cr-Clad and (**b**) Ti-Clad

tibility to oxidization. At 480 °C, the oxidation occurred even more compared to room temperature. However, oxide particles were also observed at room temperature, and it could be due to temperature increment related to friction between two surfaces.

Zinc corrosion can happen through different processes such as dissolution, formation of intermetallic compounds at the interface, and diffusion of liquid zinc along grain boundaries and depend on experimental factors such as temperature, thermal gradients, solid and liquid compositions, and velocity of the liquid metal (Balbaud-Celerier and Barbier 2001).

For investigating the corrosion resistance behavior of coatings and comparing with the base metal, five samples from each condition (base metal, Cr-Clad, Ti-Clad) were immersed in the liquid zinc and kept at 480 °C for 120, 240, 360, 720, and 840 h. After immersion, the samples in the transverse section were investigated by scanning electron microscope in order to investigate the zinc diffusion.

It was found that after 240 h noticeable concentration of zinc had diffused to the uncoated sample; however, there was no high zinc concentration in the coatings during the same time (Table 9.9).

Looking at the appearance of samples after 240 h, there was a little inclination in zinc to stick to coated samples, while a large amount of zinc was adhered to base metal (Fig. 9.11). It can be seen that corrosion in the Ti-clad starts after 360 h considering both EDS results and corrosion rate calculation. After 360 h, the liquid zinc diffused to the Ti-Clad coating and probably had reacted with the Fe which existed in the coating because of the dilution of sublayer during cladding process.

Spot EDS results showed that zinc concentration is high where a high amount of Fe exists too. The formation of δ phase $FeZn_7$ which helps to improve resistance of coating against further zinc diffusion should be underlined (Yan et al. 2006).

Furthermore, other existed compounds such as Co3Ti and FeMo in the coatings also obstruct the diffusion of zinc atoms and postpone the sublayer contact with zinc atoms. To be more specific, the presence of oxides in Ti-Clad, which is attributed to titanium oxide layers, increases the inertness of the Ti-Clad with respect to liquid zinc and can be considered as a conservative factor for Ti-Clad. The SEM micrographs and EDS results revealed that Zn existed dominantly at grain boundaries which shows that zinc atoms diffuse preferentially through grain boundaries and result in dissociation of Ti-Clad grains to zinc after 720 h; red arrows in Fig. 9.11b show diffused zinc.

For Cr-Clad, there is no obvious sign of corrosion before 720 h immersion in molten zinc. It can be concluded that Cr-Clad maintains its non-wettability until 720 h. Investigating the SEM micrographs of immersed samples, it is clear that for Cr-Clad after 720 h of immersion, a clear separation between the solidified zinc and Cr-Clad is visible which is a proof for non-wettability of Cr-Clad coating, and we can see the coating saves its integrity (Fig. 9.11a). According to EDS results, it is confirmed that the corrosion of Cr-Clad in molten zinc was controlled by depletion of elements from the coating and dissolution of them into the zinc liquid; this phenomenon would be followed by zinc substitution with coating elements and lead to separation of coating layer at longer times, and finally the sublayer would be in contact with zinc atoms and get corroded. Evaluating the EDS results for Cr-Clad

Table 9.9 Chemical composition of base metal and coating/zinc interface after immersion test (wt.%)

	Ni	Mo	Co	Cr	Ti	Zn
Substrate-120	11.3	0.8	–	16.2	–	31.2
Substrate-240	8	1.1	–	5.2	–	67.3
Cr-Clad-120	7.6	42.3	18.6	22.6	–	0.2
Cr-Clad-240	6.3	38.6	17.6	18.3	–	0.6
Cr-Clad-360	6.4	31.8	17.9	12.2	–	3.4
Cr-Clad-720	5.2	22.6	14.2	8.5	–	21.7
Cr-Clad-840	4.1	13.2	9.7	3.5	–	53.2
Ti-Clad-120	9.4	48.3	20.2	12.3	19.8	0.5
Ti-Clad-240	7.3	42.6	17.1	7.5	18.3	11.3
Ti-Clad-360	5.2	18.7	15.3	5.6	15.6	19.3
Ti-Clad-720	3.1	12.5	8.1	4.2	13.1	60.7

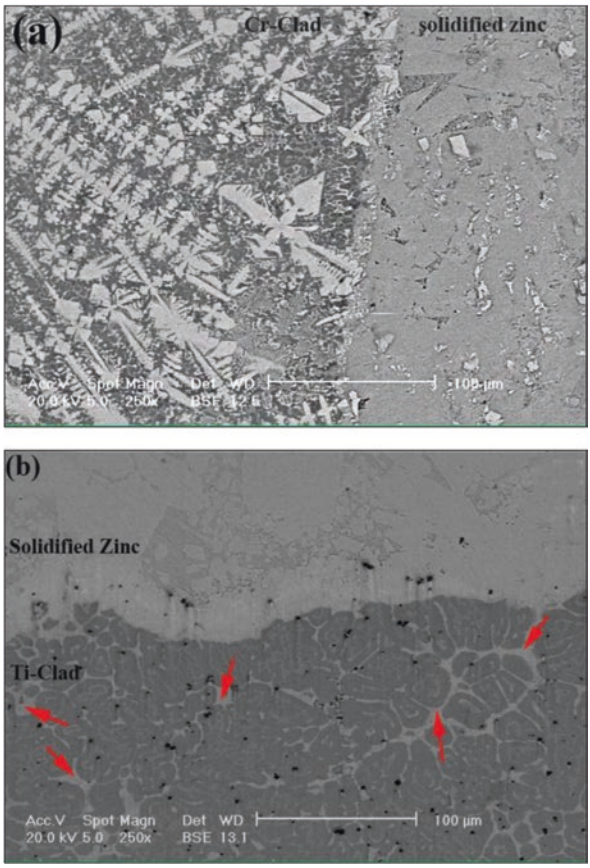

Fig. 9.11 SEM micrographs from interface of (**a**) Cr-Clad/zinc after 720 h and (**b**) Ti-Clad/zinc after 720 h

for 720 and 840 h, it is clear that zinc concentration increases in the coating by decrement in chromium concentration which can be due to similarity in their atomic radius (R_{Fe} = 0.126 nm, R_{Cr} = 0.128 nm, R_{Zn} = 0.134 nm). To be more specific, the atoms of zinc substitute with chromium atoms, and it is mutual interaction between coating and liquid zinc, while the zinc atoms are penetrating to the coating, and atoms of coating (specially chromium) are solving into liquid zinc (Fang et al. 2016).

The main reason for resistance of MoB/CoCr coating is ascribed to its non-wettability due to the existence of double boride phases which is inert to liquid zinc and helps postponing zinc penetration to substrate through the coatings (Mizuno and Kitamura 2007). The Mo-rich phase in solid solution phase inside dendrites also helps to deter the dissolution of coating and possibly helps to slow down the reaction of the alloys with molten zinc. The electrochemical corrosion is more probable to happen in interdendritic region where the concentration of Fe and Cr is higher in comparison to interdendritic regions.

Before immersion test, all the specimens were weighted. After their retrieval from molten zinc, the remnant zinc layer adhered to the specimen was cleaned using

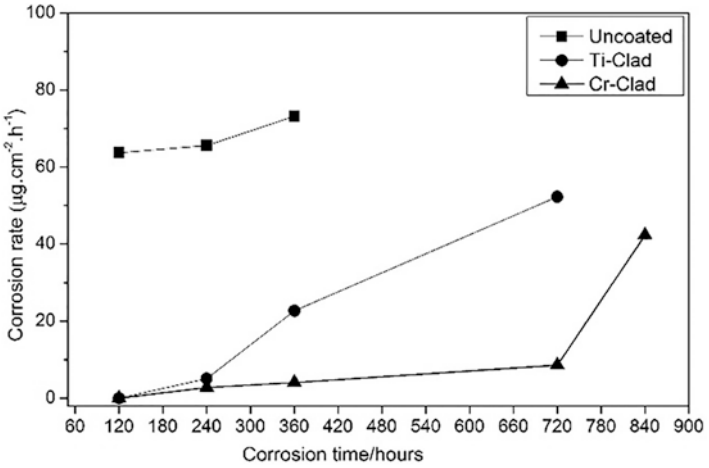

Fig. 9.12 Corrosion rate as a function of corrosion time of the specimens

dilute hydrochloric acid (3%) before determining weight loss. The corrosion rate was calculated in terms of weight loss according to Eq. (9.2):

$$R = \frac{w_1 - w_2}{s \times t} \tag{9.2}$$

where R is the corrosion rate ($mg*cm^{-2} \times h^{-1}$), W1 is the initial weight (mg), W2 is the weight after corrosion (mg), and S and t are the surface area before immersion (cm^2) and the corrosion time (h), respectively. It was revealed that Cr-Clad shows the best corrosion resistance during immersion test (Fig. 9.12).

It is obvious that 316 L stainless steel is well wetted by liquid zinc after 120 h, while two other coatings show insoluble behavior in the same time. For Ti-Clad, the incubation time can be considered 360 h because until this time there is no obvious weight loss, while this time for Cr-Clad can be assumed to be 720 h proving a better corrosion resistance in liquid zinc.

9.5 Conclusions

Conducting the pin on disk wear test at two temperatures and corrosion test in molten zinc, the main results can be summarized:

It was found that in Cr-Clad the coatings form by epitaxial growth on substrate surface, and after forming equiaxed grain region near substrate/coating interface, by increasing distance from interface to surface, the structure changes to dendritic microstructure.

Microhardness profiles revealed that there is obvious decrement in hardness from surface of coatings to interface with substrate. The main reason is the finer size of the grains at coating surface. Ti-Clad had lower hardness in comparison to Cr-Clad because of higher diffusion of Fe elements from substrate to coating in Ti-Clad.

Cr-Clad outperformed other specimens in both room temperature and 480 °C wear tests due to its finer structure and higher hardness.

All the specimens showed better wear resistance at 480 °C in comparison to ambient temperature. The main wear mechanism for coatings at both temperatures was abrasive wear, while the uncoated sample experiences adhesive wear mechanism at 480 °C.

Both clads showed high corrosion resistance in molten zinc. Incubation time for Ti-Clad and Cr-Clad can be assumed to be 360 and 720 h, respectively. While Ti-Clad gets its good corrosion resistance behavior from oxide layer formation, Cr-Clad showed the best wear resistance, thanks to its non-wettability.

References

Asphahani, A., et al. (1987). Corrosion of cobalt-base alloys. *ASM Handbook, 13*, 658–668.

Balbaud-Celerier, F., & Barbier, F. (2001). Investigation of models to predict the corrosion of steels in flowing liquid lead alloys. *Journal of Nuclear Materials, 289*(3), 227–242. https://doi.org/10.1016/S0022-3115(01)00431-7.

Fang, X., Wang, Y., Zhang, Y., Feng, S., Du, J., Liu, D., Ouyang, T., Suo, J., & Cai, S. (2016). Improving the corrosion resistance of Fe-21Cr-9Mn alloy in liquid zinc by heat treatment. *Corrosion Science, 111*, 362–369. https://doi.org/10.1016/j.corsci.2016.05.018.

Gholipour, A., Shamanian, M., & Ashrafizadeh, F. (2011). Microstructure and wear behavior of stellite 6 cladding on 17-4 PH stainless steel. *Journal of Alloys and Compounds, 509*(14), 4905–4909. https://doi.org/10.1016/j.jallcom.2010.09.216.

Halstead, A., & Rawlings, R. D. (1985). The effect of iron additions on the microstructure and properties of the "Tribaloy" Co-Mo-Cr-Si wear resistant alloys. *Journal of Materials Science, 20*(5), 1693–1704. https://doi.org/10.1007/BF00555273.

Kim, H.-J., Yoon, B.-H., & Lee, C.-H. (2003). Sliding wear performance in molten Zn–Al bath of cobalt-based overlayers produced by plasma-transferred arc weld-surfacing. *Wear, 254*(5–6), 408–414. https://doi.org/10.1016/S0043-1648(03)00186-8.

Kou, S. (2003). *Welding metallurgy* (pp. 431–446). New Jersey: Wiley.

Lin, W., & Chen, C. (2006). Characteristics of thin surface layers of cobalt-based alloys deposited by laser cladding. *Surface and Coating Technology, 200*(14–15), 4557–4563. https://doi.org/10.1016/j.surfcoat.2005.03.033.

Liu, X., Barbero, E., Xu, J., et al. (2005). Liquid metal corrosion of 316L, Fe3Al, and FeCrSi in molten Zn-Al baths. *Metallurgical and Materials Transactions A, 36*, 2049–2058. https://doi.org/10.1007/s11661-005-0325-7.

Liu, Z., Cabrero, J., Niang, S., & Al-Taha, Z. Y. (2007). Improving corrosion and wear performance of HVOF-sprayed Inconel 625 and WC-Inconel 625 coatings by high power diode laser treatments. *Surface and Coating Technology, 201*(16–17), 7149–7158. https://doi.org/10.1016/j.surfcoat.2007.01.032.

Ma, S., Xing, J., Fu, H., Yi, D., Zhang, J., Li, Y., Zhang, Z., Zhu, B., & Ma, S. (2011). Interfacial morphology and corrosion resistance of Fe–B cast steel containing chromium and nickel in liquid zinc. *Corrosion Science, 53*(9), 2826–2834. https://doi.org/10.1016/j.corsci.2011.05.020.

Majumdar, J. D., Kumar, A., & Li, L. (2009). Direct laser cladding of SiC dispersed AISI 316L stainless steel. *Tribology International, 42*(5), 750–753. https://doi.org/10.1016/j.triboint.2008.10.016.

Mizuno, H., & Kitamura, J. (2007). MoB/CoCr cermet coatings by HVOF spraying against erosion by molten Al-Zn alloy. *Journal of Thermal Spray Technology, 16*(3), 404–413. https://doi.org/10.1007/s11666-007-9046-3.

Ren, X.-J., MEI, X.-Z., & Jun, S. (2007). Materials resistance to liquid zinc corrosion on surface of sink roll. *Journal of Iron and Steel Research, International, 14*(5), 130–136. https://doi.org/10.1016/S1006-706X(08)60066-7.

Tomita, T., Tatatani, Y., Kobayashi, Y., Harada, Y., & Nakarita, H. (1993). Durability of WC/Co sprayed coatings in molten pure zinc. *ISIJ International, 33*(9), 982–988. https://doi.org/10.2355/isijinternational.33.982.

Xu, P., Lin, C. X., Zhou, C. Y., & Yi, X. P. (2014). Wear and corrosion resistance of laser cladding AISI 304 stainless steel/Al2O3 composite coatings. *Surface and Coating Technology, 238*, 9–14. https://doi.org/10.1016/j.surfcoat.2013.10.028.

Yamaguchi, H., & Hisamatsu, Y. (1979). Reaction mechanism of the sheet galvanizing. *Trans Iron Steel Inst Japan, 19*(11), 649–658. https://doi.org/10.2355/tetsutohagane1955.63.7_1160.

Yan, D., He, J., Tian, B., Dong, Y., Li, X., Zhang, J., Xiao, L., & Jing, W. (2006). The corrosion behavior of plasma sprayed Fe2Al5 coating in molten Zn. *Surface and Coating Technology, 201*(6), 2662–2666. https://doi.org/10.1016/j.surfcoat.2006.05.008.

Yan, D., Yang, Y., Dong, Y., Chen, X., Wang, L., Zhang, J., & He, J. (2012). Phase transitions of plasma sprayed Fe–Al intermetallic coating during corrosion in molten zinc at 640 °C. *Intermetallics, 22*, 160–165. https://doi.org/10.1016/j.intermet.2011.10.017.

Zhang, K., & Battiston, L. (2002). Friction and wear characterization of some cobalt- and iron-based superalloys in zinc alloy baths. *Wear, 252*(3–4), 332–344. https://doi.org/10.1016/S0043-1648(01)00889-4.

Zhang, J., Deng, C., Song, J., Deng, C., Liu, M., & Zhou, K. (2013). MoB–CoCr as alternatives to WC–12Co for stainless steel protective coating and its corrosion behavior in molten zinc. *Surface and Coating Technology, 235*, 811–818. https://doi.org/10.1016/j.surfcoat.2013.08.052.

Chapter 10
Laser Cladding of Ti Alloys for Biomedical Applications

Monireh Ganjali, Mansoureh Ganjali, S. K. Sadrnezhaad, and Yousef Pakzad

10.1 Introduction

Many people lose or experience a damaged organ or tissue due to age, illnesses, or accidents. So, the design and development of biocompatible materials with generally suitable properties called "biomaterials" for repairing or replacing diseased or damaged tissues is needed. Biomaterials are synthetic or natural substances used to improve, treat, heal, or substitute living tissues or organs, and in the design of medical implants and medical devices and diagnostic treatments in pharmaceuticals, surgeries, dentistry, nuclear medicine, and basic medical sciences (Bhat and Kumar 2013; Chaudhuri et al. 2017). Biomaterials must be blood compatible, noninflammatory, nonpyrogenic, nonallergenic, nontoxic, noncarcinogenic, chemically inert, stable, and mechanically strong enough to withstand repeated forces during a lifetime.

There are a wide range of materials such as metals, ceramics, polymers, and composites which have been investigated as biomaterials. Metals have been exclusively used almost for load-bearing implants, such as artificial joints, bone plates, screws, intramedullary nails, spinal fixations and spacers, external fixators, pacemaker cases, and dental implants. Stainless steel (Patel and Gohil 2012, Navarro et al. 2008), cobalt chromium alloys (Qizhi and George 2015), and titanium and

M. Ganjali (✉) · Y. Pakzad
Bioengineering Group, Nanotechnology and Advanced Materials Department, Materials and Energy Research Center (MERC), Tehran, Iran
e-mail: monireh_gan@merc.ac.ir

M. Ganjali
Nour Zoha Materials Engineering Research Group (NMERG), Tehran, Iran

S. K. Sadrnezhaad
Department of Materials Science and Engineering, Sharif University of Technology, Tehran, Iran
e-mail: sadrnezh@sharif.edu

P. Cavaliere (ed.), *Laser Cladding of Metals*,
https://doi.org/10.1007/978-3-030-53195-9_10

titanium-based alloys (Eisenbarth et al. 2004; Nag et al. 2009) are the most common metallic biomaterials.

Titanium and its alloys such as Ti-6Al-4 V, as one of the most promising engineering materials, have been of interest in biomedical applications due to their excellent mechanical and tribological properties. However, inertness and low biocompatibility are the most serious obstacles that hindered their usages in biomedical fields. In particular, aluminum has a neurotoxicity effect and vanadium is a strong cytotoxin element causing long-term health problems like Alzheimer's and neuropathy, and therefore, it is dangerous for Ti–6Al–4 V to remain in the human body for a long time (Geetha et al. 2008; Navarro et al. 2008). So, surface modification of titanium and its alloys seems to be necessary for enhancing their application in various fields of science and industry.

Laser technology is widely used in the surface modification of different metals, owing to their high coherence, directionality, and high energy density. Laser surface remelting (Singh et al. 2006) and laser cladding (Mukherjeea et al. 2017; Wang et al. 2008) have been studied to improve the surface properties of different types of metals. Laser cladding technique has been widely used to prepare many kinds of coatings because it can provide high production efficiency, excellent control of the deposition process, and a mechanical interlock at the interface between the coating and the substrate. In light of this, the present work aims to carry out an exploratory study on laser surface modification of Ti alloys by laser cladding.

10.2 Biomaterials

Biomaterials consist of substances without toxicity/immunological reactions in contact with the body or biological systems, which are intended to for therapeutic purposes (treat, repair, or replace a tissue function of the body). Biocompatibility is the most important and essential condition for various kinds of biomaterials to be used as a medical product (Tathe et al. 2010). Indeed, biocompatibility signifies the feature of any natural or artificial material being compatible with the living tissue. So, biocompatibility can be defined as the acceptance of an implant by the surrounding tissues and the entire tissues of the body (Park and Bronzino 2002).

In general, biomaterials should have the following properties:

- Chemical neutrality and no adverse effects on adjacent tissues
- Lifetime and fatigue strength
- No harmful effect on the metabolism of the body

All biomaterials are classified into three categories: bioinert, biodegradable, and bioactive. Bioinert is a material that does not directly bond with any of the surrounding tissues. Bioactive materials are chemically bonded with the adjacent tissues, and biodegradable materials are destroyed over time and replaced by natural substitutes. Various biomaterials include a wide range of natural or synthetic biocompatible materials that are used daily in pharmaceutical, surgery, and dental medicine. In

Table 10.1 Biomaterials, properties, and applications

Biomaterial applications	Uses of biomaterials	Types of biomaterials
Orthopedic implants	Total joint replacement	Metals and alloys such as, titanium, titanium alloys, cobalt chromium alloys, and stainless steel
	Total knee replacement	Ceramics such as, aluminum and zirconia
	Bone repair	Polymers such as, polyethylene, silicone rubber, polyurethane, polypropylene, and polymethylmethacrylate
Dental applications	Dental bridges	Ceramics such as, aluminum and zirconia
Prosthesis in cardiovascular medical devices	Cardiac pacemakers	Metals and alloys such as, stainless steel, cobalt chromium alloys, and titanium alloys
	Heart valves	Polymers such as, polyamide, polyolefin, polyesters, polytetrafluoroethylene, and polyurethanes
Ophthalmological	Intraocular lenses	Polymethylmethacrylate (PMMA), silicone, and hydrophilic and hydrophobic acrylic
Reconstructive surgery	Vascular grafts	Polymers such as, polytetrafluoroethylene, Dacron, and polyurethene
Wound healing	Synthetic sutures	Polymers such as UHMWPE
	Fracture devices	Metals such as stainless steel
Drug delivery systems	Drug eluting leads	Titanium alloys as fixation leads
		Ceramic collars surrounding the electrode tip
Bio-electrodes and sensors	Glucose monitoring biosensors	Polyurethane
		Vinyl pyridine–styrene copolymer

Data were adapted with permission from the following citation: Hassanein and Amleh (2018)

Table 10.1, a selection of different biomaterials, their properties, and applications is indicated.

10.2.1 Metallic Biomaterials

Metallic biomaterials are often used to replace the structural components of the human body because they are better than polymeric or ceramic materials in terms of tensile strength, fatigue strength, and toughness. As a result, they are widely used in various medical devices such as artificial joints, dental implants, artificial hearts, bone plates, wires, and stents. Also, metallic biomaterials due to better electrical conductivity are applied to prepare electronic parts such as heart pacemakers and artificial ears. Nowadays, the most common metallic biomaterials used are stainless steel, cobalt, titanium, and nickel, and their alloys. Some of their properties are listed in Table 10.2.

Table 10.2 Characteristics of some metals and alloys used in biomedical fields

Material	Normal analysis (w/o)	Modulus of elasticity GN/m^2 (psi $\times 10^6$)	Ultimate tensile strength MN/m^2 (ksi)	Elongation to fracture (%)	Surface
Titanium	99 + Ti	97 (14)	240–550 (25–70)	>15	Ti oxide
Titanium-aluminum-vanadium (Ti-Al-V)	90Ti-6Al-4V	117 (17)	869–896 (125–130)	>12	Ti oxide
Cobalt-chromium-molybdenum (casting)	66Co-27Cr-7Mo	235 (34)	655 (95)	>8	Cr oxide
(Co-Cr-Mo)					
Stainless steel (316 L)	70Fe-18Cr-12Ni	193 (28)	480–1000 (70–145)	>30	Cr oxide
Zirconium (Zr)	99 + Zr	97 (14)	552 (80)	20	Zr oxide
Tantalum (Ta)	99 + Ta	–	690 (100)	11	Ta oxide
Gold (Au)	99 + Au	97 (14)	207–310 (30–45)	>30	Au
Platinum (Pt)	99 + Pt	166 (24)	131 (19)		Pt

Data were adapted with permission from the following citation: Imam and Froes (2010)

10.2.1.1 Titanium and Its Alloys

Titanium and its alloys such as Ti–6Al–4V are widely used for making implants under load in dental and bone applications because of their superior mechanical properties, biocompatibility, and resistance to corrosion in a physiological environment. Titanium alloys can be classified into three main groups: α phase, β + α mixture, and β solid solution. As can be seen in Fig. 10.1, the addition of aluminum to titanium results in the stabilization of the α phase (HCP) and the production of a high-strength alloy. Also, the addition of vanadium causes the formation of β (BCC) in α background and increases the flexibility and resistance of the alloy to impact. Thus, the Ti-6Al-4V alloy is an α-bivalent alloy, which is one of the most crucial titanium alloys (Gammon et al. 2004). In β + α alloys, morphology or α phase shape plays a vital role in hammering and fatigue strength.

Currently, Ti-6Al-4V alloys are used as hip and knee joint prostheses and dental implants in the medical industry (Li et al. 2014). The hip and knee replacement traditional implants are shown in Fig. 10.2.

However, despite its remarkable advantages, the toxicity of Ti-6Al-4V components, such as aluminum and vanadium, has become an issue of concern (Okazaki and Gotoh 2005). The release of aluminum and particularly vanadium ions from this alloy can generate long-term health problems such as peripheral neuropathy, osteomalacia, and Alzheimer's disease (Lin et al. 2005).

Ti alloys have very similar mechanical properties to those of the bone. However, the low hardness and poor resistance to wear and oxidation of Ti alloys can restrict their applications, especially where tribological behavior is experienced, such as in

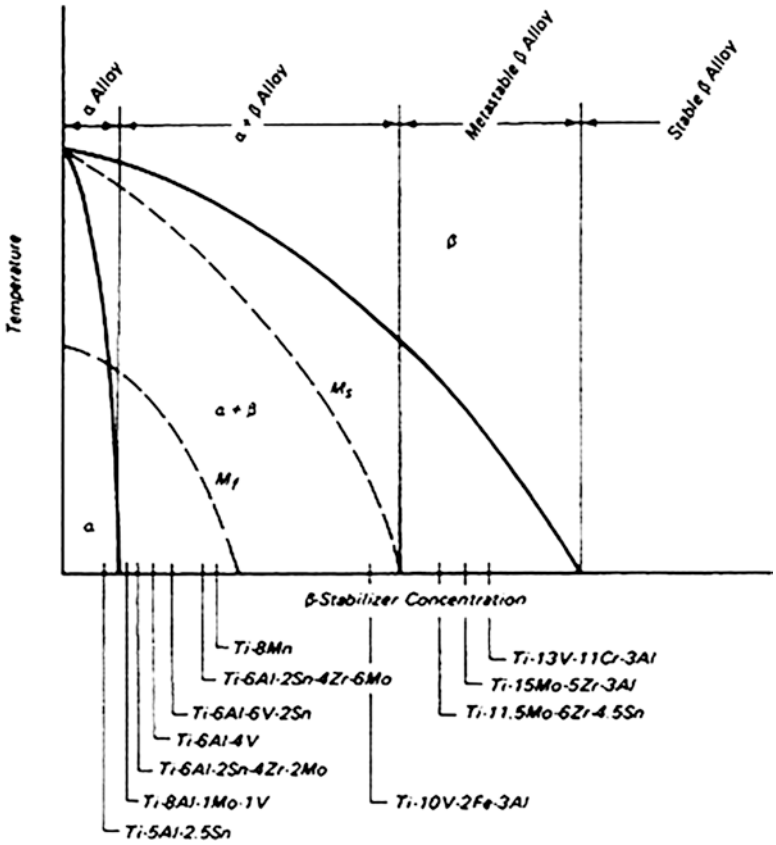

Fig. 10.1 The effects of stable elements of beta phase on the equilibrium phases of Ti alloys (Data were adapted with permission from the following citation: Lütjering et al. 2000)

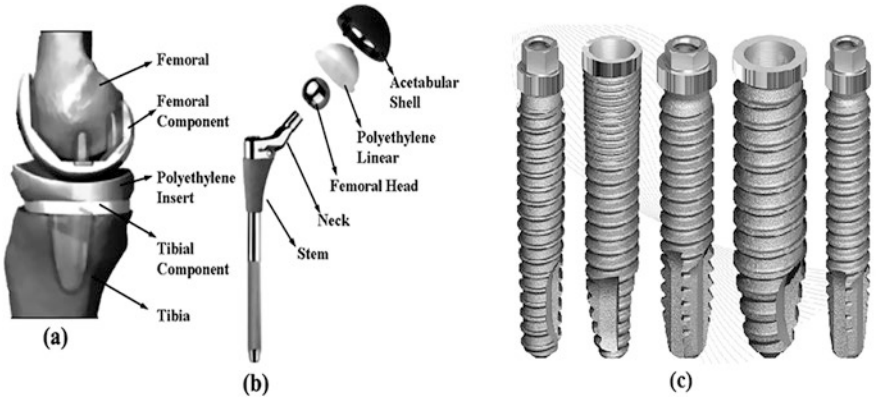

Fig. 10.2 Typical scheme of the (**a**) knee, (**b**) hip, and (**c**) dental implants (Data were adapted with permission from the following citation: Li et al. 2014, Elias et al. 2013)

valves and pin connections. Particularly, the most encountered problem by Ti alloys is in joint replacements such as total knee and hip replacements, where sliding of the ball in the socket occurs due to the movement of the hip joints; therefore, aluminum and vanadium ions are released in the body. The poor tribological properties of these alloys have limited their use in articulating the components of hip and knee prostheses. So, it is required to change the nature of the surface of Ti alloy using different surface engineering techniques.

Surface Modifications of Ti Alloys

To improve the biocompatibility and the mechanical and corrosion properties of Ti and also to enhance its surface integrity, as discussed in the previous section, Ti alloys are subjected to surface modifications by using different materials and coating techniques. The selection of materials is the key parameter in having a successful coating that effects impacts on mechanical properties of the material such as fatigue strength, hardness corrosion, and wears resistance. Metals, ceramics, polymers, and composites are used to coat metallic surfaces as a protective layer. However, a variety of coating processes and material properties can cause difficulties in choosing the best composition of the applied layer. Bioceramic materials are usually considered for this application (Salinas 2014; Peddi et al. 2008; Rodriguez et al. 2016; Kasuga et al. 2004; Braem et al. 2012). These materials and techniques will be explained in detail, in the following sections.

10.2.2 Bioceramic Materials

Bioceramics are a class of advanced ceramics that are commonly employed for repair or replacement of damaged parts in medical and dental applications (Thamaraiselvi and Rajeswari 2004; Salinas and Vallet-Regí 2013). Bioceramics are nonmetallic inorganic compounds formed from metallic and nonmetallic elements combined with ionic or covalent bonds, having high compressive strength, but low tensile strength (brittle) characteristics. The high biocompatibility of bioceramics makes these materials an ideal alternative for the reconstruction and replacement of hard tissues in the body. The biocompatibility of bioceramics can be attributed to their chemical composition. The chemical composition of bioceramics includes ions like K^+, Na^+, Mg^{2+}, and Ca^{2+} which can be found in physiological environments. The main bioceramics used in the biomedical field are shown in the Fig. 10.3.

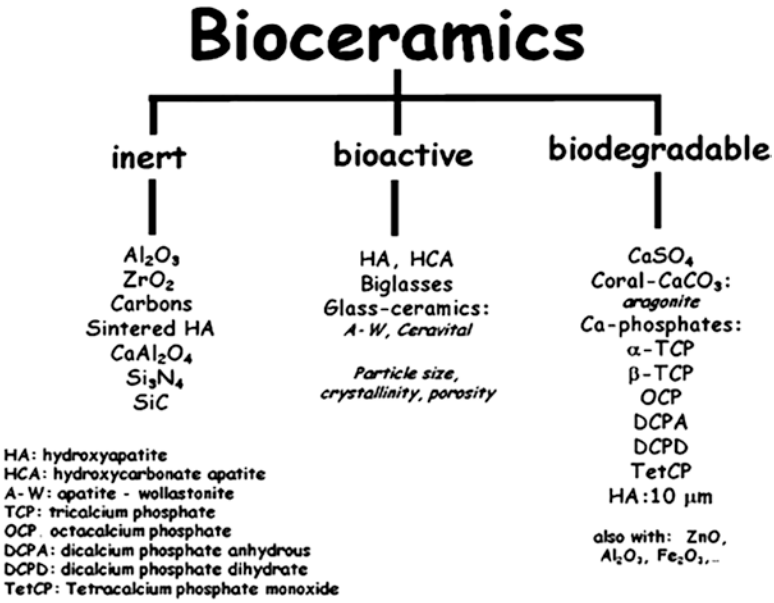

Fig. 10.3 Main bioceramics used in the biomedical field (Data were adapted with permission from the following citation: Salinas et al. 2013)

10.2.2.1 Alumina

Alumina (Al_2O_3) or aluminum oxide is the first bioceramics that is widely used in orthopedic implants in orthopedics, specifically for total hip/*knee arthroplasty*, and in dentistry due to a combination of desirable properties such as suitable biocompatibility, excellent corrosion resistance, and reasonable wear rates (Thamaraiselvi and Rajeswari 2004).

10.2.2.2 Zirconia

Zirconium dioxide *(zirconia)* ceramics have improved properties, in comparison to alumina, such as high toughness, high strength, and high-*performance abrasiveness*, and have been introduced as an *alternative* material to *alumina* (Turon-Vinas and Anglada 2018; Kumar et al. 1991). The fatigue strength of zirconia has led to producing femoral head prosthesis. Table 10.3 shows some of the applications of Al_2O_3 and ZrO_2 as implant materials.

Table 10.3 Biomedical applications of Al_2O_3 and Zro_2

Materials	Advantages	Disadvantages	Applications
Metals: stainless steel, cobalt chromium, titanium alloys, Pt, Pt–Ir alloys	High impact strength, high resistance to wear, ductile, absorption of high strain energy, high conductivity	Low biocompatibility, corrosion in physiological environment, mismatch for mechanical properties with soft connective tissue, low mechanical strength	Orthopedic load bearing and fixation devices, dental implants, neuromuscular stimulation
Ceramics: aluminum, zironia, calcium phosphate ceramics	Good biocompatibility, inert, corrosion resistance, high tensile strength, biodegradable	Undesirable surface properties, special techniques are needed for material fabrication, degradation not controllable	Hip and knee prostheses, dental implants, improving biocompatibility, temporary support, assists regeneration of natural tissues
Polymers: polyacrylates, polyesters, polyamides, polyurethanes, polyether, polyolefines, silicone rubber	Low density, easy to fabricate	Low mechanical strength; additive oligomers may cause tissue reaction	Cardiovascular, maxillofacial, soft skeletal tissue such as tendon, ligament, space filling devices, dental implants, bone cement, lens, intraocular and middle ear prostheses

Data were adapted with permission from the following citation: Balamurugan et al. (2008)

10.2.2.3 Bioactive Glass

Bioactive glasses are a group of biomaterials based on glass and can form a strong chemical bond with the tissues. However, due to their poor mechanical properties (especially weak tensile strength and fracture toughness), bioactive glasses alone cannot be used under load but can be used as coatings on metals and devices (Heimo 2017; Mozafari et al. 2013). Due to the biocompatibility of these glasses, they have been used as bone cement, bioactive coatings, and scaffolds in bone tissue engineering. The first successful use of bioactive glass was for middle ear prosthesis. Today, various clinical applications of bioactive glasses such as craniofacial procedures, grafting of benign bone tumor defects, instrumental spondylodesis, and the treatment of osteomyelitis have been reported (McAndrew et al. 2013; Lindfors et al. 2009; Frantzén et al. 2011).

10.2.2.4 Calcium Phosphates

Calcium phosphate (CaP) is the common name of a family of minerals containing calcium cations (Ca^{2+}) together with orthophosphate ($PO3^{-4}$), metaphosphate (PO^{-3}), or pyrophosphate ($P_2O_4^{-7}$) anions, and sometimes hydrogen (H^+) or

Table 10.4 Calcium phosphates and their properties

Ca:P	Mineral name	Formula	Chemical name
1.0	Monenite	$CaHPO_4$	Dicalcium phosphate (DCP)
1.0	Brushite	$CaHPO_4 + 2H_2O$	Dicalcium phosphate dehydrate (DCPD)
1.3	–	$Ca_8(HPO_4)_2(PO_4) + 5H_2O$	Octocalcium phosphate (OCP)
1.43	Whitockite	$Ca_{10}(HPO_4)_6$	–
1.5	–	$Ca_3(PO_4)_2$	Tricalcium phosphate
1.67	Hydroxyapatite	$Ca_{10}(PO_4)_6(OH)_2$	–
2.0	–	$Ca_4P_2O_9$	Tetracalcium phosphate (TTCP)

Data were adapted with permission from the following citation: Adzila et al. (2012)

hydroxide (OH^-) ions. Biocompatibility, bioavailability, and high bone resemblance make them a very suitable option for bone regeneration (Vallet-Regí and González-Calbet 2004). The most critical issue in calcium phosphates is the *calcium* and *phosphorus concentrations* and the *calcium/phosphorus ratio* in these materials, which has a significant influence on the calcium phosphate qualities. A lower Ca/P ratio increases acidity and solubility, but at a ratio of 1.67 (hydroxyapatite stoichiometry) they are decreased (Dorozhkin 2007, 2009). Table 10.4 shows several calcium phosphates and their properties.

Among the studied calcium phosphates, hydroxyapatite (HA) is the most biocompatible one because bone and teeth mineral composition is mainly composed of HA (Habraken et al. 2016). Nanosized HA may present some priorities rather than macro-scale HA (Li et al. 2008). It has been reported that ceramic biomaterials based on nanosized HA exhibit enhanced restorability and higher bioactivity (Pepla et al. 2014). Also, the release of calcium ions from nanosized HA is similar to that from biological apatite and significantly faster than that from coarser crystals (Gentile et al. 2015).

10.3 Coating Techniques

Coating methods can affect parameters such as coating-to-surface adhesion, uniformity and nonuniformity of the coating, coating thickness, etc. (Xuanyong et al. 2004; Zhecheva et al. 2005). The advantages of bonded implantation attachment include the mechanical properties of the metal section and the chemical and biological properties of the implant coating work together.

Many coating methods are used on Ti alloy substrates including plasma spray (Cooper et al. 1999), sol–gel (Pourhashem and Afshar 2014), electrophoretic deposition (Heise et al. 2018), pulsed laser deposition (PLD) (Rajesh et al. 2011; Mróz et al. 2015), and ion beam (Kim et al. 2013). Each of these methods is suitable for different applications as they offer different deposition methods, different materials, second phases, and different thicknesses and densities. As a result, mechanical stability, corrosion properties, biocompatibility (for biomedical applications), and

enhancement of material behavior for a specific type of coating have to be considered carefully (Thakare et al. 2007; Fotovvati et al. 2019; Prasad et al. 2017).

Although plasma spray is widely used in this field and has advantages such as rapid deposition rate, the high processing temperature induces dihydroxylation and decomposition of calcium phosphates like hydroxyapatite (HAp) (Heimann 2016; Demnati et al. 2014) and nonuniform coating with cracks (Choudhury and Agrawal 2012), and demands high-cost equipment and an elaborate setup. Therefore, the sol–gel deposition method due to the simplified and low-temperature processing is used in this area. However, the disadvantages of this method, such as poor adhesion between the coatings and metallic substrates and difficult porosity control, have limited its application in bioengineering (Kumar et al. 2015). So, what is the potential alternative technique to fabricate bioactive coating?

10.4 Laser Surface Treatment (LST)

On the basis of consecutive uses, the surfaces of tools and components are often investigated wear and corrosion resistance. Therefore, many techniques are used to modified surfaces. Therefore, various surface modification techniques were developed to improve their tribological properties. Among all conventional chemical and physical methods, Laser Surface Treatment (LST) is one of the most efficient techniques due to economic, fast, simple, repeatable techniques to control surface properties (Filho et al. 2011; Ghayad et al. 2015).

This approach can even be applied to repair damaged components and surfaces of tools significantly. In each of the specific applications, LST can be utilized to

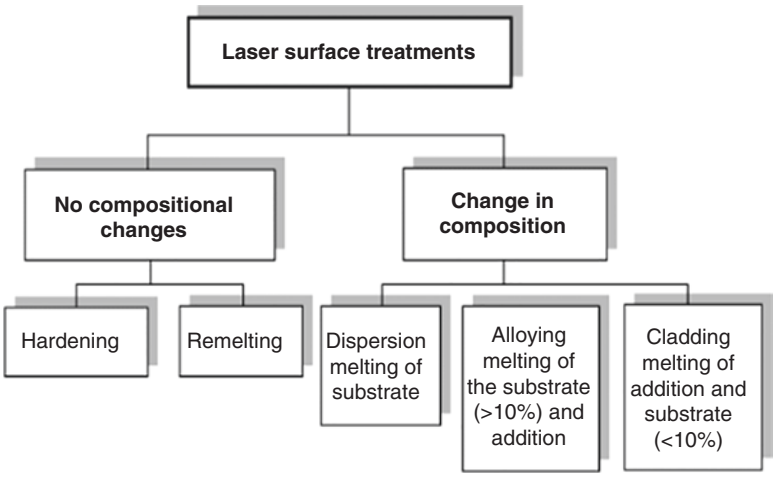

Fig. 10.4 Laser surface treatment techniques (Data were adapted with permission from the following citation: Steen 2003)

treat local repairs in flexibly and customized cover parts of components and tools. Therefore, the advantages of component surface functionalization are as follows:

- Flexible improvement and modification of tools and component surfaces to assort the collective loads
- Considerably longer components and tool life
- Broad spectrum of applications

Laser surface treatment techniques are shown in Fig. 10.4.

10.4.1 Different Laser Coating Methods for Surface Modification of Ti Alloys

On the basis of Laser Surface Treatments (LSTs), Melting (LSM), Alloying (LSA) and Cladding (LSC) are the three aspects of principal laser techniques utilized for the fabrication of wear and corrosion-resistant metallic surfaces because of the overall advantages and disadvantages of these processes to enhance wear and corrosion features.

10.4.1.1 Laser Surface Melting and Alloying

Since LSM and LSA severely relate to each other because of LSTs initial exposure to a physical phenomenon called "melting" to achieve alloying and cladding of materials, the processing has to be continued until the next stages. It is that both LSM and LSA are involved simultaneously. The alloying process is achieved during the melting process, so, by studying the alloying process, it is simultaneously possible to first express the melting processing of materials in this task.

Fulfilling laser melting on the metallic beds achieves a broad range of applications in sciences and industries due to the precise operational treatment and products with high depth/width ratios in the fusion zone, which minimizes the final amount of the affected material using laser beam scanning. The absorbed high-intensity (energy density) beam causes a fast increase of the substrate temperature. If the intensity is enough, the increasing surface temperature can reach the melting point of the substrate material. Therefore, the melting occurs on the surface of the substrate. The interface between the liquid and solid phases distributes inside the material, while the opto-thermal phenomenon causes an increase in the surface temperature. After the conducted heat spreads from the surface into the bulk material, the surface temperature rises until heat conduction and the heats of melting and evaporation modify the surface energy deposition.

In selected laser melting (SLM), the laser beam defined is focused on the metallic powder to successively melt layers, while the laser and setup parameters such as laser wavelength, power density, frequency rate, scanning rate, environmental temperature and pressure, granule size, and inner gas can be precisely controlled to

customize the products. The main goal of using the SLM technique in material surface processing is to modify their features such as wear and corrosion resistance due to the formation of a robust and homogenous structure of surface layers, avoiding any change in their chemical compositions. SLM on the surface layers causes the formation of grain refinement, ultra-high saturated solid dilutions, and good diffusion of particles, known as metallurgical changes. All these reasons should be considered to obtain a harder, stronger, and more resistant surface layer of the materials selected.

By laser beam scanning, particles on the surface of the substrate absorbed the laser wavelength and the powders in the certain paths on the metallic matrix have been locally heated until entirely be melted. However, a CAD 3D file commands where the melting will be fulfilled. Considering the ability to sufficiently manufacture of a rapid prototyping, 3D printing, or additive manufacturing, a powerful laser have been used to melting and fusing the metallic powders (Wood field et al. 2017). Although the most of SLM processings have been considered in the subcategory of selective laser sintering (SLS), SLMs can even used to producing melted powders in a solid 3D sector on the matrix accordingly (See Fig. 10.5).

Considering the above advantages, LMP can then harden alloys that cannot be hardened so adequately by other traditional material methods. Regarding, previous decades, in particular literature, the process of alloying along the melting process, a suitable application in the preparation of new and worthy products for today human needs, which, can be manufactured by proper thermal sources of high-power lasers. Figure 10.6 shows a summary of the applications of the laser in LST (Dowden 2009). In each of these types of LS processings, the laser intensity and the interaction/

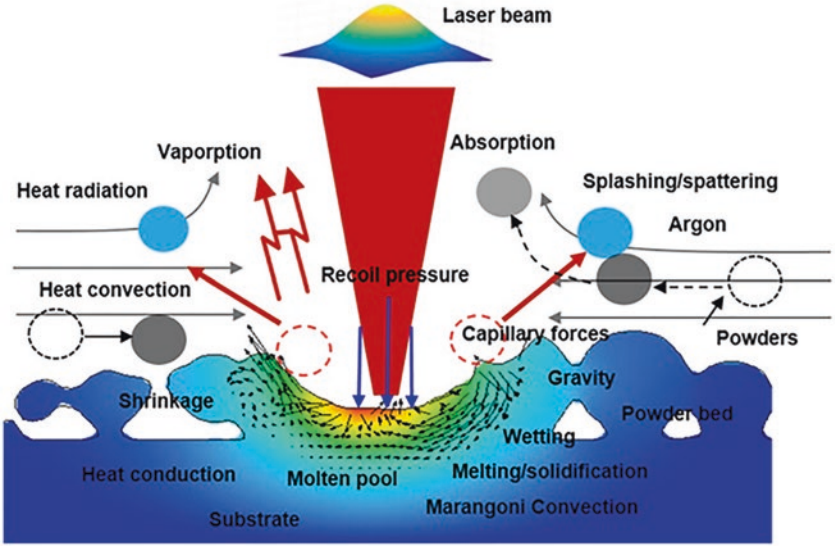

Fig. 10.5 Schematic of selective laser melting and the heat transfer in the molten pool (Data were adapted with permission from the following citation: Chen et al. 2018)

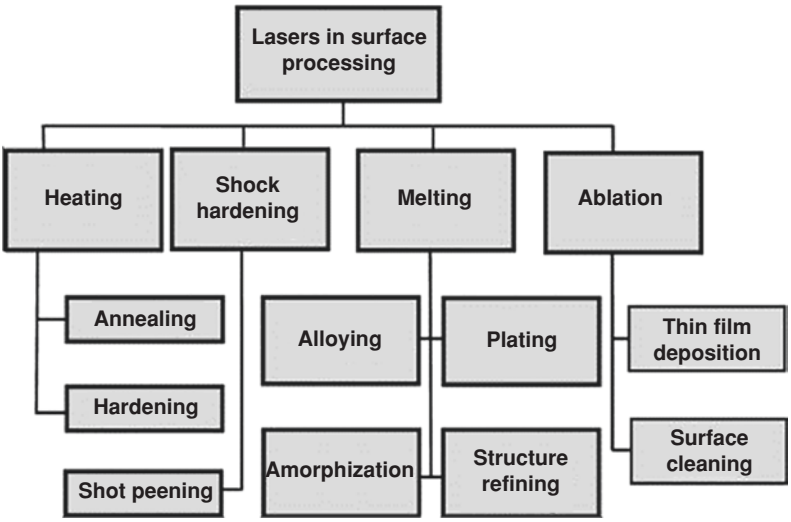

Fig. 10.6 Laser applications in surface processing (Data were adapted with permission from the following citation: Kusinski et al. 2012)

pulse duration time are specially selected in terms of acquiring the desirable temperature and phase transition.

10.4.1.2 Laser Cladding

Laser cladding (LC) for manufacturing the composite coatings is a coating technique that involves melting and adding another material as in the alloying process. A new crack- and porosity-free layer is created on the surface, in this regard (Toyserkani et al. 2005). Moreover, dilution in this process is kept to a minimum and less than the dilution required in the laser alloying process. LC can be used to manufacture a board range of surface alloys and composites with customized properties under demand. This secure processing even leads to coating multilayers with complex geometry on the material surfaces rapidly (using the laser pulse width). Besides, the modification and repairing of material surface properties are done, whereas this approach can be applied to produce 3D components (Brandt 2017; Munsch 2017).

Different Methods of Laser Cladding

There are several feeding ways of cladding a material, such as paste feeding, powder injection, and wire feeding. LC with powder injection is more general due to its almost infinite potential to change the alloy composition (Ganjali et al. 2018).

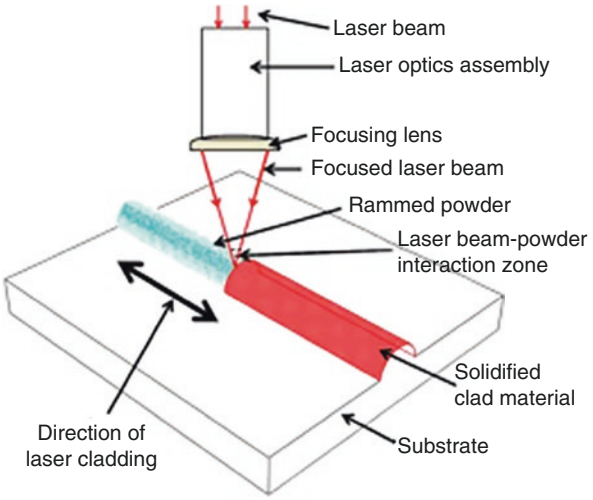

Fig. 10.7 Laser cladding by paste feeding (Data were adapted with permission from the following citation: Paul et al. 2015)

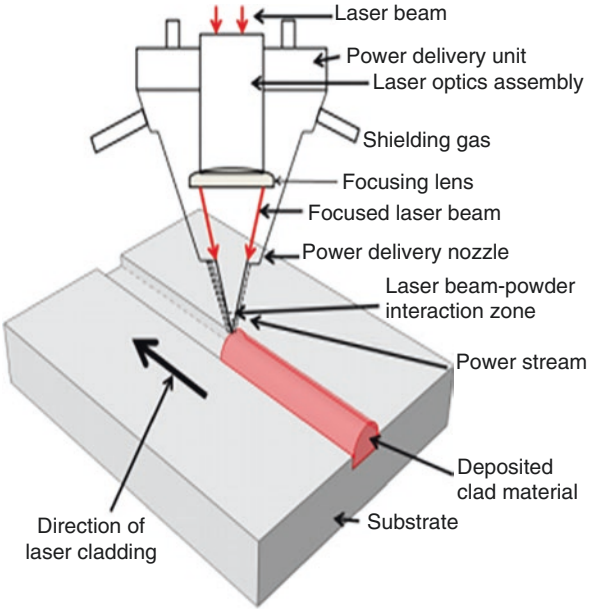

Fig. 10.8 Laser cladding by injected powder (Data were adapted with permission from the following citation: Santanu et al. 2016)

Paste Feeding

This process is a two-step approach for coating substrates. In the *first stage,* the powder is mixed with a chemical binder to ensure that it will stick to the substrate during the process and the *substrate* surface is *covered* with the paste, and in the second stage, heat provided by scanning of the laser beam is strictly transferred over the powder that melts along the substrate (Fig. 10.7). Although a homogeneous and crack-free coating with a strong metallurgical bond is formed between the liner and

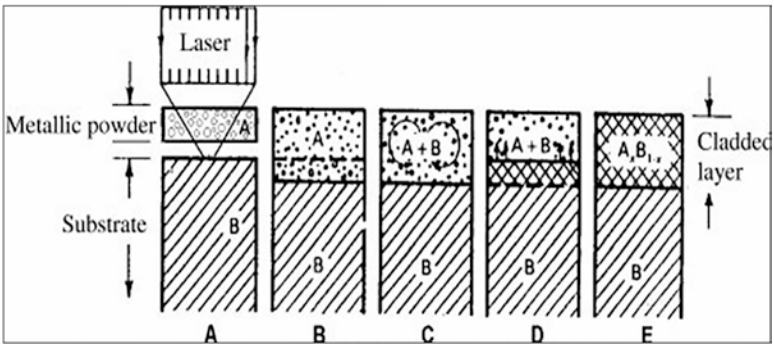

Fig. 10.9 Schematic steps involved during the laser surface cladding (Data were adapted with permission from the following citation: Picasso et al. 1994)

the substrate by this method, the method is not suitable for components with complex geometric shapes (Jayakumar et al. 2015).

Injection Powder

In this method, the powder particles are injected into the laser beam through an inert gas nozzle. Feeding powders are melted by the laser beam and a thin layer with minimum dilution is formed after solidification of the melting pool (Fig. 10.8).

To process the sample, the laser beam is placed to scan above the material surface which should be stripped by the hard material. Inert gas and the composite powder simultaneously are injected by the laser head, while the laser beam with the defined laser intensity and scanning rate is targeted, melting those powders on the surface at the same time. To accomplish this, both powder particles (metal and ceramic) and a thin layer of the substrate should absorb the laser power/energy per area, simultaneously (Fig. 10.9a). Due to the photon energy absorption, the powder and thin layer of the substrate rapidly reach their melting points. In a fraction of a milli/microsecond the liquid/solid interface is brought to the substrate (Fig. 10.9b). As is given in the formula, the height of the substrate-melted zone directly depends on the laser intensity and the interaction time. This stage involves mixing of the molten metallic powder with the substrate and the partially dissolved ceramic material using a convective fluid flow mechanism (Fig. 10.9c). Due to the half-width of laser pulse relaxed (during the decay time), the composite materials melted very fast (less than 10 m/s) and were crystallized in the molten pool as shown in Fig. 10.9. In Fig. 10.9, the solid/liquid interface, therefore, enters part A, where the composite powders existed before. Consequently, as shown in Fig. 10.9e, the cladded composite layer is uniformly formed on the substrate surface (Picasso et al. 1994; Smurov 2008).

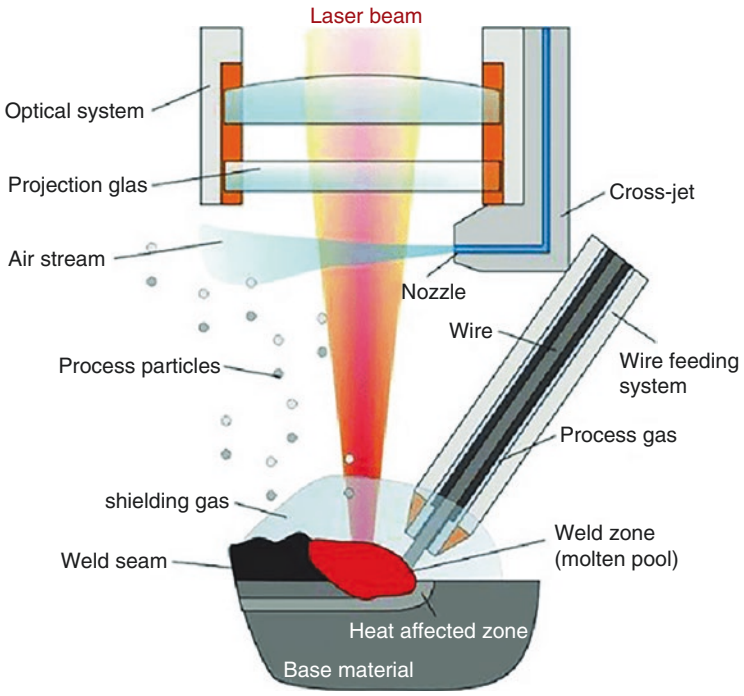

Fig. 10.10 Laser cladding with the wire feeding method (Data were adapted with permission from the following citation: Klocke et al. 2012)

Wire Feeding

The clad material is used in the wire form in this method (see Fig. 10.10). Laser cladding with wire has more advantages compared to usingboth powders and the paste feeding methods : cleaner process environment, higher material deposition efficiency, improved surface quality, and reduced material wastage, which serve to enhance the process economy (Quintino 2014).

Advantages and Disadvantages of Laser Cladding

Advantages of the laser cladding technique are as follows:

1. Low dilution (minimum %1–5) between the material cladded and the substrate
2. Laser beam as a controllable heat source with high power/energy density with the ability to focus on a tiny area
3. Controlling the coating thickness
4. Possessing a very narrow heat-affected zone (HAZ) due to the high heat created within the laser power/energy and spot size
5. Economical in terms of cost compared with conventional methods and logical guidance

However, the high cost of investment, low productivity of laser resources, and lack of control over the coating process are the disadvantages of using this cladding technology. Nowadays, with the continuing developments in the manufacturing of high-power diode lasers (HPDLs), fiber laser, and sophisticated knowledge-based control, the laser cladding process seriously has a great industrial potential for use in the coating of metals, and prototyping.

Factors Affecting the Laser Cladding Process

The selective additive materials, substrate, beam, and operating parameters substantially affect the microstructure, bonding, and quality of the cladded layer. Beam and feeding parameters are generally fixed and are dictated by the choice of equipment, lasers, and optics. The effective energy measures the amount of energy delivered to the process by the laser. This energy is principally responsible for melting the substrate surface and powder and is defined by Eq. (10.1) (Toyserkani et al. 2005):

$$E = P / VD \tag{10.1}$$

In which P – is laser power, V – is the scanning speed of the substrate, and D – is the laser beam diameter. The effective energy E is measured in units of j/cm^2.

The powder deposition density is also a good indicator of the amount of powder fed to a unit area of the substrate during deposition. The powder deposition density is calculated by Eq. (10.2) (Toyserkani et al. 2005):

$$PDD = R / VD \tag{10.2}$$

where R is the powder feed rate. The powder deposition density PDD is measured in units of g/mm^2.

As a result of increasing the scanning speed, the absorb of the laser beam by both the feeding powder and the substrate is decreased and the width, depth, and thickness of the coated layer are reduced, consequently (Vilar and Almeida 2016; Ocelík and De Hosson 2010). On the other hand, increasing the laser intensity at a lower scanning speed increase input energy density and increase clad depth after rapid solidification (Xiong et al. 2009; Tellez 2010; Hu et al. 2009; Ju et al. 2018).

The quality of the laser cladded layer is defined by the dilution ratio, so a better quality of cladded layer is required in lower dilution (Steen and Watkins 1993; Steen 2003; Hofman et al. 2011). An increase of laser power and a decrease of the laser beam spot size led to an increase in the input laser intensity, and then an increase in the dilution ratio (Pekkarinen et al. 2012; Abioye et al. 2013; Zhao et al. 2003).

The dilution rate γ is calculated by the formula (10.3) (Wu et al. 2015).

$$\gamma = b / b + h \tag{10.3}$$

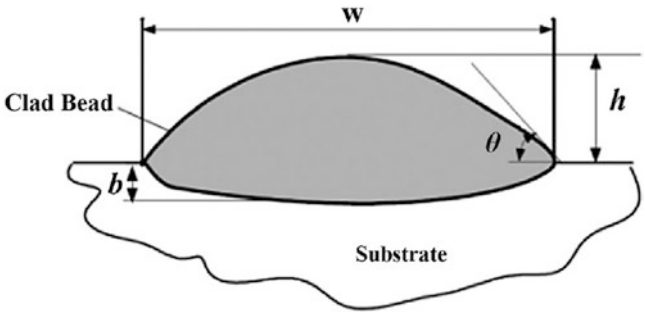

Fig. 10.11 Typical cladded cross-section with most common geometrical characteristics (Data were adapted with permission from the following citation: Toyserkani et al. 2005)

where, h – clad height, b – clad depth, w – clad width, and α – contact angle (see Fig. 10.11). The main effect of laser power and scanning speed on the cladded layer properties is shown in Fig. 10.12.

Indeed, bonding between cladding layer and substrate and fine microstructure of clad layer depends on the feeding powder shape and rate. Irregularly shaped feeding powder causes decrease flowability and as a result, the powders melt incompletely, and pores appear on the interface and surface clad layer. Moreover, the metallurgical bonding between the clad layer and substrate cannot be achieved in case of high rate feeding powder due to the partial melting of feeding powder (Frazier 2014; Sun et al. 2016).

Laser Cladding of Bioceramics – Calcium Phosphates

Many studies have been reported about laser cladding in biomedical applications (Mohammadzadeh Asl et al. 2019; Paital et al. 2010), and the effect of the pulse laser frequency (10–40 Hz) on the wettability and biocompatibility of calcium phosphate coated on the surface of samples was successfully investigated.

According to X-ray diffraction (XRD) analysis, different phases such as $CaTiO_3$, $Ca_3(PO_4)_2$, TiO_2 (anatase), and TiO_2 (rutile) in the coated layer were obtained. They showed that the hydrophilicity (wettability) of the coated samples was increased by decreasing the pulse lase frequency.

CO_2 laser was used to clad gradient coating pure $CaHPO_4{\cdot}2H_2O$, $CaCO_3$, and Ti (45–50 μm) powders on Ti-6Al-4V (Zhu et al. 2016). The bioactive results showed that there was no toxicity in the osteoclast precursors and this functional design was suitable for the growth of osteoclast precursors.

Zheng et al. (2008, 2010) investigated the microstructure and osteoblast response of gradient bioceramic coating hydroxyapatite (HAp) on a titanium alloy fabricated using LC. In another study (Lusquiños et al. 2005; Huang et al. 2013), a homogeneous HAp layer on the Ti alloy substrate and a gradient composite design by LC were fabricated. In the whole process, suitable metallurgical and chemical bonding

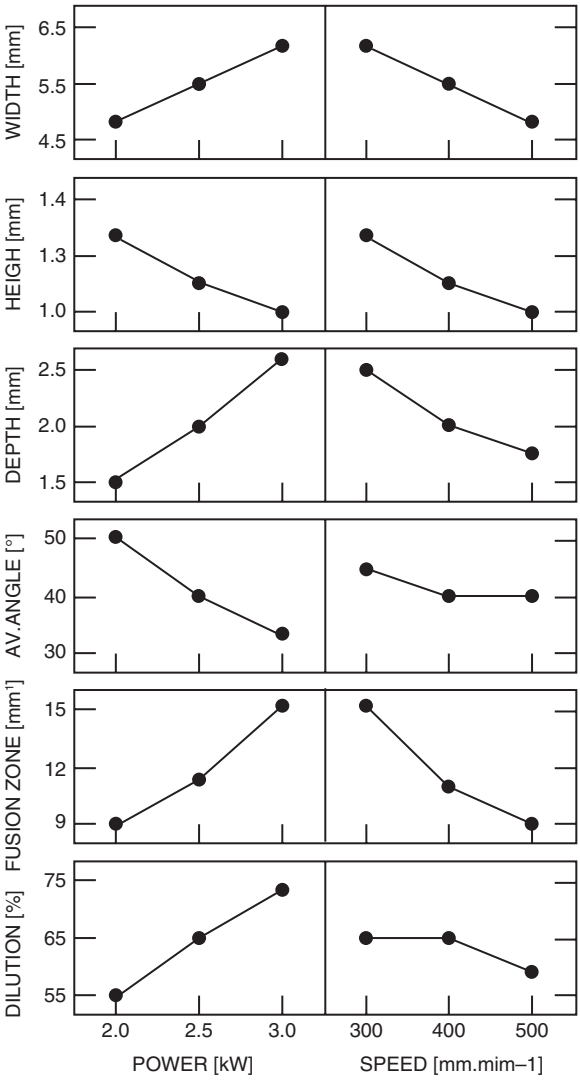

Fig. 10.12 The effect of laser power and scanning speed on the cladded layer properties (Data were adapted with permission from the following citation: Caiazzo et al. 2017)

with the substrate was achieved without any crack and pores. However, there is a limitation to using HAp in clinical research because of the defects in HAp particles, such as brittleness, weak intensity, fatigue failure, and inability to induce vascularization (Rahmandoust and Ayatollahi 2019). So, they can be used in bioresorbable composites made from HAp and biodegradable polymers. Chien et al. (2009) studied the effect of two different HAp binders on the morphology, Ca/P ratio, and hardness of Nd-YAG laser clad coatings. In this work, HAp was mixed with various binders such as water glass (WG) and polyvinyl alcohol (PVA), and then samples were cladded by a laser at two different output powers (740 and 1150 W) and at three different scanning speeds (200, 300, and 400 mm/min). They concluded that

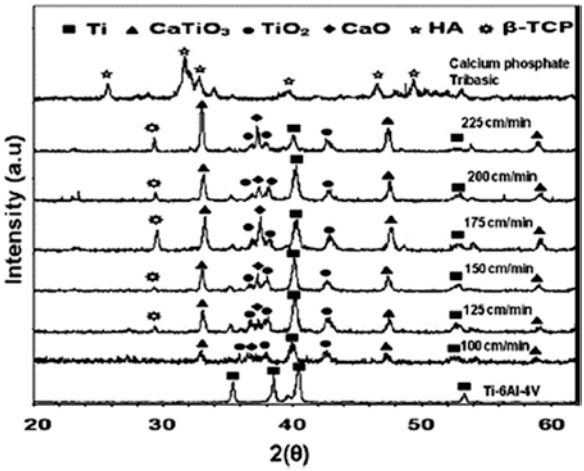

Fig. 10.13 XRD pattern of the coating at different laser scanning speeds (Data were adapted with permission from the following citation: Kurella et al. 2008)

the number and severity of the cracks formed and the porosity in the transition layer weld bead in the cladded samples, PVA and WG binder, were increased, respectively. Moreover, the hardness of the WG binder was higher than the prepared sample using the PVA binder. Recently, it has been reported that the chemical phase of the surface plays a role in Osseo-integration (Moritz et al. 2004; Tian et al. 2005; Khor et al. 2004). In this regard, LC was used for coating hydroxyapatite (HAp) on Ti alloy surfaces at multiple processing speeds (Kurella et al. 2008). They showed that the processing speeds affect the surface morphology, phase composition, and microstructure, which leads to improving the wettability in water (liquid). According to the XRD results (Fig. 10.13), at a lower laser scanning speed and a higher temperature, the wettability and, hence, biocompatibility were decreased due to the dissociation of calcium phosphate through interactions with the substrate titanium and the surrounding air.

The high dissolution rate of hydroxyapatite around the coating surface during the biological fixation effect on bone formation rate and long-term implant success. Therefore, in some cases secondary surgery is unavoidable (Qu and Wei 2006). Therefore, substitute ion such as Mg, Sr, Ag, and F acts as an inhibitor of HA nucleation and crystallization and destabilizes its structure and is decreased the c-axis of the lattice. Other weaknesses of hydroxyapatite include weak mechanical properties such as low impact resistance. These considerations have severely restricted the use of hydroxyapatite in many applications. The apatite structure is a good host for a variety of chemical ionic substituents in its construction. This substitution causes changes in some properties of apatite such as the lattice parameter, morphology, and solubility. The following section will introduce some of these materials.

Ionic Substitution in Hydroxyapatite

As mentioned above, good metallurgical and chemical bonding between the substrate and HA coating after laser cladding was achieved. But due to the presence of TCP in the cladded layer after laser treatment, the solubility of HAp is increased, and as a result, the stability of the HAp coating and also the long-term implant function are decreased (Huang et al. 2013). *Hence,* there is a *need* for the enhancement of *the solubility* of HAp. Since fluorapatite (fHAp) has lower biocompatibility degradation compared with HAp when exposed under higher laser power, it has attracted much more attention for coating on Ti alloys. Chien et al. (2014) utilized an Nd-YAG laser for HAp and fHAp coatings on Ti-6Al-4V substrates. The SEM images revealed slight differences between the surface roughness of HAp and fHAp. Also, the fHAp coated samples had a finer and denser microstructure than HAp coated samples, which led to improving the interfacial and structural strength. Meanwhile, FA has not only better chemical stability and biocompatibility than HA, but also higher interatomic bonding strength (Clarkson et al. 2000). Consequently, during the laser radiation process, FA was reported to have a more stable structure than HA.

Laser Cladding of Bioceramics – Ceramics and Bioglass Ceramics

Balovi et al. (2014) used zirconium and zirconia. Zirconium powder was mixed with the binder poly vinyl alcohol (PVA) and cold glue (CG) for coating of Ti6Al4V to improve the base material's resistance to corrosion and wear. They suggested two applications of these coatings: (1) zirconium and Zr/PVA coatings can be used to prevent the release of toxic Al and V ions in corrosive environments and (2) Zr/CG coating can be used in applications where improved hardness is required. Wang et al. (2019) investigated laser cladding of $CeO_{2/}$ Ti-based ceramic nanoparticle coatings on the Ti-6Al-4V alloy. The experimental results showed the positive effect of the addition of CeO_2 nanoparticles on the enhancement of microhardness and wear resistance of the substrate. Liu et al. (2019) studied the surface modification of the biomedical titanium alloy: micromorphology, microstructure evolution, and biomedical applications. Simulated body fluids (SBFs) results showed that the appearance of the flake-like and cotton-like morphology of apatite provides favorable conditions for osseoconnection. In a recent study by Po-Hsuen Kuo et al. (2019), SiO_2-Na_2O-CaO-P_2O_5 bioactive glass coated on the Ti-6Al-4V alloy by LC is used for bioimplant application. The SEM images of the cross-section showed good metallurgical bonding between the bio-glass coating and the substrate alloy. Meanwhile, according to the EDS results, the bioactivity decreased because of the loss of crucial species such as Na and P and addition of some elements like Ti and Al to the coating (See Fig. 10.14).

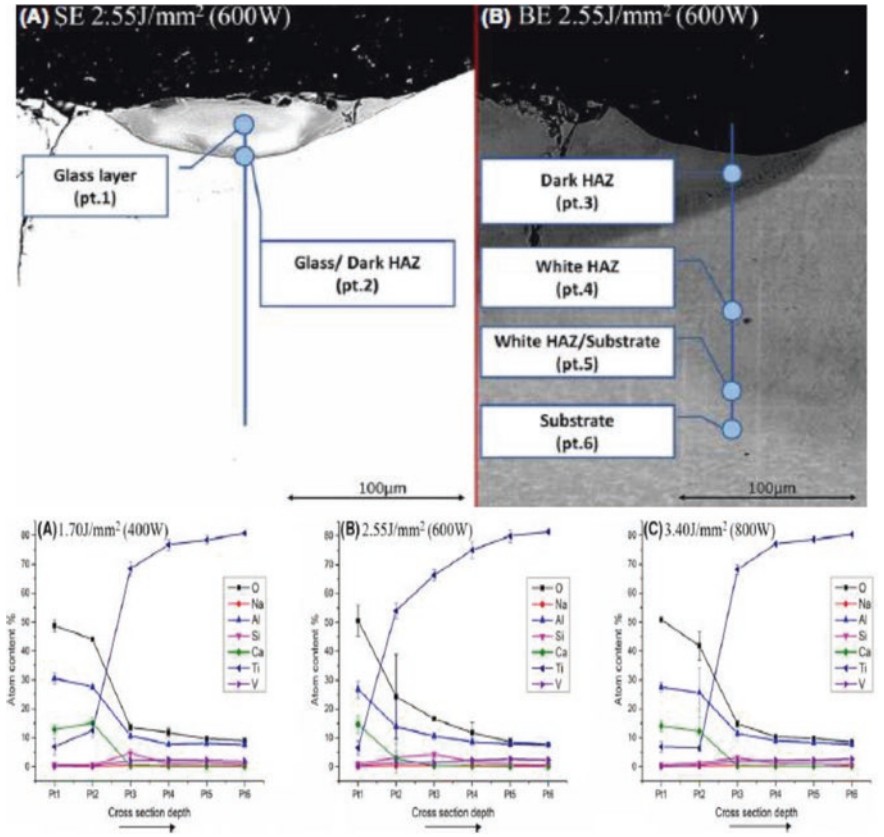

Fig. 10.14 SEM images of cross-section and EDS results of coating at different laser power; (**a**) 400 W, (**b**) 600 W, and (**c**) 800 W (Data were adapted with permission from the following citation: Kuo et al. 2019)

10.5 Conclusion

The conclusions of this work are summarized as follows:

- The application of laser cladding to generate uniform, homogeneous, compact, and well-bonded coatings on the Ti alloy substrates without the necessity of any previous treatment of the surface.
- The technique can be used to produce crack-free coating with higher microhardness and corrosion and wear resistance during the welding process and in presence of intermetallic compounds.
- Based on the literature, surface modification of Ti alloy-based biomedical devices by laser cladding could be a promising method toward more biocompatible and resistant biomedical devices.

Acknowledgments This work was partially supported by the Materials and Energy Research Center (MERC) (Grant No. 771396063).

References

Abioye, T. E., Folkes, J., & Clare, A. T. (2013). A parametric study of Inconel 625 wire laser deposition. *Journal of Materials Processing Technology, 213*, 2145–2151. https://doi.org/10.1016/j.jmatprotec.2013.06.007.

Adzila, S., Murad, M. C., & Sopyan, I. (2012). Doping metal into calcium phosphate phase for better performance of bone implant materials. *Recent Patents on Materials Science, 5*, 18–47. https://doi.org/10.2174/1874464811205010018.

Balamurugan, A., Rajeswari, S., Balossier, G., et al. (2008). Corrosion aspects of metallic implants—An overview. *Materials and Corrosion, 59*, 855–869. https://doi.org/10.1002/maco.200804173.

Baloyi, N. M., Popoola, A. P. I., & Pityana, S. L. (2014). Laser coating of zirconium and zro2 composites on ti6al4v for biomedical applications. *South African Journal of Industrial Engineering, 25*, 62–70. https://doi.org/10.7166/25-1-661.

Bhat, S., & Kumar, A. (2013). Biomaterials and bioengineering tomorrow's healthcare. *Biomatter, 3*, e24717. https://doi.org/10.4161/biom.24717.

Braem, A., Mattheys, T., Neirinck, B., et al. (2012). Bioactive glass – Ceramic coated titanium implants prepared by electrophoretic deposition. *Materials Science and Engineering: C, 32*, 2267–2273. https://doi.org/10.1016/j.msec.2012.06.013.

Brandt, M. (2017). *Laser additive manufacturing, materials, design, technologies, and applications* (1st ed.). New York: Elsevier.

Caiazzo, F., Alfieri, V., Argenio, P., et al. (2017). Additive manufacturing by means of laser-aided directed metal deposition of 2024 aluminium powder: Investigation and optimization. *Advances in Mechanical Engineering, 9*, 1–12. https://doi.org/10.1177/1687814017714982.

Chaudhuri, R., Ramachandran, M., Moharil, P., et al. (2017). Biomaterials and cells for cardiac tissue engineering: Current choices. *Materials Science and Engineering: C, 79*, 950–957. https://doi.org/10.1016/j.msec.2017.05.121.

Chen, Z., Xiang, Y., Wei, Z., et al. (2018). Thermal dynamic behavior during selective laser melting of K418 superalloy: Numerical simulation and experimental verification. *Applied Physics A, 124*, 313–329. https://doi.org/10.1007/s00339-018-1737-8.

Chien, C. S., Hong, T. F., Han, T. J., et al. (2009). Effects of different hydroxyapatite binders on morphology, Ca/P ratio and hardness of Nd-YAG laser clad coatings. *Materials Transactions, 50*, 2852–2857. https://doi.org/10.2320/matertrans.M2009245.

Chien, C. S., Liao, T. Y., Hong, T. F., et al. (2014). Surface microstructure and bioactivity of hydroxyapatite and fluorapatite coatings deposited on Ti-6Al-4V substrates using Nd-YAG laser. *Journal of Medical and Biological Engineering, 34*, 109–115. https://doi.org/10.5405/jmbe.1379.

Choudhury, P., & Agrawal, D. C. (2012). *Hydroxyapatite (HA) coatings for biomaterials* (1st ed.). London Book Chapter: Woodhead.

Clarkson, J., Hardwick, K., & Barnes, D. (2000). International collaborative research on fluoride. *Journal of Dental Research, 79*, 893–904. https://doi.org/10.1177/00220345000790040301.

Cooper, L. F., Masuda, T., Whitson, S. W., et al. (1999). Formation of mineralizing osteoblast cultures on machined, titanium oxide grit–blasted, and plasma-sprayed titanium surfaces. *The International Journal of Oral & Maxillofacial Implants, 14*, 37–47.

Demnati, I., Grossin, D., Combes, C., et al. (2014). Plasma-sprayed apatite coatings: Review of physical-chemical characteristics and their biological consequences. *Journal of Medical and Biological Engineering, 34*, 1–7. https://doi.org/10.5405/jmbe.1459.

Dorozhkin, S. V. (2007). Calcium orthophosphates. *Journal of Materials Science, 42*, 1061–1095. https://doi.org/10.1007/s10853-006-1467-8.

Dorozhkin, S. V. (2009). Calcium orthophosphates in nature, biology and medicine. *Materials, 2*, 399–498. https://doi.org/10.3390/ma2020399.

Dowden, J. (2009). *The theory of laser materials processing: Heat and mass transfer in modern technology*. Dordrecht: Springer.

Eisenbarth, E., Velten, D., Müller, M. E., et al. (2004). Biocompatibility of beta-stabilizing elements of titanium alloys. *Biomaterials, 25*, 5705–5713. https://doi.org/10.1016/j.biomaterials.2004.01.021.

Elias, C. N., Meyers, M. A., Valiev, R. Z., et al. (2013). Ultrafine grained titanium for biomedical applications: An overview of performance. *Journal of Materials Research and Technology, 2*, 340–350. https://doi.org/10.1016/j.jmrt.2013.07.003

Filho, E. A., Fraga, A. F., & Bini, R. A. (2011). Bioactive coating on titanium implants modified by Nd:YVO4 laser. *Applied Surface Science, 257*, 4575–4580. https://doi.org/10.1016/j.apsusc.2010.12.056.

Fotovvati, B., Namdari, N., & Dehghanghadikolaei, A. (2019). On coating techniques for surface protection: A review. *Journal of Manufacturing and Materials Processing, 3*, 28–50. https://doi.org/10.3390/jmmp3010028.

Frantzén, J., Rantakokko, J., Aro, H. T., et al. (2011). Instrumented spondylodesis in degenerative spondylolisthesis with bioactive glass and autologous bone: A prospective 11-year follow-up. *Journal of Spinal Disorders & Techniques, 24*, 455–461. https://doi.org/10.1097/BSD.0b013e31822a20c6.

Frazier, W. E. (2014). Metal additive manufacturing: A review. *Journal of Materials Engineering and Performance, 23*, 1917–1928. https://doi.org/10.1007/s11665-014-0958-z.

Gammon, L. M., Briggs, R. D., Packard, J. M., et al. (2004). Metallography and microstructures of titanium and its alloys. *ASM Handbook, 9*, 899–917. https://doi.org/10.1361/asmhba0003779.

Ganjali, M., Yazdanpanah, A., & Mozafari, M. (2018). *Laser deposition of nano coatings on biomedical implants*. New York Book Chapter: Elsevier.

Geetha, M., Singh, A. K., Asokamani, R., et al. (2008). Ti based biomaterials, the ultimate choice for orthopaedic implants—A review. *Progress in Materials Science, 54*, 397–425. https://doi.org/10.1016/j.pmatsci.2008.06.004.

Gentile, P., Wilcock, C. J., Miller, C. A., et al. (2015). Process optimisation to control the physicochemical characteristics of biomimetic nanoscale hydroxyapatites prepared using wet chemical precipitation. *Materials (Basel), 8*, 2297–2310. https://doi.org/10.3390/ma8052297.

Ghayad, I. M., Girgis, N. N., & Ghanem, W. A. (2015). Laser surface treatment of metal implants: A review article. *Journal of Metallurgical Engineering, 4*, 48–56. https://doi.org/10.14355/me.2015.04.006.

Habraken, W., Habibovic, P., Epple, M., et al. (2016). Calcium phosphates in biomedical applications: Materials for the future? *Materials Today, 19*, 69–87. https://doi.org/10.1016/j.mattod.2015.10.008.

Hassanein, N., & Amleh, A. (2018). Biomaterial implants: A gateway to cancer through genetics and epigenetics. Advances in modern. *Oncology Research, 04*, 15–27. https://doi.org/10.30564/amor.v4i4.194.

Heimann, R. B. (2016). Plasma-sprayed hydroxylapatite-based coatings: Chemical, Mechanical, Microstructural, and Biomedical Properties. *Journal of Thermal Spray Technology, 25*, 827–851. https://doi.org/10.1007/s11666-016-0421-9.

Heimo, Y. (2017). *Bioactive glasses: Materials, properties and applications* (2nd ed.). New York: Elsevier.

Heise, S., Wirtha, T., Höhlinger, M., et al. (2018). Electrophoretic deposition of chitosan/bioactive glass/silica coatings on stainless steel and WE43 Mg alloy substrates. *Surface and Coating Technology, 344*, 553–563. https://doi.org/10.1016/j.surfcoat.2018.03.050.

Hofman, J. T., de Lange, D. F., Pathiraj, B., et al. (2011). FEM modeling and experimental verification for dilution control in laser cladding. *Journal of Materials Processing Technology, 211*, 187–196. https://doi.org/10.1016/j.jmatprotec.2010.09.007.

Hu, W., Kang, J., & Huang, T. (2009). Effect of processing parameters on thermal phenomena in direct laser metallic powder deposition. *Tsinghua Science and Technology, 14*, 154–159. https://doi.org/10.1016/S1007-0214(09)70084-7.

Huang, A. G., Liu, Y., Hu, S. H., et al. (2013). Laser cladding of fluoridated hydroxyapatite coatings on titanium alloy for bone replacement structures. *Advances in Materials Research, 815*, 540–546. https://doi.org/10.4028/www.scientific.net/AMR.815.540.

Imam, M. A., & Froes, F. S. (2010). Low cost titanium and developing applications. *JOM, 62*, 17–20. https://doi.org/10.1007/s11837-010-0069-8.

Jayakumar, K., Kumar, S. T., & Shanmugarajan, B. (2015). Review study of laser cladding processes on Ferrous substrates. *International Journal of Advanced Multidisciplinary Research, 2*, 72–87.

Ju, J., Zhou, Y., Kang, M., et al. (2018). Optimization of process parameters, microstructure, and properties of laser cladding Fe-based alloy on42CrMo steel roller. *Materials, 11*, 2061–2076. https://doi.org/10.3390/ma11102061.

Kasuga, T., Nogami, M., Niinomi, M., et al. (2004). Calcium phosphate glass-ceramic coating on a titanium alloy. *Phosphorus Research Bulletin, 17*, 29–36. https://doi.org/10.3363/prb1992.17.0_29.

Khor, K. A., Gu, Y. W., Pan, D., et al. (2004). Microstructure and mechanical properties of plasma sprayed HA/YSZ/Ti–6Al–4Vcomposite coatings. *Biomaterials, 25*, 4009–4017. https://doi.org/10.1016/j.biomaterials.2003.10.089.

Kim, M. S., Jung, U. W., Kim, S., et al. (2013). Bone apposition on implants coated with calcium phosphate by ion beam assisted deposition in oversized drilled sockets: A histologic and histometric analysis in dogs. *Journal of Periodontal and Implant Science, 43*, 18–23. https://doi.org/10.5051/jpis.2013.43.1.18.

Klocke, F., Brecher, C., & Wegener, M. (2012). Scanner-based laser cladding. *Physics Procedia, 39*, 346–353. https://doi.org/10.1016/j.phpro.2012.10.047.

Kumar, P., Ikeuchi, K., Oka, M., et al. (1991). Low wear rate of UHMWPE against zirconia ceramic (Y-PSZ) in comparison to alumina ceramic and SUS 316L alloy. *Journal of Biomedical Materials Research, 25*, 813–828. https://doi.org/10.1002/jbm.820250703.

Kumar, A., Yadav, N., Bhatt, M., et al. (2015). Sol-gel derived nanomaterials and its applications: A review. *Research Journal of Chemical Sciences, 5*, 98–105.

Kuo, P. H., Joshi, S. S., Lu, X. A., et al. (2019). Laser coating of bioactive glasses on bioimplant titanium alloys. *International Journal of Applied Glass Science, 10*, 307–320. https://doi.org/10.1111/ijag.12642.

Kurella, A. K., Hu, M. Z., & Dahotre, N. B. (2008). Effect of microstructural evolution on wettability of laser coated calcium phosphate on titanium alloy. *Materials Science and Engineering: C, 28*, 1560–1564. https://doi.org/10.1016/j.msec.2008.04.015.

Kusinski, J., Kac, S., Kopia, A., et al. (2012). Laser modification of the materials surface layer – A review paper. *Bulletin of the Polish Academy of Sciences, Technical Sciences, 60*, 711–728. https://doi.org/10.2478/v10175-012-0083-9.

Li, L., Pan, H., Tao, J., et al. (2008). Repair of enamel by using hydroxyapatite nanoparticles as the building blocks. *Journal of Materials Chemistry, 18*, 4079–4084. https://doi.org/10.1039/B806090H.

Li, Y., Yang, C., Zhao, H., et al. (2014). New developments of Ti-based alloys for biomedical applications. *Materials, 7*, 1709–1800. https://doi.org/10.3390/ma7031709.

Lin, C. W., Ju, C. P., & Chern Lin, J. H. (2005). A comparison of the fatigue behavior of cast Ti-7.5Mo with c.p. titanium, Ti-6Al-4V and Ti-13Nb-13Zr alloys. *Biomaterials, 26*, 2899–2907. https://doi.org/10.1016/j.biomaterials.2004.09.007.

Lindfors, N. C., Heikkilä, J. T., Koski, I., et al. (2009). Bioactive glass and autogenous bone as bone graft substitutes in benign bone tumors. *Journal of Biomedical Materials Research, 90*, 131–136. https://doi.org/10.1002/jbm.b.31263.

Liu, W., Liu, S., & Wang, L. (2019). Surface modification of biomedical titanium alloy: Micromorphology, microstructure evolution and biomedical applications. *Coatings, 9*, 249–272. https://doi.org/10.3390/coatings9040249.

Lusquiños, F., Pou, J., Boutinguiza, M., et al. (2005). Main characteristics of calcium phosphate coatings obtained by laser cladding. *Applied Surface Science, 247*, 486–492. https://doi.org/10.1016/j.apsusc.2005.01.134.

Lütjering, G., Williams, J. C., & Gysler, A. (2000). *Microstructure and mechanical properties of titanium alloys*. Singapore Book Chapter: World Scientific.

McAndrew, J., Efrimescu, C., Sheehan, E., et al. (2013). Through the looking glass; bioactive glass S53P4 (BonAlive) in the treatment of chronic osteomyelitis. *Irish Journal of Medical Science, 182*, 509–511. https://doi.org/10.1007/s11845-012-0895-5.

Mohammadzadeh Asl, S., Ganjali, M., & Karimi, M. (2019). Surface modification of 316L stainless steel by laser-treated HA-PLA nanocomposite films toward enhanced biocompatibility and corrosion-resistance in vitro. *Surface and Coating Technology, 363*, 236–243. https://doi.org/10.1016/j.surfcoat.2019.02.052.

Moritz, N., Vedel, E., Ylalen, H., et al. (2004). Characterisation of bioactive glass coatings on titanium substrates produced using a CO_2 laser. *Journal of Materials Science: Materials in Medicine, 15*, 787–794. https://doi.org/10.1023/B:JMSM.0000032819.64994.42.

Mozafari, M., Salahinejad, E., Shabafrooz, V., et al. (2013). Multilayer bioactive glass/zirconium titanate thin films in bone tissue engineering and regenerative dentistry. *International Journal of Nanomedicine, 8*, 1665–1672. https://doi.org/10.2147/IJN.S42659.

Mróz, W., Bunder, B., Syroka, R., et al. (2015). In vivo implantation of porous titanium alloy implants coated with magnesium-doped octacalcium phosphate and hydroxyapatite thin films using pulsed laser deposition. *Journal of Biomedical Materials Research, 103*, 151–158. https://doi.org/10.1002/jbm.b.33170.

Mukherjeea, S., Dharab, S., & Saha, P. (2017). Laser surface remelting of Ti and its alloys for improving surface biocompatibility of orthopaedic implants. *Materials Technology: Advanced Performance Technology, 33*, 106–118. https://doi.org/10.1080/10667857.2017.1390931.

Munsch, M. (2017). *Laser additive manufacturing of customized prosthetics and implants for biomedical applications, Laser Additive Manufacturing*. New York Book Chapter: Elsevier.

Nag, S., Samuel, S., Puthucode, A., et al. (2009). Characterization of novel borides in Ti–Nb–Zr– Ta+2B metal-matrix composites. *Materials Characterization, 60*, 106–113. https://doi.org/10.1016/j.matchar.2008.07.011.

Navarro, M., Michiardi, A., Castaño, O., et al. (2008). Biomaterials in orthopaedics. *Journal of the Royal Society Interface, 5*, 1137–1158. https://doi.org/10.1098/rsif.2008.0151.

Ocelík, V., & De Hosson, J. T. M. (2010). *Thick metallic coatings produced by coaxial and side laser cladding: Processing and properties*. New York Book Chapter: Elsevier.

Okazaki, Y., & Gotoh, E. (2005). Comparison of metal release from various metallic biomaterials in vitro. *Biomaterials, 26*, 11–21. https://doi.org/10.1016/j.biomaterials.2004.02.005.

Paital, S. R., He, W., & Dahotre, N. B. (2010). Laser pulse dependent micro textured calcium phosphate coatings for improved wettability and cell compatibility. *Journal of Materials Science: Materials in Medicine, 21*, 2187–2200. https://doi.org/10.1007/s10856-010-4085-6.

Park, J. B., & Bronzino, J. D. (2002). *Biomaterials: Principles and applications* (1st ed.). New York: CRC press.

Patel, N. R., & Gohil, P. P. (2012). A review on biomaterials: Scope, applications & human anatomy significance. *International Journal of Emerging Technology and Advanced Engineering, 2*, 91–101.

Paul, S., Gupta, I., & Singh, R. K. (2015). Characterization and modeling of microscale preplaced powder cladding via fiber laser. *Journal of Manufacturing Science and Engineering, 137*, 031019–031032. https://doi.org/10.1115/1.4029922.

Peddi, L., Brow, R. K., & Brown, R. F. (2008). Bioactive borate glass coatings for titanium alloys. *Journal of Materials Science: Materials in Medicine, 19*, 3145–3152. https://doi.org/10.1007/s10856-008-3419-0.

Pekkarinen, J., Kujanpa, V., & Salminen, A. (2012). Laser cladding with scanning optics: Effect of power adjustment. *Journal of Laser Applications, 24*, 032003–032010. https://doi.org/10.2351/1.4706582.

Pepla, E., Besharat, L. K., Palaia, G., et al. (2014). Nano-hydroxyapatite and its applications in preventive, restorative and regenerative dentistry: A review of literature. *Ann Stomatol (Roma), 5*, 108–114.

Picasso, M., Marsden, C. F., Wagniere, J. D., et al. (1994). A simple but realistic model for laser cladding. *Metallurgical and Materials Transactions B: Process Metallurgy and Materials Processing Science, 5B*, 281–287.

Pourhashem, S., & Afshar, A. (2014). Double layer bioglass-silica coatings on 316L stainless steel by sol–gel method. *Ceramics International, 40*, 993–1000. https://doi.org/10.1016/j.ceramint.2013.06.096.

Prasad, K., Bazaka, O., Chua, M., et al. (2017). Metallic biomaterials: Current challenges and opportunities. *Materials (Basel), 10*, 884–907. https://doi.org/10.3390/ma10080884.

Qizhi, C., & George, T. (2015). *Biomaterials: A basic introduction* (1st ed.). New York: CRC Press.

Qu, H., & Wei, M. (2006). The effect of fluoride contents in fluoridated hydroxyapatite on osteoblast behavior. *Acta Biomaterialia, 2*, 113–119. https://doi.org/10.1016/j.actbio.2005.09.003.

Quintino, L. (2014). *Overview of coating technologies* (1st ed.). London Book Chapter: Woodhead.

Rahmandoust, M., & Ayatollahi, M. R. (2019). *Nanomaterials for advanced biological applications*. London: Springer.

Rajesh, P., Muraleedharan, C. V., Komath, M., et al. (2011). Pulsed laser deposition of hydroxyapatite on titanium substrate with titania interlayer. *Journal of Materials Science: Materials in Medicine, 22*, 497–505. https://doi.org/10.1007/s10856-011-4230-x.

Rodriguez, O., Curran, D. J., Papini, M., et al. (2016). Characterization of silica-based and borate-based, titanium-containing bioactive glasses for coating metallic implants. J. *Non-Crystalline Solids, 433*, 95–102. https://doi.org/10.1016/j.jnoncrysol.2015.09.026.

Salinas, A. J. (2014). *Silica-based ceramics: Glasses*. Hoboken: Wiley. New Jersey Book Chapter.

Salinas, A. J., & Vallet-Regí, M. (2013). Bioactive ceramics: From bone grafts to tissue engineering. *RSC Advances, 3*, 11116–11131. https://doi.org/10.1039/C3RA00166K.

Salinas, A. J., Esbrit, P., & Vallet-Regí, M. (2013). A tissue engineering approach based on the use of bioceramics for bone repair. *Biomaterials Science, 1*, 40–51. https://doi.org/10.1039/C2BM00071G.

Santanu, P., Ramesh, S., & Wenyi, Y. (2016). Thermal model for additive restoration of mold steels using crucible steel. *Journal of Manufacturing Processes, 24*, 346–354. https://doi.org/10.1016/j.jmapro.2016.06.012.

Singh, R., Kurella, A., & Dahotre, B. N. (2006). Laser surface modification of Ti—6Al—4V: Wear and corrosion characterization in simulated biofluid. *Journal of Biomaterials Applications, 21*, 49–73. https://doi.org/10.1177/0885328206055998.

Smurov, I. (2008). Laser cladding and laser assisted direct manufacturing. *Surface and Coating Technology, 202*, 4496–4502. https://doi.org/10.1016/j.surfcoat.2008.04.033.

Steen, W. M. (2003). *Laser material processing* (3th ed.). London: Springer.

Steen, W. M., & Watkins, K. G. (1993). Coating by laser surface treatment. *Journal de Physique IV France, 03*, 581–590. https://doi.org/10.1051/jp4:1993961.

Sun, Z., Tan, X., Tor, S. B., et al. (2016). Selective laser melting of stainless steel 316L with low porosity and high build rates. *Materials and Design, 104*, 197–204. https://doi.org/10.1016/j.matdes.2016.05.035.

Tathe, A., Ghodke, M., & Nikalje, A. P. (2010). A brief review: Biomaterials and their application. *International Journal of Pharmacy and Pharmaceutical Sciences, 2*, 19–23.

Tellez, A. G. M. (2010). *Fiber laser metal deposition with wire: Parameters study and temperature control*. Dissertation: University of Nottingham.

Thakare, M., Wharton, J., Wood, R., et al. (2007). Exposure effects of alkaline drilling fluid on the microscale abrasion–corrosion of WC-based hardmetals. *Wear, 263*, 125–136. https://doi.org/10.1016/j.wear.2006.12.047.

Thamaraiselvi, T. V., & Rajeswari, S. (2004). Biological evaluation of bioceramic materials: A review. *Biomaterials and Artificial Organs, 18*, 9–17.

Tian, Y. S., Chen, C. Z., Li, S. T., et al. (2005). Research progress on laser surface modification of titanium alloys. *Applied Surface Science, 242*, 177–184. https://doi.org/10.1016/j.apsusc.2004.08.011.

Toyserkani, E., Khajepour, A., & Corbin, S. (2005). *Laser cladding* (1st ed.). New York: CRC Press.

Turon-Vinas, M., & Anglada, M. (2018). Strength and fracture toughness of zirconia dental ceramics. *Dental Materials, 34*, 365–375. https://doi.org/10.1016/j.dental.2017.12.007.

Vallet-Regí, M., & González-Calbet, J. M. (2004). Calcium phosphates as substitution of bone tissues. *Progress in Solid State Chemistry, 32*, 1–31. https://doi.org/10.1016/j.progsolidstchem.2004.07.001.

Vilar, R., & Almeida, A. (2016). *Laser surface treatment of biomedical alloys*. New York Book Chapter: Elsevier.

Wang, D. G., Chen, C. Z., Ma, J., et al. (2008). In situ synthesis of hydroxyapatite coating by laser cladding. *Colloids and Surfaces, B: Biointerfaces, 66*, 155–162. https://doi.org/10.1016/j.colsurfb.2008.06.003.

Wang, H., Chen, T., Cong, W., et al. (2019). Laser cladding of Ti-based ceramic coatings on Ti6Al4V alloy: Effects of CeO2 nanoparticles additive on wear performance. *Coatings, 9*, 109–117. https://doi.org/10.3390/coatings9020109.

Wood Field, T., Lim, K., Morouço, P., et al. (2017). *Biofabrication in tissue engineering*. New York Book Chapter: Elsevier.

Wu, D., Guo, M., Ma, G., et al. (2015). Dilution characteristics of ultrasonic assisted laser clad yttria-stabilized zirconia coating. *Surface and Coating Technology, 79*, 200–204. https://doi.org/10.1016/j.matlet.2014.11.058.

Xiong, Z., Chen, G., & Zeng, X. (2009). Effects of process variables on interfacial quality of laser cladding on aeroengine blade material GH4133. *Journal of Materials Processing Technology, 209*, 930–936. https://doi.org/10.1016/j.jmatprotec.2008.03.004.

Xuanyong, L., Paul, K. C., & Chuanxian, D. (2004). Surface modification of titanium & titanium alloys. *Materials Science and Engineering R, 47*, 49–121. https://doi.org/10.1016/j.mser.2004.11.001.

Zhao, G., Cho, C., & Kim, J. D. (2003). Application of 3-D finite element method using Lagrangian formulation to dilution control in laser cladding process. *International Journal of Mechanical Sciences, 45*, 777–796. https://doi.org/10.1016/S0020-7403(03)00140-1.

Zhecheva, A., Sha, W., Malinov, S., et al. (2005). Enhancing the microstructure and properties of titanium alloys through nitriding and other surface engineering methods. *Surface and Coating Technology, 200*, 2192–2207. https://doi.org/10.1016/j.surfcoat.2004.07.115.

Zheng, M., Fan, D., Li, X., et al. (2008). Microstructure and osteoblast response of gradient bioceramic coating on titanium alloy fabricated by laser cladding. *Applied Surface Science, 255*, 426–428. https://doi.org/10.1016/j.apsusc.2008.06.078.

Zheng, M., Fan, D., Li, X., et al. (2010). Microstructure and in vitro bioactivity of laser-cladded bioceramic coating on titanium alloy in a simulated body fluid. *Journal of Alloys and Compounds, 489*, 211–214. https://doi.org/10.1016/j.jallcom.2009.09.054.

Zhu, Y., Liu, Q., Xu, P., et al. (2016). Bioactivity of calcium phosphate bioceramic coating fabricated by laser cladding. *Laser Physics Letters, 13*, 055601–055607. https://doi.org/10.1088/1612-2011/13/5/055601.

Chapter 11
Laser Cladding of Ni-Based Superalloys

Gopinath Muvvala, Sagar Sarkar, and Ashish Kumar Nath

11.1 Introduction to Ni-Based Alloys

Among all the available engineering materials, nickel and its alloys have gained wide popularity due to their ability to withstand severe operating conditions like corrosive environments both in aqueous and at high temperature, high strength at ambient and elevated temperatures, and combination of these. Apart from this, its ability to be diluted by a large number of elements or materials and retaining its ductility and strength from cryogenic to solidus temperature with the matrix being austenitic throughout the temperature range has made it a potential candidate for a wide range of applications. With appropriate alloying elements and elevated physical properties, Ni-based alloys find wide applications in marine, nuclear, power plant, petrochemical, and aerospace industries. A typical application of Ni-based alloys in gas turbine is illustrated in Fig. 11.1 (Leary et al. 2018). Air from the inlet enters the compressor unit where its pressure is increased to almost 24 times in 15 stages, each one consisting of a set of rotor and stator (Cemal et al. 2012; Eliaz et al. 2002). From the compressor, air enters at a high pressure into the combustion chamber where fuel is injected and burned raising the temperature to as high as 1930 °C, which is cooled close to 1100 °C, limited by the maximum operating temperature of materials, essentially a nickel-based alloy (Leary et al. 2018; Cemal et al. 2012). This gives a glimpse of severity of atmosphere in which nickel-based alloys can operate.

G. Muvvala (✉)
Department of Mechanical and Aerospace Engineering, Indian Institute of Technology Hyderabad, Sangareddy, India
e-mail: mgopinath@iith.ac.in

S. Sarkar · A. K. Nath
Department of Mechanical Engineering, Indian Institute of Technology Kharagpur, Kharagpur, India
e-mail: aknath@mech.iitkgp.ac.in

P. Cavaliere (ed.), *Laser Cladding of Metals*,
https://doi.org/10.1007/978-3-030-53195-9_11

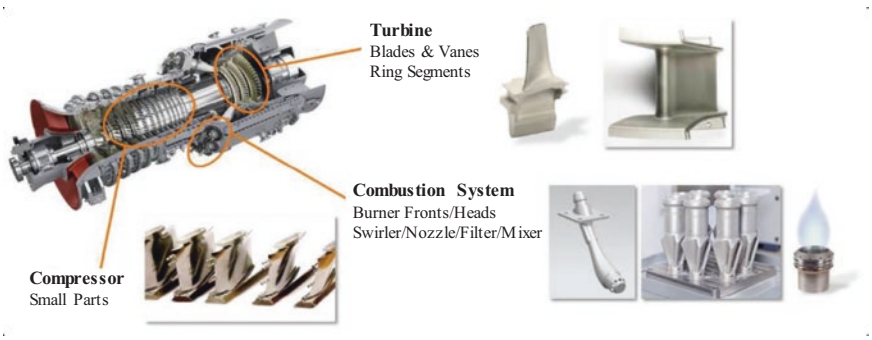

Fig. 11.1 Inconel superalloys in gas turbine applications (Leary et al. 2018)

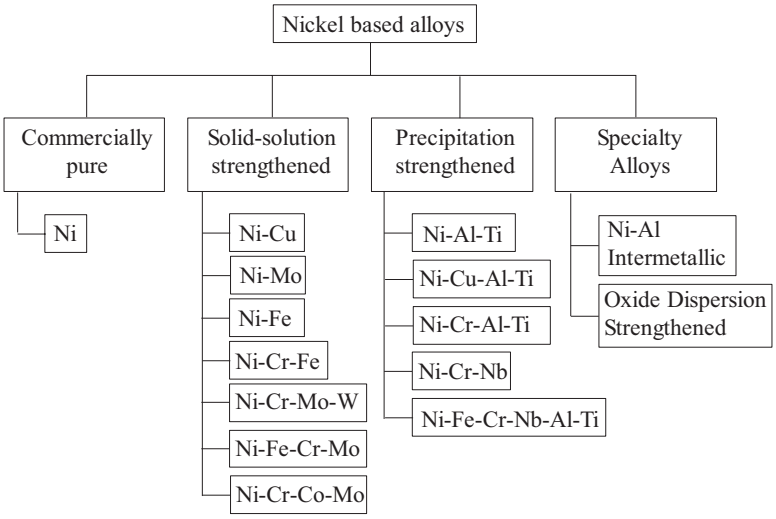

Fig. 11.2 Classification of nickel-based superalloys (DuPont et al. 2009)

11.1.1 Classification of Ni-Based Superalloys

Nickel-based superalloys can be broadly classified into four categories, as shown in Fig. 11.2. Commercially pure Ni alloys contain nickel (> 99%) and are mostly used for their corrosion resistance in caustic environments. However, they suffer from low strength and hardness. Solid solution-strengthened alloys are used in applications where a combination of moderate strength and excellent corrosion resistance is required. These are primarily strengthened by the addition of substitutional alloying elements such as Cu, Mo, Fe, Cr, and W, as shown in Fig. 11.2, which provide solid solution strengthening of austenitic microstructure. Precipitation-strengthened Ni-based alloys are used in applications where the combination of both high strength and excellent corrosion resistance is important. The development of these alloys

made the "jet age" possible. Compared to solid solution-strengthened alloys, the physical metallurgy of precipitation-strengthened Ni-based alloys is quite complex. These alloys along with solid solution strengthening elements contain Ti, Al, and Nb for precipitate formation; Cr, Al, and Ta for oxidation resistance; Cr, La, and Th for hot corrosion resistance; B and Zr for creep and stress rupture properties; and Hf for intermediate temperature ductility. A thorough study on the nickel-based alloys and their metallurgy is reported by DuPont et al. (2009) providing an exhaustive list of Ni alloys. Considering the context of this chapter and its relevance to laser cladding, the discussion is limited to two most commonly used solid solution- and precipitation-strengthened nickel-based alloys Inconel 625 and Inconel 718 and their metal matrix composite coatings.

11.2 Introduction to Laser Cladding

Before going to the details of laser cladding of nickel-based superalloys and the challenges involved, the different techniques of laser cladding and their fundamental differences are briefly discussed to understand the behaviors of same material under different processing conditions.

Laser cladding is a weld deposition technique in which the laser is used as a heat source to melt and deposit or overlay the feedstock, which may be in the form of wire or powder, onto a substrate. At the initial stage, it was very widely employed for depositing protective coatings against wear or corrosion. The main advantage stems from the fact that the process involves rapid heating followed by rapid cooling (10^3–10^6 °C/s) through self-quenching with minimum heat-affected zone and distortion and excellent metallurgical bonding. With time the process evolved into a multi-overlapped layer deposition technique which is now popularly known as **a**dditive **m**anufacturing (AM). In this process, the 3D computer-aided design (CAD) of a part to be built is first sliced into thin layers, usually 25–200 microns thick, and a 2D image of each layer is created in industry standard .stl format. Utilizing the data file, the part is built by depositing the desired material usually in the form of either powder or wire layer over layer. Utilizing laser as heat source and powder as feedstock, the process can be broadly classified into two methods, i.e., powder bed and blown powder methods, widely known as selective laser melting (SLM) and laser-engineered near net shaping (LENS) or direct metal laser deposition process (DMLD), respectively. As shown in Fig. 11.3a in powder bed method, a predefined thickness of power layer is spread on the surface of a build platform using a ceramic coater blade, followed by irradiation and melting by a focused laser beam in the selected areas as per the 2D layer data file. Again a layer of fresh powder is spread onto the already processed layer, and selective melting is carried out. The process is repeated until the component of desired height and shape is achieved. In DMLD process (Fig. 11.3b), the powder is fed coaxially along with the laser beam using a nozzle in such a way that the powder is heated up and fed into the molten pool created by the laser beam, which consolidates and forms an overlay. SLM process is

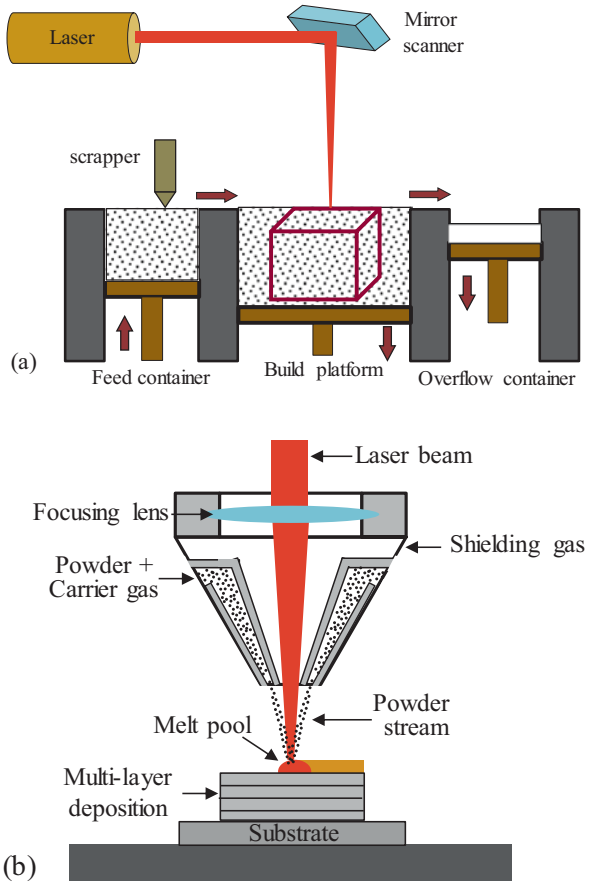

Fig. 11.3 Schematic of (**a**) SLM and (**b**) DMLD

widely used to fabricate components with complex geometries and intricate shapes directly from the CAD model, whereas DMLD process is used for refurbishment of worn-out components and to deposit protective coatings. DMLD process has been further extended to fabricate the components directly also, similar to SLM. However, DMLD is second to SLM in terms of design complexity and dimension accuracy.

Apart from the differences in the method of deposition, it is very essential to understand typical variations in the process parameters which influence the thermal history of the molten pool, surface morphology, microstructure, and mechanical properties. Table 11.1 shows the process parameters and their typical values used in SLM and DMLD process. SLM process essentially involves smaller spot diameters and layer thickness of similar ranges. In DMLD process, the spot diameter is generally in the range of less than a mm to a few mm with resulting clad track dimension of similar range. This difference essentially dictates the cooling rates which significantly affect both microstructure and mechanical properties. Molten pool in SLM process experiences a typical cooling rate of 10^6 °C/s, while it is of the order of 10^3 °C/s in case of DMLD. Table 11.2 shows the achievable mechanical properties

Table 11.1 Process parameters in SLM and DMLD process (Wu et al. 2020; Qiu et al. 2019; Kang et al. 2018; Caiazzo 2018; Ramakrishnan and Dinda 2019)

Parameter	SLM	DMLD
Laser power (P) W	200–400	400–2000
Scan speed (V) mm/min	6×10^4–30×10^4	400–800
Spot diameter (d) mm	0.04–0.1	1–3
Power density ($4P/\pi d^2$) W/mm^2	2.5×10^4–32×10^4	~50–2500

Table 11.2 [a]Achievable mechanical properties in SLM and DMLD

Alloy	Process		Yield strength (MPa)	Ultimate tensile strength (MPa)	% Elongation	Hardness
Inconel 718	SLM (Chlebus et al. 2015)	XY	1159 ± 32	1137 ± 66	8 ± 6	463 ± 8
		Z	1074 ± 42	1320 ± 6	19 ± 2	
	SLM + HT (Wang et al. 2012)	XY	1131 ± 30	1319 ± 40	16 ± 6	470 ± 15
	SLM + HIP (Moussaoui et al. 2018)	XY	1150 ± 25	1350 ± 25	25 ± 2	475 ± 15
	DMLD (Zhang et al. 2015)	XY	720 ± 25	950 ± 25	17 ± 3	285 ± 15
	DMLD+HT	XY	1062	1270	6.5	255 ± 15
	Conventional (Rao et al. 2004)	Wrought	1098 ± 70	1335 ± 60	16 ± 5	400 ± 15
		Cast	758 ± 25	862 ± 25	5 ± 2	255 ± 50
Inconel 625	SLM (Marchese et al. 2020)	XY	780 ± 25	1050 ± 30	35 ± 3	354 ± 24
		Z	620 ± 25	880 ± 10	43 ± 3	
	SLM + HT (Marchese et al. 2020)	XY	780 ± 5	1060 ± 10	38 ± 6	342 ± 10
		Z	620 ± 10	980 ± 20	45 ± 6	
	DMLD (Paul et al. 2007)	XY	572 ± 25	920 ± 15	48 ± 2	255 ± 8 (Dinda et al. 2009)
		Z	568 ± 20	925 ± 12	46 ± 2	
	Conventional (Inconel 625 data sheet)	Annealed	534 ± 120	930 ± 100	45 ± 15	188 ± 24

[a]Under optimized parameters; HT, heat treated; HIP, hot isostatic pressing

of components fabricated by SLM and DMLD processes in comparison to conventional processes. It can be observed that under optimized conditions, the mechanical properties of parts built by AM process are close or even superior for some materials, like Ni alloys, than that obtained in conventional process. However, it is observed that the strength of DMLD-built parts is usually less than that of SLM-built parts. This is essentially due the different cooling rates in two processes which dictate the segregations in nickel-based superalloys.

11.3 Cooling Rate and Its Significance in Laser Cladding Process

11.3.1 Influence of Cooling Rate on Segregations in Ni-Based Superalloys

As discussed, nickel-based alloys are used in severe environments, like high-corrosive and high-temperature applications. This is made feasible by adding appropriate alloying elements as discussed in Sect. 11.1.1. It is therefore essential to ensure their proper distribution within the material, which otherwise results in degradation of its properties. The distribution of the alloying elements within the matrix highly depends on the thermal history they undergo during deposition processes. In order to elaborate and bring out a clear understanding of this, Inconel 718 is considered for the subsequent discussion. In Sect. 11.1.1, the alloying elements and their effects on the phase strengthening as well as mechanical properties were briefly discussed. However, it is important to understand their solubility in the metal matrix which is Ni-Cr-Fe, γ-matrix in case of Inconel 718.

Inconel 718 is basically a precipitation-strengthened nickel-based superalloy that contains Nb, Ti, and Al as alloying elements. During solidification process, it is expected to form γ′ and γ“ phases, intermetallic phases based on Ni_3(Al,Ti), and Ni_3Nb having an ordered FCC L12 and a body-centered tetragonal DO_{22} structure, respectively, which are coherent with the γ-Ni solid solution matrix, i.e., Ni-Cr-Fe. The main principal strengthening mechanism involved is the antiphase boundary hardening arising from the coherent and ordered γ′ and γ” phases (Sims et al. 1987; Oblak et al. 1974). However, during the solidification process, the precipitation strengthening elements are susceptible to segregation owing to their low equilibrium distribution coefficients k as shown in Table 11.3 (Odabasi et al. 2010), which is defined as $k = C_S/C_L$, where C_S and C_L are the compositions of solid and liquid at the solid-liquid interface. However, the severity of this elemental segregation depends on the cooling or freezing rate, i.e., at higher cooling rates, the elements get trapped inside the γ-matrix improving the mechanical properties.

Figures 11.4 (Kou 2002) and 11.5 (Xiao et al. 2017) show the schematic of evolution of microstructure and its dependency on the cooling rate. During laser cladding process, the metal powder is melted along with a thin layer of substrate, both of which start solidifying as the laser beam proceeds ahead. Solidification initiates

Table 11.3 Average distribution coefficients

Process		k values of major elements						
		Nb	Al	Ti	Mo	Fe	Cr	Ni
Laser welding	2.9 kW, 39.94 mm/s	0.52	0.82	0.67	0.82	1.06	1.15	1.00
	1.5 kW, 11.85 mm/s	0.51	1.08	0.65	0.69	1.09	1.16	1.02
GTA		0.42	–	0.65	0.85	1.06	1.10	1.01
EB		0.53	–	0.71	0.69	1.05	1.04	0.96

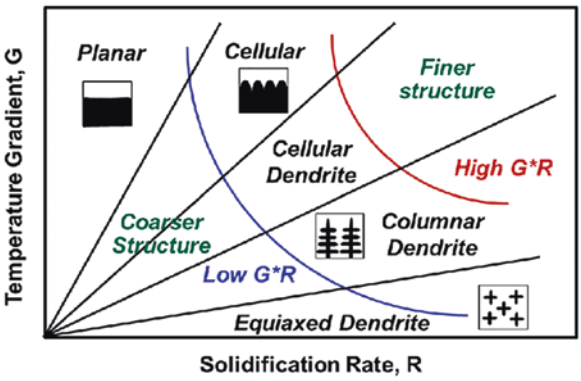

Fig. 11.4 Effect of G and R on the solidification morphology (Kou 2002)

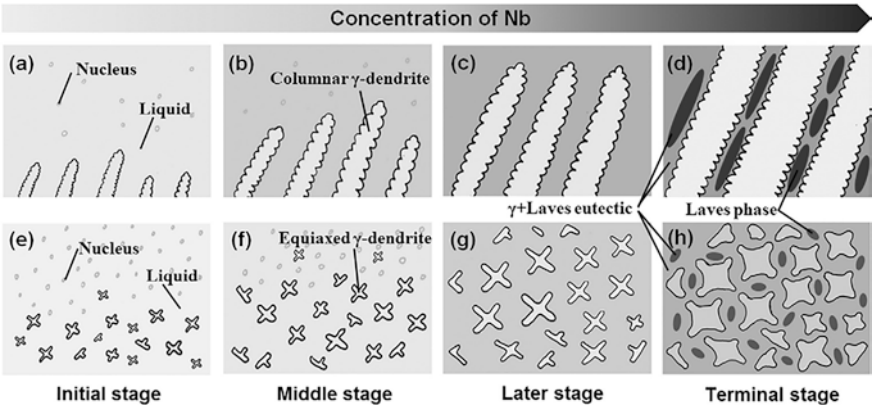

Fig. 11.5 Schematic diagram of the microstructure evolution in Inconel 718 (Xiao et al. 2017)

from the interface of molten pool and the substrate due the heterogeneous nucleation. At the initial stage, the temperature gradients (G) and the solidification rate (R) will be quite large resulting in a planar, followed by columnar or epitaxial growth, as shown in Fig. 11.4. In other words, the cooling rate which is essentially the G × R product will be very high at the initial stage of solidification resulting in fine microstructure. As the solidification proceeds, the temperature gradient and the molten pool temperature decrease which results in the formation of homogeneous nucleation sites increasing the solidification rate and equiaxed grains. As shown in Fig. 11.5, in Inconel 718, the solidification process initiates as columnar γ austenitic phase (Ni-Cr-Fe), pushing the alloying elements (Nb) into the liquid phases because of their low distribution coefficient, as shown in Table. 11.3. As the process proceeds, the concentration of alloying elements in the liquid phase increases to such an extent where it starts solidifying, forming Laves phases. This mechanism of microstructural evolution is well reported by Muvvala et al. (2017c). Figure 11.6 shows the evolution of microstructure within the molten pool as discussed above. Three distinct zones can be identified clearly, where zone 1 shows the pure

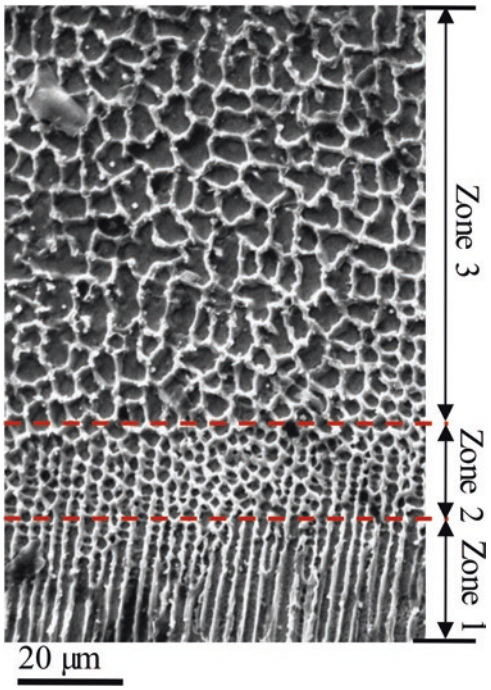

Fig. 11.6 Transition from epitaxial growth to equiaxed grains in clad zone near surface (Muvvala et al. 2017c)

epitaxial/columnar growth, followed by transition zone 2 where the epitaxial growth terminates and equiaxed grains initiate and zone 3 consisting of fully defined equiaxed grains. However, depending on the cooling rate or the molten pool lifetime, the segregation mechanism of the alloying elements varies in the laser cladding process. In case of columnar dendritic regions, where the cooling rate is expected to be maximum, alloying elements get entrapped in interdendritic regions, as shown in Fig. 11.5d, and at the top surface having relatively low cooling rates, equiaxed grains/γ-matrix start growing to sizes depending on the cooling rate pushing the alloying elements toward the grain boundaries, as shown in Fig. 11.5h. Therefore, the amount of segregation within a material essentially depends on the solidification rate which is controlled by the cooling rate and the temperature gradient. The faster the cooling rate, the lesser will be the segregation as rapid solidification results in entrapping these alloying elements. Thus, the cooling rate plays a critical role in dictating the evolution of microstructure and mechanical properties in laser cladding process.

Coming back to SLM and DMLD process, Fig. 11.7 shows the process map of cooling rate corresponding to each of these. As discussed before, it can be observed that the cooling rates are much higher in case of SLM compared to DMLD (denoted as LSF, laser solid forming) process, which essentially is the reason for superior mechanical properties in SLM parts, as shown in Table 11.2.

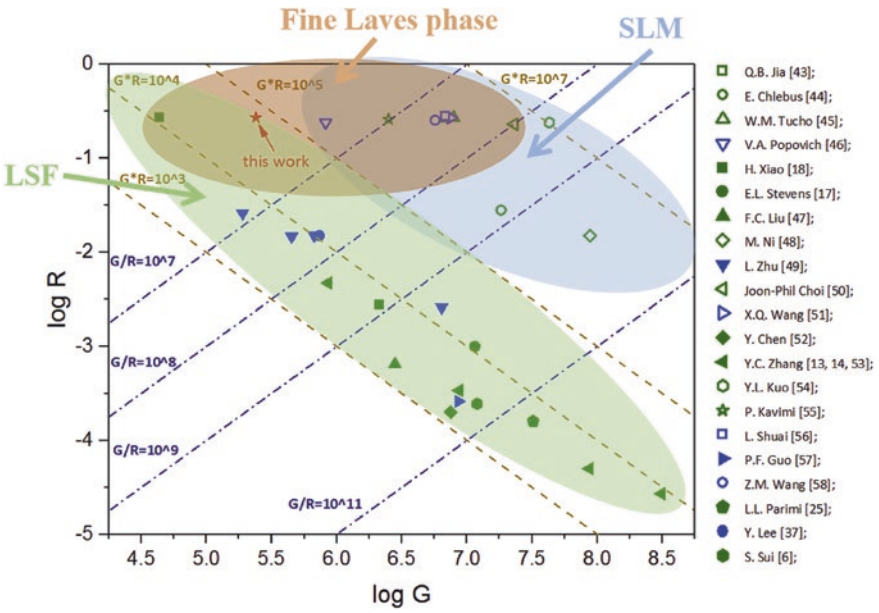

Fig. 11.7 The selection map of Laves phase morphology in Inconel 718 (Sui et al. 2019)

11.3.2 Effect of Elemental Segregation on Mechanical Properties

As discussed previously, Laves is a hexagonal close packed phase and is generally accepted as a form of $(Ni, Fe, Cr)_2(Nb, Mo, Ti)$. These are generally brittle in nature and deteriorate the mechanical properties or make the coating brittle (Gopinath et al. 2017). However, this essentially depends on their (Laves) size and distribution. Though the heat treatment could help in dissolving the Laves phase, followed by precipitation hardening, it has limitations in case of laser cladding. As laser cladding is widely used in the deposition of protective coatings or refurbishment of worn-out components, heat treatment may have adverse effects on the substrate microstructure and mechanical properties. Therefore, it is essential to control the size and shape of the Laves phase during the deposition itself. Sui et al. (2017a, b, 2019) and Ming et al. (2015) carried out a detailed research on Laves phase morphology and size on the deformation mechanism and their influence of mechanical properties at room and elevated temperatures. Laves phase deformation process includes two mechanisms, viz., fragmentation and separation from the γ-matrix as shown in Fig. 11.8. Fragmentation is essentially dominant in long-striped Laves phases during loading under room temperature due to stress concentration (Fig. 11.8a), whereas granular Laves being smaller in size move easily with γ-matrix increasing the ductility and reducing the chances of failure. Further, it can be observed that fragmentation is predominant even in case of fatigue crack

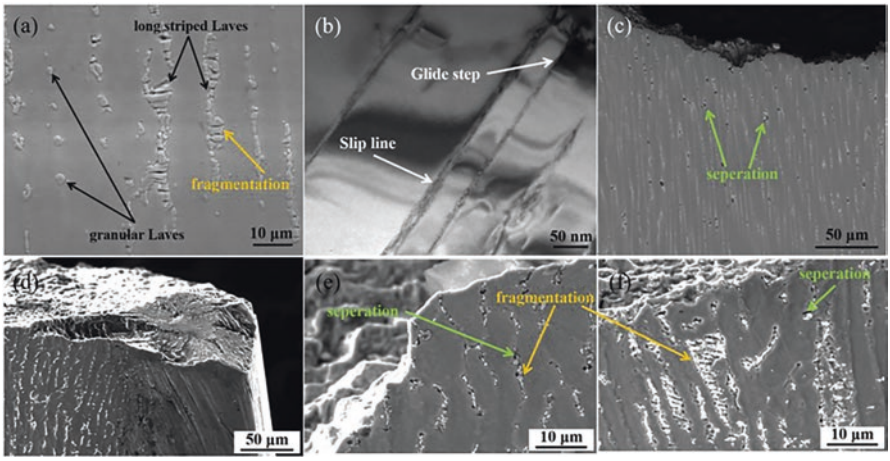

Fig. 11.8 Deformation behavior of Laves phase: (**a**) and (**b**) after the room temperature tensile test (Sui et al. 2017a); (**c**) after the stress rupture test ($T = 650$ °C, $\sigma_a = 725$ MPa) (Ming et al. 2015); (**d**), (**e**), and (**f**) after high-cycle fatigue test ($T = 650$ °C, $f = 110$ Hz, $R = 0.1$, $K_t = 1$, $\sigma_a = 750$ MPa) (Sui et al. 2017a); (**d**) in the fatigue source region; (**e**) in the fatigue crack propagation region; (**f**) in the fatigue final rupture region

propagation region (Fig. 11.8e) and the final fatigue rupture region (Fig. 11.8f). However, as shown in Fig. 11.8c, the separation is found to be the main dominating mechanism of failure in case of high-temperature rupture stress. This is also visible in case of Fig. 11.8e, f. This can be essentially attributed to the phase boundary weakening at high temperatures. Further, it is very essential to understand the influence of loading direction and orientation and shape of grains or segregating alloying elements. When the applied load or stress is parallel to the interface or boundary of the matrix and the Laves phase, high stress is required for separation, and therefore fragmentation could be dominant. However, when the applied stress is in perpendicular direction of the interface, separation could be dominant. Thus, in as-deposited additive manufactured components, directionality in mechanical properties always exists arising from the inhomogeneity in microstructure.

11.3.3 Parameters Affecting the Cooling Rate in Laser Cladding

From Sects. 11.3.1 and 11.3.2, it is evident that in laser cladding process the cooling rate or molten pool lifetime plays a significant role in determining the mechanical properties. Therefore, it is important to understand the process parameters that influence the cooling rate. Laser cladding involves a large number of process parameters, among them laser power, scan speed, spot diameter, and layer thickness or powder mass flow rate are the ones having the most significant influences, and

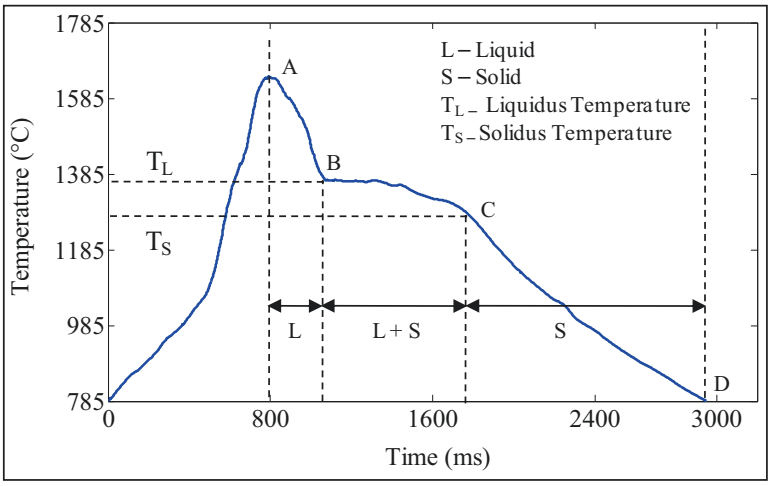

Fig. 11.9 Typical molten pool thermal cycle during the laser cladding process (Muvvala et al. 2017c)

therefore their effects are discussed in brief (Muvvala et al. 2017c). Muvvala et al. (2017c) carried out an experimental study on the influence of various process parameters on the molten pool thermal history which includes heating and cooling rates and molten pool lifetime using an IR pyrometer. Figure 11.9 shows a typical molten pool thermal history of a point during laser scan over a preplaced powder surface for cladding. It essentially consists of a heating cycle 0A and a cooling cycle AD. As the laser beam is scanned over the preplaced powder surface, the temperature at the point of laser irradiation rises rapidly melting the powder, and as the laser crosses over the point, it starts cooling. It can be observed that the cooling cycle exhibits several stages further which include cooling of molten pool (AB) and solidification shelf (BC) during which solidification process initiates (Point B) and ends (Point C) followed by solid state cooling (CD). Figure 11.10 shows typical relationships between heating and cooling rates and the molten pool lifetime (Nair et al. 2019). With increasing heating rate, cooling rate increases, and therefore the molten pool lifetime decreases which is beneficial for the mechanical properties of Ni-based coatings or components.

Figure 11.11 shows the effect of laser power and scan speed on the cooling rates (Muvvala et al. 2017c). It may be mentioned that good quality of cladding in terms of geometrical aspect and dilution was realized within the experimental range of process parameters. It can be observed that laser power has very little influence on cooling rate compared to the scan speed. At a given laser power, with the decrease of scan speed, the interaction time (ratio of laser beam diameter to scan speed) and the line energy (ratio of laser power to scan speed) both increase, and this tends to reduce the temperature gradient by heat conduction and therefore the cooling rate. However, at a given scan speed with increase in laser power, the energy density only

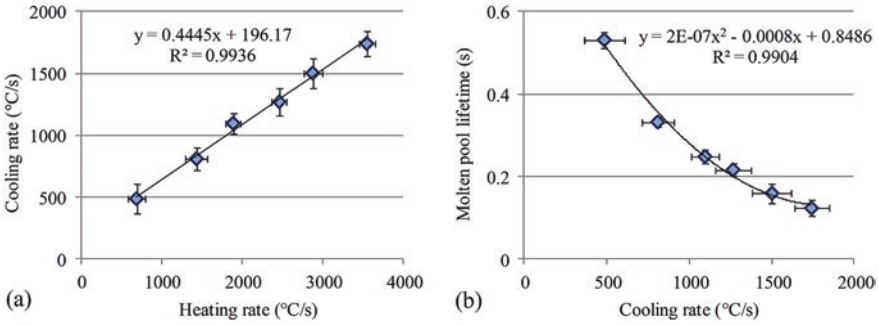

Fig. 11.10 Correlation between (**a**) heating and cooling rate and (**b**) cooling rate and molten pool lifetime (Nair et al. 2019)

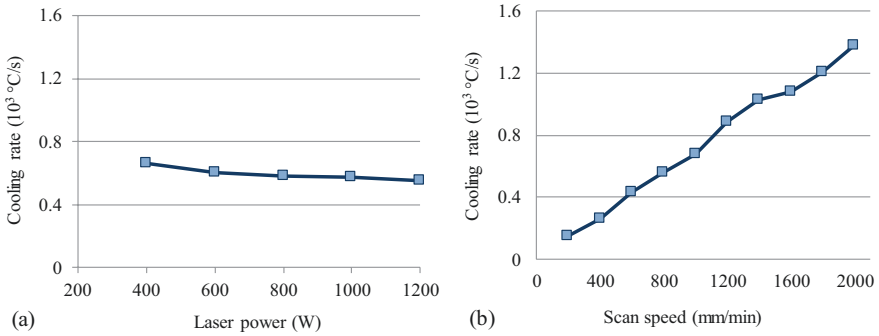

Fig. 11.11 Effect of (**a**) laser power and (**b**) scan speed on cooling rate (Muvvala et al. 2017c)

increases which tends to increase the melt pool temperature, but the onset of evaporation does not allow a significant increase in the peak temperature. Therefore, laser power has very little influence on the cooling rate. Further, the molten pool lifetime or cooling rate depends on the preplaced powder layer thickness also. As shown in Fig. 11.12, with an increase in layer thickness, the molten pool size or volume increases which tend to reduce the cooling rate. Figure 11.13 shows the variation in equiaxed grain size with the molten pool lifetime and cooling rate corresponding to different scan speeds, from which it is evident that faster cooling rates result in entrapment of alloying elements, while slower cooling rates result in severe segregations affecting the mechanical properties as discussed in previous sections.

11.3.4 Effect of Process Parameters and Cooling Rates on Surface Properties

Apart from the fabrication and refurbishment of components, laser cladding process is widely used in the field of surface engineering for depositing wear-resistant hardfacing and protective coatings against corrosion. Similar to the other mechanical

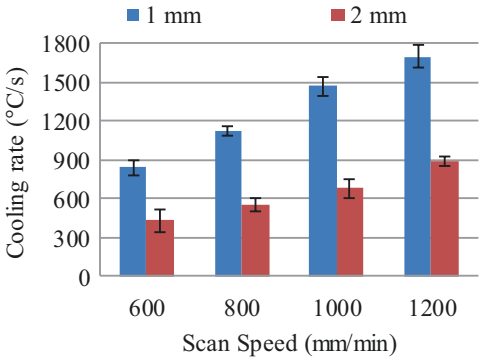

Fig. 11.12 Effect of layer thickness on cooling rate (Muvvala et al. 2017c)

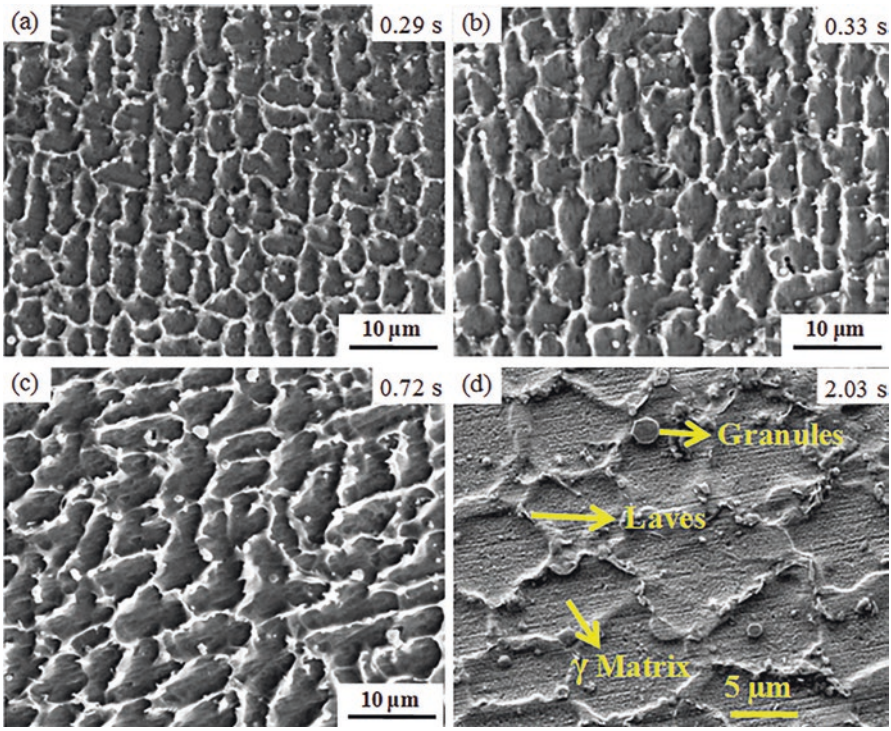

Fig. 11.13 Variation in equiaxed grain size with cooling rate, (**a**) 1050 °C/s, (**b**) 680 °C/s, (**c**) 435 °C/s, and (**d**) 152 °C/s corresponding to scan speeds of 1400, 1000, 600, and 200 mm/min, respectively

properties, cooling rate does play a significant role in determining the surface properties of coatings. Wolff et al. (2019) found that apart from the cooling rate, dilution is one of the major factors influencing the hardness in laser-deposited Inconel 718 on carbon steel. While the cooling rate was observed to reduce with the increase of laser power and powder flow rate due to the increase in the molten pool volume

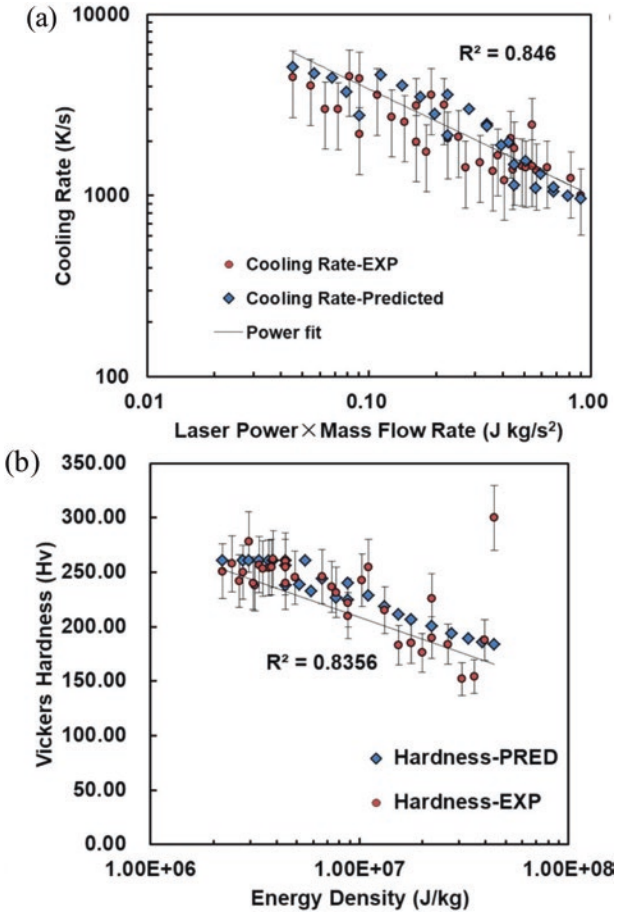

Fig. 11.14 (**a**) Effect of laser power and powder mass flow rate on cooling rate and (**b**) effect of energy density on hardness (Wolff et al. 2019)

(Fig.11.14a), the microhardness decreased with increasing laser energy per unit mass of powder deposited (Fig. 11.14b) which could be resulting from the decreased cooling rate, grain coarsening and elemental segregation, and increased dilution (Wolff et al. 2019).

In addition to the hardness, the corrosive properties of the coating also deteriorate for slower cooling rates. Luo et al. (2019) carried out a detailed research on corrosive behavior of selective laser-melted Inconel 718 with and without heat treatment and found that the Laves phase is detrimental to the corrosion properties of the coating. Figure 11.15 depicts schematically the corrosion mechanism in nickel-based alloys which experience segregation during the laser cladding process. As described earlier, Inconel 718 consists of γ-matrix as primary phase and γ′ and γ″ as secondary phases which tend to segregate at the grain boundary or interdendritic

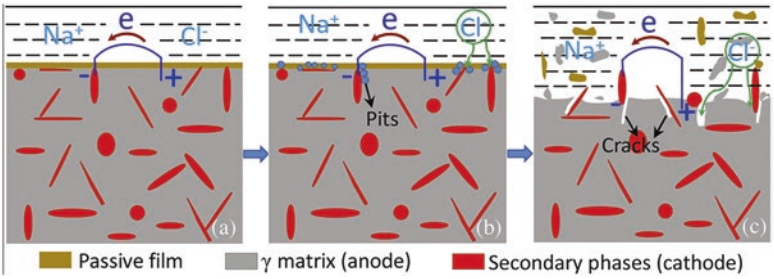

Fig. 11.15 Schematic presentations of galvanic coupling effect-induced corrosion micro-battery: (**a**) surface passivation, (**b**) formation of corrosion pits on surface passive film, (**c**) breakdown of surface passive film, dissolution of anode γ-matrix, and formation of cracks (Luo et al. 2019)

region during the deposition process. When a sample with such microstructure and phase distribution is exposed to the electric potential in a NaCl solution, the secondary phase serves as a cathode, while the γ-matrix serves as an anode (Luo et al. 2019) triggering the formation of abundant corrosion micro-batteries between Laves phases and γ-matrix due to the galvanic coupling effect, as depicted in Fig. 11.15. This results in preferential corrosion of γ-matrix. In addition, the substantial precipitation of carbides in the interdendritic region also facilitates the galvanic coupling effect. Further, this preferential corrosion also leads to the corrosion cracking, as shown in Fig. 11.15c, which is further favored by the in-built stresses.

Figure 11.16 shows the surface morphologies of Inconel 718 samples obtained by different processes after electrochemistry corrosion in 3.5 wt% NaCl solution. From Fig. 11.16a,b, the stress corrosion cracking is clearly evident in the case of as-built SLM samples. Further, in comparison to others, i.e., solution annealed and rolled samples (Fig. 11.16c–l), the corrosion cracks are markedly broadened. However, it can be observed that with heat treatment (Fig. 11.16c–h) the tendency of the corrosion cracking has completely reduced and limited to the interface of δ and γ phase which is essentially due to diffusion and dissolution of alloying element during the heat treatment process. However, as discussed previously, heat treatment may not be possible in all cases, especially in coating applications, and thus it is very essential to control the elemental segregations through proper selection of process parameters that could process the coating at rapid cooling rates.

11.4 Auxiliary Methods to Control Microstructure

From the above discussions, it is evident that controlling the microstructure and elemental segregations in nickel-based superalloys plays a vital role in dictating the mechanical properties of the laser-cladded protective coatings or components, though laser, being a rapid solidification process, still experiences elemental segregation. Also, rapid solidification results in directional solidification with

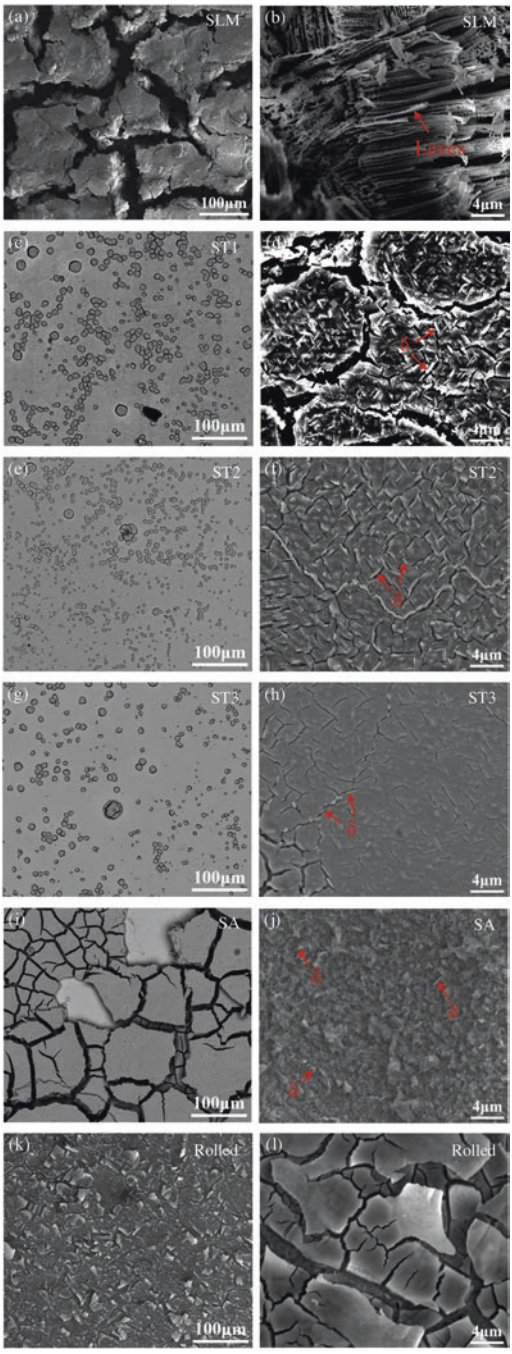

Fig. 11.16 Surface morphologies of Inconel 718 samples obtained by different processes after electrochemistry corrosion in 3.5 wt% NaCl solution: (**a**–**b**) SLM; heat treated for 1 h at (**c**–**d**) 940 °C; (**e**–**f**) 980 °C; (**g**–**h**) 1020 °C; (**i**–**j**) solution annealed at 980 °C × 1 h (air cooled) +720 °C × 8 h (furnace cooled, 50 °C/h) + 620 °C × 8 h (air cooled); (**k**–**l**) rolled (Luo et al. 2019)

inhomogeneous microstructure creating anisotropy in the mechanical as well as corrosion properties with increased residual stresses leading to cracks. So far, effects of changing the laser process parameters and thus resultant cooling rate on microstructure have been discussed. However, these changes can only influence the external heat transfer boundary of the molten pool but not the direction of the fluid movement in the molten pool. Thermo-capillary convection is one of the critical factors which govern the mechanism of metal solidification. In order to control the convection movement of the molten pool, two major external fields, namely, ultrasonic vibration and electromagnetic fields, have been applied during laser material interaction. Also, the addition of rare earth elements which acts as a surfactant is also popular in laser cladding to modify the microstructure. In the subsequent sections, these methods are described in detail:

11.4.1 Electromagnetic Field-Assisted Laser Cladding

Electromagnetic force produced by electromagnetic field changes the heat conduction and convection of the molten pool. This method is superior to ultrasonic vibration in which attenuation of the ultrasonic field in the melt pool is an issue. Three different types of electromagnetic fields, namely, single electric field, single magnetic field, and electromagnetic compound field, have been used. Single magnetic field can be further subdivided into two categories: steady magnetic field and alternating magnetic field. Schematic of laser cladding under electromagnetic field is presented in Fig. 11.17. In case of single electric field, pulsed current is used, and its electromagnetic force compresses the molten pool, resulting in reduction in porosity in the clad layer. On the other hand, single magnetic field produces Lorentz force which causes resistance for the convection in the molten pool. This can change flow velocities inside the molten pool and inhibit the surface ripple (Wang et al. 2017b) and diffusion of elements in the molten pool (Chen et al. 2016). The stirring effect caused by the electromagnetic field makes the solute and temperature field homogenize in the molten pool and causes grain refinement. Further, increased fluidity of the liquid metal reduces viscosity of the molten pool and the possibility of shrinkage of the coating (Liu et al. 2013). Steady magnetic field cannot cause great influence on the flow of the molten pool, and therefore research on combined electromagnetic fields has been exploited. By combining electric field with magnetic field, the Lorentz force can be effectively controlled to change the direction, intensity, and frequency of the magnetic and electric fields (Wang et al. 2015a). This can reduce the porosity of the clad layers (Zhang et al. 2018) and change the positions of the strengthening phase particles in the melt pool (Wang et al. 2017). A schematic showing force analysis diagram of a point in molten pool with and without electromagnetic field is presented in Fig. 11.18.

Ni-based coating such as Ni-Cr-B-Si alloys has good wear and corrosion resistance because of the presence of phases having high hardness and toughness. This coating is widely used in various industries (Savrai et al. 2016). However, the

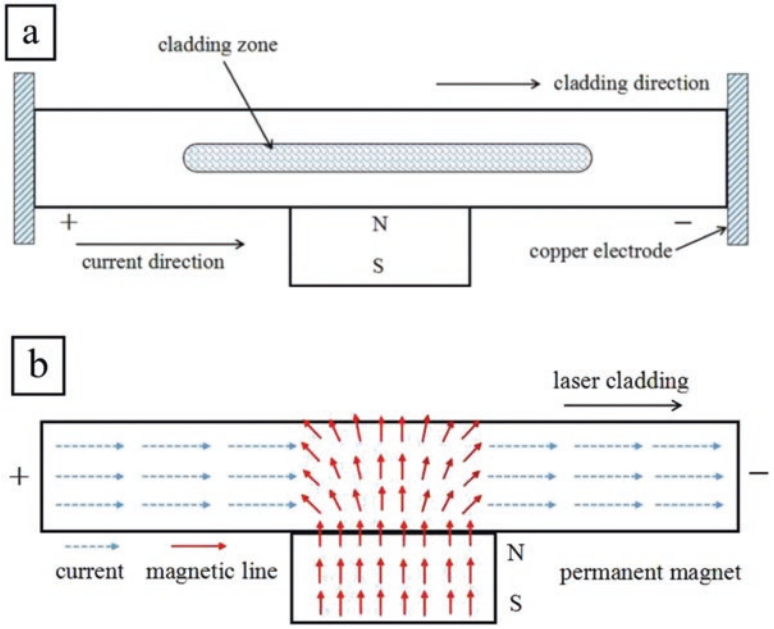

Fig. 11.17 Schematic of (**a**) laser cladding under electromagnetic field and (**b**) direction of magnetic and electric field (Zhai et al. 2019c)

presence of a variety of alloying elements in the coating can form a variety of solidification morphologies, and this may cause uneven distribution of hard phases in the matrix leading to the formation of cracks and subsequent reduction in service life of the cladded workpiece. Zhai et al. (2019c) studied the effects of electromagnetic field on microstructure, dilution, microhardness, and corrosion resistance on laser cladding of Ni-Cr-B-Si coating. A combination of four different magnetic field intensities and DC currents was tried out as given in Table 11.4, and corresponding cross-sectional SEM morphologies of the clad bead are presented in Fig. 11.19. Dilution was found to be the least under type 2 condition. Under only magnetic flux, the molten pool experiences Lorentz force directed against the fluid flow (Fig. 11.19b) which generates a decelerating flow in the molten pool. This also reduces the drag force of the fluid toward the cladding direction. Therefore, steady magnetic field is able to suppress the convection movement of the high-temperature molten material flowing into the bottom of the melt pool. As a result, because of less heat input at the molten pool and substrate interface, the penetration depth of the clad bead for type 2 condition is the least among all. With the introduction of electric field in type 3 condition, dilution increases. The presence of electric field decreases free electron density leading to decrease in conductivity of the metal and increase in electrical resistivity. Now, absorptivity of material (A) is related to electrical resistivity (ρ) according to Hagen-Rubens equation: $A = k\,(\rho/\lambda)^{1/2}$, where k = constant value of 0.365 and λ = wavelength of incident laser beam (Zhang et al. 2008c). Therefore,

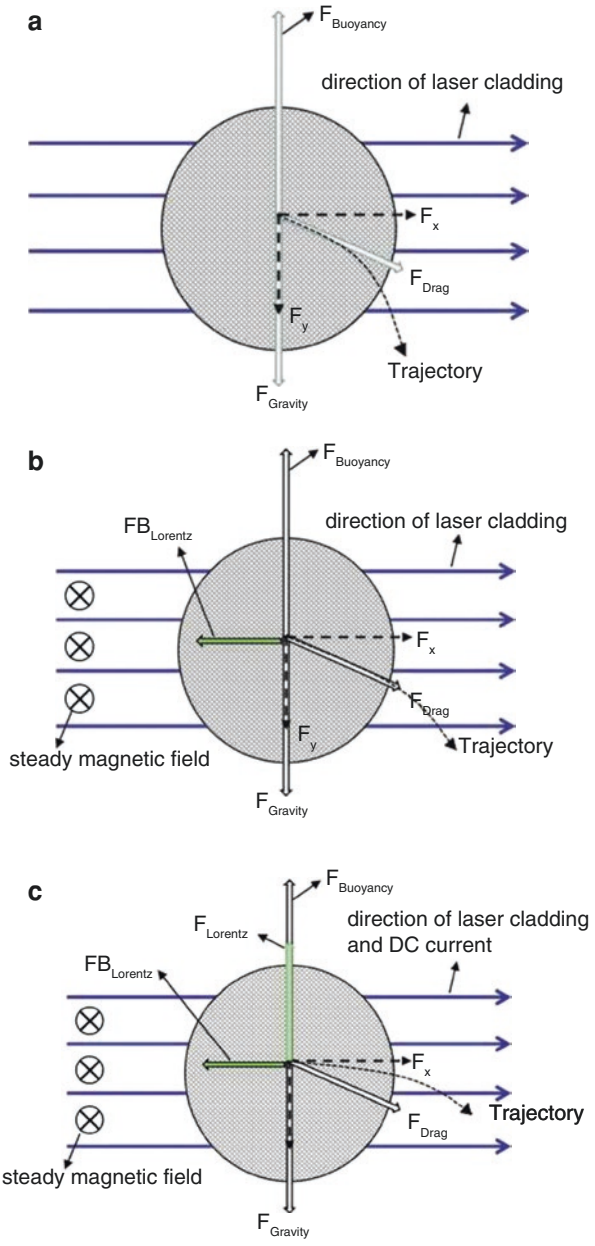

Fig. 11.18 Schematic showing force analysis diagram of a point in molten pool; (**a**) without any magnetic and electric field, (**b**) with only magnetic field, and (**c**) with electromagnetic field (Zhai et al. 2019c)

Table 11.4 Combination of different magnetic field intensities and DC currents (Zhai et al. 2019c)

	Type 1	Type 2	Type 3	Type 4
Magnetic field intensity [T]	0	0.2	0.2	0.2
DC current (A)	0	0	300	500

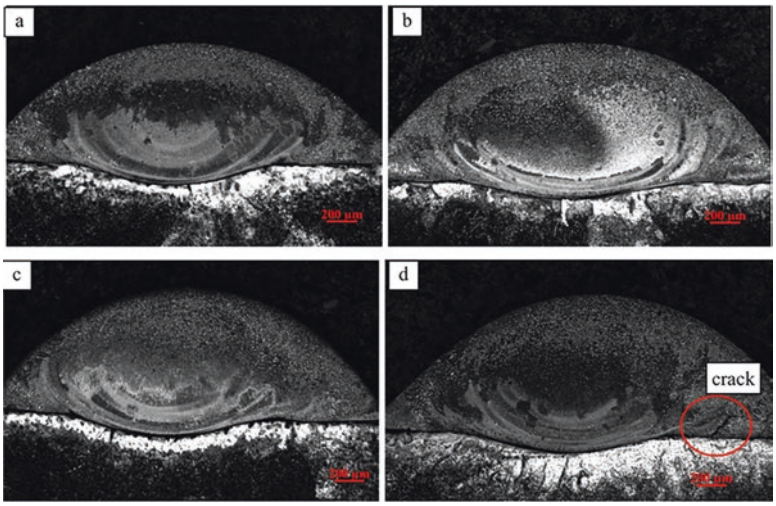

Fig. 11.19 Cross-sectional SEM morphologies of the clad bead of Ni-Cr-B-Si coating under (**a**) type 1, (**b**) type 2, (**c**) type 3, and (**d**) type 4 condition (Zhai et al. 2019c)

under type 3 condition, laser beam gets absorbed more, and consequently higher heat input leads to increase in substrate melting leading to higher dilution. Further increase in electric field (type 4 condition) causes cracks near the interface between clad layer and substrate. Increased electric field causes an increase in electromagnetic force in the upward direction (Fig. 11.19d). Once the solidification process begins, dendritic structure starts growing from the substrate which is at a relatively low temperature and forms interconnected network inside the molten pool material. As a result, molten liquid entrapped inside the dendritic network cannot be replaced by the external liquid. With increase in electromagnetic force, this entrapped liquid experiences greater upward thrust which in turn increases stress action when the solidification takes place and leads to cracking at the interface.

Zhai et al. (2019a, b) reported in the presence of alternating current, cracks can be minimized in the Ni-Cr-B-Si clad bead, as shown in Figs. 11.20 and 11.21. Diffusion of particular alloying elements inside molten pool can be controlled by using electromagnetic field. It was reported that magnetic field has effects on the diffusion of atoms in the material (Zhai et al. 2019c) following the Arrhenius equation $D = D_o \exp.(-Q/RT)$ where D = diffusion coefficient, D_o = frequency factor, R = gas constant, T = absolute temperature in Kelvin, and Q = activation energy. The factor D_o is smaller in the presence of a magnetic field, while the change in Q is negligible (Chen et al. 2016). As discussed earlier, steady magnetic field suppresses convective movement of the molten pool and thus hinders diffusion of elements leading to its accumulation and concentration. This leads to accumulation of chromium boride (CrB) phase as evident from Fig. 11.22b. With further introduction of electric field, the molten pool experiences a constant upward thrust due to electromagnetic force, and this promotes diffusion of elements to the upper part of the

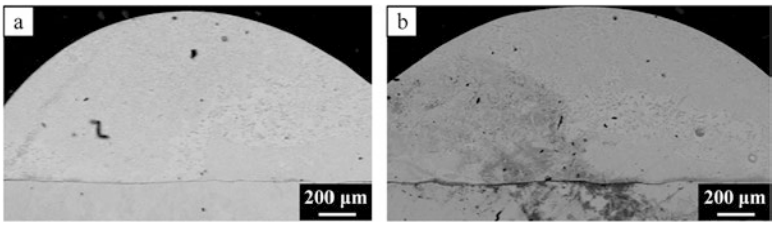

Fig. 11.20 SEM cross-sectional view of Ni-Cr-B-Si clad bead (**a**) with and (**b**) without alternating current (Zhai et al. 2019a)

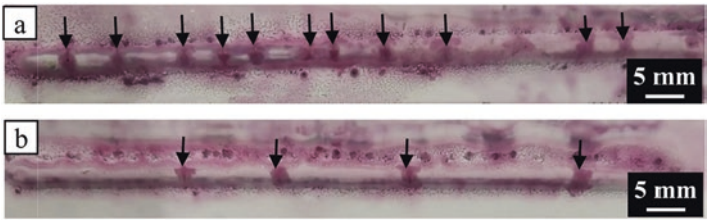

Fig. 11.21 Number of cracks in Ni-Cr-B-Si clad bead (**a**) with and (**b**) without alternating current (Zhai et al. 2019a)

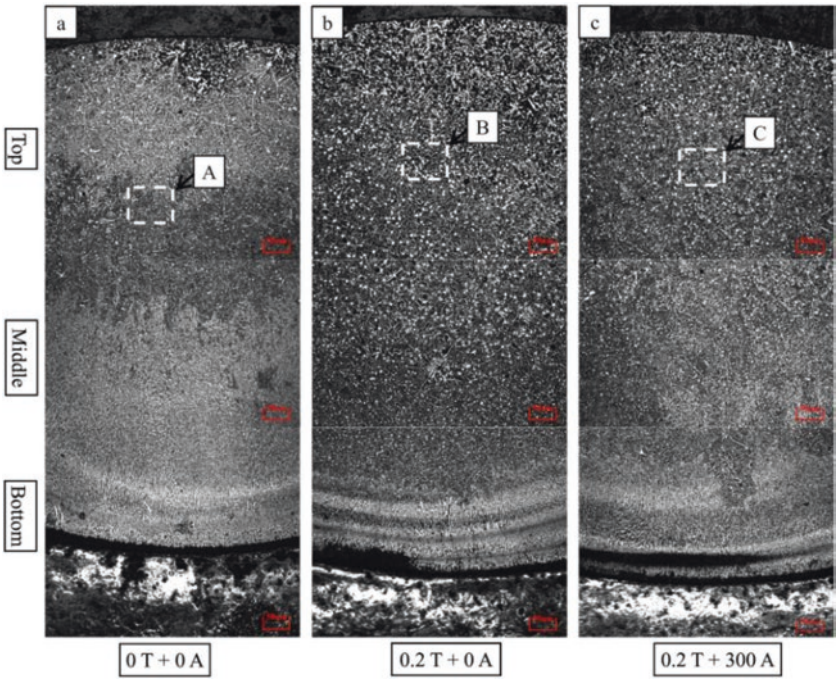

Fig. 11.22 SEM cross-sectional view of Ni-Cr-B-Si clad bead under (**a**) type 1, (**b**) type 2, and (**c**) type 3 condition; black spots contain relatively large Cr, and white color masses are CrB (Zhai et al. 2019c)

molten pool leaving relatively less elements at the middle of the clad bead. This observation can be visualized in Fig. 11.22c. Also, different morphologies of CrB are presented in Fig. 11.23 under different electromagnetic conditions. CrB having very high hardness in the range of 700 $HV_{0.2}$–1000 $HV_{0.2}$, its presence in a large number for type 2 (increase in microhardness at the bottom of the clad bead in this case may be noted) and type 3 condition increases hardness significantly, as shown in Fig. 11.24. Similar results on microhardness and corrosion resistance have also been reported by Zhai et al. (2019a) under alternating current. They reported that under alternating electric field, it is possible to promote the formation of equiaxed grains than the dendritic structure. It has been reported in the literature (Räbiger et al. 2014; Liao et al. 2007) that the electric field can improve nucleation rate and grain refinement. When current density is in certain range, i.e., $J > 2(A\Delta G)^{1/2}$, nucleation rate can be improved and grain refinement be realized (Chen et al. 2019). Due to the skin effect of alternating current, current tends to confine on the surface of the conductive melt, and since the solid resistivity is less than that of the melt, current passes through the solid phase preferentially also. Now due to the low temperature of the substrate, solidification of the melt pool begins at the bottom where the current concentrates (Fig. 11.25) and as a result the bottom of the clad bead experiences a larger current density. Increased current densities is linked to higher grain refinement and causes refinement in grains at the top and bottom of the clad bead more (Fig. 11.26). Grain refinement in the upper portion is also effected by the external environment leading to higher cooling rate. On the other hand, in the middle of the clad bead, the insufficient current density for grain refinement, Joule heating, and relatively slower cooling rates cause grain coarsening (Zhai et al. 2019c). Lu et al. (2019) studied the effect of stress distribution of the molten pool under both static and dynamic electromagnetic fields. It was found that the rotating fields have stronger ability to stabilize the stress field compared to static fields.

The above works illustrate the possibility to modify/control grain size and distribution of alloying elements, increase microhardness and corrosion resistance, and reduce the number of cracks and dilution in laser cladding of Ni-based coating by means of external magnetic or electric or combination of both either in static or rotating condition.

11.4.2 Ultrasonic Vibration-Assisted Laser Cladding Process

In the presence of ultrasonic vibration, periodical positive-negative pressure waves get generated in the molten pool. This causes two major nonlinear actions, namely, acoustic streaming and cavitation. In case of acoustic streaming, there is a steady flow that is driven by momentum transfer due to the absorption of multiple acoustic oscillations in the liquid molten material. On the other hand, cavitation is a phenomenon which causes generation of tiny bubbles/cavities and its subsequent growth, pulsation, and collapse in the liquid molten material. These two actions generate agitation in the melt pool and cause different direct and ultimate influences (Cong

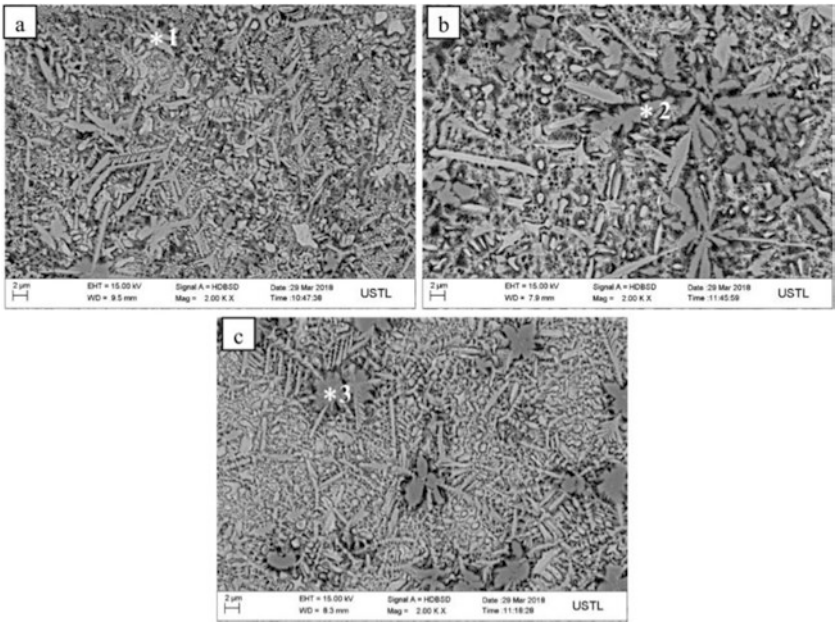

Fig. 11.23 Chromium boride (CrB) having different morphologies under (**a**) type 1, (**b**) type 2, and (**c**) type 3 condition (Zhai et al. 2019c)

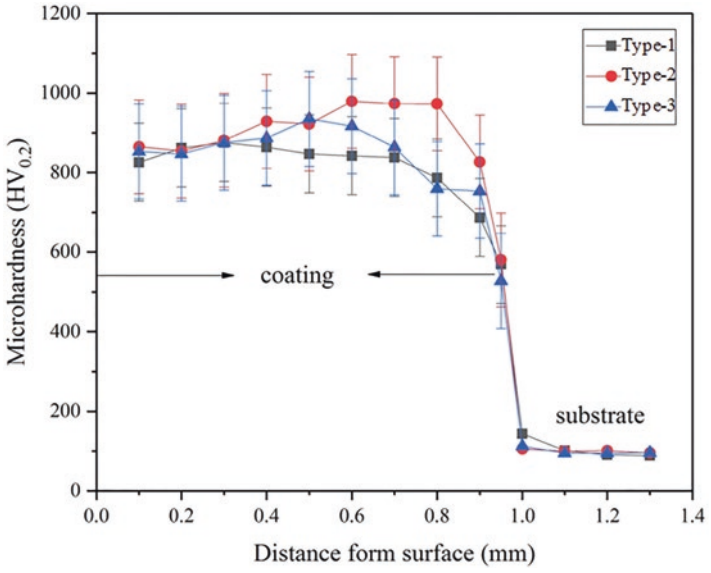

Fig. 11.24 Variation in microhardness under different electromagnetic conditions (Zhai et al. 2019c)

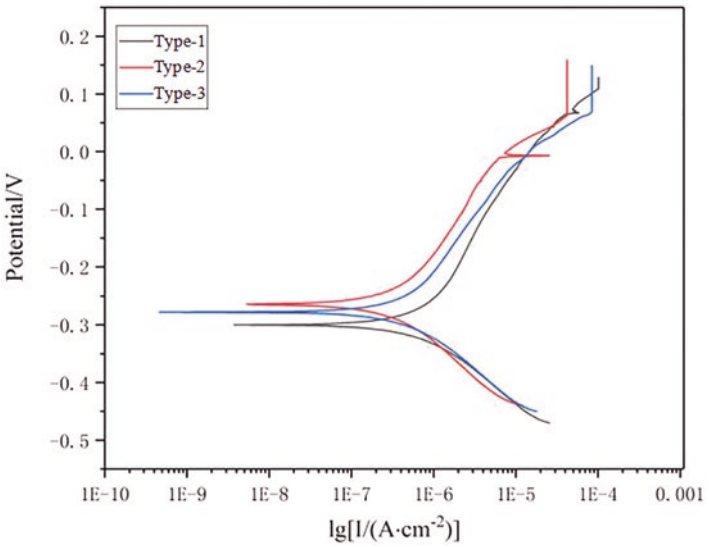

Fig. 11.25 Linear polarization curve of the Ni-Cr-B-Si clad bead with and without electromagnetic clad bead (Zhai et al. 2019c)

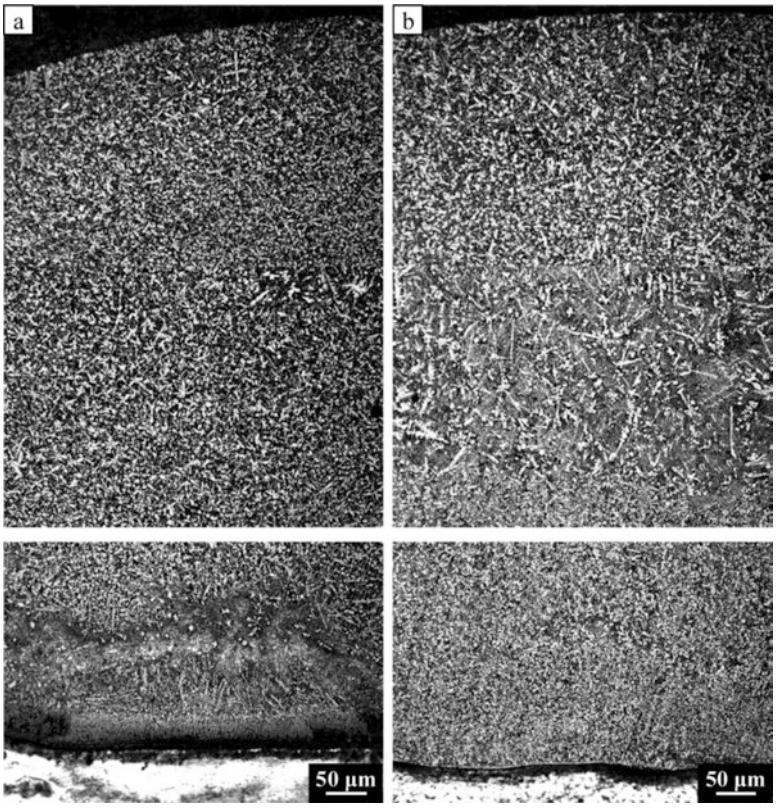

Fig. 11.26 SEM cross-sectional view of Ni-Cr-B-Si clad bead (**a**) with and (**b**) without the alternating electric field (Zhai et al. 2019a)

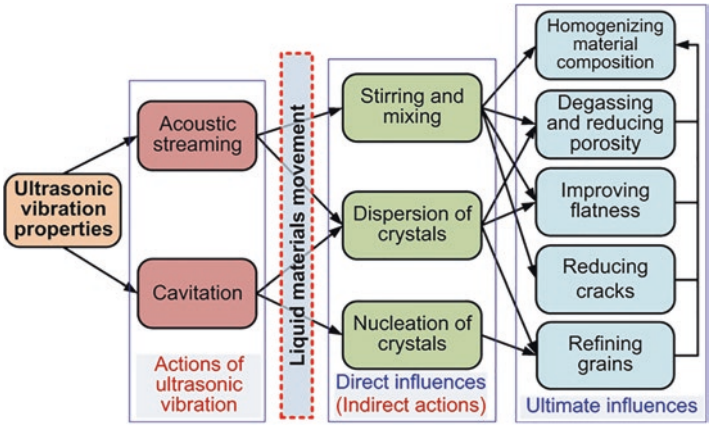

Fig. 11.27 Actions and influences of ultrasonic vibration in ultrasonic vibration-assisted melting in metal solidification processes (Cong and Ning 2017)

and Ning 2017) as summarized in Fig. 11.27. Under these influences, ultrasonic vibrations could refine grains, homogenize and redistribute alloying particles, and reduce pores and segregation; combined effect of all these can enhance mechanical and corrosion properties of the deposition. Parameters related to ultrasonic vibration-assisted melting process, i.e., DMLD, laser surface remelting, etc., include direction of vibration, ultrasonic power, frequency (commonly used 20–40 kHz), and amplitude (10–150 μm) of ultrasonic vibration, laser power, scan speed, laser spot diameter, number of layers, etc. Although various effects of ultrasonic vibration on clad quality of different materials are available in literature, only Ni-based alloy and coating are discussed here. In the next section, effects of ultrasonic vibration on grain size, porosity, segregation, and microhardness are discussed by taking an example of fabrication of IN 718 test coupons using laser-engineered net shaping (LENS) process.

Porosity is a major issue in laser cladding process. It causes reduction in fatigue life. Mostly, entrapment of gas bubbles triggers the formation of pores in the molten tracks. Acoustic streaming and cavitation effect in case of ultrasonic vibration-assisted processing generates radiation pressure waves to change the interaction between metallic liquid and entrapped gas bubbles, subsequently leading to collapse of gas-evolved pores. This is illustrated in Fig. 11.28 which shows a significant reduction in the pores in case of ultrasonic vibration-assisted processing.

Acoustic streaming and cavitation effect during microstructure formation causes formation of a large number of grain nucleation sites which results in refinement in grains (Fig. 11.29). It is well established that the grain refinement significantly increases strength and hardness of the material and a more well-arranged and homogenous microstructure reduces residual stresses caused during rapid solidification of the molten material (Furuhara and Maki 2001; Abramov 1987). The Hall-Petch equation suggests that the microhardness of any material is correlated to the

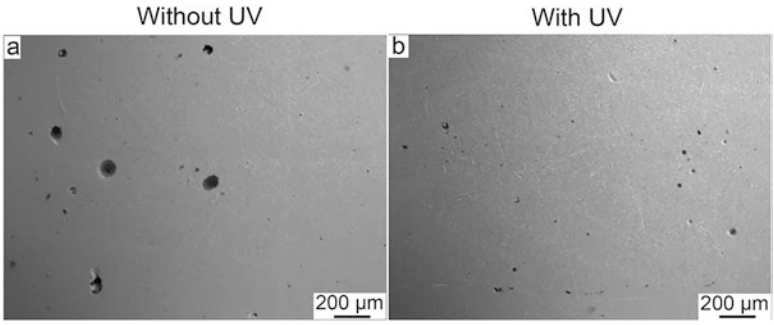

Fig. 11.28 Reduction in pores in case of ultrasonic vibration-assisted processing of IN 718 using LENS process (Ning et al. 2017)

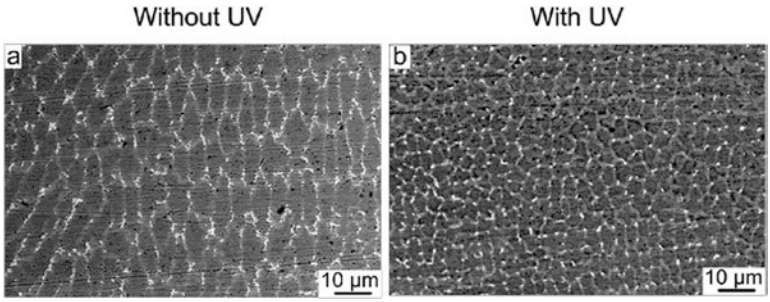

Fig. 11.29 Reduction in grain size in case of ultrasonic vibration-assisted processing of IN 718 using LENS process (Ning et al. 2017)

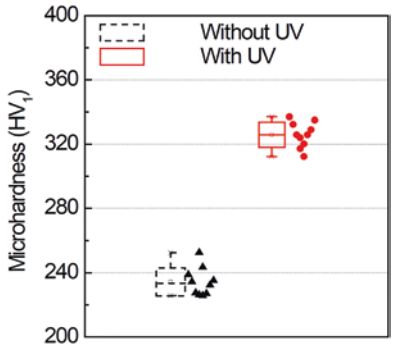

Fig. 11.30 Increase in microhardness value in case of ultrasonic vibration-assisted processing of IN 718 using LENS process (Ning et al. 2017)

reciprocal root of the grain size. Therefore, with the decrease in grain size, it is expected to increase the microhardness value for ultrasonic vibration-assisted processing, for example, as shown in Fig. 11.30.

As discussed earlier, one of the major problems in Ni-based superalloy cladding is the segregation of Laves phases which is detrimental to mechanical and corrosion

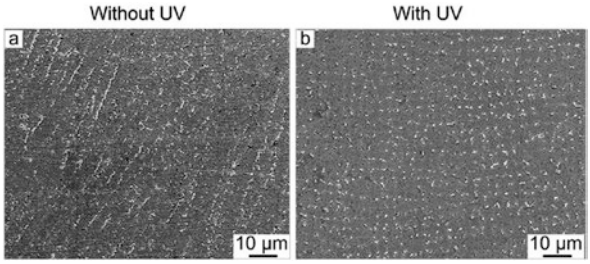

Fig. 11.31 Fragmentation of Laves phases in case of ultrasonic vibration-assisted processing of IN 718 using LENS process (Ning et al. 2017)

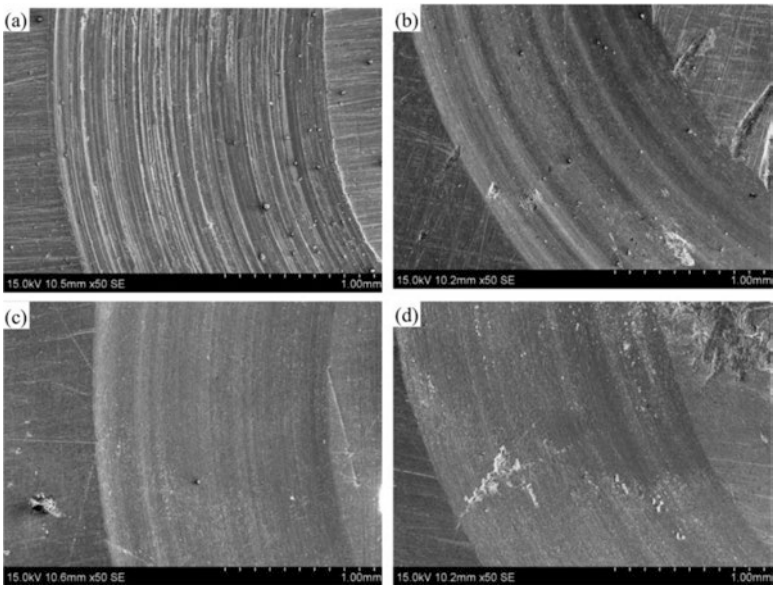

Fig. 11.32 Worn surfaces of laser-cladded WC-Ni coating (**a**) without ultrasonic vibration (**b**–**d**) and with ultrasonic vibration (Li et al. 2019)

properties due to the brittle nature of these phases. During ultrasonic vibration-assisted processing, radiation pressure of the acoustic field makes the solid-liquid interface unstable. These lead to the fragmentation of long bar-shaped Laves phases into small globular ones uniformly distributed over the matrix (Fig. 11.31). Several researchers (Li et al. 2016; Li et al. 2019) have reported increased microhardness and wear resistance in case of ultrasonic vibration-assisted laser cladding of Ni-ceramic coating (Fig. 11.32). Micro-vibration during laser cladding could make better mechanical stirring effect for mixing hard phases in the matrix resulting in more uniform microstructure.

Improvement in corrosion properties of laser cladding assisted by mechanical vibration has been realized. Liu et al. (2015) reported improved corrosion resistance (Fig. 11.33) of Ni60CuMoW laser-cladded coating. Micro-mechanical vibration

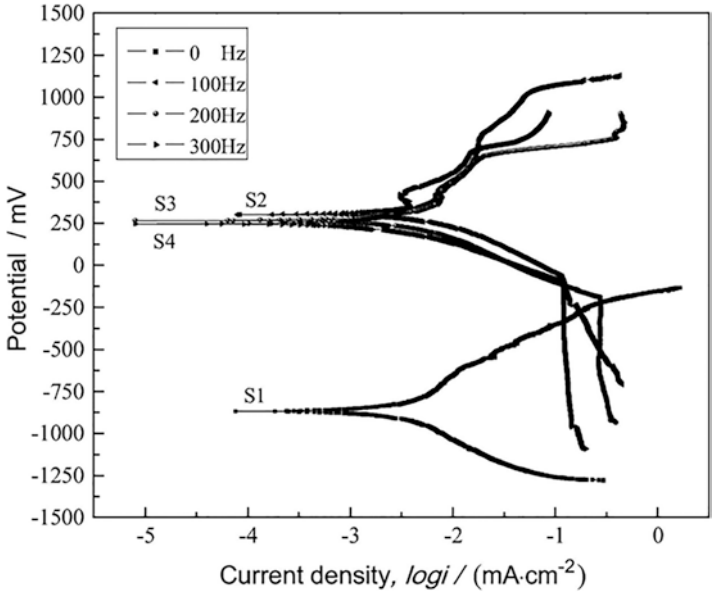

Fig. 11.33 Polarization curves of cladding Ni60CuMoW coatings with or without ultrasonic vibration in 3.5% NaCl solution (Liu et al. 2015)

improved mean particle size of the hard phases and maintained uniformity in microstructure during melting and solidification process. Uniform microstructure, high surface density, increase in Cr content in carbides, and interface bonding strength between hard phase particles and the matrix are found to be the major driving factors in improving the corrosion resistance of ultrasonic vibration-assisted deposited coating.

These studies illustrate the possibility of controlling the grain size, segregation of Laves phases, reduction of porosity, improvement of microhardness, wear, and corrosion resistance in laser cladding of Ni-based alloy using ultrasonic vibration for better mechanical and corrosion properties.

11.4.3 Rare Earth Elements Added in Nickel Coatings

Rare earth elements comprise of 15 lanthanides with atomic numbers ranging from 57 to 71 with exceptions of scandium and yttrium. The presence of these rare earth elements having large atomic radius in the solid solution causes substantial lattice distortion increasing the total energy of the system (Wang et al. 2001). These rare earth elements are mostly stable near the grain boundaries. Therefore, during the solidification process, they try to segregate at the grain boundary. This causes a drag effect on the growing crystal or grain limiting its size along and favoring formation

of new nucleation sites with time or decrease in temperature resulting not only in the refinement of microstructure but also in controlling the segregation and inhomogeneity in microstructure. Further, this results in increased area of the grain boundary restricting the crack propagation. The problem of cracks is more predominant in case of nickel-based ceramic coating due to large variation in the thermos-physical properties of the material being cladded. Li et al. (2017) studied the influence of the addition of La_2O_3 on crack susceptibility during laser cladding of Ni-based ceramic composite, and it was found that an addition of 0.6–0.8% of La_2O_3 could bring down the crack susceptibility to zero. In addition to refining the microstructure, rare earth elements also act as surfactants reducing the surface tension and interfacial energy between the crystal nucleus and the melt leading to increased wettability between the metal matrix and the ceramic phase favoring formation of shell-core structure improving the mechanical property of the coating (Niu and Chang 1999; Zhao et al. 2020). Rare earth elements also increase the latent heat of melting of the cladding materials, instigating increase in solidus temperature, and decrease liquid temperature leading to shorter solidification time resulting in finer microstructure. Further, this also limits diffusion of substrate materials into the clad material, thereby controlling the dilution. As discussed, rare earth elements reduce the solid-liquid interfacial energy, potentially reducing the Gibbs free energy required for the formation of nucleus promoting more number of nuclei. Also, the rare earth particles in some cases themselves act as nucleating sites. Therefore, the combination of drag effect, reduced solid-liquid interfacial energy, and action as heterogeneous nucleation sites results in refinement of microstructure and improved surface and mechanical characteristics. Figure 11.34 shows the effect of the addition of 6% La_2O_3 on the microstructure during laser cladding of Ni-based alloy powder (Li et al. 2017). It can be clearly observed that the addition of rare earth oxide resulted in refinement as well as the randomization of microstructure without any directionality as compared to that of cladding pure Ni-based alloy powder. Further, Li et al. (2017) also reported an increase in corrosion resistance along with the grain refinement. In addition to their chemical behavior, the particle size of the rare earth elements used also plays a critical role in controlling the microstructure as well as the surface properties. Zhang et al. (2008b) investigated the effect of the addition of nano- and micro-sized Sm_2O_3 on the microstructure and corrosive properties of laser-cladded NBA powder (NiSp475). Figure 11.35 (Zhang et al. 2008b) shows the morphology of sample surface tested for corrosion. In Fig. 11.35a, it can be observed that NBA coating without any rare earth oxide suffered severe corrosion of dendrite with significant pitting, whereas the samples with addition of 1.5% Sm_2O_3 showed a minimum corrosion with nano-sized particles (Fig. 11.35c) offering better corrosion resistance than the micro-sized particles (Fig. 11.35b). In addition to microstructure refinement and corrosion resistance, addition of rare earth materials was also reported to increase hardness and wear resistance of the coatings due to the refined microstructure with good wetting characteristics (Wang et al. 1977, 2001; Zhang et al. 2008a).

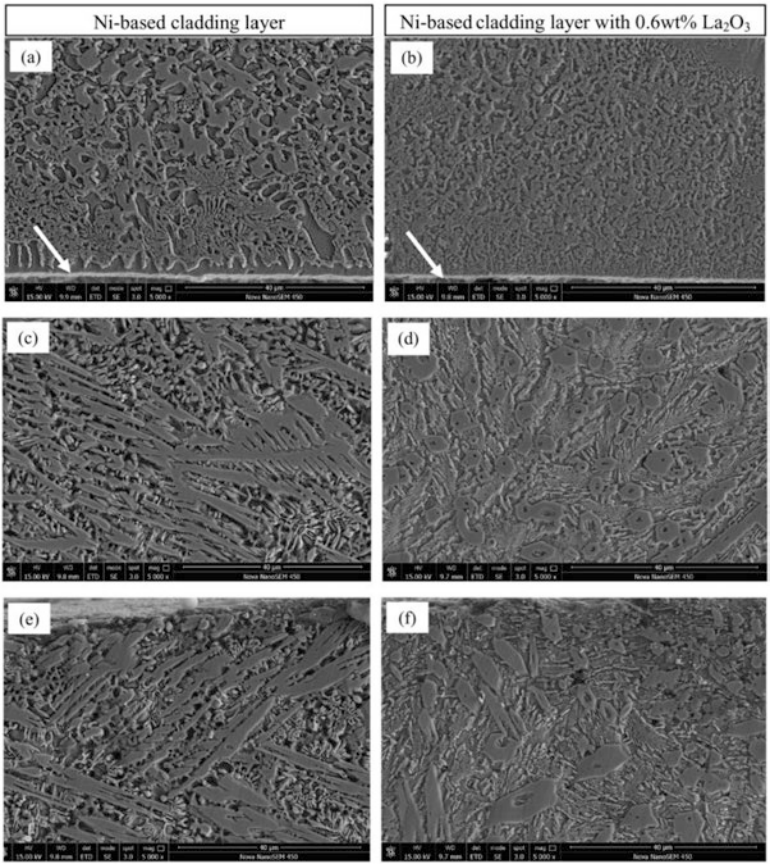

Fig. 11.34 Effect of La_2O_3 addition on microstructure refinement in Ni-based alloy powder: (**a**, **b**) bottom region, (**c**, **d**) middle region, and (**e**, **f**) upper region (Li et al. 2017)

11.5 Metal Matrix Composite Coatings of Nickel-Based Alloys

Nickel-based superalloys are generally good candidates for the development of corrosive coatings. However, they suffer from relatively poor wear resistance compared to several other superalloys like Stellite, etc. Therefore, with the increasing demand for enhanced component life, nickel-based metal matrix composite (MMC) coatings are becoming popular in almost every industry including aerospace, automobile, mining and mineral industry, etc., for armoring over turbine blade tips, pistons, valves, cylinders, drilling tools, etc., where the failure of mechanical components is generally caused by wear, erosion, and corrosion at the surface. However, these ceramic coatings experience unique problem of cracking due to rapid solidification and residual stresses, compositional changes due to their dissolution in metal matrix

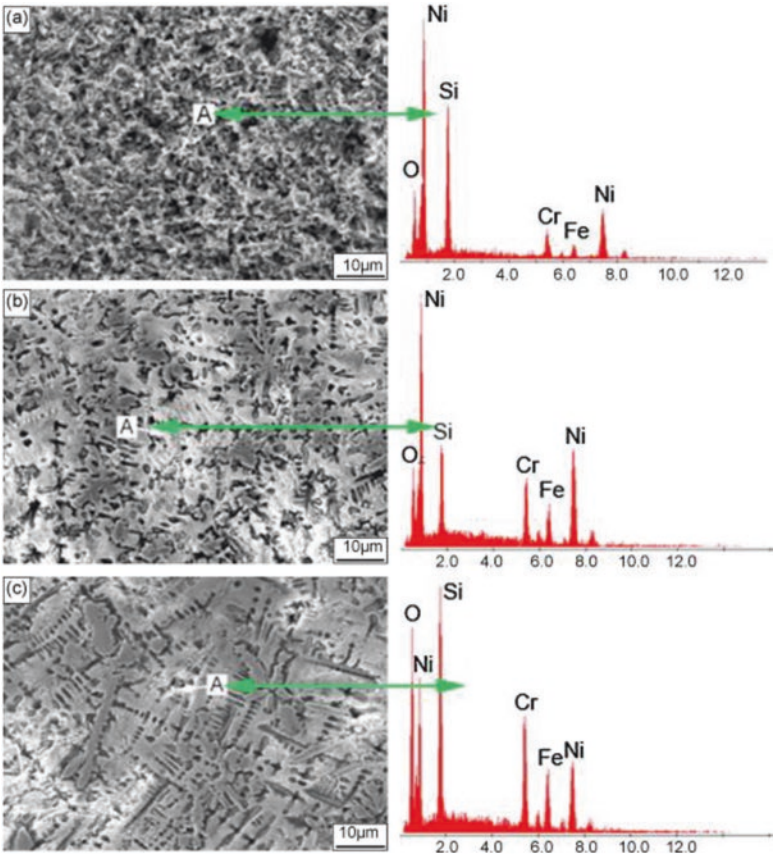

Fig. 11.35 Electrochemical corrosion morphology of the coatings: (**a**) 0% Sm_2O_3; (**b**) 1.5% m-Sm_2O_3; (**c**) 1.5% n-Sm_2O_3 (Zhang et al. 2008b)

affecting the corrosion and mechanical properties, and nonuniform distribution due to differences in their physical properties. Therefore, it is important to understand the influence of process parameters on these aspects.

As discussed in the previous section, one of the major reasons for the failure of a coating or component is the separation of the two phases upon application of load. Therefore, it is essential to establish a tailoring joint between the ceramic particles and the metal matrix. Muvvala et al. (2017a) investigated the effect of various process parameters on the tailoring of WC ceramic particles with the Inconel 718 metal matrix. Apart from the process parameters, WC wetting or tailoring is found to be a function of molten pool lifetime, as shown in Fig. 11.36. It can be observed that there is an optimum range of melt pool lifetime for the proper WC tailoring with the matrix. For a relatively short molten pool lifetime, the wetting or bonding between WC particles and the metal matrix is very poor with a distinct boundary between them. However, with increase in molten pool lifetime beyond a limit (above ~0.68 s),

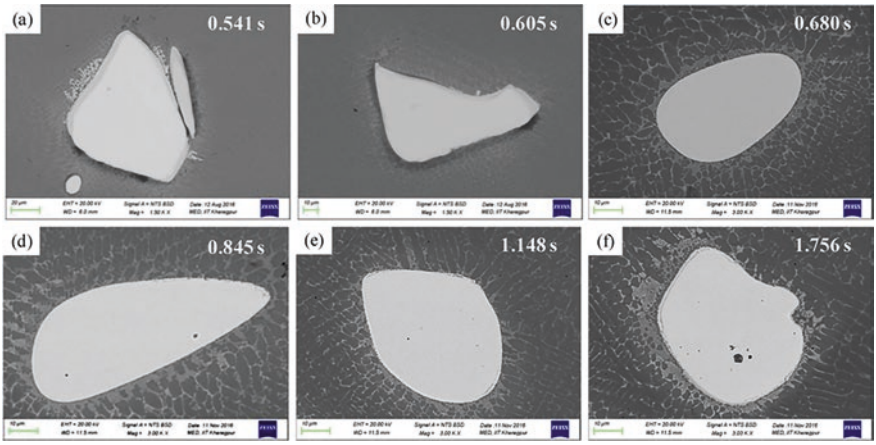

Fig. 11.36 Variation in wetting condition of ceramic particles with laser scan speed of (**a**) 1200 mm/min, (**b**) 1000 mm/min, (**c**) 800 mm/min, (**d**) 600 mm/min, (**e**) 400 mm/min, and (**f**) 200 mm/min (1200 W) (Muvvala et al. 2017a)

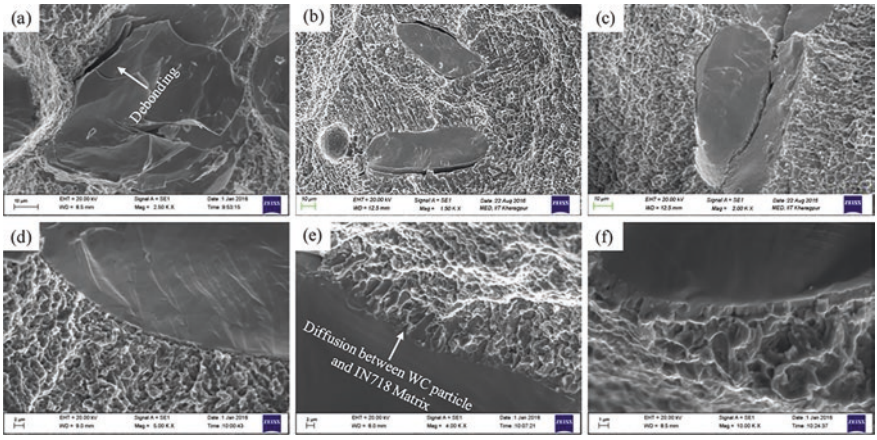

Fig. 11.37 Fracture surfaces of clad layer showing the bonding condition between the ceramic particles and the metal matrix deposited with 1200 W laser power and scan speed of (**a**) 1200 mm/min, (**b**) 1000 mm/min, (**c**) 800 mm/min, (**d**) 600 mm/min, (**e**) 400 mm/min, and (**f**) 200 mm/min (Muvvala et al. 2017a)

a clear diffusion bonding is visible tailoring the WC particles with the matrix. Figure 11.37 shows the effect of poor wetting on the fracture properties of the nickel-based coatings. A distinct delamination between the ceramic particles and the matrix is visible under the application of load. Thus, these weak interfaces act as crack initiation points resulting in premature failure of the coating under the applied load in the operation condition. Therefore, it is very essential to ensure wettability

and tailoring in ceramic MMC by controlling the process parameters to provide sufficiently slow cooling rate or long melt pool lifetime.

However, too long a melt pool lifetime could be detrimental to the quality of coating due to various effects depending on the properties of ceramic particles being added in the Ni superalloy matrix. In the case of WC particles which have a density ~16.5 g/cm^3, almost twice that of Inconel 718 and most of the other nickel-based superalloys, they tend to sink in the molten pool (Fig. 11.38). This results in a graded WC particle concentration in the coating with fewer of them on the top surface with no improvement of wear characteristic of the Ni alloy coating (Fig. 11.39) (Muvvala et al. 2017a, Fernández et al. 2015).

In addition to the issue of particle sinking, dissociation of ceramic particles is also one of the major concerns for longer melt pool lifetime in nickel-based ceramic composite coating. Figure 11.40 shows the effect of longer molten pool lifetime on the decomposition and resulting mechanical properties of the Inconel/TiC composite coating. For relatively long molten pool lifetimes, the decomposition of TiC

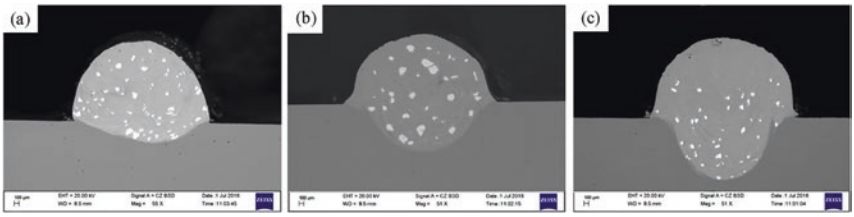

Fig. 11.38 Distribution of WC particles in clad layer: (**a**) 600 mm/min, (**b**) 400 mm/min, and (**c**) 200 mm/min (Muvvala et al. 2017a)

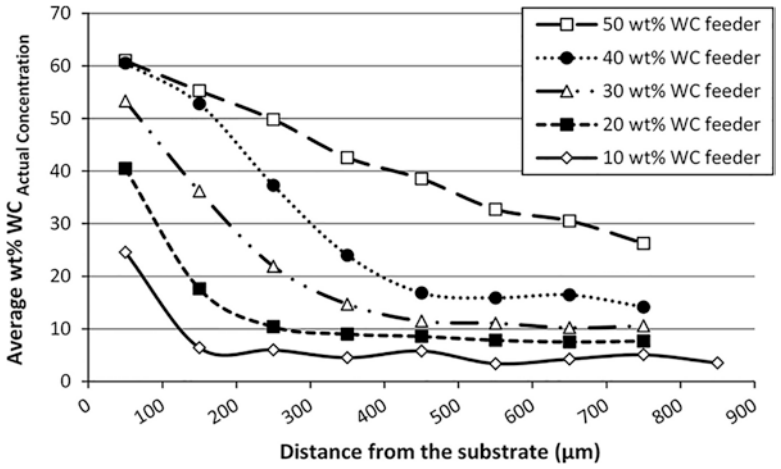

Fig. 11.39 Average wt% $WC_{actual\ concentration}$ versus the distance to the substrate in the cross section of a NiCrBSi coating for different wt% $WC_{feeder\ concentration}$ (Fernández et al. 2015)

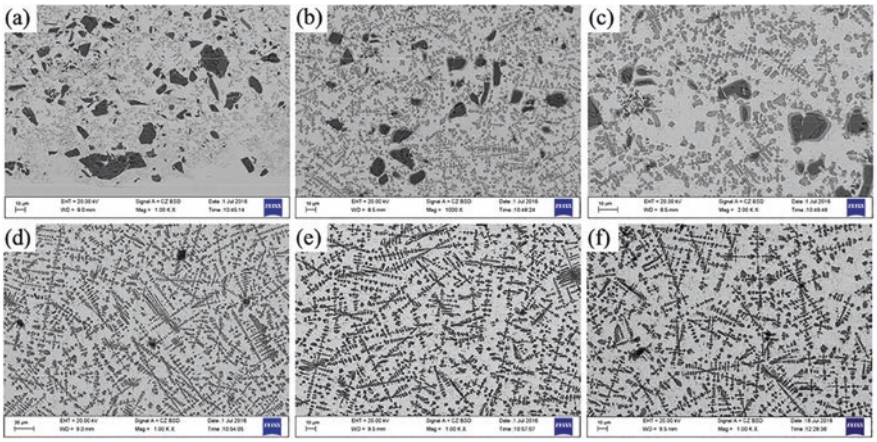

Fig. 11.40 Variation in microstructure with molten pool lifetime: (**a**) 0.281 s, (**b**) 0.3 s, (**c**) 0.429 s, (**d**) 0.487 s, (**e**) 0.899 s, and (**f**) 1.336 s (Muvvala et al. b)

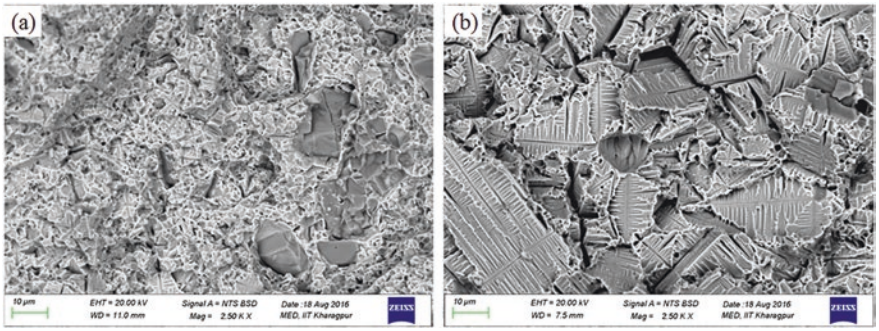

Fig. 11.41 Fracture surface of samples cladded at 1200 W laser power and (a) 1200 mm/min and (b) 400 mm/min scan speed (Muvvala et al. 2017b)

becomes severe resulting in microstructure with fully grown ceramic dendritic structure which essentially results in the brittle fracture of the coating both under wear test and tensile loading as reported by Muvvala et al. (2017b) and Liu and Shin (2017) and evident from Fig. 11.41 (Muvvala et al. 2017b).

11.6 Conclusion

Nickel-based superalloys find a wide range of applications in the field of aerospace, nuclear power plants, and many other industries owing to its excellent properties at both room and elevated temperatures. With the advancement in additive

manufacturing technology, fabrication or refurbishment of components or development of protective coatings based on nickel-based alloys also took a steep leap forward. However, they suffer from elemental segregations during the laser cladding process which are detrimental to both the surface and bulk mechanical properties. Optimizing or limiting the segregation with respect to process parameters is feasible, and this has been correlated with the cooling rate/melt pool lifetime in laser cladding process. In fact, cooling rate is found to be such a parameter which dictates the quality of the coating irrespective of process parameters and laser cladding system. In addition to the process parameters and the resulting cooling rates, external agitation of molten pool through electromagnetic field and ultrasonic vibrations and addition of rare earth elements are found to control the segregations improving the mechanical and surface properties. Further, the properties of nickel-based ceramic coating are also found possible to be controlled with the cooling rate.

Acknowledgment This work is partially supported by the Department of Science and Technology, Government of India, under the FIST Program-2007 (SR/FIST/ETII-031/2007), and Ministry of Human Resource Development and Department of Heavy Industries, Government of India, under the IMPRINT Program-2017 for Project 6917.

References

Abramov, O. V. (1987). Action of high intensity ultrasound on solidifying metal. *Ultrasonics, 25*(2), 73–82. https://doi.org/10.1016/0041-624X(87)90063-1.

Caiazzo, F. (2018). Laser-aided directed metal deposition of Ni-based superalloy powder. *Optics and Laser Technology, 103*, 193–198. https://doi.org/10.1016/j.optlastec.2018.01.042.

Cemal, M., Cevik, S., Uzunonat, Y., & Diltemiz, F. (2012). ALLVAC 718 Plus™ superalloy for aircraft engine applications. In R. Agarwal (Ed.), *Recent advances in aircraft technology*. Eskisehir: InTech. https://doi.org/10.5772/38433.

Chen, R., Wang, C. M., Jiang, P., et al. (2016). Effect of axial magnetic field in the laser beam welding of stainless steel to aluminum alloy. *Materials and Design, 109*, 146–152. https://doi.org/10.1016/j.matdes.2016.07.064.

Chen, Z. X., Ding, H. S., Chen, R. R., et al. (2019). An innovative method for the microstructural modification of TiAl alloy solidified via direct electric current application. *Journal of Materials Science and Technology, 35*(1), 23–28. https://doi.org/10.1016/j.jmst.2018.06.016.

Chlebus, E., Gruber, K., Kuźnicka, B., Kurzac, J., & Kurzynowski, T. (2015). Effect of heat treatment on the microstructure and mechanical properties of Inconel 718 processed by selective laser melting. *Materials Science and Engineering A, 639*, 647–655. https://doi.org/10.1016/j.msea.2015.05.035.

Cong, W., & Ning, F. (2017). A fundamental investigation on ultrasonic vibration-assisted laser engineered net shaping of stainless steel. *International Journal of Machine Tools and Manufacture, 121*(2017), 61–69. https://doi.org/10.1016/j.ijmachtools.2017.04.008.

Dinda, G. P., Dasgupta, A. K., & Mazumder, J. (2009). Laser aided direct metal deposition of Inconel 625 superalloy: Microstructural evolution and thermal stability. *Materials Science and Engineering A, 509*, 98–104. https://doi.org/10.1016/j.msea.2009.01.009.

DuPont, J. N., Lippold, J. C., & Kiser, S. D. (2009). *Welding metallurgy and weldability of nickel-base alloys*. Hoboken: Wiley.

Eliaz, N., Shemesh, G., & Latanision, R. M. (2002). Hot corrosion in gas turbine components. *Engineering Failure Analysis, 9*, 31–43. https://doi.org/10.1016/S1350-6307(00)00035-2.

Fernández, M. R., García, A., Cuetos, J. M., González, R., Noriega, A., & Cadenas, M. (2015). Effect of actual WC content on the reciprocating wear of a laser cladding NiCrBSi alloy reinforced with WC. *Wear, 324–325*, 80–89. https://doi.org/10.1016/j.wear.2014.12.021.

Furuhara, T., & Maki, T. (2001). Variant selection in heterogeneous nucleation on defects in diffusional phase transformation and precipitation. *Materials Science and Engineering A, 312*(1), 145–154. https://doi.org/10.1016/S0921-5093(00)01904-3.

Gopinath, M., Karmakar, D. P., & Nath, A. K. (2017). Monitoring of molten pool thermal history and its significance in laser cladding process. *Proceedings of the ASME 2017 12th international manufacturing science and engineering conference collocated with the JSME/ASME 2017 6th international conference on materials and processing. Volume 2: Additive manufacturing; Materials. Los Angeles, California, USA*. V002T01A041. https://doi.org/10.1115/MSEC2017-2657.

Inconel 625 data sheet. https://www.specialmetals.com/assets/smc/documents/alloys/inconel/inconel-alloy-625.pdf

Kang, N., Mansori, M. E., Guittonneau, F., Liao, H., Fu, Y., & Aubry, E. (2018). Controllable mesostructure, magnetic properties of soft magnetic Fe-Ni-Si by using selective laser melting from nickel coated high silicon steel powder. *Applied Surface Science, 455*, 736–741. https://doi.org/10.1016/j.apsusc.2018.06.045.

Kou, S. (2002). *Welding metallurgy* (2nd ed.). Hoboken: John Wiley & Sons Inc.

Leary, M., Mazur, M., Williams, H., Yang, E., Alghamdi, A., Lozanovski, B., et al. (2018). Inconel 625 lattice structures manufactured by selective laser melting (SLM): Mechanical properties, deformation and failure modes. *Materials and Design, 157*, 179–199. https://doi.org/10.1016/j.matdes.2018.06.010.

Li, M., Han, B., Wang, Y., Song, L., & Guo, L. (2016). Investigation on laser cladding high-hardness nano-ceramic coating assisted by ultrasonic vibration processing. *Optik, 127*, 4596–4600. https://doi.org/10.1016/j.ijleo.2016.01.194.

Li, M., Han, B., Wang, Y., & Pu, K. (2017). Effects of La_2O_3 on the microstructure and property of laser cladding Ni-based ceramic coating. *Optik, 130*, 1032–1037. https://doi.org/10.1016/j.ijleo.2016.11.111.

Li, C., Zhang, Q., Wang, F., Deng, P., Lu, Q., Zhang, Y., Li, S., Ma, P., Li, W., & Wang, Y. (2019). Microstructure and wear behaviors of WC-Ni coatings fabricated by laser cladding under high frequency micro-vibration. *Applied Surface Science, 485*, 513–519. https://doi.org/10.1016/j.apsusc.2019.04.245.

Liao, X. L., Zhai, Q. J., Luo, J. L., et al. (2007). Refining mechanism of the electric current pulse on the solidification structure of pure aluminium. *Acta Materialia, 55*(9), 3103–3109. https://doi.org/10.1016/j.actamat.2007.01.014.

Liu, S., & Shin, Y. C. (2017). The influences of melting degree of TiC reinforcements on microstructure and mechanical properties of laser direct deposited Ti6Al4V-TiC composites. *Materials and Design, 136*, 185–195. https://doi.org/10.1016/j.matdes.2017.09.063.

Liu, X. H., Ji, S. W., Jiang, Y. H., et al. (2013). Microstructure and property of Fe60 composite coatings by rotating magnetic field auxiliary laser cladding. *Chinese Journal of Lasers, 40*(1), 115–120.

Liu, H., Xu, Q., Wang, C., & Zhang, X. (2015). Corrosion and wear behavior of Ni60CuMoW coatings fabricated by combination of laser cladding and mechanical vibration processing. *Journal of Alloys and Compounds, 621*, 357–363. https://doi.org/10.1016/j.jallcom.2014.10.030.

Lu, Y., Sun, G., Wang, Z., Zhang, Y., Su, B., Feng, A., & Ni, Z. (2019). Effects of electromagnetic field on the laser direct metal deposition of austenitic stainless steel. *Optics and Laser Technology, 119*, 105586. https://doi.org/10.1016/j.optlastec.2019.105586.

Luo, S., Huang, W., Yang, H., Yang, J., Wang, Z., & Zeng, X. (2019). Microstructural evolution and corrosion behaviors of Inconel 718 alloy produced by selective laser melting following different heat treatments. *Additive Manufacturing, 30*, 100875. https://doi.org/10.1016/j.addma.2019.100875.

Marchese, G., Parizia, S., Rashidi, M., Saboori, A., Manfredi, D., Ugues, D., Lombardi, M., Hryha, E., & Biamino, S. (2020). The role of texturing and microstructure evolution on the tensile behavior of heat-treated Inconel 625 produced via laser powder bed fusion. *Materials Science and Engineering A, 769*, 138500. https://doi.org/10.1016/j.msea.2019.138500.

Ming, X. L., Chen, J., Tan, H., Yang, H. O., & Lin, X. (2015). Research on persistent fracture mechanism of laser forming repaired GH4169 superalloy. *Chin. J. Lasers., 42*, 0403005.

Moussaoui, K., Rubio, W., Mousseigne, M., Sultan, T., & Rezai, F. (2018). Effects of selective laser melting additive manufacturing parameters of Inconel 718 on porosity, microstructure and mechanical properties. *Materials Science and Engineering A, 735*, 182–190. https://doi.org/10.1016/j.msea.2018.08.037.

Muvvala, G., Karmakar, D. P., & Nath, A. K. (2017a). Monitoring and assessment of tungsten carbide wettability in laser cladded metal matrix composite coating using an IR pyrometer. *Journal of Alloys and Compounds, 714*, 514–521. https://doi.org/10.1016/j.jallcom.2017.04.254.

Muvvala, G., Karmakar, D. P., & Nath, A. K. (2017b). Online assessment of TiC decomposition in laser cladding of metal matrix composite coating. *Materials and Design, 121*, 310–320. https://doi.org/10.1016/j.matdes.2017.02.061.

Muvvala, G., Karmakar, D. P., & Nath, A. K. (2017c). Online monitoring of thermo-cycles and its correlation with microstructure in laser cladding of nickel based super alloy. *Optics and Lasers in Engineering, 88*, 139–152. https://doi.org/10.1016/j.optlaseng.2016.08.005.

Nair, A. M., Muvvala, G., & Nath, A. K. (2019). A study on in-situ synthesis of TiCN metal matrix composite coating on Ti-6Al-4V by laser surface alloying process. *Journal of Alloys and Compounds, 810*, 151901. https://doi.org/10.1016/j.jallcom.2019.151901.

Ning, F., Hu, Y., Liu, Z., Cong, W., Li, Y., & Wang, X. (2017). Ultrasonic vibration-assisted laser engineered net shaping of Inconel 718 parts: A feasibility study. *Procedia Manufacturing, 10*, 771–778. https://doi.org/10.1016/j.promfg.2017.07.074.

Niu, H. J., & Chang, I. T. H. (1999). Selective laser sintering of gas and water atomized high speed steel powders. *Scripta Materialia, 41*(1), 25. https://doi.org/10.1016/s1359-6462(99)00089-5.

Oblak, J. M., Paulonis, D. F., & Duvall, D. S. (1974). Coherency strengthening in Ni base alloys hardened by DO22 γ'' precipitates. *Metallurgical Transactions, 5*, 143–153. https://doi.org/10.1007/BF02642938.

Odabasi, A., Unlu, N., Goller, G., & Eruslu, M. N. (2010). A study on laser beam welding (LBW) technique: Effect of heat input on the microstructural evolution of superalloy Inconel 718. *Metallurgical and Materials Transactions A: Physical Metallurgy and Materials Science, 41*, 2357–2365. https://doi.org/10.1007/s11661-010-0319-y.

Paul, C. P., Ganesh, P., Mishra, S. K., Bhargava, P., Negi, J., & Nath, A. K. (2007). Investigating laser rapid manufacturing for Inconel-625 components. *Optics and Laser Technology, 39*, 800–805. https://doi.org/10.1016/j.optlastec.2006.01.008.

Qiu, C., Chen, H., Liu, Q., Yue, S., & Wang, H. (2019). On the solidification behaviour and cracking origin of a nickel-based superalloy during selective laser melting. *Materials Characterization, 148*, 330–344. https://doi.org/10.1016/j.matchar.2018.12.032.

Räbiger, D., Zhang, Y. H., Galindo, V., et al. (2014). The relevance of melt convection to grain refinement in Al–Si alloys solidified under the impact of electric currents. *Acta Materialia, 79*, 327–338. https://doi.org/10.1016/j.actamat.2014.07.037.

Ramakrishnan, A., & Dinda, G. P. (2019). Direct laser metal deposition of Inconel 738. *Materials Science and Engineering A, 740–741*, 1–13. https://doi.org/10.1016/j.msea.2018.10.020.

Rao, G. A., Srinivas, M., & Sarma, D. S. (2004). Effect of thermomechanical working on the microstructure and mechanical properties of hot isostatically pressed superalloy Inconel 718. *Materials Science and Engineering A, 383*, 201–212. https://doi.org/10.1016/j.msea.2004.05.062.

Savrai, R. A., Makarov, A. V., Soboleva, N. N., et al. (2016). The behavior of gas powder laser clad NiCrBSi coatings under contact loading. *Journal of Materials Engineering and Performance, 25*(3), 1068–1075. https://doi.org/10.1007/s11665-016-1925-7.

Sims, C. T., Stoloff, N. S., & Hagel, C. (1987). *Superalloys II*. New York: Wiley.

Sui, S., Chen, J., Fan, E. X., Yang, H. O., Lin, X., & Huang, W. D. (2017a). The influence of laves phases on the high-cycle fatigue behavior of laser additive manufactured Inconel 718. *Materials Science and Engineering A, 695*, 6–13. https://doi.org/10.1016/j.msea.2017.03.098.

Sui, S., Chen, J., Ming, X. L., Zhang, S. P., Lin, X., & Huang, W. D. (2017b). The failure mechanism of 50% laser additive manufactured Inconel 718 and the deformation behaviour of laves phases during a tensile process. *International Journal of Advanced Manufacturing Technology, 91*, 2733–2740. https://doi.org/10.1007/s00170-016-9901-9.

Sui, S., Chen, J., Ma, L., Fan, W., Tan, H., Liu, F., & Lin, X. (2019). Microstructures and stress rupture properties of pulse laser repaired Inconel 718 superalloy after different heat treatments. *Journal of Alloys and Compounds, 770*, 125–135. https://doi.org/10.1016/j.jallcom.2018.08.063.

Wang, K. L., Zhang, Q. B., Sun, M. L., & Zhu, Y. M. (1977). Effect of laser surface cladding of ceria on the wear and corrosion of nickel-based alloys. *Surface and Coating Technology, 96*, 267–271.

Wang, K. L., Zhang, Q. B., Sun, M. L., Wei, X. G., & Zhu, Y. M. (2001). Rare earth elements modification of laser-clad nickel based alloy coatings. *Applied Surface Science, 174*(3), 191–200. https://doi.org/10.1016/S0169-4332(01)00017-4.

Wang, Z., Guan, K., Gao, M., Li, X., Chen, X., & Zeng, X. (2012). The microstructure and mechanical properties of deposited-IN718 by selective laser melting. *Journal of Alloys and Compounds, 513*, 518–523. https://doi.org/10.1016/j.jallcom.2011.10.107.

Wang, L., Song, S. Y., Hu, Y., et al. (2015a). Regulation research on microstructure of laser cladding under electric-magnetic synergistic effect. *Chinese Journal of Lasers, 42*, s103005.

Wang, L., Yao, J. H., Hu, Y., et al. (2015b). Suppression effect of a steady magnetic field on molten pool during laser remelting. *Applied Surface Science, 351*(11), 794–802. https://doi.org/10.1016/j.apsusc.2015.05.179.

Wang, L., Yao, J. H., Hu, Y., et al. (2017). Influence of electric-magnetic compound field on the WC particles distribution in laser melt injection. *Surface and Coating Technology, 315*, 32–43. https://doi.org/10.1016/j.surfcoat.2017.01.116.

Wolff, S. J., Gan, Z., Lin, S., Bennett, J. L., Yan, W., Hyatt, G., Ehmann, K. F., Wagner, G. J., Liu, W. K., & Cao, J. (2019). Experimentally validated predictions of thermal history and microhardness in laser-deposited Inconel 718 on carbon steel. *Additive Manufacturing, 27*, 540–551. https://doi.org/10.1016/j.addma.2019.03.019.

Wu, H., Zhang, D., Yang, B., Chen, C., Li, Y., Zhou, K., Jiang, L., & Liu, R. (2020). Microstructural evolution and defect formation in a powder metallurgy nickel-based superalloy processed by selective laser melting. *Journal of Materials Science and Technology, 36*, 7–17. https://doi.org/10.1016/j.jmst.2019.08.007.

Xiao, H., Li, S., Han, X., Mazumder, J., & Song, L. (2017). Laves phase control of Inconel 718 alloy using quasi-continuous-wave laser additive manufacturing. *Materials and Design, 122*, 330–339. https://doi.org/10.1016/j.matdes.2017.03.004.

Zhai, L., Wang, Q., Zhang, J., & Ban, C. (2019a). Effect of alternating current electric field on microstructure and properties of laser cladding Ni–Cr–B–Si coating. *Ceramics International, 45*(2019), 16873–16879. https://doi.org/10.1016/j.ceramint.2019.05.230.

Zhai, L. L., Ban, C. Y., & Zhang, J. W. (2019b). Investigation on laser cladding Ni-base coating assisted by electromagnetic field. *Optics and Laser Technology, 114*, 81–88. https://doi.org/10.1016/j.optlastec.2019.01.017.

Zhai, L. L., Ban, C. Y., & Zhang, J. W. (2019c). Microstructure, micro-hardness and corrosion resistance of Ni-Cr-B-Si coatings under electromagnetic field auxiliary laser cladding. *Surface and Coating Technology, 358*, 531–538. https://doi.org/10.1016/j.surfcoat.2018.11.034.

Zhang, S. H., Li, M. X., Cho, T. Y., Yoon, J. H., Lee, C. G., & He, Y. Z. (2008a). Laser clad Ni-base alloy added nano- and micron-size CeO_2 composites. *Optics and Laser Technology, 40*, 716–722. https://doi.org/10.1016/j.optlastec.2007.10.007.

Zhang, S. H., Li, M. X., Yoon, J. H., & Cho, T. Y. (2008b). Characterization on the coatings of Ni-base alloy with nano- and micron-size Sm_2O_3 addition prepared by laser deposition. *Materials Chemistry and Physics, 112*, 668–674. https://doi.org/10.1016/j.matchemphys.2008.06.024.

Zhang, Y. Z., Tu, Y., Xi, M. Z., et al. (2008c). Characterization on laser clad nickel based alloy coating on pure copper. *Surface and Coating Technology, 202*(24), 5924–5928. https://doi.org/10.1016/j.surfcoat.2008.06.163.

Zhang, D., Niu, W., Cao, X., & Liu, Z. (2015). Effect of standard heat treatment on the microstructure and mechanical properties of selective laser melting manufactured Inconel 718 superalloy. *Materials Science and Engineering A, 644*, 32–40. https://doi.org/10.1016/j.msea.2015.06.021.

Zhang, N., Liu, W. W., Deng, D. W., et al. (2018). Effect of electric-magnetic compound field on the pore distribution in laser cladding process. *Optics and Laser Technology, 108*, 247–254. https://doi.org/10.1016/j.optlastec.2018.06.037.

Zhao, J., Wang, G., Wang, X., Luo, S., Wang, L., & Rong, Y. (2020). Multicomponent multiphase modeling of dissimilar laser cladding process with high-speed steel on medium carbon steel. *International Journal of Heat and Mass Transfer, 148*, 118990. https://doi.org/10.1016/j.ijheatmasstransfer.2019.118990.

Chapter 12
Laser Cladding of NiCr-Cr_2C_3 Coatings on a γ-TiAl Substrate

Pasquale Cavaliere, Seyed Erfan Aghili, Behzad Sadeghi, and Morteza Shamanian

12.1 Introduction

Laser cladding has been developed to improve the surface properties of metals and alloys. Given a base material, a new coating layer is fed on the surface, and then it is melted through a high power source provided by the laser. By moving the substrate during the process, different configurations of the cladded surface are produced (Li et al. 2019). Different ways are employed in order to deliver the coating material on the surface; mainly coaxially or from the side to the laser beam (Fig. 12.1).

Powders, after mixing with a binder, are placed on the substrate before cladding; this can be applied only on flat surfaces and the bind removal could lead to excessive porosity (Zhang et al. 2019). The powder–paste binder can be employed by depositing the coating material at the same time of laser irradiation. Here the feeding control is crucial (Liu et al. 2017; Man et al. 2008). For complex geometries, coating material supply into the form of wire is preferred. This configuration can lead to excessive porosity, cracks, and low adhesion because only a reduced portion of the laser power is absorbed (Garmendia et al. 2019). Through helium or argon gases the powder is fed into the melt pool. With this method, lower porosity coatings with improved corrosion and mechanical properties are produced. Given these advantages, powder feeding has become very widely used for laser cladding (Bourahima et al. 2019). The first employed configuration used lateral nozzles to

P. Cavaliere (✉)
Department of Innovation Engineering, University of Salento, Lecce, Italy
e-mail: pasquale.cavaliere@unisalento.it

S. E. Aghili · M. Shamanian
Department of Materials Engineering, Isfahan university of Technology, Isfahan, Iran
e-mail: e.aghili@ma.iut.ac.ir; shamanian@cc.iut.ac.ir

B. Sadeghi
State Key Lab of Metal Matrix Composites, Shanghai Jiao Tong University, Shanghai, China

P. Cavaliere (ed.), *Laser Cladding of Metals*,
https://doi.org/10.1007/978-3-030-53195-9_12

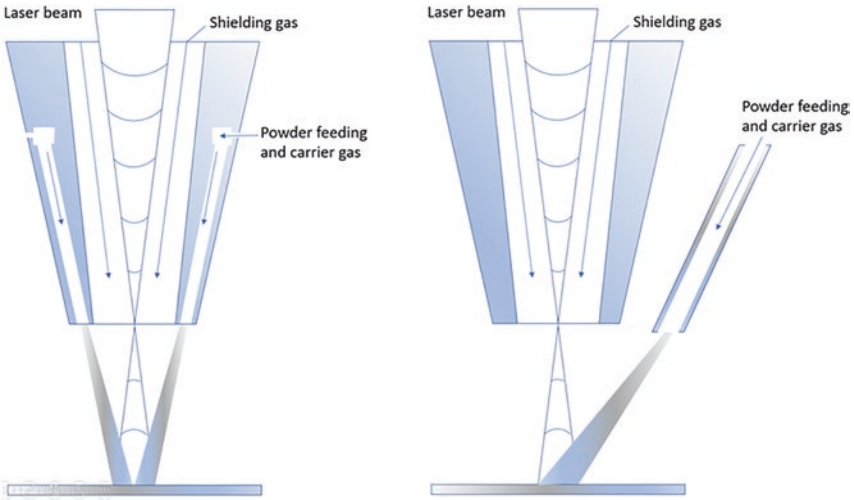

Fig. 12.1 Coaxial (left) and side (right) laser cladding

feed powders. This allows the deposition of huge volumes of powder but has the inconvenience of the possibility of moving the cladding head in just one direction (Liu et al. 2015). The process control is governed by the concentrated heat input responsible for the high precision. However, the high temperature gradients are responsible for the high thermal stresses leading to potential distortion, cracking, and delamination. So, the required quality can be reached just by the precise tuning of the employed processing parameters (Brückner and Lepski 2019). Among the main advantages of laser cladding, the possibility of mixing different types of powders to obtain functionally graded materials must be underlined. This allows for the production of additive manufactured components with various functions realized layer-by-layer (Behera et al. 2018). The clad thickness typically measures from 50 μm to 2 mm in each track. Thicker structures can be obtained by building additional layers on top of the previously deposited clad. By employing powders with optimal compositions and dimensions, high-quality metallurgical bonds can be obtained (Ma et al. 2020). Here it was demonstrated how the coatings' residual stresses decrease as the dilution increases. The description of the process is very complex due to the involvement of many physical issues such as dilution with the substrate and directional solidification, surface tensions, viscosity, Marangoni flow, electromagnetic force, and gravity (Jiang et al. 2020, Mandal et al. 2020). The process is governed by many complex parameters such as laser beam spot size, laser beam energy distribution, carrier and shielding gas used, powder feeding process, and geometry of the substrate. Process fundamentals description.

Given that the whole laser cladding process depends on the heat transfer among the laser beam, the substrate, and the power and mass transfer between the material flow and the molten surface, the main proposed approach is the employment of the well-known combined parameters (Karmakar and Ghosh 2020). Because the

process is related to so many parameters, the modeling and optimization are crucial issues. Picasso et al. (1994) indicated the laser conditions to develop a given clad height with a simple geometrical model. Lei et al. (2018) modeled the clad geometry as a function of processing parameters through complex image analyses. Reddy et al. (2018) developed a model based on a huge quantity of experimental data capable of predicting the deposition efficiency and clads' porosity. A similar approach is described by Fayaz and Kazemzadeh (2018). A precise FEM model is presented (Wirth and Wegener 2018) taking into account the heat transfer, fluid flow, surface tension, and free surface movement. Aggarwal et al. (2018) explored predictive model approaches for selecting laser cladding process settings for a desired bead geometry/overlap strategy. An empirical–statistical model for WC-Co coatings is described by Erfanmanesh et al. (2017). Ansari et al. (2016) proposed the same approach for NiCrAlY coatings on the In738 substrate. So, even if many approaches have been proposed, empirical–statistical models are very useful in understanding the complex physical phenomena of the laser cladding process. The statistical correlation between the employed processing parameters and the geometrical–microstructural features of the clad is crucial for optimal deposited coatings (Pinkerton 2015).

γ-TiAl is an excellent material for high temperature applications thanks to its properties such as low density, high specific strength and stiffness, and high elastic modulus and creep resistance. So, tribological and high-temperature oxidation properties are critically important for the component's performance (Liu and Wang 2006). NiCr base coatings can be an excellent choice to improve the required properties. In the present paper, coaxial laser cladding is modeled by relating the processing parameters to clads' geometry. The optimization allowed to identify the weight of each parameter on the clad properties and to select the best parameters in order to optimize the final microstructure of the coatings for NiCr-Cr_2C_3 deposited on the γ-TiAl substrate.

12.2 Experimental Procedure

A γ-TiAl substrate, whose dimensions were 100 × 100 × 40 mm, was employed in the present study. The substrate composition is listed in Table 12.1.

Before cladding, the surface was ground with SiC papers.

The NiCr-Cr_3C_2 (SulzerMetco, USA) powders were synthesized by mechanical milling and rounded to a nominal diameter of 50 μm for better flow into the cladding machine. Figure 12.2 shows the morphology the powder particles after exiting of the drying apparatus. Such a spherical morphology is quite suitable for the laser

Table 12.1 Composition (wt.%) of the employed substrate

Ti	Al	Cr	Nb	Others
49.35	47	1.68	1.95	0.02

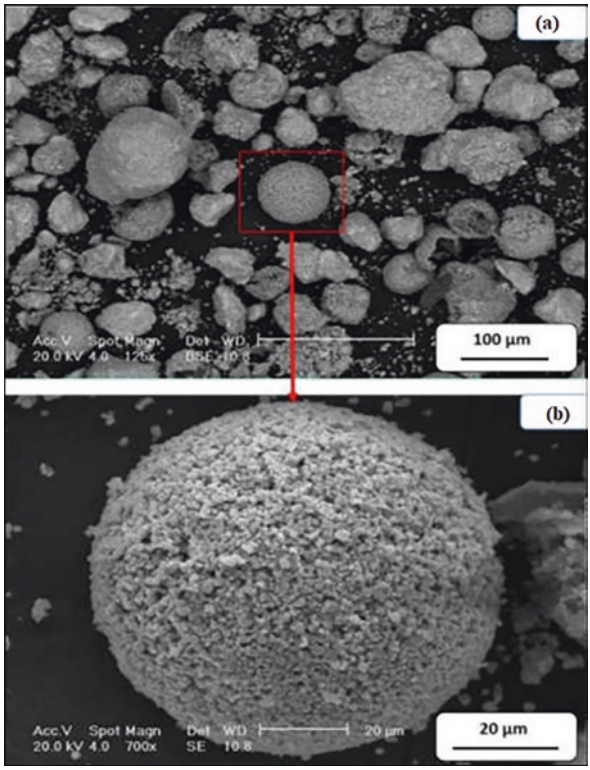

Fig. 12.2 Morphology of the powder particles of Ni (Cr)-Cr_3C_2 after the drying step

Table 12.2 Laser parameters employed in the present study

Processing parameter	
Laser power (W)	300–500
Scan speed (mm/s)	2–5
Powder feeding rate (g/min)	0.2–0.4
Shielding gas flow rate (l/min)	15
Powder carrier gas flow rate (l/min)	20

cladding process. The use of such a morphology for laser cladding is a prerequisite for achieving the best laser performance.

A powder feed unit was used to split a powder stream into four identical streams, which was then sent out by a 4-way coaxial nozzle with four individual powder streams. Argon was used as a powder carrier gas. Laser cladding was carried out using a 0.7 kw transverse-flow Nd:YAG laser materials processing system equipped with a 4-axes computer numerical controlled (CNC) machine under an Argon shielding environment. In all the experiments, the laser beam was focused exactly on the substrate surface having a spot size of 1 mm. The employed laser parameters are listed in Table 12.2.

The effective parameters employed to monitor the laser cladding process were the clad height h, the clad width W, the angle of wetting θ, and the penetration depth

b, representing the thickness of the melted substrate during the cladding process, which is just under the clad and below the substrate surface (Fig. 12.3).

One of the main effective factors on the laser cladding is the dilution that could be defined from two perspectives: geometrical and metallurgical. The melting of materials during the laser cladding leads to transfer of the materials from the substrate to the coat. Therefore, it is important to control this dilution. The metallurgical dilution (D_M) could be calculated by Eq. (12.1).

$$\left(D_M\right)=\frac{\rho_c\left(X_{c+s}X_c\right)}{\rho_s\left(X_{c+s}X_c\right)+\rho_c\left(X_{c+s}X_c\right)} \tag{12.1}$$

Where ρ_c is the density of the melted powder alloy (Kg/m^3), ρ_s is the substrate density (Kg/m^3), $X_{(c+s)}$ is the weight percent of element X in the total area of the coat zone, X_c is the weight percent of element X in alloy powder, and X_s is the weight percent of element X in the substrate. Additionally, the geometrical dilution (D_G) can be represented by Eq. (12.2).

$$\left(D_G\right)=\frac{b}{b+h} \tag{12.2}$$

It is known that to achieve an appropriate single clad track with the desired coating properties, a combined parameter of P, S, and F should be defined. Thus, in order to predict the clad geometry, a combined parameter as $P^{\alpha}S^{\beta}F^{\gamma}$ can be proposed to describe each geometrical characteristic. Here, P is the laser power, S is the scan speed, and F is the powder feeding rate. OriginPro software with a trial and error approach was employed to figure α, β, and γ, which can obtain the best linear fit with the highest R-squared. A mathematical formula was finally achieved as $y = a(x) + b$, where y is one of the geometrical characteristics of the single clad track and x is the combined parameter ($P^{\alpha}S^{\beta}F^{\gamma}$), while a and b are equation constants.

After laser cladding, the samples were cut through an electrical discharging machine in a direction perpendicular to the cladding tracks. After polishing, the samples microstructure was observed with a field emission scanning electron microscope (FESEM; MIRA3, TESCAN, Czech Republic).

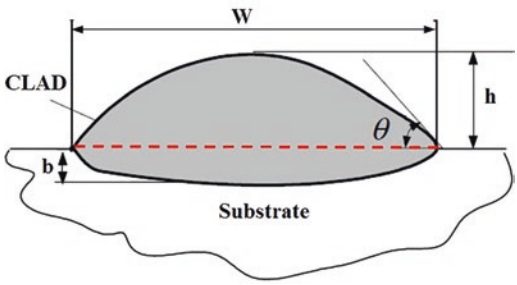

Fig. 12.3 Schematic representation of the geometrical characteristics in a single clad

12.3 Results and Discussion

Figures 12.4a–c depict the resulting geometry of single-pass laser cladding coatings for different processing parameters

At the first glance, it could be found that the single clad track geometry is affected by some relevant aspects of the laser cladding process parameters. As seen from the figures, by using $P = 300$ W, all the parameters lead to the formation of a clad on the substrate, while at higher P, the clad detached for some parameters. At a constant laser power of 400 W, with decreasing S and increasing F, poor bonding is revealed. Such conditions lead to detachment of the clad track from the substrate. Additionally, at $P = 500$ W, the detachment of the clad track from the substrate occurs by increasing S and F to 5 mm/s and 400 mg/min, respectively (Erfanmanesh et al., 2018). Moreover, based on the given equations by De Oliveira et al. (2005), the minimum required energy to melt the powder particles has a direct relationship with the feeding mass of powder into the laser. However, for the minimum employed power (300 W), well-bonded and sound single clad tracks were formed at all processing parameters in the range of $S = 2$–5 mm/s and $F = 200$–400 mg/s. Therefore, it was revealed that the required power for melting the substrate and powder particles is theoretically produced. It is worth noting that by increasing the laser power to 400 and 500 W, the cladding process for some of the samples was not successful and no cladding formed. Also, the lack of a proper cladding on the substrate in high laser powers as well as low scanning speeds was previously reported (Nabhani et al. 2018). Barekat et al. (2016) studied the laser cladding parameters for applying the Co-Cr-Mo powder as cladding on the TiAl substrate. They found that at lower values of F and S and high laser powers, the substrate is re-melted very quickly, which does not lead to the formation of clad track.

The results by Ocelik et al. (2007) on Co-based coatings on a cast iron substrate produced by a high power laser cladding process revealed that the clad track is formed at a low P and a low F as well as at a high P and a high F. In brief, by increasing the laser power and decreasing the scanning speed to 2 mm/s, the incoming energy into the molten pool greatly increases, and consequently the volume of the molten substrate increases and the turbulence of the molten pool increases. This phenomenon prevents the formation of a proper molten pool and no cladding is formed. Additionally, the low heat transfer coefficient of titanium aluminide also is important for the formation of the molten pool at high powers.

12.3.1 Effect of Processing Parameters on the Clad Height

With regards to Fig. 12.4, it could be concluded that all the parameters such as laser power, laser scanning speed, and powder particles' feeding rate affect the clad height. Keeping the laser power constant, increasing the powder particles' feeding rate leads to the enhancement of the clad height. The decrement of the scanning

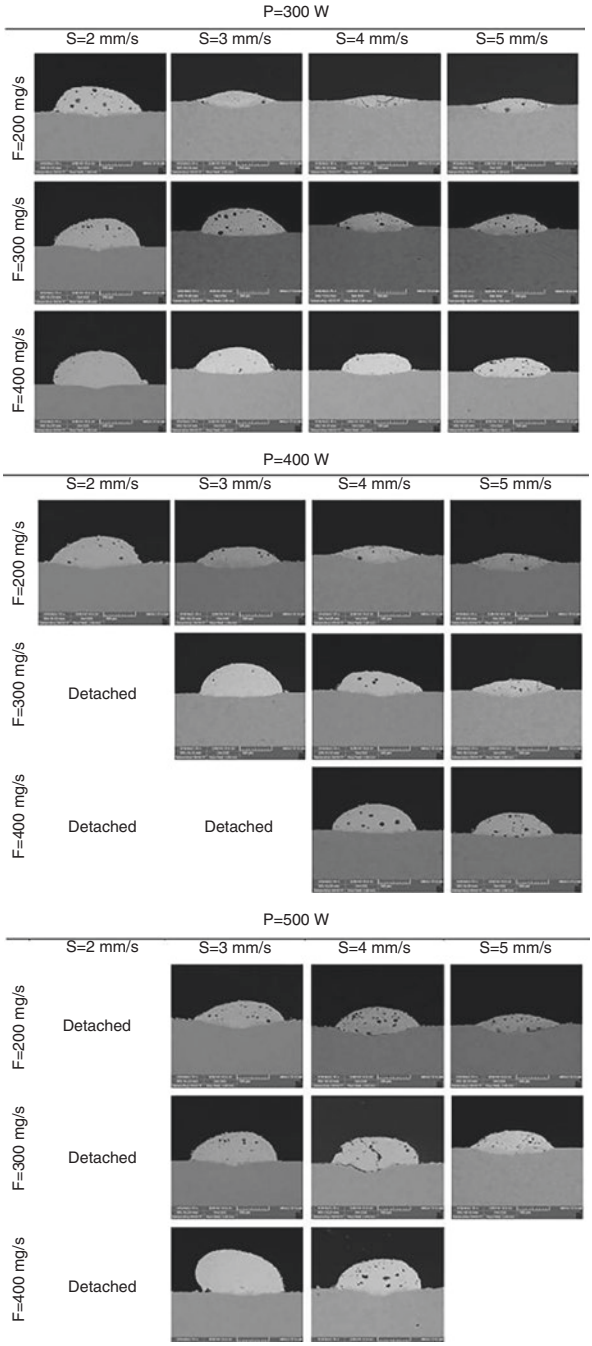

Fig. 12.4 SEM microstructure of the cross section of single clads, processed at different conditions. For each laser power, scanning speed (S) increases from left to right and powder feeding rate (F) increases from up to down

speed has the same influence on the clad height. Additionally, the clad height increases as the laser power or the powder feeding rate increases (Toyserkani et al. 2003). In justifying such behavior, it could be stated that by increasing the powder feeding rate, the mass and volume of the incoming powder into the molten pool increase per unit time as a result of the melting, and the clad height increases. In addition, by increasing the scanning speed, the duration oflaser interaction with powder particles increases, resulting in faster melting of powders leading to an increase in the clad height. The laser power has the same effect on the enhancement of the powder melting rate. The enhancement of the clad height with the increasing powder feeding rate and the decreasing scanning speed is largely described by Ansari et al. (2016). However, there is no agreement on the influence of laser power over the clad height among the researchers. Accordingly, it can thus be stated that the laser power plays a negligible role, while El Cheikh et al. (2012) pointed out the significant effect of laser power on clad height.

12.3.2 Effect of Processing Parameters on the Clad Width

The main parameters of laser cladding such as scanning rate, laser power, and powder feeding rate are quite significant for the diametric properties of the clads as seen in Fig. 12.4. One of the other main parameters that changes by varying the processing parameters is the clad width. The laser power and the scanning speed have more effect on the clad width compared to the powder feeding rate. At constant power, by increasing the laser speed, the interaction time between powder particles and the laser beam decreases and consequently the generated heat input to the center of the pool surface is decreased, resulting in a decrease in the outward shear stress on the pool surface. As a consequence, this leads to a decrease in the clad width. For example, at a laser power of 300 W and $F = 200$ mg/s, by increasing S from 2 to 5 mm/s, the clad width decreases from 1408 to 1278 μm. It is found that by increasing the laser power from 300 to 500 W, the clad width increases by about 62 μm (whereas $S = 3$ mm/s and $F = 200$ mm/gr were constant). Therefore, it can be concluded that the laser power for all values of F and S has a strong direct effect on the clad width. It can be attributed to the existence of the Marangoni and Buoyancy forces into the melt pool (Kou 2003). Among the various types of forces acting inside the melt pool, these forces showed the highest influence on the clad width. Buoyancy force originates from the differences in the liquid metal pool, while in the absence of a surface-active agent, Marangoni force, caused by the difference between surface tension in different areas of the melt pool, induced by the temperature gradients that exist across a melt pool was identified (Pinkerton 2010). It is known that the surface tension decreases with the increasing temperature. Therefore, the central zones of the melt pool, which is exactly under the laser beam, experience higher temperatures with respect to the side areas, and consequently their surface tension is lower than that of the side areas. Owing to this, the melt moves to cooler areas and consequently the clad width increases. The enhancement of the powder feeding rate

causes absorption of some of the laser energy, and thus leads to a decrease in both the heat input and the clad width. However, the observations revealed that the effect of the powder feeding rate on the clad width is lower compared to both the laser power and scanning rate. Ansari et al. (2016) reported that the clad widths, with the same values of laser power and scanning speed but different values of powder feeding rate, were approximately equal to each other.

12.3.3 Effect of the Processing Parameters on Clad Geometrical Complexity

As previously mentioned, referring to Eq. 12.2, the geometrical dilution is dependent on the penetration depth (b) as well as the clad height (h). The minimum and maximum geometrical dilutions in this study were equal to 11% and 56%, respectively. The result showed that by keeping the other parameters constant, the enhancement of laser power has a direct influence on the dilution. An increase in the laser power leads to enhancement of the heat input as well as over-melting of the substrate, and as a consequence the geometrical dilution increases. The laser scanning speed and the powder feeding rate have more interactive and complex effects on the geometrical dilution. On one hand, by decreasing the scanning speed (at constant F and P), the interaction time of the substrate and the laser beam increases and the heat input into the substrate increases. This causes an increment of the penetration depth. On the other hand, the decrement of the laser scanning speed has also a significant effect on the clad height, such that by decreasing the laser scanning speed the clad height is significantly increased. Enhancement of the powder feeding rate has impressive effects on the clad geometrical dilution, as well. By increasing the powder feeding rate into the laser per unit time, more energy is adsorbed into the powder particles, and therefore the incoming energy to the substrate decreases. This leads to a decrease in the penetration depth (Fu et al. 2002; Devesse et al. 2015).

The combined parameter derived from P, F, and S was found to be linearly dependent on the clad height, clad width, penetration depth, dilution, and wetting angle. Therefore, the next section will be focused on analyzing the obtained results of linear regression analysis in order to achieve an accurate model of the combined parameter ($P^{\alpha}S^{\beta}F^{\gamma}$) with optimal values for α, β, and γ.

By using a linear regression analysis, the linear correlation between h and the main parameters F, S, and P is achieved. Figure 12.5a shows the statistical relation between the single cladding height (h) and the combined parameter. It is worth noting that the h is directly proportional to $P^{1}S^{(-1)}F^{0.85}$ with a linear regression coefficient $R = 0.955$.

It is important to point out that a large value of R endorses the linear statistical model. Therefore, it could be concluded that the achieved combined parameter as well as the line equation are highly acclaimed, and a linear relationship between h and the combined parameter could exist. Additionally, the distribution of the residu-

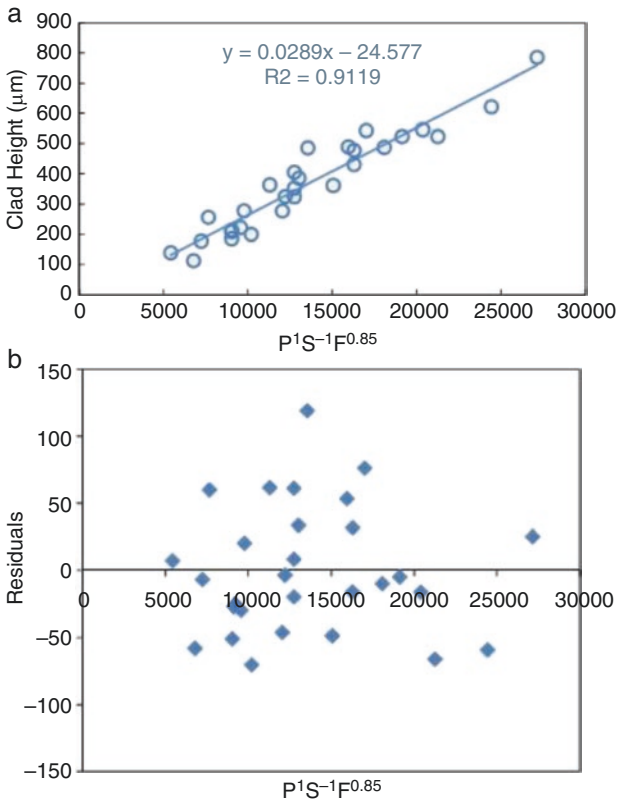

Fig. 12.5 (**a**) Dependency of the cladding height and (**b**) dependency of the value residuals on the combined parameter $P^1S^{(-1)}F^{0.85}$

als relative to the normal line is given in figure 12.5b. This shows that the distribution of the residuals is uniform. The obtained line equation of regression analysis is described by Eq. 12.3.

$$h = 0.0289\left(P^1S^{-1}F^{0.85}\right) - 24.577 \tag{12.3}$$

Therefore, the obtained model has a high reputation and accuracy. The clad height (h) is increased by increasing P and F and decreasing F. The laser power has a direct relation with the clad height, and thus has a significant effect on the clad height. On the other hand, by varying the laser power at F and S constants, the clad height changes. The influence of the laser power can be justified by stating that on increasing P, the generated temperature increases, and consequently more powder melts and the clad height increases (Tabernero et al. 2012).

With respect to the scanning speed (S) and the powder feeding rate (F), it should be mentioned that at a constant laser power, at each powder feeding rate, the clad

height increases upon decreasing the scanning speed. On the other hand, for every scanning speed, the feeding rate has the same influence on the clad height if the laser power remains constant. Generally, *F* has an inverse effect on *h*, and it reduces with increasing *S*. Moreover, the effects of *S* and *F* are such that by increasing *F* and decreasing *S*, the incoming powder volume per unit area increases, consequently more powder melts, and the clad height increases. Quantitative studies show that the cladding height is equal to 12 micron at the highest *S* and lowest *F*, while the highest height with value 784 micron is achieved at the lowest S and the highest *P* and F. For example, El Cheikh et al. (2012) have studied the laser cladding of the 316 L steel powder on a steel substrate and reported that the clad height has a direct relationship with the combined parameter $P^{(1/4)}S^{(3/4)}F^{(-1)}$ along with a linear regression coefficient of 0.944.

12.3.4 *Effect of the Processing Parameters on Clad Physical Complexity*

By using linear regression analysis, the linear correlation between W and the main parameters *F*, *S*, and *P* is achieved. In Fig. 12.6a, the correlation between *W* and $P^1S^{(-1)}F^{(-0.7)}$ is shown.

The distribution of the residuals as a function of the combined parameter $P^1S^{(-1)}F^{(-0.7)}$ relative to the normal line is also given in Fig. 12.6b. The linear regression coefficient, obtained for this condition, was equal to $R = 0.949$ which shows high accuracy of the proposed combined parameter as well as correctness of the linear equation proposed in Eq. 12.4.

$$W = 54.343\left(\mathrm{P^1S^{-1}F^{-0.7}}\right) + 1208.4 \tag{12.4}$$

The uniformity of dispersion as well as the distribution of the data showed that the achieved linear model is accurate and correct. Equation 12.4 reveals that the impression width of the single pass laser cladding (*W*) affects the three parameters *P*, *F*, and *S*. The clad width showed the aligned linear correlation with the increment of the laser power. On the other hand, by decreasing the scanning speed and the powder feeding rate, the clad width increases. The quantitative calculations revealed that *W* is about 1273 micron at the highest *S* and *F* and at the lowest *P*, while the maximum *W* was equal to 1483 micron at the lowest *S* and *F* and the highest *P*. Such findings could be attributed to the external forces and multiple forces within the melt pool, which are formed during the laser cladding process and could affect the final shape of the melt pool. The parameters such as nozzle design, powder flow setting, and the pressure of conveyance and shielding gases affect these forces. Among several variables affecting the melt pool, Buoyancy and Marangoni forces and shear stresses caused by plasma jet are the most important, the liquid metal is warmer at the center of pool surface and cooler at the edge of pool surface. Taking

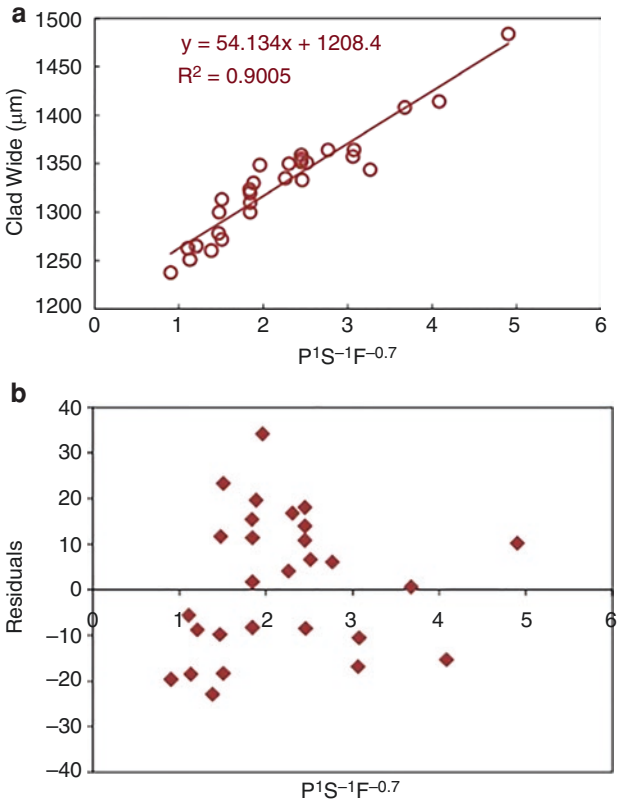

Fig. 12.6 (**a**)Variation of the single pass clad width and (**b**) distribution of the residuals, in terms of the combined parameter of $P^1S^{(-1)}F^{(-07)}$

this into account and knowing that $\partial\gamma/\partial T < 0$, the melt metal with a lower surface tension at the center is pulled outward by the cooler melt metal with a higher surface tension at the edge. In order to further explain, it should be emphasized that the outward shear stress is induced at the pool surface by the surface tension gradient along the pool surface. Finally, this causes the melt metal to flow from the center of the pool surface toward the edge and return below the pool surface (Ebrahimzadeh and Mousavi 2012).

It is worth noting that among several variables affecting the melt pool, which can determine the width and depth of the melt pool, Buoyancy and Marangoni forces and shear stress caused by plasma jet are more important. However, all the variables can be triggered by different processing parameters such as F, P, and S. Nevertheless, the laser power has the highest influence on the clad width. However, as it can be seen in the power of the F in the Eq. 12.4, the feeding rate may be considered a weak parameter in this case. By increasing the laser power, the clad width increases. On

the other hand, by decreasing the scanning speed, which results in an increase in the interaction time between the laser and materials, consequently, the input energy and then the clad width increase. By decreasing the powder feeding rate, the available powder particles decrease, and thus the heat energy distributes between less powder particles, leading to an increase in the energy and finally the increment of the clad width. Moreover, as it can be seen in Fig. 12.6a, there is some overlap in the data points. Such data points overlap corresponding to the negligible effect of the powder feeding rate on the clad width. These results clearly implied that the combined parameter found in this study for the statistical dependence of the clad width is consistent with the majority of previous works, which reported combined parameters derived from P, F, and S for the clad width. The study conducted on the thick Co-based coating on cast iron by side laser cladding revealed that there is a correlation as $PS^{(-1/2)}$ with $R = 0.9$ between W and the combined parameter (Lei et al. 2018).

Coaxial laser cladding of Ni-Cr powder on a steel substrate showed that the combined parameter $PS^{(-1/2)}$ has a direct relation to W. The linear regression coefficient $R = 0.95$ offers a high accuracy of the proposed relationship. Additionally, the laser cladding of 316 L powder on the steel substrate illustrated that $P^{(3/4)}S^{(-1/4)}$ with $R = 0.922$ have a direct relation to W (El Cheikh et al. 2012). In all previous studies, laser power and scanning speed are considered as the most effective parameters on W, and the impact of the powder feeding rate on the clad width was negligible. However, in the current study the powder feeding rate has a remarkable impact on the clad width. It seems that this could be attributed to the difference of the synthesis route for the used primary powders. The synthesized powders via the mechanical alloying route have a high level of energy, which is effective for energy absorption. On the other hand, one of the other reasons that is given here is the different particle size distribution for the used powders compared to those used in other studies. Therefore, as a result of the difference in both the synthesis route and the particle size distribution of primary powders, the role of the powder feeding rate has become more important.

12.3.5 Single Pass Clad Penetration Depth

Figure 12.7a shows the relationship between the penetration depth of the single pass clad and the combined parameter

The relationship was as $P^{0.75}S^{0.5}F^{(-1)}$. The correlation coefficient between the penetration depth and the combined parameter was $R = 0.954$, which indicated high accuracy of the achieved relationship. By taking a look at Fig. 12.7b, it could be found that the uniform distribution of the data for the proposed model showed a close approximation of the composition and data with the achieved values by the model. The linear equation obtained between the penetration depth and the main parameters is described by Eq. 12.5.

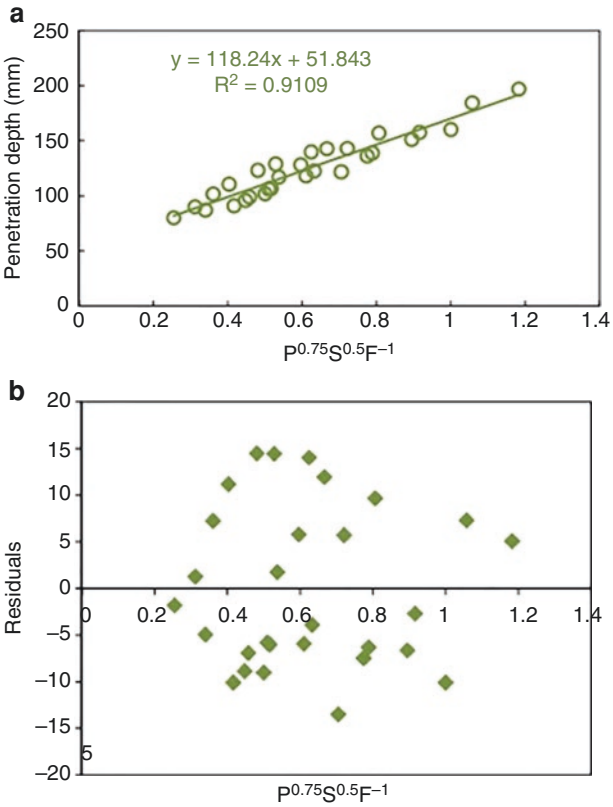

Fig. 12.7 Variation of the penetration depth for single pass clad (**a**) distribution of residuals (**b**) distribution of the residuals, in terms of the combined parameter $P^{0.75}S^{0.5}F^{(-1)}$

$$b = 118.24\left(P^{0.75}S^{0.5}F^{-1}\right) + 51.843 \tag{12.5}$$

Figure 12.7 shows that by increasing the laser power and the scanning speed as well as by decreasing the powder feeding rate, the penetration depth increases. In fact, by increasing the laser power, the input heat increases, resulting in absorbing more energy even at a constant powder feeding rate and scanning speed. Therefore, more substrate is melted. By increasing the powder feeding rate, the penetration depth decreases. Generally, both the additional powder and the substrate absorb laser beam energy and the energy is shared between them. Thus, by increasing the input powder volume, the energy consumed for melting of the substrate has a minor portion due to consumption of somewhat of input energy for melting of the extra incoming powders. Considering the scanning speed, there is a direct relationship between them, as by increasing the scanning speed, the penetration depth increases. The interaction time of powder particles with the laser beam has an opposite linear relationship with the scanning speed. The enhancement of the scanning speed

causes a decrease of the interaction and consequently decreases the input energy, while the powder volume exposed to the laser beam in unit time decreases and thus provides more energy to the substrate, which leads to an increase in the penetration depth. By comparing the obtained results in the current study and previous works, it could be concluded that the main parameters *P*, *F*, and *S* have a significant influence on the penetration depth. In addition, the most common effects on the variations of the penetration depth are shown to be the laser power and the powder feeding rate.

12.3.6 Single Pass Clad Dilution

Dilution is achieved in laser cladding processes that rely on diffusion bonding (Barekat et al. 2016). The main features of the laser cladding process are the low penetration band of the clad on the substrate as well as the low dilution with the substrate. Therefore, the study of the dilution of the clad attracts a large number of researchers' attention. The existence of dilution leads to the formation of metallurgical bonding between the clad and the substrate. In order to form a strong bond for lased clads, the molten pool must penetrate into the substrate. Additionally, the dilution phenomenon in the clad materials leads to an improvement in the clad quality. The dilution is generated via fusion bonding which is formed between the solid and liquid by fusion. The fusion bond is usually strong and has a high resistance to mechanical and thermal shocks. The melting of the substrate as well as the dilution are necessary to attain the strong bonding if the brittle phase at the interface does not form (Pinkerton 2010). Therefore, the melting of the substrate as well as the dilution is necessary; however, for high dilution values, this has a detrimental effect on the clad quality and geometry. By using linear regression analysis, the linear correlation between D and the main parameters is achieved. Figure 12.8a shows the relationship between D and the combined parameters of $S^{0.8}$ F. Figure 12.8b illustrates the distribution of the residuals drown in terms of the normal line according to the combined parameter of $S^{0.8}F^{(-0.8)}$.

The high value of the linear regression coefficient as well as the uniform dispersion of residuals reflected the accurate amount for approving the proposed linear model. This relationship is a direct relation. The linear equation of the obtained regression is described by Eq. 12.6.

$$D = 1149.6\left(S^{0.8}F^{-0.8}\right) - 8.5306 \tag{12.6}$$

Dilution is increased by increasing the scanning speed as well decreasing the powder feeding rate, while an increase or decrease of the laser power had a negligible effect on the dilution. If the laser power has a significant effect on the dilution of the clad, the clads achieved with different laser powers could not have equal dilutions even if the powder feeding rate and the scanning speed are constant. The dilution of the clads was about 11% at the highest powder feeding rate, while the

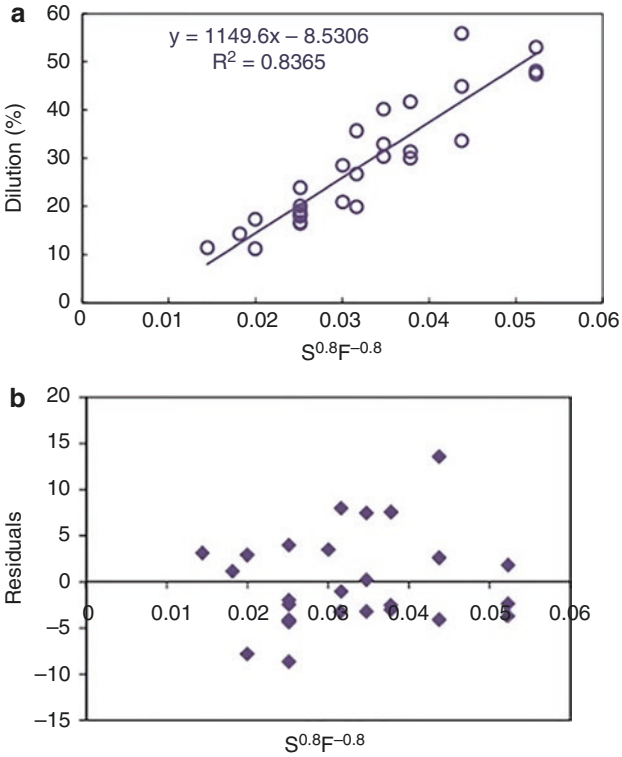

Fig. 12.8 (**a**) Variation of the dilution for single pass clad and (**b**) distribution of the residuals, in terms of the combined parameter $S^{0.8}\ F^{(-08)}$

minimum dilution was about 56% at the lowest scanning speed. Therefore, as it is shown in Fig. 12.8, dilution at the highest scanning speed and the lowest powder feeding rate is different. The main reason for the negligible effect of the laser power on the dilution could be attributed to the dilution caused by the division of the clad height to the sum of the clad height and the penetration depth. Since the laser power affects both the clad height and the penetration depth, the effect of the laser power can be eliminated by simplifying the fraction. For this reason, dilution is independent of the laser power, and therefore it could be overlooked by the effect of laser power on the dilution. On the contrary, by decreasing the laser scanning speed, the penetration depth dilution decreases. Therefore, the amount of absorbed energy is serious for both the penetration depth and dilution. It should be noted that if the amount of the incoming powder to melt pool becomes more than a threshold value, it is not possible to absorb the required amount of laser energy and the lack of substrate and coating melting would be probable. By increasing the powder feeding rate, the clad height also increases, resulting in a decrease of the penetration depth as well as the dilution. The more the powder particles penetrate the substrate, the stronger the clad forms on the substrate. Unlike the obtained results on the dilution

in previous studies, which rely on the three parameters *S*, *P*, and *F*, in this study the dilution affects the scanning speed and the powder feeing rate (Ansari et al. 2016). It seems that the reason causing such a similarity could be attributed to the Nickel-based powders used in both studies.

12.3.7 Single Pass Clad Wetting Angle

Figure 12.9a depicts the correlation between the wetting angle with the combined parameter of $P^{0.8}S^{(-0.7)}F^{1}$. The uniform distribution of the residuals relative to the model values is given in Fig. 12.9b. The wetting angle played a remarkable role to avoid porosity creation in the cladding, while overlapping individual clad tracks. By assuming that the cladding track is a hemisphere, the wetting angle can be calculated from the laser track width (*w*) and the laser clad height (*h*), as $\theta = 2$ arc tan (2 h/w). The wetting angle should be large enough to avoid the formation of porosity. In this study, the wetting angle is about 15°–94 °.

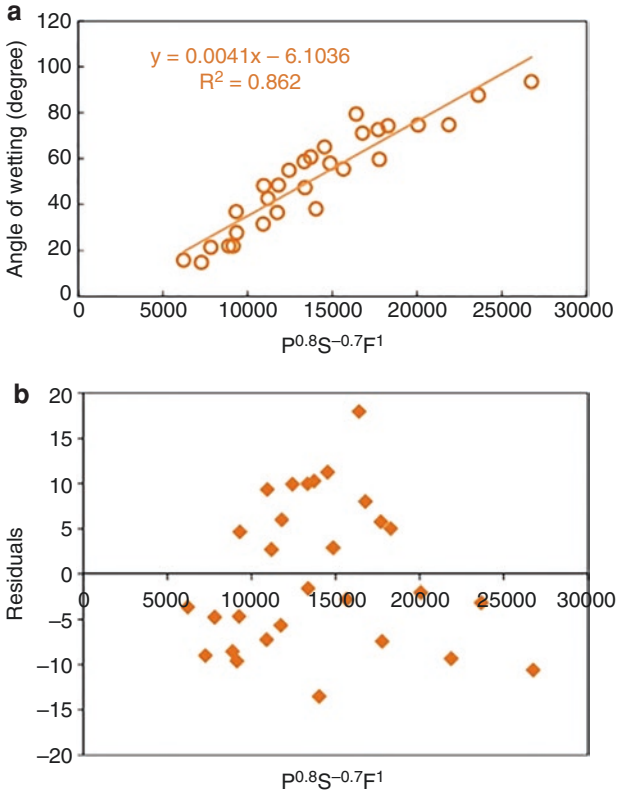

Fig. 12.9 (**a**) Variation of the wetting angle for single pass clad, (**b**) distribution of the residuals

The obtained results depict that the wetting angles have a direct relationship with the combined parameter of $P^{0.8}S^{(-0.7)}F^{1}$. The linear regression coefficient was $R = 0.928$. The obtained line equation for the wetting angle and the combined parameter is given in Eq. 12.7.

$$\theta = 0.0041\left(\mathrm{P}^{0.8}\mathrm{S}^{-0.7}\mathrm{F}^{1}\right) - 6.1036 \tag{12.7}$$

The wetting angle with laser power and the powder feeding rate have a direct relation, and a converse relation with the scanning speed. De Oliveira et al. (2005) reported that the wetting angle could change from 30°–120° and in combination of S/F with $R = 0.9$ shows a direct relationship (Costa et al. 2002). However, Ocelik et al. (2007) found that α and (P^{α}) have a relation with the combined parameter of $P^{(-1/2)}S^{(-1/2)}F^{1}$. The reported R was equal to 0.94. By eliminating the effect of P on the wetting angle, the R decreases showing the low accuracy of the obtained results. Therefore, the laser power plays a nonnegligible role due to its effect on the clad width. By decreasing the powder feeding rate, the clad height and the wetting angle decrease. The analysis of scanning speed on the wetting angle is difficult due to the fact that it is affected by both the clad width and clad height. However, it seems that by increasing the scanning speed, the wetting angle decreases.

12.3.8 Processing Map for Different Parameters

All the predicted combined parameters in this study with the best correlations and the measured geometrical characterization of single clad tracks are summarized in Table 12.3.

All the geometrical track characteristics show high values of correlation coefficient of more than 91% with their combined parameters, which reflects the high accuracy and robustness of all the directly measured quantities. It is known that for achieving a fully dense clad layer, dilution should be kept around 5–10%, while the wetting angle could be smaller than 80 for avoiding interrun porosities and achieving porosity-free clads (Jouvard et al. 1997). Such a condition leads to a porosity-free and perfect-bonded clad layer (Costa et al. 2002). Figure 12.10 shows the

Table 12.3 Combined parameters that show high correlations with geometrical characteristics of laser tracks

Quantity (y)	Combined parameter (x)	R	a	b
h(μm)	$P^{1}S^{(-1)}F^{0.85}$	0.955	0.0289	−24.577
w (μm)	$P^{1}S^{(-1)}F^{(-0.7)}$	0.949	54.134	1208.4
b(μm)	$P^{0.75}S^{0.5}F^{(-1)}$	0.954	118.24	51.843
D (%)	$S^{0.8}F^{(-0.8)}$	0.915	1149.6	−8.5306
θ (degree)	$P^{0.8}S^{(-0.7)}F^{1}$	0.928	0.0041	−6.1036

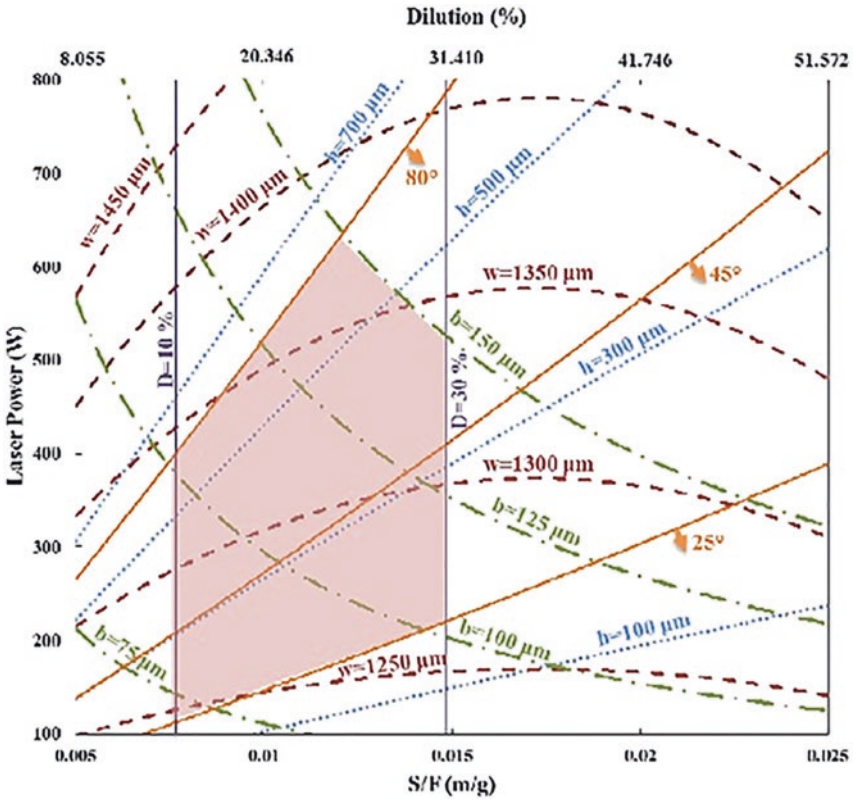

Fig. 12.10 The processing map for laser cladding of NiCr-Cr_2C_3 alloy on TiAl substrate in P vs. S/F representation

processing parameters map for the laser cladding of the NiCr-Cr_2C_3 alloy on the TiAl substrate.

The figure shows a processing map in which the vertical axis is the laser power (P) and the horizontal axis is the powder material that is fed for each unit length (S/F). By remembering the linear relationship between the wetting angle and the S/F parameter, another horizontal axis could be indicated for the wetting angle. It is known that θ could be directly achieved from each combination of processing parameters. By drawing the map, the selection of the best sample in terms of geometry characteristics will be easy. By using the map and the intended geometrical characteristics, the optimal processing parameters in terms of P, S, and F could be extracted.

On the contrary, the map could be used to predict the geometrical characteristics of the single pass clad by the selected processing parameters. Moreover, it is possible to predict the geometrical characteristics of the multi pass clad. The points on the map show all the geometrical characteristics of the model. The above horizontal axis shows dilution values. Dilution has no dependency on the laser power and has

relation with S/F; therefore, a dilution value on the above axis for each S/F value could be specified. The dilution percentages, at the constant values of 10 and 30% based on the relationship between the combined parameters and dilution, as two lines in vertical and purple, are shown in Fig. 12.10. In this map, the curved lines as dashed lines in five values of w = 1250, 1300, 1400, 1350, and 1450 micron are specified for the statistical relations between the cladding width and the combined parameter $P^1S^{(-1)}F^{(-0.7)}$. These lines are drawn as the parabolic dashed curves. With regards to these lines, it could be predicted the clad width providing that the processing parameters S, P and F are known. The statistical relations between the cladding height and the combined parameter $P^1S^{(-1)}F^{(-0.7)}$ form the parabolic dashed curves for four constant values of the cladding height (h = 100, 300, 500, and 700). These points are shown in the map in blue dashed lines. By using the lines, the cladding height for each processing parameter set could be calculated. Additionally, the orange curved line on the processing map marks the constant values of the wetting angle (25, 45, and 80 degree). However, it is worth noting that h, w, D, and θ illustrate the geometrical characteristics of the single clads, and not the final clad layer with overlapping tracks. The processing parameter indicating the successful formation of laser cladding may be marked by the shaded area, as shown in Fig. 12.10. In fact, this part of the map was selected based on the optimal parameters for the geometrical characteristics of the single clad samples. The obtained map can be employed as a guideline for selecting processing parameters. It seems that the map could demonstrate the difficulty of the laser cladding process for the studied alloy on the TiAl substrate. If the selected processing parameters such as S, P, and F locate in the shaded area, the single pass clad has proper geometrical characteristics for achieving the multi pass clads. As previously mentioned, a high density of the clad layer could be obtained by properly selecting the wetting angle. Therefore, to avoid porosity creation in the coating, while overlapping individual clad tracks, the used θ has to get decent values based on the processing map. For this purpose, the proper θ has to take values less than 80 degrees. On the other hand, due to the low values of θ, a heterogeneous clad (a low height and wide width) is formed. Therefore, the minimum of θ could be considered as 20 degrees. The dilution between 10 and 30% is acceptable for the optimal single pass clad. It should be mentioned that in multi pass clads, the portion of energy was absorbed through the former pass, and thus the input energy in the substrate decreases leading to a decrease of the dilution by 5–15% for the multi pass clads. Therefore, the clads form with the suitable dilution. This could be attributed to two reasons: first, the entrance of elements from the substrate into the clad decreases and second, fusion bond forms between the substrate and the clad and thus provides a high level of interfacial adhesion. In summary, the optimal area for the dilution is introduced as 10–30%. It should be noted that the final clad was formed with the aid of overlapping of some of the single pass clads. While the w becomes less than 1300 micron, the scanning time of the surface increases and the processing is found to be not economical. The optimal h for laser cladding in this study is between 300 and 600 micron because the final clad height is about 20–35% more than that of the single pass clad.

12.3.9 Assessment of the Optimal Clad

By considering the geometrical characteristics of the single-pass laser cladding coatings and the achieved results, it could be logical to select the formed clad with $P = 400$ W, $S = 3$ mm/s, and $F = 300$ mg/s (hereinafter called C-400-3-300), selected as the optimal clad, and therefore characterization studies have been performed on this sample. Figure 12.11 shows the EDS map of the selected clad and substrate.

Figure 12.12 depicts the XRD micrographs of the optimal clad at laser power = 400 W, scanning speed = 3 mm/s, and power feeding rate = 300 mg/s.

The primary powder blending has a chemical composition of Cr_3C_2–50 wt.% NiCr, but as Fig. 12.12 shows the clad structure contains different types of chrome carbides ($Cr_{23}C_6$, Cr_7C_3, and CrC_2) along with γ solid solution. One of the main possibilities for the formation of different types of chrome carbides during the laser cladding process is the high temperature of the melt and the partial dissolution of Cr_3C_2. This causes an increase of the chrome and carbon content into the melt pool as well as the formation of the other carbide phases during the nonequilibrium chilling. Pan et al. (2010) studied the microstructure and thermal physical parameters of Ni60-Cr_3C_2 composite coating by laser cladding. They found that $Cr_{23}C_6$, Cr_7C_3 phases exist in the produced clad. They found that this is attributed to the partial dissolution of the primary chrome carbide into the melt pool. Liu and Wang (2006) showed that Cr_7C_3 and TiC as well as γ solid solution are formed after applying the laser cladding of powder blending of Cr_3C_2–50 wt. % NiCr on the TiAl substrate.

Additionally, it was found that there is no Cr_3C_3 phase in the XRD patterns of the clad. Therefore, it could be concluded that carbon and chrome dissolution into the melt occurs and the Ti and Al elements also are introduced into the clad structure due to melting of the substrate. Yang et al. (2012) have studied the complete transformation of Cr_3C_2 to Cr_7C_3 after laser cladding of powder blending of NiCr-Cr_3C_2.

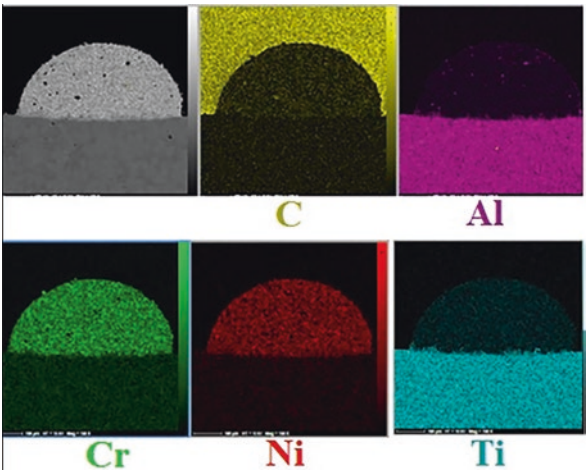

Fig. 12.11 SEM image of C-400-3-300 besides EDS elemental maps

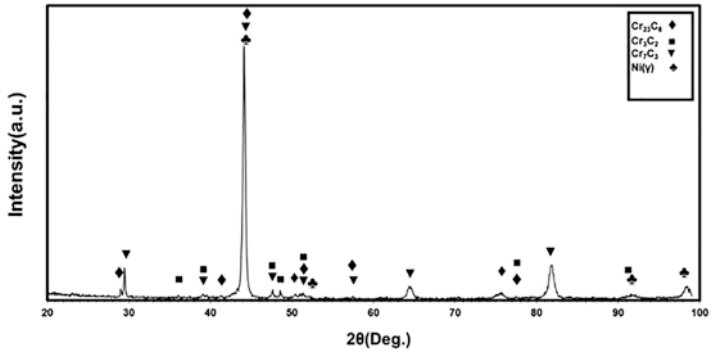

Fig. 12.12 XRD pattern of the surface of the optimal clad coating

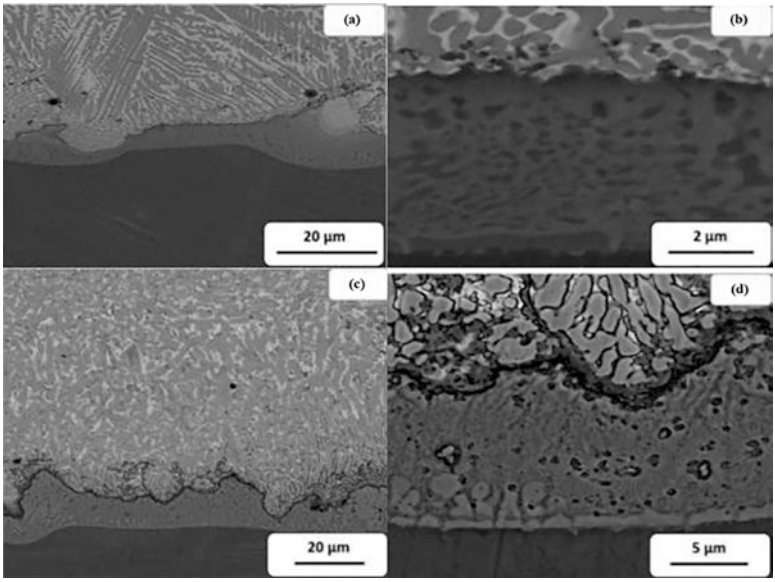

Fig. 12.13 Microstructure of the optimal clad of NiCr-Cr_3C_2 on the TiAl substrate in both engraved and nonengraved conditions

Figure 12.13 shows the microstructure of NiCr-50wt.%Cr_3C_2 coating on the TiAl substrate produced by laser cladding in engraved and nonengraved conditions. As it can be observed, there is an intermediate area between the coating and the substrate. This area is very sensitive to the engraving solution, thus it is severely corroded after engraving and consequently the identify details are missed.

Additionally, it should be noted that the metallurgical interface formed between the clad and the substrate is sound, tight, and without any defect. The presence of the metallurgical interface guarantees the proper stick during service. The existence of the interfacial region between the clad and the substrate confirms the presence of

interfacial phases. It should be stated that during the laser cladding process in addition to the powder particles feeding into the laser beam, the melt pool also is remelted leading to mixing of the melt.

In previous studies on the formation of the titanium carbide and aluminum carbide at the interface of the NiCr-Cr_3C_2 clad to the TiAl substrate (Liu and Wang 2006), the close regions to the interface are meticulously characterized by SEM. Figure 12.14 shows the microstructure of the NiCr-Cr_3C_2 clad in the regions close to the TiAl substrate. According to the color difference in backscatter electrons, they could be underlined as different phases in this region. The EDS results showed that in NiCr solid solution, different types of chrome carbides as well as titanium carbides with diameters less than 1 micron also exist in this region.

The presence of titanium carbide in this region is attributed to the substrate melt and mixing with melt caused by the melting of the powder particles of NiCr-Cr_3C_2. Figure 12.15 shows the microstructure of different regions of the NiCr-50 wt.% Cr_3C_2 clad. Since the chemical composition between the substrate and the clad shows a significant difference, epitaxial growth is not observed at the interface of the substrate and the clad. Since the direction of the heat transfer during the laser cladding process is toward the substrate, the growth direction of the columnar dendrites is opposite to the heat transfer direction. By taking a look at the microscopic images, it could be observed that by moving toward the upper regions of the clad, the microstructure becomes finer. This is attributed to both the grain growth (R) and temperature gradient (G). Theoretically, the product of G*R represents the cooling rate of the interface. In this condition, (G*R)_surface is higher than that of (G*R)_interface; therefore, the finer microstructure forms in the surface regions.

On the other hand, the average distance between the primary dendrites as well as the average distance of the secondary arms of the dendrites in the surface are less compared to the regions closer to the interface. Since, the cooling rate of the melt in the laser cladding process relative to the casting process is high, the solidification structure achieved via laser cladding is finer compared to the achieved structure

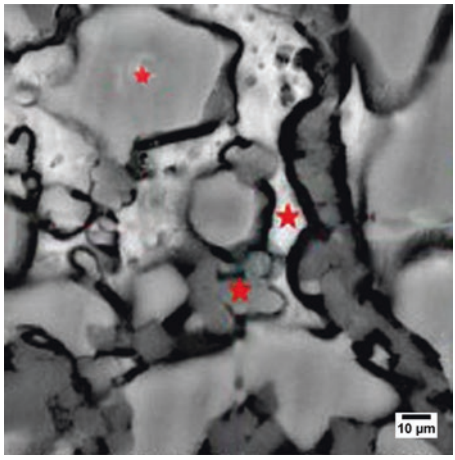

Fig. 12.14 SEM of the microstructure of the optimal clad in the close regions to the interface with the substrate

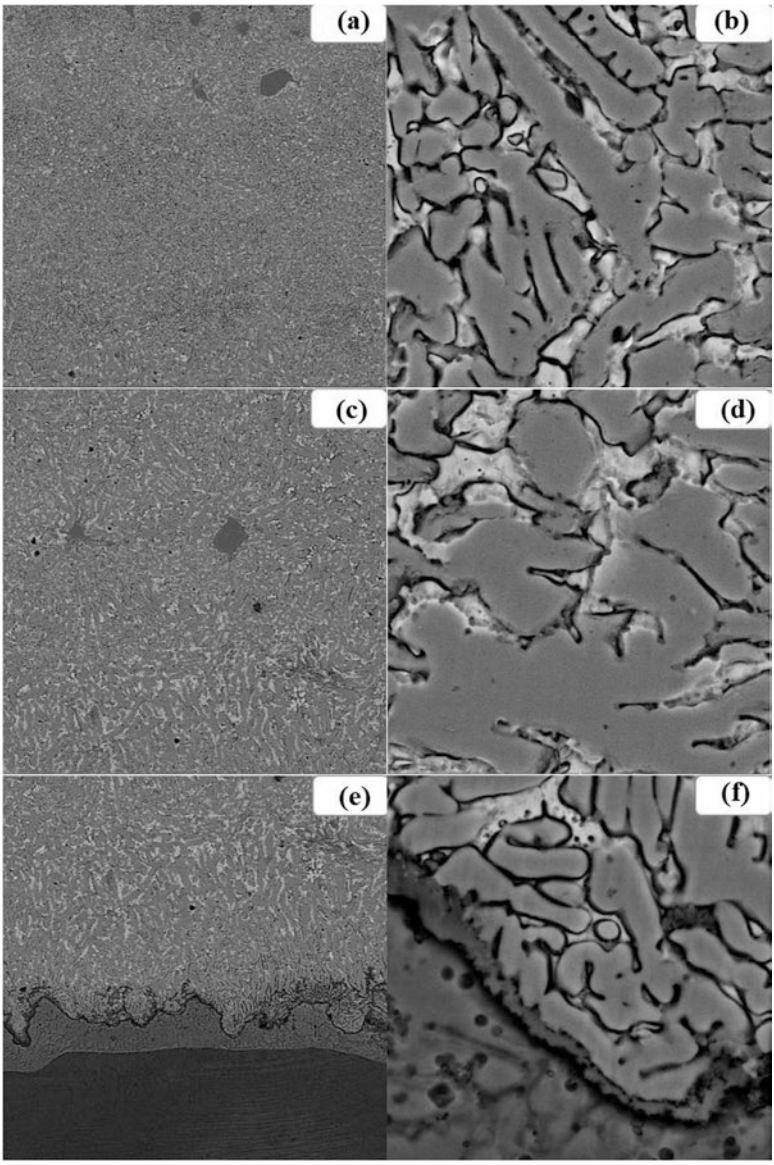

Fig. 12.15 SEM of the optimal clad (**a** and **b**) in the above region, (**c** and **d**) the intermediate region, (**e** and **f**) and the bottom region, close to the interface

with casting. On the other hand, G/R is as a decisive parameter to determine the solidification state, as with decreasing the G/R ratio, the dendrite solidification shifts toward the equiaxed solidification. Basically, by moving from the interface toward the clad, the G/R parameter value decreases. Therefore, this is why closer to the clad surface, the solidification structure tends to change to the dendrite equiaxed

structure. As shown in Fig. 12.15, the intermediate and upper regions of the clad contain coarse grains with a size of ~10 micron.

Figure 12.16 shows the high resolution of these particles besides the EDS results. The microscopic examinations revealed that the under-study phase contain 70.8 wt.% and 26.7 wt.% of chrome and carbon, respectively. However, the accurate analysis of the carbon is not possible; nevertheless, the analysis showed that the particles are probably primary chrome carbides. These carbides do not melt during the laser cladding process, and therefore remain in the structure. As previously mentioned, these particles were only observed in the upper regions of the clad.

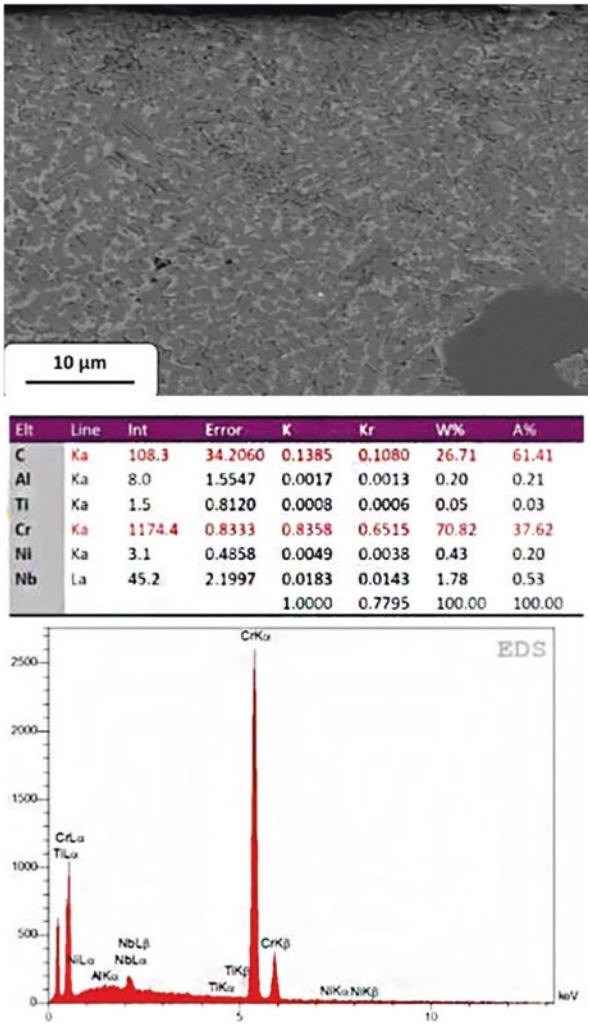

Fig. 12.16 SEM of the upper regions of the optimal clad besides EDS results

12.3.10 Microhardness of the Optimal Clad

The microhardness profiles for the optimal clad from the surface to the substrate is shown in Fig. 12.17. According to the obtained results, the average hardness of the TiAl substrate and the NiCr-Cr_3C_2 clad is equal to 320 and 820 HV. It is obvious that the presence of the different types of chrome carbides in the structure leads to a remarkable increase in the hardness of the clad compared to the substrate. In addition, the microhardness of the upper region of the clad was higher than that of the bottom region. This could be attributed to both the presence of the nonmelted particles of Cr_3C_2 close to the clad surface and to the influence of the substrate dilution on the clad in close regions to the interface.

Moreover, it should be pointed out that the microhardness obtained in this study is approximately 150 HV, which is more than that reported by Liu and Wang (2006), for the same clad of NiCr-50wt.%Cr_3C_2. The main reason for justifying such behavior could be attributed to the variety of the existing phases in the clad microstructure. On the other hand, according to the obtained XRD results, the obtained clad in this study contains different types of chrome carbides, while TiC and Cr_7C_3 phases only exist in Liu's clad. Moreover, the hardness obtained in this study is higher than that in the other studies on laser cladding of similar alloys on the γ-TiAl substrate. The main reason is the optimization of the process using three effective parameters of laser power, scanning speed, and powder feeding rate that resulted in the formation of high-quality claddings.

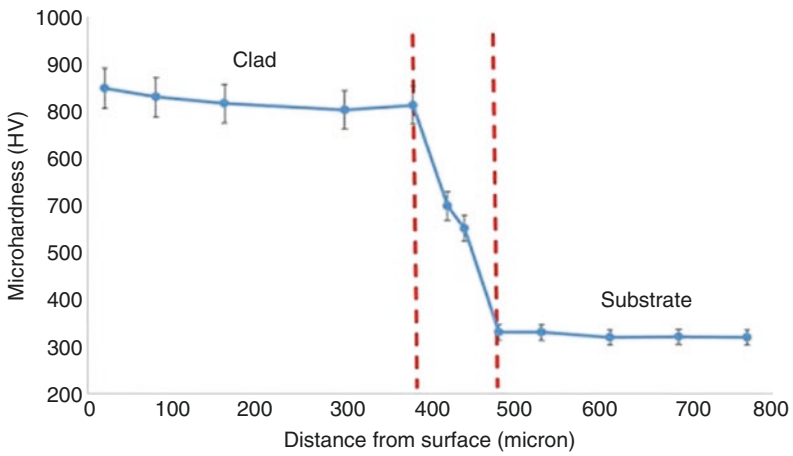

Fig. 12.17 Microhardness profile of the optimal clad from the clad to the substrate

12.4 Conclusions

NiCr-Cr_2C_3 were successfully deposited on the γ-TiAl substrate. Different processing parameters were employed in order to achieve an optimized coating in terms of strength mainly finalized for the improvement of tribological properties of the produced structure. The laser power input was optimized in order to produce sound clads. At constant laser power, increasing the powder particles' feeding rate leads to enhancement of the clad height. The decrement of the scanning speed has the same influence on the clad height. Additionally, the clad height increases as the laser power or the powder feeding rate increases. At constant power, by increasing the laser speed, the interaction time between the powder particles and laser beam decreases, and consequently the generated heat input to the center of the pool surface is decreased, resulting in a decrease in the outward shear stress on the pool surface. As a consequence, this leads to a decrease in the clad width. The clad width showed an aligned linear correlation with the increment of the laser power. On the other hand, by decreasing the scanning speed and the powder feeding rate, the clad width increases. By increasing the laser power and the scanning speed as well as by decreasing the powder feeding rate, the penetration depth increases. In fact, by increasing the laser power, the input heat increases, resulting in absorbing more energy even at a constant powder feeding rate and scanning speed. Therefore, more substrate is melted. By increasing the powder feeding rate, the penetration depth decreases. Dilution is increased by increasing the scanning speed as well decreasing the powder feeding rate.

The increasing or decreasing of the laser power had a negligible effect on the dilution. If the laser power has a significant effect on the dilution of the clad, the clads achieved with different laser powers could not have equal dilutions even if the powder feeding rate and the scanning speed are constant. The wetting angle played a remarkable role in avoiding porosity creation in the cladding, while overlapping individual clad tracks. By decreasing the powder feeding rate, the clad height and the wetting angle decrease.

The presence of different types of chrome carbides in the structure leads to a remarkable increase in the hardness of the clad compared to the substrate. In addition, the microhardness of the upper region of the clad was higher than that of the bottom region. This could be attributed to both the presence of the nonmelted particles of Cr_3C_2 close to the clad surface and to the influence of the substrate dilution on the clad in close regions to the interface.

References

Aggarwal, K., Urbanic, R. J., & Saqib, S. M. (2018). Development of predictive models for effective process parameter selection for single and overlapping laser clad bead geometry. *Rapid Prototyping Journal, 24*(1), 214–228. https://doi.org/10.1108/RPJ-04-2016-0059.

Ansari, M., Shoja Razavi, R., & Barekat, M. (2016). An empirical-statistical model for coaxial laser cladding of NiCrAlY powder on Inconel 738 superalloy. *Optics and Laser Technology, 86*, 136–144. https://doi.org/10.1016/j.optlastec.2016.06.014.

Barekat, M., Razavi, R. S., & Ghasemi, A. (2016). Nd: YAG laser cladding of Co–Cr–Mo alloy on γ-TiAl substrate. *Optics and Laser Technology, 80*, 145–152. https://doi.org/10.1016/j.optlastec.2016.01.003.

Behera, R. R., Hasan, A., Sankar, M. R., & Pandey, L. M. (2018). Laser cladding with HA and functionally graded TiO_2-HA precursors on Ti–6Al–4V alloy for enhancing bioactivity and cyto-compatibility. *Surface and Coating Technology, 352*, 420–436. https://doi.org/10.1016/j.surfcoat.2018.08.044.

Bourahima, F., Helbert, A. L., Rege, M., Ji, V., Solas, D., & Baudin, T. (2019). Laser cladding of Ni based powder on a Cu-Ni-Al glassmold: Influence of the process parameters on bonding quality and coating geometry. *Journal of Alloys and Compounds, 771*, 1018–1028. https://doi.org/10.1016/j.jallcom.2018.09.004.

Brückner, F., & Lepski, D. (2019). Laser Cladding. In J. Dowden & W. Schulz (Eds.), *The theory of laser materials processing, springer series in materials science* (Vol. 119). https://doi.org/10.1007/978-3-319-56711-2_9.

Costa, L., Felde, I., Réti, T., Kálazi, Z., Colaço, R., Vilar, R., & Verő, B. (2002). A simplified semi-empirical method to select the processing parameters for laser clad coatings. *Materials Science Forum, 414-415*, 385–394. https://doi.org/10.4028/www.scientific.net/MSF.414-415.385.

De Oliveira, U., Ocelik, V., & De Hosson, J. T. M. (2005). Analysis of coaxial laser cladding processing conditions. *Surface and Coating Technology, 197*(2–3), 127–136. https://doi.org/10.1016/j.surfcoat.2004.06.029.

Devesse, W., De Baere, D., & Guillaume, P. (2015). Modeling of laser beam and powder flow interaction in laser cladding using ray-tracing. *Journal of Laser Applications, 27*(S2), S29208. https://doi.org/10.2351/1.4906394.

Ebrahimzadeh, H., & Mousavi, S. A. A. A. (2012). Investigation on pulsed Nd: YAG laser welding of 49Ni–Fe soft magnetic alloy. *Materials and Design, 38*, 115–123. https://doi.org/10.1016/j.matdes.2012.01.037.

El Cheikh, H., Courant, B., Branchu, S., Hascoët, J.-Y., & Guillén, R. (2012). Analysis and prediction of single laser tracks geometrical characteristics in coaxial laser cladding process. *Optics and Lasers in Engineering, 50*(3), 413–422. https://doi.org/10.1016/j.optlaseng.2011.10.014.

Erfanmanesh, M., Abdollah-Pour, H., Mohammadian-Semnani, H., & Shoja-Razavi, R. (2017). An empirical-statistical model for laser cladding of WC-12Co powder on AISI 321 stainless steel. *Optics and Laser Technology, 97*, 180–186. https://doi.org/10.1016/j.optlastec.2017.06.026.

Erfanmanesh, M., Shoja-Razavi, R., Abdollah-Pour, H., & Mohammadian-Semnani, H. (2018). Influence of using electroless Ni-P coated WC-Co powder on laser cladding of stainless steel. *Surface and Coating Technology, 348*, 41–54. https://doi.org/10.1016/j.surfcoat.2018.05.016.

Fayaz, G., & Kazemzadeh, S. (2018). Towards additive manufacturing of compressor impellers: 3D modeling of multilayer laser solid freeform fabrication of nickel alloy 625 powder mixed with nano-CeO2on AISI 4140. *Additive Manufacturing, 20*, 182–188. https://doi.org/10.1016/j.addma.2018.02.001.

Fu, Y., Loredo, A., Martin, B., & Vannes, A. B. (2002). A theoretical model for laser and powder particles interaction during laser cladding. *Journal of Materials Processing Technology, 128*(1–3), 106–112. https://doi.org/10.1016/S0924-0136(02)00433-8.

Garmendia, I., Pujana, J., Lamikiz, A., Flores, J., & Madarieta, M. (2019). Development of an intra-layer adaptive toolpath generation control procedure in the laser metal wire deposition process. *Metals, 12*(3), 352. https://doi.org/10.3390/ma12030352.

Jiang, Y., Cheng, Y., Zhang, X., Yang, J., Yiang, X., & Cheng, Z. (2020). Simulation and experimental investigations on the effect of Marangoni convection on thermal field during laser cladding process. *Optik, 203*, 164044. https://doi.org/10.1016/j.ijleo.2019.164044.

Jouvard, J.-M., Grevey, D. F., Lemoine, F., & Vannes, A. B. (1997). Continuous wave Nd: YAG laser cladding modeling: A physical study of track creation during low power processing. *Journal of Laser Applications, 9*(1), 43–50. https://doi.org/10.2351/1.4745444.

Karmakar, R., & Ghosh, S. K. (2020). Effect of composition and process parameter on mechanical properties of composite coating by laser cladding: An overview. In G. Narasimham, A. Babu, S. Reddy, & R. Dhanasekaran (Eds.), *Recent trends in mechanical engineering. Lecture notes in mechanical engineering*. Singapore: Springer. https://doi.org/10.1007/978-981-15-1124-0_33.

Kou, S. (2003). *Welding metallurgy* (pp. 431–446). Hoboken: Wiley-Interscience.

Lei, K., Qin, X., Liu, H., & Ni, M. (2018). Analysis and modeling of melt pool morphology for high power diode laser cladding with a rectangle beam spot. *Optics and Lasers in Engineering, 110*, 89–99. https://doi.org/10.1016/j.optlaseng.2018.05.022.

Li, N., Huang, S., Zhang, G., Qin, R., Liu, W., Xiong, H., Shi, G., & Blackburn, J. (2019). Progress in additive manufacturing on new materials: A review. *Journal of Materials Science and Technology, 35*(2), 242–269. https://doi.org/10.1016/j.jmst.2018.09.002.

Liu, X. B., & Wang, H. M. (2006). Modification of tribology and high-temperature behavior of Ti–48Al–2Cr–2Nb intermetallic alloy by laser cladding. *Applied Surface Science, 252*, 5735–5744. https://doi.org/10.1016/j.apsusc.2005.07.064.

Liu, S., Zhang, Y., & Kovacevic, R. (2015). Numerical simulation and experimental study of powder flow distribution in high power direct diode laser cladding process. *Lasers Manuf Mater Proc, 2*(4), 199–218. https://doi.org/10.1007/s40516-015-0015-2.

Liu, J., Hu, H., Chen, C., Weng, F., & Dai, J. (2017). Research and development status of laser cladding on magnesium alloys: A review. *Optics and Lasers in Engineering, 93*, 195.210. https://doi.org/10.1016/j.optlaseng.2017.02.007.

Ma, M., Xiong, W., Lian, Y., Han, D., Zhao, C., & Zhang, J. (2020). Modeling and optimization for laser cladding via multi-objective quantum-behaved particle swarm optimization algorithm. *Surface and Coating Technology, 381*, 125129. https://doi.org/10.1016/j.surfcoat.2019.125129.

Man, H. C., Leong, K. H., & Ho, K. L. (2008). Process monitoring of powder pre-paste laser surface alloying. *Optics and Lasers in Engineering, 46*(10), 739–745. https://doi.org/10.1016/j.optlaseng.2008.05.006.

Mandal, V., Sharma, S., & Ramkumar, J. (2020). Numerical simulation of heat transfer and fluid flow in co-axial laser cladding of Ti6Al4V alloys. In M. Shunmugam & M. Kanthababu (Eds.), *Advances in simulation, product design and development* (Lecture notes on multidisciplinary industrial engineering). Singapore: Springer. https://doi.org/10.1007/978-981-32-9487-5_19.

Nabhani, M., Razavi, R. S., & Barekat, M. (2018). An empirical-statistical model for laser cladding of Ti-6Al-4V powder on Ti-6Al-4V substrate. *Optics and Laser Technology, 100*, 265–271. https://doi.org/10.1016/j.optlastec.2017.10.015.

Ocelík, V., de Oliveira, U., de Boer, M., & de Hosson, J. T. M. (2007). Thick Co-based coating on cast iron by side laser cladding: Analysis of processing conditions and coating properties. *Surface and Coating Technology, 201*(12), 5875–5883. https://doi.org/10.1016/j.surfcoat.2006.10.044.

Pan, C., Wang, H., & Wang, H. (2010). Microstructure and thermal physical parameters of Ni60-Cr3C2 composite coating by laser cladding. *Journal of Wuhan University of Technology-Materials Science Edit, 25*, 991–995. https://doi.org/10.1007/s11595-010-0136-6.

Picasso, M., Marsden, C. F., Wagniere, J.-D., Frenk, A., & Rappaz, M. (1994). Simple but realistic model for laser cladding. *Metallurgical Transactions, B, 25*(2), 281–291. https://doi.org/10.1007/BF02665211.

Pinkerton, A. (2010). Laser direct metal deposition: Theory and applications in manufacturing and maintenance. In *Advances in laser materials processing* (pp. 461–491). Elsevier. https://doi.org/10.1533/9781845699819.6.461.

Pinkerton, A. J. (2015). Advances in the modeling of laser direct metal deposition. *Journal of Laser Applications, 27*, S15001. https://doi.org/10.2351/1.4815992.

Reddy, L., Preston, S. P., Shipway, P. H., Davis, C., & Hussain, T. (2018). Process parameter optimisation of laser clad iron based alloy: Predictive models of deposition efficiency, porosity and dilution. *Surface and Coating Technology, 349*, 198–207. https://doi.org/10.1016/j.surfcoat.2018.05.054.

Tabernero, I., Lamikiz, A., Martínez, S., Ukar, E., & López de Lacalle, L. N. (2012). Modelling of energy attenuation due to powder flow-laser beam interaction during laser cladding process. *Journal of Materials Processing Technology, 212*(2), 516–522. https://doi.org/10.1016/j.jmatprotec.2011.10.019.

Toyserkani, E., Khajepour, A., & Corbin, S. (2003). Three-dimensional finite element modeling of laser cladding by powder injection: Effects of powder feedrate and travel speed on the process. *Journal of Laser Applications, 15*(3), 153–160. https://doi.org/10.2351/1.1585087.

Wirth, F., & Wegener, K. (2018). A physical modeling and predictive simulation of the laser cladding process. *Additive Manufacturing, 22*, 307–319. https://doi.org/10.1016/j.addma.2018.05.017.

Yang, M.-S., Liu, X.-B., Fan, J.-W., He, X.-M., Shi, S.-H., Fu, G.-Y., Wang, M.-D., & Chen, S. F. (2012). Microstructure and wear behaviors of laser clad NiCr/Cr3C2–WS2 high temperature self-lubricating wear-resistant composite coating. *Applied Surface Science, 258*(8), 3757–3762. https://doi.org/10.1016/j.apsusc.2011.12.021.

Zhang, Y., Xu, P., Liu, C., Ren, J., & Gong, H. (2019). The influence of carbides on the microstructure, grain growth, and oxidation resistance of nanostructured carbides-strengthened cobalt-based multi-track laser-cladding layers. *Applied Surface Science, 469*, 495–504. https://doi.org/10.1016/j.apsusc.2018.11.084.

Chapter 13
Laser Cladding of MCrAlY Alloys

Juan Carlos Pereira, Jenny Zambrano, Armando Yañez, and Vicente Amigó

13.1 Introduction

Aircraft and power-generation turbines are made from metallic components protected by TBCs. A TBC system is usually formed by a top ceramic layer (Padture et al. 2002; Cao et al. 2004) deposited onto a bond layer (Pint et al. 2010; Carpio et al. 2016) over the substrate. The materials widely used for bond coatings are composed of MCrAlY superalloys (with M = Ni, Co, Fe, or combinations of these). NiCoCrAlY and CoNiCrAlY are the most frequently used superalloys as bond coats (Schulz et al. 2003) given their good adhesion, optimal elastic modulus, high strength, and high-temperature oxidation resistance (Pomeroy 2005). These MCrAlY alloys usually contain large amounts of Cr with small additions of Y, which hardens the solid solution. The solid solution effect of these elements blocks dislocation movements through grain boundaries by enhancing the common creep resistance of MCrAlY alloys (Tancret et al. 2003). Otherwise, an Al content between 8 and 15 wt.% slows down crystal growth and results in a more thermally stable, adherent, and continuous aluminum-rich oxide layer (α-Al_2O_3) (Nijdam et al. 2006;

J. C. Pereira (✉)
LORTEK Technological Centre, Basque Research and Technology Alliance (BRTA), Arranomendia Kalea, Ordizia, Gipuzkoa, Spain
e-mail: jcpereira@lortek.es

J. Zambrano · V. Amigó
Institute of Materials Technology (ITM), Universitat Politècnica de València, Camino de Vera, Valencia, Spain
e-mail: jenzamca@upv.es; vamigo@upv.es

A. Yañez
Laboratorio de Aplicaciones Industriales del Láser. Centro de Investigaciones Tecnológicas, Universidade da Coruña, Ferrol, Spain
e-mail: armando.yanez@udc.es

P. Cavaliere (ed.), *Laser Cladding of Metals*,
https://doi.org/10.1007/978-3-030-53195-9_13

Marginean and Utu 2012). It also increases the amount of the β-(Ni,Co)Al phase, which is harder than the gamma phase in γ/β-MCrAlY coatings (Kim et al. 2009).

Nowadays, the LC process is being paid more attention as an alternative technique to manufacture TBC coatings. Laser cladding can be applied as a rapid manufacturing technique that consists in the direct deposition of metallic alloys with high melting points, such as MCrAlY alloys. Specifically, coaxial laser cladding uses a special nozzle head to create a coniform annular gap, which encircles the focused laser beam with powder to melt the powder on the surface to be coated (Fig. 13.1). The coaxial LC process has been tested to produce large dense coatings by overlapping single laser tracks (Vilar 1999; Bezençon et al. 2003; Vollertsen et al. 2005; Partes et al. 2008; Varlese et al. 2013). Even complex 3D pieces can be coated by LC using powder or solid wire as a material feedstock. In the same way, LMD processes use this principle to deposit the material layer by layer in an innovative additive manufacturing (AM) process (Segerstark et al. 2017; Singh et al. 2017; Mahamood 2018).

The continuous coatings obtained by laser-based techniques are free of pores and cracks when the process parameters are well controlled. These properties improve the resultant mechanical resistance and interfacial strength with the substrate. However, due to the brittle behavior of MCrAlY alloys at low temperatures (Texier et al. 2017), the experimental conditions must be well studied and controlled to avoid residual stresses and material defects (pores, cracks, lack of fusion, and bonding defects, among others) (Vollertsen et al. 2005; Majumdar and Manna 2011). Recent studies (Texier et al. 2016) have reported that the diffusion zone achieved between the coating and substrate is critical for optimizing the resultant mechanical properties, and it is more desirable to reduce the chemical dilution of the coating to the substrate. The elastic modulus of the bond coat is also a critical mechanical parameter as TBC systems are composed of several layers. The shear stresses expected between layers must be as low as possible to avoid delamination failures (Schulz et al. 2003; Pomeroy 2005).

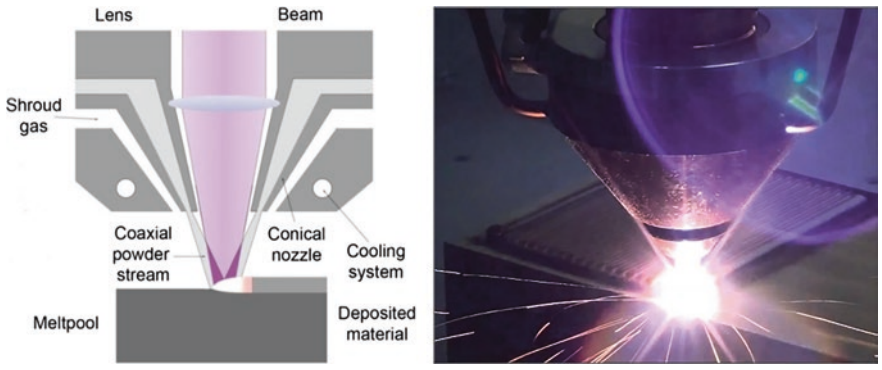

Fig. 13.1 Coaxial laser cladding. Process scheme (left) and overlay coating (right)

At high temperature, metallic materials will inevitably oxidize in different ways and under distinct conditions, while diverse interactions between chemical elements in the coating, the substrate material, and the atmosphere can be expected, including decomposition, interdiffusion, volatilization, diffusion, and oxide scale growth (Young 2008). In early stages, a fast oxidation reaction is present, and then the transient oxide products can include some metastable aluminum-rich oxides transformed during exposure to high temperature (Zhu et al. 2016). In MCrAlY bond coats, the outermost surface (opposite to the substrate) is oxidized to form a thermally grown oxide (TGO) that becomes the surface to which the subsequent layers (commonly ceramics) of TBCs adhere. The oxidation behavior of the coating and its useful life can be strongly influenced by both coating quality parameters, such as porosity level and the distribution of MCrAlY constituents during the metal deposition process (Wright and Evans 1999). In fact, the oxide scales in MCrAlY alloys, particularly NiCoCrAlY, are not pure α-Al_2O_3. So they can also contain Y-rich oxide inclusions and other common oxides like Cr_2O_3, NiO, CoO, or $(Ni,Co)(Cr,Al)_2O_4$ spinel oxides, as reported by different authors (Nijdam et al. 2006; Nijdam and Sloof 2008; Zhu et al. 2013; Ansari et al. 2017). These last spinel oxides can form and crack to eventually cause spallation of the oxide scale (Chen et al. 2005).

In this study, two MCrAlY coatings were produced by the coaxial LC process. One coat was made with a higher concentration of Ni and Al, called NiCoCrAlY. The other was prepared with a higher concentration of Co, namely, CoNiCrAlY, for comparison purposes. After finding the best experimental conditions to form dense continuous coatings using pre-alloyed powder as a feedstock material, an in-depth microstructure and mechanical characterization was performed. In order to complete the study, the elastic modulus and hardness of both the individual phases and the whole coating were evaluated by nanoindentation. To analyze the strength and fracture mechanisms of the interface between layers, a three-point bending test was used. Besides these techniques, other properties were investigated by measuring microhardness and microstructural analyses by X-ray diffraction (XRD), field emission scanning electron microscopy (FESEM), and energy dispersive spectroscopy (EDS) microanalysis. Finally, in order to evaluate high-temperature behavior, laser cladding coatings were investigated with the isothermal oxidation test in static air at 1100 °C for up to 200 h.

13.2 Materials and Laser Cladding Parameters for the MCrAlY Alloys

The feedstock materials herein used were two commercial MCrAlY pre-alloyed powders supplied by Oerlikon Metco. An Ni-rich powder called NiCoCrAlY (Amdry 365-2) was composed mainly of (wt.%) 47.1% Ni, 23% Co, 17% Cr, 12.5% Al, and 0.4% Y. The mean particle size diameter was given by the supplier as 55 μm. A Co-rich powder called CoNiCrAlY (Amdry 995C), composed of 38% Co with

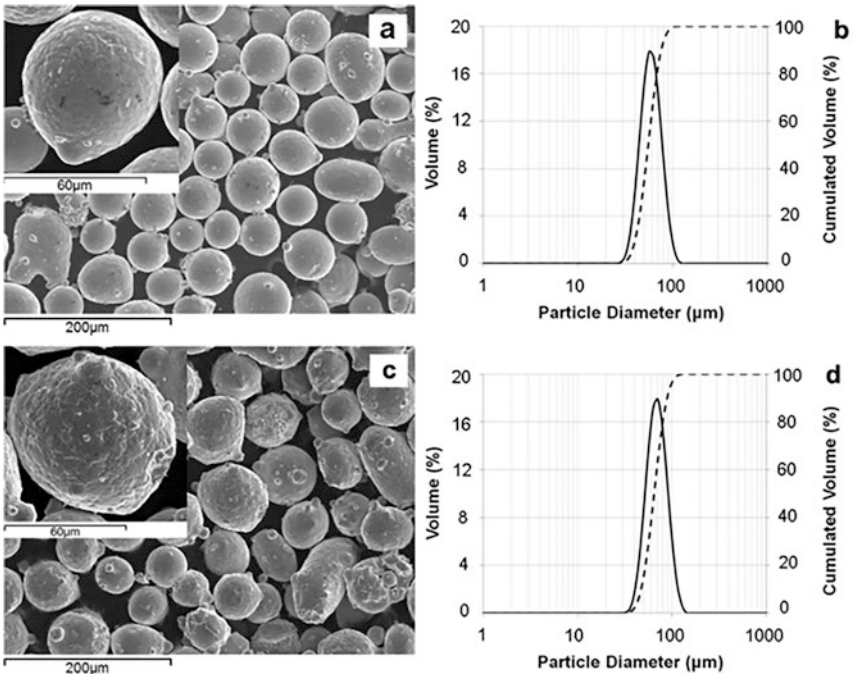

Fig. 13.2 Powder feedstock characterization. Morphological detail in SEM (20 kV SEM) of (**a**) NiCoCrAlY powder and (**c**) CoNiCrAlY powder and the particle size distribution of (**b**) the NiCoCrAlY powder and (**d**) the CoNiCrAlY powder

32% Ni, 21% Cr, 8% Al, and 0.45% Y, was used to produce the second coating, whose mean particle size diameter was 65 µm. The Gaussian particle size distribution can be seen in Fig. 13.2c,d. The morphology and size of the powder are very important for coaxial laser cladding processing because the flowability of the powder influences the coating's quality. Two phases can be distinguished in each powder's feedstock according to the XRD analysis (Fig. 13.13), which consist of γ-Ni(Cr)/Co(Ni,Cr) and β-NiAl/(Co,Ni)Al depending on the base element.

The substrate was a cold-rolled austenitic stainless steel sheet (AISI 304) with a 10-mm thickness. To study the deposition parameters in single tracks, a factorial combination of the variables to be studied (three velocities, three laser powers, and two flow rates) was proposed, which resulted in 18 tracks to be analyzed for each MCrAlY alloy. The values are summarized in Table 13.1.

An Nd:YAG solid-state laser (Rofin-Sinar DY 022) in the continuous mode and $\lambda = 1064$ nm was used. The diameter of the beam spot onto the substrate surface was 4 mm. The XYZ movement was achieved with a robotic arm (ABB IRB 2400 unit) with 6 degrees of freedom. The powder was gas assisted using a coaxial annular nozzle (Precitec YC50) and a Sulzer Metco Twin 10-C powder feeder. Helium was used as a shielding and powder carrier gas at a flow rate of 20 l/min. The other constant parameters for the LC process are shown in Table 13.2.

Table 13.1 Value of the variables for the DoE

Variable	Level 1	Level 2	Level 3
Velocity (mm/s), V	5	10	15
Laser power (W), P	1400	1700	2200
Powder feed (mg/mm), F	10	25	–

Table 13.2 Constant parameters of the laser processing to be used in this study

Parameter	Fixed value
Beam parameter product (BPP)	13 mm.Mrad
Fiber diameter	300 µm
Nozzle standoff	12 mm
Collimator lens length	200 mm
Focal lens length	200 mm
Coaxial gas	Helium @ 20 l/min
Auxiliary gas	Argon @ 15 l/min

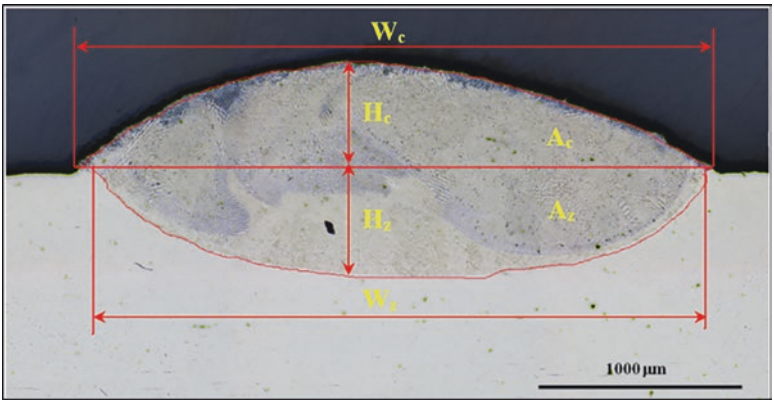

Fig. 13.3 Geometric variables measured in a single track cross section

After initially evaluating by means of a visual inspection and nondestructive testing (penetrating liquids), the quality of tracks was guaranteed. Then, the geometry of the cross section was evaluated by optical microscopy with the measurement of heights, widths, and areas. These variables to be measured are shown in Fig. 13.3 and are as follows:

H_c: Track height (µm)
W_c: Track width (µm)
A_c: Track area (µm^2)
Hz: Dilution height (µm)
W_z: Dilution width (µm)
A_z: Dilution area (µm^2)

From measuring these variables, it was possible to calculate derived parameters, such as the percentage of dilution of the clad material, $\%_{\mathrm{DIL}}$ (Eq. 13.1), the geometric aspect ratio of the track, A_r (Eq. 13.2), and the volume of deposited material, Vol (Eq. 13.3). This allowed us to take into account technical and quality criteria to select the combination of suitable LC process parameters and to then obtain satisfactory extended coatings by track overlapping. Another evaluation of the cross section of the tracks was made by optical microscopy to study the level of porosity, cracks, and other defects that could be present:

$$\%_{\mathrm{DIL}} = \frac{A_z}{A_c + A_z} \tag{13.1}$$

$$A_r = \frac{W_c}{H_c} \tag{13.2}$$

$$\mathrm{Vol}_d = A_c.V \tag{13.3}$$

Laser clads had good metallurgical bonding, as seen on the process maps for both MCrAlY alloys (Figs. 13.4 and 13.5). Here most differences in the solidification fronts are seen as the molten material strongly agitated in the melt pool driven by the Marangoni forces that resulted from variation in surface tension with temperature (Steen and Mazumder 2010), which can cause metallurgical problems due to

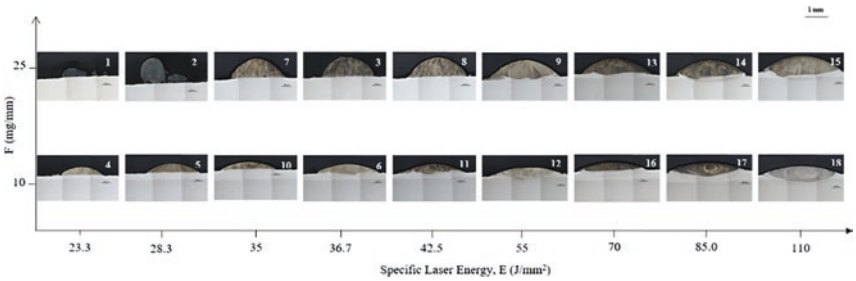

Fig. 13.4 Process map of the NiCoCrAlY laser tracks on the AISI 304 substrate

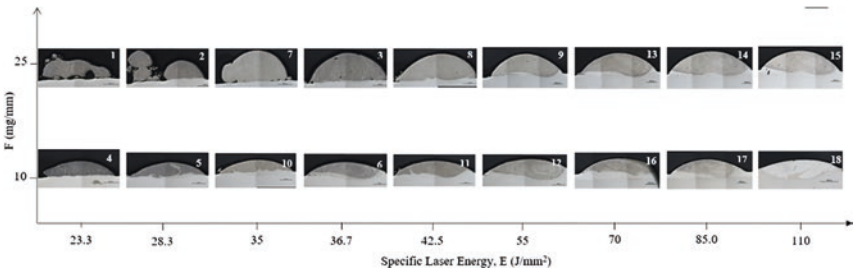

Fig. 13.5 Process map of the CoNiCrAlY laser tracks on the AISI 304 substrate

the material moving to the upper bead part from the lower region. This phenomenon also occurs in high-energy welding processes. As the energy contributed by the laser increased, the dilution of the coating material also increased; moreover, as the amount of contributed powder increased, track height also increased.

A discontinuous coating can be produced due to the lack of fusion in the overlap area in laser tracks, which is why an aspect ratio higher than or equal to 5 is recommended to obtain an adequate fusion of the clad material and to avoid porosities from appearing (Steen and Mazumder 2010). However, a high aspect ratio (above 10) can generate a very flat coating with low clad material on each track/layer, which would not be suitable for obtaining an extensive overlay coating. In this work, an aspect ratio of 8 was considered the maximum.

Several authors have agreed that an aspect ratio over 5 can be a very demanding criterion and one which entails that the dilution and thermal involvement of the substrate also increase in laser processing. So some authors have recently indicated that an aspect ratio above 2.5 could be considered satisfactory (Abioye et al. 2013; Telasang et al. 2014). Considering only the geometry of the cross section, a range of aspect ratios between 2.5 and 8 ($2.5 \leq A_r \leq 8$) can be established as the selection criterion to obtain suitable coatings by overlapping tracks.

When analyzing the values herein obtained, for both the used MCrAlY alloys, a combination of high powder flow indifferently to the employed laser energy allowed the tracks to be obtained that met the established range as a criterion for the aspect ratio (Fig. 13.6). Therefore, the low powder flow values were ruled out because they generated an excessively flat and very wide track that would not allow extensive coatings to be obtained with the suitable thickness. In particular, when F values were 25 mg/mm for the NiCoCrAlY and CoNiCrAlY superalloys, it was possible to obtain tracks with $2.5 < A_r < 5.0$ and laser energies between 35 and 100 J/mm^2.

Minimum dilution is necessary to ensure an adequate metallurgical bond between the coating and the substrate, and excessive dilution is undesirable given the need to preserve the coating's chemical composition, microstructure, and mechanical properties (Hemmati et al. 2012), in addition to reducing the heat-affected zone (HAZ) in the substrate material. For this purpose, the tracks with the lowest dilution percentage were selected.

In all the evaluated single tracks, there was a metallurgical bond with the substrate because the process parameter levels were adjusted in the initial tests to ensure that no tracks were detached, which happens at very low power or at a high scanning speed of the laser beam. As the energy contributed by the laser beam increased, dilution increased as the amount of heat added to both the powder and substrate was increased. Moreover, when the amount of powder is smaller, dilution increased as the melt pool and larger amount of energy were absorbed by the substrate material by heating and melting part of it, apart from the fact that the more the powder fed, the stronger the effect of laser beam shielding. The 4-mm diameter of the focused laser beam seemed adequate to obtain a sufficient track width to subsequently obtain satisfactory overlapping coatings.

Figure 13.7 illustrates the evolution of the dilution calculated for the different materials according to laser energy, the different combinations between the aspect

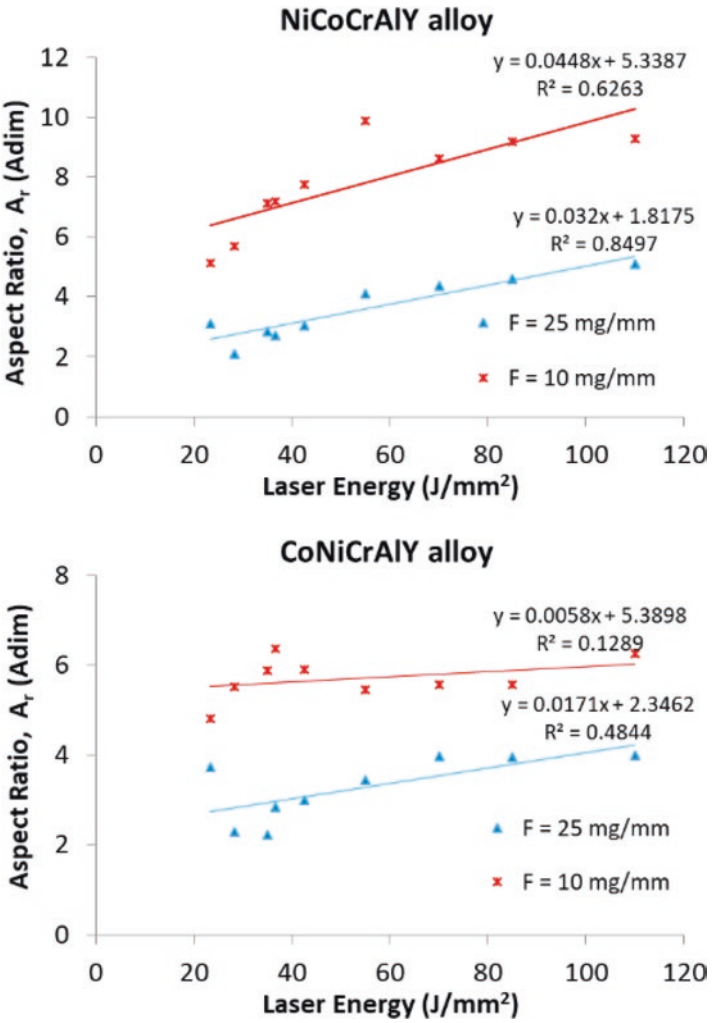

Fig. 13.6 Evolution of the aspect ratio with laser energy in laser single tracks

ratio and dilution, and the dilution zone less than 20%, highlighted with a circle. For both powders (NiCoCrAlY and CoNiCrAlY), minimum dilution was achieved (but with adequate metallurgical bonding and a low porosity level) at the highest powder flow rate and the laser energies provided below 45 J/mm^2. This would definitely rule out a low level for the powder flow rate (10 mg/mm) as it generated a very high aspect ratio (basically due to the low height of tracks) and excessive clad material dilution.

Finally, the porosity level and cracks present in the cross section of the single tracks were evaluated by an image analysis of the optical microscope micrographs shown in the process maps of Figs. 13.4 and 13.5, where the porosity level was low

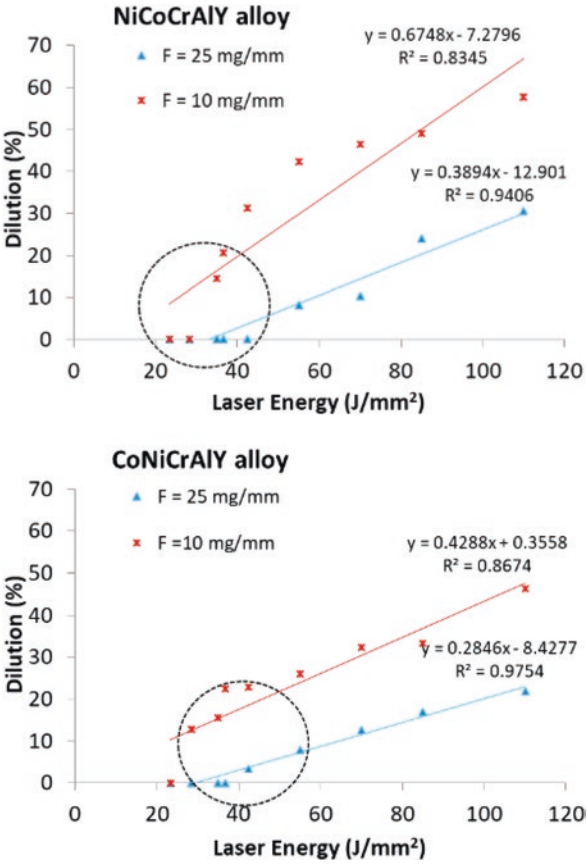

Fig. 13.7 Evolution of dilution with laser energy in laser single tracks for the MCrAlY alloys

(less than 3%), and there were no cracks in the coating material. However, in some tracks with a lower dilution percentage and a lower aspect ratio (and a high powder feed), small pores were found in the area near the interface of the clad material with the substrate, which was especially evidenced in the tracks obtained with less laser energy density, and mainly two pore types: those due to trapped gas (spherical form) and other irregular ones in the interdendritic spaces of the clad material, which could be of the shrinkage porosity type. These minor defects were hardly avoidable during the laser cladding process, first, because a high protection flow is needed to prevent the alloy's oxidation during the deposition of tracks and, second, because they form part of the nature of the MCrAlY alloys, possibly due to the aluminum in them and also to the rapid melting of the powder. Both defects were proportional to the cooling rate and have also been observed in previous works on MCrAlY coatings obtained with laser cladding (Iwamoto et al. 1998; Bezençon et al. 2003; Partes et al. 2008; Vilar et al. 2009; Vilar and Santos 2011).

The combination of processing parameters that would allow single tracks with an adequate aspect ratio (close to 3) and minimum dilution was obtained with a high

Table 13.3 Summary of the selected coaxial laser process parameters for the MCrAlY alloys

Variable	Value
Velocity (mm/s), V	15
Laser power (W), P	2200
Powder feed (mg/mm), F	25
Specific laser energy (J/mm^2), E	36.67
Geometric aspect ratio, A_r	2.75–4.71
Dilution (%), $\%_{DIL}$	0–11.92

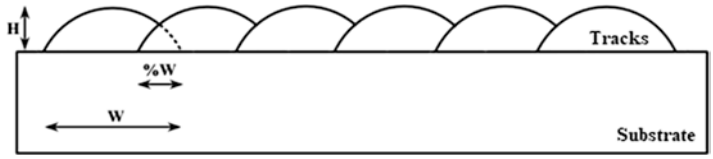

Fig. 13.8 Cross section of a laser coating obtained by track overlapping

powder feed (25 mg/mm) and laser energy densities under 45 J/mm^2 and also by working the available equipment at the highest laser power (2.2 kW) and the fastest scanning speed (15 mm/s) to increase the process' efficiency and to minimize the cooling speed. Then, the specific laser energy selected as being suitable for processing the MCrAlY superalloys would be 36.67 J/mm^2. By verifying the single tracks obtained with this combination, they had a low porosity level and showed no cracks or defects, adequate metallurgical bonding, and minimum dilution. Therefore, these would be the appropriate laser processing parameters for MCrAlY superalloys and will be used to obtain surface coatings by overlapping. The summary of the selected process parameters for the MCrAlY alloys and the aspect ratio and dilution ranges is shown in Table 13.3.

From the laser processing parameters selected as being suitable in the previous phase (Table 13.3), surface coatings were obtained by track overlapping (superposition) on a single layer. The track overlapping technique allows a coating on complex surfaces to be achieved. In Fig. 13.8, the cross section of the typical arrangement to be used to obtain a coating is shown by overlapping a percentage of track width ($\%_W$) on a single layer and on a flat surface. This study was carried out on an austenitic stainless steel sheet (10-mm thick), which was cut and cleaned by mechanical and chemical methods to ensure a clean adequate surface to clad the material.

To determine an adequate overlapping percentage, several aspects were taken into account. The first was to determine the covering height for different overlap percentages, which was obtained with geometric calculations, whereas overlapping increased, height also increased, as did the difference between the height and valley of each track making up the coating as the undulations and surface finish improved (Zhang et al. 2007; Ocelík et al. 2014). We also considered our previous experience with other alloys, which indicated a typical overlapping range between 20% and 50%. This range is similar to that in the study which reported a Ni-based superalloy (Cao et al. 2013). The literature review revealed that several authors had found a

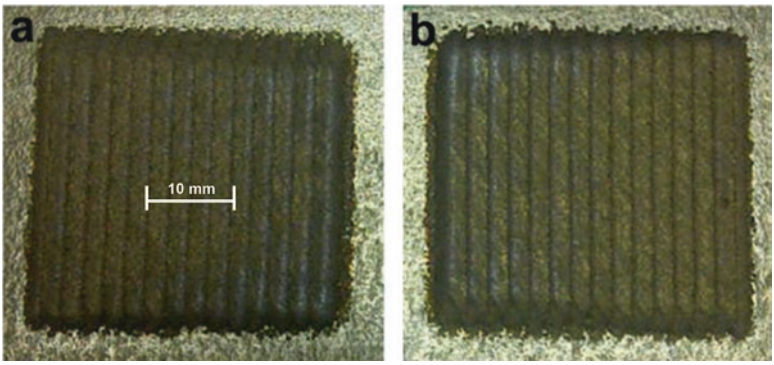

Fig. 13.9 Outeral appearance of laser coatings (**a**) NiCoCrAlY and (**b**) CoNiCrAlY

mathematical relation for appropriate overlapping based on the width and height of the single tracks obtained from a certain combination of laser processing parameters (Zhang et al. 2007; Ocelík et al. 2014). Other authors have indicated that overlapping over 32% of track width is adequate (Zhang et al. 2007) but must always be less than 70% (Li and Ma 1997).

In this work, a 40% overlapping percentage was selected as it guarantees obtaining a minimum coating thickness of around 750 μm and also minimizes the effect of undulations and lack of fusion on the coating surface. Laser cladding was carried out to obtain extensive overlay coatings (30 x 30 mm^2) on one layer. The appearance of coatings' outer surfaces is shown in Fig. 13.9.

13.3 Microstructure of the MCrAlY Laser Clad Alloys

The initial coating thickness for the NiCoCrAlY alloy was 832 ± 45 microns (Fig. 13.10a). This provided a dense coating with a homogeneous structure, and minimum dilution with the substrate was observed. The CoNiCrAlY alloy coating thickness was 715 ± 32 microns (Fig. 13.10c), with a dendritic columnar structure and small rounded pores.

The coatings' microstructures were composed of two principal phases: γ-matrix phase and β-phase. The NiCoCrAlY coating had a cellular dendritic structure (Fig. 13.11). The EDS microanalysis revealed a dendritic γ-Ni matrix phase with Cr and Co elements in solid solution and an interdendritic β-NiAl phase (dark) rich in Al with Co in solid solution. The Ni-Y-rich zones were present on some γ/β-grain boundaries.

On the CoNiCrAlY coating, a columnar dendritic structure with a planar solidification front was observed (Fig. 13.12). In this case, the interdendritic phase (dark zone) was shorter than in the nickel-based coating due to the lower Al content in this alloy. The EDS analysis also suggested hypoeutectic solidification with the γ-Co(Ni,Cr) and β-(Co,Ni)Al interdendritic phases. The γ/β-laser cladding coatings'

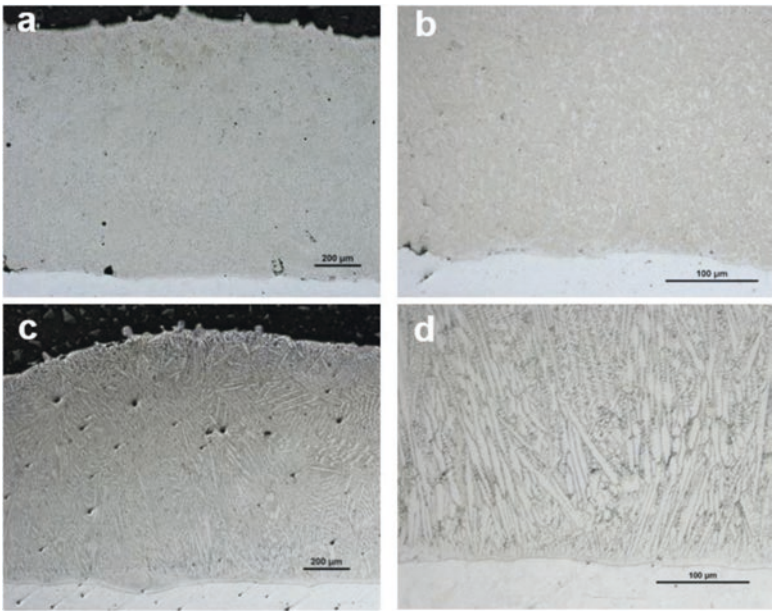

Fig. 13.10 Optical microscopy of the laser MCrAlY coatings at 50X (left) and 200X (right): (**a**) and (**b**) NiCoCrAlY, (**c**) and (**d**) CoNiCrAlY

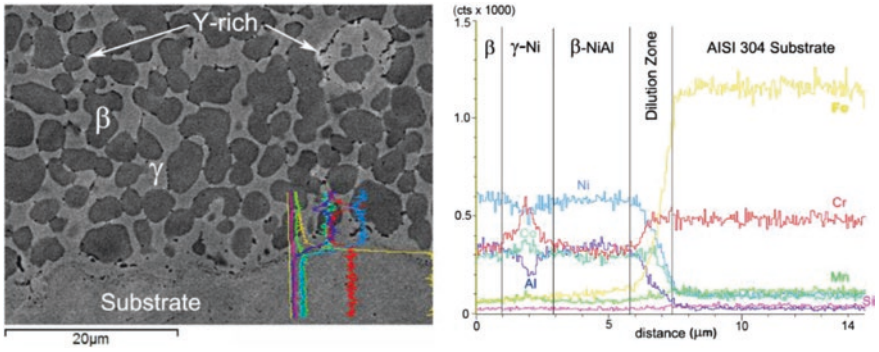

Fig. 13.11 SEM micrograph (2500X, 20 kV BSE mode) of the NiCoCrAlY laser coating, dilution, and substrate zones; line scan of the chemical composition at the interface on the right

microstructures were confirmed by the XRD analysis (Fig. 13.13). The gamma phase crystal was cubic FCC (Fm3m, space group number 225), and the beta phase was cubic BCC (Pm-3 m, space group number 221) (Dey 2003).

The primary solidification phase consisted of γ-dendrites, while the β-phase was formed in the interdendritic regions by the residual eutectic reaction at the end of solidification and solid-state precipitation. Nucleation was avoided, and the oriented cellular γ-dendrites were observed on the laser cladding coatings in the same

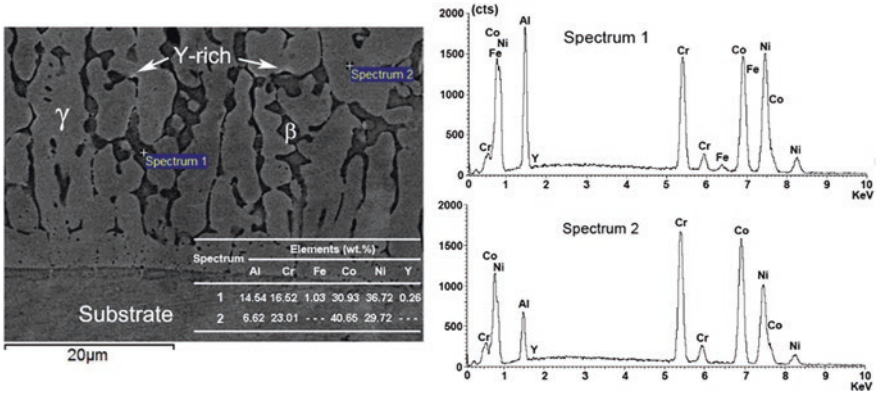

Fig. 13.12 SEM micrograph (2500X, 20 kV BSE mode) of the CoNiCrAlY laser coating area close to the interface with the substrate; chemical composition spectra with the quantification of the elements present in the two main phases on the right

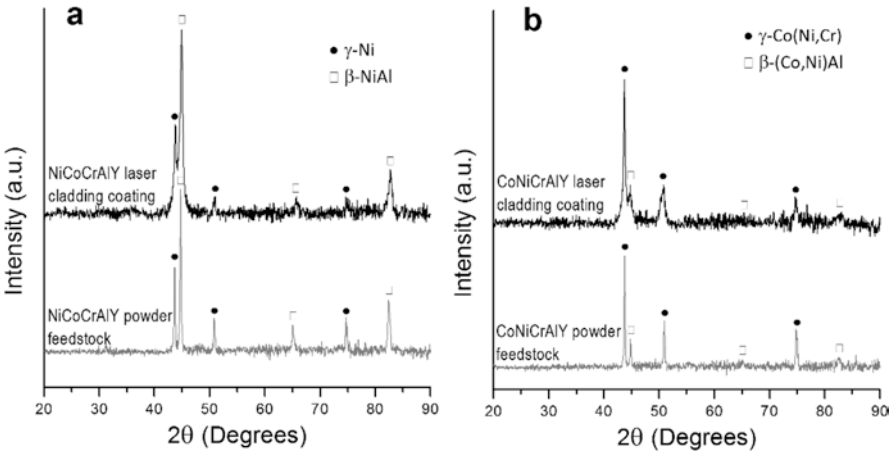

Fig. 13.13 The XRD pattern of (**a**) the NiCoCrAlY powder and LC coating and (**b**) the CoNiCrAlY powder and LC coating

orientation (vertical growth direction). Several Y-rich zones (bright white) were present in some γ/γ- and γ/β-grain boundaries. These results showed and confirmed that the yttrium-rich zones were randomly distributed but always toward the grain boundaries or around porosities on both coatings. The *Marangoni effect* (Majumdar and Manna 2011) was observed as changes in the morphology and direction of dendritic growth of the microstructure due to the in-depth gradient of the cooling rates.

The two main phases for the NiCoCrAlY laser coating were confirmed by indexing them in the electron diffraction patterns obtained with transmission electron microscopy (TEM). Figure 13.14 shows the dark field (DF) image of the NiCoCrAlY

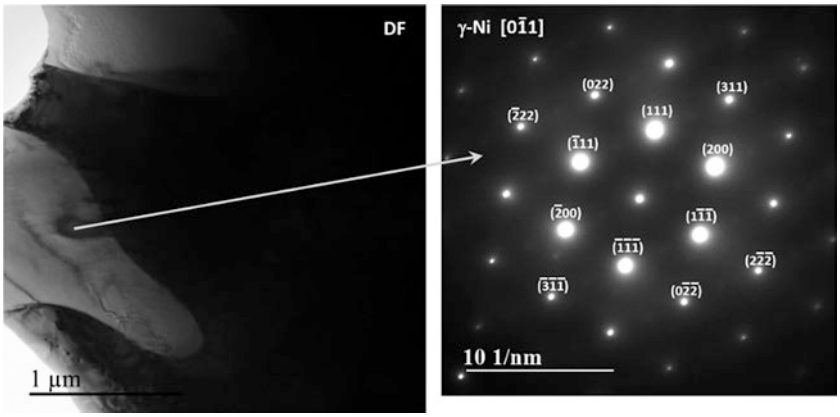

Fig. 13.14 The TEM micrograph (200 kV DF image) of the NiCoCrAlY laser coating and diffraction pattern (SADP) of the γ-Ni phase is indicated in the zone axis $\left[0\,\bar{1}\,1\right]$ (Pereira et al. 2019)

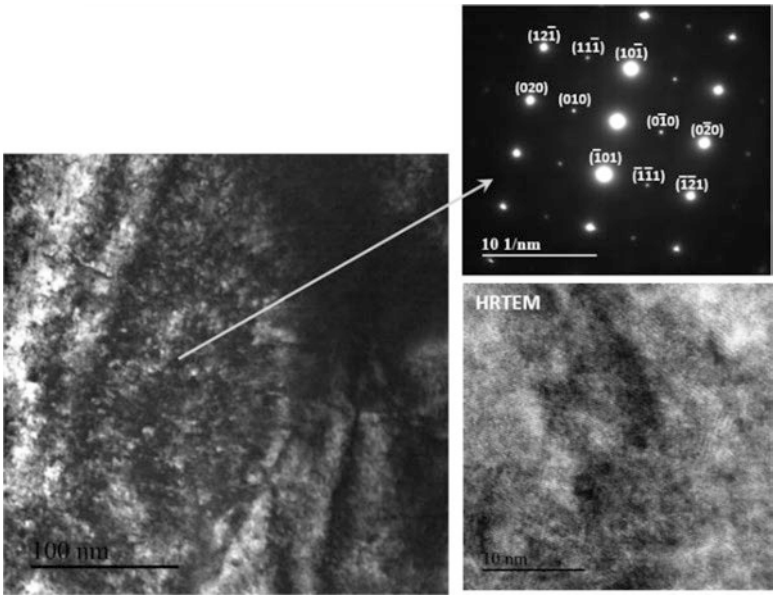

Fig. 13.15 The TEM micrograph (200 kV BF image) of the NiCoCrAlY coating and SADP corresponding to the β-NiAl phase on the zone axis [101] in high-resolution detail

coating, and on the right of Fig. 13.14, the SADP is indexed for the γ-Ni (fcc) phase on the axis of zone $\left[0\,\bar{1}\,1\right]$. Similarly, in Fig. 13.15, the bright field (BF) image corresponding to a zone of the β-phase is shown, as is the indexed SADP of this β-NiAl

phase (bcc) on the axis of zone [1 0 1]. Here, the high-resolution image of the structure of this phase is also shown (Fig. 13.15, bottom right), with different directions observed in the atomic columns of the crystalline structure.

The dilution and mixing of relevant chemical elements, such as Fe, Co, Al, and Y with Ni-Cr from the surface of the coating to the substrate, showed a gradual variation in composition, which was influenced by the obtained microstructure. With a higher iron content in the solid solution formed during the solidification in the area near the substrate, less hardness is obtained as it was measured near the dilution zone. However, a higher Al content increased hardness as this element stabilized the β-phase, which was harder than the γ-phase (Kim et al. 2009; Pereira et al. 2015b).

The amount of β-phase detected in the different coating zones doubled the γ-phase content in NiCoCrAlY compared to CoNiCrAlY, which represented two-thirds of the total composition. With the CoNiCrAlY coating (Fig. 13.16), this proportion only represented about one-fourth due to this alloy's Al content (12.5 wt.% versus 8 wt.%, respectively). This observation verified that aluminum stabilized the β-phase when obtaining MCrAlY coatings by laser cladding. Furthermore, in the interdendritic spaces at the end of the rapid solidification process, Al content above the possible eutectic composition allowed greater beta-phase formation, specifically in the NiCoCrAlY alloy with its higher aluminum content. This also influenced the high-temperature oxidation behavior in this coating, as reported in a previous work (Kim et al. 2014).

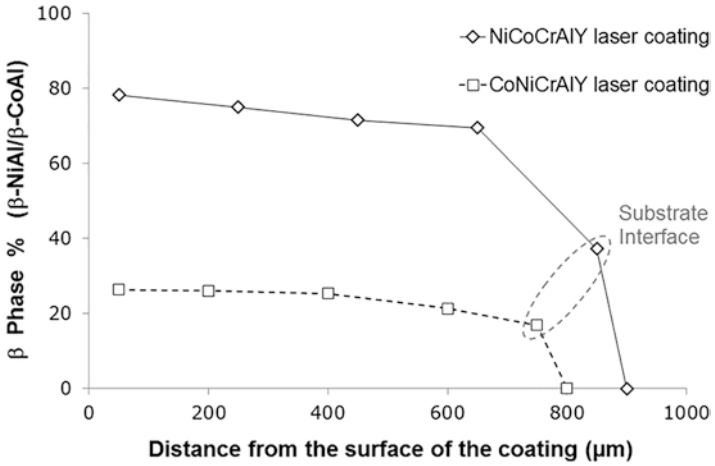

Fig. 13.16 The pattern evolution of the amount of β-phase from the surface to the substrate in the obtained γ/β-MCrAlY laser coatings

13.4 Mechanical Properties of the MCrAlY Laser Clad Alloys

The mechanical resistance and durability of a TBC depends on the mechanical characteristics of each individual layer, substrate characteristics, and their relation. In order to improve a system's resistance, coating hardness must exceed substrate hardness (Pereira et al. 2015a, c). Moreover, a gradual gradient in substrate hardness in the interface region is desirable. This is why we studied in this initial section the microhardness profile in the obtained laser coatings. The microhardness profiles obtained for both compositions are plotted in Fig. 13.17.

The average microhardness for laser coatings NiCoCrAlY and CoNiCrAlY was 492 ± 13 HV and 361 ± 15 HV, respectively, whereas the hardness for the stainless steel substrate was 234 ± 10 HV, which corroborated the greater hardness values desired for the clad material. These results also demonstrated that the microhardness behavior exhibited along the thickness of coatings was quite constant. The hardness deviation observed in certain regions was expected due to not only the dendritic to columnar transition but also to the rich β-phase content in interdendritic zones. Otherwise, the higher hardness values found in the NiCoCrAlY coating could be explained by the effect of aluminum on the formed microstructure; that is, the NiCoCrAlY alloy had a bigger amount of Al (12.5 wt.%) than the CoNiCrAlY alloy (8 wt.%), which modified the microstructure by stabilizing the β-phase, as previously described.

It has been demonstrated that the hardness acquired for the NiCoCrAlY coating was greater than that reported for conventional plasma spray and HVOF processes (Table 13.4). However, the CoNiCrAlY coating hardness resulted in a slightly lower hardness. Nevertheless, the overall quality of both studied LC coatings was enhanced

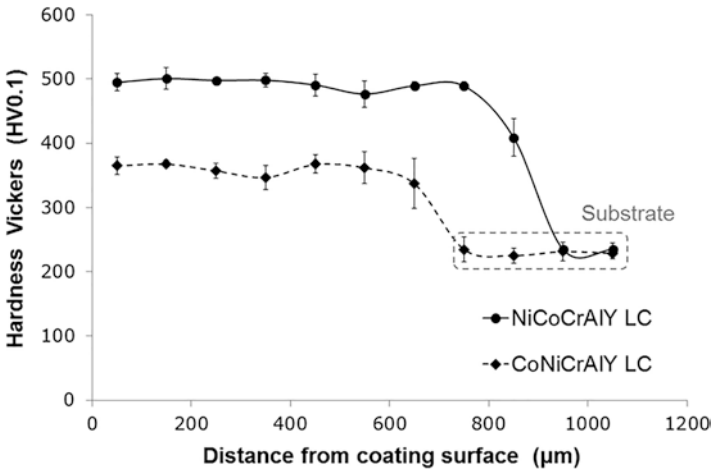

Fig. 13.17 The microhardness profile on the MCrAlY laser coatings

Table 13.4 Comparative table of the microhardness values in the MCrAlY coatings obtained by coaxial laser cladding and thermal spray processes

Coating material	Process	Microhardness (Kg/mm^2)	HV scale	References
NiCoCrAlY	Coaxial laser cladding	492 ± 13	HV0.1	Own measurements
	HVOF	434 ± 64	HV0.1	Mercier et al. (2011)
	Plasma spray	450 ± 45	HV0.1	Brodin and Eskner (2004)
CoNiCrAlY	Coaxial laser cladding	361 ± 15	HV0.1	Own measurements
	HVOF	410 ± 35	HV0.3	Scrivani et al. (2003)
	Plasma spray	155 ± 18	HV0.3	Higuera et al. (2006)

by the microstructure without observable pores, defects, or oxidized particles/material obtained with these MCrAlY alloys. The improved microstructure obtained through LC should increase the coating's durability compared with conventional thermal spray coatings.

The microhardness analysis revealed that the β-phase stabilization effect from the aluminum led to a harder coating. This hypothesis was clarified by analyzing the individual phases by nanoindentation tests run on coatings' cross sections. Figure 13.18 shows the in-depth hardness (H) and elastic modulus (E) curves obtained for the NiCoCrAlY (Fig. 13.18a) and CoNiCrAlY (Fig. 13.18b) coatings. These curves evidence several characteristics to be considered: at shallow indentation depths (below 100 nm deep), the results are useless given their highly scattered values. This phenomenon is explained by the sample's roughness and by the pure elastic deformation mechanism occurring at very low loads (Roa et al. 2012). However, two well-defined tendencies were observed within the 100–750-nm depth range.

The depth range marked in the figure was used to calculate the H and E values for each coating's individual phases. These values were subsequently assigned to the γ- and β-phases by observing the location of each imprint made using FESEM. At the maximum indentation depth, the curve converge was due to the rule of mixtures (Saha and Nix 2002; Huang et al. 2006), and these values were taken as those of the whole coating. Another analysis of individual phases is described below, although an initial inspection of these curves revealed that the H and E values for each phase were inverted to one another.

The H and E values for each identified γ/β-phase were calculated from the curves in Fig. 13.18. They are summarized in Table 13.5. These results revealed an elastic modulus value for the whole NiCoCrAlY coating of 175 ± 3 GPa and of 191 ± 3 GPa for the CoNiCrAlY coating. These E values were slightly lower than those obtained from the stainless used as the substrate (240.9 ± 7.3 GPa). Hardness was 6.2 GPa and 4.5 GPa for the NiCoCrAlY and the CoNiCrAlY coating, respectively, which corroborated the microhardness results. These characteristics suggest that failures

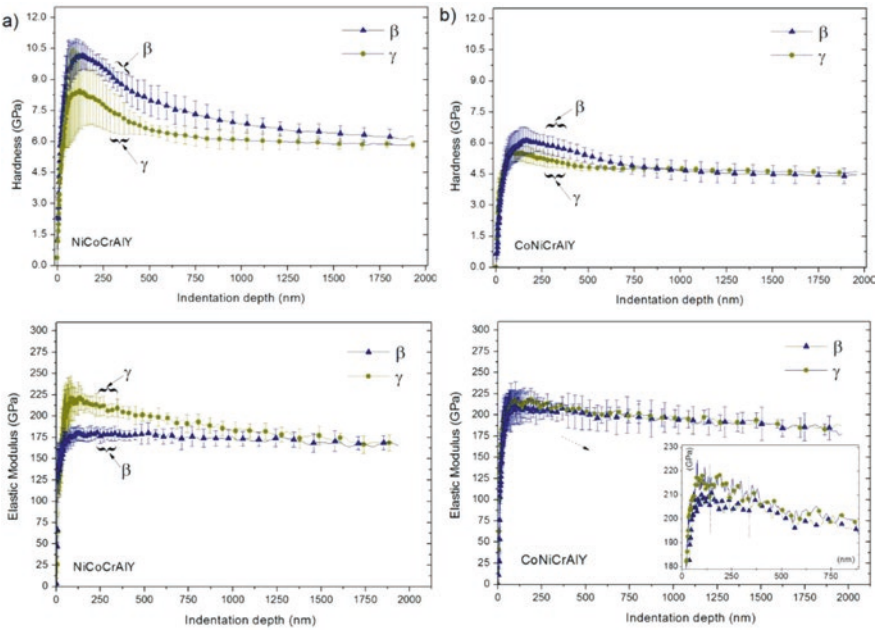

Fig. 13.18 The in-depth hardness and elastic modulus curves obtained by nanoindentation for (**a**) the NiCoCrAlY coating and (**b**) the CoNiCrAlY coating (Pereira et al. 2018)

Table 13.5 Summary of the elastic modulus and hardness values measured in each identified single phase and their contribution in the MCrAlY coatings

Alloy	Phase/material	Elastic modulus (GPa)	Hardness (GPa)
NiCoCrAlY	γ-Ni	215.4 ± 9.7	7.5 ± 0.7
	β-NiAl	178.7 ± 6.8	9.7 ± 0.4
	LC coating	175.5 ± 3.2	6.2 ± 0.1
CoNiCrAlY	γ-Co(Ni,Cr)	214.7 ± 10.9	5.3 ± 0.3
	β-(Co,Ni)Al	206.9 ± 13.0	6.0 ± 0.5
	LC coating	191.0 ± 3.4	4.5 ± 0.1

like delamination or detachment of coating must be reduced and agree with previously reported values (Saeidi et al. 2011).

The elastic modulus of the γ-phases (215 GPa and 214 GPa) were higher than for the β-phases (178 GPa and 206 GPa) for NiCoCrAlY and CoNiCrAlY, respectively. The hardness results also followed an inverse trend to the elastic moduli. The γ-phases revealed less hardness (7.5 GPa and 5.3 GPa) than the β-phases (9.7 GPa and 6.0 GPa) for NiCoCrAlY and CoNiCrAlY, respectively. The differences for each given phase were due to both coatings having similar crystallography but different chemical compositions, e.g., there is a higher proportion of Ni-Cr solid solution elements in the NiCoCrAlY coating, which led to this phase hardening. The

lower elastic modulus in the γ-Ni phase was higher than that of the β-NiAl phase due to the type of elements used in the solid solution (Co and Cr) instead of the intermetallic compounds in the aluminum-rich phase. However, the hardness of the β-NiAl phase was greater than that in γ-Ni because of the higher percentage of the stabilized β-phase. These conclusions agree with results from previous studies about coatings performed by low vacuum plasma spray (Kim et al. 2009; Webler et al. 2015) and by conventional and sintered powder metallurgy (Pereira et al. 2015b) with similar alloys.

In conclusion, the mechanical properties of the NiCoCrAlY laser coating were determined by the higher hardness and low modulus values of the β-NiAl phase, as seen in Fig. 13.19. For this coating, the biggest difference was observed between the properties of the γ/β-phases. This characteristic could affect failure resistance.

In the CoNiCrAlY coating, the difference between the mechanical properties of phases was much smaller because the β-(Co,Ni)Al phase had lower aluminum content than the β-NiAl phase. In addition, the hardness and elastic modulus were measured by the authors in an NiCrAlY laser coating (6 wt.% Al), obtained with the same LC parameters but, in this case, with the γ/γ´-microstructure to highlight the influence of Al content on the mechanical properties of the MCrAlY laser coatings. It is included in Fig. 13.19. Other authors (Webler et al. 2015) have confirmed with nanoindentation measurements that β-(Ni,Co)Al is harder than the γ-Co(Ni,Cr) phase because γ-phase has a low fraction of solid solution strengthening elements.

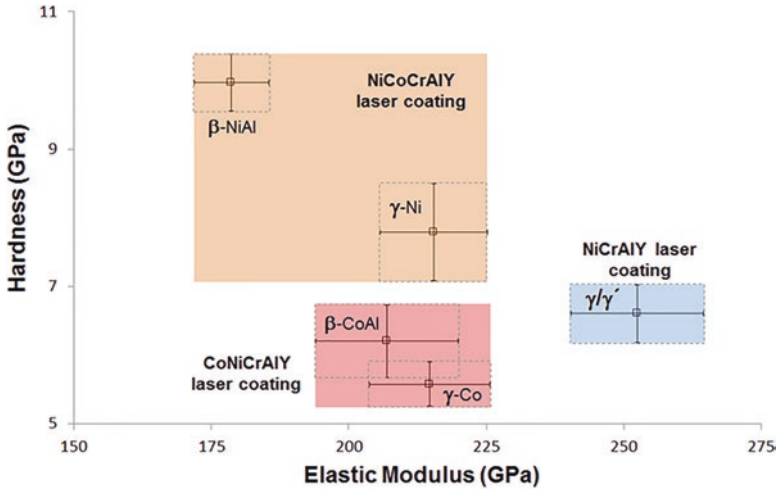

Fig. 13.19 The nanoindentation hardness and elastic modulus map for each individual phase in the MCrAlY laser coatings. The results were calculated over the 100–300 nm indentation depth

13.5 The High-Temperature Oxidation Behavior of the MCrAlY Laser Clad Alloys

Isothermal oxidation tests were conducted at 1100 °C for up to 200 h in static air in a GALLUR MC-1 furnace. Different oxidized samples were removed from the furnace at several intervals (5, 10, 25, 50, 100, and 200 h) and were air-cooled to room temperature. The increase in sample weight after the oxidation test was measured by a precision analytical balance (sensitivity of 0.01 mg). Before oxidation, the coating surface was ground to a 500 grit SiC paper (Ra = 0.17 ± 0.05 μm), and portions of the coated material were cut into samples of 7w × 7l × 0.5t mm (only the clad material). The oxidized surface was evaluated by XRD, SEM, and EDS microanalyses. The oxide layer was cut by the focused ion beam (FIB) method with a Ga column gun in a FESEM Zeiss AURIGA Compact before being analyzed by EDS in the same FESEM.

No cracks or spallation was observed on the oxidized surface after the oxidation tests at 1100 °C for 200 h. Coatings' oxidation behavior is shown according to oxidation time in Fig. 13.20. The surface weight gain in the NiCoCrAlY alloy was higher than that in the CoNiCrAlY alloy but was 50-fold less than the weight gain of the substrate (0.8184 mg/mm^2 for 200 h at 1100 °C, AISI 304).

Weight gain can be represented as a grown potential curve versus oxidation time. It is clear that, besides exhibiting less weight gain, the CoNiCrAlY alloy had a lower exponent in the weight gain law, which indicated that a stable oxide layer grows according to time. After 1 h at 1100 °C, the NiCoCrAlY alloy had already gained 15.4% more weight than the cobalt-based alloy according to the fitting mathematical model.

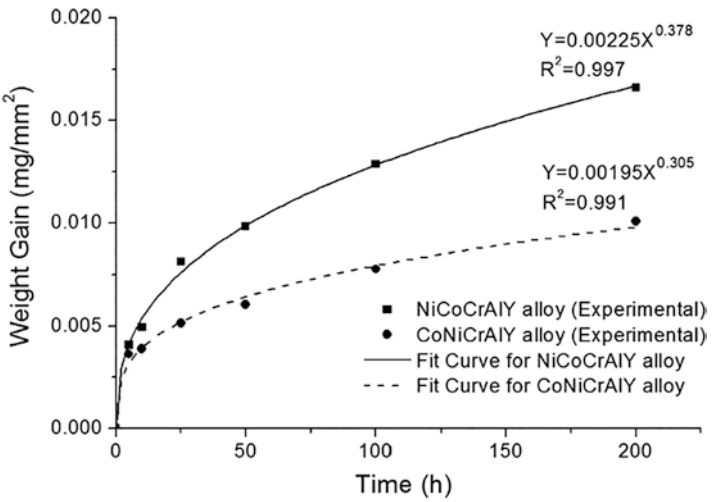

Fig. 13.20 Weight gain in the oxidation tests at 1100 °C for up to 200 h

The surface of the oxidized samples was examined by SEM-EDS, and the results are summarized in Fig. 13.21a, b**.** After 200 h at 1100 °C, the surface of the NiCoCrAlY sample appeared to be rather dense and homogeneous, with some inclusions visible as brighter objects (Fig. 13.21a). The EDS microanalysis indicated a continuous Al_2O_3 oxide layer with the NiO, CoO, Y_2O_3, and Cr_2O_3 oxides randomly distributed over the surface. NiO, CoO, and Cr_2O_3 may combine to form a $(Ni,Co)(Al,Cr)_2O_4$ spinel (Iwamoto et al. 1998). Oxide composition (types and weight percentage) was deduced by normalized stoichiometric calculations from the EDS measurements taken on the oxidized surface. This allowed us to obtain the time evolution of the oxide layer components, which is shown on the right-hand side of the surface micrograph (Fig. 13.21a). The Al_2O_3 ratio rapidly rose, presumably due to the large Al content in the alloy, which inhibited the growth of the Ni, Co, and Cr oxides. At 200 h, Al_2O_3 represented about 95% of the oxide layer.

Similar oxides were found on the surface of the CoNiCrAlY alloy. In this case, however, the lower Al content resulted in more heterogeneous oxides on the surface (as shown in Fig. 13.21b). Bigger amounts of the Ni, Cr, and Y oxides, which are larger in size, were obtained and made up approximately 64% of the oxide layer

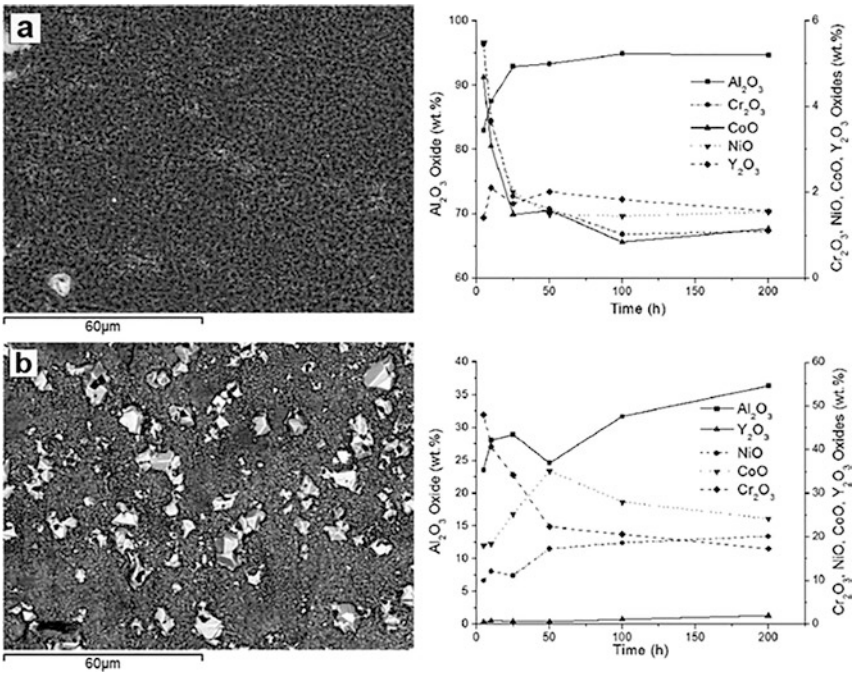

Fig. 13.21 Surface morphology and stoichiometric oxides: (**a**) BSE image of the NiCoCrAlY coating after 200 h at 1100 °C and evolution of the stoichiometric oxides for NiCoCrAlY and (**b**) BSE image of the CoNiCrAlY coating after 200 h at 1100 °C and evolution of the stoichiometric oxides for CoNiCrAlY (Pereira et al. 2015c)

composition based on stoichiometric oxide calculations for 200 h of oxidation at 1100 °C.

The morphology of the oxidized surface differed in each alloy. The oxide layer formed in the NiCoCrAlY coating had a lower roughness value and smaller regular crystals (columnar grain α-Al_2O_3) than those in the CoNiCrAlY coating (Fig. 13.21a). As a reference, the NiCoCrAlY samples oxidized for 100 h had a surface roughness (Ra) of 0.29 μm and a maximum oxide crystal height of 2078 nm. For the CoNiCrAlY coating, an irregular surface roughness with large crystals of (Co,Ni)O detected by EDS was found (Fig. 13.21b), which increased the surface roughness to 0.53 μm and the maximum height of the oxide crystals to 2853 nm at 100 h.

Many authors indicate that initial oxidation stages on MCrAlY alloys are generally preceded by the simultaneous formation of a continuous alumina layer, preceded by an initial stage of a very rapid oxidation of nonprotective oxides, such as Cr_2O_3, NiO, CoO, (Ni,Co)Cr_2O_4, and (Ni,Co)Al_2O_4 (Iwamoto et al. 1998; Nijdam et al. 2005; Toscano et al. 2006; Nijdam and Sloof 2008; Ferdinando et al. 2010; Wang et al. 2010; He et al. 2013; Zhu et al. 2013; Kaplin and Brochu 2014). Y-rich oxide inclusions can appear in the vicinity of the initial Y inclusions (Toscano et al. 2006; Nijdam and Sloof 2008) because Y is a reactive element. Alumina layer formation depends not only on the Al diffusion and the depletion of the β-NiAl phase (Kim et al. 2014) but also on the oxide inclusions on the oxide scale (Toscano et al. 2006; Nijdam et al. 2006; Nijdam and Sloof 2008; He et al. 2013).

The NiCoCrAlY laser cladding coating had a more stable Al_2O_3 TGO layer than the CoNiCrAlY coating, as suggested by the results obtained by running an EDS microanalysis of the oxidized surfaces and also by the strong peaks found in the DRX analysis (the LC-oxidized samples spectra in Fig. 13.22). The higher aluminum content of the NiCoCrAlY alloy and the initial cellular dendritic microstructure (γ/β) allowed a bigger Al_2O_3 compact single layer to grow with some Y/Al oxide inclusions (Y_2O_3/$YAlO_3$) on the Al_2O_3 oxide layer (Fig. 13.23a, c, and e). These oxide inclusions were strongly dependent on the initial Y distribution in the laser cladding coating and could affect the growth kinetics of the oxide layer. Accordingly, the fusion process that occurred during laser cladding contributed to the uniform distribution of yttrium particles and allowed a homogeneous distribution in yttrium oxides after oxidation, conversely to what occurs in the thermal spray process (with no full melting of particles).

The CoNiCrAlY oxidized coating had an oxide scale composed of two layers: a porous top layer initially formed by the CoO, NiO, Al_2O_3, and Cr_2O_3 oxides that combined to form a (Co,Ni)$(Al,Cr)_2O_4$ oxide spinel and a lower layer of stable alumina confirmed by the DRX analysis of the oxidized samples, as indicated in the FESEM images (Fig. 13.23b, d, and f). This alloy's low Al content, high cobalt-nickel proportion, and initial columnar dendritic microstructure in the coating (with a minor β-phase) affected the initial TGO scale stage. Then, the top porous nonprotective oxide layer limited oxygen diffusion to the lower Al_2O_3 layer.

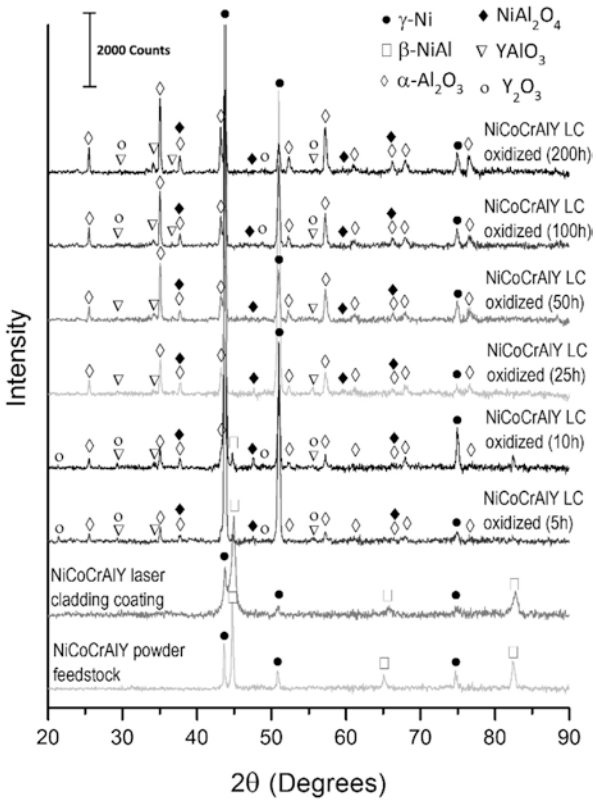

Fig. 13.22 The XRD analysis of the NiCoCrAlY powder, LC coating, and oxidized samples

Measuring oxide scale thickness according to oxidation time is shown in Fig. 13.24. The oxide layer in coatings could be similar to or thinner than that found in the MCrAlY coatings obtained by thermal spray techniques (Nijdam and Sloof 2008; Ferdinando et al. 2010; Richer et al. 2010; Song et al. 2011). This achieves more oxide grain boundaries that enhance the growth of alumina by inward oxygen diffusion (Nijdam and Sloof 2008) and the possible influence of coating/sample thickness in the high-temperature oxidation test (Toscano et al. 2006).

The thickness of the stable and continuous layer of alumina on the TGO in NiCoCrAlY laser cladding coating could be more than double that of the alumina layer obtained in the CoNiCrAlY coating (Fig. 13.24), besides being completely dense. Thus, a superior thermal barrier can be obtained using this process on an austenitic stainless steel substrate. The porous nonprotective oxide layer at the top of CoNiCrAlY TGO can be a disadvantage for applications in thermal barrier coating systems, and the porosity obtained in the top oxide layer would explain why there was a thick TGO (up to 3.5 μm) with a small weight gain (low alumina scale thickness).

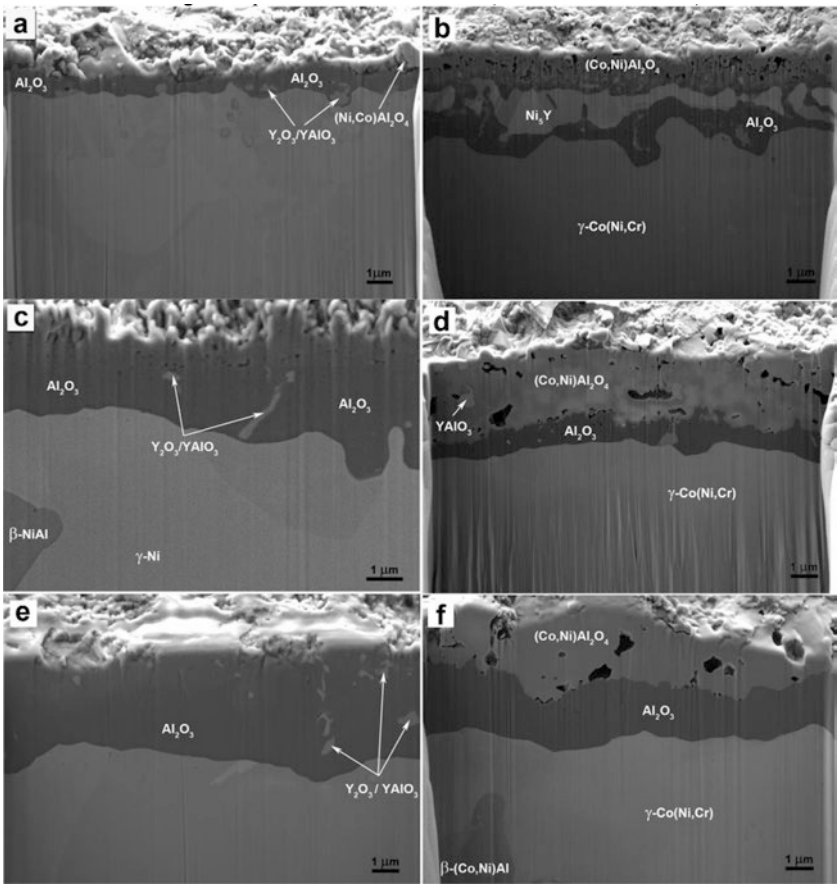

Fig. 13.23 SE images of the TGO layers in the MCrAlY laser cladding coatings oxidized (1100 °C). For 5 h of oxidation: (**a**) NiCoCrAlY and (**b**) CoNiCrAlY; for 50 h of oxidation, (**c**) NiCoCrAlY (**d**) and CoNiCrAlY; for 200 h of oxidation, (**e**) NiCoCrAlY and (**f**) CoNiCrAlY (Pereira et al. 2015c)

Near the TGO scale, a gamma phase predominates (Fig. 13.25a) in the coating due to the Al depletion zone already being evident at 50 h of oxidation. For this condition, it was possible to identify and confirm the three types of oxides visualized for this condition via the SADP analysis in TEM. The crystals of the α-Al_2O_3 dense layer (in the middle) are observed in Fig. 13.25b with their corresponding SADP. Figure 13.26 depicts the $YAlO_3$-type aluminum-yttrium oxide accompanied by a high-resolution image of the atomic arrangement of this oxide's structure. This $YAlO_3$ oxide particle is found between the alumina layer and the porous upper layer of oxides with a spinel structure.

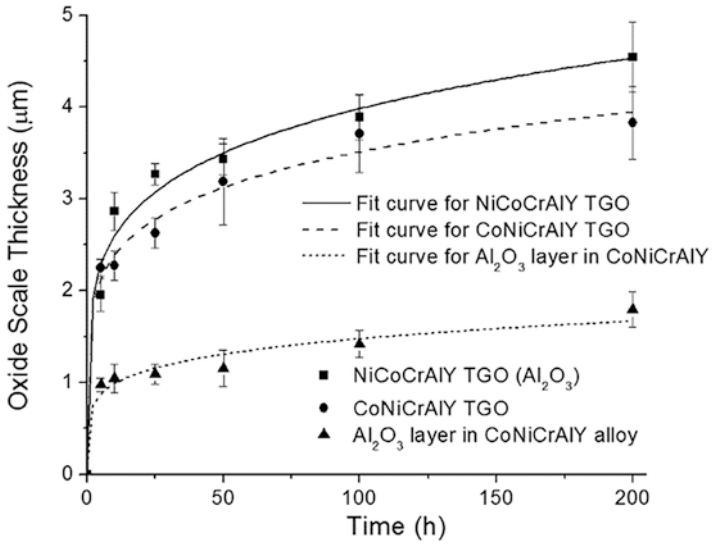

Fig. 13.24 Experimental and predicted curves for the oxide scale thickness in the MCrAlY laser cladding coatings

In the samples observed in FESEM with a longer oxidation time, this oxide type is observed as an elongated and distributed inclusion in the alumina layer. In this work, we were unable to find the $Al_5Y_3O_{12}$ phase reported for similar oxidized NiCrAlY laser coatings with higher yttrium content in the alloy (Ansari et al. 2017). The reflections of the $YAlO_3$ particle observed in the SADP (Fig. 13.26) are attributed to the alumina surrounding the particle. Hence, it is difficult to index the zone axis that corresponds to the shown electron diffraction.

The spinel oxide layer observed toward the TGO layer surface is porous, which favors the diffusion of oxygen into the TGO and, in turn, promotes the stable growth of the underlying alumina layer. Figure 13.27 shows the transmitted electron diffraction pattern and the high-resolution image of these $(Ni,Co)(Al,Cr)_2O_4$-type spinel oxides in the 50-h sample. For this coating, TGO layer densification occurred after 100 h.

Acknowledgments The authors would like to thank the SME (Electron Microscopy Service) of the Universitat Politècnica de València (UPV), Spain. This work was supported by the Spanish Ministry of Science and Innovation through Research Project MAT2011-28492-C03 and by the Generalitat Valenciana through Grant ACOMP/2013/114.

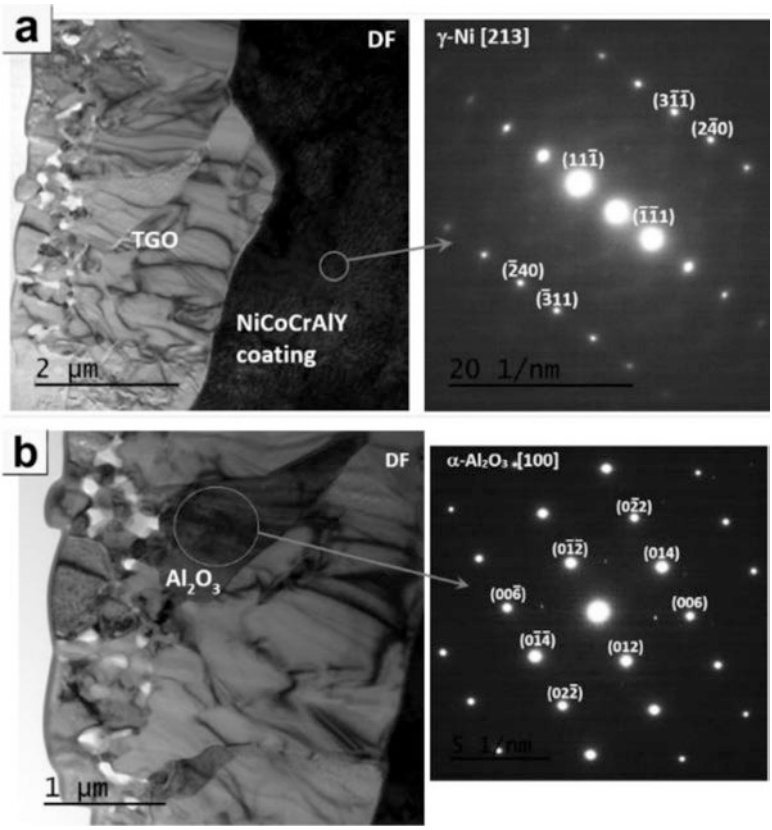

Fig. 13.25 TEM micrographs (200 kV DF image) of the NiCoCrAlY laser coating oxidized at 1100 °C for 50 h: (**a**) SADP of the NiCoCrAlY coating corresponding to the γ-Ni phase on the zone axis [213] and (**b**) SADP of an α-Al_2O_3 grain on the TGO layer on the zone axis [100]

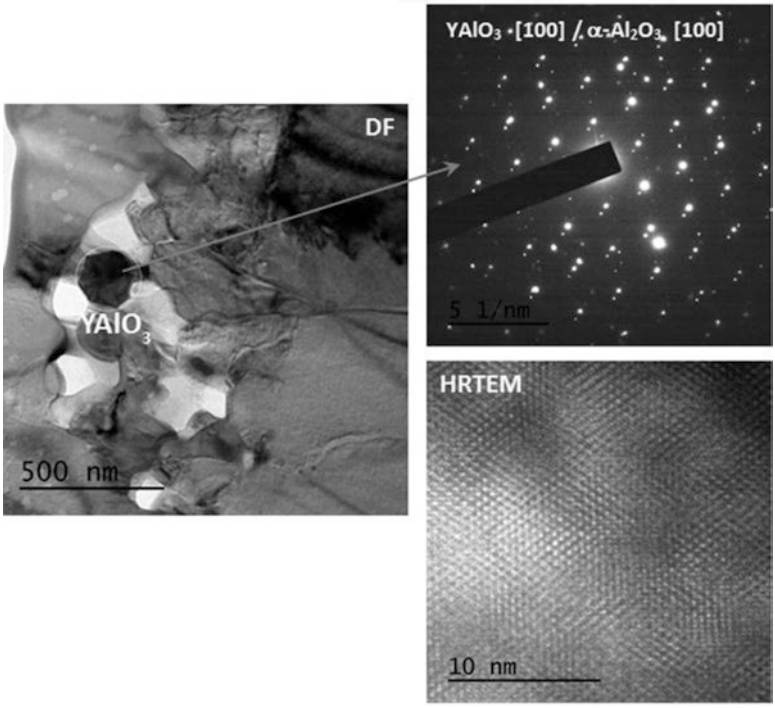

Fig. 13.26 TEM micrograph (200 kV DF image) of the oxidized NiCoCrAlY coating at 1100 °C for 50 h (left). The SADP and HRTEM images of the YAlO3 oxide indicated in the micrograph (right) (Pereira et al. 2019)

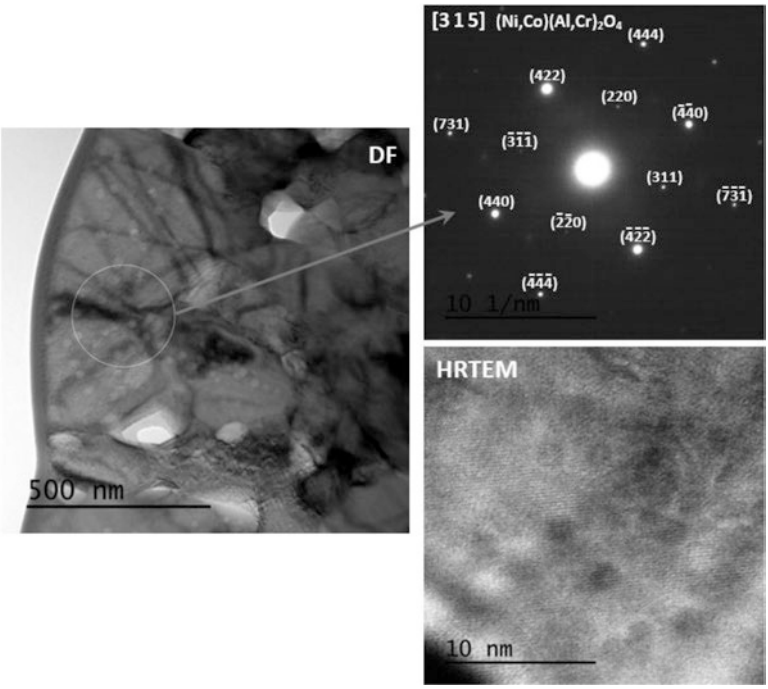

Fig. 13.27 TEM micrograph (200 kV DF image) of the NiCoCrAlY laser coating oxidized at 1100 °C for 50 h (left). The SADP and HRTEM images of the spinel $(Ni,Co)(Al,Cr)_2O_4$ oxides (right) (Pereira et al. 2019)

References

Abioye, T. E., Folkes, J., & Clare, A. T. (2013). A parametric study of Inconel 625 wire laser deposition. *Journal of Materials Processing Technology, 213*, 2145–2151. https://doi.org/10.1016/j.jmatprotec.2013.06.007.

Ansari, M., Shoja-Razavi, R., Barekat, M., & Man, H. C. (2017). High-temperature oxidation behavior of laser-aided additively manufactured NiCrAlY coating. *Corrosion Science, 118*, 168–177. https://doi.org/10.1016/j.corsci.2017.02.001.

Bezençon, C., Schnell, A., & Kurz, W. (2003). Epitaxial deposition of MCrAlY coatings on a Ni-base superalloy by laser cladding. *Scripta Materialia, 49*, 705–709. https://doi.org/10.1016/S1359-6462(03)00369-5.

Brodin, H., & Eskner, M. (2004). The influence of oxidation on mechanical and fracture behaviour of an air plasma-sprayed NiCoCrAlY bond coat. *Surface and Coatings Technology, 187*, 113–121. https://doi.org/10.1016/j.surfcoat.2003.12.021.

Cao, X. Q., Vassen, R., & Stoever, D. (2004). Ceramic materials for thermal barrier coatings. *Journal of the European Ceramic Society, 24*, 1–10. https://doi.org/10.1016/S0955-2219(03)00129-8.

Cao, J., Liu, F., Lin, X., et al. (2013). Effect of overlap rate on recrystallization behaviors of laser solid formed Inconel 718 superalloy. *Optics and Laser Technology, 45*, 228–235. https://doi.org/10.1016/j.optlastec.2012.06.043.

Carpio, P., Rayón, E., Salvador, M. D., et al. (2016). Mechanical properties of double-layer and graded composite coatings of YSZ obtained by atmospheric plasma spraying. *Journal of Thermal Spray Technology, 25*, 778–787. https://doi.org/10.1007/s11666-016-0390-z.

Chen, W. R., Wu, X., Marple, B. R., & Patnaik, P. C. (2005). Oxidation and crack nucleation/growth in an air-plasma-sprayed thermal barrier coating with NiCrAlY bond coat. *Surface and Coatings Technology, 197*, 109–115. https://doi.org/10.1016/j.surfcoat.2004.06.027.

Dey, G. K. (2003). Physical metallurgy of nickel aluminides. *Sadhana, 28*, 247–262.

Ferdinando Di, M., Fossati, A., Lavacchi, A., et al. (2010). Isothermal oxidation resistance comparison between air plasma sprayed, vacuum plasma sprayed and high velocity oxygen fuel sprayed CoNiCrAlY bond coats. *Surface and Coatings Technology, 204*, 2499–2503. https://doi.org/10.1016/j.surfcoat.2010.01.031.

He, J., Guo, H., Peng, H., & Gong, S. (2013). Microstructural, mechanical and oxidation features of NiCoCrAlY coating produced by plasma activated EB-PVD. *Applied Surface Science, 274*, 144–150. https://doi.org/10.1016/j.apsusc.2013.02.136.

Hemmati, I., Ocelík, V., & De, H. J. T. M. (2012). Dilution effects in laser cladding of Ni–Cr–B–Si–C hardfacing alloys. *Materials Letters, 84*, 69–72. https://doi.org/10.1016/j.matlet.2012.06.054.

Higuera, V., Belzunce, F. J., & Riba, J. (2006). Influence of the thermal-spray procedure on the properties of a CoNiCrAlY coating. *Surface and Coatings Technology, 200*, 5550–5556. https://doi.org/10.1016/j.surfcoat.2005.07.070.

Huang, Y., Zhang, F., Hwang, K. C., et al. (2006). A model of size effects in nano-indentation. *Journal of the Mechanics and Physics of Solids, 54*, 1668–1686. https://doi.org/10.1016/j.jmps.2006.02.002.

Iwamoto, H., Sumikawa, T., Nishida, K., et al. (1998). High temperature oxidation behavior of laser clad NiCrAlY layer. *Materials Science and Engineering A, 241*, 251–258. https://doi.org/10.1016/S0921-5093(97)00499-1.

Kaplin, C., & Brochu, M. (2014). The effect of grain size on the oxidation of NiCoCrAlY. *Applied Surface Science, 301*, 258–263. https://doi.org/10.1016/j.apsusc.2014.02.056.

Kim, D.-J., Cho, S.-K., Choi, J.-H., et al. (2009). Evaluation of the degradation of plasma sprayed thermal barrier coatings using nano-indentation. *Journal of Nanoscience and Nanotechnology, 9*, 7271–7277. https://doi.org/10.1166/jnn.2009.1786.

Kim, D., Shin, I., Koo, J., et al. (2014). Quantitative analysis on the depletion rate of β-NiAl phases in MCrAlY coating. *Journal of Mechanical Science and Technology, 28*, 513–519. https://doi.org/10.1007/s12206-013-1118-3.

Li, Y., & Ma, J. (1997). Study on overlapping in the laser cladding process. *Surface and Coatings Technology, 90*, 1–5. https://doi.org/10.1016/S0257-8972(96)03022-8.

Mahamood, R. M. (2018). Laser metal deposition of metals and alloys. In *Laser metal deposition process of metals, alloys, and composite materials* (pp. 93–118). Cham: Springer International Publishing.

Majumdar, J. D., & Manna, I. (2011). Laser material processing. *International Materials Review, 56*, 341–388. https://doi.org/10.1179/1743280411Y.0000000003.

Marginean, G., & Utu, D. (2012). Cyclic oxidation behaviour of different treated CoNiCrAlY coatings. *Applied Surface Science, 258*, 8307–8311. https://doi.org/10.1016/j.apsusc.2012.05.050.

Mercier, D., Gauntt, B. D., & Brochu, M. (2011). Thermal stability and oxidation behavior of nanostructured NiCoCrAlY coatings. *Surface and Coatings Technology, 205*, 4162–4168. https://doi.org/10.1016/j.surfcoat.2011.03.005.

Nijdam, T. J., & Sloof, W. G. (2008). Effect of Y distribution on the oxidation kinetics of NiCoCrAlY bond coat alloys. *Oxidation of Metals, 69*, 1–12. https://doi.org/10.1007/s11085-007-9080-z.

Nijdam, T. J., Jeurgens, L. P. H., & Sloof, W. G. (2005). Promoting exclusive α-Al_2O_3 growth upon high-temperature oxidation of NiCrAl alloys: Experiment versus model predictions. *Acta Materialia, 53*, 1643–1653. https://doi.org/10.1016/j.actamat.2004.12.014.

Nijdam, T. J., Kwakernaak, C., & Sloof, W. G. (2006). The effects of alloy microstructure refinement on the short-term thermal oxidation of NiCoCrAlY alloys. *Metallurgical and Materials*

Transactions A: Physical Metallurgy and Materials Science, 37, 683–693. https://doi.org/10.1007/s11661-006-0040-z.

Ocelík, V., Nenadl, O., Palavra, A., & De Hosson, J. T. M. (2014). On the geometry of coating layers formed by overlap. *Surface and Coatings Technology, 242*, 54–61. https://doi.org/10.1016/j.surfcoat.2014.01.018.

Padture, N. P., Gell, M., & Jordan, E. H. (2002). Thermal barrier coatings for gas-turbine engine applications. *Science (80-), 296*, 280–284. https://doi.org/10.1126/science.1068609.

Partes, K., Giolli, C., Borgioli, F., et al. (2008). High temperature behaviour of NiCrAlY coatings made by laser cladding. *Surface and Coatings Technology, 202*, 2208–2213. https://doi.org/10.1016/j.surfcoat.2007.09.010.

Pereira, J., Zambrano, J., Licausi, M., et al. (2015a). Tribology and high temperature friction wear behavior of MCrAlY laser cladding coatings on stainless steel. *Wear, 330*, 280–287. https://doi.org/10.1016/j.wear.2015.01.048.

Pereira, J. C., Zambrano, J. C., Afonso, C. R. M., & Amigó, V. (2015b). Microstructure and mechanical properties of NiCoCrAlYTa alloy processed by press and sintering route. *Materials Characterization, 101*, 159–165. https://doi.org/10.1016/j.matchar.2015.02.001.

Pereira, J. C., Zambrano, J. C., Tobar, M. J., et al. (2015c). High temperature oxidation behavior of laser cladding MCrAlY coatings on austenitic stainless steel. *Surface and Coatings Technology, 270*, 243–248. https://doi.org/10.1016/j.surfcoat.2015.02.050.

Pereira, J. C., Zambrano, J. C., Rayón, E., et al. (2018). Mechanical and microstructural characterization of MCrAlY coatings produced by laser cladding: The influence of the Ni, Co and Al content. *Surface and Coatings Technology, 338*, 22–31. https://doi.org/10.1016/j.surfcoat.2018.01.073.

Pereira, J. C., Echeverría, A., Afonso, C. R. M., et al. (2019). Microstructure assessment at high temperature in NiCoCrAlY overlay coating obtained by laser metal deposition. *Journal of Materials Research and Technology, 8*, 1761–1772. https://doi.org/10.1016/j.jmrt.2018.12.006.

Pint, B. A., Haynes, J. A., & Zhang, Y. (2010). Effect of superalloy substrate and bond coating on TBC lifetime. *Surface and Coatings Technology, 205*, 1236–1240. https://doi.org/10.1016/j.surfcoat.2010.08.154.

Pomeroy, M. J. (2005). Coatings for gas turbine materials and long term stability issues. *Materials and Design, 26*, 223–231. https://doi.org/10.1016/j.matdes.2004.02.005.

Richer, P., Yandouzi, M., Beauvais, L., & Jodoin, B. (2010). Oxidation behaviour of CoNiCrAlY bond coats produced by plasma, HVOF and cold gas dynamic spraying. *Surface and Coatings Technology, 204*, 3962–3974. https://doi.org/10.1016/j.surfcoat.2010.03.043.

Roa, J. J., Rayon, E., Morales, M., & Segarra, M. (2012). Contact mechanics at nanometric scale using nanoindentation technique for brittle and ductile materials. *Recent Patents on Nanotechnology, 6*, 142–152. https://doi.org/10.2174/187221012800270162.

Saeidi, S., Voisey, K. T., & McCartney, D. G. (2011). Mechanical properties and microstructure of VPS and HVOF CoNiCrAlY coatings. *Journal of Thermal Spray Technology, 20*, 1231–1243. https://doi.org/10.1007/s11666-011-9666-5.

Saha, R., & Nix, W. D. (2002). Effects of the substrate on the determination of thin film mechanical properties by nanoindentation. *Acta Materialia, 50*, 23–38. https://doi.org/10.1016/S1359-6454(01)00328-7.

Schulz, U., Leyens, C., Fritscher, K., et al. (2003). Some recent trends in research and technology of advanced thermal barrier coatings. *Aerospace Science and Technology, 7*, 73–80. https://doi.org/10.1016/S1270-9638(02)00003-2.

Scrivani, A., Bardi, U., Carrafiello, L., et al. (2003). A comparative study of high velocity oxygen fuel, vacuum plasma spray, and axial plasma spray for the deposition of CoNiCrAlY bond coat alloy. *Journal of Thermal Spray Technology, 12*, 504–507. https://doi.org/10.1361/105996303772082242.

Segerstark, A., Andersson, J., & Svensson, L.-E. (2017). Investigation of laser metal deposited alloy 718 onto an EN 1.4401 stainless steel substrate. *Optics and Laser Technology, 97*, 144–153. https://doi.org/10.1016/j.optlastec.2017.05.038.

Singh, A., Ramakrishnan, A., & Dinda, G. (2017). Fabrication of Al-11.2Si components by direct laser metal deposition for automotive applications. *Journal of Welding Joining, 35*, 67–73. https://doi.org/jwj-35-4-67.

Song, P., Subanovic, M., Toscano, J., et al. (2011). Effect of atmosphere composition on the oxidation behavior of MCrAlY coatings. *Materials and Corrosion, 62*, 699–705. https://doi.org/10.1002/maco.201005851.

Steen, W. M., & Mazumder, J. (2010). *Laser material processing* (4th ed.). London: Springer Science & Business Media.

Tancret, F., Bhadeshia, H. K. D. H., & MacKay, D. J. C. (2003). Design of a creep resistant nickel base superalloy for power plant applications: Part 1 – Mechanical properties modelling. *Materials Science and Technology, 19*, 283–290. https://doi.org/10.1179/026708303225009788.

Telasang, G., Majumdar, J. D., Padmanabham, G., et al. (2014). Effect of laser parameters on microstructure and hardness of laser clad and tempered AISI H13 tool steel. *Surface and Coatings Technology, 258*, 1108–1118. https://doi.org/10.1016/j.surfcoat.2014.07.023.

Texier, D., Monceau, D., Hervier, Z., & Andrieu, E. (2016). Effect of interdiffusion on mechanical and thermal expansion properties at high temperature of a MCrAlY coated Ni-based superalloy. *Surface and Coatings Technology, 307*, 81–90. https://doi.org/10.1016/j.surfcoat.2016.08.059.

Texier, D., Monceau, D., Crabos, F., & Andrieu, E. (2017). Tensile properties of a non-line-of-sight processed β-γ-γ′ MCrAlY coating at high temperature. *Surface and Coatings Technology, 326*, 28–36. https://doi.org/10.1016/j.surfcoat.2017.07.026.

Toscano, J., Vaβen, R., Gil, A., et al. (2006). Parameters affecting TGO growth and adherence on MCrAlY-bond coats for TBC's. *Surface and Coatings Technology, 201*, 3906–3910. https://doi.org/10.1016/j.surfcoat.2006.07.247.

Varlese, F. A., Tului, M., Sabbadini, S., et al. (2013). Optimized coating procedure for the protection of TiAl intermetallic alloy against high temperature oxidation. *Intermetallics, 37*, 76–82. https://doi.org/10.1016/j.intermet.2013.02.001.

Vilar, R. (1999). Laser cladding. *Journal of Laser Applications, 11*, 64–79. https://doi.org/10.2351/1.521888.

Vilar, R., & Santos, E. C. (2011). Structure of NiCrAlY coatings deposited on oriented single crystal Superalloy substrates by laser cladding. *Advances in Materials Research, 278*, 503–508. https://doi.org/10.4028/www.scientific.net/AMR.278.503.

Vilar, R., Santos, E. C., Ferreira, P. N., et al. (2009). Structure of NiCrAlY coatings deposited on single-crystal alloy turbine blade material by laser cladding. *Acta Materialia, 57*, 5292–5302. https://doi.org/10.1016/j.actamat.2009.06.049.

Vollertsen, F., Partes, K., & Meijer, J. (2005). State of the art of laser hardening and cladding. In E. Beyer, F. Dausinger, A. Ostendorf, & A. Otto (Eds.), *Proceedings of the third international WLT-conference on lasers in manufacturing, 14–17 June 2005* (pp. 281–305). Munich: AT-Fachverlag GmbH.

Wang, H., Zuo, D., Yan, J., et al. (2010). Effects of nanometer Al_2O_3 particles on oxidation behaviors of laser cladding low Al NiCoCrAlY coatings. *Oxidation of Metals, 74*, 49–60. https://doi.org/10.1007/s11085-010-9197-3.

Webler, R., Ziener, M., Neumeier, S., et al. (2015). Evolution of microstructure and mechanical properties of coated co-base superalloys during heat treatment and thermal exposure. *Materials Science and Engineering A, 628*, 374–381. https://doi.org/10.1016/j.msea.2015.01.060.

Wright, P., & Evans, A. (1999). Mechanisms governing the performance of thermal barrier coatings. *Current Opinion in Solid State & Materials Science, 4*, 255–265. https://doi.org/10.1016/S1359-0286(99)00024-8.

Young, D. J. (2008). *High temperature oxidation and corrosion of metals*. Amsterdam: Elsevier.

Zhang, K., Liu, W., & Shang, X. (2007). Research on the processing experiments of laser metal deposition shaping. *Optics and Laser Technology, 39*, 549–557. https://doi.org/10.1016/j.optlastec.2005.10.009.

Zhu, C., Javed, A., Li, P., et al. (2013). Study of the effect of laser treatment on the initial oxidation behaviour of Al-coated NiCrAlY bond-coat. *Surface and Interface Analysis, 45*, 1680–1689. https://doi.org/10.1002/sia.5307.

Zhu, C., Li, P., & Wu, X. Y. (2016). A study of the diffusion and pre-oxidation treatment on the formation of Al_2O_3 ceramic scale on NiCrAlY bond-coat during initial oxidation process. *Ceramics International, 42*, 7708–7716. https://doi.org/10.1016/j.ceramint.2016.01.185.

Chapter 14
Applications of Laser in Cold Spray

Ningsong Fan, Xinliang Xie, Chunjie Huang, Rocco Lupoi, and Shuo Yin

14.1 Introduction

Cold spray is a solid-state material deposition process, which was originally developed as a coating technology in the 1980s (Alkhimov et al. 1980, 1990). In this process, high-temperature compressed gases (typically nitrogen, air, or helium) are used as the propulsive gas to accelerate powder feedstock (typically metals and metal matrix composites) to a high velocity (typically higher than 300 m/s) and to induce deposition when the powders impact onto a substrate (typically metals). Figure 14.1 shows the schematic of a typical cold spray system. In contrast to conventional high-temperature deposition processes, the formation of a cold spray deposit relies largely on the particle kinetic energy prior to impact rather than the thermal energy. The feedstock used for cold spray remains solid state during the entire deposition process. Deposition is achieved through local metallurgical bonding and mechanical interlocking which are caused by localized plastic deformation at the interparticle and particle–substrate interfaces. This allows for the avoidance of defects commonly encountered in high-temperature deposition processes, such as oxidation, residual thermal stress, and phase transformation (Assadi et al. 2016; Raoelison et al. 2018; Rokni et al. 2017).

Successful deposition of a cold-sprayed deposit requires the feedstock particles to exceed a critical impact velocity (Hassani-Gangaraj et al. 2018; Meng et al. 2015;

N. Fan · R. Lupoi · S. Yin (✉)
Trinity College Dublin, Department of Mechanical and Manufacturing Engineering, The University of Dublin, Dublin, Ireland
e-mail: yins@tcd.ie

X. Xie
ICB UMR 6303, CNRS, Univ. Bourgogne Franche-Comte, UTBM, Belfort, France

C. Huang
Department of Mechanical Engineering, Helmut-Schmidt-Universität/Universität der Bundeswehr, Hamburg, Germany

P. Cavaliere (ed.), *Laser Cladding of Metals*,
https://doi.org/10.1007/978-3-030-53195-9_14

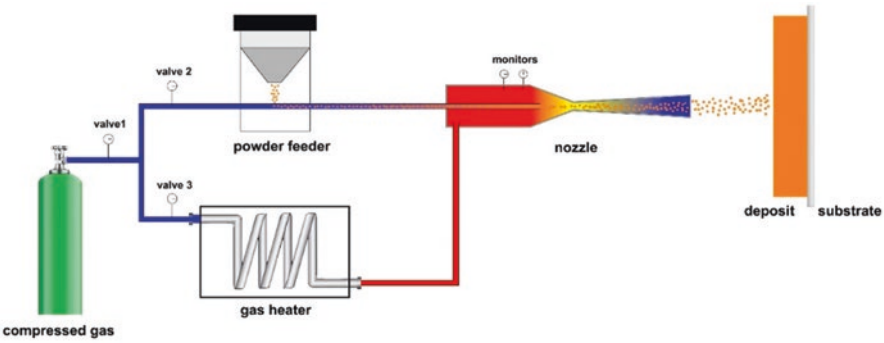

Fig. 14.1 Schematic of a typical cold spray system

Assadi et al. 2003; Raletz et al. 2006; Hassani-Gangaraj et al. 2017; Grujicic et al. 2004; Assadi et al. 2011; Schmidt et al. 2006). In cold spray, the formation of a deposit consists of two different stages. The first stage involves the deposition of an initial layer of particles where bonding occurs between feedstock particles and the substrate material; the second stage is the deposition on top of the layer(s) previously deposited, where bonding occurs between feedstock particles. Each stage has a respective critical velocity, i.e., for particle/substrate bonding and for deposit growth. Particle impact velocity must satisfy both criterions for successful deposition. In general, a higher particle velocity will result in improved deposit quality. Note that when the powder and substrate are the same material, the critical velocity can be considered as the same for both stages. Critical velocity is not a constant but depends on several factors including material type, particle size, and particle temperature. Larger particles or higher particle temperature upon impact helps to reduce critical velocity (Hassani-Gangaraj et al. 2018; Hassani-Gangaraj et al. 2017; Assadi et al. 2011; Schmidt et al. 2006; Bae et al. 2009; Yin et al. 2013).

Despite the variety of feedstocks and substrates that can be deposited with cold spray, metals deposited onto metallic substrates are still the most popular coating/substrate material combination and as a result have been intensively investigated since the inception of cold spray. In this respect, the bonding mechanism of the two metals in intimate contact is always a major research focal point. Several studies have been carried out during the past decades to improve the cold spray community's mechanistic understanding of this phenomenon (Luo et al. 2014a; Lee and Kim 2015; King et al. 2010; Klassen et al. 2016). It has been well recognized that metallurgical bonding and mechanical interlocking are two dominant mechanisms of bonding in cold spray. Metallurgical bonding is known to result from nano-scale chemical reactions at the interparticle or coating/substrate interfaces (King et al. 2010; Wang et al. 2011, 2014; Ko et al. 2015; Zhang and Zhang, 2011; Xiong et al. 2008; Kim et al. 2009). Specifically, the high-velocity impact induces high-strain-rate localized plastic deformation of the particle or the substrate at the contact interface, which in turn can result in jetting (Hassani-Gangaraj et al. 2018; Hassani-Gangaraj et al. 2019) and adiabatic shear instability (Assadi et al. 2003).

The high-velocity impact also breaks the native oxide films present on both metallic surfaces. The outward metal jet extrudes the oxide debris from the interface, allowing the intimate metal-to-metal contact. Under the localized high pressure at the contact interface, the chemical reaction can occur to form the metallurgical bonding (Assadi et al. 2003; Grujicic et al. 2004; Bae et al. 2008; Ichikawa et al. 2019; Chen et al. 2016; Kumar et al. 2017). Several experimental observations have been recognized as evidence for interfacial metallurgical bonding, including the formation of interfacial amorphous phase (Wang et al. 2014; Ko et al. 2015; Xiong et al. 2008), interfacial intermetallic layer (King et al. 2010; Kim et al. 2009), dimple-like features on fracture surfaces (Bae et al. 2009; Chen et al. 2016; Bae et al. 2012), and localized melting (Kumar et al. 2017; Li et al. 2010). Mechanical interlocking, as another important mechanism, is a nonchemical bonding phenomenon. It is represented by particles becoming mechanically embedded or trapped into the substrate materials or coatings (Yin et al. 2015; Hussain et al. 2009).

Despite the existence of the metallurgical and mechanical bonding in cold spray, such interparticle and coating/substrate bonding is not fully metallurgical. Therefore, the as-sprayed coatings typically lack cohesion and adhesion strength. In recent years, in order to improve the cohesion and adhesion strength of cold-sprayed coatings, laser technology has been applied as an assistance for the cold spray deposition. Typically, according to its application at different stages of cold spray process, the function of laser in cold spray can be classified into the follow three categories: (i) pre-laser surface treatment, (ii) in situ laser assistance, and (iii) post-laser treatment. In this chapter, a comprehensive summary will be provided to review the current work using laser to assist cold spray process.

14.2 Pre-laser Surface Treatment

Substrate topography, substrate temperature, and surface chemistry play significant roles in bond adhesion strength (Christoulis et al. 2010; Danlos et al. 2010; Perton et al. 2012; Kromer et al. 2018a). Surface pretreatments are therefore used to enhance the adhesive quality between coating and substrate by means of decreasing interfacial contaminations and increasing surface roughness or contact area of substrate with sprayed particles. Compared to conventional surface abrasive grit-blasting prior to spraying (Danlos et al. 2010), laser surfacing has been recognized as an effective substrate pretreatment method to promote significant bond strength in cold spraying.

D.K. Christoulis et al. (2010) investigated the effect of Al alloy (AISI 2017) substrate pretreated by a nano-pulsed Nd:YAG laser ablation on cold-sprayed pure Al powder adhesion and coating buildup mechanisms. The increase of laser energy density (from 1.0 to 2.2 J/E·cm^{-2}) resulted in a highly extensive melting on surface, while a relatively smoothened substrate surface was caused by increasing of laser frequency (from 37.5 to 150 Hz). It was observed that the untreated areas presented fewer adhered particles as well as nonbonded interface (Fig. 14.2a–c), while

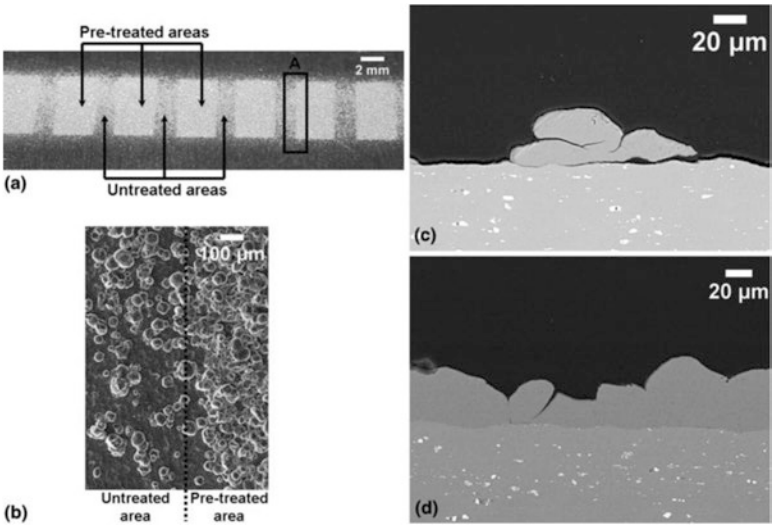

Fig. 14.2 (**a**) Macroscopic photo of the untreated and pretreated areas, (**b**) magnification of area "A" (SEM image), (**c**) SEM cross section of the untreated area, (**d**) SEM cross section of the pretreated area (2.2 J/E cm^{-2}, 18.75 Hz) (Christoulis et al. 2010)

numbers of the well-deposited particles were adhered to the laser ablated areas, forming a thin coating on the AISI 2017 substrate (Fig. 14.2d). For a further study of the cumulative effects of laser ablation and laser preheating on the adhesion of cold-sprayed coating, Y. Danlos et al. (2010) used Al6061 (18.5–74.7 µm) particles spraying onto Al2017 substrate to evaluate the deposition efficiency of coatings realized on surfaces prepared by different pretreatments. Comparing degreasing (28.09 MPa) and grit-blasting (36.1 MPa), laser ablation was proved to be useful in increasing adhesion strength (51.2 MPa) between coating and substrate, and the addition of laser heating further modified the surface topography and significantly improved coating adhesion (64.99 MPa). However, the negative effects of individual laser treatment of in situ pulsed laser ablation and continuous laser preheating on adhesion and cohesion strength of cold-sprayed Ti-6Al-4 V coatings (substrate: cylinder Ti-6Al-4V with 25 mm diameter and 10 mm thick) were found by M. Perton et al. (2012). This was attributed to the interaction between laser beam and deposited particles which in turn creates particle/particle or particle/substrate interfacial defects. On the other hand, laser preheating was proved to be beneficial for coating adhesion strength when combined with laser ablation process.

The coating delamination, cracking, or corrosion along the interface will result in a low bond strength to failure. In order to enable much stronger mechanical properties, laser surface texturing was also a critical tool for improving the performance and durability of the repaired parts by cold spraying. R. Kromer et al. (2018a) used a pulsed fiber laser operated at a diameter of 60 µm (25% larger than particle mean size) to generate two textures (Fig. 14.3a–b), corresponding to light and dense matrices of hole pattern. The deposition efficiency (DE) after one pass with respect

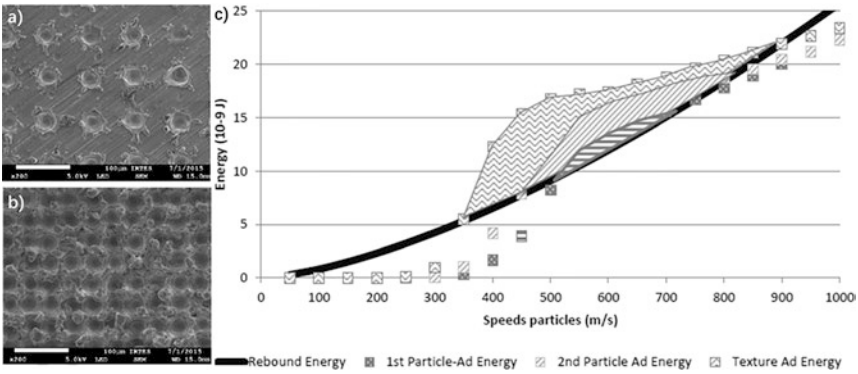

Fig. 14.3 SEM top view of textures: (**a**) distance between patterns at 150 μm, (**b**) distance between patterns at 100 μm, and (**c**) surface rebound energy and adhesion (Ad) energy function of the particle speeds (particle mean diameter = 40 μm) – particle impact on different surface shapes: first particle on raw surface, second particle on raw surface (impact on previous formed crater), and particle impact on textured surface (cavity) – the area represents the window of deposition (Kromer et al. 2018a)

to different pretreatments (GB, 12%; texture 1, 34%; and texture 2, 57%) was clarified; however, coatings showed a similar DE equal to around 67% for different pretreated substrates. Mechanical tests demonstrated that particle bonding can be improved by the textured surface via boarding the range of particle impact velocity as illustrated in Fig. 14.3c. By laser surface texturing pretreatment, R. Kromer et al. (2018b) also studied different cold-sprayed metallic coatings (Al, Ti, and Cu) onto the corresponding ceramic substrates (Al_2O_3, TiC, and Al_2O_3). Results showed that laser surface texturing increases cold-sprayed coating deposition efficiency of metallic coatings on the patterned ceramic substrates compared to raw surface.

14.3 In Situ Laser-Assisted Cold Spray (LACS)

Conventional cold spray process Laser-assisted cold spray (LACS) has been widely employed to deposit relatively soft, heat-sensitive, and oxidation-sensitive materials such as Al (Jenkins et al. 2019), Cu (Sudharshan Phani et al. 2007), Ti (Li et al. 2018a), and so on. However, it has been a challenge for high-hardness materials such as Stellite 6 and tungsten to deposit due to the poor plasticity of spraying particles. The particles experience insufficient plastic deformation during the deposition process which usually results in low deposition efficiency, porous structure, low bonding strength with substrate and poor mechanical properties of the deposit. Thus, deposition of such particles often needs higher critical impact velocities to obtain required localized plastic deformation at particle-substrate and interparticle interfaces. In order to achieve that critical velocity, unsustainable helium is usually selected as propulsive gas for particle acceleration despite its high cost. In

addition, the high gas pressure and high gas temperature are often considered as essential processing conditions which may lead to increased oxidation and phase change. If the substrate and feedstock can be softened by a heating laser during the deposition process, the powders would be easier to form deposit with better deposit properties and interface bonding. Furthermore, the propulsive gas may be replaced by nitrogen or compressed air and the need for gas heating may be eliminated, which extends the range of deposited materials and reduces the cost at the same time.

14.3.1 Working Principle of LACS

To solve this inherent problem, laser-assisted cold spray (LACS), also named supersonic laser deposition (SLD), was firstly reported by the University of Cambridge in 2009 (Bray et al. 2009). This novel hybrid manufacturing technique combines the advantages of cold spray and laser irradiation to deposit feedstock powders onto substrate. Figure 14.4 shows the laser-assisted cold spray system. A high-pressure gas supply (N_2) is divided to two streams and sent to a de Laval nozzle both directly and through powder feeder. The powder particles are accelerated to supersonic speeds in the nozzle where two streams converge and impact toward the substrate. The deposition region is simultaneously illuminated by a maximum power of 4 kW of the diode laser of 960–980 nm (LDF 4.000–100, Laserline, Germany) in order to soften the substrate and particles to allow the formation of deposits. The real-time temperature of deposition area is monitored with a pyrometer (Bray et al. 2009).

14.3.2 Microstructures and Properties of LACS Coatings

In order to investigate the powder deposition behaviour by cold spray assisted with in-situ laser irradiation, titanium powders were firstly deposited onto steel substrate using nitrogen (Bray et al. 2009). The titanium deposits fabricated using LACS showed significantly improved performance than the deposit built by conventional cold spray. The porosities of the deposits ranged from 0.3% to 0.6% which

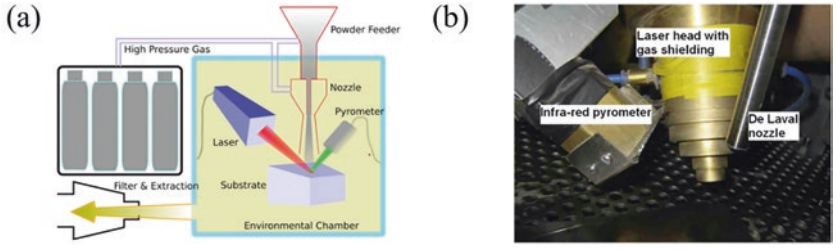

Fig. 14.4 Laser-assisted cold spray system (Bray et al. 2009)

were much lower than that of cold spray titanium deposits (2–4%). One of the concerns brought by laser heating in the process of depositiion is the oxidation of the feedstock powder. However, the level of oxygen of LACS deposit was 0.6 wt.% which was close to that of cold spray titanium deposit. Even the power of laser increased from 720 W (600 °C) to 1000 W (900 °C), the deposits had a close oxide level which could be explained by the fact that in-flight particles heated by laser for a limited period (Bray et al. 2009). The deposition mechanism of LACS titanium deposit varies from that of cold spray one. The particles experienced less overall plastic deformation compared with cold spray, but the deformation appeared on the top surface of each particle was more significant, as shown in Fig. 14.5a. By introducing high-power laser into cold spray process, both the powders and deposition region of the substrate are heated synchronously which makes them soften. Therefore, it is easier for titanium powders to embed into a heated and softened substrate or previously formed deposit layers at lower impact velocities.

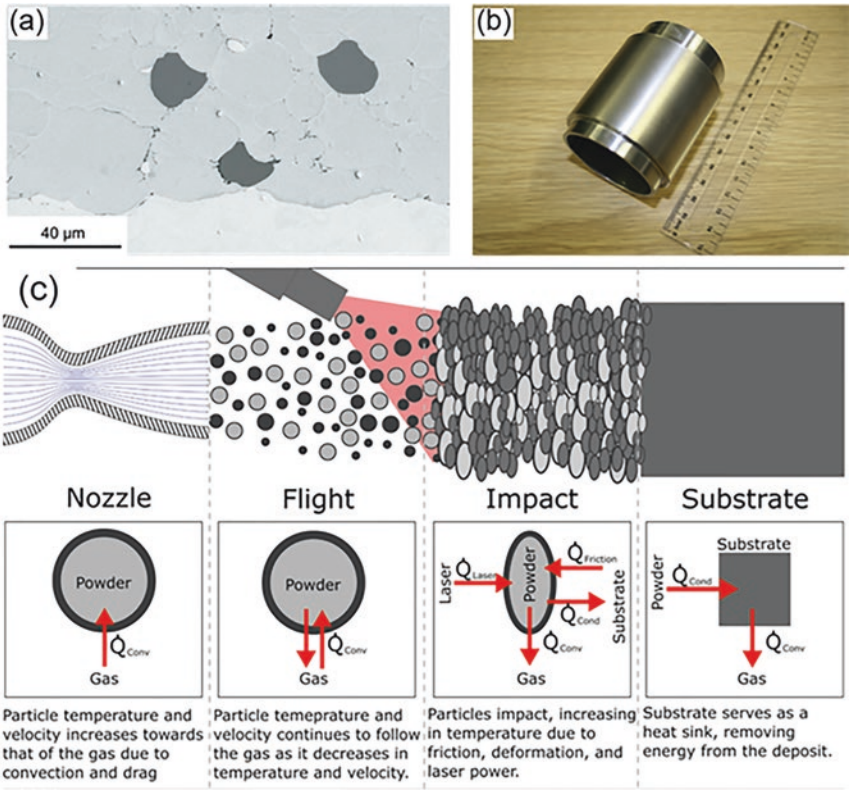

Fig. 14.5 (**a**) SEM image of titanium deposited onto steel at 500 °C with deformed particles highlighted (Bray et al. 2009); (**b**) thick titanium coating (3 mm) on a steel tube (Lupoi et al. 2011); (**c**) overview of the thermodynamic and heat transfer phenomena associated with the LACS process (Birt et al. 2017)

In 2011, based on the origin system (Bray et al. 2009), the titanium powders were deposited over a turning low-carbon steel tube, as shown in Fig. 14.5b. The machinability and ductility of titanium deposit were demonstrated in the operation of thickness reduction on a lathe, and no cracks or deposit detachment was observed. The deposit showed a low porosity, approximately 1.5 times higher microhardness than conventional pure titanium and nearly four times higher adhesion strength than the deposit produced by cold spray (Lupoi et al. 2011). Figure 14.5c shows an overview of the thermodynamic and heat transfer phenomena associated with the LACS process. The particle temperature upon impact with the substrate increased due to the in-situ laser irradation besides the plastic deformation.

After the deposition of dense titanium deposits with improved performance, the LACS was further employed to fabricate some high-hardness materials such as tungsten (Jones et al. 2014), Ni60 (Yao et al. 2015a), and Stellite 6 (Luo et al. 2012; Li et al. 2018b). Tungsten is a typical high-hardness material with the highest melting temperature among all metals. In conventional cold spray process, the high density of tungsten powders makes them difficult to accelerate to their critical velocities. Hence, high cost of helium is usually selected as processing gas (Zhang et al. 2012). Thanks to the presence of LACS, the particles can be deposited more easily at much-reduced critical velocities. The tungsten powders were deposited onto molybdenum substrate using a laser-assisted cold spray system (Jones et al. 2014). The deposit was porosity-free with approximately 95% density of wrought tungsten. Based on the three-point bend test, the tungsten deposit also exhibited tensile strength that was comparable to wrought tungsten with no evidence of deposit-substrate melting at the interface, tungsten feedstock melting, and molybdenum substrate grain growth (Jones et al. 2014). It shows potential to manufacture high performance tungsten deposits and repair X-ray targets by LACS as the impact area can be heated to above the ductile brittle transition temperature and effective bonding can be achieved without the need to melt the material.

Ni60 is another typical difficult-to-deposit material by conventional cold spray. Hard Ni60 alloy powders (58–62 HRC) were deposited on a surface-treated medium carbon steel substrate with a continuous wave diode laser heating both the powders and substrate (Yao et al. 2015a). The Ni60 deposit exhibited fine microstructure and stable phases as original powders indicating solid-state deposition characteristics. The average hardness of the LACS Ni60 deposit was up to 867 ± 24 HV0.3 due to the presence of more hard CrB ceramic and Cr_mC_n carbides (Yao et al. 2015a; Hemmati et al. 2012). The following wear test and electrochemical test indicated that the deposit also showed good sliding wear resistance and corrosion resistance.

Stellite 6® is known as a wear and corrosion resistant Co-based alloy which has been widely applied in automotive and aerospace industries. Although it has been reported that Stellite deposits were successfully manufactured by cold spray process under the optimized parameters (Magarò et al. 2019; Cinca et al. 2013), the high gas pressure (3.8–5.0 MPa) and elevated gas temperature (780–1050 °C) were indispensable during the deposition process. Even so, the deposition efficiency was relatively low (13.3 ± 1.3 ~ 21.4 ± 1.2 %) (Cinca et al. 2013). While the Stellite 6 deposits built up by LACS process with lower gas pressure (~ 3.0 MPa) and

temperature (~ 500 °C) displayed crack-free structures with low porosities, high bond strengths and good wear properties which were comparable or even better than deposits fabricated by laser cladding or high velocity oxygen fuel (HVOF) (Lupoi et al. 2011; Luo et al. 2012; Luo et al. 2013; Li et al. 2018b). The deposits retained the initial microstructure and phase of the feedstocks. The refined submicron-scale microstructure (200–400 nm) without dilution layer triggerred low friction coefficient and weight loss (Fig. 14.6b). It can be seen from Figs. 14.7 and 14.8 that the surface roughness and deposition efficiency of Stellite 6 deposits were significantly influenced by the deposition temperature from 1210 °C to 1290 °C (Li et al. 2018b). The increase of temperature at deposition site indicates the particles would obtain more thermal energy which promotes effective bonding. Based on the simulation results, the optimal deposition parameters for particle/substrate interface bonding happened when the deposition temperature reached at 1000 °C with particle diameter of 40 μm (Luo et al. 2014b). Further study indicated that the interface bonding between deposit/substrate and particle/particle was enhanced with the heated effect by laser irradiation. Dimple or tear zone was observed from the fracture surface which indicated that partial metallurgical bonding between particles resulted in improved mechanical properties (Yao et al. 2016; Luo et al. 2013).

In addition to build single material deposits, the LACS process was also employed to fabricate metal matrix composite (MMC) deposits. Tungsten carbide(WC) (Li et al. 2015a; Luo et al. 2015) and diamond (Yao et al. 2015b; Yang et al. 2015) particles were usually mixed with feedstocks as reinforced particles to further improve deposit properties. Li et al. compared the microstructure and tribology performance of WC (30 vol.%)-reinforced SS316L (70 vol.%) composite deposits manufactured by CS and LACS, respectively (Li et al. 2015a). With higher deposition temperature assisted by laser irradiation, the SS316L powders became softer which allowed more WC particles to embed in the formed deposit and thus resulted in higher WC particle concentration. This led to higher deposit density, higher interface bonding strength, and better tribological properties, as shown in Fig. 14.9. Similarly, Stellite 6 composite deposit reinforced by 30 vol.% WC particles also exhibited ideal interface bonding as shown in Fig. 14.10a-c. The EDS scanning line (Fig. 14.10d)

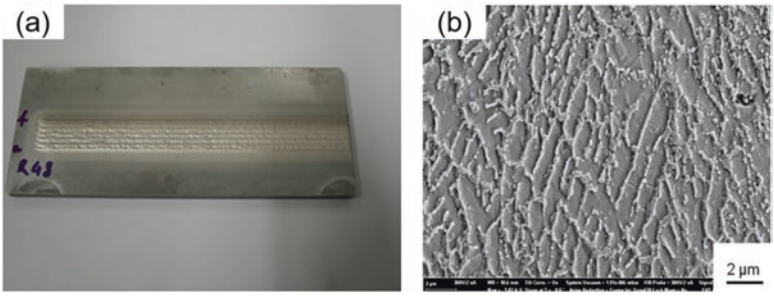

Fig. 14.6 (**a**) Stellite 6® deposit by LACS, (**b**) SEM micrograph of LACS Stellite 6 (Luo et al. 2012)

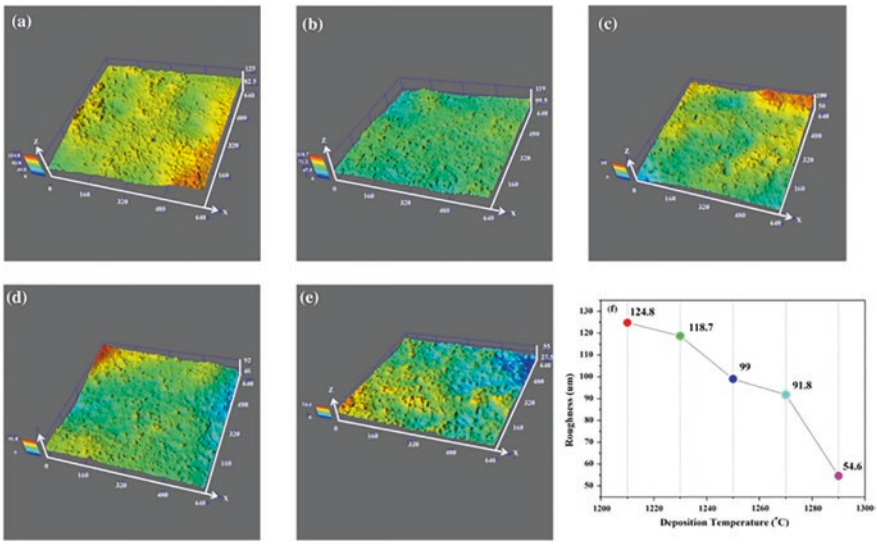

Fig. 14.7 Three-dimensional (3D) profiles of the LACS Stellite 6 coatings' surfaces: (**a**) 1210 °C, (**b**) 1230 °C, (**c**) 1250 °C, (**d**) 1270 °C, (**e**) 1290 °C, and the variation of roughness with deposition temperature (**f**) (Li et al. 2018b)

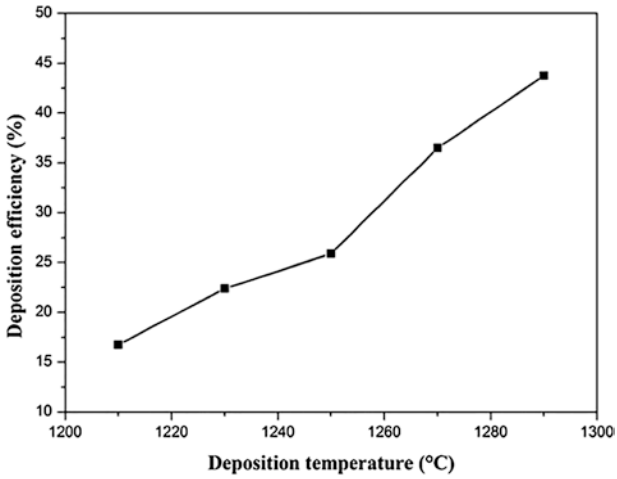

Fig. 14.8 The variation of deposition efficiency with deposition temperature (Li et al. 2018b)

showed elements interdiffusion between WC particle and Stellite 6, which was the evidence of metallurgical bonding. The heat from laser irradition and high strain rate upon impact led to an incresing temperature at the the particle contact interface thus promoting element diffusion to achieve metallurgical bonding. The bonding mechanism is coexistence of mechanical and metallurgical bonding with the effect of laser heating, while the bonding mechanism of CS is dominant mechanical

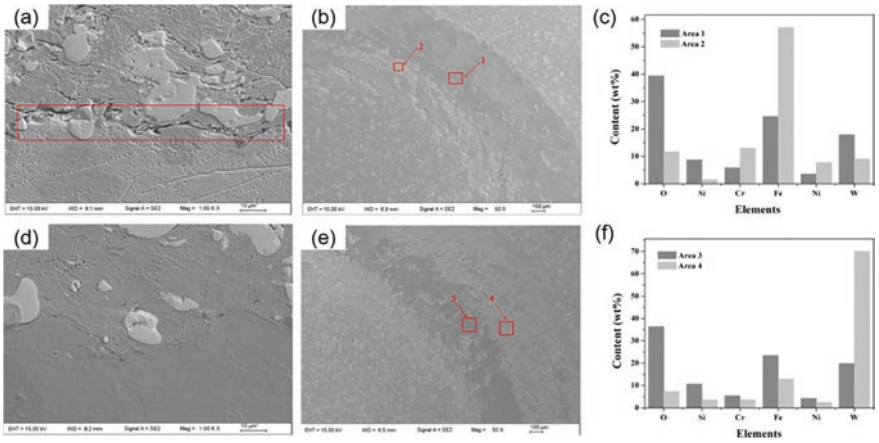

Fig. 14.9 Cold spray (top row) and laser-assisted cold spray (bottom row) deposits: (**a**, **d**) deposit/substrate interface, (**b**, **e**) worn surface morphology, and (**c**, **f**) EDS analysis of worn surface (Li et al. 2015a)

interlocking (Li et al. 2017). The investigation performed by Yao et al. found that after introducing laser into cold spray system, 20 wt.% diamond and 80 wt.% Ni60 feedstocks were successfully deposited with exhibited dense and crack-free structure. The interface bonding between deposit and substrate and between the Ni60 matrix and diamond particles was enhanced by laser irradiation. The low-temperature deposition feature of LACS is beneficial to suppress the graphitization and oxidation of diamond particles (Yao et al. 2015b; Yang et al. 2015).

Deposition temperature decided by the laser power is significant for improving deposit properties. In the investigation of austenitic steel (316L) deposit produced by LACS, it was proposed that insufficient laser power led to disruption of the deposition process stability and coating cracking. Powder detachment from the deposit was observed due to the lack of substrate heating, as shown in Fig. 14.11 a and e. The instability in deposit formation and insufficient bonding resulted in the cracks and poor structure which can be seen in Fig. 14.12a. While an exorbitant deposition temperature will also lead to the degradation of deposit performance. In the work of Luo et al., 30% WC particles were mixed with 70% Ni60 and deposited onto carbon steel substrate at various laser powers from 2.0 to 4.0 kW (Luo et al. 2015). With the increase of laser power, more pits or pores in the deposit appeared because of partially melting at higher laser power. Higher laser energy resulted in larger sizes of Ni60 particles, carbide particles, and less WC contents which triggerred reduced wear resistance of the deposit. Fe–Ni–Zr oxide dispersion strengthened steel was deposited by cold spray with and without laser. It was found that high deposition temperature induced by laser irradiation led to larger grain size, as shown in Fig. 14.13. The deposit produced with the highest laser power (1084 W) had a nearly four times larger average grain diameter than the one produced by cold spray which would be expected to result in a loss strength and toughness (Story et al. 2018).

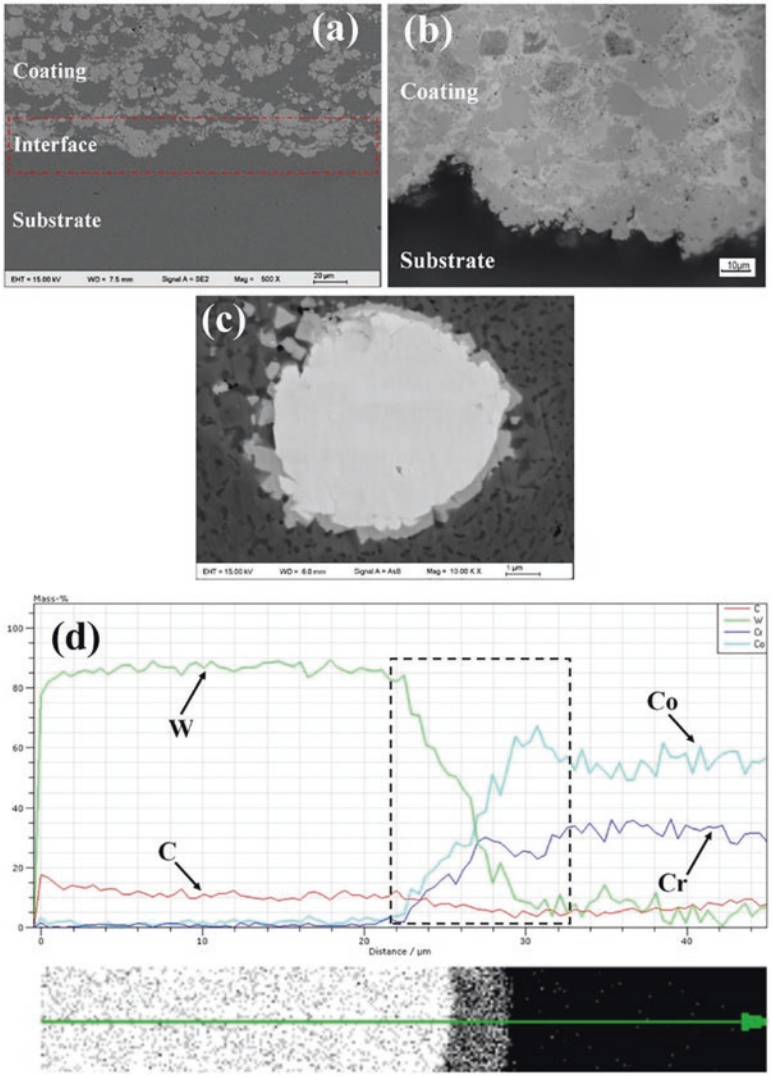

Fig. 14.10 Interface bonding in the SLD coating specimen: (**a**, **b**) coating/substrate bonding, (**c**) WC/matrix bonding, and (**d**) the EDS line scanning of the WC/matrix interface layer (Li et al. 2017)

14.4 Laser Posttreatment of Cold-Sprayed Coatings

In addition to laser-assisted cold spray (LACS), laser has also been employed to post treat the as-sprayed deposits and modify their mechanical properties (Li et al. 2020; Sun et al. 2020). In the laser remelting (LR) process, high heat input from laser beam can remelt the coating surface and form a melting pool, followed by rapid solidification. A schematic diagram of the laser post-treatment on the

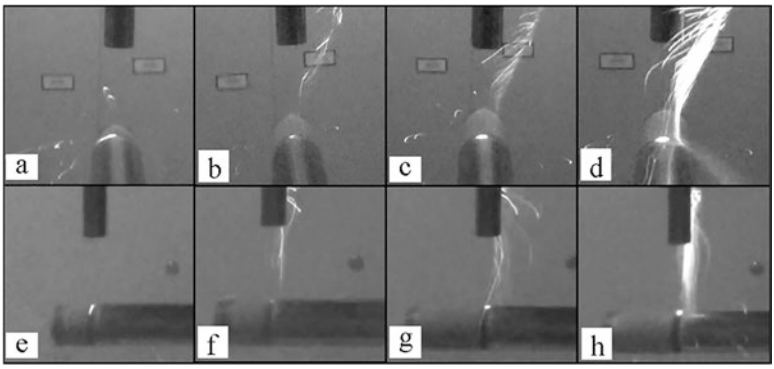

Fig. 14.11 Scheme of deposition regimes work out: (**a**, **e**) T = 700 °C, V = 15 g/min; (**b**, **f**) T = 1000 °C, V = 15 g/min; (**c**, **g**) T = 1300 °C, V = 15 g/min; (**d**, **h**) T = 1300 °C, V = 30 g/min; V, feeding velocity; T, temperature in the deposition zone (Gorunov and Gilmutdinov 2017)

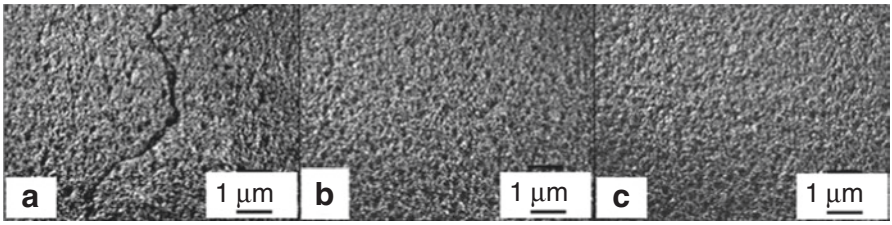

Fig. 14.12 Types of surfaces at different modes of supersonic laser deposition: (**a**) T = 700 °C, V = 15 g/min; (**b**) T = 1000 °C, V = 15 g/min; (**c**) T = 1300 °C, V = 15 g/min (Gorunov and Gilmutdinov 2017)

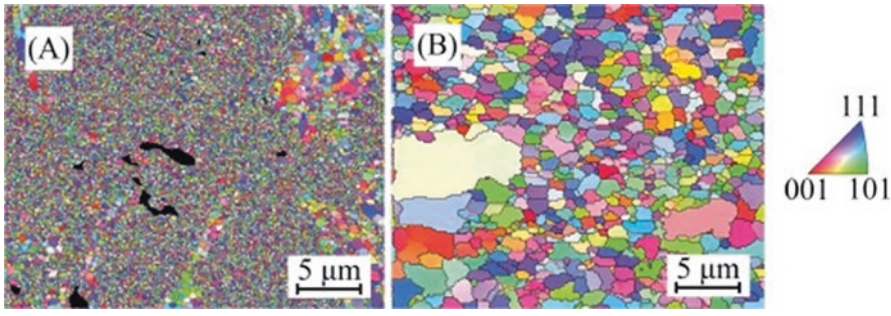

Fig. 14.13 Inverse pole figure orientation maps for deposits produced at (**a**) 320 °C, without laser, and (**b**) 950 °C, laser power: 1084 W (Story et al. 2018)

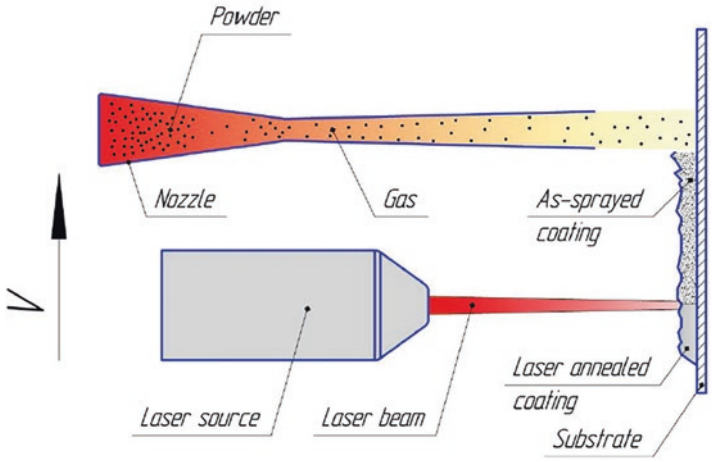

Fig. 14.14 Schematic graphs of laser posttreatment on the cold-sprayed coatings (Podrabinnik and Shishkovsky 2017)

cold-sprayed coatings is shown in Fig. 14.14. During the LR process, the coating surface morphology can be improved, and the defects within the coatings such as interconnected pores and inter-splat boundaries can be reduced or eliminated. A fine and homogenous structure resulting from rapid solidification further improves the mechanical and corrosion properties of the coating. In addition, a strategy combining cold spraying of powder mixtures and LR is capable of in situ synthesis of composites. Up to now, post-LR has been applied to treat a variety of cold-sprayed coatings including Ti and its alloy (Marrocco et al. 2011; Carlone et al. 2016; Astarita et al. 2015; Rubino et al. 2016), Ni alloy (Poza et al. 2014), stainless steels (Sova et al. 2013; Adachi and Ueda 2015), Al and its alloy (Jing and Dejun 2018; Kang et al. 2017), and metal matrix composites (Podrabinnik et al. 2015; Podrabinnik and Shishkovsky 2017; Orishich et al. 2018). The current achievements on LR of cold-sprayed coating are summarized in Table 14.1. Detailed discussions will be addressed in terms of surface morphology evolution, microstructure and phase composition evolution, composite synthesis, and mechanical and corrosion properties.

14.4.1 Surface Morphology and Roughness Evolution

LR was widely applied to modify the surface morphology of the coatings. In the as-sprayed state, the deformed particles are closely combined with a clear interface and pores between the particles (Figs. 14.15a and 14.16a). After LR, the profiles of particles disappeared by forming a much smoother surface (Figs. 14.15b and 14.16b, c). In the case of Al coating, some fine Al particles can be still observed on the coating surface after LR (Fig. 14.15d). Nevertheless, the roughness of coating surface is

Table 14.1 Summary of the research work on laser-remelting of the cold-sprayed coatings

Coatings	Substrate	Feedstocks	LR parameters	Main findings	References
Ti	Carbon steel	Pure Ti powder	CO_2 laser Laser power: 440–1000 W Scan speed: 21.6–48.3 mm/s Spot size: 0.3–1.08 mm	LR eliminates interconnected porosity that creates a high-quality barrier layer that has corrosion properties very close to the bulk Ti	Marrocco et al. (2011)
Ti	AA2024-T3	Grade 2 Ti particles	Diode laser Laser power: 220 W Scan speed: 12.5–1000 mm/min Spot diameter: 2 mm	LR produces a hard oxidized layer on Ti coating. The temper state of the aluminum substrate was not affected during the process	Carlone et al. (2016), Astarita et al. (2015), and Rubino et al. (2016)
Ti64	Ti64	Ti64 powder (size: 1–45 μm	Nd:YAG laser (1064 nm) Frequency: 12,000 HZ Laser power: 50–200 W Scan speed: 20 mm/s	After LR, the surface roughness and coating hardness became higher with higher laser power, while the tribological properties were significantly influenced by the laser power	Khun et al. (2019)
Al	S355 structural steel	Pure Al powder (20–45 μm)	2000 W all-solid fiber Laser power: 800 W Spot diameter: 5 mm	LR reduces the porosity, increase the microhardness, and improve the corrosion wear resistance of Al coatings	Jing and Dejun, (2018)
316 L stainless steel	Al	316 L stainless steel powders	Nd:YAG laser (1064 nm) Power: 500 W Scan speed: 100 mm/s	LR significantly reduces porosity and improves the corrosion resistance	Sova et al. (2013)

(continued)

Table 14.1 (continued)

Coatings	Substrate	Feedstocks	LR parameters	Main findings	References
316 L stainless steel	316 L stainless steel	316 L stainless steel powders	A semiconductor laser system, LDL160–1000 Power: 500 W Scan speed: 12 mm/s	LR densifies the microstructure by fusing and removing defects. The laser-remelted coatings protected the carbon steel substrate from corrosion in NaCl solution	Adachi and Ueda (2015)
Inconel 625	304 stainless steel	Inconel 625 powders	High-power diode laser Laser power: 70 W Scan speed: 25–50 mm/s Heat input: 14–28 J/mm	LR results in reduced interconnected porosity and increased modulus but decreased microhardness due to columnar dendritic microstructure	Poza et al. (2014)
Al–Si	Al	Pure Al powder + pure Si powder	CW ytterbium fiber laser Laser power: 200–300 W Scan speed: 1000 mm/s Hatch distance: 50 μm	After LR, the microstructure of Al–Si coating was significantly refined, and the coating surface roughness was lowered.	Kang et al. (2017)
Al/alumina–Ni composite	Al alloy	Nano-sized Al_2O_3 + Al12Si powder + Ni alloy powder	A continuous-wave ytterbium fiber laser (1075 nm) Laser power: 10–40 W Scan speed: 5–10 mm/s	LR leads to pore healing, homogenous redistribution, and intensifies intermetallic phase formation in the Ni–Al system	Podrabinnik et al. (2015) and Podrabinnik and Shishkovsky (2017)
(Ti + Al)–WC composite	—	B_4C powder WC powder Ti and Ni powder	A continuous CO_2 layer	A heterogeneous structure without pores and cracks by the consequent deposition of the powder by the CS method, followed by the laser treatment	Orishich et al. (2018)

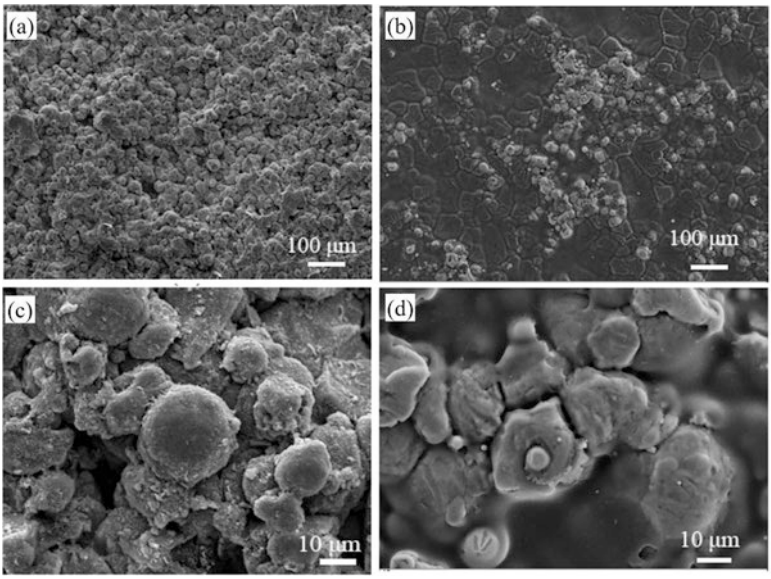

Fig. 14.15 Surface morphologies of cold-sprayed Al coating before (**a**, **c**) and after laser remelting (**b**, **d**) at different magnifications (Jing and Dejun 2018)

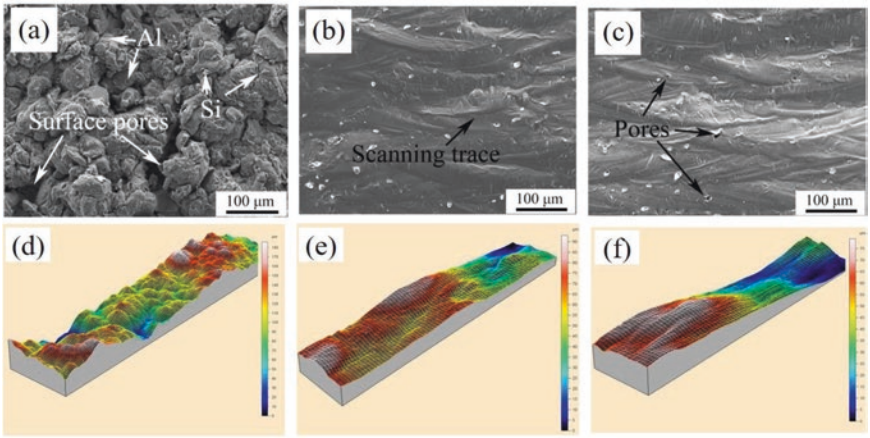

Fig. 14.16 Surface morphologies of cold-sprayed (**a**) and remelted Al-6 wt.% Si coatings at laser power of 200 W (**b**) and 300 W (**c**). (**d–f**) are the corresponding 3D profiles (Kang et al. 2017)

significantly reduced. As shown in Fig. 14.15, traces of the laser beam track and some very fine pores can be clearly seen after LR of the Al–Si coating. It was found that a higher power (300 W) can result in a large number of these pores on the coating surface. Ra of the coating decreases from 12.2 μm to about 5 μm using a laser power of 250 W. Therefore, the roughness of cold-sprayed deposits (untreated state)

could be decreased significantly after laser remelting process. In addition, it is interesting to investigate the effect of LR process on the surface morphology of the polished (smooth) coatings. The surface topographies and morphologies of the laser-treated Ti64 coatings with different laser powers are shown in Figs. 14.17 and 14.18. It was found that the surfaces of the laser-treated Ti64 coatings become rougher with higher laser power, and the highest laser power of 200 W exhibited the highest surface roughness (Khun et al. 2019). The increased roughness using high

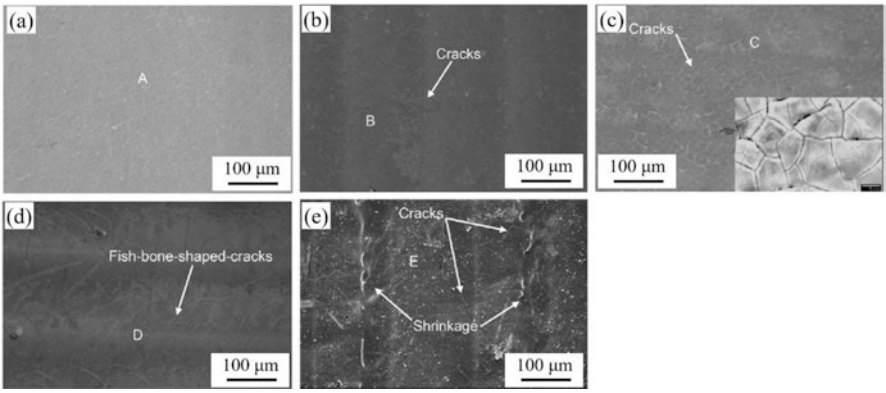

Fig. 14.17 Surface morphologies of laser-treated Ti64 coatings with laser powers of (**a**) 50 W, (**b**) 100 W, (**c**) 150 W, and (**d**) 200 W. The inset in (**b**) shows the magnified surface morphology of the same coating (Khun et al. 2019)

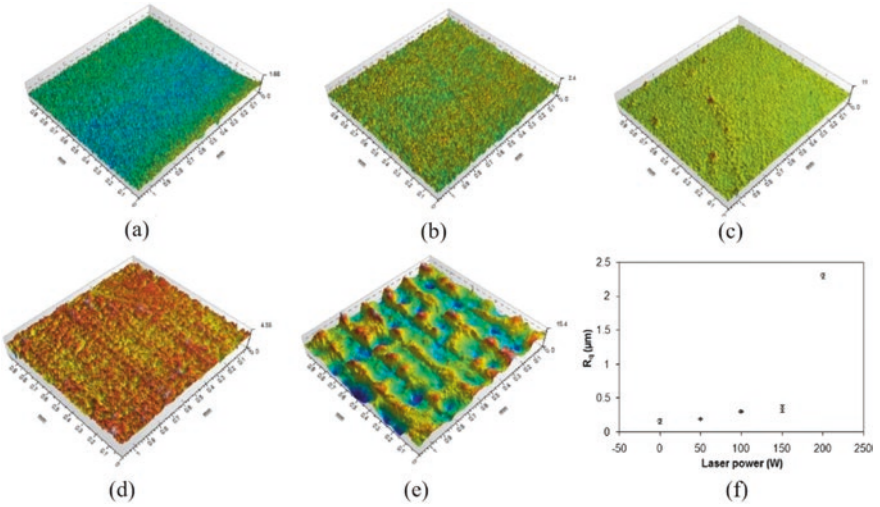

Fig. 14.18 Surface morphologies of (**a**) cold-sprayed and laser-treated Ti64 coatings with laser powers of (**b**) 50 W, (**c**) 100 W, (**d**) 150 W, and (**e**) 200 W. (**f**) Ra of untreated Ti64 coating and laser-treated Ti64 coatings with different laser powers. A laser power of 0 represents the untreated Ti64 coating (Khun et al. 2019)

laser power can be explained by the rapid cooling caused by the greatest temperature difference between the coating temperature and room temperature, which results in protruded asperities and dimples on the surface topography via the most severe surface shrinkage (Xue et al. 1997; Yilbas et al. 2011).

14.4.2 Microstructure and Phase Composition Evolution

The cold-sprayed coating is featured by a lamellar structure with interconnected pores and inter-splat boundaries resulting from insufficient plastic deformation of the particles during CS deposition. After LR, the microstructure can be completely changed. An example of the cold-sprayed Inconel 625 alloy is shown in Fig. 14.19. A significant reduction of porosity, free of cracks, and fine columnar dendritic microstructures were obtained after LR. The low secondary arm spacing was around 1 μm, indicating a very high cooling rate during solidification. A higher scan speed results in a higher cooling rate and thus a finer structure, which is consistent with selective laser melting or laser cladding process (Li et al. 2015b; Dinda et al. 2009). Compared with the microstuctures of LR Inconel 625 coating (Fig. 14.19b,c), a fast scan speed related to low thermal input limits the beneficial effect in terms of porosity reduction in the regions near the coating/substrate interface. The authors also pointed out that it is important to control the heat input by modifying the scan speed or laser power so that the substrate remelting can be avoided. Otherwise, it would lead to a reduction of coating cohesion and substrate-coating adhesion.

A significant reduction of porosity, elimination of inter-splat boundaries, and homogenous grain structure were also observed on the cold-sprayed 316 L stainless steel coating after LR, as shown in Fig. 14.20. The densification of the LR region is

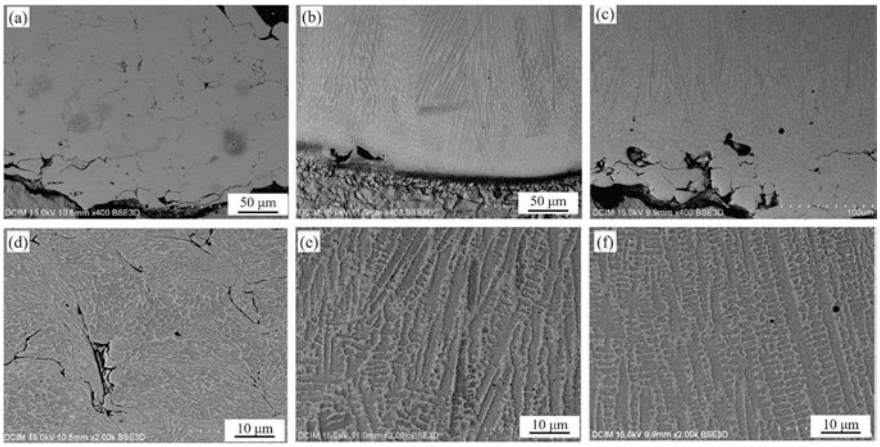

Fig. 14.19 SEM images of (**a**, **d**) cold-sprayed and laser-remelted Inconel 625 coating at scanning speed of (**b**, **e**) 25 mm/s and (**c**, **f**) 45 mm/s (Poza et al. 2014)

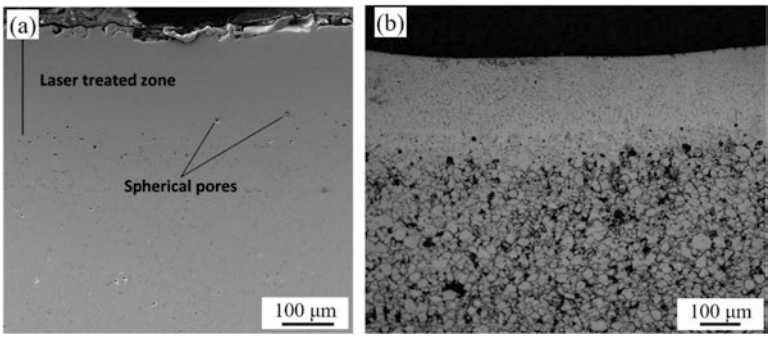

Fig. 14.20 (**a**) SEM and (**b**) optical micrograph images of 316L stainless steel coating cross section after the laser treatment (Sova et al. 2013)

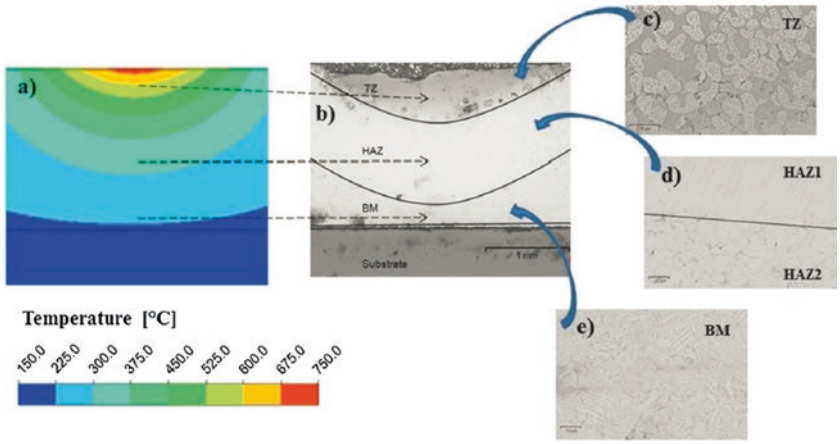

Fig. 14.21 Predicted temperature distributions and microstructures of the laser-remelted regions of cold-sprayed Ti coatings (Carlone et al. 2016)

due to its melting and porosity escaping to the free surface with the subsequent resolidification of the treated area. A few isolated spherical pores observed near the remelting interface are probably trapped gas pores, that is, the typical feature of laser-treated thermal/cold-sprayed coatings. Fine grains are mostly oriented perpendicular to the coating surface toward to the direction of cooling propagation after remelting. Since the deposited coating is thick (>2 mm), the interface of treated coatings was not influenced by surface laser treatment.

During the remelting, the region involved in the process undergoes a great thermal gradient from the remelted pool to the base material (Fig. 14.21a). Consequently, three different zones are visible in the remelted regions of Ti coatings: the treated zone (TZ), the heat-affected zone (HAZ), and the base material (BM). The microstructure in each zone is determined by both the maximum temperature achieved

and the cooling rate. The BM is characterized by a full lamellar microstructure with very thin lamellae, resulting from plastic deformation of the gas-atomized Ti powder. Compared to the BM zone, a similar structure with coarser lamellae is observed in HAZ (Fig. 14.21d). The increased lamellae size is due to a certain heat input during the remelting process. The TZ is featured by equiaxial α-grains and martensitic acicular α-grains (Fig. 14.21c). During the solidification process of this region, β-dendritic grain grows in the direction of the heat flow. When the temperature reaches the β-transus (i.e., 913 °C) and the cooling rate is high enough, diffusionless transformation from β- to α-martensitic structure occurs. Similarly, a transition zone was observed between the RZ and HAZ (Fig. 14.21d), where some acicular martensitic α-grains were formed due to the high cooling rate. The microstructure evolution within these regions can affect significantly the properties.

EDS analysis was conducted to determine the evolution of Ti and oxygen content within the remelted regions (Fig. 14.22). TZ is composed of titanium and oxygen with an atomic fraction (37% Ti and 63% O) corresponding to the stoichiometric composition of the titanium dioxide TiO2. Then, the oxygen content decreases in the direction from the surface to the inner layers of the coating. According to XRD patterns (Fig. 14.23), typical rutile peaks were found at the treated surface, while a mixture of rutile and other titanium oxides was observed in the inner layers of the TZ. The variation of phase composition in different regions can be attributed to the temperature evolution during LR process.

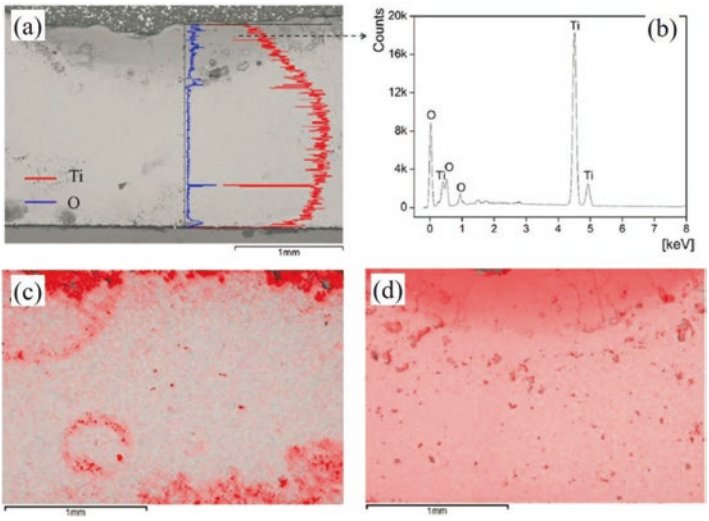

Fig. 14.22 EDX analysis for laser-remelted Ti coatings: (**a**) EDS through the thickness line scan, (**b**) titanium and oxygen intensities in the TZ; oxygen composition maps of (**c**) untreated coating and (**d**) treated coating (Carlone et al. 2016)

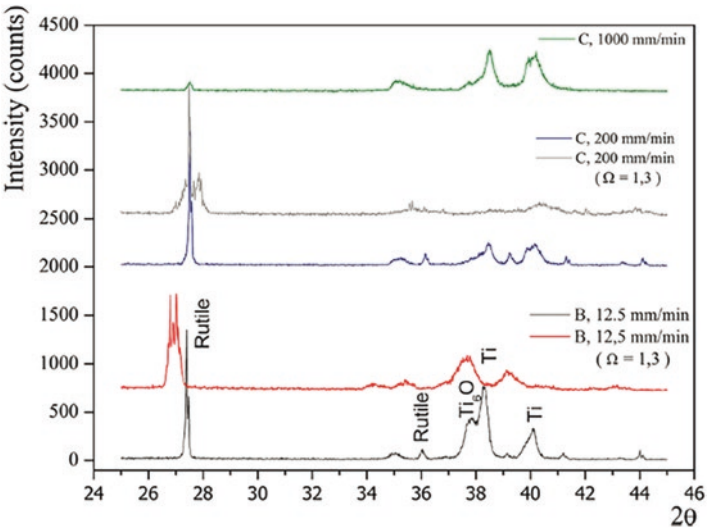

Fig. 14.23 X-ray diffraction spectra of the as-sprayed and laser-treated Ti coating (Carlone et al. 2016)

14.4.3 In Situ Synthesis of Alloy or Composite Coatings Using Powder Mixtures

Cold spray has a great flexibility in producing composite coatings by direct deposition of mixed powders. Various composites comprising of metal–ceramic mixtures and two or more metals have been fabricated successfully using cold spray. A strategy combining cold spray and LR has been developed to in situ synthesis of composites. As shown in Fig. 14.24, Al–Si (6 vol.%) alloy coating was fabricated by cold spraying of pure Al and pure Si powder mixtures, followed by LR (Kang et al. 2017). In the as-sprayed state, individual Si particles are distributed in Al matrix with clear boundaries. After LR, the Si particles disappear, while several big pores appear at the region between the laser-remelted layer and the cold-sprayed deposit. The formation of large pores is likely due to the coalescence of the smaller pores incorporated in the cold-sprayed deposit and rolled surface porosity. The small pores observed in the remelted surface layer are probably the result from some trapped gas during remelting and rapid solidification. The top surface of LR zone is characterized by equiaxed ultrafine α-Al grains due to a high cooling rate in this region. Accordingly, columnar grains that constitute the major grain morphology are presented at the bottom of the LR zone. In-between shows a mixture of equiaxed and vertical columnar grains.

In addition, nano-sized alumina ceramics was sprayed by CS process together with Al and Ni alloy powders (Podrabinnik et al. 2015). Post-LR treatment of the fabricated coatings was conducted to synthesis of AlNi–Al_2O_3 composite, which

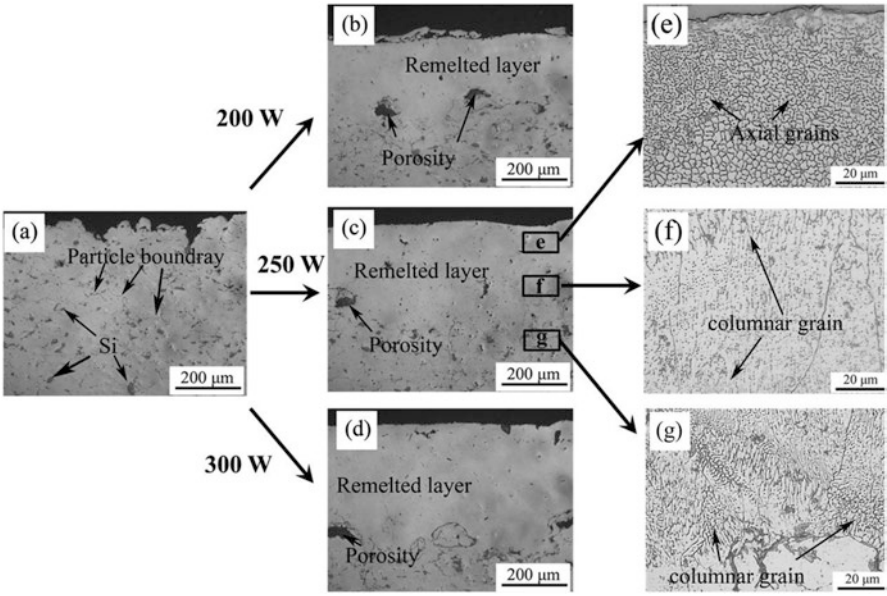

Fig. 14.24 Cross sections of (**a**) as-sprayed Al-6 vol.% Si and (**b–d**) the same sample after laser surface remelting at 200 W, 250 W, and 300 W, respectively, and (**d–f**) the corresponding microstructure of several areas (top, middle, and bottom, respectively) of the remelted layer of sample (**c**) (Kang et al. 2017)

has a great potential as a high-temperature solar selective absorbing coatings (Xue et al. 2013). As shown in Fig. 14.25, the as-sprayed coating reflects the tracks of mixing, which are improved after RL. A higher power results in a more uniform structure. It was also found that a low scan speed allows sparing time for Ni and Al diffusion redistribution and will ensure completeness of intermetallide phase formation with a smoother surface structure. Moreover, homogenous Ti–Al-based composites without pore and cracks were successfully produced by cold spraying, followed by laser action (Orishich et al. 2018).

14.4.4 Hardness Evolution and Wear Property Enhancement

The microhardness evolution within the laser-treated region depends on the microstructure, phase composition, and residual stress after LR. An example of the microhardness evolution in cold-sprayed Ti coating after LR is shown in Fig. 14.26a. On the treated coating surface, the microhardness values ranged from 700 to 1200 HV depending on the laser scan speed. A lower scan speed can lead to a higher microhardness value. Such increased microhardness is attributed to the formation of hard rutile phase due to the laser-induced thermal oxidation at the surface. At a higher

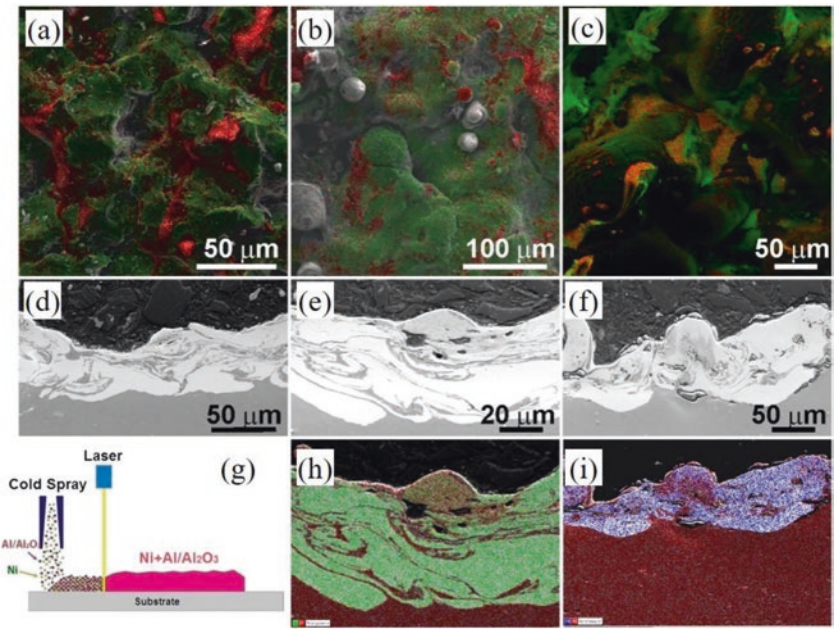

Fig. 14.25 SEM images and EDS maps of (Ni, green; Al, red color) top surfaces and cross sections of the CS coating: (**a**, **d**) the CS without LR; (**b**, **e**, and **h**) laser treated under laser power of 10 W; (**c**, **f**, and **i**) laser treated under laser power of 20 W (Podrabinnik et al. 2015)

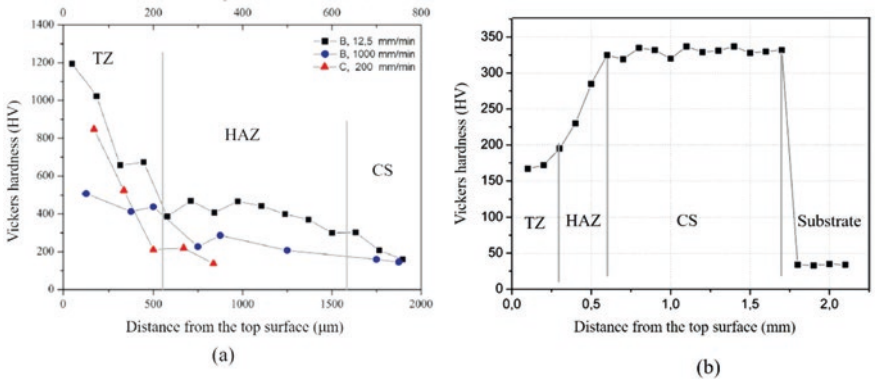

Fig. 14.26 Microhardness evolution of the laser-treated coatings: (**a**) Ti; (**b**) 316 L

scan speed (1000 mm/min), the temperature experienced by the material and the residence time were not sufficient to promote direct rutile formation and thus a lower hardness. The microhardness value for each group decreases sharply within the TZ region, followed by experiencing a gradual decrease within the HAZ. This observation is consistent well with the evolution of phase composition and microstructure (Fig. 14.21).

Figure 14.26b shows the microhardness evolution of laser-treated 316 L coating. The profile shows that the coating microhardness dramatically decreases from ~330 HV at as-sprayed zone to ~170 HV in LT zone. A gradual decrease of microhardness is observed within the HAZ of a thickness of about 300 μm. The deceased microhardness in these regions results from residual stress release induced by laser annealing. Decreased microhardness was also observed in the laser-treated Inconel 625 coating (Poza et al. 2014) due to the presence of columnar dendritic microstructure as the highly deformed as-sprayed microstructure was relaxed after LR. More heat input at a lower scan speed affects the steel substrate. Consequently, the induced Fe content from substrate into the coating leads to an increment in hardness at a lower speed. A higher elastic modulus was obtained due to the reduced porosity, but it is independent of the laser scan speed (Fig. 14.27).

Figure 14.28 (a–e) shows the wear topographies of the cold-sprayed and laser-treated Ti64 coatings with different laser powers against 100Cr6 steel balls. The untreated Ti64 coating shows a deep wear track on its surface, indicating a high wear rate (93.9 × 10–14 $m^3 \bullet N^{-1} \bullet m^{-1}$). A narrower wear track for the laser-treated Ti64 coating with 50 W (Fig. 14.9b) implies a lower wear rate than the untreated Ti64 coating. When increasing the laser power (100–200 W), the wear tracks of the coating surface become very small and not measurable. The wear track morphologies also clearly show that the Ti64 coatings treated with laser powers of 100–200 W significantly prevent their surface wear against the counter steel balls. The increased wear resistances of the coatings after LR is associated with their enhanced surface hardness.

Zhang et al. investigated the wear performance of cold-sprayed Al and laser-treated Al coatings in a 3.5 wt.% NaCl solution using different loads (Jing and Dejun 2018). It was found out that the track depth (wear rates) increased with the

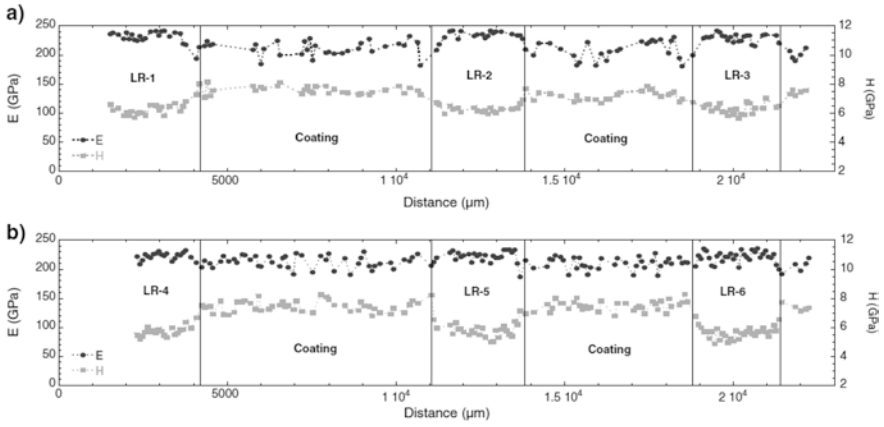

Fig. 14.27 Elastic modulus and hardness values obtained from indentation lines carried out along the transversal direction of the laser-remelted Inconel 625 coatings. (**a**) High energetic conditions: 25 mm/s, 30 mm/s, and 35 mm/s. (**b**) Less energetic conditions: 40 mm/s, 45 mm/s, and 50 mm/s (Poza et al. 2014)

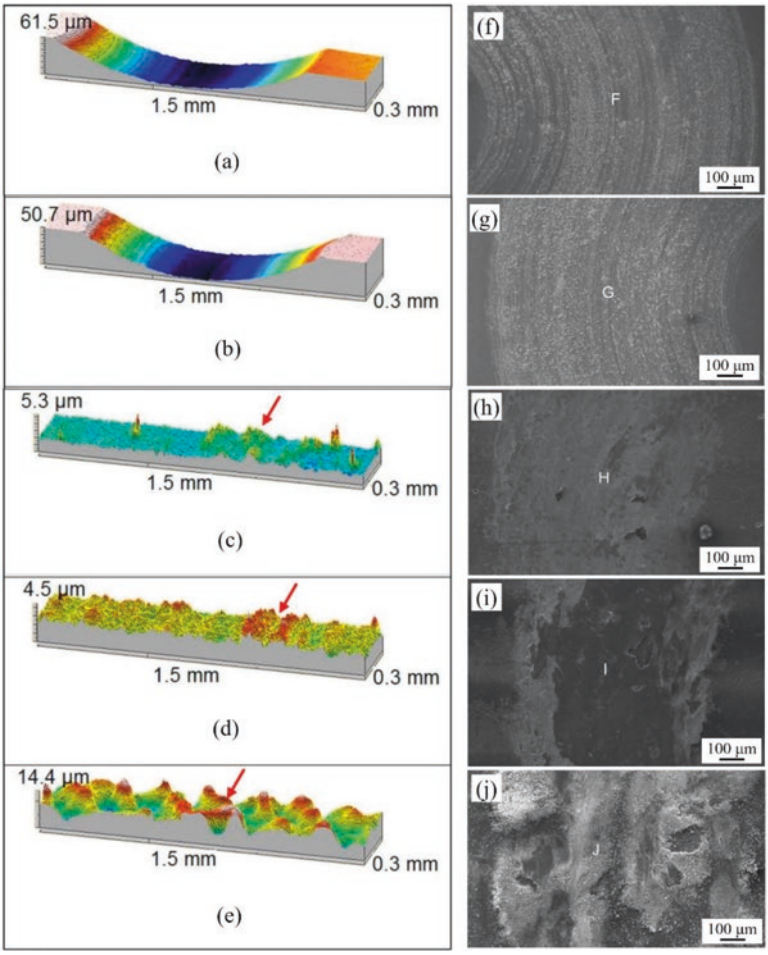

Fig. 14.28 Wear topographies and surface morphologies of (**a**, **f**) untreated Ti64 coating and laser-treated Ti64 coatings with laser powers of (**b**, **g**) 50 W, (**c**, **h**) 100 W, (**d**, **i**) 150 W, and (**e**, **j**) 200 W tested under the same conditions (Khun et al. 2019)

increase of wear loads, as shown in Fig. 14.29. This is because the increased shearing and compressive stress between the Al particles at a higher load can increase the falling probability of Al particles. The fell particles act as abrasive particles to wear the Al coating, which in turn reduces the wear resistance. After LR, the wear tracks become smoother, which is due to the dense and high hardness after LR and the finer and smoother abrasive particles. However, the wear rates of the laser-treated coatings only show a slight decrease in comparison with the untreated Al coating. As can be seen from the wear track morphology, the wear mechanism of cold-sprayed Al coating in 3.5% NaCl solution is dominated by corrosion wear under lower loads (0.5 N and 1.0 N) and abrasive wear + fatigue wear under

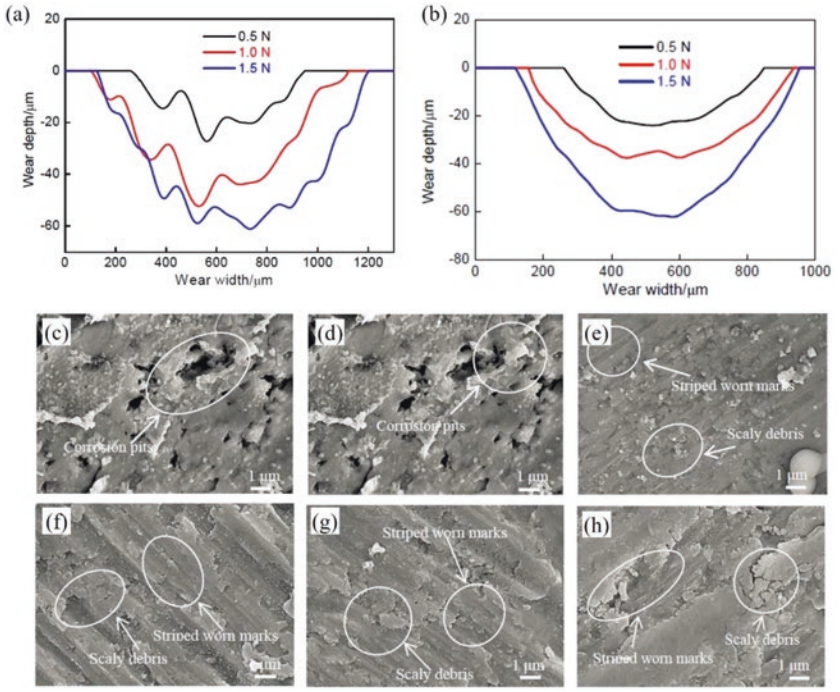

Fig. 14.29 Wear profiles of the cold-sprayed Al coating (**a**) before and (**b**) after laser remelting. (**c–e**) Morphologies of worn track on cold-sprayed Al coatings (**c–e**) before and (**f–h**) after laser remelting. (**c**, **f**) Wear load of 0.5 N; (**d**, **g**) wear load of 1.0 N; (**e**, **h**) wear load of 1.5 N (Jing and Dejun 2018)

1.5 N. Comparatively, the wear mechanical of the Al coatings after LR is dominated by abrasive wear + fatigue wear, without corrosion wear. Therefore, LR reduces the porosity of Al coating and improves its corrosion wear resistance.

14.4.5 Improvement of Corrosion Property

Figure 14.30a shows potentiodynamic polarization curves of bulk Ti, carbon steel, the as-sprayed Ti coating (on carbon steel), and the laser-treated Ti coating (on carbon steel). It can be seen that the current density of the cold-sprayed Ti coating is two orders of magnitude greater than that of bulk Ti. However, the laser-treated Ti coating has a current density virtually the same as the bulk Ti. Such significant improved corrosion property of the laser-treated Ti coating can be attributed to the reduced interconnected porosities and removed particle boundaries by LR. Since the carbon steel substrate is less noble, corrodes and corrosion pits form at the coating/substrate interface due to the interconnected pores that provide channels for corrosive solution to enter into the interior coating, forming a galvanic corrosion at

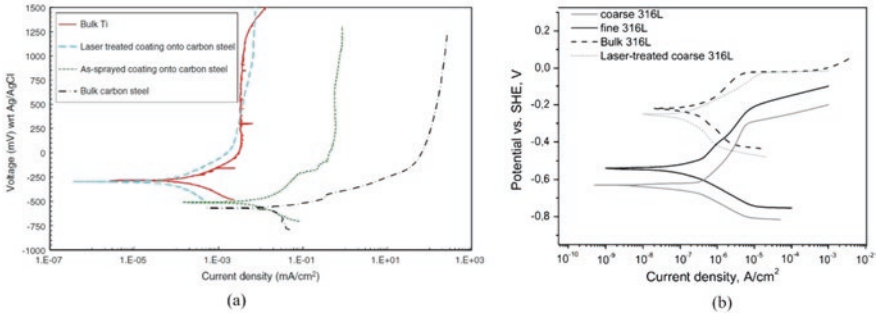

Fig. 14.30 Polarization curves obtained as-sprayed coatings, laser-treated coatings, and bulk materials: (**a**) Ti (Assadi et al. 2016), (**b**) 316 L (Sova et al. 2013)

the interface. However, the laser-treated coating/substrate interface is free from any defect or pitting. The fully dense solidification structure prevents corrosive species from penetrating the coating.

The corrosion properties of as-sprayed and laser-treated 316 L coatings were investigated by Sova et al. (2013), and they were compared to the bulk 316 L. As shown in Fig. 14.30b, the cold-sprayed 316 L coatings have lowest open circuit potential (high corrosion tendency) due to a large exposed area fraction of metal/metal interfaces with incomplete bonding and active sites resulting from severe plastic deformation. Application of surface laser posttreatment shifts the polarization curves of the coatings toward the bulk material. LR improves these interconnected pores and eliminates inter-splat boundaries, leading to a significant improvement in corrosion resistance of the cold-sprayed coatings. Similar corrosion performance on laser-remelted 316 L coating was also reported by Adachi et al. (2015). In addition, a low-temperature plasma nitriding was applied to the laser-treated cold-sprayed 316 L coating for further improving its corrosion and wear properties.

14.5 Conclusions

In summary, laser has been widely applied in cold spray process to assist the deposition of metal particles and to improve the properties of cold-sprayed coatings. Pre-laser treatment has been found to improve the adhesion strength between the coating and substrate to some extent. The in situ LACS is effective to facilitate the deposition of hard materials that are difficult to be deposited using conventional cold spray. However, in order to prevent the disadvantages caused by high temperature, the deposition temperature has to be well controlled through adjusting laser power. As the most commonly used post-laser treatment, laser remelting can homogenize the microstructure, remove the inter-splat boundaries, and reduce interconnected

porosity within the cold-sprayed coating, which promotes an increased oxidation and improved wear and corrosion properties.

References

Adachi, S., & Ueda, N. (2015). Formation of expanded austenite on a cold-sprayed AISI 316L coating by low-temperature plasma nitriding. *Journal of Thermal Spray Technology, 24*, 1399–1407. https://doi.org/10.1007/s11666-015-0278-3.

Alkhimov, A. P., Kosarev, V. F., Nesterovich, N. I., Papyrin, A. N. (1980) Method of applying coatings (SU 1618778).

Alkhimov, A. P., Kosareve, V. F., & Papyrin, A. N. (1990). A method of cold gas-dynamic spray deposition. *Doklady Akademii Nauk SSSR, 315*, 1062–1065.

Assadi, H., Gärtner, F., Stoltenhoff, T., & Kreye, H. (2003). Bonding mechanism in cold gas spraying. *Acta Materialia, 51*, 4379–4394. https://doi.org/10.1016/S1359-6454(03)00274-X.

Assadi, H., Schmidt, T., Richter, H., Kliemann, J. O., Binder, K., Gärtner, F., Klassen, T., & Kreye, H. (2011). On parameter selection in cold spraying. *Journal of Thermal Spray Technology, 20*, 1161–1176. https://doi.org/10.1007/s11666-011-9662-9.

Assadi, H., Kreye, H., Gärtner, F., & Klassen, T. (2016). Cold spraying – A materials perspective. *Acta Materialia, 116*, 382–407. https://doi.org/10.1016/j.actamat.2016.06.034.

Astarita, A., Genna, S., Leone, C., Minutolo, F. M. C., Rubino, F., & Squillace, A. (2015). Study of the laser remelting of a cold sprayed titanium layer. *Procedia CIRP, 33*, 452–457. https://doi.org/10.1016/j.procir.2015.06.101.

Bae, G., Xiong, Y., Kumar, S., Kang, K., & Lee, C. (2008). General aspects of interface bonding in kinetic sprayed coatings. *Acta Materialia, 56*, 4858–4868. https://doi.org/10.1016/j.actamat.2008.06.003.

Bae, G., Kumar, S., Yoon, S., Kang, K., Na, H., Kim, H. J., & Lee, C. (2009). Bonding features and associated mechanisms in kinetic sprayed titanium coatings. *Acta Materialia, 57*, 5654–5666. https://doi.org/10.1016/j.actamat.2009.07.061.

Bae, G., Il Jang, J., & Lee, C. (2012). Correlation of particle impact conditions with bonding, nanocrystal formation and mechanical properties in kinetic sprayed nickel. *Acta Materialia, 60*, 3524–3535. https://doi.org/10.1016/j.actamat.2012.03.001.

Birt, A. M., Champagne, V. K., Sisson, R. D., & Apelian, D. (2017). Statistically guided development of laser-assisted cold spray for microstructural control of Ti-6Al-4V. *Metallurgical and Materials Transactions A, Physical Metallurgy and Materials Science, 48*, 1931–1943. https://doi.org/10.1007/s11661-017-3970-8.

Bray, M., Cockburn, A., & O'Neill, W. (2009). The laser-assisted cold spray process and deposit characterisation. *Surface and Coatings Technology, 203*, 2851–2857. https://doi.org/10.1016/j.surfcoat.2009.02.135.

Carlone, P., Astarita, A., Rubino, F., Pasquino, N., & Aprea, P. (2016). Selective laser treatment on cold-sprayed titanium coatings: Numerical modeling and experimental analysis. *Metallurgical and Materials Transactions B: Process Metallurgy and Materials Processing Science, 47*, 3310–3317. https://doi.org/10.1007/s11663-016-0636-7.

Chen, C., Xie, Y., Yin, S., Planche, M. P., Deng, S., Lupoi, R., & Liao, H. (2016). Evaluation of the interfacial bonding between particles and substrate in angular cold spray. *Materials Letters, 173*, 76–79. https://doi.org/10.1016/j.matlet.2016.03.036.

Christoulis, D. K., Guetta, S., Irissou, E., Guipont, V., Berger, M. H., Jeandin, M., Legoux, J. G., Moreau, C., Costil, S., Boustie, M., Ichikawa, Y., & Ogawa, K. (2010). Cold-spraying coupled to nano-pulsed Nd-YaG laser surface pre-treatment. *Journal of Thermal Spray Technology, 19*, 1062–1073. https://doi.org/10.1007/s11666-010-9500-5.

Cinca, N., López, E., Dosta, S., & Guilemany, J. M. (2013). Study of stellite-6 deposition by cold gas spraying. *Surface and Coatings Technology, 232*, 891–898. https://doi.org/10.1016/j.surfcoat.2013.06.120.

Danlos, Y., Costil, S., Guo, X., Liao, H., & Coddet, C. (2010). Ablation laser and heating laser combined to cold spraying. *Surface and Coatings Technology, 205*, 1055–1059. https://doi.org/10.1016/j.surfcoat.2010.06.018.

Dinda, G. P., Dasgupta, A. K., & Mazumder, J. (2009). Laser aided direct metal deposition of Inconel 625 superalloy: Microstructural evolution and thermal stability. *Materials Science and Engineering A, 509*, 98–104. https://doi.org/10.1016/j.msea.2009.01.009.

Gorunov, A. I., & Gilmutdinov, A. K. (2017). Investigation of coatings of austenitic steels produced by supersonic laser deposition. *Optics and Laser Technology, 88*, 157–165. https://doi.org/10.1016/j.optlastec.2016.09.012.

Grujicic, M., Zhao, C. L. C., DeRosset, W. S. W., & Helfritch, D. (2004). Adiabatic shear instability based mechanism for particles/substrate bonding in the cold-gas dynamic-spray process. *Materials and Design, 25*, 681–688. https://doi.org/10.1016/j.matdes.2004.03.008.

Hassani-Gangaraj, M., Veysset, D., Nelson, K. A., & Schuh, C. A. (2017). Melting can hinder impact-induced adhesion. *Physical Review Letters*, in press, *119*, 1–5. https://doi.org/10.1103/PhysRevLett.119.175701.

Hassani-Gangaraj, M., Veysset, D., Nelson, K. A., & Schuh, C. (2018). In-situ observations of single micro-particle impact bonding. *Scripta Materialia, 145*, 9–13. https://doi.org/10.1016/j.scriptamat.2017.09.042.

Hassani-Gangaraj, M., Veysset, D., Champagne, V. K., Nelson, K. A., & Schuh, C. A. (2019). Adiabatic shear instability is not necessary for adhesion in cold spray. *Acta Materialia, 158*, 430–439. https://doi.org/10.1016/j.actamat.2018.07.065.

Hemmati, I., Ocelík, V., & De Hosson, J. T. M. (2012). Dilution effects in laser cladding of Ni-Cr-B-Si-C hardfacing alloys. *Materials Letters, 84*, 69–72. https://doi.org/10.1016/j.matlet.2012.06.054.

Hussain, T., McCartney, D. G., Shipway, P. H., & Zhang, D. (2009). Bonding mechanisms in cold spraying: The contributions of metallurgical and mechanical components. *Journal of Thermal Spray Technology, 18*, 364–379. https://doi.org/10.1007/s11666-009-9298-1.

Ichikawa, Y., Tokoro, R., Tanno, M., & Ogawa, K. (2019). Elucidation of cold-spray deposition mechanism by auger electron spectroscopic evaluation of bonding interface oxide film. *Acta Materialia, 164*, 39–49. https://doi.org/10.1016/j.actamat.2018.09.041.

Jenkins, R., Yin, S., Aldwell, B., Meyer, M., & Lupoi, R. (2019). New insights into the in-process densification mechanism of cold spray Al coatings: Low deposition efficiency induced densification. *Journal of Materials Science and Technology, 35*, 427–431. https://doi.org/10.1016/j.jmst.2018.09.045.

Jing, Z., & Dejun, K. (2018). Effect of laser remelting on friction-wear behaviors of cold sprayed Al coatings in 3.5% NaCl solution. *Materials (Basel), 11*. https://doi.org/10.3390/ma11020283.

Jones, M., Cockburn, A., Lupoi, R., Sparkes, M., & O'Neill, W. (2014). Solid-state manufacturing of tungsten deposits onto molybdenum substrates with supersonic laser deposition. *Materials Letters, 134*, 295–297. https://doi.org/10.1016/j.matlet.2014.07.091.

Kang, N., Verdy, C., Coddet, P., Xie, Y., Fu, Y., Liao, H., & Coddet, C. (2017). Effects of laser remelting process on the microstructure, roughness and microhardness of in-situ cold sprayed hypoeutectic Al-Si coating. *Surface and Coatings Technology, 318*, 355–359. https://doi.org/10.1016/j.surfcoat.2017.01.057.

Khun, N. W., Tan, A. W. Y., Sun, W., & Liu, E. (2019). Effects of Nd: YAG laser surface treatment on tribological properties of cold-sprayed Ti-6Al-4V coatings tested against 100Cr6 steel under dry condition. *Tribology Transactions, 62*, 391–402. https://doi.org/10.1080/10402004.2018.1563258.

Kim, K., Watanabe, M., Mitsuishi, K., Iakoubovskii, K., & Kuroda, S. (2009). Impact bonding and rebounding between kinetically sprayed titanium particle and steel substrate revealed by high-resolution electron microscopy. *Journal of Physics D: Applied Physics, 42*, 065304. https://doi.org/10.1088/0022-3727/42/6/065304.

King, P. C., Bae, G., Zahiri, S. H., Jahedi, M., & Lee, C. (2010). An experimental and finite element study of cold spray copper impact onto two aluminum substrates. *Journal of Thermal Spray Technology, 19*, 620–634. https://doi.org/10.1007/s11666-009-9454-7.

Klassen, T., Assadi, H., Kreye, H., & Gärtner, F. (2016). Cold spraying – A materials perspective. *Acta Materialia, 116*, 382–407. https://doi.org/10.1016/j.actamat.2016.06.034.

Ko, K. H. H., Choi, J. O. O., Lee, H., Seo, Y. K. K., Jung, S. P. P., & Yu, S. S. S. (2015). Cold spray induced amorphization at the interface between Fe coatings and Al substrate. *Materials Letters, 149*, 40–42. https://doi.org/10.1016/j.matlet.2015.02.118.

Kromer, R., Costil, S., Verdy, C., Gojon, S., & Liao, H. (2018a). Laser surface texturing to enhance adhesion bond strength of spray coatings – Cold spraying, wire-arc spraying, and atmospheric plasma spraying. *Surface and Coatings Technology, 352*, 642–653. https://doi.org/10.1016/j.surfcoat.2017.05.007.

Kromer, R., Danlos, Y., & Costil, S. (2018b). Cold gas-sprayed deposition of metallic coatings onto ceramic substrates using laser surface texturing pre-treatment. *Journal of Thermal Spray Technology, 27*, 809–817. https://doi.org/10.1007/s11666-018-0718-y.

Kumar, S., Ramakrishna, M., Chavan, N. M., & Joshi, S. V. (2017). Correlation of splat state with deposition characteristics of cold sprayed niobium coatings. *Acta Materialia, 130*, 177–195. https://doi.org/10.1016/j.actamat.2017.03.023.

Lee, C., & Kim, J. (2015). Microstructure of kinetic spray coatings: A review. *Journal of Thermal Spray Technology, 24*, 592–610. https://doi.org/10.1007/s11666-015-0223-5.

Li, W. Y., Li, C. J., & Yang, G. J. (2010). Effect of impact-induced melting on interface microstructure and bonding of cold-sprayed zinc coating. *Applied Surface Science, 257*, 1516–1523. https://doi.org/10.1016/j.apsusc.2010.08.089.

Li, B., Yao, J., Zhang, Q., Li, Z., & Yang, L. (2015a). Microstructure and tribological performance of tungsten carbide reinforced stainless steel composite coatings by supersonic laser deposition. *Surface and Coatings Technology, 275*, 58–68. https://doi.org/10.1016/j.surfcoat.2015.05.040.

Li, S., Wei, Q., Shi, Y., Chua, C. K., Zhu, Z., & Zhang, D. (2015b). Microstructure characteristics of Inconel 625 superalloy manufactured by selective laser melting. *Journal of Materials Science and Technology, 31*, 946–952. https://doi.org/10.1016/j.jmst.2014.09.020.

Li, B., Jin, Y., Yao, J., Li, Z., & Zhang, Q. (2017). Solid-state fabrication of WCp-reinforced Stellite-6 composite coatings with supersonic laser deposition. *Surface and Coatings Technology, 321*, 386–396. https://doi.org/10.1016/j.surfcoat.2017.04.062.

Li, W., Yang, K., Yin, S., Yang, X., Xu, Y., & Lupoi, R. (2018a). Solid-state additive manufacturing and repairing by cold spraying: A review. *Journal of Materials Science and Technology, 34*, 440–457. https://doi.org/10.1016/j.jmst.2017.09.015.

Li, B., Jin, Y., Yao, J., Li, Z., Zhang, Q., & Zhang, X. (2018b). Influence of laser irradiation on deposition characteristics of cold sprayed Stellite-6 coatings. *Optics and Laser Technology, 100*, 27–39. https://doi.org/10.1016/j.optlastec.2017.09.034.

Li, W., Cao, C., & Yin, S. (2020). Solid-state cold spraying of Ti and its alloys: A literature review. *Progress in Materials Science, 110*, 100633. https://doi.org/10.1016/j.pmatsci.2019.100633.

Luo, F., Cockburn, A., Lupoi, R., Sparkes, M., & O'Neill, W. (2012). Performance comparison of Stellite 6® deposited on steel using supersonic laser deposition and laser cladding. *Surface and Coatings Technology, 212*, 119–127. https://doi.org/10.1016/j.surfcoat.2012.09.031.

Luo, F., Lupoi, R., Cockburn, A., Sparkes, M., O'neill, W., & Yao, J. H. (2013). Characteristics of Stellite 6 deposited by supersonic laser deposition under optimized parameters. *Journal of Iron and Steel Research, International, 20*, 52–57. https://doi.org/10.1016/S1006-706X(13)60056-4.

Luo, X.-T., Li, C.-X., Shang, F.-L., Yang, G.-J., Wang, Y.-Y., & Li, C.-J. (2014a). High velocity impact induced microstructure evolution during deposition of cold spray coatings: A review. *Surface and Coatings Technology, 254*, 11–20. https://doi.org/10.1016/j.surfcoat.2014.06.006.

Luo, F., Cockburn, A., Cai, D., Sparks, M., Lu, Y., Ding, C., Langford, R., O'Neill, W., Yao, J., & Liu, R. (2014b). Simulation analysis of Stellite 6® particle impact on steel substrate in supersonic laser deposition process. *Journal of Thermal Spray Technology, 24*, 378–393. https://doi.org/10.1007/s11666-014-0176-0.

Luo, F., Cockburn, A., Sparkes, M., Lupoi, R., Chen, Z. J., O'Neill, W., Yao, J. H., & Liu, R. (2015). Performance characterization of Ni60-WC coating on steel processed with supersonic laser deposition. *Defence Technology, 11*, 35–47. https://doi.org/10.1016/j.dt.2014.09.003.

Lupoi, R., Sparkes, M., Cockburn, A., & O'Neill, W. (2011). High speed titanium coatings by supersonic laser deposition. *Materials Letters, 65*, 3205–3207. https://doi.org/10.1016/j.matlet.2011.07.014.

Lupoi, R., Cockburn A., Bryan C., Sparkes, M., Luo F., & O'Neill, W. (2012). Hardfacing steel with nanostructured coatings of Stellite-6 by supersonic laser deposition. Light: Science & Applications, 1, 1-6. https://doi.org/10.1038/lsa.2012.10.

Magarò, P., Marino, A. L., Di Schino, A., Furgiuele, F., Maletta, C., Pileggi, R., Sgambitterra, E., Testani, C., & Tului, M. (2019). Effect of process parameters on the properties of Stellite-6 coatings deposited by cold gas dynamic spray. *Surface and Coatings Technology, 377*, 124934. https://doi.org/10.1016/j.surfcoat.2019.124934.

Marrocco, T., Hussain, T., McCartney, D. G., & Shipway, P. H. (2011). Corrosion performance of laser posttreated cold sprayed titanium coatings. *Journal of Thermal Spray Technology, 20*, 909–917. https://doi.org/10.1007/s11666-011-9637-x.

Meng, F., Yue, S., & Song, J. (2015). Quantitative prediction of critical velocity and deposition efficiency in cold-spray: A finite-element study. *Scripta Materialia, 107*, 83–87. https://doi.org/10.1016/j.scriptamat.2015.05.026.

Orishich, A., Malikov, A., Fomin, V., Golyshev, A., Kosarev, V., Ryashin, N., & Filippov, A. (2018). Creation of heterogeneous metal-ceramic structures based on Ti, Ni and WC, B4C by the combined method of laser cladding and cold gas-dynamic spraying. *Procedia CIRP, 74*, 268–271. https://doi.org/10.1016/j.procir.2018.08.108.

Perton, M., Costil, S., Wong, W., Poirier, D., Irissou, E., Legoux, J. G., Blouin, A., & Yue, S. (2012). Effect of pulsed laser ablation and continuous laser heating on the adhesion and cohesion of cold sprayed Ti-6Al-4V coatings. *Journal of Thermal Spray Technology, 21*, 1322–1333. https://doi.org/10.1007/s11666-012-9812-8.

Podrabinnik, P. A., & Shishkovsky, I. V. (2017). Laser post annealing of cold-sprayed Al-Ni composite coatings for green energy tasks. *Procedia IUTAM, 23*, 108–113. https://doi.org/10.1016/j.piutam.2017.06.010.

Podrabinnik, P., Grigoriev, S., & Shishkovsky, I. (2015). Laser post annealing of cold-sprayed Al/alumina-Ni composite coatings. *Surface and Coatings Technology, 271*, 265–268. https://doi.org/10.1016/j.surfcoat.2014.11.042.

Poza, P., Múnez, C. J., Garrido-Maneiro, M. A., Vezzù, S., Rech, S., & Trentin, A. (2014). Mechanical properties of Inconel 625 cold-sprayed coatings after laser remelting. Depth sensing indentation analysis. *Surface and Coatings Technology, 243*, 51–57. https://doi.org/10.1016/j.surfcoat.2012.03.018.

Raletz, F. F., Vardelle, M., & Ezo'o, G. (2006). Critical particle velocity under cold spray conditions. *Surface and Coatings Technology, 201*, 1942–1947. https://doi.org/10.1016/j.surfcoat.2006.04.061.

Raoelison, R. N., Xie, Y., Sapanathan, T., Planche, M. P., Kromer, R., Costil, S., & Langlade, C. (2018). Cold gas dynamic spray technology: A comprehensive review of processing conditions for various technological developments till to date. *Additive Manufacturing, 19*, 134–159. https://doi.org/10.1016/j.addma.2017.07.001.

Rokni, M. R., Nutt, S. R., Widener, C. A., Champagne, V. K., & Hrabe, R. H. (2017). Review of relationship between particle deformation, coating microstructure, and properties in high-pressure cold spray. *Journal of Thermal Spray Technology*, 1–48. https://doi.org/10.1007/s11666-017-0575-0.

Rubino, F., Astarita, A., Carlone, P., Genna, S., Leone, C., Minutolo, F. M. C., & Squillace, A. (2016). Selective laser post-treatment on titanium cold spray coatings. *Materials and Manufacturing Processes, 31*, 1500–1506. https://doi.org/10.1080/10426914.2015.1037912.

Schmidt, T., Gärtner, F., Assadi, H., & Kreye, H. (2006). Development of a generalized parameter window for cold spray deposition. *Acta Materialia, 54*, 729–742. https://doi.org/10.1016/j.actamat.2005.10.005.

Sova, A., Grigoriev, S., Okunkova, A., & Smurov, I. (2013). Cold spray deposition of 316L stainless steel coatings on aluminium surface with following laser post-treatment. *Surface and Coatings Technology, 235*, 283–289. https://doi.org/10.1016/j.surfcoat.2013.07.052.

Story, W. A., Barton, D. J., Hornbuckle, B. C., Darling, K. A., Thompson, G. B., & Brewer, L. N. (2018). Laser assisted cold spray of Fe–Ni–Zr oxide dispersion strengthened steel. *Materialia, 3*, 239–242. https://doi.org/10.1016/j.mtla.2018.08.028.

Sudharshan Phani, P., Srinivasa Rao, D., Joshi, S. V., & Sundararajan, G. (2007). Effect of process parameters and heat treatments on properties of cold sprayed copper coatings. *Journal of Thermal Spray Technology, 16*, 425–434. https://doi.org/10.1007/s11666-007-9048-1.

Sun, W., Tan, A. W. Y., Wu, K., Yin, S., Yang, X., Marinescu, I., & Liu, E. (2020). Post-process treatments on supersonic cold sprayed coatings: A review. *Coatings, 10*. https://doi.org/10.3390/coatings10020123.

Wang, Q., Birbilis, N., & Zhang, M. X. (2011). Interfacial structure between particles in an aluminum deposit produced by cold spray. *Materials Letters, 65*, 1576–1578. https://doi.org/10.1016/j.matlet.2011.03.035.

Wang, Q., Qiu, D., Xiong, Y., Birbilis, N., & Zhang, M. X. (2014). High resolution microstructure characterization of the interface between cold sprayed Al coating and Mg alloy substrate. *Applied Surface Science, 289*, 366–369. https://doi.org/10.1016/j.apsusc.2013.10.168.

Xiong, Y., Kang, K., Bae, G., Yoon, S., & Lee, C. (2008). Dynamic amorphization and recrystallization of metals in kinetic spray process. *Applied Physics Letters, 92*, 144–147. https://doi.org/10.1063/1.2928218.

Xue, L., Islam, M., Koul, A. K., Bibby, M., & Wallace, W. (1997). Laser gas nitriding of Ti-6Al-4V. Part 2: Characteristics of nitrided layers. *Advanced Performance Materials, 4*, 389–408. https://doi.org/10.1023/A:1008696511669.

Xue, Y., Wang, C., Wang, W., Liu, Y., Wu, Y., Ning, Y., & Sun, Y. (2013). Spectral properties and thermal stability of solar selective absorbing AlNi-Al_2O_3 cermet coating. *Solar Energy, 96*, 113–118. https://doi.org/10.1016/j.solener.2013.07.012.

Yang, L., Li, B., Yao, J., & Li, Z. (2015). Effects of diamond size on the deposition characteristic and tribological behavior of diamond/Ni60 composite coating prepared by supersonic laser deposition. *Diamond and Related Materials, 58*, 139–148. https://doi.org/10.1016/j.diamond.2015.06.014.

Yao, J., Yang, L., Li, B., & Li, Z. (2015a). Characteristics and performance of hard Ni60 alloy coating produced with supersonic laser deposition technique. *Materials and Design, 83*, 26–35. https://doi.org/10.1016/j.matdes.2015.05.087.

Yao, J., Yang, L., Li, B., & Li, Z. (2015b). Beneficial effects of laser irradiation on the deposition process of diamond/Ni60 composite coating with cold spray. *Applied Surface Science, 330*, 300–308. https://doi.org/10.1016/j.apsusc.2015.01.029.

Yao, J., Li, Z., Li, B., & Yang, L. (2016). Characteristics and bonding behavior of Stellite 6 alloy coating processed with supersonic laser deposition. *Journal of Alloys and Compounds, 661*, 526–534. https://doi.org/10.1016/j.jallcom.2015.11.077.

Yilbas, B. S., Akhtar, S. S., Matthews, A., Karatas, C., & Leyland, A. (2011). Microstructure and thermal stress distributions in laser carbonitriding treatment of Ti-6Al-4V alloy. *Journal of Manufacturing Science and Engineering Transactions ASME, 133*, 1–9. https://doi.org/10.1115/1.4003523.

Yin, S., Wang, X., Suo, X., Liao, H., Guo, Z., Li, W., & Coddet, C. (2013). Deposition behavior of thermally softened copper particles in cold spraying. *Acta Materialia, 61*, 5105–5118. https://doi.org/10.1016/j.actamat.2013.04.041.

Yin, S., Xie, Y., Suo, X., Liao, H., & Wang, X. (2015). Interfacial bonding features of Ni coating on Al substrate with different surface pretreatments in cold spray. *Materials Letters, 138*, 143–147. https://doi.org/10.1016/j.matlet.2014.10.016.

Zhang, X., Ge, C., Li, Y., Guo, S., & Liu W. (2012). Experimental study of tungsten and tungsten alloy coating produced by cold gas dynamic spray and tungsten particles calculation and simulation. Acta Physica Sinica, 61, 020207. https://doi.org/10.7498/aps.61.020207.

Zhang, Y. Y., & Zhang, J. S. (2011). Recrystallization in the particles interfacial region of the cold-sprayed aluminum coating: Strain-induced boundary migration. *Materials Letters, 65*, 1856–1858. https://doi.org/10.1016/j.matlet.2011.04.014.

Index

P. Cavaliere (ed.), *Laser Cladding of Metals*,
https://doi.org/10.1007/978-3-030-53195-9